Titre: Title:	Hydrodynamics of a Gas-Solid Fluidized Bed at High Temperature in the Presence of Interparticles Forces
Auteur: Author:	Jaber Shabanian
Date:	2015
Type:	Mémoire ou thèse / Dissertation or Thesis
Référence: Citation:	Shabanian, J. (2015). Hydrodynamics of a Gas-Solid Fluidized Bed at High Temperature in the Presence of Interparticles Forces [Thèse de doctorat, École Polytechnique de Montréal]. PolyPublie. https://publications.polymtl.ca/1895/

UNIVERSITÉ DE MONTRÉAL

HYDRODYNAMICS OF A GAS-SOLID FLUIDIZED BED AT HIGH TEMPERATURE IN THE PRESENCE OF INTERPARTICLE FORCES

JABER SHABANIAN

DÉPARTEMENT DE GÉNIE CHIMIQUE

ÉCOLE POLYTECHNIQUE DE MONTRÉAL

THÈSE PRÉSENTÉE EN VUE DE L'OBTENTION

DU DIPLÔME DE PHILOSOPHIAE DOCTOR

(GÉNIE CHIMIQUE)

AOÛT 2015

UNIVERSITÉ DE MONTRÉAL

ÉCOLE POLYTECHNIQUE DE MONTRÉAL

Cette thèse intitulée:

HYDRODYNAMICS OF A GAS-SOLID FLUIDIZED BED AT HIGH TEMPERATURE IN THE PRESENCE OF INTERPARTICLE FORCES

présentée par : SHABANIAN Jaber

en vue de l'obtention du diplôme de : Philosophiae Doctor

a été dûment acceptée par le jury d'examen constitué de :

M. PERRIER Michel, Ph. D., président

M. CHAOUKI Jamal, Ph. D., membre et directeur de recherche

M. PATIENCE Gregory S., Ph. D., membre

M. PFEFFER Robert, Ph. D., membre

DEDICATION

To my beloved parents & ever-kind and supporting wife

ACKNOWLEDGEMENTS

This is the opportune moment to acknowledge all who in one way or another contributed to the completion of this thesis. First and foremost, I wish to express my deep and sincere gratitude to my supervisor Prof. Jamal Chaouki for his solid support, motivation, caring and patience, as well as providing me with an excellent atmosphere for conducting my research. His vast knowledge and logical way of thinking helped me throughout this process. It was a pleasure to work with him; the lessons he taught me go beyond what is written in this thesis and will help me in all aspects of my life.

I would like to acknowledge the members of my committee, Prof. Robert Pfeffer, Prof. Michele Perrier, Prof. Gregory S. Patience for taking interest in my work, examining my thesis and providing insightful comments.

I also wish to gratefully acknowledge the financial support of TOTAL American Services, Inc. and the Natural Sciences and Engineering Research Council of Canada (NSERC), which made this research work possible.

I deeply thank unforgettable kindness of Majid Rasouli for his caring attitude for the training of the RPT technique and the preparation of this dissertation.

Special thanks goes to my best scientific colleague, Pierre Sauriol. His kind, knowledgeable, and precious attitude made the collaboration highly beneficial for me. I was very glad to see his cute Rebecca during our collaboration. His precious comments and efforts for the improvement of the quality of the articles and assistance in conducting many high temperature tests and translating the abstract of this thesis into French is priceless.

I am so thankful to Amin Esmaeili whose friendly attitude and effective collaboration in making the optical fiber probes was really valuable. I am also deeply grateful to Farzam Fotovat for his assistance in conducting the RPT experiments as well as many valuable discussion on the field of fluidization. I would like to extend my thanks to Abdelmajid Rakin and Diego Alejandro López Del Ángel for their kind assistance during the high temperature experimental campaign.

I deeply thank my old and best friends: Majid Talebi, Khalil Shahverdi, Hesamoddin Tabatabaei, and Amirhossein Maani. Their constant support in any conditions helped me to solely look ahead. I will never forget the wonderful moments that we have had together.

I am very grateful to all my colleagues in our research group and my fellow labmates for their cooperative manner and friendly support. I would like to offer my special thanks to Milad Aghabararnejad, Mohammad Latifi, Ebrahim Alizadeh, and Hamed Bashiri for helpful discussions.

My deepest appreciation goes to the technicians in the Department of Chemical Engineering, particularly Robert Delisle, Yazid Belkhir, Tristan Ruthers, Sylvain Simard-Fleury, Guillaume Lessard, and Gino Robin for their excellent technical assistance. In addition, I wish to thank the secretaries of the Department of Chemical Engineering for helping us and providing us with an ideal atmosphere in which to advance our projects.

I genuinely express my profound gratefulness to my beloved wife, Laleh Dashtban, as I owe my success to her love, patience, heartfelt sympathy, and support.

And last but not least, from the bottom of my heart, I would like to express my endless gratitude to my mother, father, lovely brother, and in laws for the absolute support they have provided me throughout my entire life, and without whose love, spiritual encouragement and altruism I would not have finished this thesis. Words are powerless to express what I feel in my heart for them.

RÉSUMÉ

Les lits fluidisés gaz-solide sont utilisés dans un large éventail d'applications industrielles en particulier dans le cas de réactions exothermiques telles le craquage et la régénération catalytique dans le raffinage du pétrole (procédé FCC), les synthèses par oxydation partielle, la chlorination d'oxydes métalliques, la polymérisation en phase gazeuse, la combustion et la gazéification du charbon, de déchets et de biomasse. La manutention facile des solides combinée à un bon mélange de solide au sein du lit fluidisé procure aux lits fluidisés une température uniforme et une capacité intéressante de transfert de chaleur en comparaison aux autres types de réacteurs. De plus, un taux de transfert de matière élevé et une faible perte de charge contribuent à la popularité des lits fluidisés dans l'industrie. À l'échelle industrielle, les lits fluidisés sont généralement opérés à des températures élevées pour lesquelles les propriétés de transfert, des paramètres importants dans le comportement hydrodynamique, diffèrent de celles aux conditions ambiantes. Cependant, les connaissances actuelles en ce qui a trait à l'hydrodynamique des lits fluidisés opérés a température élevée sont loin d'être satisfaisantes, i.e. données insuffisantes, résultats parfois conflictuels et controversés. La source principale de cette controverse réside dans la difficulté à déterminer l'importance relative des forces interparticulaires (FIPs) et des forces hydrodynamiques (FHDs). Une attention particulière à l'évolution des FIPs est importante en raison de la tendance globale à utiliser des matières premières de qualité inférieure (e.g. charbon à haute teneur en cendres; déchets; cultures énergétiques), reconnue comme menant à la formation d'eutectiques à faible point de fusion. La présence de tels eutectiques au sein du lit fluidisé augmente les FIPs attractives ce qui peut détériorer la qualité de la fluidisation en raison de l'agglomération des particules; dans les cas extrêmes peut mener à la défluidisation du lit. Le présent travail porte sur la caractérisation hydrodynamique des lits fluidisés gaz-solides à haute température en présence de FIPs.

En raison du manque d'instruments de mesure convenables à température élevée, nous avons divisé l'étude en deux parties. La première partie visait l'investigation du comportement hydrodynamique local et global d'un lit fluidisé gaz-solide à température quasi ambiantes sujet à différentes intensités de FIPs au moyen de techniques de mesures variées. Dans la seconde partie de l'étude, le comportement hydrodynamique du lit a été observé à des températures élevées au moyen de techniques de mesures robustes (pression et température) alors que des sources de FIPs de différentes intensités étaient délibérément introduites dans le lit constitué de particules grossières.

Au cours de la première partie du travail, les FIPs attractives ont été augmentées en ajustées dans une lit fluidisé gaz-solide au moyen de l'approche par enrobage de polymère. Cette approche consiste à enrober des particules inertes sphériques au moyen d'un polymère ayant une température de transition vitreuse faible. L'intensité des FIPs résultantes varie en fonction de la température d'opération du lit fluidisé. Ainsi le lit fluidisé a été opéré à des températures avoisinant la température de transition vitreuse soit entre 20 et 40°C. Cette plage de température modeste a permis l'emploi d'une plus grande variété de techniques de mesure fiables (e.g. capteur de pression, sonde a fibre optique, poursuite d'une particule radioactive) afin de caractériser le comportement hydrodynamique en fonction des FIPs. La fluidisation des particules a été effectuée à des vite4sses superficielles allant du lit fixe au régime turbulent. Des billes de sucre, appartenant à température ambiante et sans enrobage au groupe B selon la classification de Geldart ont été choisi comme particule de référence avec les forces FIPs minimales. Dans le cas des particules enrobées, une couche uniforme d'environ 5 μm de co-polymère PMMA/PEA (poly methyl methacrylate/poly ethyl acrylate).

Les mesures de paramètres hydrodynamiques globaux : perte de charge totale, hauteur du lit fluidisé et différents signaux de pression ont montré que l'augmentation de l'intensité des FIPs pouvait altérer le comportement depuis le comportement de particules de type groupe B selon Geldart à des ^particules de groupe A ou même C. Avec l'augmentation des FIPs, on note une augmentation de la perméabilité en lit fixe, de la vitesse minimale de fluidisation (U_{mf}), de la transition au régime turbulent (U_c), et de la tendance du gaz de fluidisation à passer dans la phase d'émulsion. Inversement, la probabilité de passage de bulles dans le lit fluidisé diminue en fonction des FIPs. Un lit ayant des FIPs faibles à moyennes contient des bulles de plus petite taille lorsque fluidisé à de faible à moyenne vitesse de fluidisation dans le régime à bulle. Cependant en raison de l'augmentation du taux de croissance des bulles en fonction de la vitesse superficielle de fluidisation (U_g) à des intensités de FIPS moyennes à élevées, des bulles plus larges sont observées à des vitesse superficielles approchant et au-delà de $U_{c,No\ IPFs}$.

Une sonde à fibre optique a montré que la structure de l'hydrodynamique locale était affectée par l'intensité des FIPs. Les données recueillies au moyen de la poursuite d'une particule radioactive a servi dans certain cas à consolider les observations au moyen de la fibre optique. L'augmentation des FIPs, le lit fixe et la phase d'émulsion en régime à bulle ont montré une plus grande capacité

de rétention de gaz dans leur structure. Aussi, généralement en accord avec les mesures globales, les mesures locales montrent que le gaz de fluidisation est plus susceptible de passer dans les interstices d'un lit fluidisé cohésif lorsque dans le régime à bulle, i.e., $U_g<U_{c,No\ IPFs}$, en raison des augmentations de la porosité et la fraction de la phase d'émulsion avec l'augmentation des FIPs. La fréquence du cyclage bulle/émulsion diminue avec les FIPs, par contre la transition au régime turbulent. Étant donné que l'augmentation de FIPs augmente la taille des bulles à des vitesses superficielles près de $U_{c,No\ IPFs}$, la tendance du gaz à passer dans la phase dense pour un lit cohésif est plus faible que pour un lit sans FIPs à des $U_g>U_{c,No\ IPFs}$.

L'effet favorable des FIPs sur la répartition du gaz de fluidisation entre les phases bulle et émulsion pourrait s'avérée bénéfique sur la performance réacteur catalytique opérant dans le régime à bulle étant donné la plus grande contribution de la phase d'émulsion à accomplir la réaction catalysée par le solide. Un exercice de simulation visant à mettre en évidence cet effet a été entrepris en considérant la production d'anhydride maléique par oxydation partielle de n-butane dans un lit fluidisé dont le solide est un catalyseur à base de pyrophosphate de vanadium. Les paramètres hydrodynamiques mesurés pour des lits avec des FIPs ont été alimentés à un modèle hydrodynamique dans le modèle deux phases simple afin de simuler le réacteur sous différentes intensités de FIPs. Un modèle cinétique issue de la littérature a été utilisé. Les simulations ont confirmés l'avantage que peut représenter l'augmentation modérée des FIPs dans le cas des réactions catalysées par un solide.

La technique de poursuite d'une particule radioactive a été employée pour étudier l'influence des FIPs sur la qualité du mélange du solide dans le régime à bulle. Les résultats montrent que la période d'inactivité augmente en présence de FIPs tandis que la fréquence de cyclage et les diffusivités axiale et radiale du solide diminuent. Ces modifications des paramètres hydrodynamiques du lit fluidisé signifient que la qualité locale et globale de mélange du solide est réduite par l'augmentation des FIPs. Ainsi, l'augmentation volontaire et contrôlée des FIPs afin d'accroire la qualité du contact gaz-solide tel que dans le contexte d'une réaction catalytique doit être entreprise avec prudence afin de ne pas être pénalisé au niveau de la réduction de mélange des solides localement et globalement. En décrivant le processus d'agglomération comme une série de réaction à l'aide du temps d'inactivité déterminé expérimentalement aux diverses intensités de

FIPs, nous pouvons développer une explication fondamentale du phénomène d'agglomération montrant qu'il s'agit d'un phénomène qui a tendance à s'amplifier.

La seconde partie de l'étude visait l'analyse du comportement hydrodynamique des lits fluidisés à haute température en présence de FIPs dans un lit de particules grossières opérées dans le régime à bulles. L'augmentation des FIPs a été effectuée au moyen de la combustion de différents combustibles solides avec diverses teneurs en métaux alcalin et alcalino-terreux. Ce faisant le matériel du lit, du sable de silice, pouvait s'enrober d'une couche de composés eutectiques a faible point de fusion comparé au point de fusion du sable frais. Avec les FIPs à leur minimum (sable frais), l'augmentation de la température mène à la diminution de la taille des bulles tandis que la fréquence de passage des bulles ne varie pas significativement. L'augmentation des FIPs mène à une augmentation de la vitesse minimale de fluidisation et une multiplicité de comportements hydrodynamiques en fonction du niveau des FIPs. Les résultats obtenus dans cette partie de l'étude au moyen de techniques de mesures globales sont généralement en accord aux observations de la première partie. Ceci confirme que l'approche adoptée qui visait à entreprendre une campagne extensive à basse température sur des particules modèles peut servir à substituer certains essais à haute température pour lesquels les techniques de mesure ne sont pas adaptées afin de générer une compréhension plus approfondie du phénomène.

Avec les apports de la présente étude sur l'impact des FIPs sur l'hydrodynamique des lits fluidisés à bulles de particules grossières, une nouvelle approche pour l'anticipation de la défluidisation a été introduite. Selon cette nouvelle approche nécessite que la pression différentielle mesurée dans une section bien stabilisée du lit fluidisé diminue dans le temps en deçà d'un certain seuil et que la différence de température entre un thermocouple situé près du distributeur et les autres plus haut dans le lit dense augmente au-delà d'un seuil. Cette approche a montré qu'elle permettait d'anticiper la défluidisation du lit de quelques minutes à heures avant que la défluidisation ne se manifeste. Malgré sa simplicité, cette méthode s'est avérée robuste même face à des changements de type échelon de certains paramètres d'opération importants tels : la température du lit (±100ºC), U_g (±10%), la masse du lit (±20%). Les observations effectuées sur plusieurs incidents de défluidisation lors de la combustion du propane ou d'un autre combustible solide, la combinaison de deux valeurs seuils était requise pour la détection de la défluidisation résultant de l'agglomération des particules grossières de sable de silice (d_p=820 µm; d_p est la taille moyenne)

dans un lit fluidisé à bulles. Ces seuils agissent comme des alarmes de premier et deuxième niveaux. D'une façon similaire, la technique s'est aussi avérée utile pour l'anticipation de la défluidisation avec un lit de particules d'un sable de silice plus fin (d_p=370 μm).

ABSTRACT

Gas-solid fluidized beds are applied for a broad variety of applications in the chemical industry, such as fluidized catalytic cracking (FCC) including catalytic regeneration and other strongly exothermal processes, chlorination of metal oxides, gas-phase polymerization, and combustion or gasification of coal, waste, and biomass. Easy solids handling and good solids mixing, yielding a comparatively uniform temperature and an efficient heat exchange, high mass transfer, and low bed pressure drop are among the interesting features of these units that make them popular in industry. They are usually operated at high temperature. The hydrodynamics of gas-solid fluidized beds at thermal levels well above ambient directly affect the transfer phenomena and, thus, is a critical factor for their design and operation. Nevertheless, the present understanding of the fluidization characteristics of these systems at high temperature is far from satisfactory, i.e., findings are still controversial. The major source of this controversy is attributed to the lack of insight about the relative importance of interparticle forces (IPFs) and hydrodynamic forces (HDFs). Attention to the evolution of IPFs at elevated temperatures is important owing to the global trend to employ lower quality feedstock (e.g., high ash content coal, energy crops, and waste), known to introduce species that can result in the accumulation of low melting point eutectics. The presence of these low melting point eutectics at high temperature favor particle-particle agglomeration in the bed. In extreme cases, IPFs can fully deteriorate the fluidization state of the particles due to ongoing agglomeration, leading to complete defluidization. This research, therefore, focuses on the hydrodynamic characterization of gas-solids fluidized beds at high temperature in the presence of IPFs.

Due to a lack of proper measurement techniques at elevated temperatures, we approached this study by dividing it into two parts. The first part was aimed at exploring the fluidization behavior of a gas-solid fluidized bed at different levels of IPFs from global and local points of view. The second part focused on the hydrodynamic characterization of a gas-solid fluidized bed at high temperature while different levels of IPFs were deliberately introduced into a bed of otherwise fresh coarse particles.

The level of cohesive IPFs was increased and adjusted in a gas-solid fluidized bed with a polymer coating approach in the first part of the study. This technique is based on coating spherical inert particles with a polymer material having a low glass transition temperature in the primary step.

Since the level of IPFs achieved by this method depends on the temperature of the coated particles, they were subsequently adopted in a gas-solid fluidized bed operated at varying temperatures near the glass transition temperature of the polymer, i.e., between 20–40^{o}C. This allowed for the investigation of the effect of IPFs on the fluidization behavior of a gas-solid fluidized bed in a much friendlier environment than the conditions of a gas-solid fluidized bed at high temperature. Therefore, different reliable and accurate measurement techniques, i.e., pressure transducers, an optical fiber probe, and the radioactive particle tracking (RPT) technique, were employed for the purpose of a comprehensive hydrodynamic study. The fluidization study was attempted at different superficial gas velocities covering the fixed bed state, bubbling, and turbulent fluidization regimes. Sugar beads that belong to Geldart group B powders, referred to the fluidization behavior at ambient conditions, were adopted as the base system for which the level of IPFs was at minimum. The thickness of the uniform coating layer, i.e., PMMA/PEA (poly methyl methacrylate/poly ethyl acrylate) copolymer, was approximately 5 μm for the coated particles.

The measurements of global hydrodynamic parameters, including the total bed pressure drop profile, bed height, and different types of pressure signals, demonstrated that increasing the level of IPFs could shift the fluidization behavior of a given powder representing typical Geldart group B behavior into Geldart group A or even C behavior and increase the fixed bed permeability, the minimum fluidization velocity (U_{mf}), the transition velocity from bubbling to turbulent fluidization regime (U_c), and the propensity of the fluidizing gas to pass through a bubbling bed in the emulsion phase. Also, the passage frequency of bubbles within the bed decreased with IPFs. A bed with a low/moderate level of IPFs contained slightly smaller bubbles at low to moderate superficial gas velocities in the bubbling fluidization regime. However, due to an increased growth rate of bubble size with the superficial gas velocity (U_g) at a moderate/high level of IPFs, larger bubbles were present in the bed at gas velocities approaching and above $U_{c,No\ IPFs}$.

An optical fiber probe was exploited for the local hydrodynamic measurements to unveil the influence of IPFs on the modification of the two-phase flow structure of the bed. The data collected during the RPT tests were employed in some cases to consolidate the experimental findings achieved by the application of the optical fiber probe. Upon increasing the level of IPFs, the fixed bed and emulsion phase in the bubbling regime demonstrated a higher capacity in holding gas in their structures. Also, in broad agreement with the global measurements, the local measurements

showed that the fluidizing gas was more prone to interstitially pass through a more cohesive bed in the bubbling regime, i.e., $U_g<U_{c,No\ IPFs}$, since the emulsion phase voidage and fraction increased with IPFs. The frequency of the bubble/emulsion phase cycle decreased with IPFs. In contrast, increasing the level of IPFs led to an increase in the meso-scale transition from bubbling to turbulent fluidization regime. Since larger bubbles were presented in a bed with IPFs at superficial gas velocities close to $U_{c,No\ IPFs}$, the tendency of the gas to pass through the cohesive bed in the dense phase was lower than a bed with no IPFs at $U_g>U_{c,No\ IPFs}$.

The favorable effect of IPFs on the division of the fluidizing gas between the bubble and emulsion phases in the bubbling fluidization regime could enhance the overall performance of a catalytic bubbling gas-solid fluidized bed reactor since the efficiency of the emulsion phase in bringing about a chemical reaction between gas and solids is much higher than that of the bubble phase. Thus, a simulation study of an industrial-scale fluidized bed reactor for the production of maleic anhydride by the catalytic oxidation of n-butane over the fluidized vanadium phosphorus oxide catalyst was attempted to verify this hypothesis. The hydrodynamic parameters measured for beds at varying levels of IPFs were adopted in the two-phase flow model to describe the hydrodynamics of the simulated reactor at different levels of IPFs. A kinetic model, available in open literature, represented the reaction feature of the reactor. The simulation results confirmed the hypothesis.

The RPT technique was implemented to study the influence of IPFs on the quality of solids mixing in a bubbling gas-solid fluidized bed. The polymer coating approach was adopted to enhance and control the degree of IPFs. The analysis of the collected RPT data showed that the idle time increased in the presence of IPFs while the gross cycle frequency and the axial/radial solid diffusivities decreased. These modifications in the characteristic hydrodynamic parameters of the bed revealed that the quality of global and local solids mixing decreased in a bubbling bed with IPFs. Therefore, an increase in the level of IPFs to achieve an enhanced gas-solid contact in the bubbling regime should be cautiously applied for the purpose of improving the reaction performance of a catalytic bubbling gas-solid fluidized bed reactor. By resembling the agglomeration process to a reaction network and with the help of the calculated idle time for systems with different levels of IPFs, we could provide a fundamental understanding about why the agglomeration phenomenon, which is a major operational problem for cohesive gas-solid fluidized beds at elevated temperatures, is a self-promoting process.

The second part of the study targeted exploring the effect of temperature on the hydrodynamics of a bubbling gas-solid fluidized bed when varying degrees of IPFs were introduced into a bed of coarse particles. Increasing the level of IPFs was achieved through the combustion of different solids fuels containing varying amounts of alkali/alkali earth metals in a bubbling fluidized bed of otherwise fresh coarse particles. The bed materials could be coated with the low melting point eutectics by this technique. Upon increasing the operating temperature in a gas-solid fluidized bed of fresh coarse particles under conditions where the level of IPFs was at minimum, the bubble size decreased while the bubble passage frequency was relatively insensitive to the change. Increasing the level of IPFs led to an increase in the minimum fluidization velocity and a multiplicity of fluidization behaviors in the bubbling regime depending on the magnitude of IPFs. The results achieved in this part of the study through the global hydrodynamic measurements were in broad accordance with those obtained in the first part of this work. It proved that a suitable strategy was adopted throughout this research to provide a comprehensive understanding on the subject.

With the help of the insight gained in this study about the influence of IPFs on the hydrodynamic characteristics of a bubbling fluidized bed of coarse particles, a novel approach was introduced for the early warning of defluidization conditions. According to this method, the average differential pressure drop measured from the well stabilized section of the bed decreases over the processing time while the temperature difference between the lowermost thermocouple right above the distributor plate and others within the dense bed at the higher levels increases simultaneously when a cohesive bubbling bed of coarse particles is approaching the complete defluidization state. It demonstrated promising performance in the advanced detection of the onset of agglomeration minutes to hours before the entire defluidization of the bed. Although it is simple, the method showed a low level of sensitivity to the variation of other influential operating parameters, i.e., the bed temperature (±100^{o}C), U_g (±10%), and the bed mass (±20%). According to the observations made during many defluidization incidents, when combusting propane or a solid fuel, two pairs of detection thresholds for the opportune recognition of agglomeration in bubbling fluidized beds of coarse silica sand particles (d_p=820 μm; d_p is the average particle size) are proposed. They work as the high and high-high alarms for the purpose mentioned here. An encouraging performance was also observed from the technique for the timely recognition of agglomeration when fine silica sand (d_p=370 μm) was employed as the bed material.

TABLE OF CONTENTS

LIST OF TABLES

LIST OF FIGURES

LIST OF SYMBOLS AND ABBREVIATIONS

d_p	average particle size (μm)
HDFs	hydrodynamic forces
IPFs	interparticle forces
PEA	poly ethyl acrylate
PMMA	poly methyl methacrylate
RPT	radioactive particle tracking
U_c	transition velocity from bubbling to turbulent regime (m/s)
U_g	superficial gas velocity (m/s)
U_{mf}	minimum fluidization velocity (m/s)
$U_{c,No\ IPFs}$	transition velocity from bubbling to turbulent regime for a bed without IPFs (m/s)

LIST OF APPENDICES

CHAPTER 1 INTRODUCTION

1.1 Motivation

Gas-solid fluidized bed reactors are widely applied in the chemical industry due to their unique advantages, including favorable heat and mass transfer characteristics, uniform and controllable temperature, excellent gas-solid contact and ability to handle a wide variety of particulate properties [1-4]. Nearly all processes are operating gas-solid fluidized bed reactors at temperatures well above ambient [2, 3, 5-12].

The hydrodynamics of gas-solid fluidized beds directly affects the rates of heat and mass transfer and the reaction performance of the fluidized bed reactor. Hence, the fluidization behavior of these units at elevated temperatures is a critical factor for their design and performance assessment [5, 6]. Also, their prevalent applications along with the demand for improvements in their performance have increased the need for a better understanding of their fluidization characteristics [3]. Nevertheless, there is a limited understanding of the bed hydrodynamics at high temperature due to the lack of proper measurement techniques at super-ambient temperatures and the difficulties associated with the high temperature operation even at laboratory scales [2, 5-7, 9]. Therefore, most of our knowledge refers to ambient conditions and hydrodynamic models based on these conditions by merely changing the gas properties, i.e., its density and viscosity, are generally employed to estimate the overall performance of gas-solid fluidized bed processes at high temperature. However, this strategy overlooks possible modifications induced by temperature on the structure and dynamics of fluidized particles. Accordingly, this type of mismatch makes the accuracy of the estimation dubious [2, 5, 13]. This has been experimentally highlighted in many publications [2, 5, 6, 12-17].

Although there has been growing interest in studying the effect of temperature on fluidization behavior at elevated temperatures, findings are still controversial and an acceptable understanding of phenomena, which are responsible for changes in the flow dynamics between ambient and high temperature, has not been adequately achieved [7, 8]. Much of the controversy still remains since the relative importance of interparticle forces (IPFs) and hydrodynamic forces (HDFs) on the flow behavior of powders remains undefined [11, 13].

Increasing the system temperature increases the gas viscosity μ_g (μ_g being proportional to T^n, where n is usually between 0.6 and 1.0) and decreases the gas density ρ_g (ρ_g being inversely proportional to the absolute temperature T) [18, 19]. These changes can alter the magnitude of fluid forces acting on the particles. Electrostatic and van der Waals forces are the principal types of IPFs in a dry environment [20, 21]. The magnitude of the electrostatic forces decreases when the temperature increases [22-24] due to an increase in the electrical conductivity of particles with temperature [25, 26]. In contrast, the magnitude of the van der Waals forces acting between particles in the mutual contacts increases with the bed temperature as the molecular dipole pulsation around the contact point is enhanced by thermal excitation [27]. Also, the viscous flattening of solid particles occurring before sintering [28] leads to a larger interparticle contact area and, thus, enhances the effectiveness of the van der Waals forces. A material bridge between the particles can be present at elevated temperatures due either to the formation/addition of a liquid or to the structural/chemical changes at the particle surface, e.g., through sintering, crystallization or plastic deformation [29]. The cohesive force resulting from the material bridge, either liquid or solid, is much larger in magnitude when compared to the van der Waals and electrostatic forces [21, 29-31]. Sintering is defined by the migration of holes/lattice cavities or the movement of atoms to a less dense area of the material in the surface of particles [32], thus resulting in a solid-solid bond between the particles in contact at its final stage. The formation of a trace amount of liquid in high temperature fluidized beds is mainly the result of the presence of impurities with a low sintering temperature within the bed, which sinter/melt under the high temperature operating conditions and can further react with each other or other solids producing new compounds [33] with a low melting temperature (eutectic). For instance, in the case of the combustion and gasification of low rank coals, biomass, and wastes the ash sintering and chemical reaction between the alkali/alkali earth metal elements in the solid fuels/ash and the bed material, commonly silica sand, is known as the principal reason for the particle stickiness in the bed [34-41]. The fluidization behavior can be modified if one of the IPFs is in the same order of magnitude as the weight of the particle [35]. Therefore, it seems clear that the hydrodynamics of a gas-solid fluidized bed at high temperature is significantly more complicated than what was initially thought.

Reviewing earlier studies on the subject reveals that they dealt with the combined effects of HDFs and IPFs on bed behavior. Hence, they could ultimately prove that the thermal modification of the solid phase must be taken into account along with the variation of HDFs with no clear distinction

between the direct effects of each force group. Therefore, there is still a need to shed light on the direct influence of IPFs on bed behavior at high temperature when combined with the variation of HDFs.

Experimental studies taking into account the variations of IPFs together with HDFs and reported in the literature have mostly focused on the effect of temperature at rather low superficial gas velocities, often near the minimum fluidization/bubbling velocity. Nonetheless, fluidized bed reactors in industrial practice are mostly operated at superficial gas velocities well above the minimum fluidization velocity [42]. The bubbling and turbulent gas-solid fluidized bed reactors are among the units that have been widely employed in various industrial operations (e.g., coal combustion and gasification, production of polypropylene, drying) [1, 43]. Addressing the popular industrial applications of gas-solid fluidized beds in the bubbling and turbulent fluidization regimes, it is desirable to focus on them in this study.

1.2 Objectives

Considering the points tackled above, the main objective of this project is to "*study the hydrodynamics of a gas-solid fluidized bed at high temperature in the presence of interparticle forces"*.

To achieve this, the variations of the magnitude of IPFs and HDFs with the operating temperature must be simultaneously taken into account. Owing to the high complexity of IPFs and unavailability of a measurement technique, which can adequately determine their extent at elevated temperatures, our understanding about their variations and impact on the bed behavior under high temperature operating conditions is far from complete. Thus, a reliable and accurate technique must be adopted to deliberately introduce varying degrees of IPFs into a gas-solid fluidized bed of a given powder to study the effect of IPFs on the bed hydrodynamics. It is recommended that the fluidization behavior of the reference system be governed by HDFs. Since most of the investigations about the exclusive influence of IPFs on the fluidization characteristics of gas-solid fluidized beds have been devoted to low superficial gas velocities, there is a lack of fundamental understanding about the effect at higher gas velocities, principally in the bubbling and turbulent fluidization regimes. In addition, the harsh experimental conditions at elevated temperatures solely allows for the application of a limited number of measurement techniques for the purpose of

hydrodynamic study. Therefore, we are going to divide this research into two main parts corresponding to the targeted specific objectives as follows:

Specific objective #1:

- Investigate the influence of IPFs on the global and local hydrodynamic characteristics of a gas-solid fluidized bed at different superficial gas velocities covering the fixed bed state and bubbling and turbulent fluidization regimes at near-ambient conditions

Specific objective #2:

- Understand the fluidization behavior of a gas-solid fluidized bed at high temperature in the presence of IPFs

1.3 References

1) D. Kunii, O. Levenspiel, Fluidization Engineering, Butterworth-Heinemann, Boston, 1991.
2) B. Formisani, R. Girimonte, L. Mancuso, Analysis of the fluidization process of particle beds at high temperature, Chem. Eng. Sci. 53 (1998) 951-961.
3) S. Sanaei, N. Mostoufi, R. Radmanesh, R. Sotudeh-Gharebagh, C. Guy, J. Chaouki, Hydrodynamic characteristics of gas-solid fluidization at high temperature, Can. J. Chem. Eng. 88 (2010) 1-11.
4) T. Li, K. Pougatch, M. Salcudean, D. Grecov , Mixing of secondary gas injection in a bubbling fluidized bed, Chem. Eng. Res. Des. 87 (2009) 1451-1465.
5) H. Cui, J. Chaouki, Effects of temperature on local two-phase flow structure in bubbling and turbulent fluidized beds of FCC particles, Chem. Eng. Sci. 59 (2004) 3413-3422.
6) H. Cui, P. Sauriol, J. Chaouki, High temperature fluidized bed reactor: measurements, hydrodynamics and simulation. Chem. Eng. Sci. 58 (2003) 1071-1077.
7) T.M. Knowlton, Pressure and temperature effects in fluid-particle systems, in: W.C. Yang (Ed.), Fluidization, Solids Handling and Processing: Industrial Applications, Noyes, New Jersy, 1999, pp. 111-152.
8) J.G. Yates, Effects of temperature and pressure on gas-solid fluidization, Chem. Eng. Sci. 51 (1996) 167-205.
9) R. Girimonte, B. Formisani, The minimum bubbling velocity of fluidized beds operating at high temperature, Powder Technol. 189 (2009) 74-81.

10) H.T. Bi, J.R. Grace, Effects of pressure and temperature on flow regimes in gas-Solid fluidization systems, Can. J. Chem. Eng. 74 (1996) 1025-1027.

11) P. Lettieri, D. Newton, J.G. Yates, High temperature effects on the dense phase properties of gas fluidized beds, Powder Technol. 120 (2001) 34-40.

12) G. Raso, M. D'Amore, B. Formisani, P.G. Lignola, The influence of temperature on the properties of the particulate phase at incipient fluidization, Powder Technol. 72 (1992) 71-76.

13) P. Lettieri, J.G. Yates, D. Newton, The influence of interparticle forces on the fluidization behaviour of some industrial materials at high temperature, Powder Technol. 110 (2000) 117-127.

14) B. Formisani, R. Girimonte, G. Pataro, The influence of operating temperature on the dense phase properties of bubbling fluidized beds of solids, Powder Technol. 125 (2002) 28-38.

15) A. Chehbouni, J. Chaouki, C. Guy, D. Klvana, Effect of temperature on the hydrodynamics of turbulent fluidized beds, in: C. Laguerie, J.F. Large (Eds.) Proceedings of the 8th International Conference on Fluidization, Engineering Foundation, New York, 1995, pp. 149-156.

16) P. Cai, Y. Jin, Z.Q. Yu, Z.W. Wang, Effect of operating temperature and pressure on the transition from bubbling to turbulent fluidization, AIChE Symp. Ser. 85(270) (1989) 37-43.

17) P.K. Peeler, K.S. Lim, R.C. Close, Effect of temperature on the turbulent fluidization regime transition, in: J. Werther (Ed.) Proceedings of the 6th International Conference on Circulating Fluidized Beds, Würzburg, Germany, 1999, pp. 125-130.

18) T.M. Knowlton, Pressure and temperature effects in fluid-particle systems, in: O.E. Potter, D.J. Nicklin (Eds.) Proceedings of the 7th International Conference on Fluidization, Engineering Foundation, New York, 1992, pp. 27-46.

19) S.Y. Wu, J. Baeyens, Effect of operating temperature on minimum fluidization velocity, Powder Technol. 67 (1991) 217-220.

20) Visser, J., Van der Waals and other cohesive forces affecting powder fluidization, Powder Technol. 58 (1989) 1-10.

21) J. Shabanian, R. Jafari, J. Chaouki, Fluidization of ultrafine powders-Review, Int. Rev. Chem. Eng. (IRECHE) 4 (2012) 16-50.

22) T. Kai, S. Furusaki, Behavior of fluidized beds of small particles at elevated temperatures, J. Chem. Eng. Jpn. 18 (1985) 113-118.

23) W.O. Moughrabiah, J.R. Grace, X.T. Bi, Effects of pressure, temperature, and gas velocity on electrostatics in gas−solid fluidized beds, Ind. Eng. Chem. Res. 48 (2009) 320-325.

24) T.A. Alsmari, J.R. Grace, X.T. Bi, Effects of superficial gas velocity and temperature on entrainment and electrostatics in gas–solid fluidized beds, Chem. Eng. Sci. 123 (2015) 49-56.

25) S. Boggs, D.H. Damon, J. Hjerrild, J.T. Holboll, M. Henriksen, Effect of insulation properties on the field grading of solid dielectric DC cable, IEEE Trans. Power Delivery 16 (2001) 456-461.

26) P.K. Jain, N. Saxena, Temperature and composition dependence of electrical conductivity of Se90In10–xSbx (x=0, 2, 4, 6, 8, 10) chalcogenide glasses, J. Non-Oxide Photonic Glasses 1 (2009) 43-52.

27) H. Krupp, Particle adhesion: theory and experiment, Adv. Colloid Interface Sci. 1 (1967) 111-239.

28) H. Rumpf, Particle adhesion, in: Proceedings of the 2nd International Symposium on Agglomeration (Agglomeration 77), AIME, 1977, pp. 97-129.

29) P. Pagliai, S.J.R. Simons, D. Rhodes, Towards a fundamental understanding of defluidisation at high temperatures: a micro-mechanistic approach, Powder Technol. 148 (2004) 106-112.

30) R.A. Bowling, A theoretical review of particle adhesion, in: K. Mittal (Ed.) Particles on Surfaces 1, Plenum Press, New York, 1988, pp. 129-142.

31) J.P.K. Seville, C.D. Willett, P.C. Knight, Interparticle forces in fluidisation: a review, Powder Technol. 113 (2000) 261-268.

32) J.H. Siegell, High-temperature de fluidization, Powder Technol. 38 (1984) 13-22.

33) G. Tardos, R. Pfeffer, Chemical reaction induced agglomeration and defluidization of fluidized beds, Powder Technol. 85 (1995) 29-35.

34) A.R. Manzoori, E.R. Lindner, P.K. Agarwal, Inorganic transformation during the circulating fluid bed combustion of low-rank coals with high content of sodium and sulphur, in: Proceedings of the Engineering Foundation Conference on Inorganic Transformations and Ash Deposition During Combustion, Palm Coast, Florida, USA, 1991, pp. 735-762.

35) M. Bartels, W. Lin, J. Nijenhuis, F. Kapteijn, J.R. van Ommen, Agglomeration in fluidized beds at high temperatures: Mechanisms, detection and prevention, Prog. Energy Combust. Sci. 34 (2008) 633-666.

36) J. Werther, M. Saenger, E. U. Hartge, T. Ogada, Z. Siagi, Combustion of agricultural residues, Prog. Energy Combust. Sci. 26 (2000) 1-27.

37) W. Lin, K. Dam-Johansen, F. Frandsen, Agglomeration in bio-fuel fired fluidized bed combustors, Chem. Eng. J. 96 (2003) 171-185.

38) C. Tangsathitkulchai, M. Tangsathitkulchai, Effect of bed materials and additives on the sintering of coal ashes relevant to agglomeration in fluidized bed combustion, Fuel Process. Technol. 72 (2001) 163-183.

39) B.M. Steenari, O. Lindqvist, V. Langer, Ash sintering and deposit formation in PFBC, Fuel 77 (1998) 407-417.

40) M. Öhman, A. Nordin, B.-J. Skrifvars, R. Backman, M. Hupo, Bed agglomeration characteristics during fluidized bed combustion of biomass fuels, Energy Fuels 14 (2000) 169-178.

41) J. van Caneghem, A. Brems, P. Lievens, C. Block, P. Billen, I. Vermeulen, R. Dewil, J. Baeyens, C. Vandecastteele, Fluidized bed waste incinerators: Design, operational and environmental issues, Prog. Energy Combust. Sci. 38 (2012) 551-582.

42) I. Sidorenko, M.J. Rhodes, Pressure effects on gas-solid fluidized bed behavior, Int. J. Chem. Reactor Eng. 1 (2003) Review R5 (1-33).

43) N. Ellis, Hydrodynamics of gas-solid turbulent fluidized beds, Ph.D. dissertation, Department of Chemical and Bilogical Engineering, The University of British Columbia Vancouver, 2003.

CHAPTER 2 COHERENCE OF THE ARTICLES

Chapters 3 to 11 represent the main body of this work and include a review article, which was required to properly familiarize the reader with the different types of forces governing the hydrodynamics of a gas-solid fluidized bed, and the corresponding scientific findings achieved in this study. Each chapter consists of an individual article. A brief description of the chapter and the link in between is as follows:

- Chapter 3 presents a review article about the fluidization of ultrafine powders. Particles ranging in size from nano to about 30 microns, known as ultrafine powders, are among the particulate systems with fluidization behavior that is clearly influenced by the presence of profound IPFs. In other words, a fluidized bed of these powders is regarded as a clear example that can experience different ratios of the magnitude of IPFs/HDFs from about unity when fluidized to very high values to hardly being fluidized. This field of research has been the focus of many valuable publications and a thorough review of them has been attempted. Different types of forces that act on the fluidized particles in a gas-solid fluidized bed are primarily reviewed and correlations for the predictions of their magnitudes are reported. The relative importance of different types of IPFs with respect to each other and the weight of a particle is discussed. Thorough discussions about how these ultrafine particles become fluidized and, in particular, how different magnitudes of IPFs can result in different fluidization characteristics are provided. We believe that this part of the work offered valuable insight on the importance of IPFs in gas-solid fluidized beds and how they can alter the bed hydrodynamics. The knowledge acquired here helped with the interpretation of experimental observations made in this work yet with the application of different techniques to induce IPFs into beds of considerably larger particles than ultrafine powders.
- In chapter 4 the polymer coating approach is introduced as a superior methodology for studying the effect of IPFs on the fluidization behavior of gas-solid fluidized beds. Among its promising advantages, it reproduces and imitates the conditions found in gas-solid fluidized beds operating at elevated temperatures in a much friendlier environment (near-ambient conditions). Sugar beads representing typical Geldart group B behavior at ambient conditions were adopted as the base system for which the level of IPFs was at minimum. After applying a 5 μm uniform coating of the PMMA/PEA (poly methyl methacrylate/poly

ethyl acrylate) copolymer on the surface of these particles and subjecting them to different operating temperatures, ranging from 20–40°C, different levels of IPFs were achieved in the fluidized bed. A detailed study was attempted on the subject through the measurements of global hydrodynamic parameters, including the total bed pressure drop profile, bed height, and different types of pressure signals in this part of the work. The ability to shift the fluidization behavior of a given powder showing typical Geldart group B behavior into Geldart group A or even C behavior and the increase in the minimum fluidization velocity (U_{mf}), the transition velocity from bubbling to turbulent fluidization regime (U_c), and the tendency of the fluidizing gas to pass through a bubbling bed in the emulsion phase when the level of IPFs increased in the bed were among the most promising findings of this section of the study. The corresponding experimental results and a thorough discussion about the modification of the dilute phase characteristics in the bubbling and turbulent fluidization regimes with increasing the level of IPFs are also provided.

- Chapter 5 includes the experimental results of the effect of IPFs on the bed hydrodynamics obtained by local measurements. An optical fiber probe and the RPT technique were exploited in the bubbling and turbulent fluidization regimes for this purpose. The polymer coating approach was employed to introduce and adjust the level of IPFs in the bed. In a broad accordance with the experimental observations presented in chapter 4, the local measurements revealed that gas was more prone to pass through the bed in the emulsion phase at a given superficial gas velocity (U_g) in the bubbling regime. However, since the transition from bubbling to turbulent regime took place at a lower superficial gas velocity for a system with the lowest level of IPFs (alternatively, no IPFs), an inverted trend was observed at $U_g > U_{c,No\ IPFs}$, i.e., a higher quantity of the fluidizing gas was passing through the bed with no IPFs in the dense phase.
- Observations based on local and global measurements suggested that since the emulsion phase is more efficient than the bubble phase in bringing about a chemical reaction between gas and solids, a slight increase in the level of IPFs, far from the defluidization state, would enhance the reaction performance of a catalytic bubbling gas-solid fluidized bed reactor. This is the subject of the next part of the study, presented in chapter 6. A simulation study of an industrial-scale fluidized bed reactor was attempted to verify this hypothesis. The two-phase flow model integrated with the hydrodynamic parameters measured for beds with different

levels of IPFs described the hydrodynamics of the simulated reactor at varying degrees of IPFs. A kinetic model, available in open literature, for the partial oxidation of n-butane into maleic anhydride over the vanadium phosphorus oxide catalyst represented the reaction feature of the reactor. The simulation results demonstrated that the conjecture above is correct.

- Although increasing the level of IPFs in the bubbling regime could enhance the overall performance of a catalytic bubbling fluidized bed reactor, primary indirect observations made in chapters 4 and 5 suggest that the quality of solids mixing would, however, decrease with this change. An in-depth study was carried out with the help of the RPT technique while adopting the same polymer coating approach to increase the level of IPFs in a bed of fresh sugar beads. This part of the work is presented in chapter 7, where the experimental results confirmed the initial impression. A sharp increase in the resistance of the emulsion phase, caused by the presence of IPFs, to any changes could principally explain this modification in the bed behavior. In addition, by calculating the idle time for systems with varying degrees of IPFs and resembling the agglomeration process to a reaction network, i.e., the idle time represents the effective reaction time and all reactions follow the elementary rate law, we could provide a fundamental understanding about why the agglomeration process, which normally occurs for beds approaching complete defluidization at elevated temperature, is an auto-accelerated phenomenon.
- Chapter 8 reports the experimental findings related to the modification in the fluidization characteristics of a bubbling gas-solid fluidized bed at high temperature when varying degrees of IPFs were deliberately introduced into a bed of coarse particles. The influence of temperature on the bubbling fluidization behavior of fresh coarse particles for which the level of IPFs was at minimum was investigated at first. The bubble size decreased with temperature while the bubble passage frequency remained relatively unvaried in this case. In order to study the influence of IPFs on the bed behavior at high temperature, a fluidized bed of fresh coarse particles was initially subjected to solid fuel combustion prior to the hydrodynamic tests. This assisted with the formation and coating of the bed materials with low melting point eutectics between the SiO_2 component from the bed materials and alkali/alkali earth metals embedded in the combusting solid fuel. The fluidization study for bubbling beds with different levels of IPFs elucidated a multiplicity of behaviors depending on the magnitude of

IPFs. Appreciable similarities were observed between the experimental results achieved by the application of the polymer coating approach at near-ambient conditions and those obtained from the experimental campaign at high temperature. It confirmed the aptness of the selected methodology throughout this study.

- Chapter 9 presents a novel technique for the early recognition of agglomeration in a bubbling fluidized bed of coarse silica sand particles (d_p=820 µm; d_p is the average particle size). The new method is proposed to compensate for the main drawback of other detection approaches, i.e., the sole application of either temperature or pressure signals is insufficient to results in a simple, reliable, and robust method for the opportune detection of defluidization conditions. However, with the help of the detailed information collected from the influence of IPFs on bed behavior, the new method was established for the simultaneous applications of temperature and in-bed differential pressure signals. Although it is simple, the preliminary results of this technique for the advanced warning of agglomeration in a defluidization sample experiment obtained during the combustion of propane showed a promising performance.
- In continuation of the study presented in chapter 9, a comprehensive investigation was attempted in Appendix A to verify the applicability of this novel technique when experiencing the defluidization incident during solid fuel combustion. Comparing the performance of the novel technique with other methods reported in open literature indicated that the new monitoring approach represents an enhanced performance. Upon evaluating the sensitivity of the new method to other influential operating parameters, i.e., bed temperature (±100°C), U_g (±10%), and bed mass (±20%), and based on the observations made during many defluidization incidents, two detection thresholds for the timely recognition of agglomeration in bubbling fluidized beds of coarse silica sand particles are introduced. They function as the high and high-high alarms for the purpose mentioned here. The method also showed an encouraging efficiency for the advanced detection of agglomeration when fine silica sand (d_p=370 µm) was exploited as the bed materials. A comprehensive understanding about the evolution of the bed behavior from a normal fluidization state, where the level of IPFs was at minimum, to complete defluidization was also achieved in this study.
- Chapter 10 is a general discussion and summary of the results.
- Chapter 11 summarized the key conclusions of this study and provides recommendations for future studies.

CHAPTER 3 ARTICLE 1 : FLUIDIZATION OF ULTRAFINE POWDERS – REVIEW

Jaber Shabanian, Rouzbeh Jafari, Jamal Chaouki*

Department of Chemical Engineering, Ecole Polytechnique de Montreal, Montreal, Quebec, Canada

* Corresponding author: Tel.: +1-514-340-4711 X 4034; fax: +1-514-340-4159.

E-mail address: jamal.chaouki@polymtl.ca

(Published in International Review of Chemical Engineering (I.RE.CH.E.) 4 (2012) 16–50)

3.1 Abstract

Due to their unique properties arising from their very small primary particle size and very large surface area per unit mass, ultrafine powders are applied in a wide range of processes and their application continues to increase. Gas fluidization is one the best techniques available for dispersing and processing these particles. However, they cannot be fluidized separately and, in fact, tend to fluidize as large sized very porous aggregates. In order to achieve a proper fluidization, appropriate assisting method is required. This contribution reviews experimental and theoretical studies on gas fluidization of ultrafine particles. It includes introduction of different forces playing role on the fluidization of these powders, phenomenological discussion on how they can be fluidized, a summary of various assisting methods and their impacts for improving the fluidization quality of these powders, a summary of different experimental methods for measuring the agglomerate size followed by different modeling approaches for the prediction of this important parameter, a brief review on different applications of these particles and their bed expansion behavior. With respect to the current and upcoming applications of ultrafine powders in industrial sectors, considerable theoretical and experimental work is left for mining new opportunities in chemical engineering on the subject of fluidization of ultrafine particles.

Keywords: Fluidization, Fine and Ultrafine Powders, Nanoparticles.

3.2 Introduction

Fine powders, including ultrafine or nano size powders, play a moderate role and will be highly important in industrial applications. Processing these powders is very attractive due to their very

small primary size and large surface area-to-volume ratio [1], [2], because as in the case of gas/solid and solid/solid reactions, for example, higher reaction rates per unit volume of reactor are obtainable [3]. Nanoparticles have been used to produce catalysts, effective sorbents, drugs, cosmetics, food, plastics, biomaterials, and microelectro-mechanical systems (MEMS). In addition, they have some applications in hydrogen storage, Li-ion batteries, and fuel cells [1], [4], [5]. Therefore, it is essential to develop processing technologies that can handle large quantities of nano size particles, such as mixing, transporting, and modifying the surface properties, and to produce nanocomposities [1].

Prior to processing such materials, however, it is necessary that the nanopowders be well dispersed. Gas fluidization is one of the best techniques available to disperse and process fine particles [1], [4]. Gas-solid fluidized beds are among the unit operations, which have a number of significant advantages for processing small solid particles, including high heat and mass transfer rates, uniform and controllable bed temperature, high flowability of particles, the ability to handle a wide variety of particle properties and suitability for large-scale operations [6]-[8]. Moreover, compared to liquid-phase processing of nanoparticles, gas-phase processing reduces difficulties that arise with respect to removing impurities and drying the particles, and allows easier scale-up [4], [9].

Geldart [10] classified powders according to their primary particle size and density into four distinct groups: A, aeratable; B, sand-like; C, cohesive; and D, spoutable. On the basis of their physical properties, nano size powders fall under the Geldart group C (<30 μm) classification [11]. It has been believed that group C powders are in principle extremely hard to fluidize and, hence, can be difficult for practical use in their original separated form, not only due to the fact that the cohesive forces (such as van der Waals, electrostatic, capillary forces) in these powders are much larger than the gravitational, but also because the drag force exerted by the gas on these particles is not large enough for fluidization [12], [13]. Unlike group A and B powders, fluidization of this group of materials generally results in gas bypassing via the formation of channels and in low powder mobility. The presence of channeling in the bed gives rise to some undesirable effects, such as low bed expansion, inadequate bed pressure drop, and the creation of regions with high local gas velocities, causing undesired elutriation loss of expensive bed materials [14].

However, despite Geldart classification, there is growing experimental evidence that nanoparticles can be fluidized via the formation of agglomerates of original ultrafine particles at gas velocities

in excess of the minimum fluidization for the primary particle [12], [15]-[20]. This implies that primary particle size and density cannot be taken as representative parameters for predicting their fluidization behavior [17], [20]. In fact, because of strong interparticle forces, nanoparticles are mainly found to be in the form of large-size (100-400μm), highly porous (internal porosity>98%), fractal structured agglomerates of primary particles, rather than as isolated particles when they are subjected to gas fluidization. Therefore, gas fluidization of ultrafine powders actually refers to the fluidization of nanoparticle agglomerates and their properties (size, density, structure, etc.) highly affect the fluidization nature [1], [19]-[22].

Accordingly, it is very important to know how these agglomerate particles fluidize within the bed. In fact, fluidization behavior of highly porous agglomerates can be categorized into two distinct paths: *agglomerate particulate fluidization* (APF) and *agglomerate bubbling fluidization* (ABF). The former is characterized by very large bed expansion, homogeneous fluidization, and very low minimum fluidization velocity; the latter, instead, shows little bed expansion, high minimum fluidization velocity, and bubbling [1], [19], [20], [22].

Fluidization of nanoparticle agglomerates suffers from several problems, such as channeling, bubbling, clustering, and elutriation. As a consequence, inappropriate dispersion of nanoparticles in the gas phase and considerable gas bypassing may occur [4]. To overcome these problems and improve the fluidization quality of nanoparticle agglomerates, various assisting methods have been proposed and tested. These methods include the application of additional generated forces, for example by acoustic [23]-[27], electric [28], [29], or magnetic [30], [31] fields, or mechanical vibrations [32], [33], the use of a centrifugal fluidized bed [2], [7], [34], [35], the use of a tapered fluidized bed [36], the addition of foreign particles [12], [37], [38], and the use of micro-jets as a secondary flow in the bed [22]. The degree of fluidization enhancement achieved by applying these methods is evaluated by measuring some hydrodynamic parameters, such as minimum fluidization velocity, bed pressure drop, bed expansion, agglomerate size, degree of mixing, bubble suppression and the amount of powder elutriation, as indicators of fluidization quality.

In this chapter the studies on the fluidization of ultrafine powders will be reviewed. Firstly, different forces that directly or indirectly affect the dynamics of the fluidized bed will be introduced and correlations for the prediction of their magnitudes will be reported. Secondly, the fluidization behavior of all powders falling into Geldart group C category is phenomenologically discussed.

Thirdly, a summary of different assisting methods and their impacts for enhancing the fluidization quality of fine/ultrafine particles will be provided. Then, different experimental techniques that have been used for measuring agglomerate size will be introduced. Section six is devoted to the presentation of different modeling approaches for the prediction of agglomerate size. Different applications of ultrafine particles will be reviewed in section seven. Next, expansion behavior of the bed of fine/ultrafine particles will be discussed. Finally, a brief summary of the article will be presented.

3.3 Various forces in a gas-solid fluidized bed

In gas-solid flows, forces controlling the motions of particles can be categorized into three groups: (1) forces through the interface between particles and fluid, (2) forces imposed by external fields, and (3) forces due to the interactions between particles, interparticle forces. Although field and interparticle forces do not have a direct impact on the flow pattern in the bed, they may indirectly affect the fluid motion via particle-fluid interactions [39]. In conventional gravity driven gas-solid fluidized beds drag force, buoyant weight, and interparticle forces influence the motion of gas-solid flow. Each of these forces will be separately delineated below.

3.3.1 Drag force

The drag force F_d on a single isolated particle, with particle diameter d_p, in a uniform flow field considering superficial gas velocity u_0 and drag coefficient C_D, can be generally given by:

$$F_d = C_D \frac{\pi {d_p}^2}{4} \frac{\rho_f {u_0}^2}{2} \tag{3.1}$$

The drag coefficient is a function of the particle Reynolds number, Re_p, which is defined as:

$$Re_p = \frac{\rho_f u_o d_p}{\mu} \tag{3.2}$$

where ρ_f and μ are fluid density and viscosity, respectively. For $Re_p \ll 1$, creeping flow regime, the viscous effect dominates over the inertia and the drag coefficient can be expressed by using Stokes' law, $C_D = 24/Re_p$. On the contrary, for Re_p in the range of 700 to 10^5, the inertia effect is predominant and Newton's relation, $C_D \cong 0.44$, covers the range [39], [40]. Moreover, if a

particle is in a uniform bed of particles having bed voidage, ε, the drag force on a single particle in the bed is $\varepsilon^{-3.8}$ times that on a single isolated particle, leading to the following correlation for the drag force on a particle in a particle bed for both the Stokes' and Netwton's law regions [40]:

$$F_{d\varepsilon} = C_D \frac{\pi {d_p}^2}{4} \frac{\rho_f {u_0}^2}{2} \varepsilon^{-3.8} \quad 3.3$$

3.3.2 Buoyant weight

When the bed is fluidized, it exhibits fluid-like behavior and the density of the fluidized bed ρ_{fb} is:

$$\rho_{fb} = \varepsilon\rho_f + (1-\varepsilon)\rho_p \quad 3.4$$

where ρ_p is particle density. The buoyancy force F_b on a spherical particle is defined as [7]:

$$F_b = \frac{\pi {d_p}^3}{6} \rho_a g = \frac{\pi {d_p}^3}{6} (\varepsilon\rho_f + (1-\varepsilon)\rho_p) g \quad 3.5$$

where g is the gravity field. Accordingly, the buoyant weight W_b of the particle is:

$$W_b = gravity\ force - buoyancy\ force = \frac{\pi {d_p}^3}{6} (\rho_p - \rho_f) g\varepsilon \quad 3.6$$

3.3.3 Interparticle forces

Cohesion between particles may originate from a variety of sources. Van der Waals force, electrostatic force, and capillary force are considered as the main forces in particle adhesion [41]. These forces significantly affect the fluidization behavior of group A and, in particular group, C powders [13].

3.3.3.1 Van der Waals force

Van der Waals was the first to point out that the nonideality of gases can be explained by the existence of molecular interactions due to interacting dipoles. The dispersion effect, which is the interaction between the instantaneous dipoles formed in the atoms by their orbiting electrons, is responsible for van der Waals force [42]. The very rapidly changing dipole of one atom generates

an electric field that impacts the polarizability of a neighboring atom. The induced dipole of the neighboring atom tends to move in phase with the original dipole, producing a generalized attractive interaction known as the van der Waals force. This kind of force exists not only between individual atoms and molecules, but also between macroscopic solids. According to Krupp [43], Molerus [44] and Massimilla and Donsi [45], the van der Waals force between two smooth spheres of radius R at a separation distance Z, is given by:

$$F_{vdw} = \frac{h\bar{\omega}}{8\pi Z^2} R \left(1 + \frac{h\bar{\omega}}{8\pi^2 Z^3 H_r}\right) \quad 3.7$$

where $h\bar{\omega}$ is the Liftshits-van der Waals coefficient and a function of the nature of the bodies in contact and of the surrounding medium and H_r is the hardness of the softer of two bodies. Krupp [43] suggested a value of 4 A^o for Z, the distance where van der Waals force is maxima and a value of 10^8 N/m^2 for the hardness of undeformable solids. In the case of contact between two spherical particles of different radii, R_1 and R_2, van der Waals force can be calculated from Eq. 3.7 assuming:

$$R = \frac{R_1 R_2}{R_1 + R_2} \quad 3.8$$

Most powders have a rough surface with many asperities [46]. As a result of these asperities observed with real materials, a characterizing surface geometry and not the size of particles in contact should be considered. According to Krupp [43] and Massimilla and Donsi [45], a typical value of 0.1 μm can be considered for asperity size R_{as} and should be inserted in Eq. 3.8.

Although the relative significance of a particular form of interparticle forces strongly depends on the original properties of particles, the fluidized bed set-up and the fluidizing conditions, like moisture content [47], it is generally believed that the van der Waals force is much more significant than other types of interparticle forces for fine particles of a diameter less than 100 μm in a dry gaseous environment [13]. In addition, this force dominates over gravitational force and, hence, over fluid- dynamic forces generated in a fluidized bed under this condition [13], [48], [49]. The situation changes when porous particles or particles having a partly flattened surface, due either to their inherent structure, e.g., crystalline material, or to plastic deformation induced by pressure or an increase in temperature, are considered. For these cases, the region is extended to even larger particles [13].

3.3.3.2 Electrostatic force

In addition to van der Waals force, electrostatic force can also contribute to the adhesion of particles and, hence, their aggregation in a gaseous environment [13], [43]. During the processing of powders under dry conditions, when non-conducting particles come into contact with surfaces of dissimilar material or slide along such surfaces, this is generally accompanied by an exchange of electrons in the surface layer. This causes the particles to be electrically charged and the phenomenon is termed as a contact electrification or triboelectrification process [50], [51]. The motion of a charged particle in a gas-solid flow is influenced by the electrostatic force imposed on it by nearby charged particles. According to the well-known Coulomb's law, the electrostatic force between two charged objects, which are much smaller than the distance between them, is proportional to the product of the charges and inversely proportional to the square of the distance of separation [39]. This force is acting along a straight line from one charged object to the other and can be expressed by:

$$F_e = \frac{1}{4\pi\epsilon}\frac{q_1 q_2}{s^2} \tag{3.9}$$

where q_1 and q_2 are the charges carried by the two objects, s is the distance between the two objects, and ϵ is the permittivity of the surrounding medium.

In general, electrostatic force is insignificant compared to the first class of interparticle forces, van der Waals force [13], [51]. Moreover, this force vanishes in a humid environment due to a discharging of the system [13].

3.3.3.3 Capillary force

Capillary force, liquid-bridge force, is caused by the condensation of moisture from the surrounding gas on the surface of particles, which then forms a liquid bridge in the gap between neighboring particles, as shown in Figure 3.1. This produces a resultant attractive force between the two bodies as a result of the pressure deficiency in the bulk of the liquid and the surface tension of the liquid acting on the two particles [13], [51], [52]. The interparticle forces, which in a dry environment are principally due to van der Waals force, are then increased by this force [13]. Capillary force can dominate the gravitational force on the individual particles when the vapour pressure of the surrounding gas is close to the saturation pressure and can also be rather larger than

the maximum van der Waals force as well [49], [51]. It is practically important in agglomeration processes, driers, and some kinds of reactors and bioreactors, as for example, in drying solids where it may severely hinder the handling of powders, especially at the start [49], [51]. The liquid-bridge force is the sum of the surface tension F_γ and the pressure differential across the air-liquid interface F_p [49], [53]. By approximating the bridge profile as circular arc (torus), capillary force can be estimated according to two methods, which differ in the place where forces act [53]. The first method is the boundary method, where the total force between two equal radii of R is calculated at the liquid-solid contact, considering F_p acting at the axially projected area of the liquid contact on the sphere and F_γ acting on the three phase contact line [52]. By this method, the total force can be defined as the following:

$$F_c = 2\pi\gamma R\, sin\alpha \sin(\alpha + \beta) + \pi R^2\, \Delta p\, sin^2\alpha \qquad 3.10$$

where γ is the liquid surface tension, α is the half-filling angle, and β is the contact angle. The differential pressure Δp across the air-liquid interface is given by the Laplace-Young equation, which can be expressed by:

$$\Delta p = \gamma\left(\frac{1}{r_1} - \frac{1}{r_2}\right) \qquad 3.11$$

where r_1 and r_2 are the liquid bridge meridional curvature radius and the liquid bridge neck radius, respectively [52], [53]. The magnitude of the total force is difficult to be precisely computed by this method, even for spheres [49]. However, the second method, the gorge method, in which the total capillary force is calculated at the neck of the bridge, enables a simple and sufficiently accurate result to be obtained [49], [53]. On the basis of this method, the total force can be approximated by:

$$F_c = 2\pi\gamma R \qquad 3.12$$

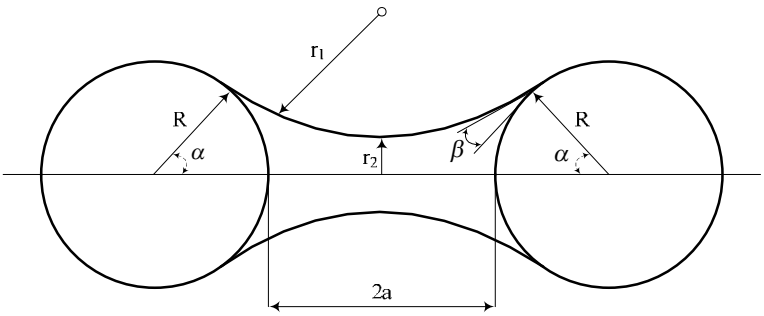

Figure 3.1: Liquid bridge between two equal size spheres. a = Half-particle distance.

According to Massimilla and Donsi [45], similar to van der Waals force, surface asperities need to be taken into account in Eq. 3.12 to have reliable value for the capillary force. It is worth mentioning that in most powder operations, vapour pressure is so low that the capillary force can be neglected [51].

A schematic comparison of different kinds of interparticle forces with that of the particle weight was provided by Seville et al. [49], as shown in Figure 3.2, for a sample particle with a particle density equal to 3×10^{-3} kg/m^3. In this figure, magnitudes of both capillary and van der Waals forces are calculated using actual particle radius and particle asperity radius, $R_{as} = 0.1\ \mu m$. Results of these calculations are plotted in the form of solid and dashed lines, respectively. It can be seen that if the gross particle radius is taken into account, a particle diameter in the order of 1 mm exhibits interparticle van der Waals force approximately equal to the particle weight, which is less plausible. On the contrary, when the latter radius is used, the equality of van der Waals force and particle weight is achieved for a $100\ \mu m$ particle size for which adhering to surfaces and resisting the force of gravity is commonly observed [49]. Also, it can be found from this figure that the magnitude of the liquid-bridge force, when present in the system, is greater than the maximum van der Waals force. Moreover, it is clear that the ratio of interparticle cohesive force to gravity force increases by a reduction in particle size.

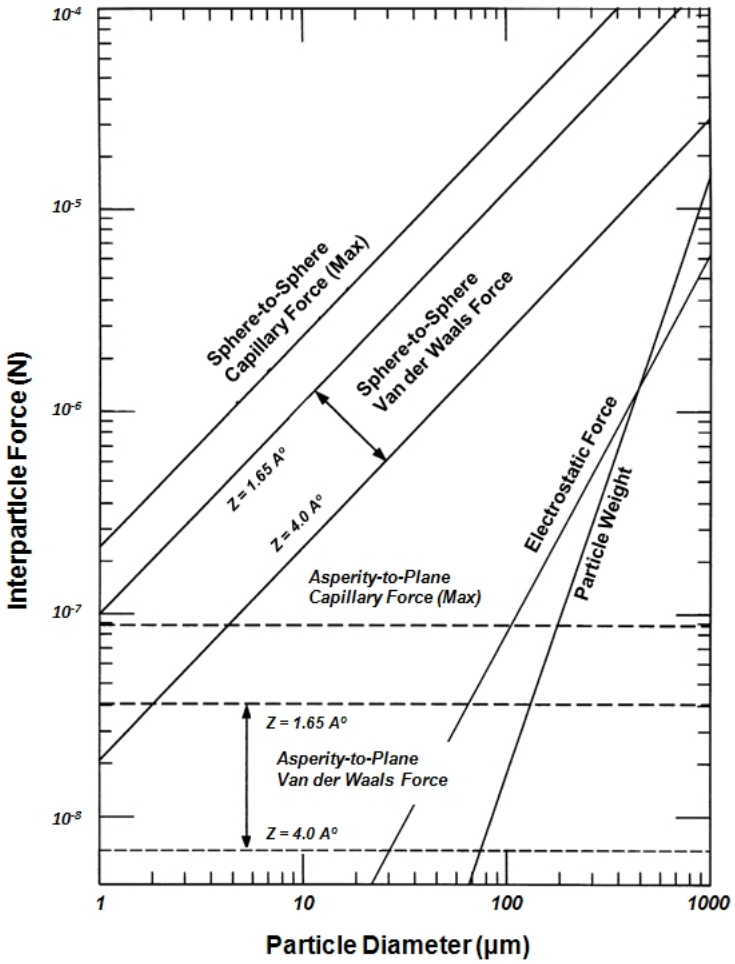

Figure 3.2: Comparison of various interparticle cohesive forces with that of the particle weight. Adapted from [49].

3.4 Fluidization of nanoparticles with high interparticle forces

According to Geldart's classification, for coarse particles of groups B and D, gravity force is always superior to interparticle forces and, hence, fluidization behavior is dominated by gravity effects. By reducing the particle size down to group A particles, the ratio of interparticle forces to the particle weight increases and these forces are of comparable magnitude for this group of materials [44]. Also, for small particles of this group, interparticle forces do not allow free fluidization in an increasing flow experiment until the drag force on the hindered bed is able to counteract the cohesion force, dislodge the particles, and restore a more normal fluidized stable state [15]. With a further decrease in particle size, entering group C region, cohesion between particles tends to predominate over the gravity force giving rise to substantial bulk adhesion that leads to significant

reduction in the permeability of the particle assembly by the interstitial gas [54]. In the case of dry fine particles ($d_p < \sim 30\ \mu m$), the interparticle forces are dominant and may exceed the particle weight by several orders of magnitude [48], [49].

Under Geldart's classification, class C covers the range of particles having a mean diameter less than $20\ \mu m$ and denoting a density difference between gas and solids larger than 1000 kg/m^3. It has been found that due to strong interparticle forces normal fluidization of these powders is extremely difficult; unlike other classes, they cannot be fluidized individually, even up to terminal velocity of original particles, and the process of fluidizing them usually involves plugging, channeling, and the formation of stable cakes [10], [15], [44], [54]. However, this is not a generalized fluidization behavior of solid materials belonging to this group. On the basis of Geldart's classification, submicron and nanoparticles are at the extreme of group C particles suggesting at first sight that the fluidization would prove impossible due to the strong interparticle forces between solids [54]. Nonetheless, it has been experimentally found that at gas velocities far above the minimum fluidization of the primary particles, such very fine powders form dynamically stable agglomerate structures, made up of the constitutive particles, in the bed and can then grow to sizes in the micron or millimeter ranges and whose fluidization behavior could therefore very well fall within groups A, B, and even C [12], [15]-[20], [55]. As these particles agglomerate into larger structures, the balance between the interparticle and inertial forces in the particulate system changes [21]. Consequently, the existence of these micro-structure agglomerates is the reason to prevent the formation of stable cohesive bonds between the primary particles and, hence, presenting a potential deviation from the theoretical behavior of cohesive materials observed in group C powders [54].

Therefore, the fine particles of group C powders can be classified into three main subclasses according to their fluidization behavior. The first subclass includes all particles that can never be fluidized under any circumstance because of extra strong adhesion forces between fine particles and between agglomerates [19], [20], [55]. For this type of particles, channeling and plugging always happens and there are two cases that show such behaviors. In one case, channels or rat-holes are directly formed from individual fine particles with a particle size in the range of several microns to tens of microns and there is a lack of adhesion forces between these powders to cause agglomeration. In the other case, channels or plugs are formed by the agglomerates of fine particles with a particle size smaller than $1\ \mu m$ and showing appreciable adhesion between agglomerates.

Experiments show that the use of external forces, like vibration, can help to break these channels and plugs to obtain stable fluidization [55]. The second and third subclasses are comprised of powders that can cross the fluidizability barrier by forming agglomerates of primary particles. However, these subclasses have some differences in their natures and are defined as agglomerate particulate fluidization (APF) and agglomerate bubbling fluidization (ABF). These behaviors can be usually found in the case of submicron and nanoparticles as well as some cases of micron size fine particles. More explanations concerning the last two subclasses are provided in the following section.

3.4.1 Agglomerate fluidization

3.4.1.1 Agglomerate particulate fluidization and agglomerate bubbling fluidization

Agglomerate fluidization is a common mode of fluidization for ultrafine particles [19]. Chaouki et al. [15] first found that at superficial gas velocities in excess of 0.04 m/s, which were far above the minimum fluidization of the original particles, the aerogel particles rearranged themselves into clusters and then these new entities fluidized uniformly and homogeneously. The agglomeration of original ultrafine particles at gas velocities much larger than incipient buoyancy conditions of the primary particles have been reported by other researchers [12], [16]-[20], [55], especially for nano size particles. This is more plausible due to the fact that cohesive forces between nanoparticles significantly increase with decreasing particle size, thus nano size powders coalesce easier than micron-size particles [20]. Accordingly, gas fluidization of nanoparticles refers to fluidization of nanoparticle agglomerates [1]. In this regard, the fluidization behavior of agglomerates can be classified as agglomerate particulate fluidization (APF) and agglomerate bubbling fluidization (ABF).

Usually, powder systems with a very small primary particle size, nanosize, and a very low bulk density can achieve APF behavior. Figure 3.3shows the sketch of the fluidization behavior of APF particles. At very low gas velocities, preferential channeling generally happens in the bed, as exhibited in Figure 3.3a, but upon increasing the superficial gas velocity, since the channels are so weak, the particles beside the channels or at the top of the bed start to fluidize first, causing the channels to break and disappear. Then the fluidized region continuously expands until the whole

bed reorganizes itself into a new uniformly fluidizing state and agglomerate fluidization is thus set into action. During fluidization, neither a dead region, nor bubbles can be found [19], [20].

Stable agglomerates, which form from the constitutive nano size particles, have snowflake like configurations and smoothly fluidize at velocities much larger than the expected minimum fluidization velocity of primary particles. The agglomerates are very light and, hence, can be easily moved with gas, even in the turbulent gas wave. By increasing the agglomerates' size, they will have high terminal velocity. For gas velocities lower than the terminal velocity of the agglomerates, they will fall back and remain in the bed. Therefore, the uniform fluidized bed has a clear solid surface in a large window of gas velocities, as shown in Figure 3.3b. A high degree of mixing is the main consequence of such freely flowing behavior that is advantageous for heat and mass transfer efficiency in the bed compared to a fixed or a bubbling fluidized bed. At higher gas velocities, the fluidized bed smoothly expands and the bed surface becomes unclear due to the entrainment of small agglomerates, as shown in Figure 3.3c. At even much higher gas velocities, pneumatic transport regime begins and masses of agglomerates are carried away and the bed will finally be empty [19], [20], as shown in Figure 3.3d.

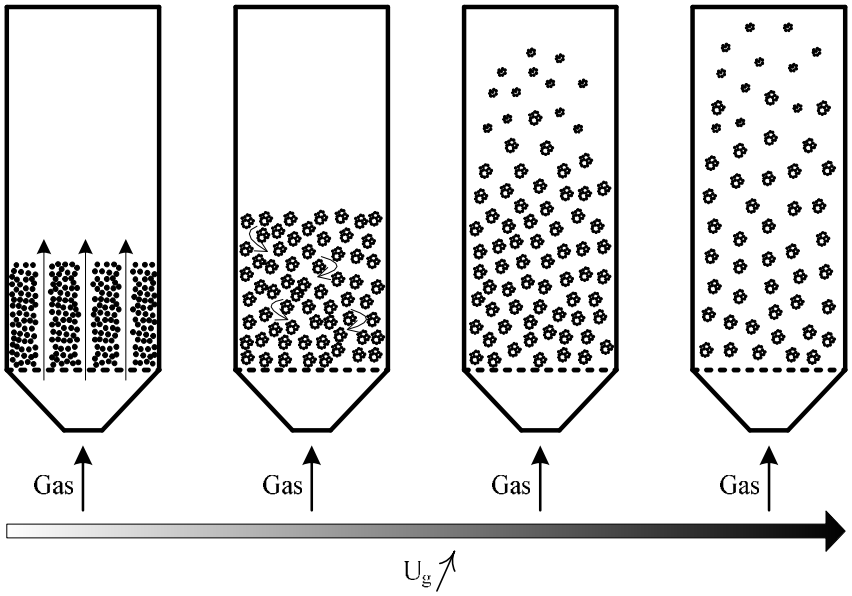

Figure 3.3: Sketch of fluidization of APF particles. Adapted from [19].

Considering the agglomerates as fluidizing particles in the bed, the expanded bed has a texture, which is very similar to the particulate fluidization in a liquid-solid system than to the bubbling fluidization in a gas-solid system. In this case, since agglomerates are so light, the density

difference between agglomerates and the surrounding gas is very close to that of liquid-solid surrounding gas is very close to that of liquid-solid systems. Therefore, nanoparticles having such homogeneous fluidization behavior are classified as agglomerate particulate fluidization, which is completely different from agglomerate bubbling fluidization [19], [20].

According to Chaouki et al. [15] and Wang et al. [19], the possibility of the occurrence of APF behavior is linked to the instability of jetting or channeling in the original fixed bed. In fact, the relative ease in dissipating channels certainly depends on the porosity of the fixed bed or in other words, on the particulate bed's bulk density. The possibility of this instability increases by decreasing the bulk density of the system and, hence, gives rise to the occurrence of agglomeration in the bed to be more feasible.

In the case of ABF, primary particles are larger (micron, submicron or nanosize) and have a higher bulk density compared with particles that show APF behavior. As a result, the particulate system is less able to easily break the channels and make the fluidizing mode a homogeneous one. Moreover, this prevents transforming the whole bed into a new system with a new effective dynamic size and apparent weight in which the hydrodynamic forces govern the gas-agglomerate interaction. In this situation, because of the partly local dominance of cohesion over the inertial force, the bed behaves like a system in between the classical group C behavior and the homogeneous fluidized bed. When these particles agglomerate during fluidization, winding channels are formed inside the bed, causing alternating fixed and fluidized regions, and accompanied by bubbling. Stratification phenomenon generally occurs for these agglomerates along the bed height, by the presence of a fixed bed or slow moving large agglomerates at the bottom, a fluidized region of smaller agglomerates in the middle and a dilute-phase region of even smaller agglomerates, including individual particles, further up in the fluidized bed [55], as depicted in Figure 3.4. Lowering the size and bulk density of primary particles are factors that can assist a bed with ABF behavior to become more similar to APF behavior.

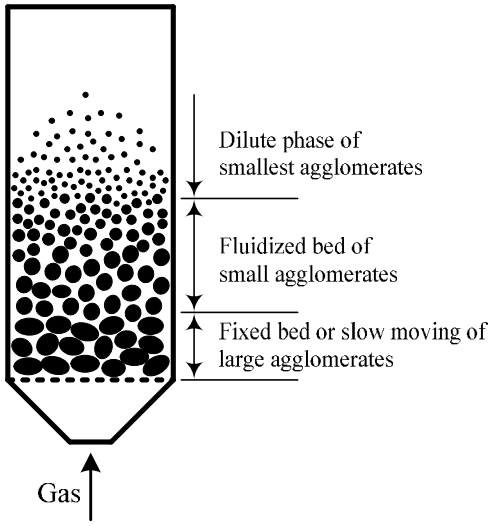

Figure 3.4: Stratification phenomenon in ABF agglomerate fluidized bed. Adapted from [55].

Considering the above-mentioned philosophy, APF agglomerates are characterized by smooth/particulate fluidization with a low minimum fluidization velocity, negligible elutriation of particles, very large bed expansion (up to five times the initial bed height), a well-defined gas-solid interface and minimal bubbling even at high superficial gas velocities. These agglomerates also have narrow agglomerate size distribution, which uniformly distribute throughout the bed. In contrast, ABF agglomerates have difficulties at low superficial gas velocities to be fluidized and show channels, slugs and spouting. Moreover, they exhibit low bed expansion (less than two times the initial bed height), high minimum fluidization velocity, large bubbles, considerable elutriation of particles, a poorly defined gas-solid interface and non-uniform distribution of agglomerates in the bed where the smaller ones appear to be fluidized in the upper part and the larger ones slowly move or are defluidized at the bottom of the bed [1], [9], [20], [22].

A summary of notable differences between ABF and APF agglomerates and their fluidization behaviors is presented in Table 3.1.

Table 3.1: Comparison of the fluidization behavior of APF and ABF [19], [20], [22]

	APF	ABF
Primary particle size	Nanoparticles	Micro, Submicron, Nanoparticles
Agglomerates	Loose, multi-stage, light in weight	Dense, single-stage, heavy in weight
Bulk density	Low (< 100 kg/m^3)	High (> 100 kg/m^3)
Fluidization characteristics	1. Low minimum fluidization velocity	1. High minimum fluidization velocity
	2. Bubbleless	2. With bubbles
	3. Bed expansion ratio is high	3. Bed expansion ratio is low
	4. Agglomerates are uniformly distributed in the bed	4. Large agglomerates are at the bottom of the bed, with small ones at the top
	5. Fluidized bed homogeneously expands, and the bed density decreases with increasing gas velocity	5. Bed expansion ratio and emulsion phase density do not change much with increasing gas velocity
	6. Negligible elutriation	6. Considerable elutriation

3.4.1.2 Agglomerate structure

The famous Geldart classification diagram predicts the fluidization behavior of powders based on the size of a single particle and the density difference between solids and fluid [49]. Although this classification has been of great value in facilitating the prediction of fluidization behavior for various particles, it suffers from some deficiencies. For example, when some fluidization operating parameters (pressure, temperature, gas properties, and effective gravitational acceleration) change, the hydrodynamic/interparticle force balance may change, this could result in a change in demarcation of particle groups [56]. Also, this simple classification cannot predict the transition from group B powders to A and even C as a result of inducing external interparticle forces to the particulate system reported by Seville and Clift [57], Rhodes et al. [58], and Shabanian et al. [59]. This deficiency can be compensated by the addition of a third axis corresponding to the magnitude of external interparticle forces into the original two dimensional Geldart's diagram. Furthermore, as pointed out in the case of agglomerate fluidization, the physical properties of primary particles cannot properly measure to predict their fluidization behavior [17], [20]. Instead, the hydrodynamic behavior of agglomerate fluidization is closely related to the properties of the agglomerates, including their size, density, structure, etc [19], [20]. In addition, various factors, such as capillary

and electrostatic attraction, geometry, and adsorption, influence the particle agglomeration process and, therefore, their fluidization. Among all these factors, agglomerate structure has vital importance for agglomerate fluidization of ultrafine powders [20].

Fluidization behavior of APF particles is quite different from normal group C powders and can be smoothly fluidized in a gas-solid particulate fluidization regime with a high bed expansion ratio and bubbleless behavior via micro-structure self agglomeration [20]. In fact, the main conditions to achieve such behavior for some nanoparticles are to have, first, a particulate system with very low bulk density and, next, fluidizing entities that are large enough for hydrodynamic forces to merely control the fluidization behavior and have strong adhesion forces in their own structures to withstand gas drag force [19]. It is rational to believe that low bulk density causes a loose agglomerate structure of bonded nanoparticles, which are strong enough to hold large amounts of gas [20].

Yao et al. [20] studied the fluidization properties of APF particles and stated that unique fluidization behavior of these powders is due to a multistage agglomerate (MSA) structure. At first, primary nanoparticles tend to arrange in a three dimensional chain-like structure, as shown in Figure 3.5, that can grow up to several hundred nanometers. These particles can be bonded together in two paths. In one path, the chain-like structure can be formed via coagulation of aerosol particles during the manufacturing process of nanoparticles. These bonds are very firm and are identified by sintered areas at the contact points between primary nanopowders. In the other way, chains form from the effect of the strong van der Waals force on such tiny particles. Chains resulting from the latter are not rigid enough and can be broken apart during fluidization, but will reform via dynamic agglomeration [21]. Overall, this three dimensional structure is the main reason for having low bulk density of these powders. Second, the three dimensional chain-like structures coalesce into larger agglomerates most of which are $1 - 100\ \mu m$ and named as simple agglomerates. Finally, many small simple agglomerates joined together and formed large agglomerates when fluidized. These large fluidized agglomerates were defined as complex agglomerates.

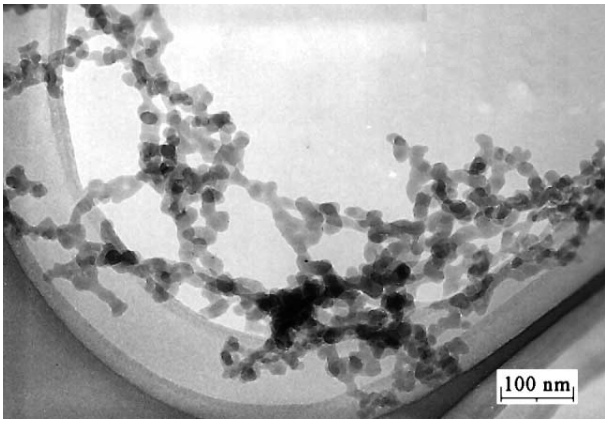

Figure 3.5: Transmission electron micrograph (TEM) of Aerosil 300, $dp = 7nm,\ \rho_b = 37.15\ kg/m^3$. Adapted from [20].

Complex agglomerates show dynamic behavior during fluidization by continuous breaking and reforming. This dynamic process is actually a balance between the separation and the congregation of simple agglomerates. Therefore, the fluidization process of APF particles can be considered as a self-rearranging process of simple agglomerates. This process finally reaches an equilibrium point at which a stable complex agglomerate size is achieved [20].

In brief, MSA structure is an important feature in the fluidization of ultrafine powders. Particles that show APF behaviors create a very porous structure in the bed due to the formation of many porous three dimensional chain-like structures and, hence, the strong adhesion forces between tiny particles are effectively diminished and the packed bed does not become compacted. Therefore, simple agglomerates are very light and have limited connecting points between each other, which allows the packed bed to be easily broken and fluidized, when gases pass through the channels [20].

However, Yao et al. [20] stated that ABF particles, unlike APF ones, possess a single-stage agglomerate (SSA) structure. Fine particles of this subclass tend to form drop-like agglomerates, such as simple agglomerates, whenever relative motion exists between particles, during packaging, handling, shipping, and storage. Generally, simple agglomerates of large size ABF particles are comprised of pile up structures, which are very unstable [55] compared to those of APF ones because of less cohesion forces that exist between the member particles. The presence of these structures rather than chain-like, which is responsible for having low bulk density in the particulate system, results in a compact nature for the packed bed. As a consequence, difficulties arise for the disintegration of channels in these beds. By decreasing the original particle size, a chain-like

structure begins to form, which not only increases the porosity of the agglomerate but also enhances their stability.

Similar to complex agglomerates of APF particles, when simple agglomerates of ABF powders are fluidized, they contribute to the dynamic process and their size and shape undergo successive changes. During fluidization, these simple agglomerates experience rearrangement with respect to their constitutive particles, or are broken apart into smaller agglomerates or even individual particles [55].

3.4.1.3 Simple classification criteria to discriminate between APF and ABF

Geldart et al. [60] presented an empirical classification criterion to predict the fluidization behavior of cohesive powders based on the so-called Hausner ratio, which is the ratio of the aerated ρ_b to tapped ρ_{tb} bulk density of the powder. According to this criterion, cohesive powders, which are difficult to fluidize, produce high Hausner ratios. It was found that powders having a ratio less than 1.25 appear to be fluidized like group A, while the fluidization behavior for powders with a ratio higher than 1.4 is clearly similar to the classical behavior of group C. Powders with the Hausner ratio between 1.25 and 1.4 possess characteristics of both A and C groups. Although, this criterion provides appreciable results for micron size fine particles, Esmaeili et al. [9] found that it cannot satisfactorily predict the APF and ABF fluidization behaviors of nano size particles.

It is believed that the bulk density of the particulate system has a crucial effect on the APF or ABF fluidization behavior of tiny particles [1], [15], [19], [20]. In this regard, according to their experimental results, Yao et al. [20] and Zhu et al. [1] reported that relatively small (<20 nm) nanoparticles with a bulk density less than 100 kg/m^3 are characterized as APF, while those with a larger size and higher bulk densities appear to behave as ABF. This criterion has been tested by many researchers and, fortunately, nearly all of them reported acceptable results with it.

In addition, Zhu et al. [1] showed that the classification criterion proposed by Romero and Johanson [61] for differentiating between homogeneous and bubbling fluidization of classical fluidized particles based on the value of a combination of dimensionless groups can substantially keep its predictive ability to distinguish whether agglomerates behave as APF or ABF. According to this classification, a bed can be smoothly fluidized if the product Π value of the combination of dimensionless groups, including the particle to fluid density ratio, the Reynolds and Froude

numbers at the minimum fluidization velocity, Re_{mf}, Fr_{mf}, and the bed height at the minimum fluidization velocity H_{mf} to column diameter D_{col} ratio, is less than 100, whereas the one with a higher product value appears to have bubbling fluidization behavior.

$$\Pi = Re_{mf}\, Fr_{mf}\, \frac{\rho_p - \rho_f}{\rho_f}\, \frac{H_{mf}}{D_{col}} < 100 \quad \text{smooth fluidization}$$

$$\Pi = Re_{mf}\, Fr_{mf}\, \frac{\rho_p - \rho_f}{\rho_f}\, \frac{H_{mf}}{D_{col}} > 100 \quad \text{bubbling fluidization}$$

Results of Zhu et al. [1] show that this criterion has very high sensitivity and is superior to simply exploiting the size and bulk density of powders to differentiate between APF and ABF behaviors of agglomerates. Table 3.2 exhibits the comparison of Romero and Johanson's criterion to that of Yao et al. [20] and Zhu et al. [1] for some ultrafine particles. It can be found from the table that for APF nanoparticles, the Π value is much less than 100, while for ABF nanoparticles, it is much higher than 100, which, in fact, shows the appreciable level of certainty of applying this criterion. Although the Romero and Johanson's criterion presents spectacular ability for the prediction of APF and ABF fluidization behavior of ultrafine powders, it was only verified for some nanoparticles [1], and more research is required to confirm this classification criterion is indeed applicable for all nanoparticles.

Table 3.2: Comparison of the predictive ability of Romero and Johanson's criterion to that of Yao et al. [20] and Zhu et al. [1] to distinguish the APF and ABF fluidization behavior of ultrafine particles. Adapted from [1]

Powder		Particle primary size (nm)	Particle bulk density (kg/m^3)	Π	Fluidization type
Trade no.	Material				
R974	SiO_2 Hydrophobic	12	33.24	0.008	APF
R104	SiO_2 Hydrophobic	12	62.90	0.197	APF
R106	SiO_2 Hydrophobic	7	41.49	0.008	APF
R972	SiO_2 Hydrophobic	16	39.00	0.010	APF
A300	SiO_2 Hydrophilic	7	39.00	1.19	APF
OX50	SiO_2 Hydrophilic	40	121.33	398	ABF
	TiO_2 Hydrophilic	21	128.29	927	ABF

3.5 Assisting methods

As discussed, the cohesive fine particles and nanopowders can be fluidized at superficial gas velocities greatly exceeding the minimum fluidization velocity of the primary particles in the form of agglomerates even without any assisting methods [62]. However, for the conventional gravity-driven fluidization of ultrafine particles, even in particulate fluidization, appreciable powder elutriation happens at the high superficial gas velocities required to fluidize the agglomerates. This loss of particles is probably the main reason that prevents the application of gas fluidization of fine particle agglomerates, especially nano-agglomerates, in industrial processes [1], [23], [63]. Moreover, although agglomeration makes it possible to fluidize ultrafine particles, it limits their potential because of the undesired decrease in specific surface area and increase in heat and mass resistances [11], [25], [34]. Therefore, it is preferable to improve the fluidization quality of these powders to work at lower gas velocities, have smaller agglomerates, and more homogeneous gas-solid flow to properly exploit their potential.

To this aim, various assisting methods have been developed. They include acoustic wave, mechanical vibration, magnetic/electric fields, the use of a centrifugal fluidized bed and a tapered fluidized bed, the addition of foreign particles, and the use of micro-jets as a secondary flow in the bed. The degree of fluidization enhancement achieved by applying these methods is evaluated by measuring some hydrodynamic parameters, such as the minimum fluidization velocity, bed pressure drop, bed expansion, agglomerate size, degree of mixing, bubble suppression and amount of powder elutriation, as indicators of fluidization quality. In this brief, these methods and their impacts on fluidization quality will be discussed.

3.5.1 Sound assisted fluidization

Various researchers have studied the phenomenology of beds of cohesive powders fluidized under the influence of acoustic fields of various sound pressure levels and frequencies. For the first time, by using an acoustic field generated by loudspeakers located at the bottom of the bed, Morse [64] found that fluidization of micron size particles under conditions where they possessed intense channeling or slugging was achieved provided an acoustic field with a frequency f_S in the range of 50 and 500 Hz, and a sound pressure level (SPL) larger than 100 dB.

Chirone et al. [65], [66] reported that the application of sound waves at a specific frequency, 120 Hz, and SPL in the range of 100–150, resulted in bubble free fluidization typical of group A powders in beds of cohesive particles of $1-45\ \mu m$ in size, as a consequence of the disaggregation of large agglomerates into smaller ones. In addition, it was noted that the high intensity sound could substantially reduce the entrainment of fine particles [65]. Extending their work, Russo et al. [67] showed that for beds of micron and submicron size particles, at a given SPL, fluidization behavior could only be improved within a certain range of sound frequencies (between 110 and 140 Hz) above/below which channeling occurred. The combined effects of gas velocity, sound frequency and pressure level on bubbling behavior were investigated by Levy et al. [68]. They found that at the natural frequency of the bed of micron size adhesive particles, high intensity sound waves caused reductions in both the minimum fluidization and minimum bubbling velocities. Also, an increase in SPL led to a decrease in bed expansion and an increase in bubble frequency. With the aid of an acoustic field having a low frequency and a high sound pressure level, Guo et al. [69] obtained a homogeneously fluidized bed for micron size fine powders.

Experimental studies to scrutinize the effect of sound wave excitation on particulate beds of nanoparticle agglomerates was started in 2004 by Zhu and coworkers [23]. They demonstrated that for SiO_2 nanoparticles with a primary particle size of 12 nm, channeling or slugging of the bed disappeared, minimum fluidization velocity was substantially reduced, and elutriation of nanoparticle agglomerates was to a large extent weakened at low frequency. By increasing the sound frequency, in the range of 200 – 600 Hz, bubbling fluidization occurred. Also, a minimum level of sound pressure, 115 dB, was required for sound waves to impact the fluidization behavior of nano-agglomerates [23]. Guo et al. [63], [70], [71] and Liu et al. [24] in a series of works showed that for particles in the range of micron, submicron, and nano size, smooth fluidization could be achieved with the help of an acoustic field at low frequencies due to disrupting large agglomerates. They noted that at a fixed sound pressure level, minimum fluidization of powders was reduced by increasing the sound frequency up to a critical value, while the reverse occurred at higher frequencies. A similar trend was observed for the agglomerate size under the effect of sound agitation for nano size particles [71]. In addition, it was found that at the same sound frequency, the quality of fluidization was significantly enhanced (agglomerate size and minimum fluidization decreased) with an increasing sound pressure level in the range of 100 – 103.4 [24], [69], [71].

Ammendola et al. [11], [25] characterized the fluidization behavior of two nanoparticles with APF and ABF behaviors under the application of acoustic fields of different SPLs and frequencies. It was noticed that either for the case of increasing SPL at a constant frequency or operating at an optimum frequency range and constant SPL, minimum fluidization velocity and agglomerate size decreased and bed pressure drop and bed expansion increased. Similar to Zhu et al. [23], they indicated that minimum SPL (SPL_{min}) was required to obtain good fluidization quality for both powders, while the SPL_{min} for APF nanoparticles was lower than for ABF ones. In addition, it was observed that the mixing of these nanopowders was intensified under the influence of sound waves from a completely segregated state in a non-assisted fluidized bed. Under the best conditions, mixing could be achieved up to microscale but not in smaller scales. A similar result was reported by Ammendola and Chirone [26] for blending two ABF nanoparticles when the bed was assisted by sound agitations. Unlike other works in the case of nano-agglomerates, Kaliyaperumal et al. [27] used a sound source under the distributor plate to study the effect of sound vibration on the fluidization behavior of nano and submicron particles. They found that acoustic waves brought about a decrease in minimum fluidization velocity and an increase in bed pressure drop and bed expansion for both kinds of particles. Similar to other studies, there was an optimum range for sound frequency and SPL_{min} was 110 dB, below which the impact of acoustic waves was insignificant. Furthermore, they observed that the best result for fluidization quality was obtained at a sound frequency close to the natural frequency of the bed.

Among the studies for enhancing the fluidization quality of fine/ultrafine powders by an acoustic field, Morse [64] and Kaliyaperumal et al. [27] positioned the sound source below the bed, while others located the source in the freeboard. Although Kaliyaperumal et al. [27] claimed that introducing acoustic waves from the bottom of the bed can lead to a more uniform agglomeration size due to absorbing more sound waves by larger agglomerates at the bottom of the bed and increasing the possibility of their disintegration, an appreciable difference between these two cases based on measurements of general fluidization parameters, such as minimum fluidization velocity, bed pressure drop, bed expansion, range of optimum sound frequency, etc., was not observed. In this regard, having a more comprehensive study, including the measurement of agglomerate size along the bed height, is required to determine whether introducing sound waves below the distributor can result in a more uniform agglomeration size in the bed or not.

There are three main issues that nearly all researchers have pointed out for sound assisted fluidization of fine/ultrafine powders. First, there is a minimum sound pressure level below which the acoustic field does not have any effect on the fluidization quality of fine powders. It can be explained as follows: since the acoustic oscillation strength is proportional to the sound pressure level [27], a minimum sound strength, or energy, is needed to initiate the fluidization or improve the fluidization quality. Secondly, by increasing the sound pressure level, since the energy given to the bed increases, the quality of the fluidization becomes better. However, at very high SPL, this might be reversed due to a higher possibility of collision between particles and agglomerates, which causes a large agglomerate size [71]. Lastly, the effect of sound frequency on fluidization quality is not monotonic and an optimum range or value has been determined for different powders most of which were close to the natural frequency of the particulate bed. The explanation of this trend is not straightforward; for low frequencies, the relative motion between smaller and larger agglomerates is practically absent and, hence, there is no break-up of agglomerates [11], [26]. In other words, a period of acoustic excitation is long with respect to the time needed for the flow of fluidizing gas to set up local channeling in the bed, which, after the initial perturbation, has recovered its adhesion [67]. For high frequencies, the sound waves are not able to propagate inside the bed [11], [26]. In fact, the sound absorption coefficient is proportional to the square of sound frequency as sound propagates through the particulate bed. Consequently, for high sound frequencies, most of the acoustic wave energy is absorbed by the upper part of the bed, if the sound source is located at the top, and reducing sound energy at the bed bottom fails to disrupt large agglomerates at the bottom of the bed and, hence, fluidization quality decreases [71]. If the source is located at the bottom of the bed, more sound energy would be absorbed by large agglomerates at the bottom and particles at the top of the bed would experience less excitation, which has a negative effect on the fluidization quality [27].

3.5.2 Vibro-fluidization

Similar to sound assisted fluidization, a considerable number of studies have been devoted to vibro-fluidization of fine/ultrafine particles. Cohesive micron and submicron powders have been successfully fluidized with the aid of mechanical vibration.

Employing a vibro-fluidized bed, Mori et al. [72] found that a wide range of fine particles down to the submicron level could be fluidized at relatively low gas velocities. According to fluidizability

of fine powders under the effect of vertical agitation, they classified group C fine particles into three subgroups: easily fluidized with large bed expansion; fluidizing powders under bubbling conditions with controllable entrainment; and non-fluidized powders even using the vibro-fluidized bed. Dutta and Dullea [14] used an external vibration and observed that the fluidization quality of micron size fine particles improved by a simultaneous increase in bed pressure drop and bed expansion accompanied by a decrease in elutriation loss. Marring et al. [73] and Noda et al. [74] reported that fluidization of cohesive powders was achieved when the bed was assisted by mechanical vibration. Through in situ agglomerate size measurement using a pulsed laser coupled with a CCD camera, Wank et al. [75] obtained that the agglomerate size of Boron Nitride powders, $5 - 11\ \mu m$, decreased by increasing the force applied to the system due to vibration.

Mawatari et al. [76] stated that increasing the vibration intensity, which is defined as vibrational acceleration to gravitational acceleration, $\Gamma = A_m \frac{(2\pi f_V)}{g}$, where the A_m is the amplitude of vibration and f_V is the frequency of vibration, for group C micron size powders led to a decrease in minimum fluidization velocity and the elimination of channels and cracks, while the bed pressure drop remained fairly constant for different vibration intensities. Comprehensive studies on the fluidization of fine particles under the application of vertical vibration were carried out by Xu et al. [77] and Xu and Zhu [47]. For a variety of micron and submicron solids, employing vibration reduced both the agglomerate size and the degree of stratification of agglomerates throughout the whole bed. Unlike Wank et al. [75], they found that agglomerate size decreased with vibration intensity up to a critical value above which the reverse trend happened. Somewhat similar results to those of Xu and Zhu [47] were reported by Valverde and Castellanos [78]. They noted that during fluidization of micron size cohesive powders assisted by vertical vibration, the homogeneous fluidization regime enlarged by increasing the vibration intensity to a critical value. With further increase, visible bubbles were developed in the bed with a similar physical mechanism for bubble formation to non-vibrated fluidized beds. Accordingly, they concluded that although vibration can reduce particle agglomeration to have APF behavior for a particulate bed of adhesive particles, agglomeration at some minimum level is required for APF behavior.

Nam et al. [32] performed the first study concerning the effect of vibration on the fluidization quality of nanoparticle agglomerates. They observed that silica nanopowders could be smoothly fluidized in the form of stable, very porous agglomerates with insignificant elutriation in the range

of vibration frequency between 30–200 Hz. It was shown that vibro-agitation was only initially required to disrupt interparticle networks in the particulate system after which aeration was sufficient to sustain the bed in a fluidized and expanded state for a long period of time. A similar result was reported by Zhang and Zhao [79] employing a horizontal vibration system for a nanoparticle fluidized bed. Nam et al. [32] also found that albeit a vibro-fluidized bed could significantly improve the fluidization quality of nanoparticles, processing the received materials by mechanical vibration was not feasible and large/hard agglomerates that existed in such powders sank to the bottom of the bed and did not break at all. Moreover, their experimental results revealed only a weak effect of vibrational parameters on the bed pressure drop and minimum fluidization velocity. Furthermore, the authors showed that nanofluidization assisted by external vibration could quickly mix nanopowders up to microscale. It was demonstrated by Hakim et al. [21] that decreasing interparticle (capillary and electrostatic) forces enhanced the fluidization quality of nanoparticles via decreasing the minimum fluidization velocity and agglomerate size. Similar results were observed when the nanoparticulate bed was subjected to mechanical vibration.

By exploiting the same experimental set-up, which was used by Nam et al. [32], Harris [80] could enhance the fluidization quality of APF nanopowders at relatively low frequencies, 16–34 Hz. For different nanomaterials Yang et al. [33] found that at certain vibration amplitudes, by increasing the vibration frequency, which was equal to an increase in vibration intensity, the minimum fluidization velocity decreased and bed pressure drop and bed expansion increased. They also showed that by employing the vibration excitation the n exponent in the Richardson-Zaki equation [81], which is an index of the degree of particulate fluidization for cohesive particles, increased by increasing the vibration frequency. Wang et al. [82] reported that for a bed of SiO_2 nanoparticles under the influence of vibration, there was a critical vibration frequency corresponding to a minimum agglomerate size. Most recently, Kaliyaperumal et al. [83] investigated the fluidization behavior of nano and submicron materials in a mechanically vibrated fluidized bed and found that the fluidization qualities of both powders were enhanced under those conditions.

Although all researchers believed that employing vibro-fluidized beds enhanced the fluidization quality of fine/ultrafine particles of group C powders, complete consensus regarding the effect of vibration on all fluidization parameters has not been achieved yet. For example, some authors reported that pressure drop increased as the vibration intensity increased [33], [82], [84], [85], some did not observe any change [32, 76], and some found that it decreased with vibration intensity [86].

Concerning the minimum fluidization velocity, Nam et al. [32] did not observe appreciable variation by vibration intensity, while some others found that it decreased as the vibration intensity increased [74], [76], [84], [86]. Moreover, there is no clear agreement on the effect of vibration strength on agglomerate size. Wank et al. [75] reported that the agglomerate size decreased up to $\Gamma = 5.5$, while Xu and Zhu [47] and Wang et al. [82] found there was a critical value of vibration intensity or frequency, much smaller than $\Gamma = 5.5$, above that agglomerate size increased rather than decreased. Therefore, though there is no doubt that vibro-fluidization is one of the useful assisting techniques for improving the fluidization quality of fine/ultrafine particles, a more comprehensive study of this method is required to clarify the exact influence of vibrational parameters, namely vibration amplitude and frequency, on the fluidization behavior of these powders.

3.5.3 Magnetically assisted fluidization

The application of an oscillating magnetic field is another beneficial assisting method to enhance the fluidization of fine/ultrafine particles. This technique has been generally implemented via the fluidization of either magnetic particles or a mixture of magnetic and nonmagnetic particles, under the exposure of an external magnetic field, which has been usually generated by a DC current [32], [87]-[91]. For the latter, both very fine and large magnetic particles have been used in experimental works. Fine magnets often create chains along the field, while large ones, which have a larger size and/or density than those of fine bed materials, do not move along with fluidized particles and mainly remain close to the gas distributor.

Zhu and Li [88], [89] began employing this technique to improve the fluidization quality of group C powders. They studied the behavior of gas-solid fluidized beds with the mixture of ferro and non-ferro-magnetic powders both in the range of type C particles in an axial uniform magnetic field. For the mixture material, the gas-solid fluidized bed was operating in agglomerate bubbling fluidization mode and, hence, they evaluated the impact of the magnetic field on the fluidization behavior through the measurement of bubble size. It was found that bubble size was highly dependent on magnetic field intensity, frequency, and the fraction of magnetic particles. At a certain field frequency, bubble size decreased as field intensity increased. Also, at a given magnetic field strength, bubble size increased by decreasing field frequency or fraction of magnets in the bed. According to their experimental observations, they believed that the magnetic field could

affect the fluidization of a fine particulate bed via the following mechanism: magnetic particles reorganized themselves to form a type of chain structure along magnetic field lines and this chain was the main reason for improving the fluidization quality for two reasons: first, the chain could easily penetrate the bubble from the top and break it due to a high ratio of gravitational force to drag force; second, the chain could restrain channeling. They noticed that the chain structures had two different actions to make the cohesive bed fluidized. Those chain structures close to the channels tried to eliminate them and increase the resistance of gas passing through the channel when the right magnetic field intensity was applied and those chains that were in the particulate body tended to disintegrate the cake structure into smaller agglomerates leading to a decrease in the resistance of the gas passing through these agglomerates. In this way the completely defluidized bed was transformed into a fluidized bed with small bubbles by applying the optimum field intensity and frequency. Similarly, Lu and Li [92] reported that the fluidization quality of the mixture of magnetic and non-magnetic cohesive type C particles was promoted with the help of a transverse rotating magnetic field. They found that magnets displayed four kinds of motions in a rotating magnetic field, which included vibrating, forming rotating chains, moving around the walls, and keeping still. As a result of these motions in the magnetic field, the channel could be eliminated, bubbles broken, and agglomerates disintegrated.

The first study to investigate the effect of an oscillating magnetic field on the fluidization of nanoparticle agglomerates was carried out by Yu et al. [30]. In their experiments large and heavy magnetic particles were used, which could not be fluidized by the action of gas drag force and remained rotating just above the gas distributor. They observed that the movement of magnetic particles, excited by an external magnetic field, greatly improved the fluidization of nanoagglomerates by disrupting large agglomerates, preventing the formation of bubbles, reducing the minimum fluidization velocity, and elutriation. By using this technique they could easily and smoothly fluidize a mixture of soft (smaller than $500\,\mu m$) and hard (larger than $500\,\mu m$) agglomerates of silica nanoparticles, indicating the appropriateness of this approach for the processing of as-received powders. Also, it was noted that mixing two different species of nanoparticles occurred on the microscale rather than the nanoscale when using magnetically assisted nanofluidization. According to Yu et al. [30], an oscillating magnetic field together with large magnets at the bottom of the bed could enhance nanoparticle fluidization in two ways: the disruption of large agglomerates into smaller ones, and transferring kinetic energy generated by

magnetic excitation to the agglomerates due to collisions. Furthermore, it was found that the fluidization of nanopowders was considerably influenced by the mass ratio of magnetic particles, intensity, and frequency of the magnetic field.

Quevedo et al. [93] employed both vibration and magnetic assistances for the fluidization of APF and ABF nanoparticles and noted that although magnetically assisted fluidization promoted the fluidization of ABF nanopowders, a combination of these methods could result in much better fluidization behavior. This might be plausible due the fact that by using the vibration, the contact points between particles/agglomerates and the wall of the bed were broken [21] and the detached entities then participated in the circulation path in the bed and fell down to the bed bottom, in the agglomerate breaking region using coarse and dense magnets, all causing greater fluidization quality. However, in the case of a single magnetic aid, it could not transmit effectively in the whole bed [35]. Zeng et al. [31], [94] reported that adding hard to fluidize nanoparticles in the bed of APF behavior, resulted in the reduction of a homogeneous operating velocity range which could be compensated with the help of an external magnetic field with the correct intensity and large heavy magnetic particles stirring at the bed bottom. Recently, Zhou et al. [95] studied the behavior of Fe_3O_4 magnetic nanoparticles in a magnetically assisted fluidized bed.

Although the magnetic nanoparticle could not be fluidized in a conventional fluidized bed, good fluidization was obtained by the addition of either a coarse steel sphere or other nonmagnetic nanopowders to the bed under the application of the magnetic field. The former acted as an agglomerate breaker and the latter as glidants to make the magnetic agglomerates more fragile, both resulted in better nanofluidization behavior.

3.5.4 Electrofluidization

The investigation of the effect of an electric field on the fluidization behavior of nanoparticles has only started in recent years and research in this field is still scarce. Kashyap et al. [96], [97] studied the influence of a horizontal electric field on a bed of 10 nm silica nanopowders in a rectangular fluidized bed. The main observation reported in their work was that the bed expansion was drastically reduced on the application of an electric field. They explained it as the result of the addition of a downward acting electric force to the gravity force. Although this result was not appropriate in the point of gas-solid contact, the authors believed that this technique would be useful for decreasing elutriation from the fluidized bed. Similarly, Valverde et al. [98] and

Quintanilla et al. [99] found that bed expansion was hindered for 12 nm silica nanoparticles when the bed was subjected to a horizontal electric field. From the analysis of agglomerate trajectories, Valverde et al. [98] estimated the electric charge per agglomerate and from that value, they concluded that the electrostatic force between agglomerates, which was caused by charges, was negligible as compared to van der Waals force. Thus, it implied that the charge of nanoparticles in the bed did not affect the agglomerate size and structure. Instead, the electric field led to pushing the agglomerates toward the lateral wall of the bed, resulting in bed compaction and the appearance of a highly heterogeneous fluidization state.

Motivated by the fact that applications of an electric field and vertical vibration can reduce the entrainment and enhance the bed expansion, respectively, Quintanilla et al. [99] studied the simultaneous effect of these fields on nanofluidization. It was found that when both techniques were applied, those conflicting effects could be practically compensated. At small amplitude vertical vibration, for which there was no bubble stimulation due to vibration, a net bed collapse from the electric field and bed enlargement from the vibration could be obtained by linear superposition of the separate effects of both fields. At large vibration amplitude and low frequencies, which aroused bubbles by vibration, the horizontal component of agglomerate flow caused by the electric field acted against bubble formation, thus, favoring bed expansion. Lepek et al. [29] found that a nonuniform alternating electric field along the bed height, while field strength was high at the bottom and very weak at the free surface, enhanced the fluidization of nanoparticle bed. The technique was suitable to achieve highly expanded fluidization for a particulate bed of unsieved nanopowders for which stratification is a common phenomenon in a conventional fluidized bed. They thought that the quality of nanofluidization was promoted in two ways. On the one hand, larger agglomerates that sank to the bottom of the bed were strongly agitated by a high intensity electric field and resulted in the destabilization of gas channels close to the gas distributor to homogenize the gas distribution in the bed and, on the other hand, since small agglomerates at the top of the bed were weakly affected by the field, excessive elutriation was avoided.

Although the above-mentioned studies tried to elucidate the influence of this method on the fluidization behavior of ultrafine powders, more study is required to completely clarify unknown points of this technique.

3.5.5 Use of a centrifugal fluidized bed

Centrifugal fluidized beds (CFB) have many advantages over conventional fluidized beds, such as increasing the incipient fluidization velocity to hinder the onset of the unstable bubbling flow regime, preventing the elutriation of particles at relatively high gas velocities by controlling the vessel rotational speed, operating in a wide range of gas velocities leading to a much higher gas throughput per unit area of distributor, high contact efficiency between gas and solid, a smaller footprint, a thin bed resulting in either no bubbles or very tiny ones, very little gas bypassing, a shorter processing time, and a small space requirement [2], [100]-[103]. Due to these benefits, employing CFB devices has been proposed by some researchers to enhance the fluidization quality of fine/ultrafine powders.

Qian et al. [7], [101] theoretically stated that under a centrifugal force, particles that belong to group C can shift to group A. To confirm the theoretical study, they showed that C powders (7 μm alumina) could fluidize in a CFB operating at a sufficiently high rotating speed to shift them into group A or B. Matsuda et al. [102], [104] found that ultrafine particles could be fluidized while forming agglomerates under high rotational acceleration G. By increasing G, the agglomerate size observed near the distributor became smaller.

Matsude et al. [34] fluidized agglomerates of nanoparticles with a primary particle size of 7 nm. They proposed an interesting energy balance model, which predicted a reduction in agglomerate size at high centrifugal forces. However, the agglomerate size to validate the model was calculated from the data on minimum fluidization velocity and using correlations of Wen and Yu [105], rather than by direct measurements. Employing APF and ABF nanoparticles, Quevedo et al. [2] and Nakamura and Watano [35] observed that the minimum fluidization velocities of nanopowders increased linearly as the centrifugal acceleration increased. However, Nakamura and Watano [35] found that the bed expansion decreased with increasing G. Also, based on measured bed expansion data and using the modified Richardson-Zaki equation coupled with fractal analysis they calculated the agglomerate size and density under different gravitational accelerations and reported that the agglomerate size decreased and its density increased by centrifugal acceleration. According to their calculations, agglomerate size and density were smaller and larger, respectively, than those found in conventional or vibration and magnetically assisted fluidized beds. Furthermore, they found that similar to results obtained for sound, vibration, and magnetic assisted nanofluidization, when two

different species of nanoparticles were fluidized in the CFB, a good degree of mixing occurred on the microscale, rather than on the nanoscale.

3.5.6 Use of a tapered fluidized bed

Operation in a tapered fluidized bed tends to simultaneously fluidize larger agglomerates of fine/ultrafine particles at the bottom of the bed and smaller ones at the top while preventing entrainment of smaller agglomerates from the top of the bed [36], [62]. Venkatesh et al. [36] showed that using a conical fluidized bed, with an expanding cross section along the gas flow direction, for micron size fine particles at high gas velocities led to a completely mixed fluidization with no segregation, while those particles could not be inherently fluidized in a conventional fluidized bed. Also, Tong et al. [106] employed a tapered fluidized bed to fluidize various ultrafine particles and found the bed was more effective than a conventional cylindrical one.

3.5.7 Addition of foreign particles

The different approaches that have been discussed vary in efficiency and from a practical perspective some of them might be difficult to implement for a large scale industrial application, whereas others might not be economically feasible except for selected applications [107]. Employing external mechanical vibration and an oscillating magnetic field are some examples for this discussion [72], [107]. Also, the widely reported sound assisting method is quite successful but like the vibration and magnetic field, it is energy intensive and brings about high elutriation rates of particulate bed materials [29], [34], [107]. The addition of foreign particles to the bed is another assisting approach, which has some advantageous over other techniques, such as no need to change the column design or obtain additional equipment or devices and studies carried out on this subject can cover a wide range of particles in terms of density, size, and shape, which means different fluidization behaviors could be observed with the mixture of powders [107]-[110].

Brereton et al. [37] and Li et al. [111] investigated the possibility of operating pure silica aerogel ($dp < 20\ \mu m$) in a circulating fluidized bed with an L-valve in the external recycle section. They found that smooth circulation of pure aerogel agglomerates was not possible due to gas and solid being unable to pass through the valve. However, by adding the correct amounts of granulate materials (Ottawa sand, $d_p = 149\ \mu m$, with sand to aerogel volume ratio ~ 4:1 and alumina particle, $d_p = 64\ \mu m$, with alumina to aerogel volume ratio ~ 1:4), much of the agglomeration was

suppressed and a mixture with free flowing characteristics, ideal for contact in a circulating fluidized bed, was obtained.

In parallel with these studies, a perfectly homogeneous fluidization of Ni/SiO_2 aerogel blended with a sufficient amount of alumina particles ($d_p = 60\ \mu m$) was reported by Klvana et al. [12] and Lauga et al. [38]. Observation using the optical microscope revealed that below the appropriate level of alumina in the admixture, in addition to aerogel particles that stuck to alumina grains, there were some aerogel particles still free, which resulted in poor fluidization behavior for the mixture. However, for mixtures having the right quantity of alumina, since there was enough available alumina surface area to collect the whole aerogel agglomerates, all of them surrounded alumina particles giving birth to hybrid particles. Considering this concept, Lauga et al. [38] could explain the experimental findings of Brereton et al. [37]. They attributed different added volumes of the two different support particles to their equal apparent available surface for catching all aerogel particles in the bed. Moreover, the authors recommended that appropriate support for improving the fluidization behavior of cohesive materials could be selected in light of the following conditions: (i) The smaller the support particles, the smaller amount of these particles are required to collect the cohesive particles. However, the resultant hybrid particles should be large enough to exhibit group A characteristics. (ii) The Liftshitz-van der Waals coefficient has to be close enough to that of cohesive particlesto promote good adhesion between the two types of particles. Later on, Zhou and Li [112] proposed a particle agglomeration number *Ae* based on the force analysis between the agglomerate body and its outer-most particle. Through the addition of a number of powders to the primary cohesive bed of SiC particles, they found that powders with $Ae \leq 40{,}000$ could be fluidized, but those with $Ae > 40{,}000$ could not. Using this strategy they were able to find the optimum amount of addition particles in the mixture to decrease the interparticle cohesive force in the original bed and improve its fluidization behavior. Ajbar et al. [110] reported that the addition of small proportions of group A particles could diminish the cohesiveness of type C powders and result in a more uniform fluidization.

The technique of foreign particle addition has received relatively a little attention for the fluidization of nanoparticle materials. In 1999, Li et al. [113] observed the same phenomenon as that of Brereton et al. [37] and Li et al. [111] when they used a mixture of $CaCO_3$ nanoparticle ($d_p = 90\ nm$) with FCC particles ($d_p = 54\ \mu m$) in a circulating fluidized bed. Song et al. [109]

experimentally studied the fluidization behaviors of SiO_2 and TiO_2 nanoparticles mixed with three different size ranges and various quantities of coarse particles of FCC, ordinary Al_2O_3 and heat-resistant Al_2O_3. They found that the fluidization behavior of the mixture significantly improved with much less nanoparticle elutriation and the best results were obtained using the $60 - 85\ \mu m$ size range that corresponds to group A classification, irrespective of the material. Similarly, enhancement in the fluidization of the hydrophilic Aerosil 200 nanoparticulate bed blended with sand particles of group A powders was reported by Ajbar et al. [107]. The authors also noted that the particle mixing approach led to much less bed entrainment compared to the sound assisting method. It is worth mentioning that results of two later studies confirm the procedure suggested by Laugu et al. [38] through which the addition of external particles enhances the fluidization quality of cohesive powders.

3.5.8 Use of micro-jets as a secondary flow in the bed

Most recently, Quevedo et al. [22] developed a new technique by which the fluidization of nanoparticle agglomerates could be greatly enhanced. It was experimentally shown that the fluidization behavior of both APF and ABF nanopowders was significantly improved by introducing a secondary gas flow to the bed, using a downward pointing micronozel in the form of a high velocity (hundreds of meters per second) microjet. For example, APF nanopowders expanded up to 50 times the initial bed height and ABF nanoparticles were changed to APF type, showing a bed expansion as much as 5 times the original bed height with the absence of bubbles. Additionally, it was found that the microjet resulted in the breakup of large agglomerates, hindering channeling, curtailing bubbling, and promoting liquid-like fluidization behavior. Moreover, the fluidization of both types of nanoparticles were accompanied by a reduction in the minimum fluidization velocity and an increase in the normalized bed pressure drop, which are proof of better fluidization quality.

Quevedo et al. [22] also studied the mixing characteristics of different nanoparticle species under the application of a microjet in the bed. More interestingly, unlike other assisting methods, which under the best conditions could achieve microscale nanomixtures, they observed that the mixing of nanoparticle species occurred on the nanoscale. By implementing discrete particle modeling to simulate the fluidization system employed by Quevedo et al. [22], van Ommen et al. [5] concluded that the enhancement of nanofluidization quality by microjet was caused by the size reduction of

agglomerates through agglomerate-agglomerate collisions in the bed. By fluidizing nanopowders in cylindrical beds with different sizes, when beds were assisted by microjets, Quevedo et al. [22] could reach similar results regarding the improvement of fluidization behavior of nanomaterials with this assisting method and, hence, confirm the easy scale-up of the technique.

The use of the microjet compared to other assisting techniques has the following advantages: it is efficient, simple to use, does not need expensive equipment nor foreign materials added to the bed, uses less energy, is easily scaled-up and can be used to blend different species of nanoparticles on the nanoscale to form nanocomposities [4]. These priorities lead to a high potential of utilization of this method for fine or nanoparticle fluidization for their various industrial applications in the near future.

Finally, to have a quick review of different assisting methods for improving the fluidization quality of fine/ultrafine particles, Table 3.3 provides a summary of the advantages and limits of these approaches.

Table 3.3: Summary of advantages and limits of different assisting methods for improving the fluidization quality of fine/ultrafine particles

Method	Advantageous	Limits
Acoustic wave	Channeling and slugging are eliminated. Minimum fluidization velocity decreases. Agglomerate size decreases. Elutriation rate decreases.	It is energy intensive. Decrease in elutriation loss is not appreciable. Operation outside the optimal ranges of SPL and f_s, not only won't improve the fluidization quality, but also deteriorates it. Operating problem with the presence of sound with high SPL. Mixing of different nanoparticles could be achieved up to microscale.
Vibro-fluidization	Channeling and slugging are eliminated. Bed pressure drop increases. Minimum fluidization velocity decreases. Agglomerate size decreases. Elutriation rate decreases.	It is energy intensive. Decrease in elutriation loss is not appreciable. Bubbles would arise at high vibration intensity. Processing of as-received fine/ultrafine particles by this approach is not feasible. Mixing of different nanoparticles could be achieved up to microscale.
Magnetically assisted fluidization	Fluidization of completely defluidized bed would be feasible. Minimum fluidization velocity decreases. Size of bubbles in bubbling fluidization regime of some micron size fine particles decreases. Elutriation rate decreases.	It is energy intensive. Decrease in elutriation loss is not appreciable. when large and dense magnets are used: The magnets mostly present at the bed bottom and the magnetic aid cannot transmit effectively in the whole bed.

		when ferro-magnetic particles with size and density similar/close to those of bed material are used: The magnets act as foreign particles and acceptance of these particles in the process is the main question.
Electrofluidization	Bed expansion increases in the case of nonuniform alternating electric field along the bed height. Elutriation rate decreases.	Bed expansion decreases and highly heterogeneous fluidized bed appears in the case of horizontal electric field.
The use of a centrifugal fluidized bed	Minimum fluidization velocity decreases. Agglomerate size decreases, smaller than those attainable by assisting the bed with acoustic, magnetic and electric fields, and mechanical vibration. Elutriation rate decreases.	Bed expansion decreases. Mixing of different nanoparticles could be achieved up to microscale. Powerful compressor is needed to supply the required fluidizing medium. Attrition is a harmful problem for this type of fluidized beds.
The use of a tapered fluidized bed	Simultaneously fluidizes large agglomerates at the bed bottom and small agglomerates at the top of the bed. Elutriation of small agglomerates is hindered.	Not reported.
Additional of foreign particles	There is no need to change the column design or obtain additional equipment. Elutriation rate decreases. Makes circulating fluidization mode of ultrafine particle agglomerates possible.	Acceptance of the presence of foreign particles in the process is under the question.
The use of micro-jet as secondary flow	Channeling is hindered. Bed pressure drop increases. Minimum fluidization velocity decreases. Bed expansion increases, much higher than those obtained by other techniques. Agglomerate size decreases. The fluidization characteristics of ABF powders change into APF ones.	Not reported.

	Mixing of different nanoparticles could be achieved up to nanoscale. It is easy to scale-up.

3.6 Experimental techniques for measuring agglomerate size

Fine/ultrafine powders tend to form agglomerates when exposed to a gas flow greatly exceeding the minimum fluidization conditions of primary particles in a gas-solid fluidized bed. Thus, agglomerates are the entities that fluidized in the bed, not the individual particles, and hence it is essential to measure the size, shape, and density of the agglomerates under different operating conditions to increase understanding of fluidization behavior of these powders [75]. Among all properties of agglomerates, their mean size, which depends on the physical properties and chemical composition of the primary particles, as well as the presence of external cohesive forces due to electrostatic effects, liquid bridge, etc., is an important factor in determining the quality of fluidization, that is, whether the fine/ultrafine particle will fluidize as APF or ABF [114], and for the performance of heat and mass transfers since particle agglomeration reduces the available fluid-solid contact area [82]. Due to the fragile nature of the agglomerates and the time-dependent process of dynamic equilibrium, the measurement of the agglomerate size poses significant challenges for the development of sampling method [47], [82].

In past years, several works have focused on determining the size of fine/ultrafine particle agglomerates. Pacek and Nienow [18] developed a technique called the “freezing method”, in which the agglomerates were frozen by spraying a binder solution of wax from the top of the bed before sampling to facilitate analysis by scanning electron microscopy (SEM). SEM analysis was also applied to agglomerates sampled directly from the fluidized bed by adhesive tape [17], [20] or aspiration [32]. In addition, agglomerates of fine particles were extracted from the bed by adhesion to a sheet of paper [41], [115]. The principal issue concerning these approaches is that the agglomerates, especially nanoparticles, are very porous and fragile, and might be broken during their removal from the bed and/or during sampling preparation for the SEM analysis [32]. Thus, intrusiveness, which might affect the agglomerate properties, is the main difficulty for these techniques.

To avoid the serious problem of sample deformation during SEM measurements, another technique, called Particle/Droplet Image Analysis (PDIA) for the direct and dynamic measurement of the agglomerate size in the splash zone of the fluidized bed was developed [1], [21], [30], [32],

[75], [116], [117]. In this technique a laser is used to illuminate the free board and the region close to the upper surface of the solid bed from behind, and shadow images of agglomerates are taken with a specially calibrated camera. Although this technique has the advantage of being dynamic and noninvasive, it is not known whether the mean agglomerate size measured in the lean section of the fluidized bed is actually representative of the mean agglomerate size in the bed itself [4]. In other words, the efficiency of the technique can be limited by stratification of agglomerates due to size dispersion, which is a common phenomenon for ABF particles, and the agglomerate samples recorded in the images close to the bed free surface could be biased towards smaller sizes [118].

An obvious limitation for the above-mentioned techniques is that they are only capable of measuring the agglomerate size in the top bed. To compensate for the deficiency of these methods, Xu and Zhu [47] developed an "online sampling technique", as depicted in Figure 3.6, which, it was claimed, is capable of sampling the agglomerates, without disrupting their sizes or structures from any parts of the bed (top, middle or bottom bed). The agglomerates are sampled in situ using a sampling idle from the top of the bed without stopping the fluidizing gas. For sampling the agglomerates in the upper layer of the bed, the idle is directly employed to pick up the agglomerates. To sample the agglomerates in the middle and bottom of the bed, an intensity-controllable vacuum is used to remove all the particulate materials above the sampling plane before taking samples with the sampling idle. After sampling, the properties of the agglomerates can be measured using SEM. To keep in mind the time-dependent process of dynamic equilibrium, agglomerate samples should be taken after a certain length of time when the bed is stabilized regarding the agglomerate size and shape under certain fluidization conditions. Although this is a promising technique for determining the agglomerate size at different levels of the bed, its result will not be reliable if particular care is not be taken during sampling removal by idle or discharging the above layers of the sampling plane by vacuum.

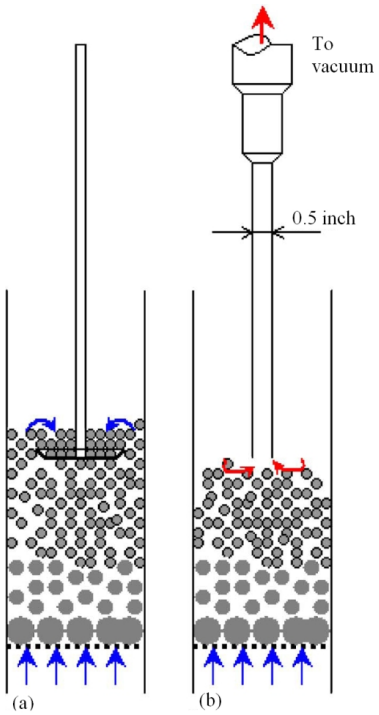

Figure 3.6: Diagram of the "online sampling technique": (a) sampling the agglomerates from the top layer of the bed; (b) removing the agglomerates from the upper layer by vacuum prior to sampling for the agglomerates on the lower layer. Adapted from [47].

As a more efficient technique, the X-ray imaging method was developed to allow fluidized beds to be studied at length scales down to 400 nm and temporal resolutions of 1ms, with the advantage of studying the bulk of the fluidized bed in an in situ, nonintrusive, and dynamic manner [54], [119], [120]. Unlike other available imaging methods, which are usually surface techniques, X-ray microtomography imaging allows us to see through the sample and reconstruct a three dimensional internal structure of the sample. Considering this ability, the authors showed that, by using this approach, it is feasible to dynamically and nondestructively determine the agglomerate size, density, and porosity, inter-agglomerate voidage, and local solid fraction, which are nearly all required information for uncovering the physics behind the fine/ultrafine particle fluidization. In addition, using high resolution X-ray imaging and the microtomography technique, changes in the agglomerate structure and density with different operating conditions can be easily seen. However, even though the technique seems to be a powerful one on the subject, it needs further development in order to respond to the low X-ray energies required for some fine powder samples.

Most recently, Quevedo and Pfeffer [114] introduced a new method through which in situ agglomerate size measurements and the imaging of fluidized nanoagglomerates were achieved by

reducing the electric charge in the bed and using Focused Beam Reflectance Measurement (FBRM) and Particle Vision Measurement (PVM) probes. The probes successfully characterized the number weighted and volume weighted agglomerate size distributions for both APF and ABP type nanoparticles. The FBRM data and PVM images showed that the probes were capable of differentiating between different types of nanoparticles (APF and ABF) and could also evaluate the effects of the microjet assisting method on the agglomerate concentration and size. Although this is a useful approach for measuring the agglomerate size and concentration, it suffers from the interference of the probes (19 and 25 mm I.D.) with the flow around them.

3.7 Models for the prediction of agglomerate size

Due to high importance of agglomerate size in the fluidization of fine/ultrafine particles, several models have been proposed to predict this parameter on the basis of the physical understanding of particle agglomeration dynamics. These models are classified into either force [15], [112], [118], [121]-[124] or energy [17], [34], [47], [71] balances around individual agglomerates, or the use of the modified Richardson-Zaki equation [1], [20], [32], [41], [115].

3.7.1 Force balance

Chaouki et al. [15] assumed that the drag force due to gas flow, which is approximately equal to gravitational force acting on an agglomerate, is equal to the van der Waals force between primary particles. Their model can be expressed as follows:

$$\frac{g(\rho_a-\rho_f)\pi {d_a}^3}{6} = 25\pi\mu\, u_{mf}\, d_a\, \frac{(1-\varepsilon_c)}{{\varepsilon_c}^3} = \frac{h\bar{\omega}}{8\pi Z^2}\left(1+\frac{h\bar{\omega}}{8\,\pi^2\, Z^3\, H_r}\right) R_{as} \qquad 3.13$$

where ε_c is the bed voidage at agglomerate minimum fluidization velocity u_{mf}, and ρ_a and d_a are the agglomerate density and size, respectively. For proper application of Eq. 3.13, the authors suggested that the particle asperity radius R_{as} with a typical order of 0.1 μm should be taken into account. Also, they postulated that since, for agglomerate fluidization, the fixed bed breaks into pieces, the agglomerate density is fairly equal to the aerated bulk density of the primary particles. Albeit the aerogel particles, which were used in their experimental work, were closer to nanoparticles than to classical group C powders, the proposed model is also capable of predicting the agglomerate size for type C fine cohesive powders.

Iwadate and Horio [121] presented a force balance model by taking into account bubbling dynamics to predict the agglomerate size in a bubbling fluidized bed of cohesive particles. In their model, the bed expansion force caused by bubbles was balanced by the agglomerate-to-agglomerate cohesive rupture force, which was approximated by van der Waals force between two spherical porous bodies. Based on the following model:

$$d_a = \frac{n_{k,mf}\, H_a\, (1-\varepsilon_a)}{12\pi\, Z^2\, D_b\, \rho_a\, g\, (-P_s)} \tag{3.14}$$

where D_b is the bubble diameter, P_s is the dimensionless particle pressure, $n_{k,mf}$ is the coordinate number of agglomerates at minimum fluidization velocity, H_a is the Hamaker constant, which is equal to $4h\bar{\omega}/3\pi$, and ε_a is the agglomerate voidage, which was measured by mercury porosimetry. Typical values for the bed of TiO_2 fine particles were suggested to be $H_a = 0.39 \times 10^{-19}\, J$, $n_{k,mf} = 4.49$, $Z = 4A^o$, and $P_s = -0.0515$. It should be noted that this model can only be used when the bed is bubbling and its application for uniform non-bubbling fluidization generally observed for APF nanoparticles is highly questionable.

Zhou and Li [112], [122] assumed that an equilibrium agglomerate size of cohesive particles in a fluidized bed can be estimated when the joint action of the collision and drag forces is balanced by the buoyant weight and the cohesive force as in the following:

$$(Kinetic\ or\ drag\ force) + (collision\ force) = (gravitational\ force - bouyacy\ force) + (cohesive\ force)$$

According to this balance, they arrived at a quadratic equation to be used for finding the agglomerate size as follows:

$$(\rho_a - \rho_f) g\, {d_a}^2 - \left[0.33\, \rho_f\, {u_0}^2\, \varepsilon^{-4.8} + \frac{0.996}{\pi}\left(\frac{\pi\, V^6\, {\rho_a}^3}{k^2}\right)^{1/5}\right] d_a + \frac{H_a}{4\pi\, Z^2} = 0 \tag{3.15}$$

where k is a function of Poisson's ratio and Young's modulus ($= 3.0 \times 10^{-6}\, Pa^{-1}$), and V is the relative velocity of agglomerates estimated by:

$$V = \left(1.5\,\overline{P_{s,n}}\,D_b\,g\varepsilon\right)^{0.5} \tag{3.16}$$

where $\overline{P_{s,n}}$ is the dimensionless average particle pressure of a non-sticky system, was taken to be 0.077. Zhou and Li [112] found that the density of agglomerates of micron and submicron particles was larger than the aerated bulk density of primary particles by a factor of 1.15, but smaller than the tapped bulk density, about 0.85 times the tapped bulk density. Through the analysis of the model, Zhou and Li [122] reported that higher gas velocity and fluid density, lower particle adhesion, and the collision between agglomerates are effective for agglomerate size reduction. As pointed out by Yang [62], the authors used a constant drag coefficient around the agglomerate, an assumption that is only valid for the high Reynolds number (turbulent flow), and compared the results of the model with experiments for which the Reynolds number around the agglomerates was very low (viscous flow). Accordingly, this model cannot be applied for nanoparticle fluidization in which fluidization is occurring at a creeping flow.

A predictive equation to find the agglomerate size in a fluidized bed of micron size cohesive particles was proposed by Castellanos et al. [123] through studying the limit of mechanical stability of the agglomerate suspended in the gas flow field. Their predictive equation stemmed from a local force balance between shear and adhesion forces on a particle at the outer layer of the agglomerate. In the fluidized bed of micron size primary particle agglomerates, particles tend to agglomerate due to interparticle attractive force. Besides this, the weight of the agglomerate, which is a body force acting uniformly through the agglomerate, is balanced by a hydrodynamic drag force, which acts mainly at the surface of the agglomerate because of the flow screening effect. Consequently, shear forces distributed across the agglomerate grow as the agglomerate size increases, and eventually curtails its growth. The authors suggested that the response of the agglomerate resembles that of a spring subjected to a typical strain:

$$\gamma_s \sim \frac{N_a\,m_p\,g}{K_c\,R_a} \tag{3.17}$$

where N_a is the number of particles in the agglomerate, m_p is the particle mass, K_c is the agglomerate spring constant, and R_a is the agglomerate radius. The agglomerate spring constant was given by $\xi/{k_a}^{\theta}$, where ξ is the interparticle attractive force constant, k_a is the ratio of the agglomerate size d_a to particle size d_p, and θ is the elasticity exponent, $\theta = 3$ was considered for a three

dimensional case. In this context, the local shear force F_s acting on the agglomerate was estimated as follows:

$$F_s \sim \xi \gamma_s \frac{d_p}{2} \sim N_a\, m_p\, g\, {k_a}^2 \tag{3.18}$$

Considering the just presented concept, the particles would continue adhering to the agglomerates as long as the interparticle attractive force F_{IPF} is larger than F_s. Therefore, based on this method, the condition $F_{IPF} = F_s$ results in a criterion by which the agglomerate size can be predicted as follows:

$$Bo_g \sim {k_a}^{D_a+2} \tag{3.19}$$

where Bo_g is the granular Bond number, which is the ratio of the interparticle attractive force to particle weight ($Bo_g = F_{IPF}/m_p\, g$), and $D_a = \frac{\ln N_a}{\ln k_a}$ which is the fractal dimension of the agglomerate, was taken to be 2.5 similar to the diffusion-limited-agglomeration model introduced by Witten and Sander [125]. Experimental results of Castellanos et al. [41] showed that D_a for micron size agglomerates was a robust parameter and was always about 2.5, which confirms this choice. Finally, through this criterion the agglomerate size is expressed as follows:

$$d_a = d_p \left(\frac{F_{IPF}}{(1/6)\pi\, \rho_p\, g\, {d_p}^3} \right)^{1/(D_a+2)} \tag{3.20}$$

The difference between this force balance with the one developed by Chaouki et al. [15] is that the former is a balance between shear and cohesion forces on the agglomerate in the local scale, while in the latter, the local interparticle attractive force was equated to the global drag force on the agglomerate [118].

As previously mentioned, the essential difference between agglomerates of micron size particles and those for APF nanoparticles is that the former forms simple agglomerates from primary fine particles, whereas the latter, as was studied by Yao et al. [20], possesses multistage agglomeration starting from the primary nanoparticle, passing through the three dimensional chain-like structure, simple and complex agglomerates, each of the three were shaped from many components of the previous stage. Postulating the limits to the agglomeration of simple agglomerates to complex

agglomerates in the fluidized bed of nanoparticles is governed by the same physical mechanism as for fine micron size particles, Valverde and Castellanos [124] proposed a new criterion similar to Eg. (19) for the case of nanoparticles as follows:

$$Bo_g^* \sim (k^*)^{D^*+2} \tag{3.21}$$

where $Bo_g^* = F^*/(N_s\, m_p\, g)$ is the ratio of the cohesive force between simple agglomerates to the weight of the simple agglomerate, N_s is the number of primary nanoparticles in each simple agglomerate, k^* is the ratio of complex agglomerate size d^{**} to simple agglomerate size d^* ($k^* = d^{**}/d^*$), $D^* = \ln N^*/\ln k^*$ is the fractal dimension of the complex agglomerates, and N^* is the number of simple agglomerates in the complex agglomerate. Also, they considered $F^* = F_{vdw}$. By assuming a reasonable value for simple agglomerate size, even though they could have good results with this criterion for different nanoparticles, this approach has two main problems in practice. First, the size of simple agglomerates has to be known a priori and, second, it does not account for previous stages of formation of 3D chain-like structures and simple agglomerates [118].

To compensate for these deficiencies, Valverde and Castellanos [118] came up with a new and simple model for calculating the agglomerate size of nanoparticles by merely knowing the primary particle size and density, fractal dimension, and attractive force. They proposed to use Eq. 3.19 for each one of the steps of formation of nanoparticle agglomerates. In addition, they assumed that different agglomeration stages has the same fractal dimension equal to global fractal dimension $D_a = 2.5$. Experimental results of Wang et al. [117] and Nam et al. [32] confirmed this assumption. On the basis of these hypotheses and considering the general fractal dimension $D_a = \ln N_a/\ln k_a$, where, in the case of nanoparticles, N_a is regarded as the total number of primary particles in the complex agglomerate and $k_a = d^{**}/d_p$ as the ratio of the complex agglomerate size to primary nanoparticle size, the following correlation for the prediction of complex agglomerate size was achieved:

$$d^{**} = d_p{}^{D_a(D_a+1)/(D_a+2)^2} (2R_{as})^{(D_a+4)/(D_a+2)^2}\, \Lambda^{-1/(D_a+2)}\, Bo_g{}^{(D_a{}^2+6(D_a+2))/(D_a+2)^3} \tag{3.22}$$

where $\Lambda = \mathrm{g_{ef}}/\mathrm{g}$ is the ratio of effective acceleration $\mathrm{g_{ef}}$ to gravitational acceleration, which is an important parameter for centrifugal and vibro-fluidized beds, and Bo_g is the nanoparticle Bond

number calculated as the ratio of attractive force between primary nanoparticles to the weight of the primary nanoparticles, defined as follows:

$$Bo_g = \frac{F_{IPF}}{(1/6)\pi\ \rho_p\ g\ {d_p}^3} \tag{3.23}$$

Interparticle attractive force between primary nanoparticles F_{IPF} was considered as the summation of van der Waals and capillary forces ($F_{IPF} = \frac{H_a\ d_p}{24\ Z^2} + \frac{\pi\gamma\ d_p}{2}$) to cover both hydrophobic and hydrophilic nanoparticles. Also, the interparticle attractive force between three dimensional chain-like structures and simple agglomerates was equated to van der Waals force, considering $R_{as} = 0.1\ \mu m$, as in the following:

$$F_{vdw-II} = \frac{H_a\ R_{as}}{12\ Z^2} \tag{3.24}$$

Eq. 3.24 is another correlation that has been used by some authors to calculate the van der Waals force between two hard spherical particles ($H_r \gg$). Eq. 3.7, which is a more general correlation for the computation of van der Waals force, is equal to Eq. 3.24 for hard particles and considering $H_a = 4h\bar{\omega}/3\pi$. In order to discriminate the van der Waals force estimated by Eq. 3.24 to that of Eq. 3.7, we symbolize the force as F_{vdw-II} in Eq. 3.24.

It is worth mentioning that Eq. 3.22 predicts that the agglomerate size should not depend essentially on the properties of the environmental gas, like gas viscosity. This was experimentally checked by Valverde et al. [126] in which they used different gases as fluidizing medium for nanoparticles and found that the gas type had negligible effect on the agglomerate size.

3.7.2 Energy balance

Following similar reasoning to Chaouki et al. [15], Morooka et al. [17] assumed that the agglomerate will disintegrate if the collision energy is greater than the energy that is required to break the agglomerate into two parts (i.e., the energy due to the interparticle forces). Employing this philosophy, the equilibrium size of agglomerates can be calculated by:

$$(energy\ generated\ by\ laminar\ shear) + (kinetic\ energy\ of\ agglomerate)$$

$$= (energy\ required\ to\ break\ up\ the\ agglomerate)$$

$$3\pi\mu\, u_{mf}\, {d_a}^2 + \left(\frac{\pi}{6}\right)\rho_e\, {d_a}^3 \left(\frac{{u_{mf}}^2}{2}\right) = E_{break} \tag{3.25}$$

where ρ_e is the density of the emulsion phase in the fluidized bed and E_{break} is the energy needed to disrupt the agglomerate, which is given as:

$$E_{break} = \left(\frac{\pi}{2}\right) {d_a}^2 \sigma\, Z \tag{3.26}$$

where Z is the distance at which van der Waals force is maximized and, as previously mentioned, is approximately equal to 4 A^o, and σ is the maximum tensile strength, which can be approximated using the Rumpf [127] theory, supposing that forces are transmitted at coordinate points of particles forming the agglomerate:

$$\sigma = \frac{(1-\varepsilon_a)}{\varepsilon_a\, {d_p}^2}\, F_{IPF} \tag{3.27}$$

Agglomerate voidage ε_a was approximated by $1 - \rho_a/\rho_p$. Since they carried out their experiments in a dry environment, van der Waals force was dominant over other types of interparticle forces and, hence, $F_{IPF} = F_{vdw}$. Using Eqns. 3.7, 26, and 27, E_{break} can be expressed as follows:

$$E_{break} = \frac{{d_a}^2\, h\bar{\omega}\, R_{as}}{16\, Z\, {d_p}^2} \left(\frac{1-\varepsilon_a}{\varepsilon_a}\right) \left(1 + \frac{h\bar{\omega}}{8\,\pi^2\, Z^3\, H_r}\right) \tag{3.28}$$

Although this model paved the path for using energy balance modeling to estimate the agglomerate size, Zhou and Li [112] believed that the first term in left hand side of Eq. 3.25, which is related to energy generated by laminar shear, should not be involved in the total energy balance and also it was not true to use the minimum fluidization velocity as the characteristic velocity of agglomerates. Similar criticism concerning the inappropriateness of employing the minimum fluidization velocity as the relative velocity between two agglomerates was highlighted by Xu and Zhu [47].

In a centrifugal fluidized bed of nanoparticles, Matsuda et al. [34] presented an energy balance equation based on attainable energy and agglomerate disintegration energy. They assumed that there exists an attainable energy E_a for the disintegration of agglomerates proportional to ${g_{ef}}^r$ and

r was adjusted to 0.4 to fit the model to their experimental results. For the basis of their model, they modified the agglomerate disintegration energy presented by Morooka et al. [17] by considering that energy consumption for breaking powder should consider the energy required per unit-weight of agglomerate, rather than only focusing on the disintegration of a given agglomerate. This is due to the fact that the required energy for agglomerate disruption increases as the agglomerate size decreases. Accordingly, the energy consumption for the disintegration of agglomerate per unit-weight of agglomerate E_{dw} was described by using the density of agglomerate as in the following:

$$E_{dw} = E_{break}\ \frac{1}{(1/6)\pi\ \rho_a\ {d_a}^3} = \frac{3\ h\bar{\omega}\ R_{as}}{8\pi Z \rho_a d_a {d_p}^2}\left(\frac{1-\varepsilon_a}{\varepsilon_a}\right)\left(1+\frac{h\bar{\omega}}{8\ \pi^2\ Z^3\ H_r}\right) \tag{3.29}$$

and by substituting (ρ_a/ρ_p) into $(1-\varepsilon_a)$, Eq. 3.29 reforms as

$$E_{dw} = \frac{3\ h\bar{\omega}\ R_{as}}{8\pi Z\ (\rho_p-\rho_a)\ d_a {d_p}^2}\left(1+\frac{h\bar{\omega}}{8\ \pi^2\ Z^3\ H_r}\right) \tag{3.30}$$

In this context, by considering $E_a = c_a\ \Lambda^{0.4}$, where c_a is a parameter that depends on the operating conditions and experimental apparatus design, the disintegration of agglomerates occurs when $E_a > E_{dw}$ and stops when E_a is equivalent to E_{dw}. Consequently, the size of the agglomerate can be expressed as the following when $E_a = E_{dw}$:

$$d_a = \frac{3\ h\bar{\omega}\ R_{as}}{8\pi Z\ c_a(\rho_p-\rho_a)\ {d_p}^2\ \Lambda^{0.4}}\left(1+\frac{h\bar{\omega}}{8\ \pi^2\ Z^3\ H_r}\right) \tag{3.31}$$

The main critique regarding this model is that the agglomerate size to validate the model was calculated from the data on minimum fluidization velocity and using correlations of Wen and Yu [105], rather than by direct measurements.

Xu and Zhu [47] and Guo et al. [71] used the energy balance strategy and proposed models to predict the agglomerate size in the case of assisting fluidization using external fields, such as the vibration and acoustic field. The general form of energy balance was expressed as, the agglomerate tends to break down when the total energy due to collision E_{coll} and the external field E_{ext} exceeds the energy due to the cohesion E_{coh}. In this regard, the general energy balance is given by:

$$E_{coll} + E_{ext} = E_{coh} \tag{3.32}$$

Xu and Zhu [47] used the following correlation to calculate the collision energy:

$$E_{coll} = 0.104\pi\, \rho_a {d_a}^3\, V^2 \tag{3.33}$$

They believed that employing Eq. 3.16 for calculating the relative agglomerate velocity, which was proposed by Zhou and Li [112], [122], or replacing it by the minimum fluidization velocity, following Morooka et al. [17], are not appropriate ways to estimate the relative velocity of agglomerates. This is due to the fact the using Eq. 3.16 results in the relative velocity being as high as the gas velocity, and in some cases even much higher than that, and employing the second approach yields overlooking the effect of the superficial gas velocity on the agglomerate size. In this regard, the authors approximated V as:

$$V = 0.1\sqrt{u_0\, u_{mf}} \tag{3.34}$$

Also, the contribution of vibration, as the external field, in breaking agglomerates was expressed as:

$$E_{ext} = E_{vib} = \frac{0.01\,\pi^3}{3}\, \rho_a {f_v}^2 {A_m}^2 {d_a}^3 \tag{3.35}$$

Finally, by using the energy balance the agglomerate size was given as follows:

$$d_a = \frac{\frac{\pi}{96}\, 1.61\, {\varepsilon_a}^{-1.48}\, \frac{1-\varepsilon_a}{\varepsilon_a}\, \frac{H_a}{d_p}\, \frac{1}{Z}}{0.104\pi\, \rho_a\, V^2 + \frac{0.01\,\pi^3}{3}\, \rho_a {f_v}^2 {A_m}^2} \tag{3.36}$$

A comparison between the results of the model and experiments for beds of micron size fine particles, while agglomerate size were measured by an "online sampling technique", showed the acceptable accuracy of the model. Albeit this model was validated for micron size particles, it is also capable of predicting the agglomerate size of nanoparticles, as well.

Considering the energy given by the external field as sound wave energy E_{sou}, and the presence of critical values for sound frequency f_{sc} and sound pressure level SPL_c, as discussed in section 3.5.1,

and using the general energy balance like Eq. 3.32, Guo et al. [71] could achieve the following equation to predict the agglomerate size for beds of submicron and nanoparticles:

$$d_a = \left\{\left(h\bar{\omega}/16Z{d_p}^2\right)((1-\varepsilon_a)/\varepsilon_a)(1+h\bar{\omega}/8\,\pi^2\,Z^3\,H_r) - (\pi/4)k_{at}10^{-12+SPL}\,e^{(SPL-SPL_c)/SPL_c}\right\} / 0.104\pi\,\rho_a\,V^2 \quad 3.37$$

where k_{at} is the attenuation coefficient, which is a function of the sound frequency ratio and the sound pressure ratio as in the following:

$$k_{at} = f(\frac{f_s}{f_{sc}}, \frac{SPL - SPL_c}{SPL_c}) \quad 3.38$$

3.7.3 Modified Richardson-Zaki equation

Fitting the bed expansion data to the modified Richardson-Zaki (R-Z) empirical equation is another method that has been used to obtain information about the agglomerate size. Originally, the R-Z equation was developed to describe the bed expansion behavior of homogeneous liquid-solid fluidized beds. However, it was found that the equation can be also applied for smooth fluidization of a non-cohesive gas-solid system and takes the form

$$\frac{u_0}{u_{p0}} = (1-\emptyset)^n \quad 3.39$$

where u_0 is the superficial gas velocity (which for uniform fluidization must be equal to the initial settling velocity u_s in sedimentation), $\emptyset$ is the particle volume fraction, the R-Z exponent n is close to 5.0 for the Stokes-flow regime, and u_{p0} is the terminal velocity for a single particle, expressed by

$$u_{p0} = \frac{\rho_p\,g\,{d_p}^2}{18\,\mu} \quad 3.40$$

By using the R-Z equation for fine cohesive particles in a homogeneous fluidization regime, Vlaverde et al. [115] found that the terminal settling velocity of fluidizing entities was higher than the terminal velocity of a single particle, which indicated the agglomerate fluidization for those particles. Thus, it was noted that for the case of agglomerate fluidization, the terminal settling

velocity of agglomerate u_{tsa} rather than the velocity for the primary particle should be used in the R-Z equation, which introduced the first modification of this equation. It should be taken into account that the R-Z equation is only valid for APF beds since the superficial gas velocity is equal to the initial settling velocity. While for ABF beds, since u_0 is appreciably larger than u_s due to the bypass of a substantial volume of gas by bubbles, the R-Z equation cannot be applied [1], [4], [41], [115], [124].

Considering these issues, to predict the agglomerate size, Yao et al. [20] fitted their bed expansion experimental data of APF nanopowders to the modified R-Z equation

$$\frac{u_0}{u_{tsa}} = (1 - \emptyset)^n \tag{3.41}$$

Consequently, they could obtain the fitting parameters u_{tsa} and n from experimental results. To calculate the agglomerate size from these data, similar to Chaouki et al. [15], they approximated the agglomerate density to the bulk density of the primary nanoparticles and employed the following correlation for terminal settling velocity of the agglomerate

$$u_{tsa} = \frac{\rho_a \, g \, {d_a}^2}{18 \, \mu} \tag{3.42}$$

Although the proposed method is much simpler than the force and energy balance modeling approaches and requires much fewer parameters to be estimated or fitted, it has a major inconvenience. The problem concerning the Yao et al. approach is that they obtained values of n as low as 3, while since the Reynolds number for nanofluidization is typically very small [1], the R-Z exponent cannot deviate too much from $n \approx 5$. As pointed out by Valverde and Castellanos [118], this problem originates from neglecting the screen effect of agglomerates. Thus, the next modification on the R-Z equation was to consider the gas flow screening by agglomerates.

In order to implement the second modification, Valverde et al. [115] and Castellanos et al. [41] assumed that the agglomerates behave like hard spheres with a hydrodynamic radius equal to their radius of gyration, thus it was possible to use the agglomerate volume fraction $\emptyset_a$ instead of the particle volume fraction $\emptyset$ in the modified R-Z equation as follows:

$$\frac{u_0}{u_{tsa}} = (1 - \emptyset_a)^n \quad 3.43$$

Agglomerates of fine particles have fractal structures [32], [41], [115] for which a number of primary particles in the agglomerate N_a can be approximated by the following:

$$N_a = {k_a}^{D_a} \quad 3.44$$

where k_a is the ratio of the agglomerate size d_a to primary particle size d_p, and D_a is the fractal dimension. In this regard, the terminal settling velocity of agglomerate relates to the terminal velocity of the primary particle as follows:

$$u_{tsa} = \frac{u_{p0}\, N_a}{k_a} \quad 3.45$$

and agglomerate volume fraction to particle volume fraction as

$$\emptyset_a = \frac{\emptyset\, {k_a}^3}{N_a} \quad 3.46$$

Substituting Eqs. 3.45 and 46 in Eq. 3.43 yields

$$\frac{u_0}{u_{p0}} = \frac{N_a}{k_a}\left(1 - \emptyset \frac{{k_a}^3}{N_a}\right)^n \quad 3.47$$

By using this approach and fitting the bed expansion experimental data of APF nanoparticles to Eq. 3.47, fitting parameters and, hence, N_a and k_a are determined. Accordingly, agglomerate size can be calculated by $d_a = k_a \times d_p$. In addition to agglomerate size, it is possible to determine the agglomerate density and inter-agglomerate voidage, which are advantages of this method. This approach was used by Nam et al. [32] for the nanoparticle fluidized bed and it could accurately predict the agglomerate size in comparison with the measured data by employing a laser-based planar imaging analysis carried out for images at the splash zone of the bed. They have also reported that with n values in the range of 4 to 6, the fractal dimension, number of primary particles, and diameter of the agglomerates were insensitive to the value of the R-Z exponent n.

Zhu et al. [1] tried to solve this problem by postulating that the density of the agglomerate remains almost constant before ρ_{a0} and during fluidization. A combination of this assumption with an overall mass balance on the powder in the fluidized bed, by ignoring the elutriation and particle adhesion to the walls of the column, yields

$$\varepsilon = 1 - \frac{H_0}{H}\,(1 - \varepsilon_0) \tag{3.48}$$

where H_0 is the fixed bed height, H is the bed height during fluidization, and ε_0 is the fixed bed voidage. By considering Eq. 3.41, but in the form of bed voidage as in the following:

$$\frac{u_0}{u_{tsa}} = \varepsilon^n \tag{3.49}$$

Eq. 3.46 reforms as

$${u_{tsa}}^{1/n} - {u_{tsa}}^{1/n}(1 - \varepsilon_0)\,\frac{H_0}{H} = {u_{tsa}}^{1/n} \tag{3.50}$$

By drawing a plot of ${u_{tsa}}^{1/n}$ vs. H_0/H and forming a linear regression for experimental bed expansion data of APF powders, the terminal settling velocity of agglomerate u_{tsa} and the bed voidage at fixed bed ε_0 can be determined. Accordingly, the agglomerate density before/during fluidization can be estimated as follows:

$$\rho_a = \rho_{a0} = \frac{\rho_b}{(1 - \varepsilon_0)} \tag{3.51}$$

and, finally, the agglomerate size can be calculated from Stokes law, Eq. 3.42. Zhu et al used $n = 5.0$ in their calculation, since the flow was in creeping motion, and found that while their approach was simpler than that of Nam et al. [32], the predictions of both approaches were very close to each other. Moreover, the authors showed that the prediction of their model was fairly well compared to the agglomerate size measured by the in situ optical measurement technique on the lean zone of the fluidized bed.

Results of the calculation of agglomerate size using different models reviewed in this section together with the physical properties of applied powders are summarized in Table 3.4.

Table 3.4: Results of the calculation of agglomerate size using different predictive models

Source	Trade no.	Material	d_p (μm)	ρ_p (kg/m^3)	Fluidization aid	Calculated d_a (μm)
Chaouki et al. [15]		Cu/Al_2O_3 aerogels	<0.01	1200 - 1500		245 - 264
Morooka et al. [17]		Si_3N_4	0.13	2910		350
Iwadate and Horio [121]		TiO_2	0.27	4250		172
Zhou and Li [112, 122]		SiC	1.82	3210		635
		TiO_2	0.6	3880		529
		SiO_2	4.6	2000		330
Yao et al. [20]	R812s	SiO_2	0.007	2560		230
	TS530	SiO_2	0.009	2560		277
	R504	SiO_2	0.012	2560		238
	R972	SiO_2	0.016	2560		277
	Aerosil 300	SiO_2	0.007	2560		286
	Aerosil 150	SiO_2	0.014	2560		331
Matsuda et al. [34]		TiO_2 Hydrophilic	0.007	4000	Centrifugal field	239
					$\Lambda = 9.1$	159
					$\Lambda = 25.2$	99
					$\Lambda = 82.5$	
Nam et al. [32]	R974	SiO_2 Hydrophobic	0.012	2200	Vibration	160
Zhu et al. [1]	R974	SiO_2 Hydrophobic	0.012	2560		211
	R805	SiO_2 Hydrophobic	0.012	2560		279
	R104	SiO_2 Hydrophobic	0.012	2560		245
	R711	SiO_2 Hydrophobic	0.012	2560		207
	COK84	SiO_2-Al_2O_3: 7-1	0.012	2740		316
	R106	SiO_2 Hydrophobic	0.007	2560		201
	A 300	SiO_2 Hydrophilic	0.007	2560		296

	R972	SiO_2 Hydrophobic	0.016	2560		195
Xu and Zhu [47]		Talc	4.1	2720	No vibration	390
		$CaCo_3$	5.5	2700		230
					With Vibration	247
						190
Guo et al. [71]		SiO_2 Hydrophilic	0.0075	2560	Sound assisted at SPL = 100	63
		SiO_2 Hydrophobic	0.0075	2560		89
		SiO_2 Hydrophilic	0.50	2560		92
Valverde and Castellanos [118]	R974	SiO_2	0.012	2560		172
	R974	SiO_2	0.012	2560	Magnetic field	172
	R974	SiO_2	0.012	2560	Sound assisted	172
	R974	SiO_2	0.012	2560		172
	A 300	SiO_2 Hydrophilic	0.007	2200	Initial vibration	307
	A 300	SiO_2 Hydrophilic	0.007	2200		188
					Preheating	
		TiO_2 Hydrophilic	0.007	4000		180
		TiO_2 Hydrophilic	0.007	4000	Centrifugal field	111
		TiO_2 Hydrophilic	0.007	4000	$\Lambda = 5$	93
					$\Lambda = 37$	
					$\Lambda = 82$	

3.8 Applications

Fine particles with their high surface area and unique properties are very attractive for many applications. Control over their size, shape, consistency and composition are necessary and important to ensure their specific commercial applications and to comply with application requirements. Challenges explained in previous sections limit large-scale application of the nanoparticle fluidized bed. Most applications have only been developed in laboratories or small-scale production. However, in recent years the production of material with unique specification by nanoparticle fluidization has attracted a lot of attention. The subject is particularly important in food and pharmaceutical industries where drying, cooling, coating, and granulation are frequent applications of a fluidized bed of fine powders. Using one or more of the assisting methods to obtain homogeneous fluidization of nano-agglomerates can be further processed in large quantities in the dry state using unit operations, such as reaction, coating, granulation, mixing, drying, and adsorption.

One of the most common applications of a nano-particle fluidized bed is coating and encapsulations. Wank et al. [128] carried out Atomic Layer Deposition (ALD) of alumina (Al_2O_3) on a wide size distribution of hexagonal boron nitride platelet-like particles that were fluidized as aggregates in the fluidized bed. They found that the individual primary particles, rather than the aggregates, were coated with a nano-thick ceramic film using ALD. Cohesive primary particles that fluidized as aggregates in a fluidized bed can be individually coated when the surface reaction is dominant. Fluidization of nano-agglomerates can also be used for the production of more advanced materials via coating processes. Esmaeili et al. [129] applied nano-particle fluidization for coating aluminum powders with polymer, which is known as a solution to protect them from a non-desirable reaction, such as oxidation. Ultrafine alumina powders are being recognized as a good candidate for diverse combustion applications, such as additives in solid rocket propellants and metallic fuel in explosive formulations. The nano-sized aluminum powder showed a burning rate 5-10 times greater than micro-sized ones when used in a gas generator fuel. They can be used to achieve more complete combustions. The enhanced properties are due to their large specific surface area, which provides these powders with a high reactivity and makes them particularly difficult to maintain in an un-oxidized state.

Encapsulating nanoparticles with polymers also has applications for medical purposes. For example, the high mechanical and thermal properties of zirconia had led to its use in applications requiring high temperature, high strength, toughness, and aesthetic shade. For this reason zirconium oxide has been extensively used in medical and dental applications. To manufacture an artificial denture, zirconia powder on a nanometer scale is densified under high pressure and temperature to obtain a dense ignot, which will be formed to the desired shape via milling by diamond burs. In this process, zirconia powder must be applied on a nanometer scale to avoid anisotropy in the final product. The hard processing of dense sintered zirconia is very time consuming and costly due to wear and tear on the milling instrument. One possible solution is to encapsulate the zirconia nanoparticles beforehand with a thin layer of polymers, which is uniformly applied around the particles, thus eliminating drawbacks in the milling process [9].

Nanoparticles also have been used to solve environmental issues. Nishii et al. [130] achieved high-density compacts without the use of a binder to avoid dust formation. The cohesiveness of fine particles was advantageously exploited in pressure swing granulation to make weakly consolidated agglomerates. Catalytic gas-solid reaction is another application of the nano-particle fluidized bed. Klvana et al. [12] developed a new process for hydrogenation of toluene by the use of a Ni/SiO_2 aerogel catalyst, which can yield the high concentration needed in the process. Matsuda et al. [131] used a fluidized bed of ultrafine particle photo-catalyst for the treatment of NO_x since the amount of NO_x removal is thought to be dependent on the specific surface area of photo-catalyst.

Carbon nanotubes (CNTs) are very promising materials in a wide range of potential applications, e.g., as hydrogen storage media, selective absorption agents, catalyst supports, microelectronic devices, reinforcement materials and so on. Catalytic chemical vapour deposition (CCVD) in a fluidized bed is one of the successful techniques to synthesize CNTs. Fluidization is a process of choice for the large scale production of CNTs because such reactors provide a large effective surface area and plenty of space for the growth of CNTs. In addition, it provides good conditions for rapid heat and mass transfer. Recently, the production of multi-walled carbon nanotubes (MWNT) using fluidized bed reactors has been of interest to researchers. Corris et al. [132] employed a fluidized bed reactor for the production of multi-walled carbon nano-tubes with an iron-supported catalyst by the catalytic chemical vapor deposition process. Multi-walled carbon nano-tubes and single walled carbon nano-tubes are expected to usher in significant breakthroughs in the technology of electronic and engineering materials. The fluidized bed can provide the large-

scale synthesis of this material for commercial applications. Qian et al. [133] also prepared carbon nano-tubes from ethylene decomposition over the Fe/Al_2O_3 catalyst in a so-called nano-agglomerate fluidized bed reactor. Carbon nano-tube with good morphology, narrow diameter distribution and fewer lattice defects were produced. Large-scale production of carbon nano-tubes with uniform properties will be feasible since the flow dynamic, available space for growing, and the mass and heat transfer rate can be controlled.

3.9 Expansion of the bed of fine/ultrafine particles

In this section the aim is to determine which of the different forms of the R-Z equation available in the literature is the most appropriate one for predicting the expansion behavior of the bed of fine/ultrafine particles. In this regard, it is of prime importance to be taken into account that the parameters used in the right correlation should reveal the physics of the bed.

Richardson and Zaki [81] developed Eq. 3.52 to describe the sedimentation and homogeneous fluidization of uniformly sized noncohesive particles ($d_p > 100\mu m$) fluidized with different liquids.

$$\frac{u_{0l}}{u_{p0}} = \varepsilon^n = (1-\emptyset)^n \qquad 3.52$$

where u_{0l} is the superficial liquid velocity, u_{p0} is the velocity required to give $\varepsilon = 1$ that is theoretically equal to the terminal velocity for an isolated particle, n is the so-called R-Z exponent, and $\emptyset$ is the particle volume fraction. According to Richardson and Zaki [81], sedimentation of suspension and homogeneous fluidization are equivalent processes. In their experimental work, they observed that the settling velocity of a vertical suspension at a given solid concentration $u_s(\emptyset)$ was equal to the upward superficial velocity of the liquid required to maintain the fluidized bed at the same solid concentration. They showed that the parameter n can be correlated to terminal velocity Reynolds number Re_t, based on the diameter and terminal velocity of a single particle, as follows:

$$n = 4.65, \qquad (Re_t \leq 0.2)$$

$$n = 4.35\, Re_t^{-0.03}, \qquad (0.2 < Re_t \leq 1.0)$$

$$n = 4.45\, Re_t^{-0.01}, \quad (1.0 < Re_t < 500)$$

$$n = 2.39, \quad (Re_t \geq 500) \qquad 3.53$$

Surprisingly, researchers have found that plotting the homogeneous bed expansion data of fine particles in a gas-solid fluidization system as $\log u_0$ against $\log \varepsilon$ showed the straight line characteristics of liquid-solid systems. However, the n exponent in Eq. 3.52, when the superficial gas velocity u_0 instead of u_{0l} was used for gas-solid system, was somewhat larger than predicted for fluidization of uniform spheres with a liquid and u_{p0} was generally greater than the free falling velocity of the particle [134]-[137]. Accordingly, authors tried to relate this phenomenon to the role of interparticle forces for fine cohesive powders since interparticle forces are virtually absent in a liquid fluidized system [134], whereas it is not the case for gas-solid fluidization of fine cohesive particles.

Geldart and Wong [134] studied the expansion characteristics of homogeneous fluidized beds of a wide range of powders having a mean particle size of 3.0 to $125\mu m$ at ambient conditions using various gases, such as air, argon, nitrogen and arction-12. By using the original R-Z equation for a gas-solid system as given in Eq. 3.54, they found that the n exponent increased as the particle size decreased and the materials became more cohesive. In fact, the n exponent was around 4.65 for group A powders and became significantly larger, even as large as 60.0, for those powders, which showed a higher degree of cohesiveness.

$$\frac{u_0}{u_{p0}} = \varepsilon^n = (1 - \emptyset)^n \qquad 3.54$$

Geldart and Wong regarded the values of n/4.65 > 1 as indicative of the presence of interparticle forces in the gas-solid fluidized system. According to this and on the basis of their experimental results, they correlated the n/4.65 ratio to the Hausner ratio, which itself is a good reflection of the degree of cohesivity of fine particles in the gas-solid system, as follows:

$$\frac{n}{4.65} = \left(\frac{HR}{1.11}\right)^{4.16} \qquad 3.55$$

Also, they observed that for noncohesive particulate materials, which were uniformly fluidized in a laminar flow regime, the terminal velocity for an isolated particle calculated from the Stokes's equation, u_{p0}, was close to the velocity extrapolated from Eq. 3.54 at $\varepsilon = 1$, ${u_{p0}}^*$. In contrast, for the cohesive group C particles, the ${u_{p0}}^*/u_{p0}$ was significantly higher than 1. On the basis of their experimental results, since those materials having n/4.65 > 1 also had a value of ${u_{p0}}^*/u_{p0} > 1$, they correlated these two ratios as follows:

$$\frac{n}{4.65} = 1.26 \left(\frac{{u_{p0}}^*}{u_{p0}}\right)^{0.132} \qquad 3.56$$

According to what was proposed by Geldart and Wong [134], to predict the homogeneous bed expansion behavior of fine cohesive particles in a gas-solid fluidized bed using Eq. 3.54, the value of n index can be predicted from Eq. 3.55 by having the value of the Hausner ratio for the powder, and ${u_{p0}}^*/u_{p0}$ from n through Eq. 3.56, while u_{p0} is calculated from Stokes's equation using the mean particle size.

As can be found from this strategy, the accuracy of the prediction is highly dependent on the experimentally determined value of the Hausner ratio. However, although Geldart and Wong [134] showed that this method can have acceptable results for micron size fine particles, the applicability of this method for prediction of the uniform bed expansion behavior of nanoparticles is highly questionable because, as noted by Esmaeili et al. [9], the Hausner ratio is not a good indication of the fluidization behavior of nano size particles. Next, and more importantly, although the value of n index in this strategy is reflective of the cohesiveness inside the bed and increases by increasing the bed cohesivity, this form of R-Z equation is not a good phenomenological representation of the bed expansion behavior of fluidizing entities inside the bed of fine/ultrafine powders. As previously stated, fine/ultrafine primary particles tend to cross the fluidizability barrier by forming agglomerates of the primary powders. When these agglomerates uniformly expand in their stable fluidization regime, hydrodynamic forces are dominant forces in this gas-solid system [19] and, hence, having a form of R-Z equation with a value of n exponent near 5.0 in laminar flow regime, as noted by Geldart and Wong [134], would be a better choice for this case in which interparticle forces are fairly absent between fluidizing entities. In this form, the value of n index, $n \cong 5.0$,

phenomenologically represents the physics of agglomerate fluidization of fine/ultrafine particles, when they smoothly expand in the bed.

To confirm this fact, it was noted by Zhu et al. [1] that the Reynolds number for APF nanoparticle agglomerates, which can fluidize uniformly without any bubbles, is typically very small (Re < 1) and, hence, Stokes flow prevails for them. Therefore, the R-Z exponent cannot deviate too much from $n \approx 5$ [1]. Also, it was shown by Nam et al. [32] that a R-Z exponent of n = 5.0 is valid for APF nanoparticle aggregates.

In order to have a form of R-Z equation that describes well the physics of agglomerate fluidization of fine/ultrafine particles, it is necessary to make two more modifications to Eq. 3.54. First, since agglomerates of primary particles are fluidizing entities in a gas-solid fluidized bed of fine/ultrafine particles, substituting the u_{p0} by the terminal velocity of the agglomerates u_{tsa} is required. Second, again, due to the preceding stated reason and noting the fact that these agglomerates have fractal structures, which effectively screen the gas flow as gas flow inside the aggregates is negligible compared to the flow outside [123], it requires the use of agglomerate concentration $\emptyset_a$ rather than solid concentration in Eq. 3.54. All points discussed here direct us to the modified Richardson-Zaki equation coupled with fractal analysis proposed by Valverde et al. [115], Castellanos et al. [41], and Nam et al. [32], which is expressed as follows:

$$\frac{u_0}{u_{tsa}} = (1 - \emptyset_a)^{5.0} \tag{3.57}$$

or by using the concept of fractal analysis, which was explained in section 3.7.3, it can be given in a more complete form as the following:

$$\frac{u_0}{\frac{N_a}{k_a}\, u_{p0}} = \left(1 - \emptyset \frac{{k_a}^3}{N_a}\right)^{5.0} \tag{3.58}$$

It is stressed here that Eq. 3.57 or 58 is the most appropriate form of R-Z equation for prediction of the bed expansion behavior of agglomerate fluidization of fine/ultrafine particles, which each of its components phenomenologically describes the physics behind the fluidization of these materials. It is worth recalling here that for the other forms of R-Z equation, which were proposed by Yao et al. [20], Eq. 3.41, only replaces the particle falling velocity by the agglomerate settling

velocity in Eq. 3.54 and, hence, doesn't consider all required modifications that should be done on Eq. 3.54 for agglomerate fluidization of fine/ultrafine powders. The inability of this form for prediction of bed expansion behavior of agglomerate fluidization of ultrafine particles can be found in the experimental results of Yao et al. [20] where the predicted values of n exponent for beds of APF agglomerates for which, as noted above, the Reynolds number is very low and laminar flow condition is dominating, were as low as 3, which is typically close to the values of n reported for the turbulent regime of liquid-solid fluidization of non-agglomerated particles [81].

Even though it is expressed that Eq. 3.58 is much better than the form of R-Z equation proposed by Geldart and Wong [134], which based on their experimental observations can be given as the following:

$$\frac{u_0}{u_{p0}{}^*} = \frac{u_0}{u_{tsa}} = (1-\emptyset)^n \qquad 3.59$$

Eq. 3.59 was very effective in determining the degree of importance of interparticle forces in beds of micron size fine particles by merely evaluating the magnitude of n index from their uniform bed expansion data. Therefore, it is highly interesting to check whether Eq. 3.59 keeps its predictive ability for reflecting the degree of cohesivity by values of n exponent in beds of other fine/ultrafine materials, especially nanoparticles, that have been used by different researchers to verify Eq. 3.58 or not. Frankly speaking, the left hand sides of both Eqs. 3.58 and 59 for a specific bed of fine/ultrafine particulate bed with a specific agglomerate size are equivalent because both indicate that agglomerates of the primary particles are fluidizing entities in the system and, hence, the terminal velocity of agglomerate is used in both correlations. Therefore, in order to calculate the value of n exponent in Eq. 3.59 from the bed expansion data attainable from Eq. 3.58, the right hand side of these two correlations should be equivalent, too. By doing so, the mean values of n exponent for different solid systems, in their own homogeneous bed expansion regime, are calculated and presented in Table 3.5.

As can be found in Table 3.5, similar to what was reported by Geldart and Wong [134], Eq. 3.59 predicts values of n larger than 4.65 for gas-solid systems of micron size fine particles. The most striking result is found for the system of nanoparticle for which $n = 350$ is calculated. As expected, the magnitude of interparticle force for a bed of nano size particle is much greater than the bed of the same type of material but with larger size particles and this can be clearly found from the value

of n index reported for this size of powder in Table 3.5. Albeit this verification was done for one nanoparticle material here, performing the same type of calculations by having the bed expansion data for other nano size powders seems necessary to confirm the ability of Eq. 3.59 for predicting the importance of interparticle forces in a gas-solid system of ultrafine particles by merely providing the homogeneous bed expansion data of the system.

Table 3.5: Calculation of n exponent of Eq. 3.59 for fine/ultrafine powders used by different researchers to verify Eq. 3.58

Source	Material	$d_p\ (\mu m)$	$\rho_p\ (kg/m^3)$	N_a	D	Calculated n for Eq. 3.59
Valverede et al. [115]	Xerographic toner	8.53	1199	96	2.6190	11.17
Castellanos et al. [41]	Copolymer styrene n-buthylmethacyrylate	7.8	1135	63	2.5323	12.70
		11.8		23.7	2.5120	10.51
		15.4		12.4	2.4990	9.42
		19.1		9.6	2.5080	8.64
Nam et al. [32]	Aerosil R974	0.012	2200	4.047×10^{10}	2.5371	350.22

3.10 Future work

Research on the concept of fluidization of fine/ultrafine particles has been conducted over the last three decades. However, although many valuable studies have been carried out, there is not a well-matured knowledge in the field and, hence, fine cohesive powders, including ultrafine or nano size powders, play a moderate role in industrial applications nowadays. Nonetheless, it is highly expected that theses powders will be significantly important in industrial applications in the near future due to their special characteristics, namely their very small primary size and large surface area-to-volume ratio. Therefore, much more scientific efforts are required to expand the knowledge for ultrafine particle fluidization in order to facilitate the implementation of large scale industrial processes involving these materials.

First and foremost, introducing a simple and robust criterion for predicting APF/ABF behavior of ultrafine powders or modifying the existing ones seems essential. As discussed before, the one which was proposed by Yao et al. [20] and Zhu et al. [1] is simple and only requires the primary particle size and bulk density. However, even though it could have acceptable results for different

nanoparticle samples, it is not robust enough for the purpose. On the other hand, the other criterion, which was proposed by Romero and Johanson [61], has very good sensitivity to APF and ABF behaviors as long as there is a good evaluation of the minimum fluidization velocity of the powders, which itself is a challenging task for such fine and ultrafine cohesive particles. Another problem with this criterion is that it was only verified for some nano size particles. Thus, performing more studies seems essential to check whether this classification criterion is applicable for all nanopowders or not.

Second, it was noted in previous sections that effective fluidization of fine/ultrafine cohesive particles is often not possible without an assisting method; different groups of researchers showed that the fluidization quality of these powders could, however, be greatly enhanced when an appropriate assisting method was applied. Apart from all the research work that has been performed in this part, there are still many holes remaining to be filled in order to understand better the exact performance of each technique. Improving the fluidization quality of fine/ultrafine particles with the combination of the proposed methods is the matter, which has received little attention among researchers, whereas this might be a helpful solution for increasing the efficiency of assisting approaches. Furthermore, coming up with novel assisting methods demanding low energy and cost, that are easy to implement and scale up together with considerable efficiency in practice is highly appreciated.

Third, the mean agglomerate size is an important parameter to be evaluated, when a bed of ultrafine powders is fluidizing, due to its substantial impact on the quality of fluidization, the heat and mass transfer efficiencies and on the overall performance of the fluidized bed. In this regard, considerable efforts have been devoted to measure and predict this parameter. Concerning the online measurement of the agglomerate size, it seems that the X-ray imaging technique is a powerful one, which can provide researchers with plenty of structural and dynamic information about the fluidized bed of ultrafine particles in a noninvasive manner. However, further development is required for the technique to respond to the low X-ray energies needed for some fine powder samples. In parallel and most necessarily, more studies are required to present a simple model for predicting the agglomerate size from some preliminary information, including the physical properties of the particulate material, interparticle attractive forces, and operating parameters independent of the introduction of many fitting parameters to be assumed. The simple model proposed by Valverde and Castellanos [118] would be a sample for such modeling.

Nonetheless, it predicts the same agglomerate size for non-assisted, sound-assisted, magnetically-assisted fluidized beds and also for the bed assisted by mechanical vibration, whereas, according to the experimental results reported by different researchers that cannot be the case. In addition, it is of great importance to experimentally verify whether the superficial gas velocity affects the mean agglomerate size or not. If it does, it is highly appreciated to be considered when models will be presented for estimating agglomerate size. This is the case when an agreement among the research community does not exist and it needs to be well clarified with the help of experimental results.

As suggested by van Ommen and Pfeffer [4], another virtually unexplored field is the modeling of reactions taking place in a fluidized bed of ultrafine particles. Considering the fact that one agglomerate of ultrafine particles can easily consist of too many primary particles, a large range of length scales plays a role in this modeling and, hence, a multi-scale modeling approach would be an appropriate one for this purpose [4].

One of the critical applications of the nanoparticle fluidized bed is for encapsulation of nanoparticles. Coating or encapsulating nanoparticles with polymers is desired in many applications to improve their chemical stability, reduce their toxicity, and facilitate their storage, transport, and processing. In two particular applications of nanoparticle coating, we can specify the encapsulation of zirconia and aluminum nanoparticles. These nanoparticles are very promising materials in industrial applications. Over the last few years, the introduction of zirconium oxide-based ceramics into the field of dentistry has been greatly appreciated. On the other hand, ultrafine aluminum powder is being recognized as a good candidate for diverse combustion applications, such as additives in solid rocket propellants and metallic fuel in explosive formulations. The common method for encapsulation of nanoparticles is slurry based methods in which small amounts of catalyst is dissolved in an organic solvent, where nanoparticles have already been dispersed. Some drawbacks, however, arise when the process is carried out in the liquid phase, as the polymerization reaction must be followed by additional steps to isolate the coated particles. After encapsulation, the reaction slurry must be filtered to separate the coated particles from the solvent. This step is usually accompanied by washing the encapsulated powders to eliminate solvent impurities, catalyst and the nonreacted monomers. Then, the coated particles must be completely dried in an oven overnight. Subsequently, the dried particles form a hard bulk material, which needs to be grinded to obtain finely coated particles. To accomplish all of the aforementioned additional processes requires more than the polymerization reaction time itself, which usually lasts

only a few minutes. Accordingly, the encapsulation process costs for a liquid–solid reaction, particularly when dealing with large amounts of particles, are significant. In addition, under these conditions, it is difficult to ensure a complete removal of the impurities in the solvent and to obtain the desired particle size by grinding the bulk material recovered from the process. To overcome these issues Esmaeili et al. [129] for the first time used a fluidized bed reactor for encapsulating nanoparticles by the polymerization compounding approach using Ziegler–Natta catalysts. The polymerization reaction was carried out using a solvent-free process in a gas-solid fluidized bed reactor. This direct gas–solid reaction greatly simplified collecting the particles of interest after polymerization because there was none of the extra steps often found in encapsulation processes, such as filtering and drying. Although the concept has been approved on a lab scale, scaling up of such a process still is a big challenge. It is necessary to evaluate fluidization quality on a large scale and define proper operating conditions to be able to encapsulate nanoparticles at that scale. In parallel, more studies relating to the coating of ultrafine particles with a thin layer of organic and/or inorganic materials to achieve a specific physical, chemical, optical, and electrical property are required to be performed. All of these studies should be directed to the ideal conditions of coating the individual nanoparticles, rather than their agglomerates, in the simplest practical way.

3.11 Summary

Ultrafine powders, nanoparticles, have received widespread interest in recent years due to their unique properties arising from their very small primary particle size and very large surface area. They have been used to produce catalysts, effective sorbents, drugs, cosmetics, food and plastics. In addition, they have some applications in hydrogen storage, Li-ion batteries, and fuel cells. In parallel with plenty of academic attention on the fluidization of nanoparticles, it is a highly probable that these powders will be incorporated as part of large-scale industrial processes. Accordingly, it will require large quantities of ultrafine particles to be handled and processed in many cases. Prior to processing such materials, however, it is necessary that the nano-sized particles be well dispersed. Gas fluidization is one of the best techniques available to disperse and process fine particles. Gas-solid fluidized beds are among the unit operations, which have a number of significant advantages for processing small solid particles, including high heat and mass transfer rates, uniform and controllable bed temperature, the ability to handle a wide variety of particle properties and suitability for large-scale operations. Since the fluidization of nanoparticles happens

in an agglomerate state, the properties of fluidized agglomerates, rather than those of primary powders, determine the fluidization characteristics of the bed. Thus, it is very important to know how these aggregate particles fluidize within the bed. Fluidization of nanoparticle agglomerates suffers from several problems, such as bubbling, channeling, clustering, and entrainment. Therefore, inappropriate dispersion of nanoparticles in the gas phase and considerable gas bypassing may occur. Moreover, for the conventional gravity-driven fluidization of nanoparticles, even in particulate fluidization, appreciable powder elutriation happens at the high superficial gas velocities required to fluidize the nano-aggregates. This loss of particles is probably the main reason that prevents the application of gas fluidization of nano-agglomerates in industrial processes. To overcome these problems and improve the fluidization quality of nanoparticle agglomerates, various assisting methods have been proposed and tested. These methods include vibration, ultra-sound, the application of magnetic and electric fields, the use of a rotating fluidized bed, the use of a conical fluidized bed, the addition of foreign particles and the use of micro-jets as a secondary flow in the bed. The degree of fluidization enhancement achieved by applying these methods is evaluated by measuring some hydrodynamic parameters, such as minimum fluidization velocity, bed pressure drop, bed expansion, agglomerate size, degree of mixing, bubble suppression and amount of powder elutriation, as indicators of fluidization quality.

This review intended to provide a comprehensive review of current ultrafine powder fluidization technology. It discussed the challenges associated with widespread application of these powders in industries and explained the fundamentals of nanoparticle fluidization along with the details necessary to understand the process complexity and come up with reliable solutions. It gives in-depth coverage of state-of-the-art international research experiences of nanoparticle fluidization at the edge of scientific inquiry and emerging technologies.

Fluidization of the nanoparticle is state of the art. Engineers and scientists in the chemical and pharmaceutical fields as well as in the areas of agriculture, food, ceramics, electronics and solid-catalyzed reactions need to broaden their current level of knowledge. The engineering data available for its implementation are limited and this subject requires more research. More studies are necessary to describe how the assisting method can improve the quality of fluidization and how operating parameters can be adjusted to achieve desirable homogeneity. It can be suggested to perform different tests at a wide range of vibration (f=0-50 Hz) and monitor bubble formation at different vibration intensities. Size and propagation also can be studied. Enhancing

nanofluidization with an electrostatic field also needs extensive studies. This can be done for a variety of nanoparticles at different electrostatic fields. Pre-charging powders prior to fluidization could also be considered as an alternative subject or other design parameters, like distributer geometry, the effect of internals, and heat and mass transfer, could attract the researcher's attention to fill the holes in the body of knowledge.

3.12 Nomenclature

3.12.1 Acronyms

ABF	agglomerate Bubbling Fluidization
APF	agglomerate Particulate Fluidization
MSA	multi-stage agglomerate
SPL	sound pressure level
SPL_c	critical sound pressure level
SPL_{min}	minimum sound pressure level
SSA	single-stage agglomerate

3.12.2 Symbols

A_e	agglomerate number
A_m	vibration amplitude, m
Bo_g	granular Bond number
Bo_g^*	granular Bond number of simple agglomerate
C_a	parameter used for definition of E_a, J/kg
C_D	drag coefficient
d_a	agglomerate size, m
d_p	particle size, m
d^*	simple agglomerate size, m

d^{**}	complex agglomerate size, m
D_a	fractal dimension
D_b	bubble diameter, m
D_{col}	column diameter, m
D^*	fractal dimension of the complex agglomerates
E_a	attainable energy, J/kg
E_{break}	energy required to break an agglomerate, J
E_{coh}	cohesion energy, J
E_{coll}	collision energy, J
E_{dw}	agglomerate disruption energy per unit weight of agglomerate, J/kg
E_{ext}	energy given to the system by external field, J
E_{vib}	vibration energy, J
E_{sou}	sound wave energy, J
f_s	sound frequency, Hz
f_{sc}	critical sound frequency, Hz
f_v	vibration frequency, Hz
F_b	buoyant force, N
F_c	capillary force, N
F_d	drag force, N
F_e	electrostatic force, N
F_{IPF}	interparticle attractive force, N
F_p	force due to pressure difference across the air-liquid interface, N
F_s	shear force, N
F_{vdw}	van der Waals force, N

F_γ	surface tension force, N
F^*	interparticle attractive force between simple agglomerates, N
Fr_{mf}	froude number at u_{mf}
g	gravity field acceleration, m/s^2
g_{ef}	effective acceleration, m/s^2
H	bed height, m
H_a	hamaker constant, J
H_{mf}	bed height at u_{mf}, m
H_r	hardness, N/m^2
H_0	fixed bed height, m
$h\bar{\omega}$	liftshits-van der Waals coefficient, J
k	function of Poisson's ration and Young's modulus, Pa^{-1}
k_a	ratio of agglomerate size to particle size
k_{at}	sound attenuation coefficient, s
k^*	ratio of complex agglomerate size to simple agglomerate size
K_c	agglomerate spring constant
m_p	particle mass, kg
n	richardson-Zaki exponent
$n_{k,mf}$	coordinate number of agglomerates at u_{mf}
N_a	number of particles in an agglomerate
N_s	number of primary nanoparticles in a simple agglomerate
N^*	number of simple agglomerates in a complex agglomerate
P_s	dimensionless particle pressure
$\overline{P_{s,n}}$	dimensionless average particle pressure of non-sticky system

q_i	charges carried by objects, i = 1,2, C
R	particle radius, m
R_a	agglomerate radius, m
R_{as}	particle asperity radius, m
Re_{mf}	reynolds number at u_{mf}
Re_p	particle Reynolds number
Re_t	terminal velocity Reynolds number
s	distance between two objects, m
u_{mf}	agglomerate minimum fluidization velocity, m/s
u_{p0}	terminal velocity of a single particle, m/s
$u_{p0}{}^*$	velocity extrapolated from Eq. 3.52 at $\varepsilon = 1$, m/s
u_s	initial settling velocity, m/s
u_{tsa}	terminal settling velocity of agglomerate, m/s
u_0	superficial gas velocity, m/s
u_{0l}	superficial liquid velocity, m/s
V	relative velocity of agglomerates, m/s
W_b	buoyant weight, N
Z	separation distance between particles, m

3.12.3 Greek letters

α	half-filling angle
β	contact angle
γ	liquid-surface tension, N/m
γ_s	agglomerate spring strain, N/m

ε	bed voidage
ε_a	agglomerate voidage
ε_0	fixed bed voidage
ϵ	permittivity of the surrounding, F/m
θ	elasticity exponent
μ	fluid viscosity, Pa.s
ξ	interparticle attractive force constant
ρ_a	agglomerate density, kg/m^3
ρ_{a0}	agglomerate density before fluidization, kg/m^3
ρ_b	aerated bulk density of primary particles,
ρ_e	density of emulsion phase in fluidized bed, kg/m^3
ρ_f	fluid density, kg/m^3
ρ_{fb}	density of fluidized bed, kg/m^3
ρ_p	particle density, kg/m^3
ρ_{tb}	tapped bulk density, kg/m^3
σ	maximum tensile strength of agglomerate, Pa
ϕ	particle volume fraction
ϕ_a	agglomerate volume fraction
Γ	vibration intensity
Δp	differential pressure across air-liquid interface, Pa
Λ	ratio of effective acceleration to gravity field acceleration

3.13 References

[1] C. Zhu, Q. Yu, R. N. Dave, R. Pfeffer, Gas fluidization characteristics of nanoparticle agglomerates, *AIChE J.* 51 *(2005) 426-439.*

[2] J. Quevedo, R. Pfeffer, Y. Shen, R. Dave, H. Nakamura, S. Watano, Fluidization of nanoagglomerates in a rotating fluidized bed, *AIChE J.* 52 *(2006) 2401-2412.*

[3] E. Jaraiz, S. Kimura, O. Levenspiel, Vibrating beds of fine particles: Estimation of interparticle forces from expansion and pressure drop experiments, *Powder Technol.* 72 *(1992) 23-30.*

[4] J. R. van Ommen, R. Pfeffer. Fluidization of Nanopowders-Experiments, Modeling, and Applications, *13th International Conference on Fluidization, Gyeong-ju, Korea, 16-21 May (2010).*

[5] J. R. van Ommen, D. M. King, A. Weimer, R. Pfeffer, B. G. M. van Wachem, Experiments and modelling of micro-jet assisted fluidization of nanoparticles, *13th International Conference on Fluidization, Gyeong-ju, Korea, 16-21 May (2010).*

[6] D. Kunii, O. Levenspiel, *Fluidization Engineering* (Butterworth-Heinemann, 1991).

[7] G. H. Qian, I. Bágyi, I. W. Burdick, R. Pfeffer, H. Shaw, J. G. Stevens, Gas–solid fluidization in a centrifugal field, *AIChE J.* 47 *(2001) 1022-1034.*

[8] S. Sanaei, N. Mostoufi, R. Radmanesh, R. Sotudeh-Gharebagh, C. Guy, J. Chaouki, Hydrodynamic characteristics of gas–solid fluidization at high temperature, *Can. J. Chem. Eng.* 88 *(2010) 1-11.*

[9] B. Esmaeili, J. Chaouki, C. Dubois, An evaluation of the solid hold-up distribution in a fluidized bed of nanoparticles using radioactive densitometry and fibre optics, *Can. J. Chem. Eng.* 86 *(2008) 543-552.*

[10] D. Geldart, Types of gas fluidization, *Powder Technol.* 7 *(1973) 285-292.*

[11] P. Ammendola, R. Chirone, F. Raganati, Fluidization of binary mixtures of nanoparticles under the effect of acoustic fields, *Adv. Powder Technol.* 22 *(2011) 174-183.*

[12] D. Klvana, J. Chaouki, C. Lauga, C. Chavarie, D. Kusohorsky, G. Pajonk, Study of the performance of fluidization Ni/SiO2 aerogel for toluene hydrogenation, *6th International Conference on Fluidization, Banff, Canada (1989).*

[13] J. Visser, Van der Waals and other cohesive forces affecting powder fluidization, *Powder Technol.* 58 *(1989) 1-10.*

[14] A. Dutta, L.V. Dullea, Effects of external vibration and the addition of fibers on the fluidization of a fine powder, *AIChE Sym. Ser.* 87 *(1991) 38–46.*

[15] J. Chaouki, C. Chavarie, D. Klvana, G. Pajonk, Effect of interparticle forces on the hydrodynamic behaviour of fluidized aerogels, *Powder Technol.* 43 *(1985) 117-125.*

[16] Chavarie, C., K. Dobson, R. Clift and J. P. K. Seville, Study on the fluidization of group C aerogel powders by spontaneous dynamic agglomeration, *37th Canadian Chemical Engineering Conference, Montreal, Canada (1987).*

[17] S. Morooka, K. Kusakabe, A. Kobata, Y. Kato, Fluidization state of ultrafine powders, *J. Chem. Eng. J.* 21 *(1988) 41–46.*

[18] A. W. Pacek, A. W. Nienow, Fluidisation of fine and very dense hardmetal powders, *Powder Technol.* 60 *(1990) 145-158.*

[19] Y. Wang, F. Wei, Y. Jin, T. Luo, Agglomerate particulate fluidization and E-particles, *Third Joint China/USA Chemical Engineering Conference (CUChE-3)*, Beijing, China (2000).

[20] W. Yao, G. Guangsheng, W. Fei, W. Jun, Fluidization and agglomerate structure of SiO2 nanoparticles, *Powder Technol.* 124 *(2002) 152-159.*

[21] L. F. Hakim, J. L. Portman, M. D. Casper, A. W. Weimer, Aggregation behavior of nanoparticles in fluidized beds, *Powder Technol.* 160 *(2005) 149-160.*

[22] J. A. Quevedo, A. Omosebi, R. Pfeffer, Fluidization enhancement of agglomerates of metal oxide nanopowders by microjets, *AIChE J.* 56 *(2010) 1456-1468.*

[23] C. Zhu, G. Liu, Q. Yu, R. Pfeffer, R. N. Dave and C. H. Nam, Sound assisted fluidization of nanoparticle agglomerates, *Powder Technol.* 141 *(2004) 119-123.*

[24] H. Liu, Q. Guo, S. Chen, Sound-Assisted Fluidization of SiO2 Nanoparticles with Different Surface Properties, *Ind. Eng. Chem. Res.* 46 *(2007) 1345-1349.*

[25] P. Ammendola, R. Chirone, F. Raganati, Sound assisted fluidization of Al2O3and Fe2O3 nanoparticles, *AIChE Annual Meeting, Salt Lake City, US, November 7-12 (2010).*

[26] P. Ammendola, R. Chirone, Aeration and mixing behaviours of nano-sized powders under sound vibration, *Powder Technol.* 201 *(2010) 49-56.*

[27] S. Kaliyaperumal, S. Barghi, J. Zhu, L. Briens and S. Rohani, Effects of acoustic vibration on nano and sub-micron powders fluidization, *Powder Technol.* 210 *(2011) 143-149.*

[28] J. M. Valverde, J. M., M. J. Espin, M. A. S. Quintanilla, A. Castellanos, Electrofluidized bed of silica nanoparticles, *J. Electrostatics* 67 *(2009) 439-444.*

[29] D. Lepek, J. M. Valverde, R. Pfeffer, R. N. Dave, Enhanced nanofluidization by alternating electric fields, *AIChE J.* 56 *(2010) 54-65.*

[30] Q. Yu, R. N. Dave, C. Zhu, J. A. Quevedo, R. Pfeffer, Enhanced fluidization of nanoparticles in an oscillating magnetic field, *AIChE J.* 51 *(2005) 1971-1979.*

[31] P. Zeng, T. Zhou, J. Yang, Behavior of mixtures of nano-particles in magnetically assisted fluidized bed, *Chem. Eng. Process.* 47 *(2008) 101-108.*

[32] C. H. Nam, R. Pfeffer, R. N. Dave, S. Sundaresan, Aerated vibrofluidization of silica nanoparticles, *AIChE J.* 50 *(2004) 1776-1785.*

[33] J. Yang, , T. Zhou, L. Song, Agglomerating vibro-fluidization behavior of nano-particles, *Adv. Powder Technol.* 20 *(2009) 158-163.*

[34] S. Matsuda, H. Hatano, T. Muramoto, A. Tsutsumi, Modeling for size reduction of agglomerates in nanoparticle fluidization, *AIChE J.* 50 *(2004) 2763-2771.*

[35] H. Nakamura, S. Watano, Fundamental particle fluidization behavior and handling of nano-particles in a rotating fluidized bed, *Powder Technol.* 183 *(2008) 324-332.*

[36] R. D. Venkatesh, J. Chaouki, D. Klvana, Fluidization of cryogels in a conical column, *Powder Technol.* 89 *(1996) 179-186.*

[37] C. Brereton, J. Chaouki, J. R. Grace, R. Legros, J. Yeung, Hydrodynamic behavior of a silica aerogel powder in a circulating fluidized bed, *37th Canadian Chemical Engineering Conference, Montreal, Canada (1987).*

[38] C. Lauga, J. Chaouki, D. Klvana, C. Chavarie, Improvement of the fluidisability of Ni/SiO2 aerogels by reducing interparticle forces, *Powder Technol.* 65 *(1991) 461-468.*

[39] L. S. Fan, C. Zhu, *Principles of Gas–Solid Flows* (Cambridge University Press, 1998).

[40] L. G. Gibilaro, *Fluidization Dynamics* (Butterworth Heinemann, 2001).

[41] A. Castellanos, J. M. Valverde, M. A. S. Quintanilla, Aggregation and sedimentation in gas-fluidized beds of cohesive powders, *Phys. Rev. E* 64 *(2001) 041304.*

[42] F. London, The general theory of molecular forces, *Trans. Faraday Soc.* 33 *(1937) 8-26.*

[43] H. Krupp, Particle Adhesion: Theory and Experiment, *Adv. Colloid Interface Sci.* I *(1967) 111.*

[44] O. Molerus, Interpretation of Geldart's type A, B, C and D powders by taking into account interparticle cohesion forces, *Powder Technol.* 33 *(1982) 81-87.*

[45] L. Massimilla, G. Donsì, Cohesive forces between particles of fluid-bed catalysts, *Powder Technol.* 15 *(1976) 253-260.*

[46] T. G. Mason, A. J. Levine, D. Ertascedil, T. C. Halsey, Critical angle of wet sandpiles, *Phys. Rev. E* 60 *(1999) R5044.*

[47] C. Xu, J. Zhu, Experimental and theoretical study on the agglomeration arising from fluidization of cohesive particles--effects of mechanical vibration, *Chem. Eng. Sci.* 60 *(2005) 6529-6541.*

[48] J. M. Valverde, A. Ramos, A. Castellanos, P. Keith Watson, The tensile strength of cohesive powders and its relationship to consolidation, free volume and cohesivity, *Powder Technol.* 97 *(1998) 237-245.*

[49] J. P. K. Seville, C. D. Willett, P. C. Knight, Interparticle forces in fluidisation: a review, *Powder Technol.* 113 *(2000) 261-268.*

[50] A. G. Bailey, Electrostatic phenomena during powder handling, *Powder Technol.* 37 *(1984) 71-85.*

[51] K. Rietema, *The Dynamics of Fine Powders* (Elsevier Science Publishers LTD, 1991).

[52] G. Lian, C. Thornton, M. J. Adams, A Theoretical Study of the Liquid Bridge Forces between Two Rigid Spherical Bodies, *J. Colloid Interface Sci.* 161 *(1993) 138-147.*

[53] T. Weigert, S. Ripperger, Calculation of the Liquid Bridge Volume and Bulk Saturation from the Half-filling Angle, *Part. Part. Syst. Charact.* 16 *(1999) 238-242.*

[54] O. Gundogdu, U. Tuzun, Gas Fluidisation of Nanoparticle Assemblies: Modified Geldart classification to account for multiplescale fluidisation of agglomerates and clusters, *KONA* 24 *(2006) 3-14.*

[55] Z. Wang, M. Kwauk, H. Li, Fluidization of fine particles, *Chem. Eng. Sci.* 53 *(1998) 377-395.*

[56] H. Cui, J. Chaouki, Interparticle forces in high temperature fluidization of geldart a particles, *China Particuology* 2 *(2004) 113-118.*

[57] J. P. K. Seville, R. Clift, The effect of thin liquid layers on fluidisation characteristics, *Powder Technol.* 37 *(1984) 117-129.*

[58] M. J. Rhodes, X. S. Wang, A. J. Forsyth, K. S. Gan, S. Phadtajaphan, Use of a magnetic fluidized bed in studying Geldart Group B to A transition, *Chem. Eng. Sci.* 56 *(2001) 5429-5436.*

[59] J. Shabanian, F. Fotovat, J. Bouffard, J. Chaouki, Fluidization Behavior in a Gas-Solid Fluidized Bed with Thermally Induced Inter-particle Forces, *10th International Conference*

On Circulating Fluidized Beds And Fluidization Technology- CFB-10, Engineering Conferences International. Sunriver Resort, Oregon, US, May 1-5, (2011).

[60] D. Geldart, N. Harnby, A. C. Wong, Fluidization of cohesive powders, *Powder Technol.* 37 *(1984) 25-37.*

[61] J. B. Romero, L. N. Johanson, Factors affecting fluidized bed quality, *Chem. Eng. Prog. Sym. Ser.* 58 *(1958) 28-37.*

[62] W. C. Yang, Fluidization of fine cohesive powders and nanoparticles—a review, *J. Chin. Inst. Chem. Eng.* 36 *(2005) 1–15.*

[63] Q. Guo, Y. Li, M. Wang, W. Shen, C. Yang, Fluidization Characteristics of SiO2 Nanoparticles in an Acoustic Fluidized, *Chem. Eng. Technol.* 29 *(2006) 78-86.*

[64] R. D. Morse, Sonic Energy in Granular Solid Fluidization, *Ind. Eng. Chem. Res.* 47 *(1955) 1170-1175.*

[65] R. Chirone, L. Massimilla, S. Russo, Bubbling fluidization of a cohesive powder in an acoustic field, *Fluidization VII (1992) 545–553.*

[66] R. Chirone, L. Massimilla, S. Russo, Bubble-free fluidization of a cohesive powder in an acoustic field, *Chem. Eng. Sci.* 48 *(1993) 41-52.*

[67] P. Russo, R. Chirone, L. Massimilla, S. Russo, The influence of the frequency of acoustic waves on sound-assisted fluidization of beds of fine particles, *Powder Technol.* 82 *(1995) 219-230.*

[68] E. K. Levy, I. Shnitzer, T. Masaki and J. Salmento, Effect of an acoustic field on bubbling in a gas fluidized bed, *Powder Technol.* 90 *(1997) 53-57.*

[69] Q. Guo, H. Liu, W. Shen, X. Yan, R. Jia, Influence of sound wave characteristics on fluidization behaviors of ultrafine particles, *Chem. Eng. J.* 119 *(2006) 1-9.*

[70] Q. Guo, M. Wang, Y. Li and C. Yang, Fluidization of Ultrafine Particles in a Bubbling Fluidized Bed with Sound Assistance, *Chem. Eng. Technol.* 28 *(2005) 1117-1124.*

[71] Q. Guo, X. Yang, W. Shen and H. Liu, Agglomerate size in an acoustic fluidized bed with sound assistance, *Chem. Eng. Process.* 46 *(2007) 307-313.*

[72] S. Mori, A. Yamamoto, S. Iwata, T. Harahan, I. Yamada, Vibro-fluidization of Group C particles and its industrial applications, *AIChE Sym. Ser.* 86 *(1990) 88–94.*

[73] E. Marring, A. C. Hoffmann, L. P. B. M. Janssen, The effect of vibration on the fluidization behaviour of some cohesive powders, *Powder Technol.* 79 *(1994) 1-10.*

[74] K. Noda, , Y. Mawatari, S. Uchida, Flow patterns of fine particles in a vibrated fluidized bed under atmospheric or reduced pressure, *Powder Technol.* 99 *(1998) 11-14.*

[75] J. R. Wank, , S. M. George, A. W. Weimer, Vibro-fluidization of fine boron nitride powder at low pressure, *Powder Technol.* 121 *(2001) 195-204.*

[76] Y. Mawatari, T. Koide, Y. Tatemoto, S. Uchida, K. Noda, Effect of particle diameter on fluidization under vibration, Powder Technol. 123 (2002) 69-74.

[77] C. Xu, Y. Cheng, J. Zhu, Fine particle fluidization-effects of mechanical/acoustic vibration, *Fluidization XI, (2004) 627–634.*

[78] J. M. Valverde, A. Castellanos, Effect of vibration on agglomerate particulate fluidization, *AIChE J.* 52 *(2006) 1705-1714.*

[79] W. Zhang, M. Zhao, Fluidisation behaviour of silica nanoparticles under horizontal vibration, *J. Exp. Nanosci.* 5 *(2010) 69-82.*

[80] A. T. Harris, On the vibration assisted fluidisation of silica nanoparticles, *Int. J. Nanotechnol.* 5 *(2008) 179-194.*

[81] J. F. Richardson, W. N. Zaki, Sedimentation and fluidization. Part 1., *Trans. Inst. Chem. Eng.* 32 *(1954) 35-52.*

[82] H. Wang, T. Zhou, J. S. Yang, J. J. Wang, H. Kage, Y. Mawatari, Model for Calculation of Agglomerate Sizes of Nanoparticles in a Vibro-fluidized Bed, Chem. Eng. Technol. 33 (2010) 388-394.

[83] S. Kaliyaperumal, S. Barghi, L. Briens, S. Rohani, J. Zhu, Fluidization of nano and sub-micron powders using mechanical vibration, *Particuology* 9 *(2011) 279-287.*

[84] S. M. Tasirin, N. Anuar, Fluidization Behavior of Vibrated and Aerated Beds of Starch Powders, *J. Chem. Eng. J.* 34 *(2001) 1251-1258.*

[85] E. K. Levy, B. Celeste, Combined effects of mechanical and acoustic vibrations on fluidization of cohesive powders, *Powder Technol.* 163 *(2006) 41-50.*

[86] K. Erdész, A. S. Mujumdar, Hydrodynamic aspects of conventional and vibrofluidized beds--a comparative evaluation, *Powder Technol.* 46 *(1986) 167-172.*

[87] J. Arnaldos, J. Casal, A. Lucas, L. Puigjaner, Magnetically stabilized fluidization: modelling and application to mixtures, *Powder Technol.* 44 *(1985) 57-62.*

[88] Q. S. Zhu, H.Z. Li, Fluidization of group C powder with external magnetic force, *Fifth China-Japan Symposium on Fluidization, Nagoya, Japan (1994).*

[89] Q. Zhu, H. Li, Study on magnetic fluidization of group C powders, *Powder Technol.* 86 *(1996) 179-185.*

[90] W. Y. Wu, , A. Navada, S. C. Saxena, Hydrodynamic characteristics of a magnetically stabilized air fluidized bed of an admixture of magnetic and non-magnetic particles, *Powder Technol.* 90 *(1997) 39-46.*

[91] V. L. Ganzha, S. C. Saxena, Heat-transfer characteristics of magnetofluidized beds of pure and admixtures of magnetic and nonmagnetic particles, *IJHMT* 41 *(1998) 209-218.*

[92] X. Lu, H. Li, Fluidization of CaCO3 and Fe2O3 particle mixtures in a transverse rotating magnetic field, *Powder Technol.* 10 *(2000) 66-78.*

[93] J. A. Quevedo, J. Flesch, R. Pfeffer, R. Dave, Evaluation of assisting methods on fluidization of hydrophilic nanoagglomerates by monitoring moisture in the gas phase, *Chem. Eng. Sci.* 62 *(2007) 2608-2622.*

[94] P. Zeng, T. Zhou, G. Chen, Q. Zhu, Behavior of mixed ZnO and SiO2 nano-particles in magnetic field assisted fluidization, *China Particuology* 5 *(2007) 169-173.*

[95] Zhou, L., R. Diao, T. Zhou, H. Wang, H. Kage, Y. Mawatari, Behavior of magnetic Fe3O4 nano-particles in magnetically assisted gas-fluidized beds, *Adv. Powder Technol.* 22 *(2011) 427-432.*

[96] M. Kashyap, D. Gidaspow, T. W. Tsai, Effect of electric field on the hydrodynamics of nanoparticles in a rectangular fluidized bed, *AIChE Annual Meeting, San Francisco, CA, US, (2006).*

[97] M. Kashyap, D. Gidaspow, M. Driscoll, Effect of electric field on the hydrodynamics of fluidized nanoparticles, *Powder Technol.* 183 *(2008) 441-453.*

[98] J. M. Valverde, M. A. S. Quintanilla, M. J. Espin, A. Castellanos, Nanofluidization electrostatics, *Phys. Rev. E* 77 *(2008) 031301.*

[99] M. A. S. Quintanilla, J. M. Valverde, A. Castellanos, D. Lepek, R. Pfeffer, R. N. Dave, Nanofluidization as affected by vibration and electrostatic fields, *Chem. Eng. Sci.* 63 *(2008) 5559-5569.*

[100] M. A. Howley, R. Pfeffer. The hydrodynamics of a rotating fluidized bed, *AIChE Annual Meeting, Cicinati, Ohio, US, October 30 - November 04 (2005).*

[101] G. H. Qian, R. Pfeffer, H. Shaw, J. Stevens, Fluidization of group C particles using rotating fluidized beds, *Fluidization X Engineering Foundation, (2001) 509-516.*

[102] S. Matsuda, H. Hatano, K. Tsuchiya, Effects of Operating Conditions on Photocatalytic Reduction of NOx in Fluidized Beds of TiO2, *Fluidization IX, Engineering Foundation, (1998) 701-708.*

[103] E. K. Levy, W. J. Shakespears, A. T. Raissi, J. C. Chen, Particle elutriation from centrifugal fluidized beds, *AIChE Symp. Ser. 77 (1981) 86–95.*

[104] S. Matsuda, H. Hatano, T. Nuramoto, A. Tsutsumi, Particle and Bubble Behavior in Ultrafine Particle Fluidization with High G, *Fluidization X, Engineering Foundation, (2001) 501–508.*

[105] C. Y. Wen, Y. H. Yu, Mechanics of fluidization, *Chem. Eng. Prog. Symp. Ser.* 62 *(1966) 100-111.*

[106] H. Tong, O. Qiu, H. Li, Fluidization Characteristics of Ultrafine Particles in Conical Bed, *Fluidization IX, Engineering Foundation, (2004) 715-722.*

[107] A. Ajbar, Y. Bakhbakhi, S. Ali, M. Asif, Fluidization of nano-powders: Effect of sound vibration and pre-mixing with group A particles, *Powder Technol.* 206 *(2011) 327-337.*

[108] T. Zhou, H. Li, Effects of adding different size particles on fluidization of cohesive particles, *Powder Technol.* 102 *(1999) 215-220.*

[109] L. Song, T. Zhou, J. Yang, Fluidization behavior of nano-particles by adding coarse particles, *Adv. Powder Technol.* 20 *(2009) 366-370.*

[110] A. Ajbar, K. Alhumazi, M. Asif, Improvement of the Fluidizability of Cohesive Powders through Mixing with Small Proportions of Group A Particles, *Can. J. Chem. Eng.* 83 *(2005) 930-943.*

[111] H. Li, R. Legros, C. M. H. Brereton, J. R. Grace, J. Chaouki, Hydrodynamic behaviour of aerogel powders in high-velocity fluidized beds, *Powder Technol.* 60 *(1990) 121-129.*

[112] T. Zhou, H. Li, Estimation of agglomerate size for cohesive particles during fluidization, *Powder Technol*. 101 *(1999) 57-62.*

[113] H. Li, R. Hong, Z. Wang, Fluidizing ultrafine powders with circulating fluidized bed, *Chem. Eng. Sci.* 54 *(1999) 5609-5615.*

[114] J. A. Quevedo, R. Pfeffer, In Situ Measurements of Gas Fluidized Nanoagglomerates, *Ind. Eng. Chem. Res.* 49 *(2010) 5263-5269.*

[115] J. M. Valverde, M. A. S. Quintanilla, A. Castellanos, P. Mills, The settling of fine cohesive powders, *EPL* 54 *(2001) 329.*

[116] X. S. Wang, V. Palero, J. Soria, M. J. Rhodes, Laser-based planar imaging of nano-particle fluidization: Part I--determination of aggregate size and shape, *Chem. Eng. Sci. 61 (2006) 5476-5486.*

[117] X. S. Wang, V. Palero, J. Soria, M. J. Rhodes, Laser-based planar imaging of nano-particle fluidization: Part II--mechanistic analysis of nanoparticle aggregation, *Chem. Eng. Sci.* 61 *(2006) 8040-8049.*

[118] J. M. Valverde, A. Castellanos, Fluidization of nanoparticles: A simple equation for estimating the size of agglomerates, *Chem. Eng. J.* 140 *(2008) 296-304.*

[119] P.M. Jenneson, O. Gundogdu, In situ x-ray imaging of nanoparticle agglomeration in fluidized beds, *Appl. Phys. Lett.* 88 *(2006) 034103-3.*

[120] O. Gundogdu, P. Jenneson, U. Tuzun, Nano particle fluidisation in model 2-D and 3-D beds using high speed X-ray imaging and microtomography, *J. Nanopart. Res.* 9 *(2007) 215-223.*

[121] Y. Iwadate, M. Horio, Prediction of agglomerate sizes in bubbling fluidized beds of group C powders, *Powder Technol.* 100 *(1998) 223-236.*

[122] T. Zhou, H. Li, Force balance modelling for agglomerating fluidization of cohesive particles, *Powder Technol.* 111 *(2000) 60-65.*

[123] A. Castellanos, , J. M. Valverde, M. A. S. Quintanilla, Physics of Compaction of Fine Cohesive Particles, *Phys. Rev. Lett.* 94 *(2005) 075501.*

[124] J. M. Valverde, A. Castellanos, Fluidization of nanoparticles: A modified Richardson-Zaki Law, *AIChE J.* 52 *(2006) 838-842.*

[125] T. A. Witten, L. M. Sander, Diffusion-Limited Aggregation, a Kinetic Critical Phenomenon, *Phys. Rev. Lett.* 47 *(1981) 1400.*

[126] J. M. Valverde, M. A. S. Quintanilla, A. Castellanos, D. Lepek, J. Quevedo, R. N. Dave, R. Pfeffer, Fluidization of fine and ultrafine particles using nitrogen and neon as fluidizing gases, AIChE J. 54 (2008) 86-103.

[127] H. Rumpf, Zur Theorie der Zugfestigkeit vom Agglomeraten bei Kraftubertragung an Kontaktpunkten, *Chemie Ingenieur Technik* 42 *(1970) 538-542.*

[128] J. R. Wank, S. M. George, A. W. Weimer, ALD of aluminum films on nanosized boron nitride particles in a fluidized bed, *AIChE annual meeting, San Francisco, CA, USA (2003).*

[129] B. Esmaeili, J. Chaouki, C. Dubois, Encapsulation of nanoparticles by polymerization compounding in a gas/solid fluidized bed reactor, *AIChE J.* 55 *(2009) 2271-2278.*

[130] K. Nishii, Y. Itoh, N. Kawakami, M. Horio, A pressure swing granulation, A novel binderless granulation by cyclic fluidization and gas flow compaction, *Powder Technol.* 74 *(1993) 1-6.*

[131] S. Matsuda, H. Hatano, A. Tsutsumi, Ultrafine particle fluidization and its application to photocatalytic NOx treatment, *Chem. Eng. J.* 82 *(2001) 183-188.*

[132] M. Corris, B. Caussat, A. Ayral, J. Durand, Y. Kihn, P. Kalck and P. Serp, Carbon nano-tubes produced by fluidized bed catalytic CVD: first approach of the process, *Chem. Eng. Sci.* 58 *(2003) 4475-4482.*

[133] W. Qian , F. Wei, Z. Wang, T. Liu, H. Yu, G. Luo, L. Xiang, X. Deng, Production of carbon nano-tubes in a packed bed and fluidized bed, *AIChE J.* 49 *(2003) 619-625.*

[134] D. Geldart, A. C. Y. Wong, Fluidization of powders showing degrees of cohesiveness--I. Bed expansion, *Chem. Eng. Sci.* 39 *(1984) 1481-1488.*

[135] L. Massimilla, G. Donsì, C. Zucchini, The structure of bubble-free gas fluidized beds of fine fluid cracking catalyst particles, *Chem. Eng. Sci.* 27 *(1972) 2005-2015.*

[136] P. Lettieri, D. Newton, J. G. Yates, Homogeneous bed expansion of FCC catalysts, influence of temperature on the parameters of the Richardson-Zaki equation, *Powder Technol.* 123 *(2002) 221-231.*

[137] K. Godard, and J. F. Richardson, The Behaviour of Bubble-Free Fluidized Beds, *I. Chem. E. Sym. Ser.* 30 *(1968) 126-135.*

CHAPTER 4 ARTICLE 2: HYDRODYNAMICS OF A GAS–SOLID FLUIDIZED BED WITH THERMALLY INDUCED INTERPARTICLE FORCES

Jaber Shabanian, Jamal Chaouki*

Department of Chemical Engineering, Ecole Polytechnique de Montreal, Montreal, Quebec, Canada

* Corresponding author: Tel.: +1-514-340-4711 X 4034; fax: +1-514-340-4159.

E-mail address: jamal.chaouki@polymtl.ca

(Published in Chemical Engineering Journal 259 (2015) 135–152)

4.1 Highlights:

- The effect of interparticle forces on hydrodynamics of gas-solid fluidized bed is studied.
- The fluidization characteristics of the bed can be greatly influenced by interparticle forces.
- The minimum fluidization velocity increases with interparticle forces.
- The gas is more prone to pass through the bed in the emulsion phase when interparticle forces increase.
- Enhancing interparticle forces will increase the bubbling to turbulent regime transition velocity.

4.2 Abstract

In this study, a polymer coating approach was applied to increase and adjust the level of cohesive interparticle forces (IPFs) in a gas-solid fluidized bed. This novel approach is based on coating spherical inert particles with a polymer material having a low glass transition temperature followed by using the coated particles in a gas-solid fluidized bed. Since the level of artificial IPFs inside the bed depends on the temperature of the coated particles, it was simply controlled by the temperature of the inlet air. Accordingly, the system temperature was gradually varied near and slightly above the glass transition temperature of the polymer, between 20–40°C, to investigate the influence of IPFs on the fluidization behavior of the bed at different superficial gas velocities, covering fixed bed state, bubbling, and turbulent fluidization regimes. The study of hydrodynamics

was carried out through the visual observation of bed height, the measurement of bed pressure drop, and the recording pressure signals in the windbox and dense bed. Experimental results indicated that enhancing the level of IPFs in the bed can alter the fluidization behavior of the bed from Geldart (Geldart, D., 1973) group B behavior to Geldart group A and even Geldart group C behaviors, result in a fixed bed with a looser structure that can hold more gas inside, increase the characteristic fluidization velocities, such as minimum fluidization velocity and transition velocity from a bubbling to turbulent fluidization regime, increase the tendency of the fluidizing gas passing through the emulsion phase in the bubbling regime, and result in a noticeably larger bubble size at gas velocities slightly higher than the bubbling to turbulent transition velocity of the bed without IPFs.

Keywords: Gas-solid fluidized bed, Interparticle forces, Hydrodynamics, Global measurements.

4.3 Introduction

Together with the basic physical properties of powder, such as particle density, size, shape and roughness, interparticle forces (IPFs) are among the most important parameters affecting the fluidization behavior of particulate materials. In regard to the significance of IPFs, it has been well demonstrated that the flow dynamics of Geldart [1] group C powders is mainly governed by IPFs [2]. This results in completely different behavior compared to the other groups of Geldart classification with low or no IPFs. In addition, research studies on the subject of the hydrodynamics of a gas-solid fluidized bed at high temperatures clearly pointed out that some peculiar phenomena, which happen at elevated temperatures, cannot be solely explained in light of the influence of this variable on the properties of the fluidizing gas [3-11]. In fact, it turns out to be obvious that the simultaneous influence of the operating temperature both on the gas phase and the solid phase, considered as variations in IPFs, must be taken into account to describe these behaviors well. Therefore, it is highly necessary to clearly address how IPFs can change the fluidization dynamics of a gas-solid fluidized bed.

Different approaches have been used by researchers to investigate the influence of IPFs on the fluidization behavior of gas-solid fluidized beds. However, easy and accurate control of the level of IPFs that are uniformly distributed throughout the particulate media is the most important criterion for the selection of a method by which IPFs are introduced into a bed of powders. Also,

to tackle what was found at high temperatures, the methodology can be chosen to imitate the cohesive behavior found at extreme operating temperatures in a friendlier environment. Techniques that have been applied include the following: increasing the level of van der Waals forces by reducing the mean particle size [12-16]; intensifying the amount of capillary force by adding a cohesive agent into the bed [17, 18]; application of a magnetic field around the bed [19-21]; and increasing the bed temperature to a high value while cured particles, doped silica catalysts and Ballotini particles with the potassium acetate, were used as bed materials [10, 11].

Each of these approaches has specific difficulties in practice. Basically, the magnitude of van der Waals interparticle forces becomes considerably small compared to the hydrodynamic forces (HDFs) for particles in excess of 100 μm in size [22, 23]. Accordingly, in order to use van der Waals forces to study the behavior of the bed in the presence of IPFs, it is required to utilize particles smaller than 100 μm in size. For larger particles for which HDFs are dominant, IPFs can be introduced by the addition of a cohesive agent into the bed. However, it is challenging with this approach to have uniform distribution of the liquid phase throughout the particulate bed [24, 25]. This results in interparticle force anisotropy inside the bed. Additionally, the application of this technique limits the fluidization study at only low superficial gas velocities. In the third technique, the ferromagnetic particles repel each other when they are perpendicular to the magnetic field and attract each other when they are parallel. This results in mal-distribution of IPFs around the particles, thus, yielding anisotropic attraction/repulsion in the bed [26]. Moreover, there is little degree of similarity between the flow dynamics of a cohesive bed obtained from this approach and those that are normally found in industrial applications. It is due to the fact that IPFs attained by this methodology are aligned with the magnetic field following a specific direction [27]. For the last approach, it requires operating the gas-solid fluidized bed at high temperatures. Application of this method is limited by the expensive capital and operational costs of experimental work at elevated temperatures as well as the lack of proper hydrodynamic measurement techniques, which are applicable for such operating conditions [28].

Shabanian et al. [29] and Bouffard et al. [27] have recently presented a novel approach by which cohesive IPFs are introduced into the bulk of particulate materials through modification of particle surface properties accompanied by the adjustment of the operating temperature in the system. This novel technique is called polymer coating approach. It uses spherical inert particles, which are coated with polymer material having a low glass transition temperature (9^{o}C) by an atomization

process. The polymer material is a copolymer PMMA/PEA (Poly Methyl MethAcrylate/Poly Ethyl Acrylate) contained in a polymer suspension called Eudragit NE30D. By changing the operating temperatures slightly above the glass transition temperature of the polymer, e.g., between 20–40^{o}C, the polymer properties are modified in a way that the artificial cohesive IPFs between the coated particles can be varied significantly. In this way the degree of cohesivity inside the bulk of materials can be simply controlled by the temperature of the inlet air in a stable and reproducible manner. More conceptual information concerning this approach can be found in Bouffard et al. [27].

A number of promising benefits can be achieved by applying the polymer coating approach to enhance the level of IPFs inside the gas-solid fluidized bed. Unlike the van der Waals force method, there is no concern regarding the sole application of very fine particles. Since the degree of cohesivity obtained by this technique is directly associated with the temperature of the surface of the coated particles and there is a uniform temperature profile inside the gas-solid fluidized bed, cohesive IPFs attained by this approach are uniformly distributed throughout the bed. Also, a fluidization study can be conducted at both low and high superficial gas velocities with no restrictions. More interestingly, this technique is practical for reproducing and imitating the conditions found in gas-solid fluidized beds operating at elevated temperatures in a much friendlier environment. Accordingly, unlike high temperature operation, which is limited by a few measurement techniques for hydrodynamic study, since this method requires working at operating temperatures slightly above the glass transition temperature of the polymer (9^{o}C), different measurement techniques can be easily applied for hydrodynamic study. Preliminary results of the application of this method for the introduction of IPFs into a gas-solid fluidized bed showed promising performance [29].

To the authors' knowledge almost all experimental data that have been collected by researchers regarding the influence of IPFs on the fluidization behavior of gas-solid fluidized beds are at fairly low superficial gas velocities, near the minimum fluidization/bubbling velocity [10-20]. Until now, there is no reported data about the effect of IPFs on the bed hydrodynamics at moderate and high gas velocities. Therefore, it is interesting to use the polymer coating approach considering all of its advantages to investigate the effect of IPFs on the hydrodynamics of a gas-solid fluidized bed not only at low gas velocities but also at velocities well above the minimum fluidization velocity covering both bubbling and turbulent fluidization regimes. In the present study, experimental observations, measurements of bed pressure drop and gauge/differential pressure fluctuations in

the windbox and dense bed have been used to characterize the hydrodynamics of a gas-solid fluidized bed with different levels of IPFs.

4.4 Methodology

The experimental campaign initially required producing uniformly coated particles with a thin layer of coating polymer on the surface of the base particles. This was achieved in a spheronizer machine through an atomization process. Subsequently, the coated particles were used in a gas-solid fluidized bed apparatus and subjected to various operating temperatures by which the polymer properties and the level of IPFs were altered.

4.4.1 Particle coating process

The first experimental step was to prepare coated particles with a thin and uniform layer of polymer coating on the surface of the base particles. Copolymer PMMA/PEA contained in a polymer suspension, Eudragit NE30D, was used as the coating material. The inert base powders used in this work were a 450–720 μm cut of spherical sugar beads (d_p=580 μm, ρ_p=1556 kg/m^3), which can be classified as Geldart group B powders at ambient conditions (d_p is the mean particle size and ρ_p is the particle density). These beads could easily accept the PMMA/PEA material as coating and, hence, satisfied the requirements.

Coated sugar beads were produced through an atomization process. During this process the polymer suspension, which consists of a solution of the copolymer PMMA/PEA in a 2 to 1 ratio in water (Mass %: Water 70.0; PMMA/PEA 28.66; Noxynol100 1.33), was coated on the surface of the sugar beads. The particles were simultaneously dried by the heated air to attain a uniform coating layer on the surface of the base particles. The coating process was conducted in the spheronizer machine with a two-substance atomizer (BETE XA-SR 050). A schematic of this process can be seen in Figure 4.1. The heated air was introduced into the processing chamber at a specific flow rate and temperature. Adjustments of the gas flow rate and operating temperature during the coating process were done to ensure an adequate drying rate throughout the process and to prevent particle adhesion. The atomizer was fed with the coating solution using a peristaltic pump with a flowrate close to 1 g/min and compressed air, which allowed the formation of a very fine coating droplets. This, in fact, is essential for an efficient coating process. Also, conducting

the coating process at a very low flowrate of polymer solution, 1 g/min, ensured the good distribution of a thin coating of film on all the particles inside the spheronizer chamber. It is worth mentioning that with all these measures appreciable similarity was found between the particle size and density measurements from different samples selected from various locations in the spheronizer chamber at the end of the coating process and also in different days. This confirmed the repeatability of the effective coating process. Table 4.1briefly reports operating parameters related to the coating process of the sugar beads.

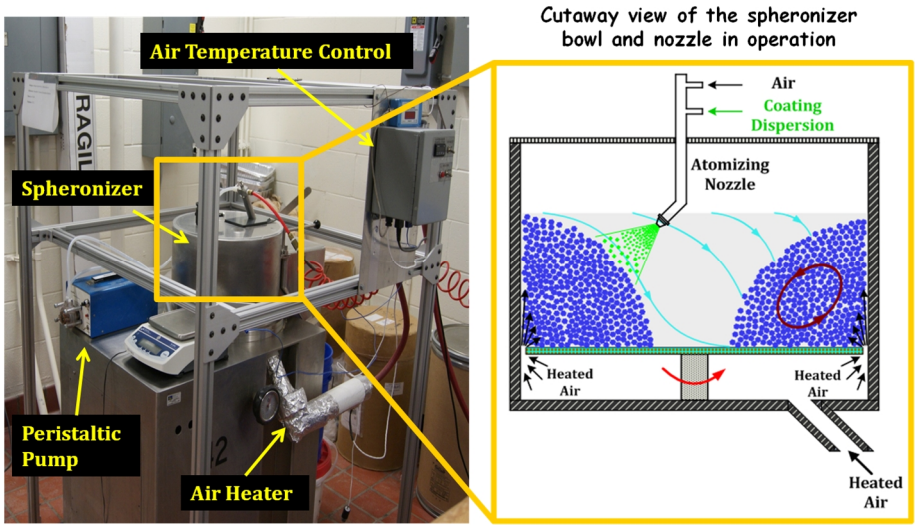

Figure 4.1: Schematic of the spheronizer machine and the atomization nozzle during the coating process.

The characteristics of the final coated beads are presented in Table 4.2. It is important to mention that having achieved a thin coating layer during the coating process, variations in particle size and density for sugar beads were approximately only 1% for both parameters. Therefore, the fresh and coated sugar beads held very similar characteristics from Geldart classification's point of view.

Table 4.1: Operating parameters of the coating process.

Disc rotational rate (rpm)	230
Air flowrate (cfm)	25
Air temperature (°C)	30
Coating solution flowrate (g/min)	1
Atomization pressure (Kpa)	200

Table 4.2: Characteristics of the final coated particles.

Materials	*Quantity*
Spherical sugar beads	3.0 (kg)
PMMA/PEA	0.10 (kg)
Mass percentage of coating	3.4 %
Thickness of coating layer	~ 5 μm

4.4.2 Experimental set-up

All experiments for the hydrodynamic study were conducted in an atmospheric pressure cold fluidized bed made of a transparent Plexiglas tube with a 15.2 cm internal diameter and 3.0 m in height. With the help of an external cyclone at the air outlet of the column entrained particles were returned back into the freeboard of the bed. Dried and filtered air was used as fluidizing gas and supplied to the bed through a perforated distributor plate. The distributor plate was 1 cm thick and made from aluminum. It consisted of 157 holes 1 mm in diameter arranged in 1 cm triangular pitch.

The fluidizing air was heated up by an electrical heater before entering the fluidized bed. Accordingly, it was used to adjust the operating temperature of the system at a desired process set-point. The air flowrate was controlled by a calibrated rotameter and an orifice plate connected to a water manometer to cover a wide range of gas velocities in the bed. In this regard, different superficial gas velocities were used at each temperature tested, up to 1.3 m/s, covering the packed bed state, bubbling and turbulent fluidization regimes.

In order to investigate the effect of IPFs on the fluidization behavior of a gas-solid fluidized bed, uncoated/fresh and coated sugar beads were separately used in the fluidizing column at different operating temperatures. Experiments of fresh sugar beads, as a base system without IPFs, were conducted at 20°C. However, in order to achieve different levels of IPFs inside the bed, experiments with the coated sugar beads were performed at 20°C, 30°C, and 40°C. From this point onwards, for simplicity, we refer to these systems with their different operating temperatures in abbreviated form, SB20, CSB20, CSB30, and CSB40, which stand for fresh sugar beads at 20°C and coated sugar beads at 20°C, 30°C, and 40°C, respectively. It should be noted that the variations of air viscosity and density in the 20°C to 40°C temperature range used in the present work are 5% and 6%, respectively. These variations are relatively negligible compared to the degree of variation of cohesive IPFs, which can be achieved by the polymer coating approach for the same process temperature range. Therefore, different behaviors found from systems operated at different temperatures were principally attributed to the variation in the level of IPFs. For all experiments the same amount of material was fed into the column, 4.0 kg. It resulted in an initial bed height of approximately 26 cm (h/D ≈ 1.70) at ambient conditions (h is the bed height and D is the column diameter).

At each experimental temperature, fluidization tests were conducted with the purpose of hydrodynamic study through the experimental observations and the global measurements of pressure signals. Three graduated scales stuck on the outer surface and around the periphery of the transparent fluidizing column approximately $2\pi/3$ apart from each other were used to read the bed height. The average bed height was subsequently calculated based on the three bed height readings. A differential pressure transducer (MODUS, R32-100, 0–100 in water) was applied to measure the bed pressure drop across the whole bed with the aid of a pressure tap located just above the distributor plate. Also, two gauge pressure transducers were used to measure pressure signals in the dense bed and windbox (in-bed: OMEGA, PX309-002GI, 0–2 psig; windbox: Honeywell, model SA, 0–50 psig). Since an in-bed gauge pressure transducer responds to every pressure fluctuation that occurs within the bed [30], analysis of the time series of the pressure signals obtained from this transducer gives global insight to what's occurring inside the bed. The pressure port related to the in-bed gauge pressure measurement was positioned at 17.5 cm in height above the distributor plate. Furthermore, in-bed dynamic differential pressure fluctuations were recorded with an appropriate pressure transducer (OMEGA, PX272-20DI, 0–20 in water). The

corresponding pressure ports were located at equal axial distance to the pressure port connected to the in-bed gauge pressure transducer on either sides of it (10–25 cm above the distributor plate). Since the response of the differential pressure transducer is affected by the pressure fluctuations occurring between its ports [30], placement of the differential pressure transducer with this configuration made it possible to track the phenomenon happening inside the stabilized dense bed with another set of glasses. The pressure signals were acquired at the sampling frequency of 400 Hz for a period of four minutes with the help of a 16 bit A/D data acquisition board using the Labview 9.0.1® program. The fluidizing column used in this study with the special placements of different measurement ports are schematically shown in Figure 4.2.

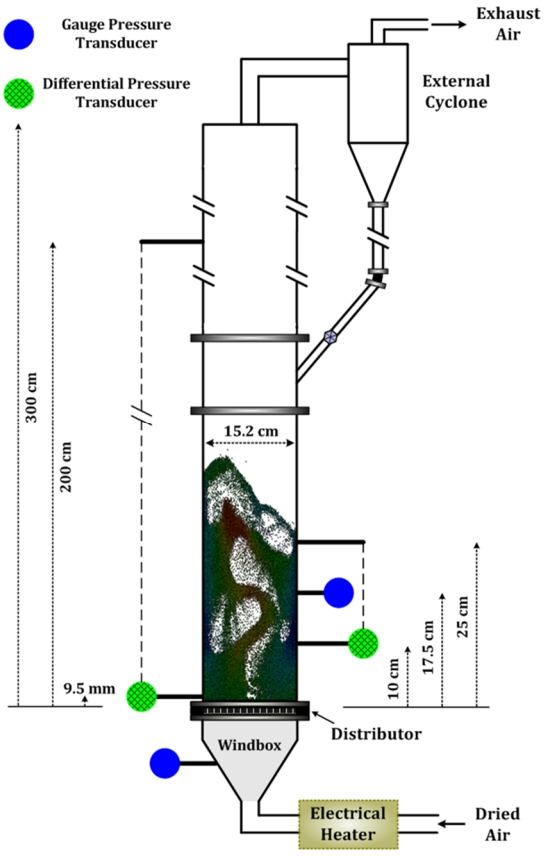

Figure 4.2: Schematic diagram of experimental cold model column equipped with pressure transducers.

4.5 Analysis of pressure signals

In general, pressure fluctuations obtained from a gas-solid fluidized bed contain a considerable amount of information about the hydrodynamics of the bed when the pressure is sampled at a sufficiently high frequency [31]. They include the effect of many different dynamical phenomena

taking place in fluidized beds, such as bubble formation, coalescence, and eruption, bed mass oscillation, etc. [32-34]. Therefore, detailed information on the dynamic characteristics of the gas-solid fluidized bed can be obtained from scrutinizing the pressure fluctuations. Different analysis methods have been used to treat the gauge and differential pressure signals acquired during the experimental campaign to provide clear insight into the impact of IPFs on the fluidization behavior of a gas-solid fluidized bed. It is worth mentioning that all pressure signals that were applied in this study to be analyzed with different methods were obtained after subtracting a moving average with 0.2 Hz from the primary signal. This was performed to eliminate the effect of gas flow rate fluctuations on the signals.

4.5.1 Bed pressure drop profile

The conventional method of bed pressure drop variation as a function of superficial gas velocity can be applied as the first indication of fluidization behavior. It has been well demonstrated that HDFs dominate the hydrodynamics of powders showing typical behavior of Geldart group B particles [22]. They form bubbles at the minimum fluidization velocity U_{mf} [1]. Also, their bed pressure drop profile reaches a plateau without illustrating an overpressure compared to the pressure drop resulting from the weight of the bed following a linear increase in the bed pressure drop with the gas velocity in the packed bed state [35]. However, the magnitude of IPFs is comparable with that of HDFs for Geldart group A powders [22]. Basically, there is a degree of overshoot at U_{mf} for the bed pressure drop profile of these particles. It originates from the tensile strength that is created in the bulk of the materials due to IPFs. The presence of IPFs for these powders is indeed responsible for the prevention of the bed to be easily fluidized at U_{mf} while they exhibit normal fluidization at gas velocities above the minimum bubbling velocity, U_{mb} [18, 36]. Unlike Geldart group A and B powders, fluidization dynamics of powders with Geldart group C characteristics is dominated by IPFs [2]. Powders with these behaviors are difficult to fluidize normally. Due to the considerable amount of cohesive IPFs they normally form channels and rat holes at low gas velocities while part of the bed might lift upward at higher gas velocities, especially in small diameter fluidizing columns [1]. These characteristics are generally translated into erratic behavior in the bed pressure drop profile, either a considerably smaller bed pressure drop than the bed apparent weight per unit area because of the formation of cracks/channels or an appreciably larger bed pressure drop due to the upward lift of the whole bed or part of it [37]. Accordingly, the

evaluation of the bed pressure drop profile can be used for the determination of the influence of IPFs on the fluidization quality and to check whether the HDFs or IPFs dominate the fluidization behavior. In addition, the minimum fluidization velocity, which is an important parameter to describe the fluidization of powders and is required for the initial design and subsequent scale-up and operation of gas-solid fluidized bed reactors, can be determined using the bed pressure drop profile.

4.5.2 Standard deviation

The most common method for analyzing pressure fluctuations in the time domain is to evaluate the amplitude of signals, which is generally expressed in the form of standard deviation. For a series of pressure sampling points, p_i (i = 1, 2, 3, …, N), the standard deviation σ can be calculated as the following:

$$\sigma = \sqrt{\frac{1}{N-1}\sum_{i=1}^{N}(p_i - \bar{p})^2} \qquad 4.1$$

where N is the number of data points at the sampling time interval and $\bar{p}$ is the mean value of the pressure time series p_i [38]. The bubbling phenomenon is basically the most influencing phenomenon, which diverges the bed from its steady behavior [39]. Since the standard deviation is a measure of data set dispersion from its mean value (corresponding to the steady behavior of the bed), the standard deviation of in-bed pressure signals has an intense interrelation with mean bubble size. Accordingly, the change in the amplitude with the superficial gas velocity has been used to identify the transition velocity between regimes, e.g., from bubbling to turbulent fluidization regime [40-42].

4.5.3 Power spectral density

The power spectral density (PSD) of a signal is a frequency domain analysis. It represents the contribution of every frequency in the spectrum to the power of the overall signal. The PSD can be evaluated by the magnitude of the square of Fourier transform of the original signal. The variance of such estimation for PSD does not decrease with an increase in the number of data points. In order to diminish the variance, the signal can be repeatedly divided into sub-spectra and an average

of a number of sub-spectra can be considered as an estimate for PSD [38]. This is, in fact, the Welch method of PSD estimation [43]. The number of sub-spectra is chosen in a manner to achieve a satisfactory compromise between frequency resolution and variance. Accordingly, the pressure time series can be divided into K segments of distinct length of M_s. The PSD of each sub-spectra can be evaluated as:

$$P_{xx}^{i}(f) = \frac{1}{\sum_{m=1}^{M_s} w^2(m)} \left[\sum_{m=1}^{M_s} p_i(m)\, w(m)\, e^{-2j\pi mf} \right]^2 \tag{4.2}$$

where $p_i(m)$, $w(m)$, j, and f are the sampled pressure time series, window function, complex number, and frequency, respectively. Using Hamming window w while there are no overlaps between windows, the averaged PSD can be estimated as follows:

$$P_{xx}(f) = \frac{1}{K} \sum_{i=1}^{K} P_{xx}^{i}(f) \tag{4.3}$$

The Hamming window used in the Welch method is defined as follows [44]:

$$w(n) = 0.54 - 0.46 \cos\left(\frac{2\pi n}{M_s - 1}\right) \tag{4.4}$$

In the frequency domain, the amplitude, dominant frequency, and frequency distribution of PSD of pressure fluctuations can be analyzed and applied as an index of flow pattern inside the bed. It can be additionally used for qualitative characterization of the regime transition [41, 45, 46].

4.5.4 Estimation of bubble size by signal decomposition approach

Pressure fluctuations in a gas-solid fluidized bed exhibit a complex structure since they arise from different sources. Pressure waves originating from different sources have different propagation velocities. Fast-travelling pressure waves include those waves that are generated by bubble formation, coalescence, breakage, and eruption, bed mass oscillations, and gas flow fluctuations [33]. These waves can be propagated with a velocity in the range of 5–30 m/s, with the higher limit (~30 m/s) for voidage close to minimum fluidization conditions and decreasing rapidly to about 10 m/s with bed voidage increasing to that at U_{mb} [34]. Therefore, they can instantaneously be

registered anywhere in the bed, even in the windbox [32]. Nonetheless, slowly propagating pressure fluctuations stem from the passage of rising gas bubbles inside the bed [33]. These waves propagate at the same velocities as the bubble rise velocities, normally less than 2 m/s [47]. Since the passage of bubbles creates local pressure fluctuations, these phenomena can only be measured locally in the bed and not in the windbox. Therefore, by comparison of absolute/gauge pressure fluctuations that are simultaneously measured in the windbox and dense bed the bubble-passage-induced pressure components can be identified. Van der Schaaf et al. [33] proposed a frequency-domain-based approach by which PSD of in-bed absolute/gauge pressure fluctuations can be decomposed into two separate parts, a coherent component (COP) and an incoherent component (IOP), relative to the pressure signals recorded in the windbox. This approach is also known as incoherent analysis or IOP method. According to this approach, the fast-travelling waves are considered as the coherent part between two pressure time series and the incoherent part is related to the bubble-passage-induced waves. The coherence of two pressure signals, p_x in the windbox and p_y in the bed, can be quantified by calculation of a coherence function, $\Upsilon_{xy}^2(f)$, as the following:

$$\Upsilon_{xy}^2(f) = \frac{P_{xy}(f)\, P_{xy}^*(f)}{P_{xx}(f)\, P_{yy}(f)} \tag{4.5}$$

where $P_{xx}(f)$ and $P_{yy}(f)$ are the PSDs of the windbox and the in-bed gauge pressure signals, respectively, whereas $P_{xy}(f)$ is their cross PSD and $P_{xy}^*(f)$ is the conjugate of $P_{xy}(f)$. The coherence function ranges from 0 to 1, with zero representing completely unrelated PSD of two signals and unity indicating fully related PSDs. Subsequently, COP can be estimated as follows:

$$COP(f) = \Upsilon_{xy}^2 P_{yy}(f) \tag{4.6}$$

and IOP as:

$$IOP(f) = (1 - \Upsilon_{xy}^2)\, P_{yy}(f) \tag{4.7}$$

Davidson [48] proposed that the amplitude of bubble-passage-induced pressure fluctuations is proportional to the gas bubble diameter D_b. Therefore, the amplitude of IOP in the time-domain is related to the bubble diameter and, hence, the bubble size in the gas-solid fluidized bed can be estimated by [33]:

$$D_b \approx \frac{\sigma_{xy,i}}{\rho_p\, g\, (1 - \varepsilon_{mf})} \quad 4.8$$

where ε_{mf} is the bed voidage at minimum fluidization conditions, and $\sigma_{xy,i}$ is the standard deviation of IOP, which based on Parseval's theorem can be calculated as follows [33]:

$$\sigma_{xy,i}^2 = \int_0^\infty IOP_{xy}(f)df \quad 4.9$$

Since the incoherent component of in-bed absolute/gauge pressure signals is related to gas bubbles, which are generated in the vicinity of the pressure sensor, the bubble size obtained from Eq. 4.8 is basically for the region near the transducer [49]. It should be noted that the incoherent analysis does not directly result in actual bubble size but a characteristic length scale, which is proportional to the mean bubble size. Moreover, the bubble length scale that is estimated by this method is irrespective of the bubble shape and its spatial distribution [50].

4.5.5 Estimation of the frequency of macro-structures by wavelet analysis

In order to assess the distribution of the fluidizing gas between the bubble and emulsion phases using the measured pressure signals, information about the frequency of bubbles extra to their size is required to be known. It was reported by Fan et al. [51] that the dominant frequency in the PSD of gauge pressure signals in the bubbling regime could be attributed to the frequency of bubble passage in the bed. However, the precision of this method, the determination of a peak in the resulted frequency spectrum, is principally low. Also, Kage et al. [52] found that the dominant frequency from the absolute pressure signals corresponds to the bubble eruption frequency detected at the bed surface. Therefore, it is difficult to extract the frequency of bubble passage in the bed by direct application of the PSD of pressure signals.

Zhao and Yang [53] demonstrated that the original pressure signals registered from a gas-solid fluidized bed could be decoupled by wavelet analysis into three main frequency scales. This stems from the fact that gas-solid fluidization can be treated as a multi-scale phenomenon with components on three distinct frequency scales [54]. The low frequency components with large amplitude of fluctuation correspond to macrostructures of fluidized bed (mainly bubbles). The medium frequency structures belong to the meso-structures and reflect dynamic features of particle

clusters. The high frequency components associated with micro-structures, which originate from the motion of a single particle and measured noises in the fluidized bed [53, 55]. Johnsson et al. [38] showed that the phenomena of different scales can be identified in a logarithmic scale of PSD of pressure signals. Hence, after identification of the frequency range representing the macro-structures following the same strategy introduced by Johnsson et al. [38], the wavelet analysis [53, 56] can be employed to decouple the original pressure signals in different windows of frequencies. Subsequently, the pressure signal related to the macro-structures can be reconstructed using one/more detail signals considering the principles of the wavelet (noting the range of frequencies that is covered by each detail and approximation signals). Then, the peak frequency of the reconstructed signals can be calculated and attributed to the frequency of the macro-structures, which could be a well representative of the frequency of bubble passage in the bed.

4.6 Results and discussion

4.6.1 Measurement of Hausner ratio

In order to ascertain that by application of the polymer coating approach the level of IPFs increases in the bed when the operating temperature increases, the measurements of Hausner ratio were performed for fresh sugar beads and coated ones at different temperatures ranging between 20^{o}C to 40^{o}C. The Hausner ratio is defined as the ratio of aerated bulk density ρ_{ab} to tapped bulk density ρ_{tb} of powder [12]. According to the empirical classification criterion presented by Geldart et al. [12], cohesive powders that are difficult to fluidize produce high Hausner ratios. It was found that powders having a ratio less than 1.25 appear to be fluidized like Geldart group A particles, while the fluidization behavior for powders with a ratio higher than 1.4 is identical to the classical behavior of Geldart group C particles [12]. Results of these measurements are presented in Figure 4.3. It can be found that the Hausner ratio progressively increased with the operating temperature. This approves that the level of IPFs achieved by the application of the polymer coating approach increases with the operating temperature.

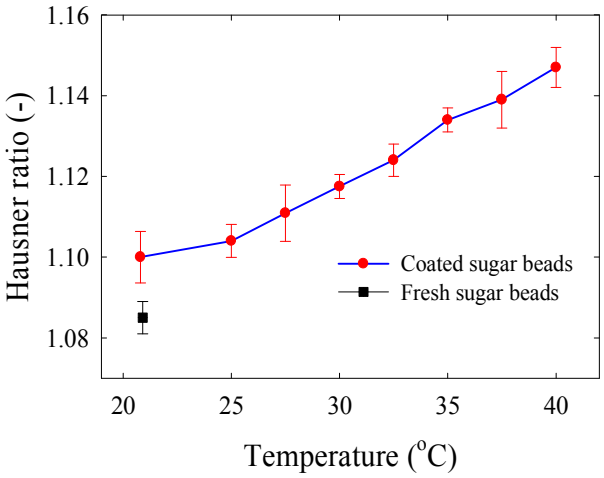

Figure 4.3: Hausner ratios of fresh and coated sugar beads at different temperatures.

It is worth mentioning that although, as will be discussed later, CSB40 showed identical behavior to the typical Geldart group C particles at fairly low gas velocities, the value of the Hausner ratio for the coated sugar beads at 40°C was smaller than 1.4 in comparison with the Geldart's representation. It should be kept in mind that the criterion presented by Geldart to predict the fluidization behavior of cohesive and non-cohesive micron size fine particles based on the values of the Hausner ratio was established for particles that were naturally cohesive, principally by the dominance of van der Waals forces. Accordingly, for the very fine Geldart group C particles, smaller than 30 µm, it is expected that the size of cavities formed between particles in the packing is in the same order or even slightly larger than that of the particle size. Hence, once an aerated packed bed of these particles is successively tapped, a completely dense packed bed can be eventually attained due to the well arranged placement of very fine particles next to each other in the packing. This yields a value higher than 1.4 for the Hausner ratio. However, if virtual IPFs, e.g., by the polymer coating approach, are introduced into the particulate bed while the base particles are fairly coarse, about 600 µm in size, there could not be a considerable difference between the aerated and tapped packed beds. It is due to the fact that the voidage of a completely tapped packed bed of coarse particles could be higher than that of very fine particles. Therefore, the marginal values of the Hausner ratio established by Geldart for the naturally cohesive powder cannot be essentially valid for all kinds of cohesive particulate beds. Similarly, Esmaeili et al. [57] found that the Hausner ratio criterion introduced by Geldart cannot satisfactorily predict the

Agglomerate Particulate Fluidization (APF) and Agglomerate Bubbling Fluidization (ABF) [2] behaviors of nano size cohesive particles.

4.6.2 Bed pressure drop profile

The bed pressure drop was first measured while increasing the fluidizing velocity in small steps ("Fluidizing" curve). Once the bed became well fluidized, the superficial gas velocity U_g was decreased till all contents of the bed settled down and the bed pressure drop was recorded with the same procedure ("Defluidizing" curve).

Figure 4.4 illustrates the results of the measured bed pressure drop for beds with different levels of IPFs during increasing and decreasing fluidizing velocity branches. It can be found for SB20 that at gas velocities below U_{mf} the bed pressure drop continuously increased with fluidizing velocity. At minimum fluidization velocity, bubbles formed inside the bed and the bed pressure drop became practically constant without showing any overpressure at U_{mf}. These behaviors are similar to those of typical Geldart group B powders. However, when CBS20 was used in the bed, a slightly lower pressure drop was recorded for its packed bed in comparison with SB20. This was followed by a small overpressure in the fluidizing curve while the bed became completely fluidized at a slightly higher velocity than U_{mf} for SB20. The presence of an overshoot for the bed pressure drop profile at velocities close to U_{mf} is due to the adhesion forces by which particles act on each other and on the walls of the fluidized bed apparatus [35, 58, 59]. This phenomenon is normally found for powders showing Geldart group A behavior. By increasing the level of IPFs inside the bed of coated sugar beads with increasing the bed temperature to 30°C, CSB30, it was noted that the packed bed had an even lower pressure drop than CSB20. Also, the degree of overshooting in the fluidizing curve for CSB30 was considerably larger than CSB20. It represents a higher degree of impact of IPFs on the fluidization behavior of CSB30. This was accompanied by further increase in U_{mf}. It is important to mention that for CSB20 and CSB30, due to the cohesive IPFs that were obtained by the polymer coating approach, the bed was prevented from homogeneous expansion for gas velocities that coincide with the overpressure in the bed pressure drop profile. Both systems formed bubbles once they became fluidized. This will be discussed in detail in section 4.6.3.

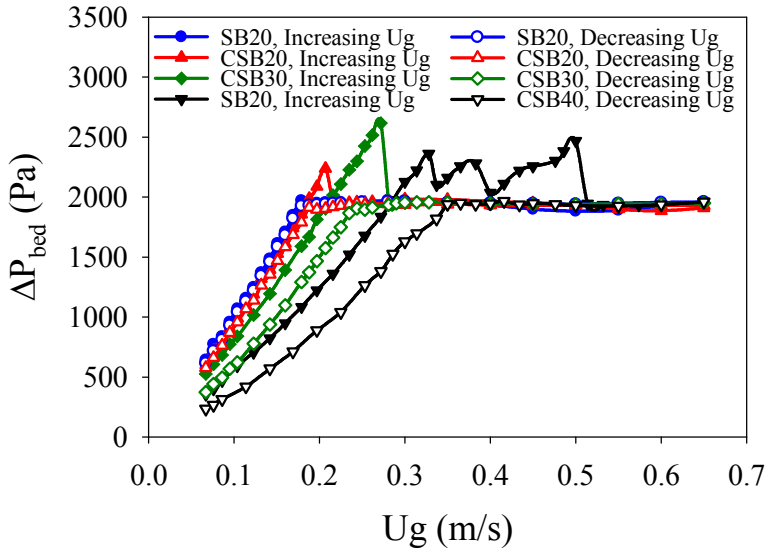

Figure 4.4: Bed pressure drop profile during increasing and decreasing velocity passes.

The highest level of IPFs was achieved for CSB40. In the fixed bed state, this bed showed the least resistance to the passage of the gas through the bed, which resulted in the smallest bed pressure drop compared to the other systems. The fluidization of CSB40 characterized by the presence of an over-pressure in the fluidizing bed pressure drop profile at velocities even higher than U_{mf} of CSB30, formation of cracks and rat holes at low fluidizing velocities, and lifting a portion of the bed as a slug rather than fluidizing it at mediate velocities. These are identical to classical characteristics of Geldart group C powders, which are supported by the erratic behavior in the fluidizing curve shown in Figure 4.4. For CSB40 increasingly higher velocities were needed to achieve complete fluidization. These results show that an increase of the level of IPFs can cause the fluidization behavior of the bed to change from Geldart group B behavior to Geldart group A and even Geldart group C behaviors. In addition, Figure 4.4 shows that U_{mf} increases when the role of cohesive IPFs is enhanced in the bed.

Figure 4.4 further indicates that the bed pressure drop profiles for SB20 during the increasing and decreasing velocity passes are well matched. This implies that the only resistance that the drag force, due to the gas flow rate, should overcome to fluidize the bed is its buoyant weight. However, hysteretic behavior can be seen for the fluidization-defluidization cycles of systems with IPFs inside. Such behavior is basically caused by the impact of IPFs on the bed behavior. For these systems, during the increasing fluidizing velocity pass, the drag force should compensate both the

buoyant weight of the bed and the yield stress of the packed bed due to IPFs in order to make the bed fluidized. This results in the appearance of an overshoot in the bed pressure drop profile in the fluidizing branch. It can be found from the fluidizing-defluidizing bed pressure drop profiles plotted in Figure 4.4 that the more the bed was influenced by IPFs, the larger was the deviation obtained between the curves. Similar behaviors were found by Lettieri et al. [11], who investigated the effect of IPFs on the fluidization behavior of a doped silica catalyst with potassium acetate at high temperatures. Espin et al. [60] had also reported the same trend while horizontal magnetic fields of different strengths were applied to a Geldart A steel powder.

4.6.3 Bed height and packed bed permeability

The variation of the fixed and fluidized bed heights for fresh and coated sugar beads are presented in Figure 4.5. It shows that by increasing the level of IPFs in the bed, the fixed bed height and, correspondingly, the fixed bed voidage, increased. This can be, in fact, translated into a reduction in the coordination number of a single particle in the packing with enhancing IPFs. The coordination number $\mathcal{K}$ of an individual particle in the packing is defined as the total number of contact points with surrounding particles [35]. Once IPFs are present in the bed, part of the weight of a single particle in the packing can be sustained with these forces and, hence, they prevent particles from shearing off to sideward positions. Accordingly, particles are piled up in the vertical direction with relatively little sideward support, leaving more voids in the packing. This, in turn, brings about a lower coordination number for the particles while the packing holds higher porosity.

Raso et al. [7], Formisani et al. [3], and Xu and Zhu [6] reported that voidages of the loosely settled beds of a wide range of particles from Geldart C to B increased with temperature. They referred these variations, in the total absence of gas flow, to modifications in particulate phase properties, namely a growth of IPFs stabilizing a looser solid lattice. Experimental results of this study affirm these opinions and indicate that a fixed bed with higher IPFs can be stabilized with a looser structure and hold more gas inside. Similar findings have been reported by Rhodes et al. [20] and Espin et al. [60] while IPFs were induced into the system using a magnetic field.

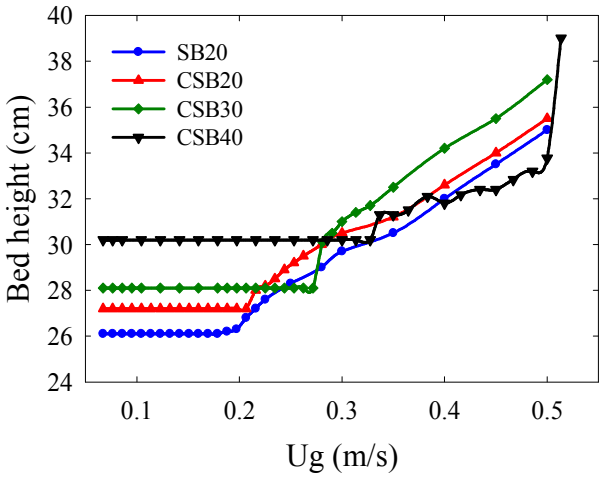

Figure 4.5: Effect of IPFs on the fixed and fluidized bed heights.

Having the bed pressure drop profile and the fixed bed height, the permeability of the packed bed χ can be evaluated. It is an important parameter, which shows the capability of the packing for letting a fluid to pass it under the influence of a pressure gradient and can be estimated by the following [35]:

$$\chi = \frac{\Delta h\, U_g}{\Delta P} \tag{4.10}$$

According to Carman [61] the bed pressure drop increases linearly with the gas velocity below U_{mf} at a low Reynolds number. It can be described by the following:

$$\frac{\Delta P}{\Delta h} = \frac{180}{{d_p}^2} \frac{(1-\varepsilon)^2}{\varepsilon^3} \mu_g\, U_g \tag{4.11}$$

where ΔP is the bed pressure drop at the superficial gas velocity U_g, μ_g is the viscosity of the flowing gas, and ε is the bed voidage. Therefore, the permeability is a strong function of packing porosity as in the following:

$$\chi = \frac{\varepsilon^3\, {\mathrm{d_p}}^2}{180\, \mu_g\, (1-\varepsilon)^2} \tag{4.12}$$

The calculated permeability values of different packings in this study are presented in Figure 4.6. It can be found from this figure that with enhancing the role of IPFs, the permeability of the packing

increased. This is consistent with the higher fixed bed height and the smaller packed bed pressure drop found for the systems with a higher degree of IPFs while the same amount of material was fed in the bed for different cases.

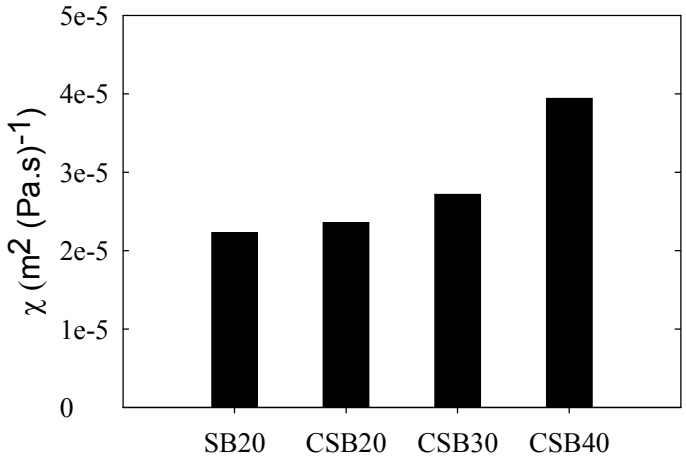

Figure 4.6: Effect of IPFs on the permeability of the particle packing.

According to Rietema [35] the emulsion phase in a bubbling fluidized bed can be considered to be completely stabilized between two bubble passages. Therefore, the more porous solid structure that was noted for the packed bed state with increasing IPFs can be extended into the fluidized state. This means that the fluidized bed can also hold more gas inside when the level of IPFs is increased. In other words, it is expected that the portion of the fluidizing gas passing through the bed in the emulsion phase increases with IPFs. The experimental bed expansion readings are used to verify this statement.

The total volume of the bed is made of bubble volume and emulsion phase powder:

$$hA = \sum V_B + \frac{\sum V_p}{(1 - \varepsilon_e)} \qquad 4.13$$

where A is the cross-sectional area of the fluidizing column, $\sum V_B$ is the total bubble volume within the bed, $\sum V_p$ is the total volume of particles forming the bed, and ε_e is the emulsion phase voidage. Since there are no bubbles at U_{mf}:

$$h_{mf}A = \frac{\sum V_p}{(1 - \varepsilon_{mf})} \quad 4.14$$

where h_{mf} is the bed height at the minimum fluidization state. Also, since the fluidizing gas in the bed can be thought of as divided into bubble and emulsion phases:

$$\sum V_B = (1 - f_e)hA \quad 4.15$$

where f_e is the emulsion phase fraction. Based on Eqs. 4.13 to 15, it can be deducted that:

$$f_e = \frac{(1 - \varepsilon_{mf})\, h_{mf}}{(1 - \varepsilon_e)\, h} \quad 4.16$$

Aided by the common assumption that the emulsion phase retains the same voidage as at minimum fluidization, Eq. 4.16 is simplified as follows:

$$f_e = \frac{h_{mf}}{h} \quad 4.17$$

In order to estimate the volumetric flow rate of gas flowing through the emulsion phase V_e^*, it necessitates having knowledge of the bubble flow rate V_B^*. This, in turn, requires knowledge of the average bubble rise velocity U_B in the bed. Assuming that the bubble length scale that is estimated by the IOP method [33] (using the gauge pressure signals recorded 17.5 cm above the distributor plate) represents the mean bubble size (D_b) in the bed, it is then possible to calculate the corresponding mean bubble rise velocity from the commonly used equation presented by Davidson and Harrison [62] as follows:

$$U_B = 0.71\sqrt{g\, D_b} + (U_g - U_{mf}) \quad 4.18$$

where g is the gravity acceleration. Accordingly, V_e^* can be calculated as:

$$V_e^* = U_g A - (1 - f_e)\, U_B A \quad 4.19$$

Figure 4.7 presents the values estimated for V_e^* in the cases of SB20, CSB20, and CSB30 in the bubbling regime. It clearly shows that, as expected, V_e^* increased with IPFs. This means that the

tendency of the fluidizing gas passing through the bed in the emulsion phase increased with IPFs in the bubbling regime. Since a better gas-solid contact is achieved in the emulsion phase, this is a promising finding. It suggests that a slight increase in the level of IPFs inside the bubbling bed while it is far enough from the defluidization condition can offer an appreciable advantage for systems requiring good gas-solid contacting, like FCC regeneration.

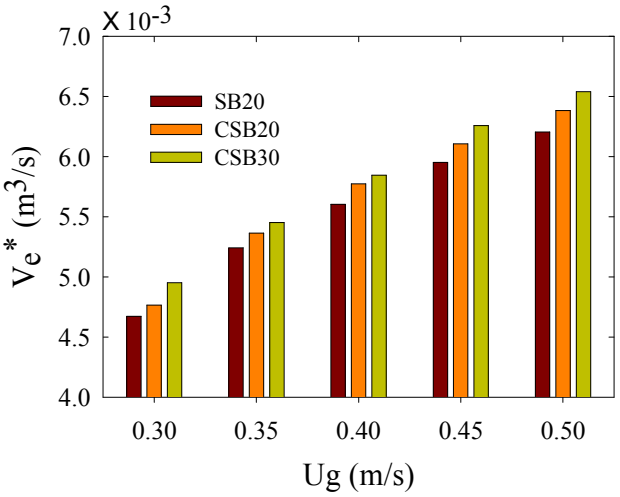

Figure 4.7: Effect of IPFs on V_e^*.

In general, U_{mf} is equal to U_{mb} for a non-cohesive bed of Geldart group B powders. Accordingly, no homogeneous bed expansion can be observed with these powders. The bed expansion evolution that was observed for SB20 follows the typical trend for non-cohesive, i.e., Geldart group B, powders. For typical Geldart group A powders, which are naturally cohesive due to their fine particle size, uniform bed expansion is exhibited between U_{mf} and U_{mb}. This occurs simultaneously with the overpressure in the bed pressure drop profile. Nonetheless, although based on the bed pressure drop analysis CSB20 and CSB30 demonstrated comparable behavior to the typical Geldart group A behavior, no bubble free bed expansion was observed for these beds for gas velocities that coincide with the overpressure in the bed pressure drop profile in the fluidizing branch.

Different behaviors found regarding the bed expansion in this study compared to the typical Geldart group A behavior can be explained by taking into account how this phenomenon happens for Geldart group A powders and the concept of the polymer coating approach for enhancing IPFs in the particulate system. Generally, IPFs and HDFs compromise with each other for Geldart group

A particles. For these powders, van der Waals forces are the main IPFs that present in a dry gaseous environment [63]. When the gas velocity is below U_{mf} no rearrangement occurs in the initial state of the packing. Once the gas velocity exceeds U_{mf}, since the drag force and van der Waals forces are of comparable magnitude, particles can wiggle at their places. This can result in a small rearrangement in the packing, which yields the formation of larger cavities between particles and, eventually, a slight increase in the bed height. In this way, a new structure with fewer contact points (lower coordination number) forms in the bed while the elasticity modulus of the weak solid-like lattice decreases into a new value. By increasing the gas velocity in the homogeneous fluidized bed, the bed expands as long as the gas velocity is lower than the critical velocity, U_{mb}. The expansion, however, occurs in small steps and not continuously. Finally, at the critical superficial gas velocity of U_{mb} the bed holds a specific structure where the maximum tensile strength of the bed exceeds and it becomes unstable with the formation of bubbles [35]. Such behavior of the classical Geldart A powders resembles the behavior of a plastic material in its elastic region, which stretches under the tensile stress and cracks when the yield stress is passed.

The thickness of the coating layer, the process temperature, the polymer chain molecular weight, the level of entanglement of polymer chains, the area of contact as well as the contact time are among the most important parameters affecting the adhesion force between two polymer layers in the polymer coating approach for induction of IPFs in a particulate system. The effective adhesion energy W achieved by this technique can be estimated by:

$$W = W_r\,[1 - \exp(-a{t_c}^b)] \qquad 4.20$$

where W_r is the maximum adhesion energy between the coated particles, which occurs when the polymer chains have enough time to diffuse and relax at the contact point. This characteristic time is named as the reptation time t_D. The particle contact time is t_c and the regression constants a and b vary with the polymer properties, such as the polymer structure, the polymer reptation time, and the molecular weight. When two polymer layers are disconnected with a high debonding velocity V_d, the cohesive energy increases with the contact time, until it reaches the maximum value W_r. When the debonding velocity is very low or when the contact time is larger than the reptation time, the adhesion energy can be considered constant at the maximum value [27].

Basically, the longest contact time between particles in a bubbling fluidized bed occurs in the emulsion phase, which is equal to the idle time. For resin beads with a 550-750 μm diameter and particle density of 1100 kg/m^3, the idle time is about 100 ms at a gas velocity equal to 0.3 m/s [64]. A particle contact time in order of the idle time in a bubbling fluidized bed results in an effective adhesion energy (much) smaller than the maximum adhesion energy depending on the polymer properties and the process temperature. However, since polymer chains can easily relax at the contact point while the bed is fixed for a time period in order of or larger than the reptation time, the effective adhesion energy can easily reach its maximum value. According to the evaluation that was done by Bouffard et al. [27] for the PMMA/PEA polymer layers with thicknesses of 3.5 and 7 μm at process temperatures of 10^{o}C and 45^{o}C, the level of IPFs obtained by the polymer coating approach using this polymer material could be clearly higher than the weight of the particle, or the drag force resulting from the gas flow at the theoretical U_{mf}. Correspondingly, when the theoretical U_{mf} is exceeded, since the drag force is lower than the artificial IPFs in the system (for the cases of CSB20, CSB30), it cannot wiggle the particles in the bed. Hence, the bed resists to any modification on its structure and stays at its initial state without any change in the coordination number of particles in the packing. By increasing the gas velocity, the drag force becomes closer to the level of IPFs at the interparticle contact point. Eventually, at the critical velocity U_{mf} ($\cong U_{mb}$), the buoyant weight of the bed and the yield stress due to IPFs are compensated by the drag force. Hence, the bed starts to be fluidized with the appearance of bubbles in the bed. This behavior looks like the normal behavior of brittle materials when subjected to tensile stress, which suddenly breaks when the yield stress is exceeded without showing significant deformation (strain).

It is worth mentioning that the phenomenon that was observed for CSB20 and CSB30 in this study corroborates the hypothesis that was posed by Xie and Geldart [65] that a large increase in IPFs can reduce or even prevent homogeneous expansion. Xie [66] postulated that the Geldart Number (Ga=U_{mb}/U_{mf}) can be related to the mechanical properties of a powder. According to Xie, a powder with a high Geldart Number has a certain plasticity, which can be expanded, contracted, and bent around corners. A low Geldart Number implies a brittle fluidization state in which a small change can result in instability in the uniform fluidized bed by forming bubbles or switching into the packed bed. Expansion behaviors found for typical Geldart groups A and B powders and those of this study support this opinion.

4.6.4 Standard deviations of in-bed gauge and differential pressure signals

The simplest analysis in the time domain that can be done on the recorded pressure signals in the fluidized state is to plot a sequence of these data points to qualitatively look for the effect of an operating variable (the IPFs) on the bed behavior. Samples of original in-bed gauge pressure signals as a function of time at three different gas velocities for SB20 and CSB40, which had the minimum and maximum level of IPFs, respectively, are plotted in Figure 4.8. For each velocity, signals are presented in windows of identical width for comparison of amplitudes. For all cases no clear periodicity can be found in the signals, which confirms the presence of multiple bubbles in these systems that results in a complex flow in the bed. It can be found from Figure 4.8 that at U_g=0.35 m/s, the amplitudes of pressure signals for SB20 were higher than for CSB40. This implies that the sizes of bubbles were larger for SB20 at this operating condition. At U_g=0.65 m/s, however, the trend became reversed most probably due to the presence of larger bubbles for CSB40. Normally, by increasing the gas velocity the amplitudes of pressure signals increased up to the transition velocity from bubbling to turbulent regime and then reduced with superficial gas velocity. Figure 4.8c shows pressure signals for SB20 at U_g=1.1 m/s while the bed was operating in the turbulent regime. Very small amplitudes and a random nature of pressure fluctuations could be found for this system, which indicate there was a high degree of homogeneity of the bed in the turbulent regime. On the contrary, at U_g=1.1 m/s, CSB40 was still at the transition state between the bubbling and turbulent regimes and characterized with much larger amplitudes of pressure signals. It is worth mentioning that similar trends were observed with the in-bed differential pressure fluctuations, as well.

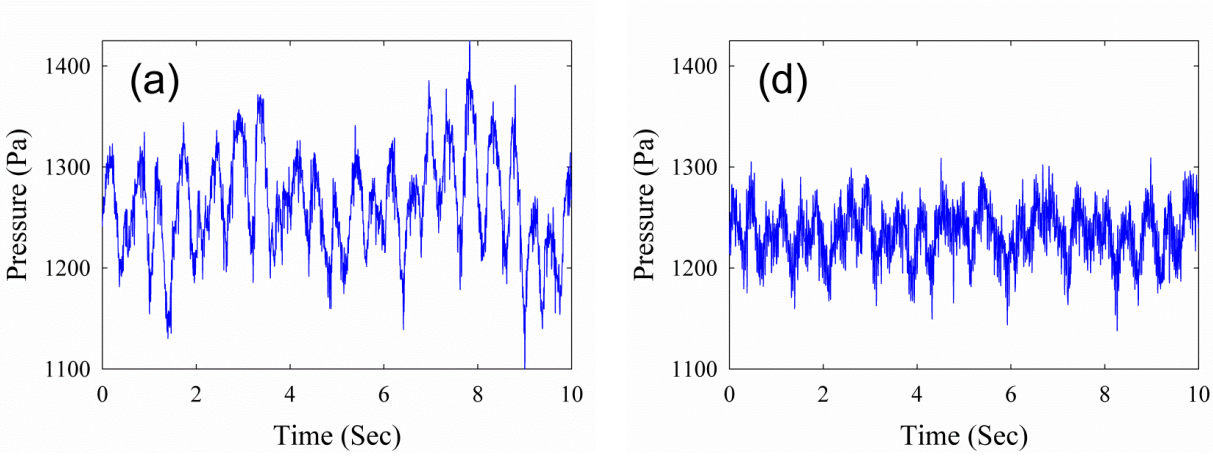

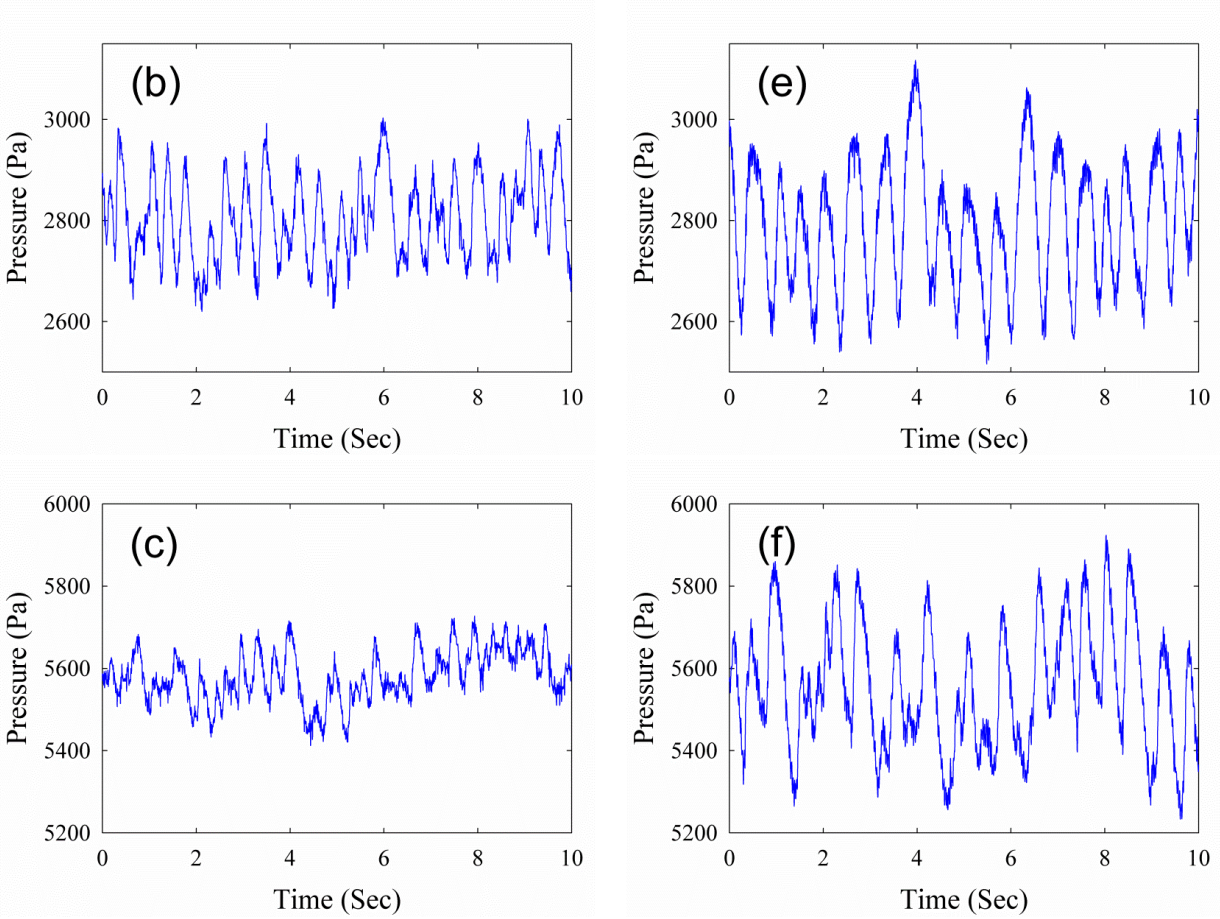

Figure 4.8: Time sequence of the in-bed gauge pressure fluctuations for SB20 and CSB40 at different gas velocities. a) SB20, U_g=0.35 m/s, b) SB20, U_g=0.65 m/s, c) SB20, U_g=1.10 m/s, d) CSB40, U_g=0.35 m/s, e) CSB40, U_g=0.65 m/s, f) CSB40, U_g=1.10 m/s.

The standard deviations of in-bed gauge and differential pressure fluctuations for different operating conditions are presented in Figure 4.9. Figure 4.9a shows that by increasing the superficial gas velocity for SB20 the standard deviation of pressure fluctuations continuously increased due to the predominance and increase in bubble formation and coalescence up to the critical transition velocity from bubbling to turbulent regime, U_c. With further increase in gas velocity the standard deviation decreased since bubble breakage became dominant and the gradual disappearance of bubbles/voids occurred in the turbulent regime. According to Yerushalmi and Cankurt [40], the gas velocity at which the standard deviation reached its maximum is referred to as U_c. Inspecting Figure 4.9a reveals that at gas velocities well below U_c, namely $U_{mf,SB20} < U_g < 3U_{mf,SB20}$, the standard deviations of pressure fluctuations are lower for beds with a higher degree of IPFs, at a constant superficial gas velocity. This can be attributed to the fact that the emulsion

phase in the bubbling regime, in a similar manner to the packed bed, could hold more gas inside its structure when the level of IPFs was increased in the bed [67]. Accordingly, at a given fluidizing gas throughput, a smaller volume of the gas was available to form bubbles. Therefore, smaller bubbles were formed inside the bed, which resulted in weaker standard deviations of pressure fluctuations. This also means that at such operating conditions, the tendency of the gas passing through the bed in the interstitial phase increased with IPFs. This is consistent with what has already been discussed in section 4.6.3 using the bed height (global) measurements. Also, experimental results using a solid concentration optical fiber probe validated this opinion in light of local measurements [29, 67]. Based on these observations it can be concluded that if the level of IPFs is slightly increased in a gas-solid fluidized bed, which is operating at low/moderate gas velocities of the bubbling regime and far from the defluidization condition, it can offer appreciable advantage for systems requiring good gas-solid contacting. According to the experimental results of this study, the corresponding range of gas velocities falls in $U_{mf,No\ IPFs} < U_g < 3U_{mf,No\ IPFs}$. This interval can vary depending on the level of IPFs together with the physical properties of the fluidizing gas and particles.

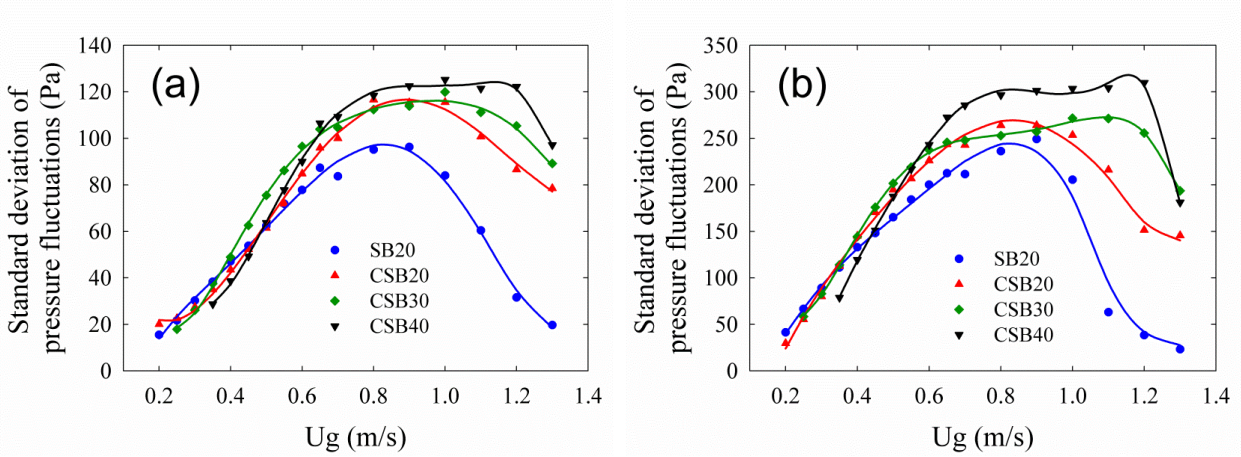

Figure 4.9: Effect of IPFs on standard deviations of in-bed a) gauge and b) differential pressure fluctuations.

Figure 4.9a also shows that the growth rate of standard deviations of pressure fluctuations with gas velocity increased with IPFs. This yields standard deviation curves for different systems that experience a trend inversion at mediate gas velocities in the bubbling regime; higher standard deviation was obtained for the bed with higher IPFs at gas velocities above 0.65 m/s. This implies that bubbles grew faster with the superficial gas velocity when the level of IPFs was increased in the bed. This phenomenon can be explained by a reduction in the fluidity of particles with

increasing IPFs. According to the bubble break up theory on the instability of its roof [68], bubble splitting occurs once the stalactite of particles forms from its roof. In this regard, since the fluidity of particles diminished with enhancing IPFs, the formation of stalactites of particles on the bubble's roof reduced. Correspondingly, the bubble splitting rate decreased with IPFs and the bubble size increased more rapidly for cases with higher IPFs. This results in an increased slope in the standard deviations of pressure fluctuations with superficial gas velocity in the bubbling regime.

It can be further found from Figure 4.9a that with additional increase in gas velocity the standard deviation of gauge pressure fluctuations reached its peak and then decreased while the fluidization regime changed from bubbling to turbulent. It shows that the transition between bubbling and turbulent regimes was a perspicuous transition with respect to U_g for SB20. However, the transition between these regimes slowly occurred in a span of gas velocities when IPFs were present in the bed. This took place more slowly and over a wider range of gas velocities by enhancing IPFs. In other words, the bed with IPFs resisted against the regime transition from bubbling to turbulent and this became more highlighted when the degree of IPFs was enhanced. In addition, it can be found from Figure 4.9a that increasing IPFs in the bed shifted the regime transition to a higher gas velocity.

Basically, very strong particle-particle collisions are responsible for vigorous solid mixing and enhanced energy dissipation in the bed, which subsequently result in the formation of aggregate flows as characteristics of the turbulent regime [69]. As was discussed earlier, in the case of SB20 the fluidizing gas was more prone to pass through the bed in the bubble phase while it was operating in the bubbling regime. Accordingly, the influential action of bubbles was predictable for SB20 and more particle-particle collision with high intensity could take place in the bed. This, in turn, could result in early transition from a bubbling to turbulent fluidization regime. Nevertheless, less bubbling activity was anticipated for beds with enhanced IPFs due to the higher tendency of the gas to interstitially pass through the bed. Also, since a more diluted emulsion phase was obtained when the level of IPFs was increased [67], a larger free space was available for particles to move freely and, hence, collision opportunities could reduce. Additionally, the bed with IPFs seems to be capable of dampening the received energy from the drag force through the interparticle contacts. Thus, a higher gas velocity was needed to supply the required energy for intensifying the particle-particle collisions to the critical level after which the continuous emulsion phase was mainly

disintegrated, making bubbles/voids become smaller and the corresponding classical aggregate flows form in the bed.

The trends that can be seen for the standard deviations of pressure fluctuations in the turbulent regime (Figure 4.9) would offer that increasing IPFs can shift the transport velocity U_{tr} to higher values. Indeed, it was visually observed that the amount of solids that was elutriated with the fluidizing gas in the turbulent regime reduced with IPFs.

Normally, particles that are presented in the freeboard of a bubbling gas-solid fluidized bed are those in the wake of bubbles that are thrown into the freeboard after bursting bubbles at the surface of the bed [70]. Since particles in the wake of the bubbles are in close contact with other particles in the emulsion phase, the rate of ejection of a wake's particles into the freeboard can decrease due to the presence of cohesive IPFs at the interparticle contact points. Moreover, a temporary (dynamic) agglomerate of primary particles may exist in the freeboard because of IPFs with the effective size of the fluidized particulate material larger than the primary particles. This helps them to return back to the dense bed. It is worth mentioning that experimental findings and visual observations of this study are consistent with the experimental observations reported by other researchers, who found that the elutriation rate, measured at constant gas velocity, reduced by decreasing the particle size from a typical Geldart group A into Geldart group C powders [71, 72]. They argued that the increase in the level of IPFs was responsible for such behavior.

By scrutinizing Figure 4.9a and b, very good agreements can be found between variations of standard deviations of in-bed gauge and differential pressure fluctuations with gas velocity for systems with different amounts of IPFs. In this regard, the experimental findings, which were inferred by the analysis of standard deviations of in-bed gauge pressure fluctuations, were supported by the dynamic differential pressure signals recorded for the stabilized central part of the fluidized bed.

4.6.5 Power spectral densities of in-bed gauge and differential pressure signals

In addition to standard deviations of in-bed gauge and differential pressure fluctuations, the PSD of these signals, in the frequency domain, was analyzed. Results of this analysis for SB20 and CSB40 at three different gas velocities are plotted in Figure 4.10. The curves that are presented here were obtained by using a Hamming window and the original time series signal was divided

into different sub-spectra with an equal number of samples (8192) according to the recommendation of Johnsson et al. [38].

It can be seen from Figure 4.10 that in all cases the high intensity components of PSDs of gauge and differential signals were concentrated in the range of 0–4 Hz. At low gas velocities, PSDs were featured by a higher dominant frequency with smaller peak intensity. Comparing PSDs of gauge or differential signals of SB20 and CSB40 at this condition (U_g=0.35 m/s; Figure 4.10a, d) reveal that the frequency spectrums were broader for SB20 while they contained more intense peaks at corresponding dominant frequencies. This implies that a higher number of small bubbles with larger sizes than those of CSB40 were simultaneously occurring for SB20. This is consistent with the analysis of standard deviation. By increasing the gas velocity up to U_g=0.8 m/s (Figure 4.10b, e) the dominant frequency shifted toward smaller frequencies while the intensity of the peak drastically increased. This can be explained by an increase in the superficial gas velocity that can result in both increasing bubble size and the number of bubbles, but principally increasing bubble size. Inspecting Figure 4.10b and c reveals that although the energy level of PSDs increased for both systems, CSB40 held more intense peaks. In other words, a similar inversion trend that was observed with the standard deviation analysis can be seen here, as well. This indicates that the bed with a higher degree of IPFs had larger bubbles at mediate gas velocities ($U_g > 3U_{mf,SB20}$). At higher gas velocities (U_g=1.1 m/s), SB20 was operating in the turbulent regime with small transient voids, continuously splitting and coalescing, while CSB40 was still at the bubbling to turbulent transition boundary. It can be found from Figure 4.10c and f that PSDs of SB20 considerably changed through the reduction of the amplitude of PSD and spreading PSD over higher frequencies. By comparing PSDs of gauge and differential pressure signals of CSB40 at U_g=0.8 m/s and U_g=1.1 m/s it can be noticed that the wideness of intense peaks around the dominant frequency were (slightly) increased. This shows that the number of large bubbles increased in the bed to overcome the resistance that CSB40 was showing against the transition from bubbling to turbulent regime. Furthermore, the considerable difference that can be seen for PSDs of CSB40 in comparison with those of SB20 at U_g=1.1 m/s confirms the delayed regime transition for CSB40 in accordance with the standard deviation analysis.

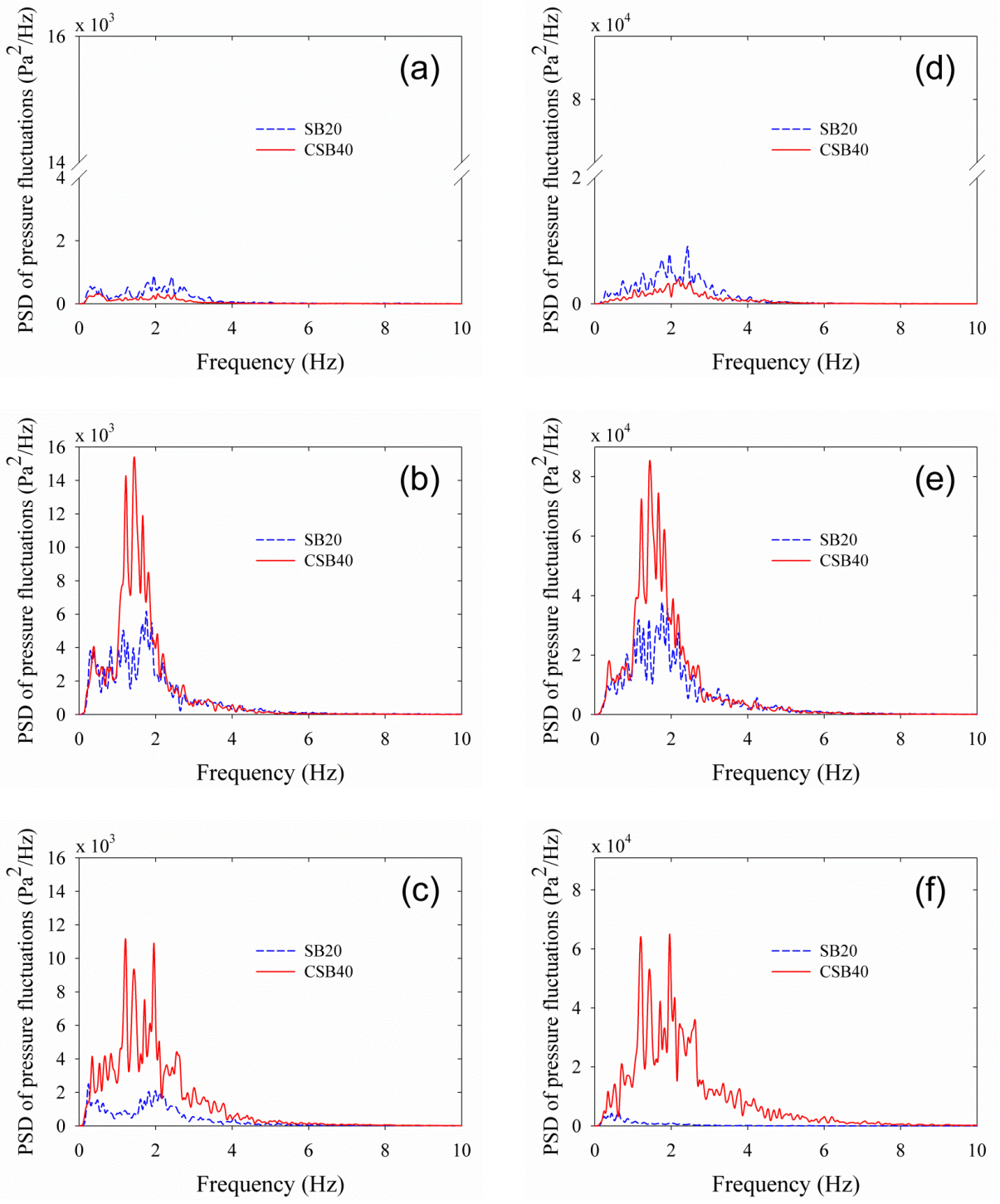

Figure 4.10: PSD of in-bed gauge and differential pressure signals for SB20 and CSB40. a) gauge, U_g=0.35 m/s, b) gauge, U_g=0.8 m/s, c) gauge, U_g=1.1 m/s, d) differential, U_g=0.35 m/s, e) differential, U_g=0.8 m/s, f) differential, U_g=1.1 m/s.

4.6.6 Bubble activity and estimation of bubble size

The IOP method suggested by van der Schaaf et al. [33] was employed with the gauge pressure signals recorded in the windbox and dense bed to quantify the length scale of the passing bubbles in fluidized beds with different levels of IPFs. The method uses a frequency-domain-based coherence function, which is a degree of relevance of these signals. In general, a low and high coherence correspond to the dominance of bubbles passage and fast-travelling waves on the recorded in-bed gauge/absolute pressure signals, respectively [33]. An average coherence $\overline{\Upsilon_{xy}^2}$ in the frequency range of 0-10 Hz was proposed by Cai et al. [73] as the following:

$$\overline{\Upsilon_{xy}^2} = \frac{1}{10}\int_0^{10} \Upsilon_{xy}^2(f)\ df \qquad 4.21$$

to quantify the extent of similarity between the signals at the two measuring levels of the bed.

The average coherence function was calculated for different systems and illustrated in Figure 4.11. As can be seen, for each system, this parameter increased with the gas velocity up to a maximum value and then decreased with a further increase in the gas flow rate. A similar trend was also observed for this variable for a bed of 78 μm FCC particles by Zhang et al. [47]. Such behavior can be explained by referring to the concept of incoherent analysis. At low gas velocities, since there is a little impact of fast travelling waves (fluctuations in the gas flow rate, bubble formation, coalescence, break-up and eruption, and the bed mass oscillation) on the registered pressure signals, pressure waves due to the passage of even small bubbles can constitutively form the small amplitude in-bed gauge pressure signals. Therefore, the similarity of gauge pressure signals recorded in the windbox and dense bed is low at this condition albeit the propagation rate of fast-travelling waves is high. By increasing the gas velocity, bubbles become larger and can have greater impact on the in-bed recorded pressure signals due to their axial movements. However, the fast-travelling waves contribute more effectively in the formation of the final pressure fluctuations. Hence, the average coherence function increases with the superficial gas velocity up to a maximum. The peak in the average coherence took place at velocities slightly smaller than U_c identified by the standard deviation analysis. It should be noted that the fast-travelling waves can be seriously attenuated in the presence of bubbles, especially in fluidized beds with high bubble volume fractions [74]. A further increase in gas velocity, while bubbles are changing their identity into

small transient voids, reduces the intensities of fast-travelling waves due to strong attenuation caused by the presence of plenty of voids in the bed. In addition, pressure waves generated by passage of the numerous small voids can have an appreciable

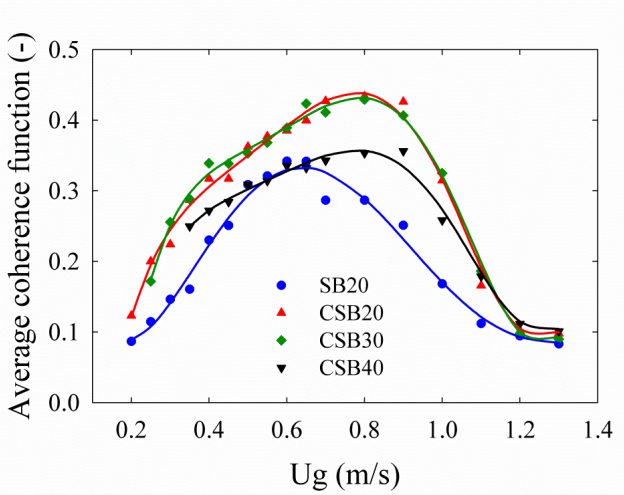

Figure 4.11: Effect of IPFs on the average coherence function.

contribution in the formation of the final pressure fluctuations with small amplitude in the turbulent regime. Accordingly, the average coherence drastically decreases at high gas velocities.

Scrutinizing Figure 4.11 reveals that the average coherence function at different superficial gas velocities was higher for beds with IPFs compared to SB20 (without IPFs). This suggests that the hydrodynamics of the bed with IPFs was less affected by the bubble/void activity. It could be concluded that an increase in the level of IPFs could bring about a reduction in the quality of solid mixing in the bed because of less bubble activity. This is while it was found that the quality of gas-solid contact could improve in the bubbling regime when the level of IPFs was increased. Therefore, increasing the amount of IPFs in the bed with the purpose of achieving better gas-solid contact should be cautiously applied to reach an optimized operating performance.

It can be additionally found from Figure 4.11 that among beds with IPFs, CSB20 illustrated the largest average coherence function and it decreased by enhancing IPFs while the coherence function of CSB40 was still higher than SB20. This behavior can be explained by noting the fact that by increasing the level of IPFs the fixed bed and the emulsion phase voidages increased [67]. As for example, the fixed bed voidage increased from 0.47 for CSB20 to 0.53 for CSB40. Such an increase in the packed bed voidage, which can be extended into the fluidized state, can impressively attenuate the fast-travelling waves in the bed and, hence, reduce the average coherence function.

Figure 4.12 presents the bubble diameter (length scale) estimated by the IOP method as a function of gas velocity. The bubble diameters estimated by this approach, increased approximately linearly with increasing the superficial gas velocity below its maximum value in the bubbling regime for all systems studied. It shows that a bed with a higher degree of IPFs contained slightly smaller bubbles at low gas velocities ($U_{mf,SB20} < U_g < 3U_{mf,SB20}$). Also, the growth rate of the bubble size with the gas velocity increased with IPFs. It resulted in larger bubbles for more cohesive beds at moderate and high gas velocities ($U_g > 3U_{mf,SB20}$). Moreover, it can be noticed that the velocity at which the maximum bubble size occurred shifted toward higher gas velocities by increasing the level of IPFs. This means that the transition velocity from bubbling to turbulent regime delayed with IPFs. Interestingly, all findings are in agreement with the results of the standard deviation and PSD analyses presented in sections 4.6.4 and 4.6.5.

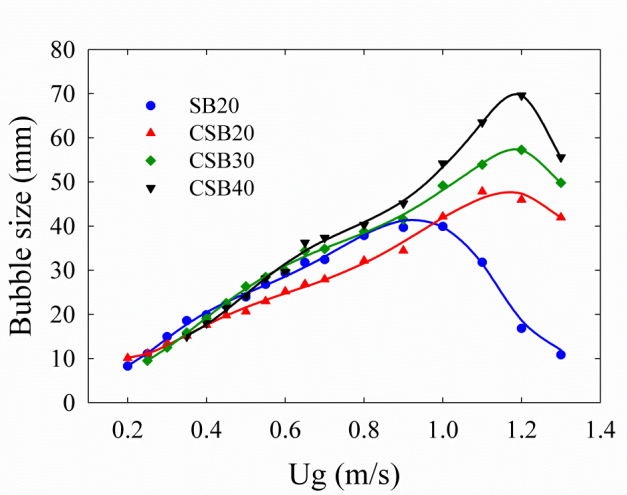

Figure 4.12: Effect of IPFs on the bubble size estimated by incoherence analysis.

Figure 4.12 further demonstrates that at gas velocities higher than 1.1 m/s while SB20 was operating well in the turbulent regime and other systems were at the regime transition conditions, markedly smaller bubbles/voids can be found for SB20, a system without IPFs. Since a bed with large bubbles suffers from gas bypassing and a much better quality of solid mixing is obtained in the turbulent regime, a better overall performance of the gas-solid fluidized reactor is predictable when a bed without IPFs is operated at the above range of superficial gas velocities. Experimental results of local measurements reported in a separate work by the present authors [67] confirm that the highest amount of gas passing through the emulsion phase was observed for the bed without IPFs under the same operating conditions.

4.6.7 Estimation of the frequency of macro-structures

In order to evaluate the frequency of macro-structures in fluidized beds with different levels of IPFs, the frequency range of these structures at different operating conditions was primarily identified by plotting the PSD of the gauge pressure signals in a logarithmic scale following Johnsson et al. [38]. It was noted that the macro-structures at different operating conditions were presented in the range of frequencies smaller than 3.25 Hz. Subsequently, the wavelet analysis (up to 10^{th} level) was applied to decompose the original gauge pressure signals into different details and an approximation signals each containing frequency information in a specific range. A second order Daubechies wavelet (db2) was selected as the wavelet function in the present study. After decoupling the original signals, considering the sampling frequency of 400 Hz for the recorded pressure signals, details of D7 to D10 covering the range of frequencies between 0.19–3.25 Hz were employed to reconstruct the signals representing the macro-structures. The average peak frequency of the reconstructed signals, nominating the frequency of the macro-structures that could properly represents the frequency of bubble passage in the bed, was calculated afterwards.

The frequency of the macro-structures for beds with different levels of IPFs as a function of gas velocity is plotted in Figure 4.13. It illustrates that for each system tested, the frequency of the macro-structures initially increased with the gas velocity up to a partial maximum. This could basically represent the range of gas velocities required for bubbling activity of small bubbles to be well developed in the bed. It then gradually decreased with the gas velocity to reach a minimum. In this interval, the bubble coalescence could dominate over the bubble formation yielding the presence of fewer number of bubbles yet larger in size in the bed. The frequency of the macro-structures subsequently increased with further increase in the gas velocity. This could be principally attributed to the replacement of large bubbles by plenty of small bubbles/voids after the bubbling to turbulent regime transition. Increase in the number of large bubbles even before the completion of the bubbling to turbulent regime transition for beds with IPFs, which was previously noted in Figure 4.10, could be another reason for this variation. This could help these beds to overcome the resistance shown against the regime transition. For the superficial gas velocities higher than 1.1 m/s, depending on the level of IPFs in the bed, the frequency of the macro-structures eventually started to decrease again. This reduction could be associated with the disappearance of bubbles/voids with the purpose of moving toward formation of a homogeneous bed at high velocities of the turbulent regime. Similar trend for the variation of the frequency of bubbles

passing by the front tip of a solids concentration optical fiber probe with the gas velocity was noted by Shabanian and Chaouki [67].

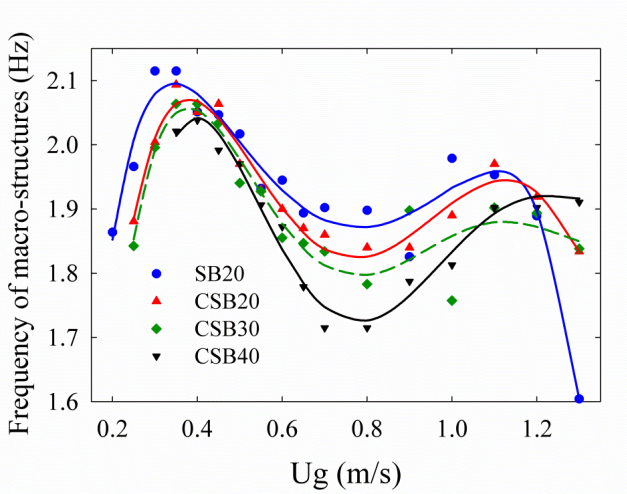

Figure 4.13: Effect of IPFs on the frequency of macro-structures in the fluidized bed.

Figure 4.13 also depicts that the frequency of the macrostructures decreased by enhancing the degree of IPFs in the bed. By considering Figure 4.12 in conjunction with Figure 4.13, it can be found that at low gas velocities, namely $U_{mf,SB20} < U_g < 3U_{mf,SB20}$, since the bubble size is slightly smaller and they form less frequently for beds with IPFs inside, the fluidizing gas was more prone to pass through the bed in the emulsion phase. This is in close agreement with the results presented in Figure 4.7. At higher gas velocities, typically $3U_{mf,SB20} < U_g < U_{c,SB20}$, although the bed with a high level of IPFs could hold slightly larger bubbles, the tendency of the gas could be still higher to pass through the bed in the emulsion phase in a more cohesive bed since the frequency of the macro-structures was perceptibly lower. At the superficial gas velocities higher than $U_{c,SB20}$, where SB20 was operating in the turbulent regime while other beds were still experiencing the bubbling to turbulent regime transition, the frequency of the macro-structures for different systems was drawing near to each other. These findings along with the presence of much smaller bubbles/voids for SB20 would offer that, different from the bubbling regime, the tendency of the fluidizing gas interstitially passing through the bed is higher for a bed with a lower degree of IPFs under this operating condition. Quantitative values presented by Shabanian and Chaouki [67] for the distribution of the fluidizing gas between the bubble and emulsion phases under the similar operating conditions confirm these implications.

The sequential transition from bubbling to turbulent regime for systems with different levels of IPFs played a great role on the inversion trend found at superficial gas velocities slightly higher than $U_{c,No\ IPFs}$. Further increase in the superficial gas velocity higher than U_c for systems with IPFs led to the formation of smaller voids and further disintegration of the emulsion phase in the bed. This principally resulted from the progressive dominance of HDFs over IPFs. It can eventually yield the presence of approximately identical fluidization behavior for beds with different levels of IPFs at very high superficial gas velocities.

Although a better gas solid contact was noted in the bubbling regime when the level of IPFs was increased with the polymer coating approach, its direct application at high temperatures may not be feasible for three reasons. First, the polymer coating approach is based on the utilization of a polymer material and most polymers have low melting temperatures. Second, the polymer coating approach requires the application of specific based particles that accept the polymer coating. Hence, this method cannot be applied to any of the particles used in gas-solid fluidized beds. Third, in order to take advantage of the polymer coating approach, the base particles should be coated with the polymer material. In the case of catalyst particles, this means annihilating the active sites of catalysts, which is strongly undesirable. In contrast, there are other feasible approaches to intentionally induce a slight increase in the level of IPFs in gas-solid fluidized beds operating at elevated temperatures. Alternate approaches when the gas-solid fluidized bed is obliged to work at high operating temperatures are the addition of fines (<45 μm) [75, 76], the application of bed materials with a smaller mean particle size [77-79], and doping the catalyst particles with a small amount of materials with a low sintering temperature [10, 11].

4.7 Conclusion

The effect of IPFs on the fluidization behavior of a gas-solid fluidized was investigated with the help of the polymer coating approach and global hydrodynamic measurements. The analysis of experimental results demonstrated that IPFs could have great influence on the hydrodynamic properties of both fixed and fluidized beds. It was found that U_{mf} increased by increasing the level of IPFs in the bed. The results also indicated that by enhancing IPFs the tendency of the fluidizing gas passing through the bed in the emulsion phase increased at low gas velocities in the bubbling regime. It was highlighted through the presence of slightly smaller bubbles that were passing in the bed with a lower frequency. For the coarse sugar beads used in the this study, the corresponding

range of gas velocities falls in $U_{mf,No\ IPFs} < U_g < 3U_{mf,No\ IPFs}$. It was also noted that the bubble growth rate was higher for a bed with stronger IPFs. It resulted in slightly larger bubbles at higher velocities of the bubbling regime ($3U_{mf,No\ IPFs} < U_g < U_{c,No\ IPFs}$). Despite this fact, the frequency of the macro-structures was discernibly lower for a more cohesive bed in the same range of gas velocities. Hence, the fluidizing gas could still be more prone to interstitially pass through the bed when the level of IPFs was enhanced under the identical operating conditions. This observation implies that by a slight increase in the level of IPFs for a bubbling gas-solid fluidized bed, while it is far enough from the defluidization condition, the distribution of the fluidizing gas between the bubble and emulsion phases can be modified towards the emulsion phase, where a better gas-solid contact can be achieved, to improve the overall performance of the system. It should be noted that the marginal superficial gas velocity inferred from this study ($3U_{mf,No\ IPFs}$) depends on the level of IPFs and the physical properties of the fluidizing gas and particulate materials.

It was further found that by enhancing the degree of cohesive IPFs in the system U_c increased. Experimental results showed that at gas velocities slightly higher than $U_{c,No\ IPFs}$ appreciably smaller bubbles/voids were found for the system without IPFs while the frequency of the macro-structures for beds with different levels of IPFs were drawing near to each other. This suggests that an improved performance of the gas-solid fluidized bed reactor could be achieved with a less cohesive bed at superficial gas velocities slightly above $U_{c,No\ IPFs}$. It is due to the better quality of solid mixing in the turbulent regime and less gas bypassing by the bubbles.

4.8 Nomenclature

4.8.1 Acronyms

ABF	agglomerate bubbling fluidization
APF	agglomerate particulate fluidization
COP	coherent component
CSB20	coated sugar beads at 20^{o}C
CSB30	coated sugar beads at 30^{o}C
CSB40	coated sugar beads at 40^{o}C

Ga	Geldart number
HDFs	hydrodynamic forces
IOP	incoherent component
IPFs	interparticle forces
PEA	poly ethyl acrylate
PMMA	poly methyl methAcrylate
PSD	power spectral density
SB20	fresh sugar beads at 20^{o}C

4.8.2 Symbols

a	constant in Eq. 4.20 (sec^{-b})
A	cross-sectional area of the fluidizing column (m^2)
b	constant in Eq. 4.20 (-)
D	column diameter (m)
d_p	mean particle diameter (μm)
D_b	bubble diameter (m)
f	frequency (Hz)
f_e	emulsion phase fraction (-)
g	gravity acceleration (m/s^2)
h	bed height (m)
h_{mf}	bed height at minimum fluidization state (m)
j	complex number (-)
K	number of segments (-)
M_s	number of data points in each segment (-)
N	number of data points (-)

p_i	pressure signal (Pa)
p_x	pressure signals recorded in the windbox (Pa)
p_y	in-bed gauge pressure signals (Pa)
$\bar{p}$	mean value of the pressure signals (Pa)
P_{xx}	average power spectral density of gauge pressure signals recorded in the windbox (Pa^2/Hz)
$P_{xx}{}^{i}$	power spectral density of each segment (Pa^2/Hz)
P_{xy}	cross power spectral density of gauge pressure signals recorded in the windbox and in the dense bed (Pa^2/Hz)
P_{xy}^*	conjugate of P_{xy} (Pa^2/Hz)
P_{yy}	average power spectral density of in-bed gauge pressure signals (Pa^2/Hz)
t_c	contact time (sec)
t_D	reptation time (sec)
U_B	bubble rise velocity (m/s)
U_c	transition velocity from bubbling to turbulent regime (m/s)
$U_{c,CSB40}$	transition velocity from bubbling to turbulent regime for CSB40 (m/s)
$U_{c,No\ IPFs}$	transition velocity from bubbling to turbulent regime for a bed without IPFs (m/s)
$U_{c,SB20}$	transition velocity from bubbling to turbulent regime for SB20 (m/s)
U_g	superficial gas velocity (m/s)
U_{mb}	minimum bubbling velocity (m/s)
U_{mf}	minimum fluidization velocity (m/s)
$U_{mf,No\ IPFs}$	minimum fluidization velocity for a bed without IPFs (m/s)
$U_{mf,SB20}$	minimum fluidization velocity for SB20 (m/s)
U_{tr}	transport velocity (m/s)

V_d debonding velocity (m/s)

V_B^* bubble flow rate (m^3/s)

V_e^* volumetric flow rate of gas flowing through the emulsion phase (m^3/s)

w window function (-)

W effective adhesion energy (J)

W_r maximum adhesion energy (J)

4.8.3 Greek letters

ε bed voidage (-)

ε_d emulsion phase voidage (-)

ε_{mf} minimum fluidization voidage (-)

$\mathcal{K}$ coordination number (-)

μ_g gas viscosity (Pa.s)

ρ_{ab} aerated bulk density (kg/m^3)

ρ_p particle density (kg/m^3)

ρ_{tb} tapped bulk density (kg/m^3)

σ standard deviation of pressure signals (Pa)

$\sigma_{xy,i}$ standard deviation of IOP (Pa)

χ permeability of the packed bed ($m^2(Pa.s)^{-1}$)

ΔP bed pressure drop (Pa)

ΣV_B total bubble volume within the bed (m^3)

ΣV_e total volume of particles forming the bed (m^3)

Υ_{xy}^2 coherence function (-)

$\overline{\Upsilon_{xy}^2}$ average coherence function (-)

4.9 Acknowledgment

The authors are grateful to the Total American Services, Inc. and the National Sciences and Engineering Research Council of Canada (NSERC) for supporting this work.

4.10 References

1) D. Geldart, Types of gas fluidization, Powder Technol. 7 (1973) 285-292.
2) J. Shabanian, R. Jafari, J. Chaouki, Fluidization of ultrafine powders-Review, Int. Rev. Chem. Eng. (IRECHE) 4 (2012) 16-50.
3) B. Formisani, R. Girimonte, L. Mancuso, Analysis of the fluidization process of particle beds at high temperature, Chem. Eng. Sci. 53 (1998) 951-961.
4) B. Formisani, R. Girimonte, G. Pataro, The influence of operating temperature on the dense phase properties of bubbling fluidized beds of solids, Powder Technol. 125 (2002) 28-38.
5) R. Girimonte, B. Formisani, The minimum bubbling velocity of fluidized beds operating at high temperature, Powder Technol. 189 (2009) 74-81.
6) C. Xu, J.X. Zhu, Effect of gas type and temperature on fine particle fluidization, China Particuology 4 (2006) 114-121.
7) G. Raso, M. D'Amore, B. Formisani, P.G. Lingola, The influence of temperature on the properties of the particulate phase at incipient fluidization, Powder Technol. 72 (1992) 71-76.
8) S. Rapagna, P.U. Foscolo, L.G. Gibilaro, The influence of temperature on the quality of gas fluidization, Int. J. Multiphase Flow 20 (1994) 305-313.
9) Y. Zhong, Z. Wang, Z. Guo, Q. Tang, Defluidization behavior of iron powders at elevated temperatures: Influence of fluidizing gas and particle adhesion, Powder Technol. 230 (2012) 225-231.
10) P. Lettieri, J.G. Yates, D. Newton, The influence of interparticle forces on the fluidization behavior of some industrial materials at high temperature, Powder Technol. 110 (2000) 117-127.
11) P. Lettieri, D. Newton, J.G. Yates, High temperature effects of the dense phase properties of gas fluidized beds, Powder Technol. 120 (2001) 34-40.
12) D. Geldart, N. Harnby, A.C. Wong, Fluidization of cohesive powders, Powder Technol. 37 (1984) 25-37.

13) M. Baerns, Effect of interparticle adhesive forces on fluidization of fine particles, Ind. Eng. Chem. Fundam. 5 (1966) 508-516.

14) A.R. Abrahamsen, D. Geldart, Behavior of gas-fluidized beds of fine powders Part I. Homogeneous expansion, Powder Technol. 26 (1980) 35-46.

15) A.R. Abrahamsen, D. Geldart, Behavior of gas-fluidized beds of fine powders Part II. Voidage of dense phase in bubbling beds, Powder Technol. 26 (1980) 47-55.

16) D. Geldart, A.R. Abrahamsen, Homogeneous fluidization of fine powders using various gases and pressures, Powder Technol. 19 (1978) 133-136.

17) J.P.K. Seville, R. Clift, The effect of thin liquid layers on fluidization characteristics, Powder Technol. 37 (1984) 117-129.

18) L.J. McLaughlin, M.J. Rhodes, Prediction of fluidized bed behavior in the presence of liquid bridge, Powder Technol. 114 (2001) 213-223.

19) J.A. Agbim, A.W. Nienow, P.N. Rowe, Inter-particle forces that suppress bubbling in gas fluidized beds, Chem. Eng. Sci. 26 (1971) 1293-1294.

20) M.J. Rhodes, X.S. Wang, A.J. Forsyth, K.S. Gan, S. Phadtajaphan, Use of a magnetic fluidized bed in studying Geldart Group B to A transition, Chem. Eng. Sci. 56 (2001) 5429-5436.

21) W.Y. Wu, A. Navada, S.C. Saxena, Hydrodynamic characterization of a magnetically stabilized air fluidized bed of an admixture of magnetic and non-magnetic particles, Powder Technol. 90 (1997) 39-46.

22) J.P.K. Seville, C.D. Willett, P.C. Knight, Interparticle forces in fluidization: a review, Powder Technol. 90 (1997) 39-46.

23) A.J. Forsyth, S. Hutton, M.J. Rhodes, Effect of cohesive interparticle force on the flow characteristics of granular material, Powder Technol. 126 (2002) 150-154.

24) N. Fraysse, H. Thomé, L. Petit, Humidity effects on the stability of sandpile, Eur. Phys. J. B, 11 (1999) 615-619.

25) S.M. Iveson, J.A. Beathe, N.W. Page, The dynamic strength of partially saturated powder compacts: the effect of liquid properties, Powder Technol. 127 (2002) 149-161.

26) G. Lumay, N. Vandewalle, Controlled flow of smart powders, Phys. Rev. E, 78 (2008) 061302.

27) J. Bouffard, F. Bertrand, J. Chaouki, S. Giasson, Control of particle cohesion with a polymer coating and temperature adjustment, AIChE J. 57 (2012) 3685-3696.

28) H. Cui, J. Chaouki, Effects of temperature on the local two-phase flow structure in bubbling and turbulent fluidized beds of FCC particles, Chem. Eng. Sci. 59 (2004) 3413-3422.

29) J. Shabanian, F. Fotovat, J. Bouffard, J. Chaouki, Fluidization behavior in a gas-solid fluidized bed with thermally induced inter-particle forces, in: T.M. Knowlton (Ed.), Proceedings of the 10th International Conference on Circulating Fluidized bed and Fluidization Technology (CFB-10), Engineering Conferences International, New York, 2011, pp. 738.

30) J.F. Davidson, The two-phase theory of fluidization: successes and opportunities, AIChE Symp. Ser. 281 (1991) 1-12.

31) F. Ghasemi, J. Rudd van Ommen, M. Sahimi, Analysis of pressure fluctuations in fluidized beds. I. Similarities with turbulent flow, Chem. Eng. Sci. 66 (2011) 2627-2636.

32) J. van der Schaaf, J.C. Schouten, C.M. van den Bleek, Origin, propagation and attenuation of pressure waves in gas-solid fluidized beds, Powder Technol. 95 (1998) 220-233.

33) J. van der Schaaf, J.C. Schouten, F. Johnsson, C.M. van den Bleek, Non-intrusive determination of bubble and slug length scales in fluidized beds by decomposition of the power spectral density of pressure time series, Int. J. Multiphase Flow 28 (2002) 865-880.

34) H.T. Bi, J.R. Grace, J. Zhu, Propagation of pressure waves and forces oscillations in gas-solid fluidized bed and their influences on diagnostics of local hydrodynamics, Powder Technol. 82 (1995) 239-253.

35) K. Rietema, The dynamics of fine powders, Elsevier Science Publishers LTD, New York, 1991.

36) J.M. Valverede, Fluidization of fine powders: Cohesive versus dynamical aggregation, Springer, Part. Technol. Ser. 18 (2013).

37) Q. Guo, M. Wang, Y. Lim C. Yang, Fluidization of ultrafine particles in a bubbling fluidized bed with sound assistance, Chem. Eng. Technol. 28 (2005) 1117-1124.

38) F. Johnsson, R.C. Zijerveld, J.C. Schouten, C.M. van den Bleek, B. Leckner, Characterization of fluidization regimes by time-series analysis of pressure fluctuations, Int. J. Multiphase Flow 26 (2000) 663-715.

39) H.W. Kwon, Y. Kange, S.D. Kim, M. Yashima, L.T. Fam, Bubble-chord length and pressure fluctuations in three-phase fluidized beds, Ind. Eng. Chem. Res. 33 (1994) 1852-1857.

40) J. Yerushalmi, N.T. Cankurt, Further studied of the regimes of fluidization, Powder Technol. 24 (1979) 187-205.

41) A. Chehbouni, J. Chaouki, C. Guy, D. Klvana, Characterization of the flow transition between bubbling and turbulent fluidization, Ind. Eng. Chem. Res. 33 (1994) 1889-1896.

42) H.T. Bi, N. Ellis, I.A. Abba, J.R. Grace, A state-of-the-art review of gas-solid turbulent fluidization, Chem. Eng. Sci. 55 (2000) 4789-4825.

43) P.D. Welch, The use of a fast Fourier transform for the estimation of power spectra, IEEE Trans. on Audio and Electroacoustics, AU-15 (1967) 70-73.

44) L.D. Enochson, R.K. Otens, Programming and analysis for digital time series data; shock and vibration monograph series, Department of Defense, Shock and Vibration Information Center, Washington, DC, USA, 1968.

45) S. Satij, L.S. Fan, Characterization of slugging regime and transition to turbulent regime for fluidized beds of large coarse particles, AIChE J. 31 (1985) 1554-1562.

46) D. Bazic, D. Ahchieva, E. Piskova, S. Heinrich, Z. Grbavcic, Hydrodynamics of shallow fluidized bed of coarse particles, Chem. Eng. J. 114 (2005) 47-54.

47) Y. Zhang, H.T. Bi, J.R. Grace, C. Lu, Comparison of decoupling methods for analyzing pressure fluctuations in gas-fluidized beds, AIChE J. 56 (2010) 869-877.

48) J.F. Davidson, Symposium on fluidization discussion, Trans. Inst. Chem. Eng. 39 (1961) 230-232.

49) M. Liu, Y. Zhang, H. Bi, J.R. Grace, Y. Zhu, Non-intrusive determination of bubble size in a gas-solid fluidized bed: An evaluation, Chem. Eng. Sci. 65 (2010) 3485-3493.

50) M. Rüdisüli, T.J. Schildhauer, S.M.A. Biollaz, A. Wokaun, J.R. van Ommen, Comparison of bubble growth from pressure fluctuation measurements to optical probing and literature correlations, Chem. Eng. Sci. 74 (2012) 266-275.

51) L.T. Fan, T.C. Ho, S. Hiraoka, W. P. Walawender, Pressure fluctuations in a fluidized bed, AIChE J. 27 (1981) 388-396.

52) H. Kage, N. Iwasaki, H. Yamaguchi, Y, Matsuno, Frequency analysis of pressure fluctuation in fluidized bed plenum, J. Chem. Eng. Japan, 24 (1991) 76-81.

53) G.-B. Zhao, Y.-R. Yang, Multiscale resolution of fluidized bed pressure fluctuations, AIChE J. 49 (2003) 869-882.

54) S. Sasic, B. Leckner, F. Johnsson, Characterization of fluid dynamics of fluidized beds by analysis of pressure fluctuations, Prog. Energy Combust. Sci. 33 (2007) 453-469.

55) M.R. Tamadondar, R. Zarghami, H. Azizpour, N. Mostoufi, J. Chaouki, R. Radmanesh, Using S-statistics for investigating the effect of temperature on hydrodynamics of gas-solid fluidization, Particuology 11 (2013) 288-293.

56) J.R. van Ommen, S. Sasic, J. van der Schaaf, S. Gheorghiu, F. Johnsson, M.-O. Coppens, Time-series analysis of pressure fluctuations in gas-solid fluidized beds – A review, Int. J. Multiphase Flow 37 (2011) 403-428.

57) B. Esmaeili, J. Chaouki, C. Dubois, An evaluation of the solid hold-up distribution in a fluidized bed of nanoparticles using radioactive densitometry and fiber optics, Can. J. Chem. Eng. 86 (2008) 543-552.

58) K. Rietema, H. W. Piepers, The effect of interparticle forces on the stability of gas-fluidized beds –I. Experimental evidence, Chem. Eng. Sci. 45 (1990) 1627-1639.

59) X.S. Wang, F. Rahman, M.J. Rhodes, Nanoparticle fluidization and Geldart's classification, Chem. Eng. Sci. 62 (2007) 3455-3461.

60) M.J. Espin, J.M. Valverde, M.A.S. Quintanilla, A. Castellanos, Stabilization of gas-fluidized beds of magnetic powders by a cross-flow magnetic field, J. Fluid Mech. 680 (2011) 80-113.

61) P.C. Carman, Fluid flow through granular beds, Trans. Inst. Chem. Eng. 15 (1937) 150-167.

62) J.F. Davidson, D. Harrison, Fluidised particles, Cambridge University Press, Cambridge, 1963.

63) J. Visser, Van der Waals and other cohesive forces affecting powder fluidization, Powder Technol. 58 (1989) 1-10.

64) M. Stein, Y.L. Ding, J.P.K. Seville, D.J. Parker, Solid motion in bubbling gas fluidized beds, Chem. Eng. Sci. 55 (2000) 5291-5300.

65) H.Y. Xie, D. Geldart, Fluidization of FCC powders in the bubble-free regime: effect of types of gases and temperature, Powder Technol. 82 (1995) 269-277.

66) H.Y. Xie, Fluidization of fine particles, Ph.D. Dissertation, University of Bradford, Bradford, UK, 1993.

67) J. Shabanian, J. Chaouki, Local characterization of a gas-solid fluidized bed in the presence of thermally induced interparticle forces, Chem. Eng. Sci. submitted for publication.

68) R. Clift, J.R. Grace, The mechanism of bubble break-up in fluidized beds, Chem. Eng. Sci. 27 (1927) 2309-2310.

69) J. Li, J.A.M. Kuipers, Effect of pressure on gas-solid flow behavior in dense gas-fluidized beds: discrete particle simulation study, Powder Technol. 127 (2002) 173-184.

70) D. Kunii, O. Levenspiel, Fluidization Engineering, Butterworth-Heinemann, Boston, 1991.

71) K. Smolders, J. Baeyens, Elutriation of fines from gas fluidized beds: mechanisms of elutriation and effect of freeboard geometry, Powder Technol. 92 (1997) 35-46.

72) D. Geldart, A.C.Y. Wong, Entrainment of particles from fluidized beds of fine particles, AIChE Symp. Ser. 83 (1987) 1-9.

73) N. Mostoufi, J. Chaouki, On the axial movement of solids in gas-solid fluidized beds, Chem. Eng. Res. Des. 78 (200) 911-920.

74) P. Cai, Y. Jin, Z.Q. Yu, Z.W. Wang, Mechanism of flow regime transition from bubbling to turbulent fluidization, AIChE J. 36 (1990) 955-956.

75) P. Cai, Z. Miu, Z.Q. Yu, Y. Jin, Mathematic feature and analyzing methods of pressure fluctuation signal from a gas-solid fluidized bed, Chem. Metall. Eng. 11 (1990) 114-122 (in Chinese).

76) J.G. Yates, D. Newton, Fine particle effects in a fluidized-bed reactor, Chem. Eng. Sci. 41 (1986) 801-806.

77) M. Pell, S.P. Jordan, Effects of fines and velocity on fluid bed reactor performance, AIChE Symp. Ser. 262 (1988) 68-73.

78) J.H. Siegell, Defluidization phenomena in fluidized bed of sticky particles at high temperature, Ph.D. Dissertation, The City University of New York, 1976.

79) J.H. Siegell, High-temperature defluidization, Powder Technol. 38 (1984) 13-22.

80) P. Compo, R. Pfeffer, G.I. Tardos, Minimum sintering temperatures and defluidization characteristics of fluidizable particles, Powder Technol. 51 (1987) 85-101.

CHAPTER 5 ARTICLE 3: LOCAL CHARACTERIZATION OF A GAS–SOLID FLUIDIZED BED IN THE PRESENCE OF THERMALLY INDUCED INTERPARTICLE FORCES

Jaber Shabanian, Jamal Chaouki*

Department of Chemical Engineering, Ecole Polytechnique de Montreal, Montreal, Quebec, Canada

* Corresponding author: Tel.: +1-514-340-4711 X 4034; fax: +1-514-340-4159.

E-mail address: jamal.chaouki@polymtl.ca

(Published in Chemical Engineering Science 119 (2014) 261–273)

5.1 Highlights:

- The effect of interparticle forces on local hydrodynamics of gas-solid fluidized bed is studied.
- The dynamic two-phase flow structure of the bed can be greatly influenced by interparticle forces.
- Enhancing interparticle forces will increase the tendency of the gas passing through the bed in the emulsion phase.
- Increasing interparticle forces will increase the meso-scale bubbling to turbulent regime transition velocity.

5.2 Abstract

This article reports the results obtained from an extensive experimental campaign aimed at investigating the effect of interparticle forces (IPFs) on the local flow structure of a gas-solid fluidized bed. A polymer coating approach was used to enhance and control the degree of cohesive IPFs in a gas-solid fluidized bed. In this work, the local transient solids concentration (bed voidage) was carefully measured with the help of an accurate optical fiber probe at different temperatures and gas velocities covering both bubbling and turbulent fluidization regimes. Also, the Radioactive Particle Tracking (RPT) technique was employed to track the trajectory of a tracer mimicking the behavior of solid particles in two systems, one with the least amount of IPFs in the bubbling regime and the other with the highest amount. Experimental results showed that by increasing the level of

IPFs in the bed, the fixed bed and emulsion phase voidage in the bubbling regime increased and demonstrated higher capacities in holding gas inside their structures. In addition, the emulsion phase fraction increased, the tendency of the fluidizing gas passing through the bed in the emulsion phase enhanced in the bubbling regime, the frequency of the bubble/emulsion phase cycle decreased, and the meso-scale transition from bubbling to turbulent fluidization regime delayed until reaching higher superficial gas velocities.

Keywords: Gas-solid fluidized bed, Interparticle forces, Hydrodynamics, Local measurements.

5.3 Introduction

Gas-solid fluidized beds are used extensively in industries for mixing, drying, adsorption, agglomeration/granulation of particles, and catalytic and non-catalytic reactions because of their excellent mixing ability and high heat and mass transfer rates between particles and fluidizing medium in situations of relatively low pressure drops (Vazquez et al., 2007; Si and Guo 2008; van Ommen and Mudde 2012). It has been verified by observation and experiments that a two-phase flow structure with a dynamic distribution of phases with voidage from ε_{mf} (bed voidage at minimum fluidization) to 1 exists for bubbling and turbulent fluidized beds (Davidson et al., 1985; Cui et al., 2000; Cui et al., 2001b). In the bubbling regime, the dilute/bubble phase (the dispersed phase), which mainly contains gas, and the dense/emulsion phase (the continuous phase), which mainly contains particles, form the two phases. However, in the turbulent regime, elongated and irregular bubbles and violently moving solid clusters are recognized as the two extreme phases of the flow structure while there is no obvious distinction between these two phases (Lin et al., 2001; van Ommen and Mudde 2012).

In general, bubbling and turbulent gas-solid fluidized beds, which operate at high solids concentration, are known as intrinsically complex systems due to the sophisticated dynamic behavior of both gas and solids flow structure formation and evolution (Li et al., 1998; Li 2000; Zhu et al., 2008). This is caused by the non-linear interaction between gas and solids, which can strongly influence the gas-solid distribution between bubble and emulsion phases while its variation can have considerable effect on the various processes taking place in the bed (van Ommen and Mudde 2012). For instance, on the one hand, the presence of bubbles results in particles mixing in the bed and, hence, enhancing the heat and mass transfer rates (van der Schaaf et al., 2002). On

the other hand, since the gaseous reactants in the bubble phase are hardly in contact with the catalyst particles (van der Schaaf et al., 2002), and the emulsion phase is a lot more efficient in bringing about the chemical reaction between gas and solids (Rowe et al., 1978), the presence of bubbles can yield a decrease in the conversion of gaseous reactants in the gas-solid fluidized bed reactor. In this regard, any operating variable that can alter the dynamic gas-solid distribution in the bed can subsequently have an influential impact on the apparent reaction and heat/mass transfer rates in the fluidized bed and, furthermore, on the overall reaction rate in fluidized bed reactors.

Interparticle forces (IPFs) are among the most important parameters that can affect the fluidization characteristics of the particulate materials. In regard to the importance of IPFs, there is no question that the fluidization behavior of very fine Geldart group C powders (Geldart 1973) is dominated by IPFs (Shabanian et al., 2012). Many empirical observations reported in the literature have clearly shown that different types of fluidization behavior may be exhibited by the same powder depending on the operating conditions (gas viscosity, gravity, gas adsorption, temperature, pressure, presence of eutectics) (Rietema and Piepers 1990; Rietema 1991; Poletto et al., 1993; Rapagna et al., 1994; Tardos and Pfeffer 1995; Xie and Geldart 1995; Formisani et al., 1998; Lettieri et al., 2000; Formisani et al., 2002; Li and Kuipers 2002; Lin et al., 2002; Cui and Chaouki 2004; Zhong et al., 2012). This is, in fact, in close relation with the variation in the balance between IPFs and hydrodynamic forces (HDFs) in the particulate system. Variation in the level of IPFs due to any operational reason is inevitable, especially in the near future due to the necessity of extreme conditions operation of low quality feedstocks while the local flow structure of the gas-solid fluidized beds in the presence of this influential operating parameter is poorly understood. Thus, it is essential to understand the flow structure of the bed in the presence of IPFs in order to efficiently ameliorate the design and operation of industrial gas-solid fluidized beds.

Different approaches have been applied by researchers to study the effect of IPFs on the hydrodynamic behavior of gas-solid fluidized beds. Nonetheless, simple and precise control of the level of IPFs, which are uniformly distributed throughout the bed, with the least amount of implementational and operational limitations for the approach by which cohesive IPFs are introduced into the bed of powders are the most important criteria for the selection of an appropriate method for this purpose. Among the different approaches and in light of its valuable advantages, it has been demonstrated in earlier works by the present authors (Shabanian et al., 2011; Shabanian and Chaouki 2013; Shabanian and Chaouki 2014) that the polymer coating approach (Shabanian

et al., 2011; Bouffard et al., 2012) is a superior method for investigating the influence of IPFs on the fluidization behavior of a gas-solid fluidized bed. With this method, the cohesive IPFs are introduced into the bulk of particulate materials by modifying the particle surface properties and adjusting the system temperature. More details about this approach can be found elsewhere (Bouffard et al., 2012).

To the author's knowledge there are only a limited number of studies (Willett 1999; Seville et al., 2000) about the influence of IPFs on the local hydrodynamics of gas-solid fluidized beds at relatively low superficial gas velocities, close to the minimum fluidization velocity U_{mf} of a system without IPFs. Also, there is no clear information about the effect of IPFs on the detailed hydrodynamics of gas-solid fluidized beds at moderate and high superficial gas velocities (bubbling and turbulent fluidization regimes). In parallel, it is widely accepted that for a better understanding of the flow dynamics of multiphase systems it is of prime importance to know the inner details of such systems. In this respect, the objective of the present study is to provide clear insight into the influence of IPFs on the local dynamic flow structure of the bed. The solids concentration optical fiber probe and Radioactive Particle Tracking (RPT) technique were employed in this work while beds with different levels of IPFs were achieved with the assistance of the polymer coating approach.

5.4 Methodology

The experimental work initially required the production of base particles coated with a thin and uniform layer of polymer on the surface. This was achieved through an atomization process in a spheronizer machine. In the following step, the coated particles were used in a gas-solid fluidized bed and subjected to different operating temperatures by which the properties of the PMMA/PEA (Poly Methyl MethAcrylate/Poly Ethyl Acrylate) coating and the observed IPFs were changed.

5.4.1 Particle coating process

The first experimental step was to prepare base particles uniformly coated with a thin polymer film. The polymer material that was coated on the surface of the base particles was copolymer PMMA/PEA, which was contained in a polymer suspension called Eudragit NE30D. A 450–700 μm cut of spherical sugar beads (d_p=580 μm, ρ_p=1556 kg/m^3), which is classified as Geldart group

B particles at ambient conditions, was selected as the inert base particles. These particles can easily accept the PMMA/PEA polymer coating on their surfaces.

The polymer suspension, which consists of a solution of copolymer PMMA/PEA in a 2 to 1 mass ratio in water (%Mass: Water 70.0; PMMA/PEA 28.66; Noxynol100 1.33), was coated on the surface of the sugar beads through an atomization process to produce the coated particles. This process was achieved in a spheronizer machine, where the coated particles were simultaneously dried by the heated air to attain a uniform coating film on the surface of the base particles. Details of the coating procedure and its operating conditions can be found elsewhere (Shabanian et al., 2011; Shabanian and Chaouki 2013; Shabanian and Chaouki 2014).

The thickness of the coating layer at the end of the coating process was approximately 5.0 μm. With such a thin coating layer variations in particle size and density for sugar beads were about only 1% for both parameters. This implies a close similarity of the fresh and coated sugar beads from Geldart classification's point of view.

5.4.2 Hydrodynamic study

All experiments for the hydrodynamic study were carried out under atmospheric pressure in a cold gas-solid fluidized bed. The column was made of a transparent Plexiglas pipe with a 15.2 cm internal diameter and was 3.0 m in height. A cyclone, placed at the air outlet of the column, returned back the entrained particles to the freeboard of the bed. Dried and filtered air, as fluidizing gas, was introduced into the bed through a perforated distributor plate. The distributor plate was 1 cm thick and made of aluminum. It consisted of 157 holes 1 mm in diameter arranged in a 1 cm triangular pitch. To minimize the electrostatic effect, the whole bed was electrically grounded.

In order to investigate the influence of IPFs on the hydrodynamic characteristics of a gas-solid fluidized bed fresh/uncoated and coated sugar beads were separately used in the fluidizing column at different operating temperatures. Experiments of fresh sugar beads as the base system without IPFs were carried out at 20^{o}C while experiments with coated sugar beads were conducted at 30^{o}C, 35^{o}C and 40^{o}C to achieve different levels of IPFs inside the bed. Hereafter, for the sake of simplicity, we call these systems with their different operating temperatures in abbreviated form SB20, CSB30, CSB35, and CSB40, which stand for uncoated sugar beads at 20^{o}C and coated sugar beads at 30^{o}C, 35^{o}C, and 40^{o}C, respectively. It is worth emphasizing that variation in the air

viscosity and density in the 20ºC to 40ºC temperature range are 5% and 6%, respectively. These variations are relatively negligible compared to the amount of variation in the level of IPFs, which stems from the polymer coating approach for the same temperature range. Different superficial gas velocities were used for each temperature tested (up to 1.3 m/s), covering both bubbling and turbulent fluidization regimes. Procedures for adjusting the bed temperature and gas flow rate control were similar to what have been outlined previously (Shabanian and Chaouki 2014).

In the first part of the experimental work for the present study, a fluidization study was performed at each operating temperature by measuring instantaneous local bed voidage with a reflective type solids concentration optical fiber probe. The same amount of material, 4.0 kg, was introduced into the column for all experiments with the optical fiber probe, which resulted in a static bed height of approximately 26 cm ($h/D_c \approx 1.70$) at ambient conditions. The probe was placed at the bed center and an axial position of 20 cm above the distributor plate at various operating conditions for all the experiments. This axial position for the probe ensured it was far enough from the turbulent effects of the distributor plate. The optical fiber probe used in the experiments was made in-house. To minimize the probe impact on the local flow field and further measurement accuracy, it was developed with a 3.0 mm diameter tip and 4.7 mm diameter body. The probe contained 72 emitting and receiving plastic fiber strands, each having a 250 μm diameter with the core refractive index and numerical aperture of 1.49 and 0.5, respectively. These fiber strands were arranged in an alternative array, corresponding to emitting and receiving layers of the fibers at the center of the probe tip. With this arrangement the difficulty of a "blind zone" found in regular parallel fiber probes (Cui et al., 2001; Liu et al., 2003) can be effectively diminished. This is due to the presence of plenty of fine emitting and receiving fiber strands at the tip of the probe, which are uniformly mixed together to function in a similar manner to a single-fiber probe.

The in-house fabricated optical probe was employed in conjunction with an optical fiber solids concentration measurement device (PV-4A Particle Velocity Analyzer, manufactured by the Chinese Academy of Science) to obtain signals of dynamic local bed voidage in the bed. To ensure the validity and repeatability of the sampled signals, the instantaneous local bed voidage data were acquired for a period of four minutes with the sampling frequency of 400 Hz at each operating condition. The calibration curve of normalized voltage responding to solids concentration developed by Cui et al., (2001a) was used to calculate the local bed voidage data from the recorded voltage data as the following:

$$\frac{1-\varepsilon}{1-\varepsilon_{mf}} = \frac{0.4\,u^*}{1.4-u^*} \qquad 5.1$$

where ε is the local bed voidage and

$$u^* = \frac{V-V_0}{V_{mf}-V_0} \qquad 5.2$$

where V, V_0, V_{mf} are acquired voltages under operating conditions, for an empty column, and at the minimum fluidization state.

The second part of the experimental work was carried out with the RPT technique by introducing 3 kg of particulate material into the bed. These experiments were conducted for SB20 and CSB40, systems with the least and highest amount of IPFs, at two different superficial gas velocities (0.30 and 0.50 m/s) in the bubbling regime. The radioactive tracer was made of a mixture of scandium oxide and epoxy glue with a density and size close to those of the bed material. The radioactive tracer was then activated to 60 μCi. The long half-life of radioactive scandium made it feasible to continuously run the experiment for an extended period. To track the tracer in the bed, twelve NaI scintillation detectors were located around the fluidized bed rig with an axial position of 0–35 cm in height from the distributor plate. The sampling time in the experiments was 10 ms and each experiment lasted 4 hours. Details of the RPT experiments and the tracer position reconstruction can be found elsewhere (Larachi et al., 1995).

5.5 Results and discussion

5.5.1 Effect of IPFs on ε_{mf}

Prior to performing any measurements at each operating temperature with the optical fiber probe, it had to be calibrated between the two extreme local bed voidages (ε_{mf} and 1, corresponding to the minimum fluidization state and the empty bed, respectively). The variations of ε_{mf} for fresh and coated sugar beads are reported in Table 5.1. The mean values presented in the table are an average of, at least, ten repetitions. It shows that ε_{mf}, which was equal to the fixed bed voidage ε_0, increased with IPFs. This indicates that the fixed bed could hold more gas inside its structure once IPFs were enhanced in the bed. This behavior can be explained noting the fact that when IPFs were

present in the bed, part of the weight of a single particle could be sustained with these forces. This yielded a reduction in the free movement of the particle in the packing and, hence, prevented solids from shearing off to neighboring cavities in the packing. Therefore, particles piled up in the vertical direction and a packing with a higher porosity was achieved. This result affirms the arguments of Formisani et al., (1998), and Xu and Zhu (2006) about the increase in ε_0, in the complete absence of gas flow, at high temperatures for particles of Geldart groups A, B, and C because of an increase in IPFs.

Table 5.1: Variation of ε_{mf} with IPFs

System	ε_{mf}	Standard deviation of ε_{mf} readings
SB20	0.47	0.0015
CSB30	0.49	0.0025
CSB35	0.50	0.0019
CSB40	0.53	0.0015

5.5.2 Effects of IPFs on averaged local bed voidage & Eulerian solid velocity field

The time-averaged local bed voidage ε_m of recorded signals as a function of superficial gas velocity U_g for beds with different levels of IPFs is illustrated in Figure 5.1. In all cases, by increasing the gas velocity ε_m quickly increased, reached a relatively stable region, and then further increased at higher gas velocities. Figure 5.1 shows that for each superficial gas velocity tested, although ε_m for SB20 and CSB30 was fairly comparable, it basically decreased with IPFs. Increasing the level of IPFs from SB20 to CSB40, for instance, resulted in a typical relative reduction of 5% of ε_m under the conditions studied. This reveals that particles can be fluidized more easily in a bed with a lower degree of IPFs. However, ε_m for different systems was almost similar to each other at gas velocities higher than 1.2 m/s. It could be due to the severe action of the fluidizing gas on the fluidized particles, which weakened the influence of IPFs on the local flow structure of the bed. It is worth remembering that ε_m only shows a compromised variation in the local flow structure of the bed due to operational reasons, which includes the contributions of both bubble and emulsion phases. Therefore, more analyses were required to be conducted on the instantaneous local bed voidage data to clearly highlight the effect of IPFs on the flow dynamics of the bed.

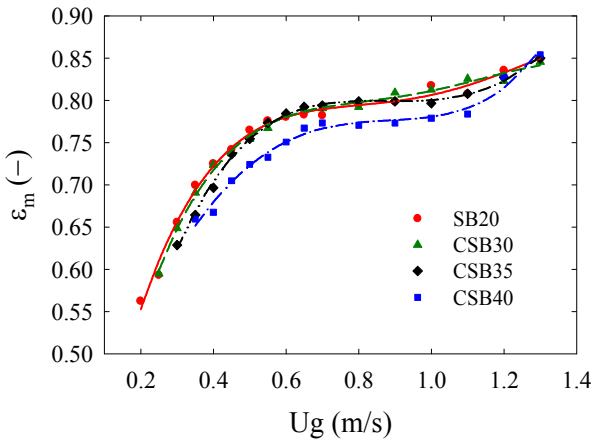

Figure 5.1: Effect of IPFs on the time-averaged local bed voidage.

Figure 5.2 presents the calculated Eulerian solid velocity field from the original radioactive particle trajectory at superficial gas velocities tested for SB20 and CSB40. It shows that the main solid flow pattern in all cases was a straight upward movement of solids to the splash zone through the central region of the bed and a downward movement along the annulus. This figure depicts that both the active height of the bed and the solid velocity increased with increasing the superficial gas velocity as a result of greater bubble activity in the bed. It is also apparent that an increase in the level of IPFs can effectively modify the solid flow structure of the bed. For instance, the solid flow pattern for CSB40 at 0.30 m/s deviated from the typical pattern. The particles travelled upward along the annulus in the bottom layer and then were directed to the central region at an intermediate height of the bed. Above the intermediate layer, the solid flow pattern was identical to the typical solid flow pattern. This type of flow pattern can be explained by the fact that since there was a considerable amount of IPFs in the bed and the gas velocity was relatively low, it was easier for the gas to break down the particle-wall contacts rather than the particle-particle contacts in the bulk of the bed. Hence, the solids circulation at the bottom section of the bed started from regions close to the wall. However, by increasing the gas velocity, since the fluidizing gas had enough power to find its path from the center of the bed at the bottom section, the upward movement of solids started from the central region. Nonetheless, it is clear from Figure 5.2c and d that the stabilized flow pattern started at slightly higher levels of the bed height when IPFs were increased.

a **b**

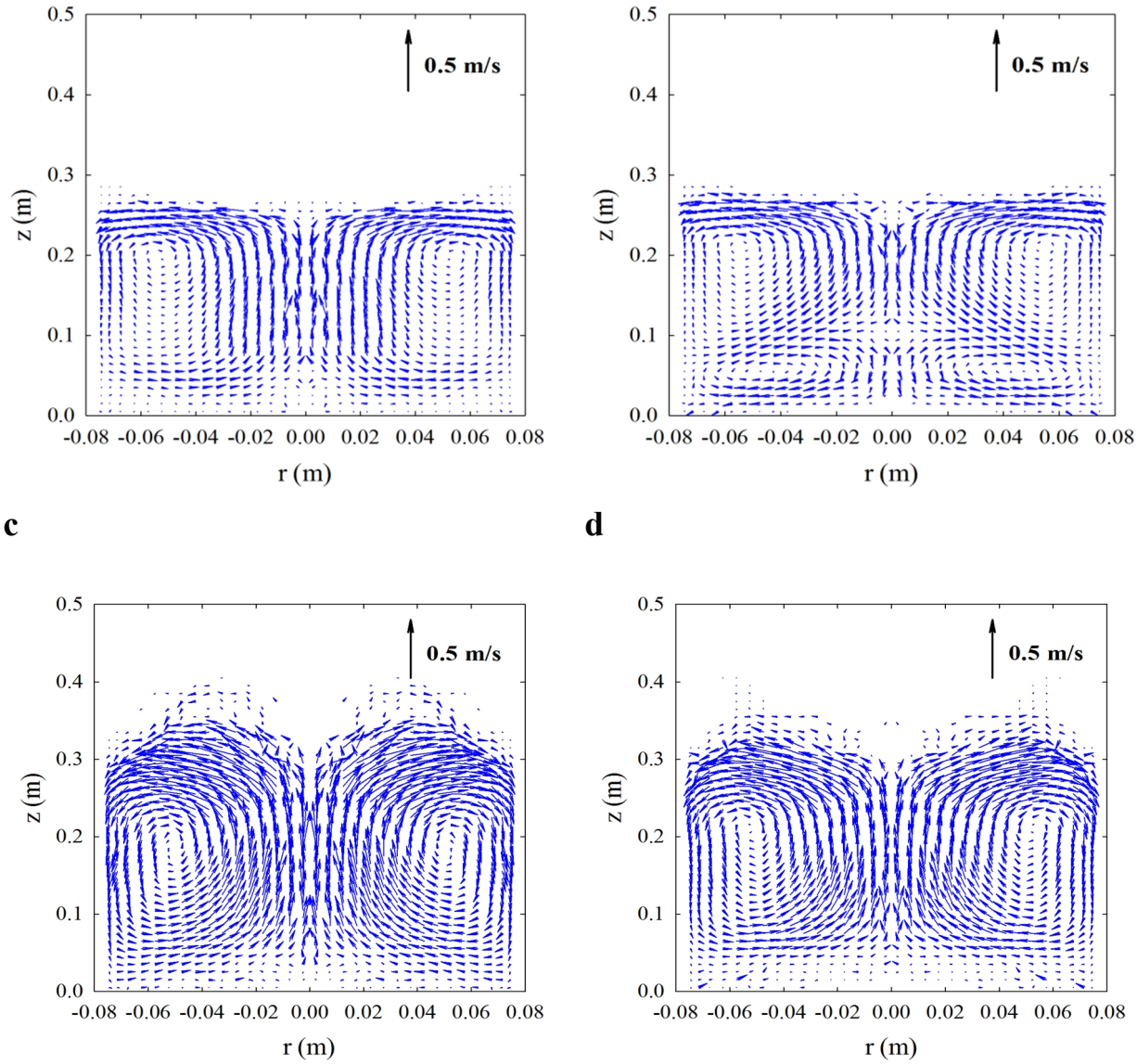

Figure 5.2: Effect of IPFs on the Eulerian velocity field of solids a) SB20, U_g=0.30 m/s, b) CSB40, U_g=0.30 m/s, c) SB20, U_g=0.50 m/s, d) CSB40, U_g=0.50 m/s.

It can be further found from Figure 5.2 that the magnitude of the arrows in the whole bed decreased with IPFs, especially at the center of the bed. It is representative of the solid velocity in this section that is in close relation to the bubble rise velocity and size. This observation is consistent with the analysis of pressure signals (Shabanian and Chaouki 2014) and values of bubble contact times obtained by the local bed voidage measurements, which will be discussed later. This confirms the presence of smaller bubbles for beds with more cohesive IPFs at superficial gas velocities well below the transition velocity from a bubbling to turbulent regime. The reduction in the average particle velocity due to the presence of IPFs was also reported by Willett (1999). The level of IPFs

was increased in a bed of 1-mm ballotini particles through the addition of a very small amount of involatile oil. The particle motion was monitored by tracking a single radioactive tracer particle with the help of the Positron Emission Particle Tracking (PEPT) technique. Therefore, this qualitative comparison on the solid flow pattern in beds with different levels of IPFs confirmed that additional analyses were required to be conducted on the instantaneous local bed voidage data.

5.5.3 Effects of IPFs on fluctuation amplitude of local bed voidage signals

The standard deviations of local bed voidage fluctuations σ under different operating conditions are plotted in Figure 5.3. Similar to the evolution of ε_m with the gas velocity, the standard deviation increased first with the gas velocity to reach a plateau at intermediate velocities for all systems. Nevertheless, it began to decrease with a further increase in gas velocity, which was accompanied by an additional increase in ε_m. All curves plotted in Figure 5.3 also show two clearly discoverable points, the starting and final points of the plateau. According to Zhu and Zhu (2008), this range of gas velocities with a relatively constant σ reflects the bubbling to turbulent transition on meso-scale. This is actually different from the quick regime transition that was found with the pressure fluctuations for SB20, which was reported elsewhere (Shabanian and Chaouki 2014). Similar behavior was noted by Zhu and Zhu (2008) and Zhu et al., (2008) with a bed of 65 μm FCC powders using measurements of pressure and solids concentration fluctuations.

Basically, the transition velocity from bubbling to turbulent fluidization regime U_c based on the pressure fluctuations is defined as the gas velocity at which the standard deviation of pressure fluctuations reaches its maximum (Yerushalmi and Cankurt 1979). With this widely used technique, the transition is generally a perspicuous transition. This velocity distinguishes the condition at which big bubbles are replaced by smaller and transient voids (Bi and Grace 1995). Since pressure fluctuations represent the overall hydrodynamic behavior (Zhu and Zhu 2008) and bubble activities (formation, coalescence, axial movement, and eruption) are the main source of pressure oscillations in the bed (van der Schaaf et al., 2002; Punčochář and Drahoš 2005), the bubbling to turbulent transition velocity determined from the pressure amplitude is closely related to a change in bubble phase/behavior (Zhu and Zhu 2008). However, since the local bed voidage fluctuations principally reflect the solids dynamic behavior, applying its standard deviation to determine the transition from bubbling to turbulent fluidization regime results in a gradual transition. This is related to the emulsion phase transition that lasts over a range of gas velocities

(U_{c1}– U_{c2}) (Zhu and Zhu 2008). Since the well defined two-phase flow structure in the bubbling regime, dispersed bubble phase and continuous emulsion phase, is replaced by an unstable two-phase flow structure of clusters and broth in the turbulent regime (Ellis et al., 2004), the local bubbling to turbulent regime transition attained by the amplitude of the local bed voidage fluctuations is a result of the disappearance of the stable two-phase flow structure. Therefore, U_{c1} (the gas velocity at which the amplitude of local bed voidage fluctuations reaches its maximum) represents the beginning of the breakdown of the stable emulsion phase and U_{c2} (the gas velocity at which the amplitude of local bed voidage fluctuations begins to decrease with U_g) marks the completion of this breakdown (Zhu and Zhu 2008). By this definition, U_{c1} is considered as the velocity of the incipient turbulent fluidization and U_{c2} as the velocity of complete entry into the turbulent fluidization regime on a meso-scale.

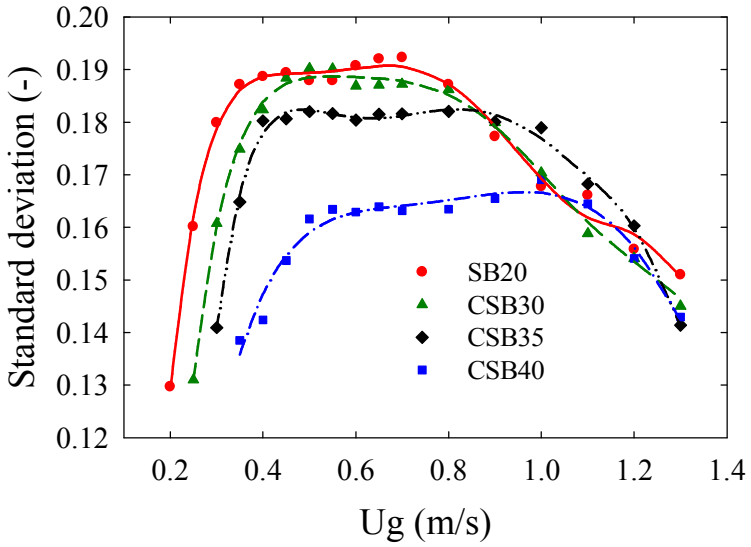

Figure 5.3: Effect of IPFs on the standard deviation of local bed voidage fluctuations.

Figure 5.3 further illustrates that U_{c1} and U_{c2} increased with IPFs and the local flow regime transition took place over a wider range of gas velocities. It indicates that the breakdown of the continuous emulsion phase started at a higher gas velocity due to cohesive IPFs, which enhanced the tensile strength of the emulsion phase. Also, it reveals that the complete breakdown of this phase required more energy from the fluidizing gas to entirely overcome the attractive IPFs at the interparticle contact points. Thus, a bed with IPFs resisted the bubbling to turbulent regime transition while it eventually happened at a higher gas velocity. These findings are consistent with

the analysis of standard deviation of pressure fluctuations reported in a separate work by the present authors (Shabanian and Chaouki 2014). It is also worth mentioning that the magnitude of the local bed voidage fluctuations was lower for the bed with higher IPFs while all systems were operating in the bubbling regime. It implies that there was a more intensive flow fluctuation in the bed with a lower amount of IPFs and it became more uniform for the bed with a larger amount of IPFs. However, the amplitude of fluctuations was relatively comparable for all systems at high gas velocities of the turbulent regime. This could be due to the intense action of the fluidizing gas and considerable reduction in the idle time (Stein et al., 2000) of the system during which the coated particles could be in contact with each other. This reduction, in turn, substantially decreased the effective adhesion energy resulting from the polymer coating approach (Shabanian and Chaouki 2014).

5.5.4 Effect of IPFs on two-phase flow characteristics

5.5.4.1 Probability density distribution of the instantaneous local bed voidage

The probability density distributions of the local bed voidages from ε_{mf} to 1 for fluidized beds with different levels of IPFs were calculated and plotted in Figure 5.4 to identify the gas-solid distribution in the two-phase flow structure and its dependence on IPFs. A bimodal probability density distribution in transient local bed voidage signals can be found in all operating conditions. The first peaks, which are characterized by low voidages, are related to the emulsion phase and indicate the continuity of this phase with high solids fractions. The second peaks at high voidages represent the bubble phase, which are characterized by a continuous gaseous phase with low solids fractions.

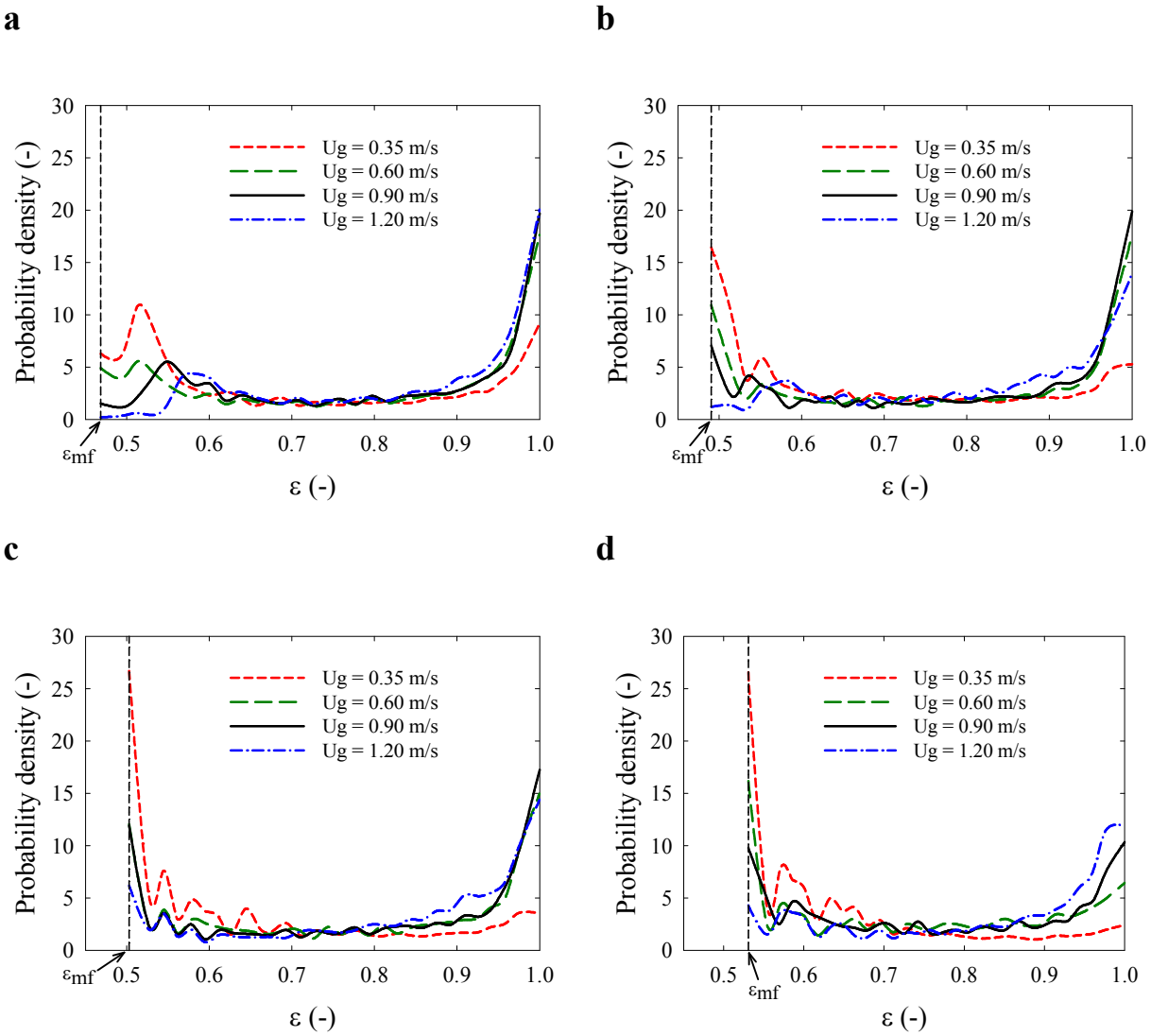

Figure 5.4: Comparison of the probability density distribution of the instantaneous local bed voidage at different U_g and levels of IPFs in the bed. a) SB20, b) CSB30, c) CSB35, d) CSB40.

It can be found that variations in operating conditions, either changing U_g or the level of IPFs, can change the shape of the probability density distribution curves. At a given degree of IPFs, with increasing U_g, the probability of the emulsion phase decreased/shifted to higher voidages and that of the bubble phase increased. It means that the hydrodynamics of the bed modified by increasing U_g through increasing the portion of the bubble phase while decreasing the emulsion phase, which is more diluted, so that higher voidages form in the bed. On the other hand, by increasing the level of IPFs, the probability of the emulsion and bubble phases increased and decreased, respectively. This reveals that the probability density distribution of the local bed voidage for beds with IPFs

was different from SB20, without IPFs, even if they had equal time-averaged voidages in some conditions (refer to Figure 5.1). In fact, SB20 had a low probability at and close to the saturation voidage ε_{mf} (emulsion phase) while beds with IPFs had a high probability in this region and it was enhanced by increasing the IPFs. Additionally, the reduction that was observed in the probability of pure bubbles by enhancing IPFs can be attributed to the presence of more particles in the bubble phase under such operating conditions. These observations show that the local flow structure that was partially dominated by the bubble phase for SB20 altered toward dominance of the emulsion phase in systems with higher levels of IPFs. Consequently, it means that at a given fluidizing gas throughput, by enhancing IPFs, the dominant mechanism for the gas-solid interaction changed and the gas tended to pass through the bed in the emulsion phase rather than the bubble phase.

5.5.4.2 Time-averaged voidages of bubble and emulsion phases

To further understand how IPFs affect the local two-phase flow structure of the bed, hydrodynamic parameters corresponding to both bubble and emulsion phases were calculated. The method of minimum probability of local bed voidage (Cui et al., 2000) was used to distinguish the bubble phase from the emulsion phase in the instantaneous local bed voidage signals. With this approach, the probability density distribution of the local bed voidage against the local bed voidage from ε_{mf} to 1 is analyzed and the local voidage with the minimum probability between the two probability density peaks is taken as the division voidage ε_{div} between the emulsion and bubble phases (Cui et al., 2000). Consequently, at a given time for each operating condition, if the local voidage measured by the probe was higher than ε_{div}, it was considered as a bubble phase passing by the front tip of the probe; otherwise, the local bed voidage was taken as an emulsion phase.

Following identification of the bubble and emulsion phases in the original local bed voidage data, the time-averaged voidages of bubble and emulsion phases, ε_b and ε_e, respectively, were calculated at each operating condition. Figure 5.5 illustrates the variations of these parameters as a function of superficial gas velocity for systems differing in the level of cohesive IPFs. It can be found that, for each system tested, ε_e rapidly increased with the gas velocity up to a relatively stable level that lasted over a range of gas velocities. This velocity range interestingly matches the range of gas velocities with a relatively constant σ in Figure 5.3 for the corresponding systems. The ε_e then increased with a further increase in the gas velocity when the bubbling regime transferred to the turbulent regime on a meso-scale. The presence of this type of evolution for ε_e with the superficial

gas velocity confirms that the bubbling to turbulent transition velocity obtained from the amplitude of the local bed voidage signals does correspond to the emulsion phase transition.

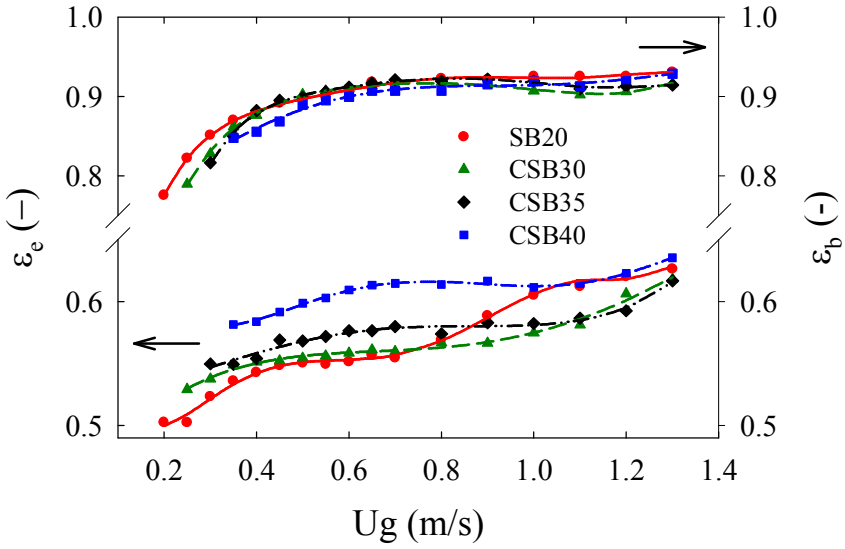

Figure 5.5: Effect of IPFs on the time-averaged bubble and emulsion phase voidages.

Figure 5.5 shows that for the gas velocities below 0.7 m/s where all systems were operating in the bubbling regime ε_e progressively increased with IPFs. This proves that the emulsion phase in an identical manner to the packed bed state could hold more gas inside its structure when IPFs were enhanced in the bed. This result confirms Rietema's (1991) opinion about the temporal stability of the emulsion phase between two bubble passages. According to Rietema, during this interval, the structure of the emulsion phase resembles the homogeneously expanded fixed bed while the degree of stability increases with the level of IPFs. This is also a promising finding, which indicates that at a specific gas velocity, by increasing the level of IPFs in the bed, the fluidizing gas is more prone to be present in the emulsion phase. Accordingly, since a better gas-solid contact is achieved in the emulsion phase, a slight increase in the level of IPFs inside the bed while it is far from the defluidization condition can offer an appreciable advantage for systems requiring good gas-solid contacting, like FCC regeneration. It is worth noting that this observation is in good agreement with the experimental results of Row et al., (1978) and Yates and Newton (1986). They reported that increasing the amount of fines (< 45 μm), which can be translated into an increase in the degree of IPFs in the bed, resulted in an increase in the interstitial gas flow rate and emulsion phase voidage. An increase in voidage of the emulsion phase was also reported by Rietema (1991)

through fluidizing fresh cracking catalysts with three different gases (methane, nitrogen, and argon) at gas pressures up to 15 bar. In addition, he found that the increase in the emulsion phase voidage was accompanied by an increase in the elastic modulus of the particulate bed with the gas pressure. Accordingly, he attributed this modification to an increase in the level of IPFs in the system.

By increasing the gas velocity above 0.7 m/s, SB20 transferred into the turbulent regime first while the regime transition took place at higher U_g for systems with higher levels of IPFs. Since the breakage of the emulsion phase completed for SB20 under this operating condition, ε_e began to increase again with U_g. Although ε_e for SB20 considerably increased in the turbulent regime, it became comparable to the ε_e of CSB40 at its stable level during which it was operating in the bubbling regime. This implies that if it is required to reach a specific emulsion phase voidage (hence, gas flow rate in the emulsion phase) in the fluidized bed while there are some operational limitations, like the attrition of the particulate materials, which requires working at a low/moderate fluidizing gas flow rate, this can be simply achieved by enhancing IPFs in the fluidized bed while it is far from the defluidization state. Drying certain foods and pharmaceutical particulate materials in gas-solid fluidized beds and gas-gas chemical reactions with the help of expensive solid catalysts that can be easily attrited in gas-solid fluidized beds are typical examples regarding this requirement. In addition, it can be found in Figure 5.5 that ε_e for systems with different levels of IPFs was drawing near to each other at velocities close to the maximum superficial gas velocity tested, U_g=1.3 m/s. This indicates that at very high U_g the role of IPFs on the local hydrodynamics of the bed weakened.

For almost all systems tested, ε_b quickly increased at gas velocities slightly above the corresponding minimum fluidization velocity. It represents the range of gas velocities required for bubbling activity to be well developed in the bed. After this initial step, a little change was observed in ε_b upon increasing U_g. Figure 5.5 further depicts that ε_b slightly decreased when the level of IPFs was increased in the bed. This means that bubbles contained more solids when IPFs were enhanced. According to the minimum probability approach (Cui et al., 2000), all voidages higher than ε_{div} are considered as local voidages for the bubble phase element, thus, ε_b only reports a mean value for these voidages. Therefore, in order to have better knowledge about the evolution of the local bed voidage in this range, cumulative probability density distribution of local bed voidage signals for SB20 and CSB40 at different velocities were calculated and plotted in

Figure 5.6. It can be seen from this figure that contributions of intermediate voidages in the evolution of the cumulative probability density distribution were more pronounced for CSB40. However, contributions of voidages in the range of $0.9 < \varepsilon < 1$ were more significant for SB20. This reveals that most of the bubbles in SB20 were closer to the pure bubble while bubbles with more solids fractions form the main population of bubbles for CSB40 with IPFs inside.

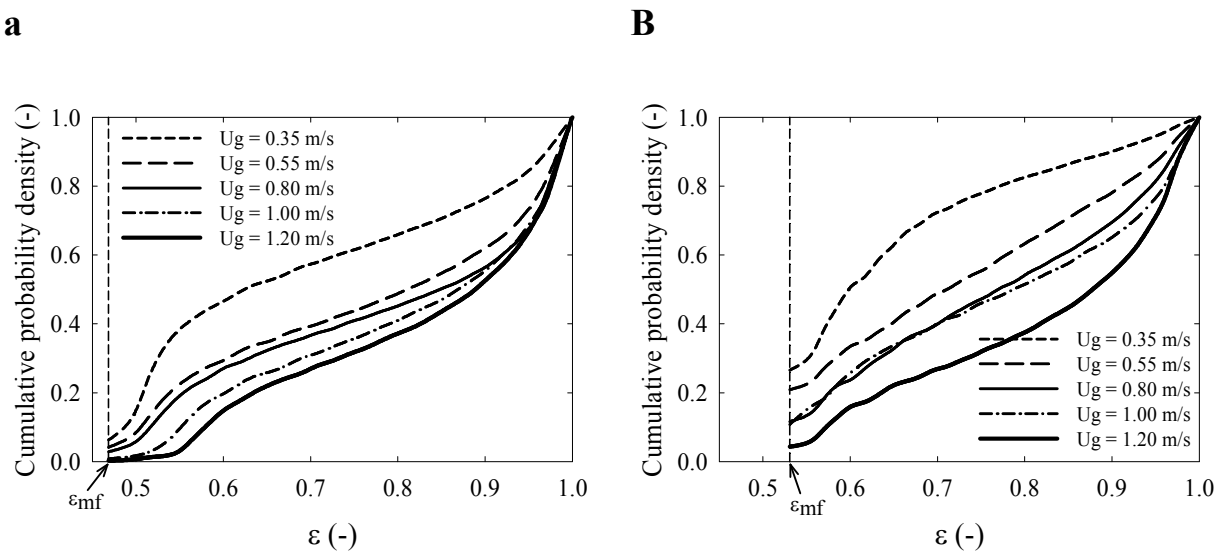

Figure 5.6: Comparison of the cumulative probability density distribution of the instantaneous local bed voidage at different U_g and levels of IPFs in the bed. a) SB20, b) CSB40.

5.5.4.3 Emulsion phase fraction

For the next step, the emulsion phase fraction f_e, which is the time fraction of the emulsion phase from the local bed voidage signals, was calculated at each operating condition as the following (Cui et al., 2000):

$$f_e = \frac{\varepsilon_b - \varepsilon_m}{\varepsilon_b - \varepsilon_e} \qquad 5.3$$

Figure 5.7 presents the variation of f_e with superficial gas velocity and IPFs. It can be noted that for each operating temperature, f_e quickly reduced with U_g at low gas velocities since the bubbling phenomenon was under development to be dominant in the bed. At intermediate gas velocities, f_e somehow leveled off; this is more obvious for SB20. It could be the result of two competing phenomena that counterbalanced their effects. On the one hand, part of the excess gas compared to lower gas velocities could be devoted to completion of the emulsion phase breakage and making it

more diluted. On the other hand, the rest of the excess gas could either contribute to the formation of slightly bigger bubbles with relatively lower frequency before the completion of the bubbling to turbulent regime transition or the formation of smaller bubbles with higher frequency after the regime transition. In this regard, both bubble and emulsion phases could experience such gradual evolutions while portions of these phases in the local flow structure of the bed remained relatively unchanged. Similar behavior for f_e can be also found in the experimental results of Cui et al., (2001b) for 70 µm FCC and 385 µm sand particles, differing in the range of gas velocities at which this plateau-like region can be observed. At higher U_g, while the bed was operating in the turbulent regime, small bubbles/voids were frequently passing by the front tip of the probe and the emulsion phase changed its entity into clusters of particles with higher voidages. This, in turn, resulted in a further decrease in f_e due to the increase in the portion of the dilute phase in the bed.

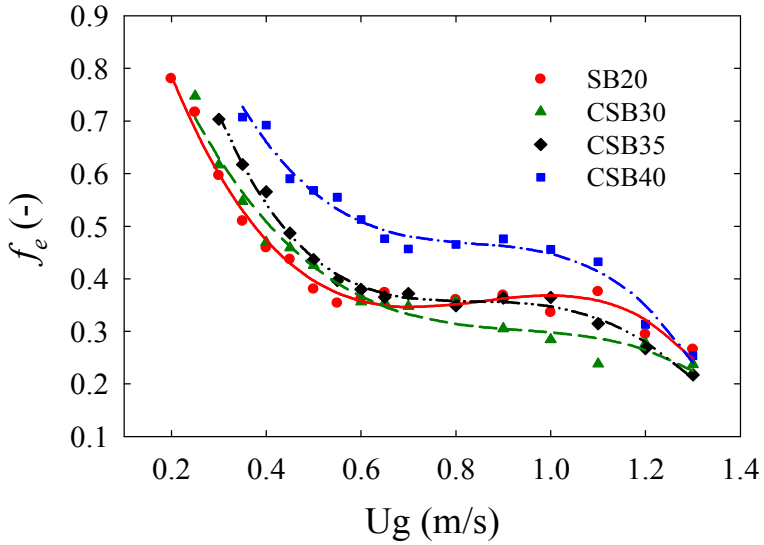

Figure 5.7: Effect of IPFs on the emulsion phase fraction.

Comparing the emulsion phase fraction of systems with different levels of IPFs in Figure 5.7 reveals that f_e successively increased with IPFs when all of them where operating in the bubbling regime, namely for U_g < 0.7 m/s. Consequently, by increasing the level of IPFs in a bubbling gas-solid fluidized bed the two phase flow structure of the bed tended to be comprised of more emulsion phase that had a higher capacity for holding the fluidizing gas inside its structure. This, subsequently, implies that at a specific superficial gas velocity in the bubbling regime, the tendency of gas flowing in the emulsion phase increased with IPFs.

The radioactive particle trajectory, registered in the bubbling regime, had been employed to verify whether or not the single point local measurement by the optical fiber probe is in agreement with the local behavior throughout the whole bed. Figure 5.8 illustrates the influences of superficial gas velocity and IPFs on the probability density of vertical particle velocity during the RPT experiment. As demonstrated in this figure, the distribution of vertical particle velocity at different operating conditions exhibited a Gaussian-like function while the maximum distribution took place in the vicinity of zero velocity. This indicates that particles spent more time wandering in the emulsion phase, where because of random walking or Brownian motion of the particles, the vertical particle velocity was very close to zero (Stein et al., 2000; Mostoufi and Chaouki 2004). Figure 5.8 shows that by increasing the superficial gas velocity, the probability of the particle velocity close to zero decreased and the Gaussian-like function broadened over a wider range of velocities. It indicates that the probability of particles being caught in the bubbles, where they move more rapidly in the wake, drift or as descending clusters, increased with U_g.

Figure 5.8 further depicts that IPFs had a dissimilar effect on the probability of the vertical particle velocity in comparison with the superficial gas velocity. By increasing the level of IPFs, the intensity of the peak close to zero increased. This reveals that by enhancing IPFs in the particulate bed fewer particles were picked up by the ascending bubbles. In other words, the more cohesive fluidized bed can be comprised more of the emulsion phase in which particles are experiencing Brownian motion. Therefore, RPT results clearly support the experimental finding with the analysis of the single point local bed voidage signals expressing that f_e increases with IPFs in the bubbling regime. Moreover, Figure 5.8 implicitly unveils that increasing the level of IPFs in the bubbling regime yielded an increase in the portion of the fluidizing gas that interstitially passed through the bed.

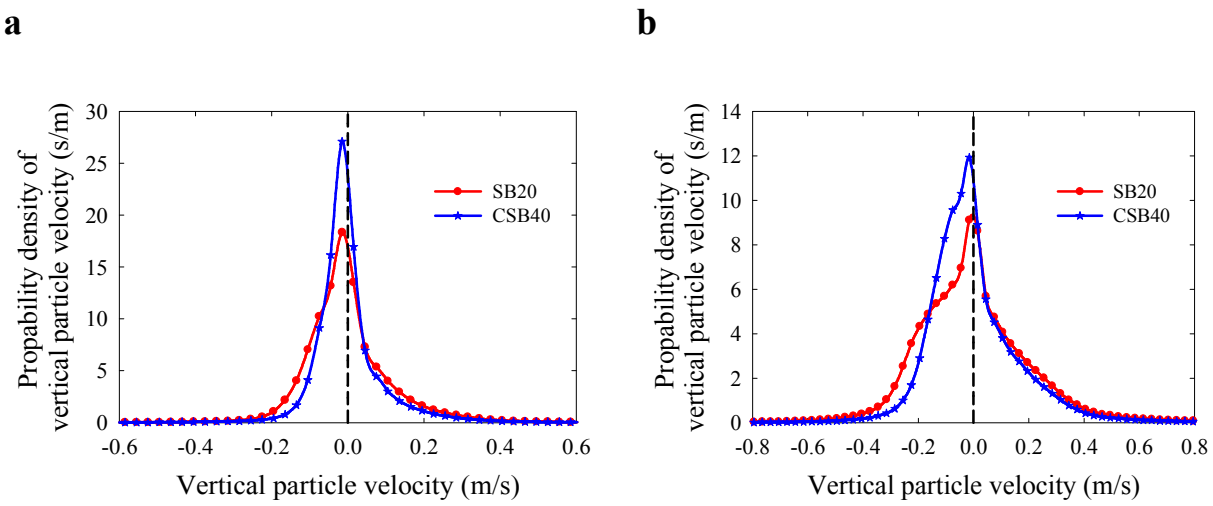

Figure 5.8: Effect of IPFs on the probability density of vertical particle velocity. a) U_g=0.30 m/s, b) U_g=0.50 m/s.

The variation of f_e with IPFs was more complicated at higher gas velocities and inversion trends can be seen for systems with different levels of IPFs. It is clear from Figure 5.7 that the plateau occurred in the range of gas velocities slightly below U_c and lasted up to gas velocities well above U_c for SB20. However, it mainly took place at gas velocities below the corresponding U_c for systems with IPFs. Basically, the emulsion phase could expand more easily and experience a higher voidage after the regime transition when there were no IPFs in the bed. This is while this capability was reduced by increasing IPFs. This can be simply inferred from Figure 5.5 while the rate of increase in ε_e after the transition of the fluidization regime from bubbling to turbulent was appreciably higher for systems with lower/no IPFs. Therefore, the extension of the stable level in the case of SB20 above U_c could be explained by noting the fact that the swarm of particles in the turbulent region could be further diluted with the fluidizing gas to benefit operation with constant f_e. At gas velocities above U_g=1.1 m/s for SB20, the f_e decreased due to the dominance of bubble/void activity in increasing the portion of the dilute phase compared to the dilution capability of the emulsion phase. Also, disintegration of the emulsion phase into its constituent particles followed by their entrainment through the ascending voids can promote these changes. Nonetheless, when IPFs were enhanced in the bed, the emulsion phase hardly allows more gas to enter into its structure. Accordingly, the additional gas at superficial gas velocities slightly below U_c would tend to appear in the bubble phase and form bigger bubbles. The impact of this increase in bubble size could be high enough to relatively increase the portion of the bubble phase while it

was not compensated with a reduction in the bubble frequency. Therefore, f_e remained constant for a shorter range of gas velocities and began to decrease as the gas velocity reached the corresponding U_c.

It can be further found from Figure 5.7 that f_e was almost similar for systems with different levels of IPFs at velocities close to the maximum superficial gas velocity tested in this study, U_g=1.3 m/s. This indicates that at a very high superficial gas velocity there was a limited impact of IPFs on the local flow structure of the bed due to the dominance of strong HDFs over IPFs in the bed.

5.5.4.4 Distribution of the fluidizing gas between the bubble and emulsion phases

In order to quantitatively evaluate the influence of IPFs on the distribution of the fluidizing gas between the bubble and emulsion phases in the vicinity of the optical fiber probe's tip, the bubble rise velocity U_B and the superficial gas velocity of the emulsion phase U_e were calculated using the experimental results. Indeed, U_B and U_e are correlated with the emulsion phase fraction and the superficial gas velocity as follows:

$$U_g = f_e U_e + (1 - f_e) U_B \qquad 5.4$$

To fulfill this evaluation, it requires having knowledge of the bubble rise velocity, which is closely related to the bubble size. Liu et al., (2010) conducted measurements of bubble size in a fluidized bed of 78 μm FCC particles utilizing both dual intrusive optical fiber probes and non-intrusive pressure sensors. For the latter, they applied the spectral decomposition approach presented by van der Schaaf et al., (2002) on the recorded pressure signals in the windbox and dense bed. They found that bubble chord lengths obtained by optical probe signals overestimated the values of bubble sizes calculated by the model presented by Horio and Nonaka (1987), which is probably the most accurate correlation for predicting bubble diameter in fluidized beds of Geldart group A particles (Liu et al., 2010). On the contrary, the values of bubble length scales estimated by the spectral decomposition approach were in close agreement with those estimated by the Horio and Nonaka (1987) equation. Experimental measurements of bubble size by the application of dual optical fiber probes vertically aligned in a fluidized bed of 380 μm sand particles carried out by Fotovat et al., (2013) also demonstrated the same deficiency, i.e., overestimation of bubble chord lengths obtained by the optical probe measurements.

The spectral decomposition method (van der Schaaf et al., 2002) was used in the present study to estimate the bubble length scale in the vicinity of the optical fiber probe. The gauge pressure signals registered in the windbox and 17.5 cm in height above the distributor plate were employed for this method. Pressure measurements were simultaneously carried out with the local bed voidage measurements with the same sampling frequency of 400 Hz. The spectral decomposition method does not directly yield actual bubble size but a characteristic length scale that is proportional to the average bubble size (Rüdisüli et al., 2012). Similar to Liu et al., (2010) and Zhang et al., (2010), a proportionality constant of unity is considered in this study. In general, the bubble size obtained by the spectral decomposition approach is for the region close to the in-bed pressure transducer (Liu et al., 2010). Since the in-bed pressure sensor was placed in an axial position very close to the optical probe's location in this study, it is assumed that the bubble length scales estimated by this approach closely represent the average size of bubbles passing by the front tip of the probe.

According to Karimipour and Pugsely (2011) the correlation presented by Mori and Wen (1975) yields the best estimations for bubble size in fluidized beds of Geldart group B particles in the case of the perforated distributor plate. It is thus chosen in this work to verify the appropriateness of the bubble length scale estimations attained by the spectral decomposition method. It is given by Mori and Wen (1975) as follows:

$$\frac{D_{bm} - D_b}{D_{bm} - D_{b0}} = \exp(-0.3\ \frac{h}{D_c}) \tag{5.5}$$

where D_{b0} is the initial bubble size, D_{bm} is the maximum bubble size due to total bubble coalescence, D_b is the bubble size, h is the height above the distributor plate, and D_c is the column diameter. D_{b0} and D_{bm} can be expressed as follows:

$$D_{b0} = 0.347 \left(\mathrm{A_c}\ \frac{\left(\mathrm{U_g} - \mathrm{U_{mf}}\right)}{\mathrm{N_{or}}} \right)^{0.4} \tag{5.6}$$

$$D_{bm} = 0.652 \left(\mathrm{A_c} \left(\mathrm{U_g} - \mathrm{U_{mf}} \right) \right)^{0.4} \tag{5.7}$$

where A_c is the cross-sectional area of the column, and N_{or} is the number of orifices on the perforated distributor plate.

Figure 5.9 depicts values of bubble size estimated by the spectral decomposition approach and those calculated by the Mori and Wen (1975) equation in the vicinity of the in-bed gauge pressure sensor for beds with different levels of IPFs in their corresponding bubbling regimes. This figure clearly shows that values of bubble length scales estimated by the spectral decomposition method are in good agreement with the values calculated by the Mori and Wen (1975) correlation, especially for systems with no or low IPFs. It confirms the suitability of the selected approach for the estimation of the bubble size. Deviations that can be found between the estimations of these approaches for beds with high amounts of IPFs affirm that the growth rate of bubble size with the superficial gas velocity increased with IPFs. This is consistent with the results reported by Shabanian and Chaouki (2014) using measurements of pressure signals. This also illustrates the necessity of developing predictive correlations describing the bubble properties in beds with different levels of IPFs.

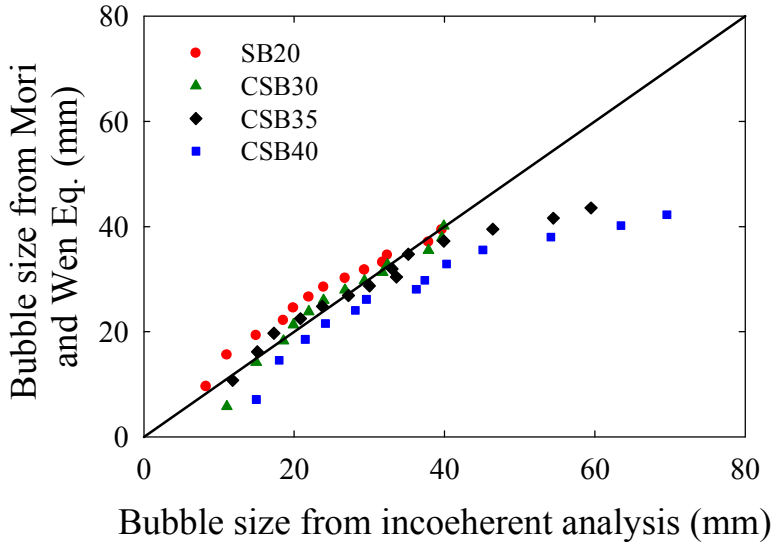

Figure 5.9: Bubble sizes estimated from Mori and Wen (1975) Eq. and spectral decomposition method.

Following the estimation of the bubble size from the spectral decomposition approach at different operating conditions, the corresponding bubble rise velocity was calculated from the commonly used literature correlation of Davidson and Harrison (1963) as the following:

$$U_B = 0.71\sqrt{g\,D_b} + (U_g - U_{mf}) \qquad 5.8$$

where g is the gravity acceleration. Subsequently, U_e was calculated from Eq. 5.4 with the help of values of f_e and U_B calculated/estimated at each operating condition.

Variations of U_e and U_B with the superficial gas velocity and IPFs are plotted in Figure 5.10. It can be clearly established from this figure that the tendency of the fluidizing gas passing through the bed in the emulsion phase was higher for beds with higher amounts of IPFs in the bubbling regime. However, a different trend was noted at high gas velocities. The U_e for SB20, a system without IPFs, steeply increased with gas velocities higher than 0.9 m/s. In fact, SB20 represented the highest amount of fluidizing gas passing in the emulsion phase for gas velocities higher than 1.2 m/s. This can be attributed to the lowest resistance that the emulsion phase in the case of SB20 was showing in spite of more dilution due to the absence of IPFs. The presence of considerably smaller bubbles for SB20 compared to systems with IPFs under this operating condition (Shabanian and Chaouki 2014) played a great role in this evolution, too. This finding suggests that if there is no operational limitation to process the gas-solid fluidized bed around gas velocities where a system without IPFs is in the turbulent regime and the one with IPFs is in the bubbling regime, better reaction performance is predictable for the bed without IPFs. This could be related to better gas-solid contact because of more gas flowing in the emulsion phase under such operating conditions together with the improved quality of solid mixing that can be achieved in the turbulent regime.

Figure 5.10 also demonstrates that although there was an increased tendency of gas passing through the emulsion phase in the bubbling regime that can improve the gas-solid contact in the bed, the amount of fluidizing gas flowing through the bubble phase decreased in this regime. This can be inferred as the presence of restrictions in the formation and development of bubbles in the bed, which can have a negative impact on the quality of solid mixing in the bed. It is well recognized that the quality of solid mixing, particularly the local solid mixing, in a gas-solid fluidized bed is a crucial parameter in the case of very rapid reactions, where reactants convert to products before the bubble reaches the surface of the bed or interacts with the other bubbles in the bed (Mostoufi and Chaouki 2001). Therefore, an increase in the level of IPFs with the purpose of having better gas-solid contact in the bubbling regime could be an appropriate operating solution in the case of slow reactions, which are not controlled by the transfer phenomena.

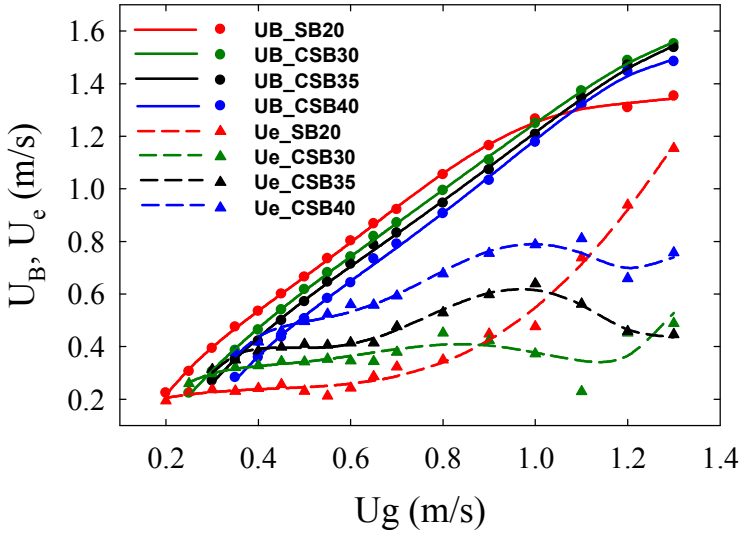

Figure 5.10: Effect of IPFs on the bubble rise velocity and the superficial gas velocity of emulsion phase.

5.5.4.5 Bubble/emulsion cycle frequency

To specify how the fluidization intensity, which is in close relation to the quality of solid mixing in the bed, is influenced by IPFs, the frequency of the bubble/emulsion phase cycle was analyzed via the local bed voidage signals. Results of this analysis for different operating conditions are presented in Figure 5.11. It shows that for each system tested, the frequency of the bubble/emulsion cycle first increased with the gas velocity to reach a partial maximum. It then experienced a gradual reduction with U_g up to the transition velocity from bubbling to turbulent regime and, subsequently, increased with a further increase in U_g. It is worth mentioning that to calculate the frequency of the bubble/emulsion phase cycle no filtering was applied on the detected bubble phases with voidages higher than ε_{div}, which was determined with the help of the minimum probability approach (Cui et al., 2000). Consequently, the values obtained by this method included all bubbles, even those with very small contact times by the front tip of the optical probe.

Figure 5.12 illustrates typical plots of probability density distributions of bubble contact time with the optical fiber probe at different gas velocities for SB20. In fact, the bubble contact time is related to its dimension, the longer the bubble contact time, the larger its dimension will most likely be (Cui and Chaouki 2004). By considering Figure 5.11 in conjunction with Figure 5.12, it can be found that plenty of small bubbles passed by the front tip of the probe at low gas velocities (U_g=0.35

m/s). However, by increasing U_g toward U_c, larger bubbles with longer contact times with the probe formed in the bed while the net bubble frequency and, thus, the frequency of the bubble/emulsion phase cycle decreased. By increasing the gas velocity above U_c larger bubbles were replaced by smaller bubbles/voids. This is obvious from a reduction in the probability of longer contact times and an increase in the probability of shorter contact times. The exchange of large bubbles with small voids during the bubbling to turbulent regime transition was accompanied by an increase in the bubble/void frequency in the bed.

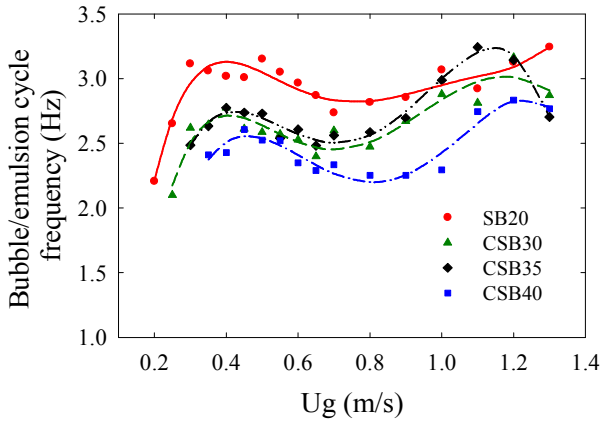

Figure 5.11: Effect of IPFs on the bubble/emulsion cycle frequency.

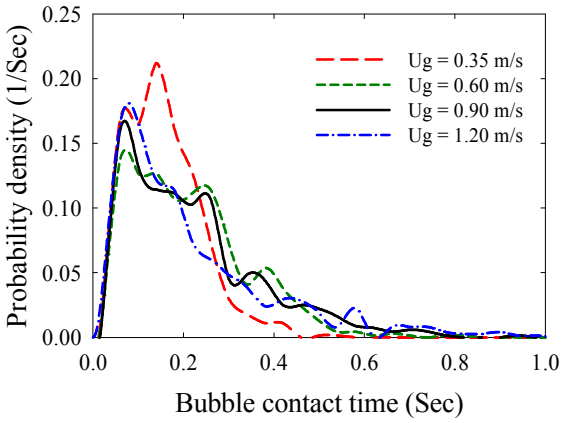

Figure 5.12: Typical plots of the probability density distribution of bubble contact times at different gas velocities for SB20.

It can be noted from Figure 5.11 that the frequency of the bubble/emulsion phase cycle decreased with IPFs. Basically, the frequency of the bubble/emulsion phase cycle represents the incidence of phase change in the fluidized bed, which cycles repeatedly over time on a macro-scale (Cui and Chaouki 2004). When the frequency of the bubble/emulsion phase cycle increases, the fluidization activity is enhanced and, consequently, more intense fluidization with better solid mixing is achieved in the bed. Accordingly, by increasing the level of IPFs inside the bed less intense fluidization can be achieved and lower quality solid mixing is predictable for the bed. It can therefore be concluded that enhancing cohesive IPFs in the bubbling bed with the purpose of achieving better gas-solid contact should be compromised with the quality of solid mixing in the bed to reach an optimized operating performance.

5.5.4.6 Bubble contact time

In order to characterize the effect of IPFs on the bubble contact time/dimension, plots of probability density distributions of bubble contact time for systems differing in levels of IPFs at three different gas velocities are presented in Figure 5.13. The mean contact time at each operating condition was illustrated with an arrow in the figure. It can be found that a bed with higher IPFs contained smaller bubbles at low gas velocity, while smaller bubbles were noted for the bed with a lower degree of IPFs at medium gas velocity. A similar inversion trend in the variation of bubble size was reported in a separate work by the present authors (Shabanian and Chaouki 2014) using the recorded pressure signals from beds with different levels of IPFs. At high gas velocity in the turbulent regime, the local fluidization behaviors of systems with different amounts of IPFs were approaching each other in the presence of a slight difference between the mean bubble contact times and the corresponding probability density distributions.

The inversion trend observed in Figure 5.13 could be explained by noting the variation of ε_e and a reduction in the fluidity of particles with IPFs. It was found that when a cohesive bed was operating at a low gas velocity in the bubbling regime, the emulsion could hold more gas inside its structure. Accordingly, at the same superficial gas velocity, a smaller portion of the fluidizing gas passed through the bed in the form of bubbles, causing a reduction in bubble size with IPFs. However, the presence of IPFs reinforced the emulsion phase and prevented it from disintegrating. In other words, the fluidity of particles decreased with IPFs and, hence, prevented the stalactites of particles from easily forming on the bubble's roof. The formation of stalactites of particles from the bubble's roof is responsible for bubble splitting according to the bubble break-up theory (Clift and Grace 1972). Since the stalactites of particles could shape less frequently in the bed when IPFs were enhanced, bubbles grew faster with U_g. This eventually resulted in larger bubbles with otherwise less frequency for the bed with more profound IPFs.

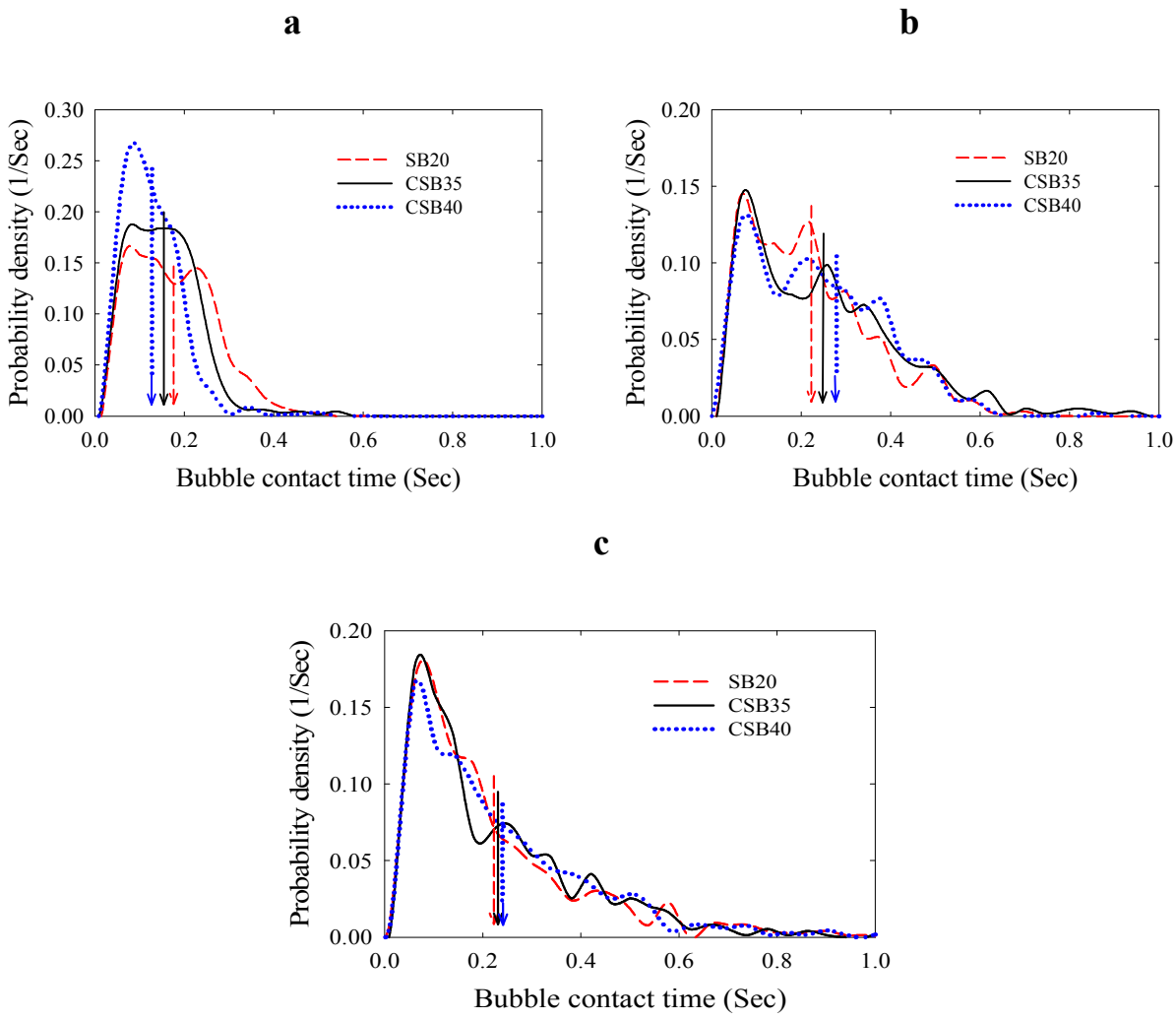

Figure 5.13: Effect of IPFs on the probability density distribution of bubble contact times: a) U_g=0.40 m/s, b) U_g=0.80 m/s, c) U_g=1.20 m/s.

At gas velocities higher than U_c, since the breakage of the emulsion phase was approximately completed, it could be further diluted with the fluidizing gas and disintegrated into clusters. This helped to hinder the successive increase in the bubble size. In addition, since the degree of impact of IPFs on the flow structure of the bed greatly decreased at high gas velocities because of an appreciable decrease in the ratio of the magnitude of IPFs/HDFs, systems with different levels of IPFs were almost exhibiting similar hydrodynamic behavior, including the bubble size.

5.6 Conclusion

The polymer coating approach was applied in this work to investigate the effect of IPFs on the local flow structure of a gas-solid fluidized bed. Experimental results showed that the dynamic

two-phase flow structure of the bed was greatly influenced by IPFs in both bubbling and turbulent fluidization regimes. This was more pronounced for the bubbling regime due to the higher ratio of the magnitude of IPFs/HDFs. It was observed that increasing the level of IPFs in the bed resulted in an increase in the tendency of the fluidizing gas passing through the bed in the emulsion phase in the bubbling regime. This is a promising finding, which indicates that by a slight increase in the level of IPFs while it is far from the defluidization condition the gas distribution balance between phases is more prone toward the emulsion phase, where a better gas-solid contact can be achieved. It was also found that increasing the level of IPFs with the purpose of enhancing the gas-solid contact should be cautiously applied since it could have a negative impact on the quality of solid mixing in the bed. It was further noted that U_c, on the meso-scale, increased with IPFs. Different from the bubbling regime, the amount of gas flowing in the emulsion phase was higher for a bed without IPFs in the turbulent fluidization regime. It suggests that an improved overall performance of the fluidized bed reactor under such operating conditions can be achieved with beds with the minimum amount of IPFs.

These findings corroborate that the design and operation of gas-solid fluidized beds under extreme conditions or in the presence of any impurities by which IPFs are inevitably present in the system cannot be only based on the variation of HDFs. The variations of IPFs must be considered, as well. As shown in the present study, the presence of IPFs affects some critical characteristics of the local flow structure in the bed. Accordingly, understanding such effects is essential for the successful design and operation of gas-solid fluidized beds.

5.7 Nomenclature

5.7.1 Acronyms

CSB30	coated sugar beads at 30^{o}C
CSB35	coated sugar beads at 35^{o}C
CSB40	coated sugar beads at 40^{o}C
HDFs	hydrodynamic Forces
IPFs	interparticle Forces

PEA	poly Ethyl Acrylate
PMMA	poly Methyl MethAcrylate
SB20	fresh sugar beads at 20°C

5.7.2 Symbols

A_c	cross-sectional area of the column (m^2)
d_p	mean particle diameter (μm)
D_b	bubble size (m)
D_{bm}	maximum bubble size due to total bubble coalescence (m)
D_{b0}	initial bubble size (m)
D_c	column diameter (m)
f_e	emulsion phase fraction (-)
g	gravity acceleration (m/s^2)
h	height above the distributor plate (m)
N_{or}	number of orifices on the perforated distributor plate (m)
u^*	parameter in Eq. 5.1 (-)
U_B	bubble rise velocity (m/s)
U_c	transition velocity from bubbling to turbulent regime (m/s)
U_{c1}	velocity of the incipient turbulent fluidization regime on a meso-scale (m/s)
U_{c2}	velocity of the complete entry into the turbulent fluidization regime on a meso-scale (m/s)
U_e	superficial gas velocity of emulsion phase (m/s), ($U_e = U_i$)
U_g	superficial gas velocity (m/s)

U_{mf}	minimum fluidization velocity (m/s)
V	acquired voltage under operating condition (v)
V_{mf}	acquired voltage at minimum fluidization state (v)
V_0	acquired voltage at empty column (v)

5.7.3 Greek letter

ε	local bed voidage (-)
ε_b	time-averaged bubble phase voidage (-)
ε_{div}	division voidage between the emulsion and bubble phases (-)
ε_e	time-averaged emulsion phase voidage (-)
ε_m	time-averaged local bed voidage (-)
ε_{mf}	minimum fluidization voidage (-)
ε_0	fixed bed voidage (-)
ρ_p	particle density (kg/m^3)

5.8 Acknowledgement

The authors wish to acknowledge the financial support provided for this work by the Total American Services, Inc. and the National Sciences and Engineering Research Council of Canada (NSERC). We would like to thank Amin Esmaeili and Mikaeil Leduc for their help with the fabrication of the optical fiber probe. We are also grateful to Michael Butler for activation of the radioactive tracer at the Nuclear Reactor section of McMaster University.

5.9 References

Bi, H.T., Grace, J.R., 1995. Effect of measurement method on the velocities used to demarcate the onset of turbulent fluidization. The Chemical Engineering Journal and the Biochemical Engineering Journal 57, 261-271.

Bouffard, J., Bertrand, F., Chaouki, J., Giasson, S., 2012. Control of particle cohesion with a polymer coating and temperature adjustment. AIChE Journal 57, 3685-3696.

Clift, R., Grace, J.R., 1972. The mechanism of bubble break-up in fluidised beds. Chemical Engineering Science 27, 2309-2310.

Cui, H., Chaouki, J., 2004. Effects of temperature on local two-phase flow structure in bubbling and turbulent fluidized beds of FCC particles. Chemical Engineering Science 59, 3413-3422.

Cui, H., Mostoufi, N., Chaouki, J., 2000. Characterization of dynamic gas-solid distribution in fluidized beds. Chemical Engineering Journal 79, 133-143.

Cui, H., Mostoufi, N., Chaouki, J., 2001a. Comparison of measurement technique of local particle concentration for gas–solid fluidization, in: Kwauk, M., Li, J., Yang, W.C., (Eds.) Fluidization X, United Engineering Foundation, New York, pp. 779-786.

Cui, H., Mostoufi, N., Chaouki, J., 2001b. Gas and solids between dynamic bubble and emulsion in gas-fluidized beds. Powder Technology 120, 12-20.

Davidson, J.F., Clift, R., Harrison, D., 1985. Fluidization (2nd ed.). Academic Press, NewYork.

Davidson, J.F., Harrison, D., 1963. Fluidised Particles. Cambridge University Press, Cambridge.

Ellis, N., Bi, H.T., Lim, C.J., Grace, J.R., 2004. Hydrodynamics of turbulent fluidized beds of different diameters. Powder Technology 141, 124-136.

Formisani, B., Girimonte, R., Mancuso, L., 1998. Analysis of the fluidization process of particle beds at high temperature. Chemical Engineering Science 53, 951-961.

Formisani, B., Girimonte, R., Pataro, G., 2002. The influence of operating temperature on the dense phase properties of bubbling fluidized beds of solids. Powder Technology 125, 28-38.

Fotovat, F., Chaouki, J., Bergthorson, J., 2013. The effect of biomass particles on the gas distribution and dilute phase characteristics of sand–biomass mixtures fluidized in the bubbling regime. Chemical Engineering Science 102, 129-138.

Geldart, D., 1973. Types of gas fluidization. Powder Technology 7, 285-292.

Horio, M., Nonaka, A., 1987. A generalized bubble diameter correlation for gas-solid fluidized beds. AIChE Journal 33, 1865-1872.

Karimipour, S., Pugsley, T., 2011. A critical evaluation of literature correlations for predicting bubble size and velocity in gas-solid fluidized beds. Powder Technology 205, 1-14.

Larachi, F., Chaouki, J., Kennedy, G., 1995. 3-D mapping of solids flow fields in multiphase reactors with RPT. AIChE Journal 41, 439-443.

Lettieri, P., Yates, J.G., Newton, D., 2000. The influence of interparticle forces on the fluidization behaviour of some industrial materials at high temperature. Powder Technology 110, 117-127.

Li, J., 2000. Compromise and resolution—Exploring the multi-scale nature of gas–solid fluidization. Powder Technology 111, 50-59.

Li, J., Kuipers, J.A.M., 2002. Effect of pressure on gas–solid flow behavior in dense gas-fluidized beds: a discrete particle simulation study. Powder Technology 127, 173-184.

Li, J., Wen, L., Wei, G., Cui, H., Jingqiang, R., 1998. Dissipative structure in concurrent-up gas–solid flow. Chemical Engineering Science 53, 3367-3379.

Lin, C.-L., Wey, M.-Y., You, S.-D., 2002. The effect of particle size distribution on minimum fluidization velocity at high temperature. Powder Technology 126, 297-301.

Lin, Q., Wei, F., Jin, Y., 2001. Transient density signal analysis and two-phase micro-structure flow in gas–solids fluidization. Chemical Engineering Science 56, 2179-2189.

Liu, J., Grace, J.R., Bi, X., 2003. Novel multifunctional optical-fiber probe: I. Development and validation. AIChE Journal 49, 1405-1420.

Liu, M., Zhang, Y., Bi, H., Grace, J.R., Zhu, Y., 2010. Non-intrusive determination of bubble size in a gas–solid fluidized bed: An evaluation. Chemical Engineering Science 65, 3485-3493.

Mori, S., Wen, C.Y., 1975. Estimation of bubble diameter in gaseous fluidized beds. AIChE Journal 21, 109-115.

Mostoufi, N., Chaouki, J., 2001. Local solid mixing in gas-solid fluidized beds. Powder Technology 114, 23-31.

Mostoufi, N., Chaouki, J., 2004. Flow structure of the solids in gas-solid fluidized beds. Chemical Engineering Science 59, 4217-4227.

Poletto, M., Salatino, P., Massimilla, L., 1993. Fluidization of solids with CO2 at pressures and temperatures ranging from ambient to nearly critical conditions. Chemical Engineering Science 48, 617-621.

Punčochář, M., Drahoš, J., 2005. Origin of pressure fluctuations in fluidized beds. Chemical Engineering Science 60, 1193-1197.

Rapagna, S., Foscolo, P.U., Gibilaro, L.G., 1994. The influence of temperature on the quality of gas fluidization. International Journal of Multiphase Flow 20, 305-313.

Rietema, K., 1991. The dynamics of fine powders. Elsevier Science Publishers LTD, New York.

Rietema, K., Piepers, H.W., 1990. The effect of interparticle forces on the stability of gas-fluidized beds--I. Experimental evidence. Chemical Engineering Science 45, 1627-1639.

Rowe, P.N., Santoro, L., Yates, J.G., 1978. The division of gas between bubble and interstitial phases in fluidised beds of fine powders. Chemical Engineering Science 33, 133-140.

Rüdisüli, M., Schildhauer, T. J., Biollaz, S.M.A., Wokaun, A., van Ommen, J.R., 2012. Comparison of bubble growth obtained from pressure fluctuation measurements to optical probing and literature correlations. Chemical Engineering Science 74, 266-275.

Seville, J.P.K., Willett, C.D., Knight, P.C., 2000. Interparticle forces in fluidization: a review. Powder Technology 133, 261-268.

Shabanian, J., Chaouki, J., 2013. Pressure signals in a gas-solid fluidized bed with thermally induced inter-particle forces, in: Kuipers, J.A.M., Mudde, R.F., van Ommen, J.R., Deen, N.G., (Eds.), The 14th International Conference on Fluidization–From Fundamentals to Products, , ECI Symposium Series.

Shabanian, J., Chaouki, J., 2014. Hydrodynamics of a gas-solid fluidized bed with thermally induced interparticle forces. Chemical Engineering Journal, submitted for publication.

Shabanian, J., Fotovat, F., Bouffard, J., Chaouki, J., 2011. Fluidization behavior in a gas-solid fluidized bed with thermally induced inter-particle forces, in: Knowlton, T.M., (Ed.), Proceedings of the 10th International Conference On Circulating Fluidized Beds And Fluidization Technology (CFB-10), Engineering Conferences International, New York, pp. 738.

Shabanian, J., Jafari, R., Chaouki, J., 2012. Fluidization of ultrafine powders-Review. International Review of Chemical Engineering (IRECHE) 4, 16-50.

Si, C.D., Guo, Q.J., 2008. Wavelet analysis of particle concentration signals in an acoustic bubbling fluidized bed. Chemical Engineering & Technology 31, 1597-1604.

Stein, M., Ding, Y.L., Seville, J.P.K., Parker, D.J., 2000. Solids motion in bubbling gas fluidised beds. Chemical Engineering Science 55, 5291-5300.

Tardos, G., Pfeffer, R., 1995. Chemical reaction induced agglomeration and defluidization of fluidized beds. Powder Technology 85, 29-35.

van der Schaaf, J., Schouten, J.C., Johnsson, F., van den Bleek, C.M., 2002. Non-intrusive determination of bubble and slug length scales in fluidized beds by decomposition of the power spectral density of pressure time series. International Journal of Multiphase Flow 28, 865-880.

van Ommen, J.R., Mudde, R.F., 2012. Measuring the gas-solids distribution in fluidized beds: A Review. International Journal of Chemical Reactor Engineering 6, 1-29.

Vazquez, C., Nombela, J.L., Sobrino, C., de Vega, M., Zubia, J., Montero, D.S., 2007. Plastic fiber-optic probes for characterizing fluidized beds in bubbling regime. 16th International Conference on Plastic Optical Fiber (POF), Turin, Italy.

Willett, C.D., 1999. The micromechanics of wet particulate materials. Ph.D. Thesis, University of Birmangham.

Xie, H.Y., Geldart, D., 1995. Fluidization of FCC powders in the bubble-free regime: effect of types of gases and temperature. Powder Technology 82, 269-277.

Xu, C., Zhu, J.X., 2006. Effects of gas type and temperature on fine particle fluidization. China Particuology 4, 114-121.

Yerushalmi, J., Cankurt, N.T., 1979. Further studies of the regimes of fluidization. Powder Technology 24, 187-205.

Yates, J.G., Newton, D., 1986. Fine particle effects in a fluidized-bed reactor. Chemical Engineering Science 41, 801-806.

Zhang, Y., Bi, H. T., Grace, J.R., Lu, C., 2010. Comparison of decoupling methods for analyzing pressure fluctuations in gas-fluidized beds. AIChE Journal 56, 869-877.

Zhong, Y., Wang, Z., Guo, Z., Tang, Q., 2012. Defluidization behavior of iron powders at elevated temperature: Influence of fluidizing gas and particle adhesion. Powder Technology 230, 225-231.

Zhu, H., Zhu, J., 2008. New investigation in regime transition from bubbling to turbulent fluidization. The Canadian Journal of Chemical Engineering 86, 553-562.

Zhu, H., Zhu, J., Guozheng, L., Fengyun, L., 2008. Detailed measurements of flow structure inside a dense gas-solids fluidized bed. Powder Technology 180, 339-349.

CHAPTER 6 ARTICLE 4: PERFORMANCE OF A CATALYTIC GAS-SOLID FLUIDIZED BED REACTOR IN THE PRESENCE OF INTERPARTICLE FORCES

Jaber Shabanian, Jamal Chaouki*

Department of Chemical Engineering, Ecole Polytechnique de Montreal, Montreal, Quebec, Canada

* Corresponding author: Tel.: +1-514-340-4711 X 4034; fax: +1-514-340-4159.

E-mail address: jamal.chaouki@polymtl.ca

(Published in International Journal of Chemical Reactor Engineering (2015), doi: 10.1515/ijcre-2014-0106)

6.1 Abstract

The influence of interparticle forces (IPFs) on the hydrodynamics of a gas-solid fluidized bed was experimentally investigated with the help of a polymer coating approach. The results showed that the presence of IPFs in the bed can considerably change the hydrodynamic parameters. The tendency of the fluidizing gas passing through the bed in the emulsion phase increased with IPFs in the bubbling regime. The performance of a fluidized bed reactor was then studied through simulation of a reactive catalytic system using three different hydrodynamic models: (a) a simple two-phase flow model, (b) a dynamic two-phase flow model, and (c) a dynamic two-phase flow model, integrating the effects of superficial gas velocity and IPFs. The simple two-phase flow model was found to underestimate the reactor performance for catalytic reaction most likely due to the oversimplified assumptions involved in this model. Also, the simulation results showed that modification of the bed hydrodynamics due to IPFs resulted in a better performance for a bubbling fluidized bed reactor. This suggests that the hydrodynamic models should take into account the effects of superficial gas velocity and variation in the ratio of the magnitude of IPFs/hydrodynamic forces, due to any operational reason, to yield a more reliable evaluation of the performance of the fluidized bed reactor.

Keywords: Gas-solid fluidized bed reactor, Interparticle forces, Reactor simulation, Two-phase flow model.

6.2 Introduction

Gas-solid fluidized bed reactors are widely used in the chemical process industry, where they are usually operated at high temperatures and/or high pressures. Heat and mass transfer properties of gas-solid fluidized beds are greatly influenced by hydrodynamic properties [1]. This, in turn, can have a large impact on the reaction performance of the fluidized bed reactor. Therefore, the hydrodynamics of gas-solid fluidized bed reactors under extreme conditions are one of the most important factors for their design and performance evaluation [2].

Prior experimental studies demonstrated that the sole consideration of the variations of gas properties, namely its density and viscosity, due to the variation in operating conditions cannot adequately predict the bed hydrodynamics at extreme conditions [3-14]. Researchers thus suggested that to achieve a satisfactory understanding of the bed hydrodynamics at extreme conditions, modifications in the solid phase, i.e., interparticle forces (IPFs), must be taken into account, as well. The variation of the Hamaker constant with the operating temperature [15], the increase in the tendency of gas adsorption on the surface of fluidized particles at high pressures [4, 16], the formation of eutectics and the tendency of bed particles to sinter together at high temperatures [6, 17, 18] are clear examples of the importance of this obligation. Therefore, it is highly necessary to clearly understand the influence of IPFs on the fluidization behavior of the bed.

Earlier studies of the group [19, 20] demonstrated that the polymer coating approach [19, 21] is a superior method to investigate the effect of IPFs on the behavior of a gas-solid fluidized bed. It offers promising advantages, including the simple and accurate control of the level of IPFs in the bed by only adjusting the inlet gas temperature, the uniform distribution of IPFs throughout the whole bed as a result of the uniform thermal property of the gas-solid fluidized bed, and the capability to apply the method at both low and high gas velocities. It was thus used in this study to achieve different levels of IPFs in the bed.

Predicting the performance and scale-up of fluidized bed reactors are essential for the appropriate development of new chemical processes [22]. The two-phase flow modeling (i.e., bubble and emulsion phases) is extensively used for modeling the hydrodynamic properties of gas-solid fluidized bed reactors. The simple two-phase flow model (STPFM) postulates the presence of two extreme phases in the bed, i.e., the solid-free bubble phase and the emulsion phase at minimum fluidization state [23, 24]. However, the presence of solid particles in bubbles and the interstitial

gas flow rate in excess of the minimum fluidization condition has been shown by researchers [1, 25-31]. Hence, a dynamic two-phase flow model (DTPFM) representing a dynamic gas-solid distribution between the two phases was proposed by Cui et al. [30]. It is well known that the assumptions of the STPFM are principally valid for superficial gas velocities close to the minimum fluidization [32] whereas the DTPFM can be used over a wide range of superficial gas velocities, covering both bubbling and turbulent fluidization regimes.

In order to investigate the effect of modification of the bed hydrodynamics due to IPFs on the overall reaction performance of a gas-solid fluidized bed reactor, a catalytic example reaction was simulated under different operating conditions in the present study. An industrial-scale fluidized bed reactor for production of maleic anhydride (MAN) by the catalytic oxidation of n-butane (n-C4) over the fluidized vanadium phosphorus oxide (VPO) catalyst was selected for this purpose. The hydrodynamic parameters measured for fluidized beds with different levels of IPFs were employed for the simulation study.

6.3 Experimental

The first step in the experimental campaign was to prepare base particles uniformly coated with a thin PMMA/PEA (poly methyl methacrylate/poly ethyl acrylate) coating film. Spherical sugar beads that are 450–700 μm (d_p=580 μm, ρ_p=1556 kg/m^3), Geldart group B particles, which accept the PMMA/PEA coating, were selected as the inert base particles in this work (d_p is the mean particle size and ρ_p is the particle density). The coated particles were produced through an atomization process in a spheronizer machine. The particles were simultaneously dried with the heated air introduced into the processing chamber. The thickness of the coating film was approximately 5 μm at the end of the coating process. With such a thin coating layer there was only about a 1% difference in the particle density and size for sugar beads after the coating process. This implies that the fresh and coated sugar beads held similar hydrodynamic characteristics according to the Geldart's [33] classification. More detailed information about the coating procedure and its operating conditions can be found elsewhere [19, 20].

The fresh sugar beads and the coated particles were separately used in a cold gas-solid fluidized bed for hydrodynamic study. The bed was made of a Plexiglas tube with a 15.2 cm ID and 3.0 m in height. It was working under atmospheric pressure. Dried and filtered air was employed as the

fluidizing gas and introduced into the bed through a perforated distributor plate (consisting of 157 holes 1 mm in diameter). In order to investigate the influence of IPFs on the fluidization characteristics of the bed, experiments with the fresh sugar beds as the base system without IPFs were carried out at 20ºC whereas experiments with the coated sugar beads were conducted at 40ºC. From this point onwards, we call these systems with their corresponding operating temperatures as SB20 and CSB40, which stand for fresh sugar beads at 20ºC and coated sugar beads at 40ºC. Table 6.1 reports the minimum fluidization velocity, U_{mf}, the minimum fluidization voidage, ε_{mf}, and the transition superficial gas velocity from bubbling to turbulent fluidization, U_c, for SB20 and CSB40. They obtained through bed pressure drop measurements, visual observations, and standard deviation analysis of in-bed gauge pressure signals, respectively. Different superficial gas velocities (up to 1.3 m/s, covering both bubbling and turbulent fluidization regimes) were used for each system tested.

Table 6.1: Basic hydrodynamic parameters of SB20 and CSB40

System	U_{mf} (m/s)	ε_{mf} (-)	U_c (m/s)
SB20	0.18	0.47	0.90
CSB40	0.34	0.53	1.20

A set of pressure transducers and a solids concentration optical fiber probe (parallel optical fiber bundle probe [34] with 3.0 mm diameter tip and 4.7 mm diameter body) were used for the purpose of hydrodynamic study. Gauge pressure signals were measured in the dense bed (17.5 cm above the distributor plate; OMEGA, PX309-002GI, 0–2 psig) and in the windbox (Honeywell, model SA, 0–50 psig). Measurement of the instantaneous local bed voidage was achieved with the help of the solids concentration optical fiber probe located at the center of the column and 20 cm in height above the distributor plate. Both of these measurements were simultaneously carried out for a period of four minutes with the sampling frequency of 400 Hz at each superficial gas velocity, U_g, and temperature tested. The optical fiber probe was calibrated according to the calibration curve developed by Cui et al. [34]. For the fluidization tests 4.0 kg of material were poured into the column, which resulted in a static bed height of approximately 26 cm at ambient conditions.

6.4 Experimental results and discussion

According to the concept of the two-phase flow modeling, the gas and solids in the fluidized bed are divided into two distinct phases: the bubble and emulsion phases. Therefore, the chemical conversion resulting from a gas-gas catalytic or gas-solids reaction is highly dependent on the distribution of gas and solids between these phases. Hence, the hydrodynamic study was mainly focused on the influence of IPFs on the two-phase flow structure of the bed.

The probability density distributions of the local bed voidages of SB20 and CSB40 from the corresponding εmf to 1 at different gas velocities in bubbling and turbulent regimes are presented in Figure 6.1. It shows that for both systems tested increasing Ug resulted in a decrease in the probability of the emulsion phase (first peak at low voidages) and an increase in the probability of the bubble phase (second peak at high voidages). This implies that increasing Ug altered the local flow structure of the bed toward the presence of a more bubble/dilute phase in the bed. However, increasing the level of IPFs had different effects on the probabilities of the emulsion and bubble phases, i.e., they increased and decreased with IPFs, respectively. This is more obvious at low and moderate gas velocities while the probability density distributions of SB20 and CSB40 became almost identical at higher gas velocities, where the level of hydrodynamic forces (HDFs) tended to dominate the magnitude of IPFs. It can be inferred from these observations that enhancing IPFs promoted the local bed hydrodynamics toward the formation of more emulsion phase in the bed, notably in the bubbling regime. Accordingly, it indicates that at a given fluidizing gas throughput, the dominant mechanism for the gas-solid interactions modified in the bed by increasing the level of IPFs as the fluidizing gas was more prone to pass through the bed in the emulsion phase rather than the bubble phase.

The method of minimum probability [30] was used to distinguish each phase from the instantaneous local bed voidage data. The time-averaged voidages of bubble and emulsion phases, ε_b and ε_e, respectively, and the emulsion phase fraction, f_e, were subsequently calculated. Figure 6.2 exhibits the variations of ε_b and ε_e with U_g for the systems tested. It shows that for both SB20 and CSB40, the emulsion phase held voidages higher than the local bed voidage at the corresponding minimum fluidization condition. Also, ε_b for both systems was lower than the voidage (ε) of the solid-free bubble (ε=1). These observations reveal that the oversimplified assumptions of the STPFM do not apply to SB20 and CSB40. In other words, the emulsion phases of these systems

could support the passage of a higher volumetric flow rate of gas compared to the corresponding minimum fluidization condition and the quantity of gas flowing in the form of bubbles was smaller than could be expected from the STPFM for both systems.

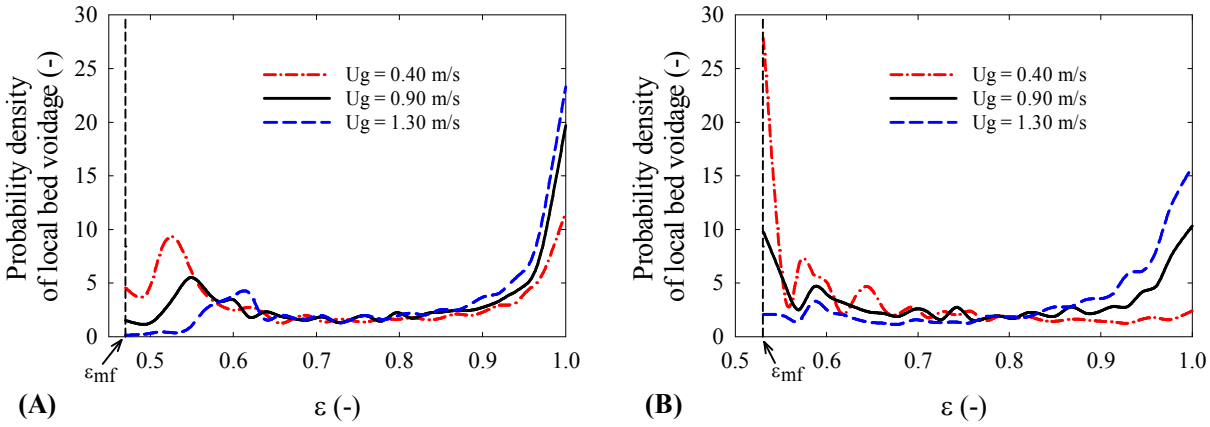

Figure 6.1: Dependence of probability density distribution of local bed voidage on IPFs

Figure 6.2 also illustrates that for each system tested both ε_b and ε_e rapidly increased with U_g to reach a relatively stable level. The ε_b then persistently increased with U_g with a very small slope. However, ε_e remained (approximately) constant for a range of gas velocities and further increased with U_g at higher gas throughput. The initial increase in ε_b with U_g could be attributed to the range of gas velocities required for the bubbles to be well developed in the bed. The further gradual increase in ε_b represents the progressive evolution of bubbles toward the solid-free bubble. The increase in ε_e at velocities before the plateau-like region could be explained by the initial increase in the permeability of the emulsion phase to reach its maximum strain while keeping its continuity. The presence of a stable level for ε_e at intermediate gas velocities represents its resistance against the complete breakdown of its continuous structure. By increasing U_g the continuous structure of the emulsion phase eventually disintegrates, the stable level vanishes, and the fluidized bed transfers into the turbulent regime with an unclear boundary between the cluster and broth. This can be found through a second increase in ε_e at higher gas velocities.

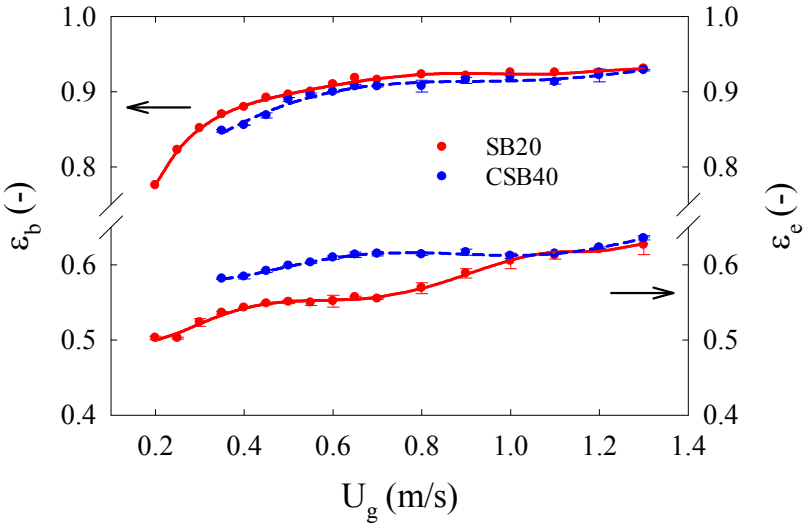

Figure 6.2: Dependence of time-averaged bubble and emulsion phase voidages on IPFs

Figure 6.2 depicts that by increasing the level of IPFs ε_b slightly decreased over the whole range of gas velocities tested. This means a bed with a higher level of IPFs can have more solid particles in its bubble phase. Hence, it can enhance the chemical reaction taking place in this phase. The figure further elucidates that the plateau-like region of ε_e shifted to a higher U_g and covered a wider range of gas velocities for CSB40. The εe considerably increased with IPFs for gas velocities lower than 0.9 m/s. It suggests that the capacity of the emulsion phase for holding gas increased with IPFs over this span of gas velocities. This can have a favorable effect on the chemical conversion in the gas-solid fluidized bed reactor since a good gas-solid contact can be achieved in the emulsion phase. This finding is in accordance with the experimental observation of Rietema [4], who found that ε_e for a bed of fresh catalytic cracking increased with the operating pressure. Since the increase in ε_e was accompanied by an increase in the elastic modulus of the particulate bed, Rietema argued this modification was due to an increase in the level of IPFs in the bed. At higher gas velocities ε_e for systems with different levels of IPFs approached each other as a result of the dominance of strong HDFs over IPFs in the bed.

The variation of f_e, which is defined as the time fraction of the emulsion phase from the local bed voidage signals [10], as a function of U_g is plotted in Figure 6.3. It can be found that, for each system tested, f_e initially decreased with U_g, reached a plateau, and further decreased at higher gas velocities. The quick decrease at low gas velocities can be related to the development of the bubbling phenomenon in the bed. The stable level principally reveals the resistance showed by the

emulsion phase to maintain its continuous structure. The further decrease of f_e at high gas velocities (particularly, in the turbulent regime) could be due to the presence of a highly diluted and a relatively homogeneous flow structure in the bed.

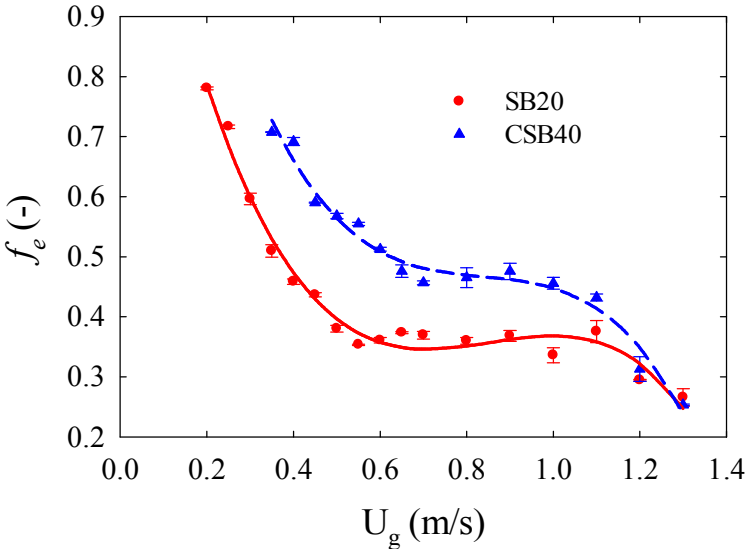

Figure 6.3: Dependence of emulsion phase fraction on IPFs

Figure 6.3 also illustrates that CSB40 was comprised of considerably more emulsion phase in comparison with SB20. This is pronounced for gas velocities smaller than 1 m/s. At gas velocities higher than 1.2 m/s, where the bed was greatly influenced by the strong action of HDFs, no difference can be seen in f_e for SB20 and CSB40. Therefore, the experimental results suggest that since an increase in the level of IPFs yields an increase in the emulsion phase fraction while it can hold more gas inside its structure, the tendency of the fluidizing gas passing through the bed in the emulsion phase can increase with IPFs.

In order to verify this argument, the distribution of the fluidizing gas between the bubble and emulsion phases was quantitatively evaluated for SB20 and CSB40 in the vicinity of the optical probe's tip. The bubble rise velocity, U_b, and the superficial gas velocity of the emulsion phase, U_e, were evaluated for each system. The U_g, f_e, U_b, and U_e are correlated as follows:

$$U_g = f_e U_e + (1 - f_e) U_b \qquad 6.1$$

By having knowledge about the variation of the bubble size in the vicinity of the probe's tip, U_b can be calculated with the commonly used equation presented by Davidson and Harrison [24] as follows:

$$U_b = 0.71\sqrt{g\,d_b} + (U_g - U_{mf}) \quad 6.2$$

where d_b is the average bubble size. Subsequently, U_e can be calculated from Eq. 6.1 at each operating condition.

The gauge pressure signals registered in the windbox and dense bed were used to estimate the bubble size in the region close to the optical fiber probe's tip. This was done with the help of the frequency-domain-based decomposition method [35]. The results are plotted in Figure 6.4. It shows that CSB40 contained slightly smaller bubbles at low gas velocities (U_g<3$U_{mf,SB20}$). This can be explained by the higher capacity of the emulsion phase in holding the fluidizing gas inside its structure; hence, a lower quantity of gas contributed to the formation of bubbles, which resulted in slightly smaller bubbles in the bed. Nevertheless, larger bubbles were noted at higher gas velocities. In other words, the growth rate of the bubble size with U_g increased with IPFs. Also, the transition velocity from bubbling to turbulent regime, where large bubbles are replaced by smaller ones [36], increased with IPFs. These behaviors could be attributed to the reduction in the rate of bubble splitting with IPFs. In fact, the emulsion phase became stabilized against any changes that could be imposed on its structure in a bed with (strong) IPFs. Thus, the stalactite of particles on the bubble's roof, which is responsible for the bubble splitting [37], formed less frequently, yielding the appearance of larger bubbles in the bed. The last observation revels that a higher amount of energy was required to be transferred to the bed with an enhanced level of IPFs by the fluidizing gas to transfer the fluidization regime from bubbling to turbulent. An increase in U_c helped to completely break down the reinforced emulsion phase and replace the large bubbles by small and transient voids.

Figure 6.4 also demonstrates that SB20 contained considerably smaller bubbles at gas velocities higher than 1.0 m/s. It reveals that over this range of gas velocities, where SB20 was operating in the turbulent regime and CSB40 was operating close to the corresponding U_c, a higher quantity of gas bypassing could happen for CSB40. This can have a negative impact on the overall reaction performance of the reactor.

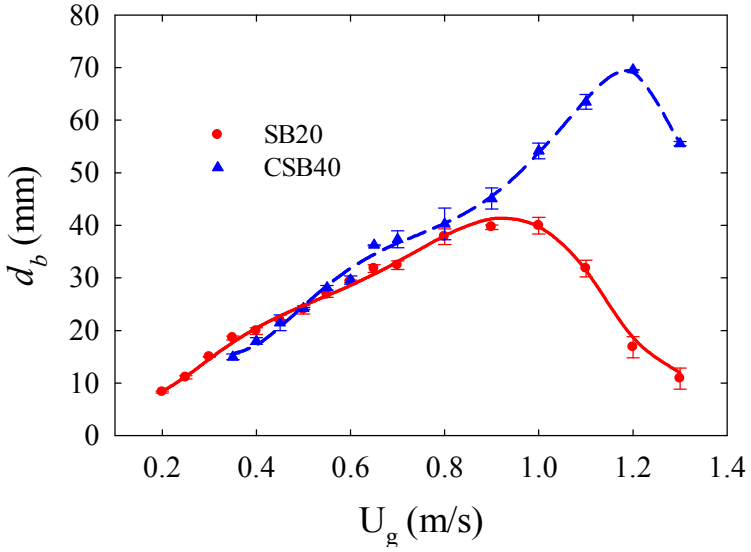

Figure 6.4: Dependence of bubble size on IPFs

Variations of U_e and U_b for SB20 and CSB40 as function of U_g are plotted in Figure 6.5. It evidently shows that, for gas velocities smaller than 1.0 m/s, the tendency of the fluidizing gas to pass through the bed in the emulsion phase was higher for CSB40. This is in good accordance with the experimental results reported by Row et al. [27] and Yates and Newman [28]. They found that increasing the fines (< 45 µm) content, which can increase the level of IPFs in the bed, resulted in an increase in the quantity of the fluidizing gas interstitially passing the bed in the bubbling regime. It can be found from Figure 6.5 that the interstitial gas flow rate was higher for SB20 at $U_g > 1.2$ m/s. These trends confirm the arguments that were advanced after scrutinizing the effect of IPFs on other hydrodynamic parameters measured in this study.

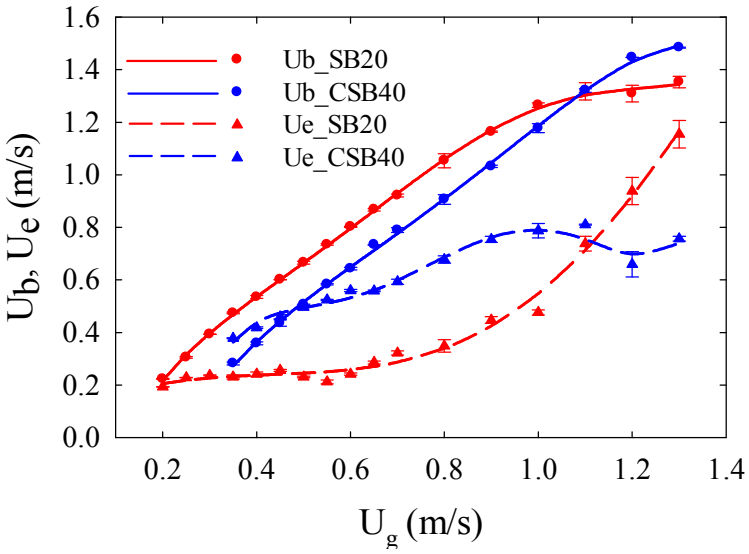

Figure 6.5: Dependence of bubble rise velocity and superficial gas velocity of the emulsion phase on IPFs

6.5 Reactor simulation

For reactive systems, the emulsion phase is more efficient in bringing about the chemical reaction between gas and solids [27]. Therefore, a slight increase in the level of IPFs in a bubbling gas-solid fluidized bed reactor, far from defluidization conditions, can be considered as an operating measure to improve the reactor performance. To verify this hypothesis, a typical industrial-scale catalytic reactor was simulated under different operating conditions. Simulations were achieved using the STPFM and DTPFM that accounted for modifications in the fluidization behavior of the bed due to both U_g and IPFs. Hydrodynamic parameters measured during the experiments were used for this purpose.

6.5.1 Hydrodynamic model

The general hypotheses associated with all the hydrodynamic models exploited in the present study are as follows:

- The reactor operates at steady-state condition.
- Due to the great radial homogeneity in large turbulent fluidized beds (I.D. > 0.5 m) [38] there is a negligible radial concentration gradient within the bed. Hence, it was neglected

in the mole balance equation. An identical condition was assumed for the large industrial-scale fluidized bed in the bubbling regime.

- The bubble diameter is considered to be constant along the bed height.
- Due to the negligible wall effects in an industrial-scale fluidized bed [39-41], it is reasonable to apply the hydrodynamic parameters measured from the center of a 15.2 cm column in the simulation study.
- There is a uniform temperature profile throughout the whole bed [42]. Therefore, the physical properties of the fluidizing gas, kinetic constants, and hydrodynamic parameters remain unchanged along the bed.

The STPFM was chosen as the base hydrodynamic model in this work. Since the bubble phase is considered to be free of solids in this model, the catalytic reaction solely occurs in the emulsion phase. For the STPFM the superficial gas velocity in the emulsion phase is considered to be equal to U_{mf} and it holds the same structure as the minimum fluidization condition ($\varepsilon_e=\varepsilon_{mf}$). However, in a real gas-solid fluidized bed, the bubble phase contains a lot of particles and the emulsion phase is more diluted than the minimum fluidization condition [30]. Also, the bubble and emulsion phases can exhibit dynamic evolution with a series of voidages between the extreme voidages ε_{mf} and 1 [43]. Thus, the progress of the chemical reaction should be taken into account in both the bubble and emulsion phases [22]. In addition, the DTPFM seems to be more representative of the actual flow structure of the fluidized bed. In this regard, the second hydrodynamic model uses the DTPFM with the hydrodynamic parameters measured for SB20 to consider the effect of U_g on the overall performance of the reactor. In order to integrate the effects of U_g and IPFs on the reactor performance, the hydrodynamic parameters measured for CSB40 were employed with the DTPFM as the third hydrodynamic model. The general mass balance and mass transfer equations used for the simulation study based on the two-phase concept of fluidization are given in Table 6.2. The required fluidization parameters for all three models are listed in Table 6.3.

Table 6.2: General mass balance and mass transfer equations

Mole balance for species i in the bubble phase	$\frac{dC_{i,b}}{dz} = \frac{R_{i,b}\,(1-\varepsilon_b)\rho_p - K_{be}\,(C_{i,b} - C_{i,e})}{U_b}$
Mole balance for species i in the emulsion phase	$\frac{dC_{i,e}}{dz} = \frac{R_{i,e}\,f_e\,(1-\varepsilon_e)\rho_p + K_{be}\,(1-f_e)\,(C_{i,b} - C_{i,e})}{U_e\,f_e}$
Mean concentration of species i	$C_i = \frac{U_b\,(1-f_e)}{U_g}\,C_{i,b} + \frac{U_e\,f_e}{U_g}\,C_{i,e}$
Bubble to emulsion gas interchange coefficient (K_{be}) [42]	$\frac{1}{K_{be}} = \frac{1}{K_{bc}} + \frac{1}{K_{ce}}$
	$K_{bc} = 4.5\left(\frac{U_e}{d_b}\right) + 5.85\left(\frac{{D_{AB}}^{0.5}\,g^{0.25}}{{d_b}^{1.25}}\right)$,
	$K_{ce} = 6.77\left(\frac{0.71\sqrt{g\,d_b}\,D_{AB}\,\varepsilon_e}{{d_b}^3}\right)^{0.5}$

Required correlations and information for calculation of D_{AB} were extracted from Treybal [44], Poling [45], and Yaws [46].

Table 6.3: Fluidization specifications of all three hydrodynamic models

Parameters	Simple two-phase flow model, SB20	Dynamic two-phase flow model, SB20	Dynamic two-phase flow model, CSB40
Average bubble phase voidage (ε_b)	$\varepsilon_b = 1$	$\varepsilon_b = f(U_g)$	$\varepsilon_b = f(U_g, IPFs)$
Average emulsion phase voidage (ε_e)	$\varepsilon_e = \varepsilon_{mf}$	$\varepsilon_e = f(U_g)$	$\varepsilon_e = f(U_g, IPFs)$
Emulsion phase fraction (f_e)	$f_e = \frac{(U_g - U_{mf})}{(U_b - U_{mf})}$	$f_e = f(U_g)$	$f_e = f(U_g, IPFs)$
Bubble rise velocity (U_b)) [24]	$U_b = 0.71\sqrt{g\,d_b} + (U_g - U_{mf})$	$U_b = 0.71\sqrt{g\,d_b} + (U_g - U_{mf})$	$U_b = 0.71\sqrt{g\,d_b} + (U_g - U_{mf})$
Superficial gas velocity of the emulsion phase (U_e))	$U_e = U_{mf}$	$U_e = \frac{U_g - U_b\,(1-f_e)}{f_e}$	$U_e = \frac{U_g - U_b\,(1-f_e)}{f_e}$

6.5.2 Kinetic model

In order to evaluate the reaction performance of a fluidized bed reactor, a reactive system for the production of maleic anhydride (C4H2O3) by the partial oxidation of n-butane over the vanadium phosphorous oxide catalyst was selected. The kinetics of this reaction has been the subject of many investigations [47-58]. A particular kinetic model for this reaction system is the widely cited work

of Centi et al. [48] in which the authors developed the model from the empirical data generated in an isothermal steady-state tubular fixed bed reactor, where the oxygen was supplied to the catalyst from the gas phase. It is worth mentioning that since gas-solid fluidized bed reactors show complex hydrodynamic behavior for deriving the kinetic information corresponding to bed materials, small fixed bed reactors for which the hydrodynamics could be confidentially described should be used to obtain the kinetic data [59]. Subsequently, the overall performance of a reactive system can be evaluated through the combination of information about the reactor's input, kinetics, and contacting pattern (hydrodynamics) [60].

According to Centi et al. [48] the reaction kinetics of n-C4 over VPO catalyst can be described by a triangular network of reactions. It can be illustrated as follows [48]:

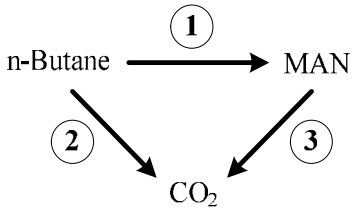

The reactions involved in this pathway with their corresponding rate equations have been proposed by Centi et al. [48] as follows:

$$nC_4H_{10} + 3.5O_2 \rightarrow MAN + 4H_2O, \qquad r_1 = \frac{k_1 K_B C_B {C_O}^{\alpha}}{1 + K_B C_B} \tag{6.3}$$

$$nC_4H_{10} + 6.5O_2 \rightarrow 4CO_2 + 5H_2O, \qquad r_2 = k_2 {C_O}^{\beta} \tag{6.4}$$

$$MAN + 4.5O_2 \rightarrow 4CO_2 + H_2O, \qquad r_3 = k_3 C_{MAN} \left(\frac{{C_O}^{\gamma}}{{C_B}^{\delta}}\right) \tag{6.5}$$

where r1 is the rate of MAN formation from n-C4, r2 is the rate of CO2 formation from n-C4, r3 is the rate of MAN decomposition to CO2, and CB, CO, and CMAN denote the concentrations of n-C4, oxygen and MAN, respectively. The kinetic parameters are presented in Table 6.4. The absence of internal diffusion effects was verified by the authors for the catalyst particles prepared in the form of cylindrical pellets (2 mm length, 4 mm OD, and 2 mm ID). Hence, the presented kinetic model can be rationally applied to a fluidized bed of (virtual) catalysts with a mean particle size about 600 μm, identical to the sugar beads used in this study.

Table 6.4: Kinetic parameters (@ 340°C)

Parameter	Value (units)
k_1	6.230×10^{-7} ($mol^{(1-\alpha)}L^{\alpha}/(gr.s)$)
k_2	9.040×10^{-7} ($mol^{(1-\beta)}L^{\beta}/(gr.s)$)
k_3	0.966×10^{-7} ($mol^{(\delta-\gamma)}L^{(1-\delta+\gamma)}/(gr.s)$)
K_B	2616 (L/mol)
α	0.2298
β	0.2298
γ	0.6345
δ	1.151

The selective partial oxidation of n-butane to maleic anhydride in a steady-state gas-solid fluidized bed reactor involves two reactions, which occur simultaneously with respect to the selective activity of the VPO catalyst. It includes selective oxidation of n-C_4 by an oxidized catalyst and reoxidation of the reduced catalyst by molecular oxygen. In order to assure that both steps keep up continuously in a fluidized bed reactor, a higher than stoichiometric amount of oxygen is required [61]. Since the oxidation and regeneration steps intricately occur under this condition, researchers generally lump these steps in an overall kinetic model, known as the redox model [49, 62, 63]. The Langmuir-Hinshelwood type rate expression developed by Centi et al. [48] for the partial oxidation of n-C_4 follows the same strategy. Hence, it satisfies the requisite and can be practically used for simulating a steady-state gas-solid fluidized bed reactor designated for the production of MAN from n-C_4.

6.5.3 Simulation results and discussion

The three hydrodynamic models were coupled with the kinetic model and solved for an industrial-scale reactor under different operating conditions (described in Table 6.5). It was postulated in the simulation that complete oxidation of n-C_4 and MAN were the only undesired reactions in the reaction network and no carbon monoxide was produced by the partial oxidation of these reactants. The overall reaction rates for all of the species involved in the kinetics are summarized in Table 6.6.

Table 6.5: Operating conditions for the simulation

Parameter	Value (unit)
D_c	2 (m)
H	6 (m)
d_p	580 (μm)
ρ_p	1556 (kg/m^3), SB20
	1540 (kg/m^3), CSB40
ε_{mf}	0.47 (-), SB20
	0.53 (-), CSB40
T	340 (^{o}C)
P	202.65 (kPa)
U_g	0.4 – 1.3 (m/s)
y_{B0}	5 (% v/v)

Table 6.6: Overall reaction rates

Species i	R_i
n-C_4H_{10}	$-r_1 - r_2$
O_2	$-3.5r_1 - 6.5r_2 - 3r_3$
MAN	$r_1 - r_3$
CO_2	$4r_2 + 4r_3$
H_2O	$4r_1 + 5r_2 + r_3$

The simulation results for the three hydrodynamic models were considered for analysis in terms of the conversion of n-C4, X = (CB0 – CB)/CB0, the selectivity of MAN, S = CMAN/(CB0 – CB), and the yield of MAN produced, Y = CMAN/CB0, where CB0 is the concentration of n-C4 fed to the reactor. Figure 6.6 illustrates the overall performance curves predicted by the three models over a wide range of superficial gas velocities, 0.4 – 1.3 m/s. It shows that the conversion decreases with U_g for all models. This could be principally due to less residence time of the reactants at higher gas velocities in the reactor. In addition, since the emulsion phase is the main constituent of the two-phase flow structure of the fluidized bed at low gas velocities and it is concentrated in solids (catalysts), a higher reaction rate and, hence, a higher conversion can be achieved. However, by increasing U_g, since the bubble phase fraction (1 - f_e) increases in the bed (e.g., see Figure 6.3)

while it is less concentrated in solids, the reactants are less converted to products when passing through the bed. This leads to a reduction in the overall conversion. An identical trend can be found for the yield of MAN produced. Nonetheless, the selectivity of MAN represents a different behavior and increases with U_g for all hydrodynamic models tested. The kinetics of oxidation of MAN can explain this different effect. It can be found from eq. 6.5 that the rate of MAN oxidation is inversely related to the concentration of the n-C4. Thus, since the conversion of n-C4 decreases with Ug, a higher concentration of n-C4 can be attained at higher gas velocities yielding a reduction in the rate of MAN oxidation. This can, consequently, increase the selectivity of the MAN at higher gas velocities.

Figure 6.6 also exhibits that the STPFM predicts lower n-C4 conversion than the DTPFMs at all gas velocities. This can be attributed to the fact that the STPFM neglects the presence of solid particles in the bubble phase. Therefore, since according to this model no catalytic reaction takes place in the bubbles, a lower conversion of n-C4 is predictable for the simulated reactor performance using this model. The same trend can be noted for the yield of MAN produced. However, the STPFM predicts higher selectivity than both DTPFMs. This can be justified noting the kinetics of MAN oxidation along with a lower n-C4 conversion achieved by the STPFM.

Comparing the reactor performance using the DTPFM for beds with and without IPFs reveals that the n-C4 conversion and the MAN yield are higher for a bed with IPFs at gas velocities below 1.1 m/s. Since both DTPFMs are coupled with the same kinetic model and the comparison is made at the same U_g, the spread in the prediction data only results from the hydrodynamic changes due to the presence of IPFs. The simulation results show that the presence of IPFs in the system leads to a typical average increase of 7% in the n-C4 conversion and the MAN yield over the range of gas velocities between 0.60 – 1.0 m/s. This difference can be mostly due to the increase in the tendency of the fluidizing gas to pass through the bed in the emulsion phase, which has already been discussed about in the previous section. Scrutinizing the trends of these parameters at $U_g > 1.2$ m/s shows an inversion trend, i.e., a bed without IPFs exhibits a better performance under this operating condition. An increase in the amount of gas bypassing a bed affected by the presence of IPFs at high gas velocities ($U_g > U_{c,No\ IPFs}$) can explain this change. Lastly, a slight decrease (< 0.5%) in the selectivity of MAN over the whole range of gas velocities can be found for a bed with IPFs from the simulation results. The kinetics of MAN oxidation and the increase in the n-C_4 conversion for a reactor with an enhanced level of IPFs can explain this reduction.

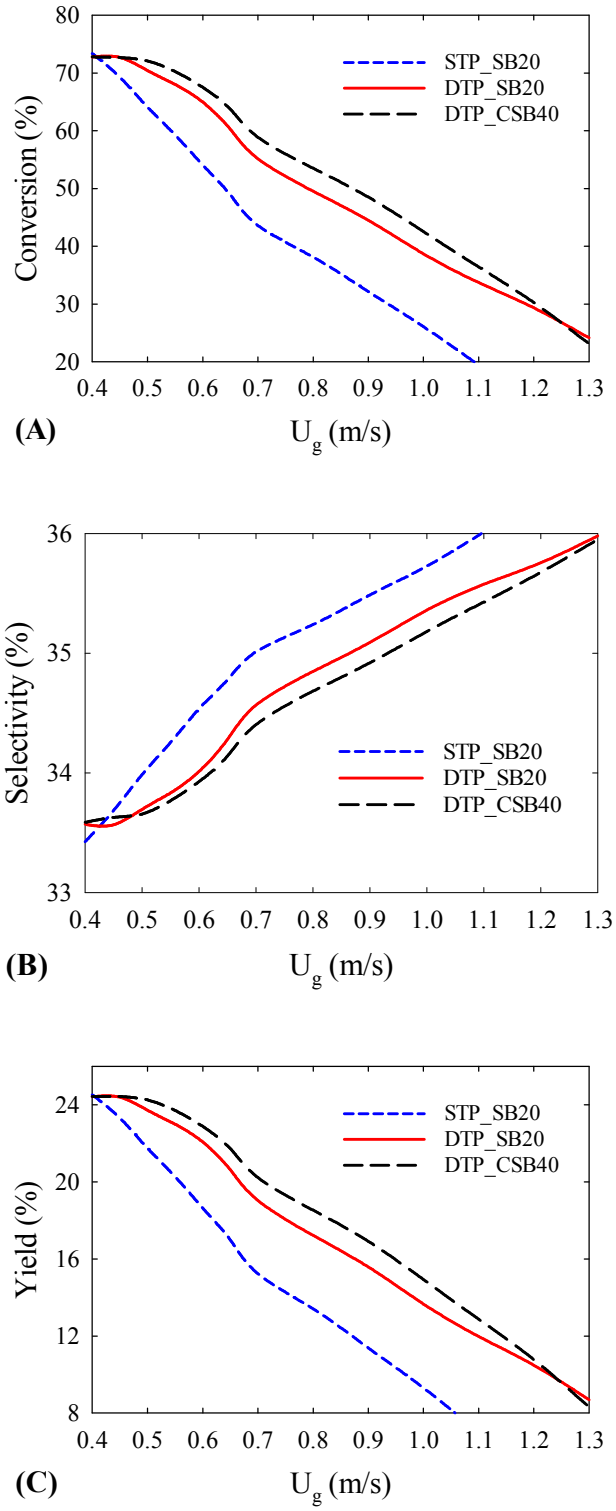

Figure 6.6: Prediction of performance of the fluidized bed reactor for all three hydrodynamic models at different superficial gas velocities: (A) n-butane conversion, (B) MAN selectivity, (C) MAN yield

These results confirm that an increase in the level of IPFs, while the bed is operating far from defluidization conditions and at gas velocities below U_c for a bed without IPFs, $U_{c,No\text{-}IPFs}$, to restrict the gas bypassing problem, can be favorably applied to enhance the reaction performance of a gas-solid fluidized bed reactor. Therefore, even though the bed hydrodynamics is principally governed by U_g, the variation of the level of IPFs due to any operational reason must be taken into account to achieve a proper prediction of the overall performance of the gas-solid fluidized bed reactor.

6.6 Conclusion

The analysis of experimental results showed that the presence of IPFs in the gas-solid fluidized bed led to a significant modification of the bed hydrodynamics. The distribution of the fluidizing gas between the bubble and emulsion phases was greatly influenced by IPFs. The fluidizing gas was more prone to pass through the bed in the emulsion phase over the range of gas velocities below $U_{c,No\text{-}IPFs}$. The predictions of an industrial-scale reactor performance clearly demonstrated that the hydrodynamic changes resulting from enhancing the role of IPFs in the bed can improve the overall performance of the reactor. It suggests that a slight increase in the level of IPFs in the bed, far from defluidization conditions, can result in an appreciable increase in the performance of bubbling fluidized bed reactors requiring good gas-solid contacting. At gas velocities higher than $U_{c,No\ IPFs}$, however, an increase in the level of IPFs can reduce the reactor performance due to the gas bypassing problem originating from the presence of much larger bubbles in the bed.

6.7 Nomenclature

6.7.1 Acronyms

CSB40	coated sugar beads at 40ºC
DTPFM	dynamic two-phase flow model
HDFs	hydrodynamic forces
IPFs	interparticle forces
MAN	maleic anhydride
PEA	poly ethyl acrylate

PMMA	poly methyl methacrylate
STPFM	simple two-phase flow model
SB20	fresh sugar beads at 20°C
VPO	vanadium phosphorus oxide

6.7.2 Symbols

C_B	concentration of n-butane (mol/L)
C_{B0}	concentration of n-butane fed (mol/L)
C_i	mean concentration of species i (mol/L)
$C_{i,b}$	concentration of species i in the bubble phase (mol/L)
$C_{i,e}$	concentration of species i in the emulsion phase (mol/L)
C_{MAN}	concentration of MAN (mol/L)
C_O	concentration of oxygen (mol/L)
d_b	average bubble size (m)
d_p	mean particle size (μm)
D_{AB}	gas diffusion coefficient (m^2/s)
D_c	reactor diameter (m)
f_e	emulsion phase fraction (-)
g	gravity acceleration (m/s^2)
H	height of reactor (m)
k_1	rate constant for MAN formation ($mol^{(1-\alpha)}\ L^{\alpha}/(g.s)$)
k_2	rate constant for CO_2 formation ($mol^{(1-\beta)}\ L^{\beta}/(g.s)$)
k_3	rate constant for MAN decomposition ($mol^{(\delta-\gamma)}\ L^{(1-\delta+\gamma)}/(g.s)$)
K_{bc}	bubble to cloud gas interchange coefficient (1/s)
K_{be}	bubble to emulsion gas interchange coefficient (1/s)

K_B adsorption equilibrium constant for n-C_4 in Centi et al. [48] kinetics (L/mol)

K_{ce} cloud to emulsion gas interchange coefficient (1/s)

P pressure (kPa)

r_1 rate of MAN formation (mol/(g.s))

r_2 rate of CO_2 formation (mol/(g.s))

r_3 rate of MAN decomposition (mol/(g.s))

$R_{i,b}$ overall reaction rate of species i in the bubble phase (mol/(g.s))

$R_{i,e}$ overall reaction rate of species i in the emulsion phase (mol/(g.s))

S selectivity of MAN, number of moles of MAN produced per moles of n-C_4 converted (-)

T temperature (^oC)

U_b bubble rise velocity (m/s)

U_c transition velocity from bubbling to turbulent regime (m/s)

$U_{c,No-IPFs}$ transition velocity from bubbling to turbulent regime for a bed without IPFs (m/s)

U_g superficial gas velocity (m/s)

U_{mf} minimum fluidization velocity (m/s)

$U_{mf,SB20}$ minimum fluidization velocity for SB20 (m/s)

U_e superficial gas velocity of emulsion phase (m/s)

X conversion of n-C_4, number of moles of n-C_4 converted per moles of n-C_4 fed (-)

y_{B0} feed n-C_4 concentration (% v/v)

Y yield of MAN, number of moles of MAN produced per moles of n-C_4 fed (-)

z distance above the distributor plate (m)

6.7.3 Greek letters

$\alpha, \beta, \gamma, \delta$ exponents in Centi et al. [48] rate expressions (-)

ε local bed voidage (-)

ε_b time-averaged bubble phase voidage (-)

ε_e time-averaged emulsion phase voidage (-)

ε_{mf} minimum fluidization voidage (-)

ρ_p particle density (kg/m^3)

6.8 Acknowledgements

The authors greatly appreciate the financial support of the Total American Services, Inc. and the National Sciences and Engineering Research Council of Canada (NSERC).

6.9 References

1) Werther, J., 1978. Effect of gas distributor on the hydrodynamics of gas fluidized beds. German Chemical Engineering 1, 166-174.
2) Cui, H., Sauriol, P., Chaouki, J., 2003. High temperature fluidized bed reactor: measurements, hydrodynamics and simulation. Chemical Engineering Science 58, 1071-1077.
3) Rietema, K., Piepers, H.W., 1990. The effect of interparticle forces on the stability of gas-fluidized beds--I. Experimental evidence. Chemical Engineering Science 45, 1627-1639.
4) Rietema, K., 1991. The Dynamics of Fine Powders, Elsevier Science Publishers LTD, New York.
5) Poletto, M., Salatino, P., Massimilla, L., 1993. Fluidization of solids with CO_2 at pressures and temperatures ranging from ambient to nearly critical conditions. Chemical Engineering Science 48, 617-621.
6) Tardos, G., Pfeffer, R., 1995. Chemical reaction induced agglomeration and defluidization of fluidized beds. Powder Technology 85, 29-35.
7) Xie, H.Y., Geldart, D., 1995. Fluidization of FCC powders in the bubble-free regime: effect of types of gases and temperature. Powder Technology 82, 269-277.
8) Formisani, B., Girimonte, R., Mancuso, L., 1998. Analysis of the fluidization process of particle beds at high temperature. Chemical Engineering Science 53, 951-961.

9) Lettieri, P., Yates, J.G., Newton, D., 2000. The influence of interparticle forces on the fluidization behaviour of some industrial materials at high temperature. Powder Technology 110, 117-127.

10) Cui, H., Chaouki, J., 2004. Effects of temperature on local two-phase flow structure in bubbling and turbulent fluidized beds of FCC particles. Chemical Engineering Science 59, 3413-3422.

11) Cui, H., Chaouki, J., 2004. Interparticle forces in high temperature fluidization of geldart a particles. China Particuology 2, 113-118.

12) Xu, C., Zhu, J.X., 2006. Effects of gas type and temperature on fine particle fluidization. China Particuology 4, 114-121.

13) Zhong, Y., Wang, Z., Guo, Z., Tang, Q., 2012. Defluidization behavior of iron powders at elevated temperature: Influence of fluidizing gas and particle adhesion. Powder Technology 230, 225-231.

14) Shabanian, J., Sauriol, P., Rakib, A., Chaouki, J., 2014. Characterization of gas-solid fluidization at high temperature by analysis of pressure signals. in Proceedings of the 11th International Conference on Fluidized Bed Technology (CFB-11), Beijing, China.

15) Krupp, H., 1967. Particle adhesion: theory and experiment. Advances in Colloid and Interface Science 1**,** 111-239.

16) Xie, H.Y., 1997. The role of interparticle forces in the fluidization of fine particles. Powder Technology 94, 99-108.

17) Bartels, M., Lin, W., Nijenhuis, J., Kapteijn, F., van Ommen, J.R., 2008. Agglomeration in fluidized beds at high temperatures: Mechanisms, detection and prevention. Progress in Energy and Combustion Science 34, 633-666.

18) Siegell, J.H., 1984. High-temperature de fluidization. Powder Technology 38, 13-22.

19) Shabanian, J., Fotovat, F., Bouffard, J., Chaouki, J., 2011. Fluidization behavior in a gas-solid fluidized bed with thermally induced inter-particle forces. in Proceedings of the 10th International Conference on Circulating Fluidized Beds and Fluidization Technology (CFB-10), Knowlton, T.M. (Editor), Sunriver Resort, Oregon, US.

20) Shabanian, J., Chaouki, J., 2013. Pressure signals in a gas-solid fluidized bed with thermally induced inter-particle forces. in Proceedings of the 14th International Conference on

Fluidization – From Fundamentals to Products, Kuipers, J.A.M., Mudde, R.F., van Ommen, J.R., Deen N.G. (Editors), Noordwijkerhout, the Netherlands.

21) Bouffard, J., Bertrand, F., Chaouki, J., Giasson, S., 2012. Control of particle cohesion with a polymer coating and temperature adjustment. AIChE Journal 57, 3685-3696.
22) Mostoufi, N., Cui, H., Chaouki, J., 2001. A comparison of two- and single-phase models for fluidized-bed reactors. Industrial & Engineering Chemistry Research 40, 5526-5532.
23) Toomey, R.D., Johnstone, H.F., 1952. Gaseous fluidization of solid particles. Chemical Engineering Progress 48, 220–225.
24) Davidson, J.F., Harrison, D., 1963. Fluidised particles, Cambridge University Press, Cambridge.
25) De Vries, R.J., van Swaaij, W.P.M., Mantovani, C., Heijkoop, A., 1972. Design criteria and performance of the commercial reactor for the Shell Chlorine Process. in Proceedings of the Second International Symposium on Chemicla Reaction Engineering, Amesterdam, B9 (59 - 69).
26) Aoyagi, M., Kunii, D., 1974. Importance of dispersed solids in bubbles for exothermic reactions in fluidized beds. Chemical Engineering Communications 1, 191-197.
27) Rowe, P.N., Santoro, L., Yates, J.G., 1978. The division of gas between bubble and interstitial phases in fluidised beds of fine powders. Chemical Engineering Science 33, 133-140.
28) Yates, J.G., Newton, D., 1986. Fine particle effects in a fluidized-bed reactor. Chemical Engineering Science 41, 801-806.
29) Chaouki, J., Gonzales, A., Guy, C., Klvana, D., 1999. Two-phase model for a catalytic turbulent fluidized-bed reactor: Application to ethylene synthesis. Chemical Engineering Science 54, 2039-2045.
30) Cui, H., Mostoufi, N., Chaouki, J., 2000. Characterization of dynamic gas-solid distribution in fluidized beds. Chemical Engineering Journal 79, 133-143.
31) Cui, H., Mostoufi, N., Chaouki, J., 2001. Gas and solids between dynamic bubble and emulsion in gas-fluidized beds. Powder Technology 120, 12-20.
32) Jafari, R., Sotudeh-Gharebagh, R., Mostoufi, N., 2004. Performance of the wide-ranging models for fluidized bed reactors. Advanced Powder Technology 15, 533-548.
33) Geldart, D., 1973. Types of gas fluidization. Powder Technology 7, 285-292.

34) Cui, H., Mostoufi, N., Chaouki, J., 2001. Comparison of measurement technique of local particle concentration for gas–solid fluidization. in Proceedings of Fluidization X, Kwauk, M., Li, J., Yang, W.C. (Editors), Beijing, China, pp. 779-786.

35) van der Schaaf, J., Schouten, J.C., Johnsson, F., van den Bleek, C.M., 2002. Non-intrusive determination of bubble and slug length scales in fluidized beds by decomposition of the power spectral density of pressure time series. International Journal of Multiphase Flow 28, 865-880.

36) Bi, H.T., Grace, J.R., 1995. Effect of measurement method on the velocities used to demarcate the onset of turbulent fluidization. The Chemical Engineering Journal and the Biochemical Engineering Journal 57, 261-271.

37) Clift, R., Grace, J.R., 1972. The mechanism of bubble break-up in fluidised beds. Chemical Engineering Science 27, 2309-2310.

38) Ege, P.E., 1995. Investigation of the flow structure of turbulent fluidized beds. Ph.D. dissertation, University of Trondheim, Norway.

39) Glicksman, L.R., McAndrews, G., 1985. The effect of bed width on the hydrodynamics of large particle fluidized beds. Powder Technology 42, 159-167.

40) Krishna, R., van Baten, J.M., Ellenberger, J., 1998. Scale effects in fluidized multiphase reactors. Powder Technology 100, 137-146.

41) Rüdisüli, M., Schildhauer, T.J., Biollaz, S.M.A., van Ommen, J.R., 2012. Scale-up of bubbling fluidized bed reactors - A review. Powder Technology 217, 21-38.

42) Kunii, D., Levenspiel, O., 1991. Fluidization Engineering. Butterworth-Heinemann, Boston.

43) Li, J., Wen, L., Qian, G., Cui, H., Kwauk, M., Schouten, J.C., van den Bleek, C.M., 1996. Structure heterogeneity, regime multiplicity and nonlinear behavior in particle-fluid systems. Chemical Engineering Science 51, 2693-2698.

44) Treybal, R.E., 1981. Mass-Transfer Operations. McGraw-Hill, London.

45) Poling, B.E., Prausnitz, J.M., O'Connell, J.P., 2001. The Properties of Gases and Liquids. McGraw-Hill, New York.

46) Yaws, C.L., 1999. Chemical Properties Handbook. McGraw-Hill, New York.

47) Varma, R.L., Saraf, D.N., 1979. Selective Oxidation of C4 hydrocarbons to maleic anhydride. Industrial & Engineering Chemistry Product Research and Development 18, 7-13.

48) Centi, G., Fornasari, G., Trifiro, F., 1985. n-Butane oxidation to maleic anhydride on vanadium-phosphorus oxides: kinetic analysis with a tubular flow stacked-pellet reactor. Industrial & Engineering Chemistry Product Research and Development 24, 32-37.

49) Schneider, P., Emig, G., Hofmann, H., 1987. Kinetic investigation and reactor simulation for the catalytic gas-phase oxidation of n-butane to maleic anhydride. Industrial & Engineering Chemistry Research 26, 2236-2241.

50) Bej, S.K., Rao, M.S., 1991. Selective oxidation of n-butane to maleic anhydride. 1. Optimization studies. Industrial & Engineering Chemistry Research 30, 1819-1824.

51) Sharma, R.K., Cresswell, D.L., Newson, E.J., 1991. Kinetics and fixed-bed reactor modeling of butane oxidation to maleic anhydride. AIChE Journal 37, 39-47.

52) Mills, P.L., Randall, H.T., McCracken, J.S., 1999. Redox kinetics of VOPO4 with butane and oxygen using the TAP reactor system. Chemical Engineering Science 54, 3709-3722.

53) Huang, X.-F., Li, C.-Y., Chen, B.-H., Silveston, P.L., 2002. Transient kinetics of n-Butane oxidation to maleic anhydride over a VPO catalyst. AIChE Journal 48, 846-855.

54) Dente, M., Pierucci, S., Tronconi, E., Cecchini, M., Ghelfi, F., 2003. Selective oxidation of n-butane to maleic anhydride in fluid bed reactors: detailed kinetic investigation and reactor modelling. Chemical Engineering Science 58, 643-648.

55) Lorences, M.J., Patience, G.S., Díez, F.V., Coca, J., 2003. Butane oxidation to maleic anhydride: kinetic modeling and byproducts. Industrial & Engineering Chemistry Research 42, 6730-6742.

56) Lorences, M.J., Patience, G.S., Díez, F.V., Coca, J., 2004. Transient n-butane partial oxidation kinetics over VPO. Applied Catalysis A: General 263, 193-202.

57) Gascón, J., Valenciano, R., Téllez, C., Herguido, J., Menéndez, M., 2006. A generalized kinetic model for the partial oxidation of n-butane to maleic anhydride under aerobic and anaerobic conditions. Chemical Engineering Science 61, 6385-6394.

58) Shekari, A., Patience, G.S., 2013. Transient kinetics of n-butane partial oxidation at elevated pressure. The Canadian Journal of Chemical Engineering 91, 291-301.

59) Grace, J.R., 1986. Fluidized beds as chemical reactors. in Gas fluidization technology, Geldart, D., (Editor), John Wiley & Sons, Chichester.

60) Levenspiel, O., 1999. Chemical Reaction Engineering. 3rd ed., John Wiley & Sons, New York.

61) Contractor, R.M., 1999. Dupont's CFB technology for maleic anhydride. Chemical Engineering Science 54, 5627-5632.

62) Mars, P., van Krevelen, D.W., 1954. Oxidations carried out by means of vanadium oxide catalysts. Chemical Engineering Science 3, 41-59.

63) Buchanan, J.S., Sundaresan, S., 1986. Kinetics and redox properties of vanadium phosphate catalysts for butane oxidation. Applied Catalysis 26, 211-226.

CHAPTER 7 ARTICLE 5: INFLUENCE OF INTERPARTICLE FORCES ON SOLIDS MOTION IN A BUBBLING GAS-SOLID FLUIDIZED BED

Jaber Shabanian, Jamal Chaouki*

Department of Chemical Engineering, Ecole Polytechnique de Montreal, Montreal, Quebec, Canada

* Corresponding author: Tel.: +1-514-340-4711 X 4034; fax: +1-514-340-4159.

E-mail address: jamal.chaouki@polymtl.ca

(Submitted to Powder Technology)

7.1 Highlights:

- The effect of interparticle forces on solids motion in a bubbling gas-solid fluidized bed is studied.
- Increasing the level of interparticle forces increases the tendency of gas passing through the bed in the emulsion phase.
- The quality of solids mixing can be greatly influenced by interparticle forces.
- The presence of interparticle forces in a bubbling gas-solid fluidized bed decreases the quality of global and local solids mixings.

7.2 Abstract

This article presents some observations of the effect of interparticle forces (IPFs) on solids motion in a gas-solid fluidized bed operated in the bubbling fluidization regime and at atmospheric pressure. The radioactive particle tracking (RPT) technique was adopted to observe the solids flow pattern and quantify spherical equivalent bubble size, distributions of upward and downward-moving clusters and idle and bubble-induced times, cycle frequency, and axial/radial solids diffusivities. The level of cohesive IPFs was increased and controlled in the fluidized bed with a polymer coating approach. Experimental results showed that the presence of IPFs could effectively modify the solids flow pattern in a bubbling gas-solid fluidized bed. The influence was more pronounced at low gas velocity, where the ratio of the magnitude of IPFs to hydrodynamic forces

was high. At constant superficial gas velocity, beds with IPFs contained smaller bubbles indicating a higher tendency of gas entering the emulsion phase compared to the bubble. The evaluation of different solids mixing characteristic parameters showed that the favorable effect of IPFs on the division of the fluidizing gas between the bubble and emulsion phases was accompanied by reductions in the quality of global and local solids mixing.

Keywords: Gas-solid fluidized bed, Bubbling regime, Interparticle forces, Solids motion, Particle tracking.

7.3 Introduction

Bubbling gas-solid fluidized beds are extensively employed for several chemical processes due to their unique operational advantages, such as intense solids mixing, good gas-solids contact, fuel flexibility, as well as efficient heat transfer [1, 2]. These attractive features are driven by the bubble-induced solids circulation within the bed [2, 3]. Solids are carried up to the bed surface in the wake of bubbles, or gas voids, and in the drifts formed behind the bubbles [4]. A down flow of solids through the emulsion phase is present to keep the bed continuity. These sequences yield an axial circulation of solids in the bed, called gross circulation of solids. Simultaneously, a lateral mixing of solids occurs either in the bed, i.e., within the bubble wake and between the wake and the emulsion, or at the bed surface. The former is caused by the lateral movement of bubbles due to interaction and coalescence with neighboring bubbles while the latter is the result of the eruption of bubbles [5-7].

Solids motion directly affects heat and mass transfer rates and, in turn, the overall reaction rate in fluidized bed reactors [5]. Thus, it plays a crucial role in controlling product quality and productivity in such devices [3]. Solids mixing can be influenced by numerous parameters, such as bubble size and rise velocity, particle size and density, interaction between gas and solids and between gas/suspended solids and the column wall, bed geometry, and the ratio of bed height to column diameter [1, 7-9]. In addition, interparticle forces (IPFs) can alter the bed hydrodynamics [10-12]. Changes in the cohesive flow behavior of powders that are observed at high temperatures in many industrial processes, such as drying pharmaceutical granules, curing ceramics, and the combustion of solid fuels [13, 14] confirm the importance of this factor. Also, hydrodynamic observations at high pressures and/or temperatures demonstrated that the sole consideration of a

modification in gas properties resulting from a variation in operating conditions cannot adequately predict fluidization behavior under extreme conditions [12, 15-21]. Accordingly, any attempt to better understand the fluidization characteristics, in particular solids motion, in the presence of IPFs, which would yield a more precise design of fluidized beds, is of great interest.

It has been demonstrated in earlier studies of the group [10, 11, 22, 23] that the polymer coating approach [22] is a superior technique to introduce and control the level of IPFs in a gas-solid fluidized bed. Spherical inert powders are primarily coated with a polymer material having a low glass transition temperature (9^{o}C) and subsequently adopted in a fluidized bed for hydrodynamic study at different levels of cohesive IPFs in this methodology. The degree of IPFs is controlled by the thickness of the coating and system temperature.

The complex solids motion in bubbling fluidized beds poses a significant challenge and a technological risk to plant designers and investors. Despite the fact that many industrial bubbling fluidized bed reactors are operating under conditions where a discernible magnitude of IPFs is present, surprisingly little has been reported in the literature on the detailed influence of IPFs on the solids motion in these beds. Accordingly, this study is aimed at deploying the time-position data obtained by the nonintrusive radioactive particle tracking (RPT) technique to explore the movement of solids in bubbling gas-solid fluidized beds with different levels of IPFs. The polymer coating approach was exploited in this work to increase the level of cohesive IPFs in the bed.

7.4 Experimental

The experimental campaign was divided into two parts. The first part was aimed at the preparation of base particles uniformly coated with a thin layer of PMMA/PEA (poly methyl methacrylate/poly ethyl acrylate). The second part focused on the application of powders with different cohesive properties in a gas-solid fluidized bed for hydrodynamic study.

Spherical sugar beads, which accept the PMMA/PEA coating, were selected as the inert base powders. The mean particle size d_p and the particle density ρ_p were 580 μm and 1556 kg/m^3, respectively. These particles belong to group B powders of the Geldart classification [24] at ambient conditions. The coated sugar beads were produced through an atomization process in a spheronizer machine. The thickness of the uniform coating layer was approximately 5 μm at the end of the coating process. Differences in the particle size and density of the fresh and coated sugar

beads were only about 1% for both parameters. This means that both powders held similar fluidization characteristics from Geldart classification's point of view. Details of the coating process and its operating conditions are described elsewhere [11, 22, 23].

The experimental set-up utilized for the fluidization study consisted of a RPT system and an atmospheric pressure gas-solid fluidized bed, built as a Plexiglas cylindrical column with an inner diameter equal to 15.2 cm and 3.0 m in height. Air, adopted as the fluidizing gas, entered the bed through a perforated distributor plate made from aluminum with 157 holes 1 mm in diameter arranged in a 1 cm triangular pitch. Upon demand, air was heated to the desired temperature with the help of an electrical heater located before the windbox. The RPT system included 12 NaI scintillation detectors, which were distributed on three principle planes having four detectors with a 90^o spatial angle between two neighboring detectors in each plane. The planes were configured approximately 10 cm apart to entirely cover an axial position of 0-35 cm in height from the distributor plate. The adjacent planes were staggered 45^o to keep the farthest distance between detectors on alternate planes [25].

According to earlier studies of the group [10, 11, 22, 23] the highest level of IPFs was observed for the coated sugar beads at 40^{o}C. Therefore, in order to investigate the influence of IPFs on solids motion in a bubbling gas-solid fluidized bed, fresh sugar beads at 20^{o}C (SB20), a system without IPFs, and coated sugar beads at 40^{o}C (CSB40) were selected. The RPT experiments were carried out at low and moderate superficial gas velocities, U_g=0.30, 0.50 m/s, in the bubbling regime for each system. For all experiments the same amount of particulate material, 3.0 kg, was introduced into the column. It yielded an initial bed height of approximately 20.5 cm ($h/D_c \approx 1.35$) at ambient conditions (h is the bed height and D_c is the column diameter). The minimum fluidization velocity U_{mf} was experimentally determined by the measurement of bed pressure drop profile. It was 0.16 m/s and 0.25 m/s for SB20 and CSB40, respectively.

To reflect the dynamic fluidization behavior, a radioactive particle tracer was fabricated from a mixture of scandium oxide and epoxy glue mimicking the size and density of the bed material. The radioactive tracer was subsequently activated to 60 μCi. The long half-life of the produced isotope ^{46}Sc allowed the experiment to be run for a long period. The gamma-rays emitted by the tracer were counted by detectors and recorded by a high speed data acquisition system. These counts were analyzed later to calculate the coordinates of the tracer. Details of the RPT experiments and inverse

reconstruction strategy for determining the tracer position are described elsewhere [26-28]. In each experiment, the position of the tracer was monitored every 10 ms for 4 hrs.

7.5 Results and discussion

7.5.1 Solids flow pattern

Figure 7.1 presents solids flow patterns for SB20 and CSB40 at the tested superficial gas velocities. The mean particle flow was predominantly upward at the center of the bed followed by a continuous down flow of solids near the wall for SB20 at U_g=0.30, 0.50 m/s and CSB40 at U_g=0.50 m/s. It reveals that solids, in these cases, smoothly ascended with the rising bubbles in the bed center from the bottom layer to the splash zone, where they exhibited a fast horizontal displacement from the center to the wall. They subsequently moved downward along the annulus to keep the bed continuity. However, CSB40 represented a complex solids flow pattern with four active circulation cells within the whole bed at U_g=0.30 m/s. Under this condition, the dominant pattern was a down flow of solids at the bed center, which deflected the upward solids movement/bubbles toward the wall at regions close to the air distributor. At an intermediate height of the bed, the upward travelling particles encountered the solids flow returning from the top section of the bed at the annulus. The two solids flows then merged and were directed toward the vessel center-line, where the particles redistributed between the bottom and top circulation cells. This behavior can be attributed to the great influence of IPFs on the bed behavior for CSB40 at U_g=0.30 m/s. It led air bubbles close to the distributor level to preferentially break the particle-wall contacts rather than the solid-solid contacts in the bulk of solids. Therefore, the particles started their upward movements along the wall at the bottom section of the bed. Nonetheless, due to a stronger action of the fluidizing gas on the particles at U_g=0.50 m/s, air bubbles were able to break the interparticle contacts in the bulk of solids and the upward movement of solids and bubbles commenced from the central region of the bed.

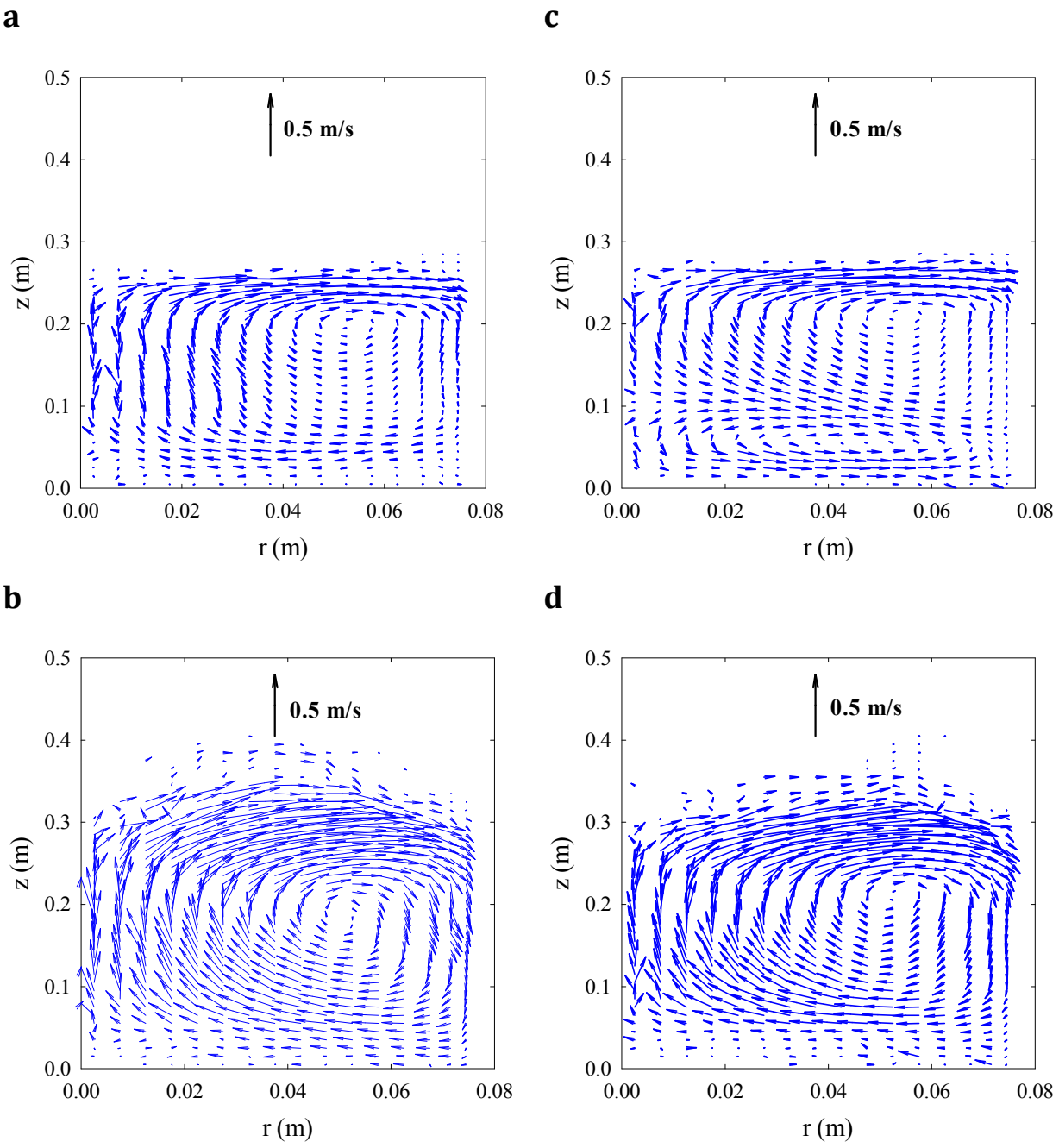

Figure 7.1 : Influence of IPFs on flow pattern of solids. a) SB20, U_g= 0.30 m/s; b) SB20, U_g= 0.50 m/s; c) CSB40, U_g= 0.30 m/s; d) CSB40, U_g= 0.50 m/s.

Figure 7.1 also illustrates that a well-developed flow pattern started at higher levels when IPFs were present. It infers that the lowermost section of the bed is less involved in the global solids recirculation when the level of IPFs increases. This observation suggests that the presence of IPFs

in a bubbling gas-solid fluidized bed can introduce a temperature gradient between the lowermost section of the bed and the higher levels of the bed.

It is evident in Figure 7.1 that the magnitude of upward arrows, representing the upward particle velocity, decreased with IPFs. A similar observation, i.e., a decrease in particle mobility in beds of spherical lead-glass ballotini after the addition of a very small amount of involatile oil was also reported by Willett [29]. The upward velocity of solids is in close relation with the bubble rise velocity since bubbles typically pass upward through the bed carrying particles in their wake. Accordingly, the peak upward particle velocities at each level of the bed are associated with the bubble velocity [3]. Following Fan et al. [2, 8, 30] the average upward velocity of solids within the top 10% of the vertical particle velocity U_z map was calculated from the RPT data to represent the bubble rise velocity in each layer. The experimental data acquired in this study indicated (not shown here) that the selection of the top 10% of the upward particle velocity was an appropriate choice to be significantly higher than velocities of particles outside the bubble stream. For this evaluation, the bed was divided into a number of layers, each 1 cm in height, and the calculation was conducted in each layer. Following the estimation of the bubble rise velocity under different operating conditions, the corresponding bubble size at each level of the bed was calculated from the correlation presented by Fan et al. [30] as follows:

$$d_B = \left(\frac{U_w - 1.6\, {D_c}^{1.35}\, (U_g - U_{mf})}{1.81\, {D_c}^{1.35} + 0.711\, g^{0.5}} \right) \tag{7.1}$$

where d_B is the spherical equivalent diameter of the bubble, U_w is the solids velocity in the bubble wake, which is comparatively equal to the bubble rise velocity, and g is the gravitational acceleration. Fan et al. [30] validated this correlation with the most frequently used literature correlations for particles with Archimedes Ar numbers in the range of 4,260-10,175. Since the Archimedes numbers of SB20 and CSB40 were respectively 10,650 and 8,905, it was assumed that the equivalent bubble size estimated by this approach closely represented the average bubble size in the systems tested in this study.

Variations of d_B with the bed height under different operating conditions are plotted in Figure 7.2. The values reported in this figure are in good agreement with the visual observations and those calculated by the spectral decomposition method [31], which employs pressure signals registered

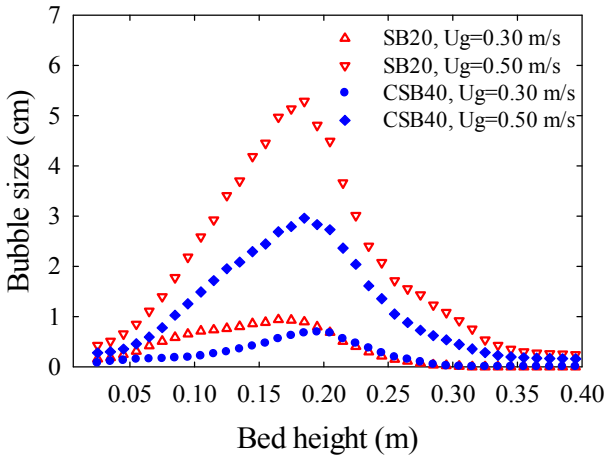

Figure 7.2: Influence of IPFs on bubble size.

in the windbox and dense bed. It shows that for systems representing typical bed behavior by a straight upward movement of bubbles from the distributor level to the splash zone, d_B constantly increased when the bubble was rising within the fluidized bed. The CSB40 at U_g=0.30 m/s, however, exhibited a complex behavior while the constant increase in d_B launched at levels higher than 10 cm in height above the distributor plate. The presence of two sets of circulation cells in this system can explain this different behavior. A sharp decrease in d_B at the top section of the bed, i.e., h>20 cm, obviously corresponds to the splash zone, where bubbles broke and experienced a complete decay. A more gradual decrease in d_B at the splash zone for CSB40 suggests that a milder ejection of particles into the freeboard existed when the level of IPFs was increased in the bed. This observation demonstrates that the presence of IPFs in the dense bed prevented particles from being easily transferred to the freeboard. It can subsequently delay the transition velocity from bubbling to turbulent regime and reduce the elutriation rate. This argument is consistent with the experimental findings employing global hydrodynamic measurements about the influence of IPFs on fluidization behavior reported by the present authors [10, 11], Smolders et al. [32], and Geldart and Wong [33].

Figure 7.2 further elucidates that beds with IPFs contained smaller bubbles in the bubbling regime. This implies that at an identical throughput of the fluidizing gas, the tendency of gas to pass through the bed in the emulsion phase increases by enhancing IPFs. This is a promising finding since this type of modification in the distribution of gas between the bubble and emulsion phases can improve the overall performance of a catalytic bubbling gas-solid fluidized bed reactor due to a better gas-

solid contact that can be achieved in the emulsion phase. It was validated in a separate work by the group [34]. The presence of gas bubbles in bubbling fluidized beds has a dual impact on the bed behavior. On the one hand, it provides particle mixing. On the other hand, it decreases the reactor performance because there is an inadequate gas-solid contact between the catalyst particles and the gaseous reactants in the bubble phase [31]. Accordingly, the favorable effect of IPFs on the division of the fluidizing gas between two phases should be coupled with their impact on the quality of solids mixing to clearly delineate the influence of IPFs on the hydrodynamics of a bubbling gas-solid fluidized bed.

7.5.2 Clusters and characteristic times

Solids in a dense gas-solid fluidized bed do not move independently but rather as clusters [35]. They spend time in the bubble wake, drift, and emulsion phase [3]. Particles/clusters in the wake and drift experience an upward movement while those in the emulsion phase exhibit a Brownian-like motion, moving randomly in different directions [36, 37]. Since the drift is the result of the wake shedding into the emulsion phase, it has less velocity than the wake yet considerably higher than the emulsion phase [3, 37]. In light of the gulf streaming that is present in a bubbling fluidized bed, the annulus region is normally devoid of bubbles. Thus, the tracer particle during its downward movement in this region can survive a certain distance without being disrupted by the bubbles [36]. If solids random walking movements during which particles are wandering in the emulsion phase are filtered from the tracer trajectory, the clusters in the bed can be classified into two principal types, ascending clusters (in the wake, drift, and emulsion) and descending clusters (in the emulsion). Mostoufi and Chaouki [36] developed an algorithm to distinguish ascending and descending clusters based on the trajectory of the tracer moving inside the bed. The algorithm is established on the fact that if the tracer is attached to an ascending or descending cluster, the axial coordinates of the tracer trajectory would be a straight line with a positive or negative slope, respectively. The straight line portions in the trajectory associate with the constant velocity of clusters. It, consequently, means that stable ascending/descending clusters are only detected by this algorithm. Detailed description of the algorithm can be found elsewhere [36].

An in-house computer program was developed following the algorithm introduced by Mostoufi and Chaouki [36] and searched for the linear segments of the trajectory for a set of at least 40 consecutive points with a correlation coefficient higher than 0.98. Figure 7.3. illustrates the velocity

distributions of ascending and descending clusters for SB20 and CSB40 at gas velocities tested in this study. The evolution of the velocity distributions of upward moving clusters in these systems was similar to that observed by Mostoufi and Chaouki [36] for sand particles (d_p=385 μm) at moderate gas velocities of the bubbling regime ($U_g \approx 2U_{mf}$) with relatively no sharp peak corresponding to bubbles and a wide peak corresponding to ascending clusters. This evolution reveals that at low and moderate superficial gas velocities, particles tended to spend most of their time in the emulsion phase rather than associating themselves with the bubbles. By increasing the gas velocity the velocity span of both types of clusters became wider and shifted toward higher velocities. It indicates that by increasing the fluidizing gas velocity, the degree of heterogeneity of the bubbling bed increased while more particles were being picked up by faster bubbles and descending clusters were heading downward at a higher velocity to compensate for the upward movement of ascending clusters.

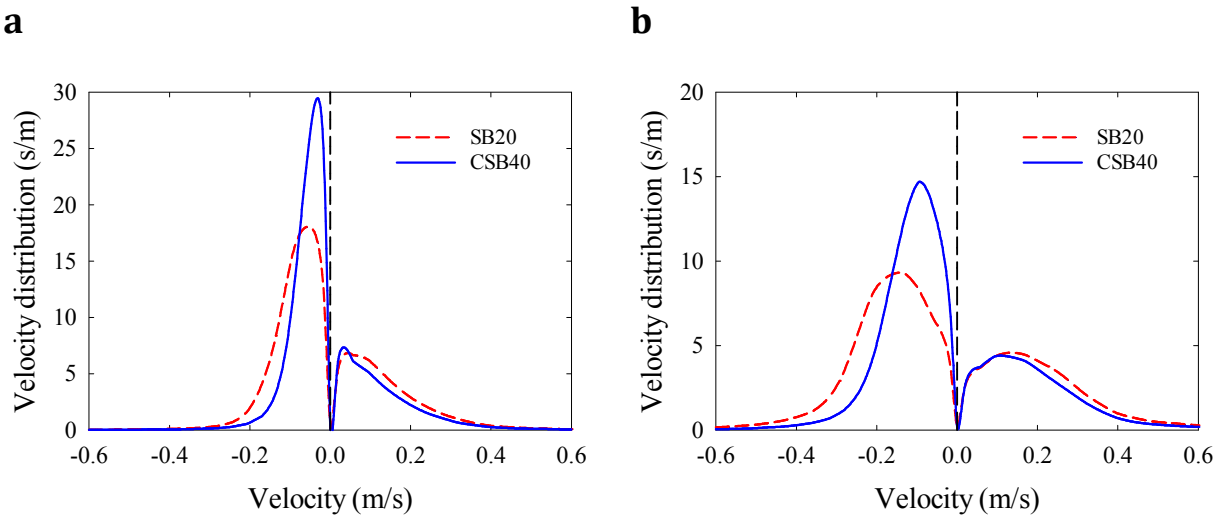

Figure 7.3: Influence of IPFs on the velocity distributions of ascending and descending clusters. a) U_g=0.30 m/s, b) U_g=0.50 m/s.

Figure 7.3 also demonstrates that the presence of IPFs resulted in a narrower velocity distribution toward lower velocities for both upward and downward moving clusters. It infers that clusters experienced a higher level of difficulty to move freely in beds with IPFs. This effect is well pronounced for descending clusters. It can be ascribed to the stronger action of HDFs on ascending clusters in the wake/drift, which can diminish the influence of IPFs on these clusters. However, for

descending clusters, which are present in the emulsion phase, the resistance caused by IPFs in the bulk of solids can effectively reduce their downward speed. Approaching the peaks of ascending and descending clusters in the velocity distribution plot by enhancing IPFs suggests that the bubbling bed would exhibit more homogeneous/less chaotic behavior. In other words, the presence of IPFs in a bubbling gas-solid fluidized bed can lower the quality of solids mixing.

Idle time as proposed by Stein et al. [3] is the time that particles spend in the emulsion phase. The residence times of particles in the wake and drift, corresponding to the upward movement, were respectively named as jump time and relaxation time [3]. According to Stein et al. [3], when solids velocity is higher than the gas velocity at minimum fluidization they are no longer part of the emulsion phase. They are otherwise considered to be part of a drift/wake. The jump and relaxation times are lumped together as bubble-induced time in this study.

Distributions of the idle and bubble-induced times were calculated from the analysis of RPT data and are shown in Figure 7.4. Figure 7.4a exhibits that an increase in the superficial gas velocity resulted in a shorter residence of particles in the emulsion phase that was repeated at a higher frequency. An increase in the level of IPFs inversely influenced the distribution of the idle time, i.e., a longer idle time with a less frequent displacement of particles between phases. Figure 7.4b illustrates that an increase in the superficial gas velocity slightly broadened the distribution of the bubble-induced time and increased the particles' lift frequency by the moving bubbles. In contrast, the presence of IPFs in the bed appreciably decreased the frequency of the tracer lift in the bubble-induced phase (wake and drift) while the peak bubble-induced duration times were approximately identical. The observed variations in characteristic times can greatly influence the hydrodynamic behavior of a fluidized bed. For instance, long idle time promotes agglomeration by sintering and, hence, defluidization in the case of gas-solid fluidized beds operated at temperatures above the sintering temperature of the bed materials [38]. Also, by considering the bubble phase as a kinetic energy source and the emulsion phase as a kinetic energy sink [3], long idle time coupled with the less frequent bubble-emulsion phase exchange means that particles spent less time in an energetic state and, hence, less kinetic energy transferred between wake and emulsion occurred. Accordingly, the presence of IPFs in a bubbling gas-solid fluidized bed can decrease the wake-emulsion solids exchange and, in turn, can decrease the quality of local solids mixing. In addition, the experimental results illustrated in Figure 7.4 demonstrate that the presence of IPFs had more evident impact on descending clusters, corresponding to the emulsion phase.

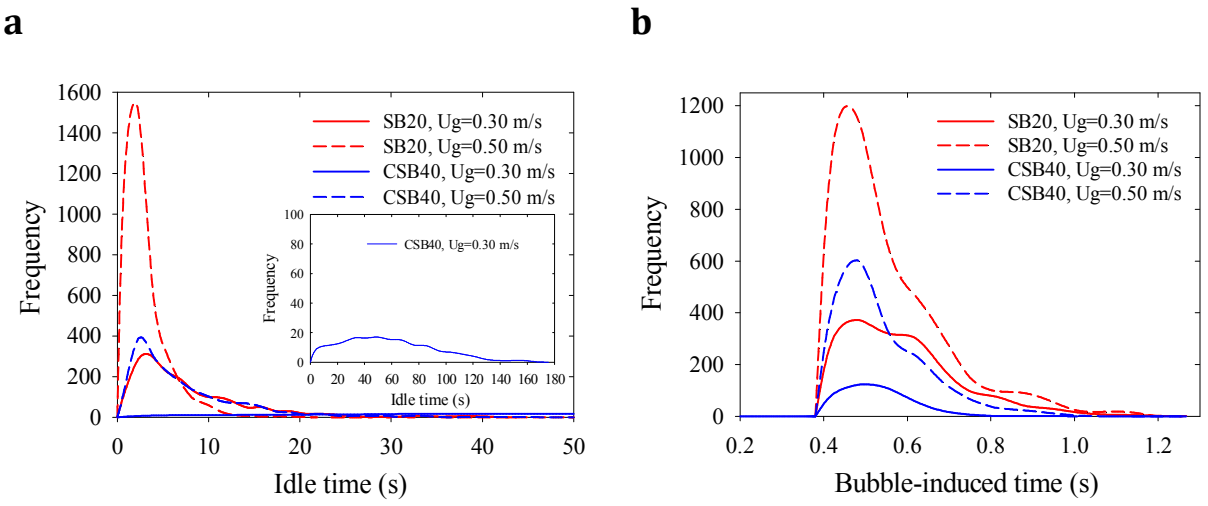

Figure 7.4: Influence of IPFs on characteristic times. a) idle time, b) bubble-induced time.

The idle time serves as the effective contact period for the agglomeration process to advance in a bubbling fluidized bed. If the agglomeration phenomenon is simply approached by a reaction network, as presented below, while the idle time represents the effective reaction time and all reactions follow the elementary rate law [39], the concentration of large agglomerates in the bed can be calculated as follows:

$$A + A \xrightarrow{r_1} (2A) \qquad r_1 = K_1 {C_A}^2, \qquad C_{2A} = K_1 {C_A}^2 t \tag{7.2}$$

$$A + (2A) \xrightarrow{r_2} (3A) \qquad r_2 = K_2 C_A C_{2A}, \qquad C_{3A} = K_1 K_2 {C_A}^3 \frac{t^2}{2} \tag{7.3}$$

$$A + (3A) \xrightarrow{r_3} (4A) \qquad r_3 = K_3 C_A C_{3A}, \qquad C_{3A} = K_1 K_2 K_3 {C_A}^4 \frac{t^3}{6} \tag{7.4}$$

...

$$A + ((i-1)A) \xrightarrow{r_{(i-1)}} (iA) \qquad r_{(i-1)} = K_{(i-1)} C_A C_{(i-1)A}, \qquad C_{iA} = (K_{(i-1)}!) {C_A}^i \frac{t^{(i-1)}}{(i-1)!}, \quad i = 2, 3, \dots, n \tag{7.5}$$

where A represents a single particle, r_i is the rate of formation of an agglomerate consisting of i single particles, K_i is the agglomeration rate constant corresponding to r_i, C_{iA} is the concentration of an agglomerate consisting of i single particles in the bed, and t is the reaction time, which is

equal to the corresponding idle time. It was assumed in the above simplified network that an intermediate agglomerate formed temporarily in the bed to exclusively participate in the formation of a larger agglomerate with one more unit particle. The C_{iA} in a convenient manner can be defined as the number of particles consisting of i single particles per unit mass of bed material. The level of IPFs progressively increases in a bed that is approaching a complete defluidization condition. Based on the results presented in Figure 7.4a it can be inferred that the idle time continuously increases during this pass; the rate of increase in idle time enhances with the ratio of the magnitude of IPFs/HDFs. Also, according to Eqs. (2)-(5), the concentration of larger agglomerates in the bed is a stronger function of the reaction time, i.e., the idle time. Consequently, it can be concluded that the agglomerate size exponentially increases from the onset of agglomeration up to the entire defluidization of the bed.

Since the probability of solid and liquid bridge formation between two particles, corresponding to the sintering and eutectic formation processes, in a cohesive bubbling bed in the vicinity of complete defluidization at elevated temperatures increases with the contact time of colliding particles, the agglomeration phenomena is a self-promoting process. This is a common problem in olefin-polymerization processes [40], where a large fluidized bed of polymer particles completely defluidizes within a short period of time (< 1hr) when agglomerates the size of a tennis ball are detected inside the bed. The simulation study of the agglomeration phenomenon in an air-polyethylene fluidized bed consistently showed that the mass distribution of agglomerates rapidly grows when the inlet gas temperature was higher than the softening temperature of polyethylene particles [41]. Agglomeration due to the presence of molten silicates during combustion of biomass with high alkali content at elevated temperatures was also regarded as an auto-accelerated process [42]. The results presented in Fig. 4a with the analogy approached above can phenomenologically explain why agglomerates exponentially enlarge when a bed is moving toward a complete defluidization state.

7.5.3 Global solids mixing

Solids mixing is important in the design and operation of gas-solids fluidized beds due to its direct effect on temperature control, heat transfer, position, the number of solids feed and withdrawal points, and chemical conversion [4, 44]. Solids mixing is generally believed to be driven by two principal mechanisms: i) convective mixing due to the gross circulation of solids, ii) dispersive

mixing due to solids turbulent motion [5, 44]. The former mechanism governs the global solids mixing process in the bed while the latter controls the local solids mixing [5]. Uniform temperature is vital in chemical reactions if products are sensitive to variations in bed temperature [45]. The temperature gradient appears if the overall solids circulation flux is not high enough [4]. Stein et al. [46] defined the cycle frequency, as the average frequency that a tracer particle moves from below 30% of the dense bed height to the top 30% and returns back to the same height, as a characteristic of the global solids mixing in the bed. Based on this definition, a computer program was developed to identify the cycles through the bed from the time-position trajectory of particles obtained during the RPT experiments.

An evaluation of the cycle frequency under different operating conditions was carried out and the results are plotted in Figure 7.5. It demonstrates that the cycle frequency increased due to the superficial gas velocity for both SB20 and CSB40 in the bubbling regime. It can be ascribed to the increase in the capability of larger bubbles for carrying a higher amount of particles at a higher speed to the splash zone. This increased upward-moving solids flux requires a higher downward solids flow to maintain the dense bed continuity. However, the presence of IPFs in the bed led to a decrease in the cycle frequency. This observation could be principally attributed to the presence of smaller bubbles that move less frequently through the bed with higher levels of IPFs (in the range of the gas velocities studied) [10, 11]. In addition, a lesser degree of particle mobility within the emulsion phase with a greater level of resistance driven by the presence of IPFs can promote this reduction trend. Since the high degree of solids mixing is responsible for the uniformity of temperature and composition in the fluidized bed [45], Figure 7.5 reveals that increasing the level of IPFs in a bubbling gas-solid fluidized bed decreased the quality of global solids mixing in the bed. This can subsequently introduce a temperature non-uniformity along the bed height, which is in accordance with the results presented in section 7.5.1.

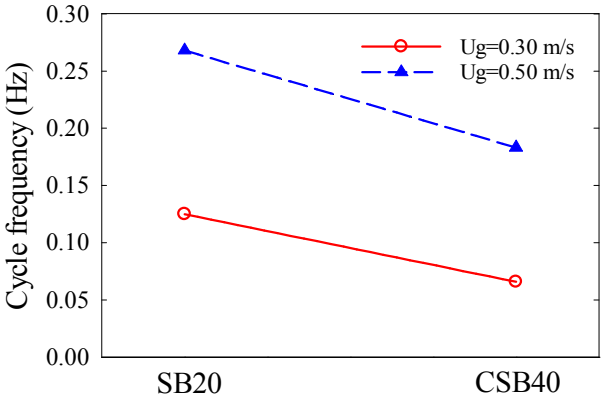

Figure 7.5: Influence of IPFs on cycle frequency.

7.5.4 Local solids mixing

Reaction conversion in a gas-solid fluidized bed is basically governed by two phenomena: reaction rate and mass transfer between the bubble and emulsion phases [47]. The importance of the hydrodynamics, particularly the local solids mixing, increases when the rate of reaction increases. It is crucial when dealing with very fast catalytic and/or extremely exothermic reactions [5, 47]. The creation of hot spots in the bed and low conversion at the outlet are direct consequences of poor solids mixing [5]. The local solids mixing can be evaluated through determining the solids diffusivity in gas-solid fluidized bed. Mostoufi and Chaouki [5] introduced a method to evaluate the solids diffusivity from the particle trajectory in the Lagrangian coordinates. For this purpose, a large number of particle tracers should be injected in a small cell in the bed. However, since the RPT experiment involves only one tracer, the ergodicity theorem [48] should be employed to process the data obtained in the RPT experiments. By applying this method, two sample reconstructions of the self-diffusion of l000 labeled solid particles versus time for SB20 and CSB40 at U_g=0.50 m/s are provided in Figure 7.6. It qualitatively shows that particles in a bed without IPFs, SB20, can spread over the whole bed considerably faster compared to CSB40, which was influenced by the presence of IPFs.

The frequency of macro-structures, which appropriately represents the frequency of bubble passage within the bed, in the operating conditions of Figure 7.6 was estimated to be approximately 2 Hz [11], i.e., a bubble passed from/around the injection cell every ~500 ms. This infers that the virtual tracers were principally dispersed as a result of particle movement within the emulsion phase that was minimally disturbed by moving bubbles in the time interval exhibited in Figure 7.6. Since

bubble movement is the main reason for solids movement, the typical solids dispersion profiles illustrated in Figure 7.6 are not a picture of the sole dispersion phenomenon. However, it can well represent how fast particles can be locally mixed by virtue of the presence of a concentration gradient to form a uniform distribution throughout the bed, where no more dispersion occurs. Therefore, it can be concluded that a cohesive gas-solid fluidized bed in the bubbling regime would have a lower quality of local solids mixing.

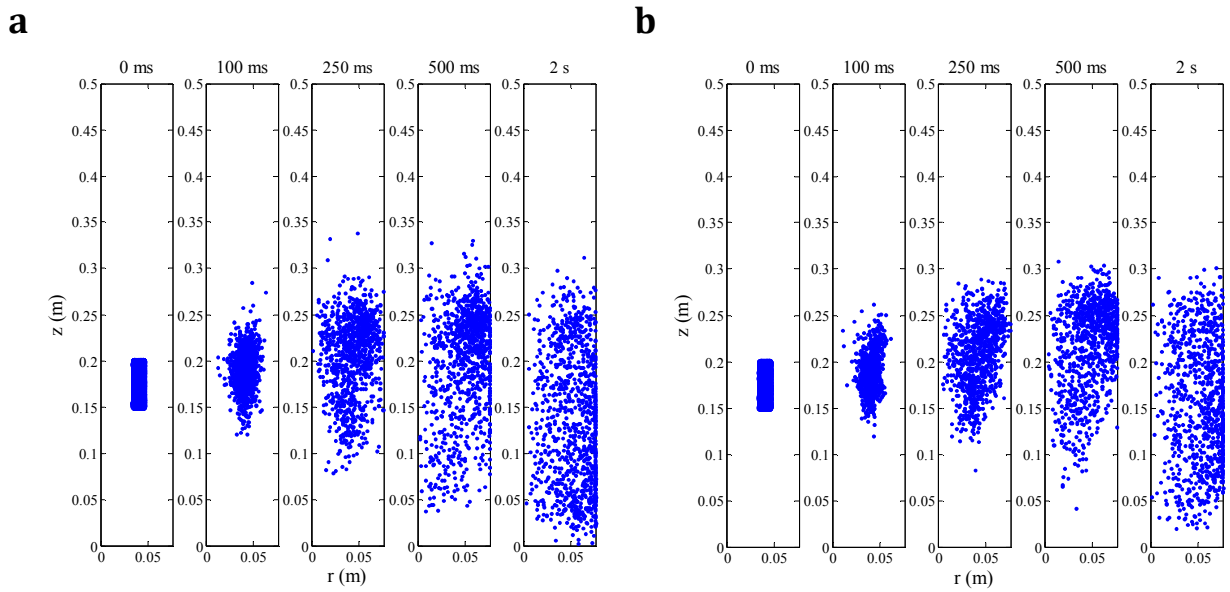

Figure 7.6: Self-diffusion of 1000 labeled tracers virtually injected in the imaginary compartment 35<r<45 mm, 150<z<200 mm at U_g=0.50 m/s. a) SB20, b) CSB40.

Following the algorithm introduced by Mostoufi and Chaouki [5], the values of axial and radial solids diffusivities, D_z and D_r, respectively, were evaluated to quantitatively verify this statement. Since the operating height of the bed in the conducted experiments was not high enough to observe a definite trend in the calculated variables with respect to the axial position, the averages of D_z and D_r over axial direction are plotted in Figure 7.7 as a function of radial position. In order to prevent jet turbulence and bubble eruption effects in the results, a layer of the bed close to the distributor plate and the top were excluded from the average. Figure 7.7 shows that D_z and D_r were lower close to the column wall and increased by moving towards the bed center, reached a maximum value at the halfway radial positions (in most cases), and further decreased near the center. An identical observation was reported by Mostoufi and Chaouki [5] for a dense gas-solid fluidized bed of sand particles (d_p=385 μm). Since the solids diffusivity is a function of the shear rate in the

suspension [5, 49], the variations of D_z and D_r with respect to the radial position cannot be explained by the wall effect but with the variation of velocity gradient [5]. Trends of the axial and radial velocity gradients in the radial direction observed in this study and shown in Figure 7.8, were similar to those recognized by Mostoufi and Chaouki [5] for sand particles. This, in turn, affirms their argument. Figure 7.8 depicts that the axial velocity gradients were remarkably larger than the radial velocity gradients. D_z for all systems was consistently an order of magnitude larger than D_r. It reveals that the local solids mixing in the axial direction was many times faster than the lateral mixing. It is directly related to the natural tendency of bubbles to vertically move in the fluidized bed rather than laterally.

From Figure 7.7, it is seen that diffusivities in both directions increased with the superficial gas velocity. It could be attributed to a higher turbulent activity of bubbles at higher gas velocities in the bubbling regime, which led to a better quality of solids mixing in the bed. Figure 7.7 further demonstrates that the solids diffusivity coefficients decreased with IPFs approving the unfavorable impact of IPFs on the quality of local solids mixing for a bubbling gas-solid fluidized bed. A decrease in solids mobility inside the bed due to a decrease in the bubble size and an increase in the resistance of the emulsion phase in spite of any changes resulting from the presence of IPFs can explain this effect.

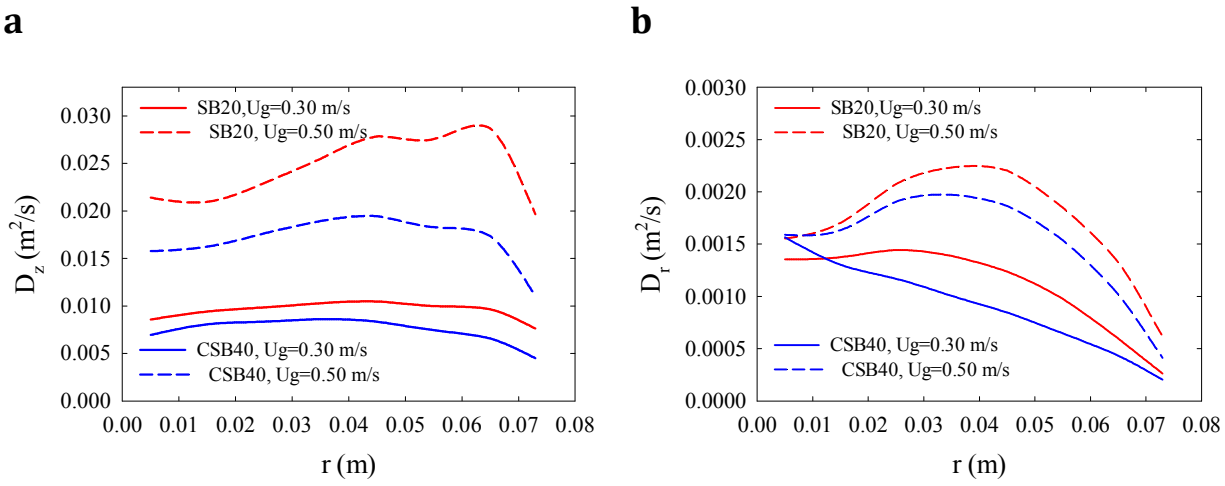

Figure 7.7: Influence of IPFs on local solids mixing. a) axial solids diffusivity, b) radial solids diffusivity.

Mostoufi and Chaouki [5] proposed that the axial solids diffusivity is a linear function of the velocity gradient as follows:

$$D_z = \alpha\gamma_z + D_{z,0} \qquad 7.6$$

where α is the slope, γ_z is the axial velocity gradient, and $D_{z,0}$ is the solids diffusivity at the zero gradient condition, i.e., solids diffusivity in a constant velocity field. According to their experimental results, the slope was principally a function of the particle diameter in a dense gas-solid fluidized bed. In order to study the influence of IPFs on the relationship between the solids diffusivity and the velocity gradient, the axial solids diffusivity for different systems is plotted against the axial velocity gradient in Figure 7.9. It shows that the value of α is independent of IPFs. The results also confirm that the slope is not a function of the bed voidage for a bubbling dense gas-solid fluidized bed. However, IPFs could effectively modify $D_{z,0}$. Figure 7.9 illustrates that $D_{z,0}$ for different systems linearly correlated with the excess gas velocity, $U_g - U_{mf}$, as $D_{z,0} = 0.64(U_g - U_{mf})$. Hence, $D_{z,0}$ simultaneously varied with the excess gas velocity and IPFs. A similar trend (not shown here) was observed for the radial diffusivity at the zero gradient condition, too. Therefore, since the level of IPFs in a gas-solid fluidized bed can change due to any operational reason, an appropriate hydrodynamic correlation must include the contribution of IPFs in addition to HDFs.

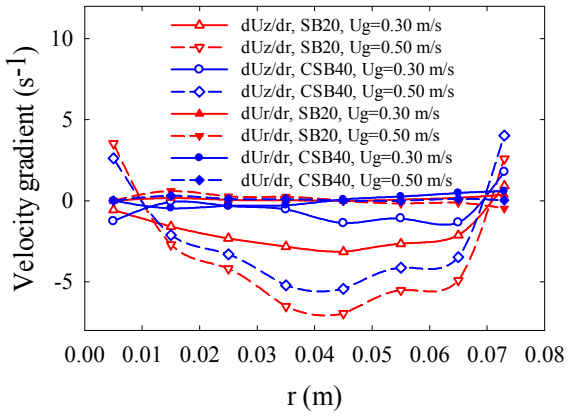

Figure 7.8: Influence of IPFs on axial and radial solids velocity gradient.

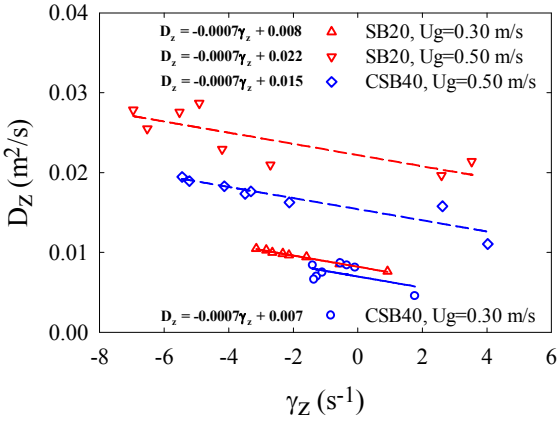

Figure 7.9: Axial solids diffusivity as a function of axial solids velocity gradient.

7.6 Conclusion

The influence of IPFs on the solids flow pattern and the quality of solids mixing was examined by the time-position trajectory of particles acquired by the RPT technique in a bubbling gas-solid

fluidized bed. A polymer coating approach was applied to introduce and control the level of IPFs in the bed. The experimental results showed that IPFs could greatly influence the solids flow pattern in the bed. At low gas velocity, where a higher value of the ratio of the magnitude of IPFs/HDFs could present, particles showed less tendency to be involved in the gross circulation. Also, the onset of the gross cycle shifted to slightly higher levels in cohesive beds. These modifications in the solids flow pattern suggest that particles in a cohesive bubbling fluidized bed tend to contribute less in the transfer of heat within the bed. Hence, the presence of a temperature gradient along the bed height is anticipated. This finding is pivotal in the early detection of defluidization conditions, where the level of IPFs continuously increases over time, or in the case of processes where a uniform temperature profile throughout the bed is required.

The evaluation of the bubble size demonstrated that IPFs led to the presence of smaller bubbles in the range of gas velocities tested in the bubbling regime. It indicates that the tendency of gas to interstitially pass through the bed in the emulsion phase was enhanced by the presence of IPFs. This is a favorable modification in the distribution of the fluidizing gas between the bubble and emulsion phases, since a better gas-solid contact can be achieved in the emulsion phase. However, analysis of the experimental data revealed that the quality of solids mixing, in particular the local solids mixing, decreased with IPFs. Therefore, an increase in the level of IPFs in a bubbling gas-solid fluidized bed with the purpose of achieving better gas-solid contact should be cautiously applied to obtain an optimized performance. Finally, although the superficial gas velocity principally governs the bed hydrodynamics, the variation in the ratio of the magnitude of IPFs/HDFs must be taken into account to achieve a proper prediction of the overall performance of a gas-solid fluidized bed reactor.

7.7 Nomenclature

7.7.1 Acronyms

Ar	Archimedes number
CSB40	coated sugar beads at 40^{o}C
HDFs	hydrodynamic forces
IPFs	interparticle forces

PEA	poly ethyl acrylate
PMMA	poly methyl methacrylate
RPT	radioactive particle tracking
SB20	fresh sugar beads at 20ºC

7.7.2 Symbols

A	single particle (-)
C_{iA}	concentration of an agglomerate consisting of i single particles ($1/m^3$)
d_p	mean particle size (μm)
d_B	spherical equivalent diameter of bubble (m)
D_c	column diameter (m)
D_r	radial diffusivity (m^2/s)
D_z	axial diffusivity (m^2/s)
$D_{z,0}$	axial diffusivity at zero velocity gradient (m^2/s)
g	gravitational acceleration (m/s^2)
h	bed height (m)
K_i	agglomeration rate constant corresponding to r_i (m^3/s)
r	radial coordinate (m)
r_i	rate of formation of an agglomerate consisting of i single particles ($1/(m^3.s)$)
t	reaction time (s)
U_g	superficial gas velocity (m/s)
U_{mf}	minimum fluidization velocity (m/s)
U_W	solids velocity in bubble wake (m/s)
U_z	vertical particle velocity (m/s)

$U_g - U_{mf}$ excess gas velocity (m/s)

z axial coordinate (m)

7.7.3 Greek letters

α constant in Eq. 7.2 (m^2)

γ_z axial velocity gradient, $[dU_z/dr]$ (s^{-1})

ρ_p particle density (kg/m^3)

7.8 Acknowledgements

The authors wish to express their appreciation to the Total American Services, Inc. and the National Sciences and Engineering Research Council of Canada (NSERC) for their financial support of this work under the Grant number IRCPJ 412045-10. We also acknowledge the assistance of Michael Butler for activation of the radioactive tracer at the Nuclear Reactor section of McMaster University.

7.9 References

1) D. Kunii, O. Levenspiel, Fluidization Engineering, Butterworth-Heinemann, Boston, 1991.
2) X. Fan, D.J. Parker, Z. Yang, J.P.K. Seville, J. Baeyens, The effect of bed materials on the solid/bubble motion in a fluidised bed, Chem. Eng. Sci. 63 (2008) 943-950.
3) M. Stein, Y.L. Ding, J.P.K. Seville, D.J. Parker, Solids motion in bubbling gas fluidised beds, Chem. Eng. Sci. 55 (2000) 5291-5300.
4) J. Baeyens, D. Geldart, Solids Mixing, in: D. Geldart (Ed.), Gas Fluidization Technology, John Wiley & Sons Ltd., New York, 1986, pp. 97-122.
5) N. Mostoufi, J. Chaouki, Local solid mixing in gas-solid fluidized beds, Powder Technol. 114 (2001) 23-31.
6) M.J. Rhodes, X.S. Wang, M. Nguyen, P. Stewart, K. Liffman, Study of mixing in gas-fluidized beds using a DEM model, Chem. Eng. Sci. 56 (2001) 2859-2866.
7) H.R. Norouzi, N. Mostoufi, Z. Mansourpour, R. Sotudeh-Gharebagh, J. Chaouki, Characterization of solids mixing patterns in bubbling fluidized beds, Chem. Eng. Res. Des. 89 (2011) 817-826.

8) X. Fan, Z. Yang, D.J. Parker, Impact of solid sizes on flow structure and particle motions in bubbling fluidization, Powder Technol. 206 (2011) 132-138.

9) G.R. Duursma, D.H. Glass, S.J.L. Rix, M.I. Yorquez-Ramirez, PIV investigations of flow structures in the fluidised bed freeboard region, Powder Technol. 120 (2001) 2-11.

10) J. Shabanian, J. Chaouki, Local characterization of a gas–solid fluidized bed in the presence of thermally induced interparticle forces, Chem. Eng. Sci. 119 (2014) 261-273.

11) J. Shabanian, J. Chaouki, Hydrodynamics of a gas–solid fluidized bed with thermally induced interparticle forces, Chem. Eng. J. 259 (2015) 135-152.

12) J. Shabanian, P. Sauriol, A. Rakib, J. Chaouki, Characterization of gas-solid fluidization at high temperature by analysis of pressure signals, in: Proceedings of the 11th International Conference on Fluidized Bed Technology (CFB-11), Beijing, 2014.

13) P. Pagliai, S.J.R. Simons, D. Rhodes, Towards a fundamental understanding of defluidisation at high temperatures: a micro-mechanistic approach, Powder Technol. 148 (2004) 106-112.

14) I. Tomasetta, The effect of temperature on flow properties of powders, Ph.D. dissertation, Universita Degli Studi Salerno, 2012.

15) K. Rietema, The Dynamics of Fine Powders, Elsevier Science Publishers Ltd., New York, 1991.

16) H.Y. Xie, The role of interparticle forces in the fluidization of fine particles, Powder Technol. 94 (1997) 99-108.

17) G. Tardos, R. Pfeffer, Chemical reaction induced agglomeration and defluidization of fluidized beds, Powder Technol. 85 (1995) 29-35.

18) B. Formisani, R. Girimonte, L. Mancuso, Analysis of the fluidization process of particle beds at high temperature, Chem. Eng. Sci. 53 (1998) 951-961.

19) P. Lettieri, J.G. Yates, D. Newton, The influence of interparticle forces on the fluidization behaviour of some industrial materials at high temperature, Powder Technol. 110 (2000) 117-127.

20) H. Cui, J. Chaouki, Effects of temperature on local two-phase flow structure in bubbling and turbulent fluidized beds of FCC particles, Chem. Eng. Sci. 59 (2004) 3413-3422.

21) Y. Zhong, Z. Wang, Z. Guo, Q. Tang, Defluidization behavior of iron powders at elevated temperature: Influence of fluidizing gas and particle adhesion, Powder Technol. 230 (2012) 225-231.

22) J. Shabanian, F. Fotovat, J. Bouffard, J. Chaouki, Fluidization behavior in a gas-solid fluidized bed with thermally induced inter-particle forces, in: T.M. Knowlton (Ed.), Proceedings of the 10th International Conference on Circulating Fluidized Beds and Fluidization Technology (CFB-10), Engineering Conferences International, New York, 2011.

23) J. Shabanian, J. Chaouki, Pressure signals in a gas-solid fluidized bed with thermally induced inter-particle forces, in: J.A.M. Kuipers, R.F. Mudde, J.R. van Ommen, N.G. Deen (Eds.), The 14th International Conference on Fluidization–from Fundamentals to Products, ECI Symposium Series, Noordwijkerhout, 2013.

24) D. Geldart, Types of gas fluidization, Powder Technol. 7 (1973) 285-292.

25) S. Roy, F. Larachi, M.H. Al-Dahhan, M.P. Dudukovic, Optimal design of radioactive particle tracking experiments for flow mapping in opaque multiphase reactors, Appl. Radiat. Isot. 56 (2002) 485-503.

26) F. Larachi, G. Kennedy, J. Chaouki, A γ-ray detection system for 3-D particle tracking in multiphase reactors, Nucl. Instrum. Methods Phys. Res., Sect. A 338 (1994) 568-576.

27) F. Larachi, J. Chaouki, G. Kennedy, 3-D mapping of solids flow fields in multiphase reactors with RPT, AIChE J. 41 (1995) 439-443.

28) M. Rasouli, F. Bertrand, J. Chaouki, A multiple radioactive particle tracking technique to investigate particulate flows, AIChE J. 61 (2015) 384-394.

29) C.D. Willett, The micromechanics of wet particulate materials (Ph.D. Thesis), University of Birmingham, 1999.

30) X. Fan, D.J. Parker, B. Armstrong, Prediction of bubble behaviour in fluidised beds based on solid motion and flow structure, Chem. Eng. J. 140 (2008) 358-369.

31) J. van der Schaaf, J.C. Scouten, F. Johnsson, C.M. van den Bleek, Non-intrusive determination of bubble and slug length scales in fluidized beds by decomposition of the power spectral density of pressure time series, Int. J. Multiphase Flow 28 (2002) 865-880.

32) K. Smolders, J. Baeyens, Elutriation of fines from gas fluidized beds: mechanisms of elutriation and effect of freeboard geometry, Powder Technol. 92 (1997) 35-46.

33) D. Geldart, A.C.Y. Wong, Entrainment of particles from fluidized beds of fine particles, AIChE Symp. Ser. 83 (1987) 1-9.

34) J. Shabanian, J. Chaouki, Performance of a catalytic gas-solid fluidized bed reactor in the presence of interparticle forces, Int. J. Chem. Reactor Eng. (2015) accepted for publication.

35) N. Mostoufi, J. Chaouki, On the axial movement of solids in gas-solid fluidized beds, Chem. Eng. Res. Des. 78 (2000) 911-920.

36) N. Mostoufi, J. Chaouki, Flow structure of the solids in gas-solid fluidized beds, Chem. Eng. Sci. 59 (2004) 4217-4227.

37) R. Radmanesh, Fluidized bed biomass gasification (Ph.D. Thesis), Ecole Polytechnique de Montreal, 2006.

38) J.P.K. Seville, H. Silomon-Pflug, P.C. Knight, Modelling of sintering in high temperature gas fluidization, Powder Technol. 97 (1998) 160-169.

39) H.S. Fogler, Elements of Chemical Reaction Engineering, 4th ed., Pearson Education Inc., Upper Saddle River, New Jersey, 2006.

40) L.A. Noble, Method of preventing or reducing polymer agglomeration on grid in fluidized-bed reactors, US Patent (2012) US 8,129,482 B2.

41) Z. Mansourpour, N. Mostoufi, R. Sotudeh-Gharebagh, Investigating agglomeration phenomena in an air-polyethylene fluidized bed using DEM–CFD approach, Chem. Eng. Res. Des. 92 (2014) 102-118.

42) G. Olofsson, Z. Ye, I. Bjerle, A. Andersson, Bed agglomeration problems in fluidized-bed biomass combustion, Ind. Eng. Chem. Res. 41 (2002) 2888-2894.

43) D. Moslemian, M.M. Chen, B.T. Chao, Experimental and numerical investigation of solids mixing in a gas fluidized bed, Part. Sci. Technol. 7 (1989) 335-355.

44) D. Moslemian, Study of solids motion, mixing, and heat transfer in gas fluidized beds (Ph.D. Thesis), Illinois University, 1987.

45) M. Stein, T.W. Martin, J.P.K. Seville, P.A. McNeil, D.J. Parker, Positron Emission Particle Tracking: Particle Velocities in Gas Fluidized Beds, Mixers and other Applications, in: J. Chaouki, F. Larachi, M.P. Dudukovic (Eds.), Non-invasive Monitoring of Multiphase Flows, Elsevier, Amsterdam, 1997, pp. 309–333.

46) M.M. Yazdanpanah, A. Forret, T. Gauthier, A. Delebarre, Modeling of CH4 combustion with NiO/NiAl2O4 in a 10 kW_{th} CLC pilot plant, Appl. Energy 113 (2014) 1933-1944.

47) A.S. Monin, A.M. Yaglom, J.L. Lumley, Statistical Fluid Mechanics: Mechanics of Turbulence, Vol. 1., MIT Press, Cambridge, 1971.

48) E.C. Eckstein, D.G. Bailey, A.H. Shapiro, Self-diffusion of particles in shear flow of a suspension, J. Fluid Mech. 79 (1977) 191-208.

CHAPTER 8 ARTICLE 6: FLUIDIZATION CHARACTERISTICS OF A BUBBLING GAS-SOLID FLUIDIZED BED AT HIGH TEMPERATURE IN THE PRESENCE OF INTERPARTICLE FORCES

Jaber Shabanian, Jamal Chaouki*

Department of Chemical Engineering, Ecole Polytechnique de Montreal, Montreal, Quebec, Canada

* Corresponding author: Tel.: +1-514-340-4711 X 4034; fax: +1-514-340-4159.

E-mail address: jamal.chaouki@polymtl.ca

(Submitted to Chemical Engineering Journal)

8.1 Highlights

- The hydrodynamics of a bubbling gas-solid fluidized bed was studied at high temperature.
- The investigation was attempted in the virtual absence and presence of interparticle forces.
- Smaller bubbles passed through a bed of coarse particles at elevated temperatures.
- The presence of interparticle forces led to a multiplicity of behaviors.

8.2 Abstract

The fluidization behavior of bubbling fluidized beds of coarse particles were investigated between 700 and 1000°C for superficial gas velocities ranging from 0.6–1.5 m/s. The objective of the study was to highlight the modification in the bed behavior with the operating temperature at conditions under which the role of hydrodynamic forces (HDFs) or interparticle forces (IPFs) was dominant. To this end, the experimental work was divided into two phases. In the first phase, the influence of temperature on the hydrodynamics of a bubbling fluidized bed of coarse particles for which HDFs were dominant was investigated. In the second phase, the surface characteristics of the fluidized particles were primarily modified through the formation of eutectics resulting from a chemical reaction between the bed material and alkali/alkali earth metal based reagents that were introduced into the bed throughout periods of solid fuel combustion at elevated temperatures. It thus triggered changes in their fluidization characteristics with increasing temperature while IPFs were present in the bed. Experimental results revealed that the flow dynamics of a bubbling bed of coarse particles

at high temperature was principally influenced by the variation of the gas density with temperature when IPFs did not play a discernable role. Nevertheless, with the presence of different levels of IPFs in the bed, a multiplicity of behaviors was realized at elevated thermal levels. Thus, a great deal of attention to the physical and/or physico-chemical changes of the fluidized particles with increasing temperature along with the variation of the physical properties of the fluidizing gas must be taken into account in order to arrive at the successful design and reliable operation of gas-solid fluidized beds at high temperature.

Keywords: Gas-solid fluidized bed, Bubbling regime, Hydrodynamics, High temperature, Interparticle forces.

8.3 Introduction

Gas-solid fluidized beds have been commonly employed in chemical industries in such areas as fluidized catalytic cracking, catalytic oxidation, combustion and gasification of different solid fuels, and polymerization [1, 2], often operating at high temperature with respect to the particles being fluidized in the bed. Since they offer critical advantages, such as the ability to provide high heat and mass transfer rates, high combustion efficiency, low emission levels, and good fuel flexibility to process a broad variety of solid fuels (biomass, various waste materials, low grade coal) or blends (co-firing with conventional fuels) [3-6], they will find many additional industrial applications in the near future that will coincide with the rarefication of conventional resources. Therefore, a comprehensive understanding of the fluidization characteristics of a fluidized bed at high temperature is of prime importance to establish successful design criteria for this technology.

Research on the effect of temperature on the hydrodynamic aspects of gas-solid fluidized beds was started in the mid-1970s yet findings are still controversial to provide a satisfactory understanding of the phenomena that is responsible for changes in the fluidization behavior between the ambient and high temperature [2, 7]. The major source of this controversy is ascribed to the lack of insight about the relative importance between hydrodynamic forces (HDFs) and interparticle forces (IPFs) [8, 9]. Although some researchers attempted to approach this difference on the sole basis of variation in HDFs [10-15], it has been proven that most of the conventional models/equations, which were based purely on hydrodynamic principals, became increasingly inaccurate when the temperature increased [16-18]. It is believed to be the direct consequence of ignoring the

modification in the solid phase, i.e., level of IPFs, at thermal levels well above the ambient temperature. Some peculiar observations were reported for the bed behavior at high temperature, which could not be solely explained in light of changes in the fluidizing gas properties. They include an increase in the settled bed voidage ε_0 in the complete absence of gas flow [4, 19-23], an increase in the minimum fluidization and bubbling voidages (ε_{mf} and ε_{mb}, respectively) [4, 19-21, 23-27], the presence of an overshoot at the minimum fluidization velocity U_{mf} in the bed pressure drop profile for powders showing typical Geldart group B [28] behavior at ambient conditions [29, 30], or the presence of a more profound overshoot at U_{mf} for powders exhibiting typical Geldart group A characteristics at room temperature [8, 9] as well as the concave trend for the variations of U_{mf} and the interstitial gas velocity U_i with the system temperature for fine particles [4, 8, 21, 26, 30]. Thus, it turned out to be obvious that the combined effects of HDFs and IPFs govern the bed hydrodynamics though their relative importance and the way in which IPFs, in particular, influence the bed behavior is not clear.

Increasing the system temperature decreases the gas density ρ_g (ρ_g being inversely proportional to the absolute temperature T) and increases the gas viscosity μ_g (μ_g being proportional to T^n, where n is usually between 0.6 and 1.0) [31, 32]. These changes can in turn modify the magnitude of fluid forces exerted on the particles. Van der Waals and electrostatic forces are the main types of IPFs in a dry environment [33, 34]. The magnitude of the van der Waals forces acting between particles in mutual contact enhances with an increase in the bed temperature as the molecular dipole pulsation around the contact point is enhanced by thermal excitation [35]. Also, the viscous flattening of solid particles occurring before sintering [36] gives place to a larger interparticle contact area, promoting the effectiveness of the van der Waals forces. The electrostatic forces, which are only important for particles larger than 50 microns in diameter [37], become less influential at higher thermal levels [18, 38, 39] due to an increase in the electrical conductivity of particles as the temperature increases [40, 41]. The presence of a material bridge between the particles at high temperature can arise either from the formation/addition of a liquid or the structural/chemical changes at the particle surface, e.g., through sintering, crystallization or plastic deformation [42]. The cohesive force resulting from the material bridge, either liquid or solid, is much larger in magnitude than the van der Waals and electrostatic forces [34, 37, 42, 43]. Sintering originates from the migration of holes/lattice cavities or the movement of atoms to a less dense

area of the material on the surface of particles [44] and yields a solid-solid bond between the particles in contact at its final stage. The formation of a trace amount of liquid in high temperature fluidized beds is principally due to the presence of impurities with a low sintering temperature within the bed, which sinter/melt at the operating temperature and can further react with each other or other solids producing new compounds [45] with a low melting temperature (eutectic), which liquefy under the operating conditions. For instance, in the case of the combustion and gasification of biomass, wastes, and low rank coals the ash sintering and chemical reaction between the alkali/alkali earth metal elements in the solid fuels/ash and the bed material, commonly silica sand, is known as the major source of particle stickiness in the bed [6, 46-52]. If one of the IPFs is in the same order of magnitude as the weight of the particle, the particles are called sticky and the fluidization behavior can be modified [6]. Therefore, it seems clear that the fluidization characteristics of a gas-solid fluidized bed at elevated temperatures are significantly more complicated than what was initially thought.

Reviewing extensive studies on the influence of temperature on the gas-solid fluidization behavior reveals that they can be categorized into five groups: i) literature studies that were devoted to low gas velocities, either for the fixed bed state or near the minimum fluidization/bubbling velocity [4, 8-15, 19-27, 29, 30, 53-75], which do not generate considerable industrial interest; ii) studies to model the limiting state of defluidization when fluidizing pure material at high temperature [76-81]; iii) investigations about the influence of bed temperature on the transition velocity from bubbling to turbulent fluidization regime U_c [82-85]; iv) research that focused on the variation of entrainment rate with an increase in temperature [18, 86-92]; and v) detailed studies that concentrated on the bubbling and turbulent bed behaviors by the application of appropriate measurement techniques [16, 17, 93-98]. Since earlier studies on the subject dealt with the combined effects of HDFs and IPFs on bed behavior, they could ultimately prove that the thermal modification of the solid phase must be taken into account along with the variation of HDFs with no clear distinction between the direct effect of each force group. Detailed fluidization dynamics of gas-solid fluidized beds in which the properties of fluidized particles experience a modification during the process, particularly as a result of the presence of a liquid deposit on the particle surface at high temperature, has rarely been reported in the literature. Hence, there is still a need to delineate the direct influence of IPFs on bed behavior at elevated temperatures when integrated with the variation of HDFs.

The objective of the present study is to explore the bubbling fluidization behavior of coarse particles in the presence of different levels of IPFs at high temperature. A wide range of operating conditions, temperatures between 700 and 1000^{o}C and superficial gas velocities ranging from 0.6–1.5 m/s, relevant to industrial fluidized bed combustion and gasification of different solid fuels, was selected. The fluidization characteristics of fresh coarse silica sand and olivine particles, nominated systems that are minimally influenced by IPFs, were initially studied. In the second step, different levels of IPFs were deliberately introduced into beds of these coarse particles through the deposition of a liquid layer on the surface of the particles. This was achieved during the combustion of different solid fuels, embedding alkali/alkali earth metal based reagents, at different temperatures for a certain period of time. The spent particles with different magnitudes of IPFs were subsequently subjected to hydrodynamic tests at high temperature to achieve the aim of the study.

8.4 Experimental

Figure 8.1 shows a schematic of the atmospheric pressure pilot scale fluidized bed adopted in this study. The refractory lined apparatus was capable of operating at 1050^{o}C. It consisted of a windbox with a lateral natural gas burner/air entry, a fluidizing/reaction section that was 20 cm I.D. and 97 cm in height, an expansion section with a 60 cm I.D. and 48 cm tall, and an external cyclone to recover the entrained fly ashes produced during the combustion of solid fuels. Dry and filtered air, as a fluidizing medium, was supplied to the bed through a stainless steel bubble cap distributor plate with 9 caps each having 4 holes 6.35 mm in diameter on its perimeter. The unit temperature was monitored with 14 OMEGA type K thermocouples located along the axis, from the windbox to the expansion zone. They assisted in controlling the operating temperature, verifying the expanded bed height, and providing a local measure of the bed behavior. The global hydrodynamic measurements were achieved by four pressure transducers: an absolute pressure transducer (OMEGA, PX309-100A5V, 0-100 Pisa) in the windbox, a gauge pressure transducer (OMEGA, PX309-002G5V, 0-2 Psig) at 30 cm in height above the distributor plate within the dense bed, a differential pressure transducer (JUMO, 404304/000-414-415-28-298, 0-160 mbar) to measure the bed pressure drop (5-130 cm in height), and a differential pressure transducer (JUMO, 404304/000-414-415-28-298, 0-100 mbar) to acquire the in-bed differential pressure signals (15-45 cm above the distributor plate). Since in-bed gauge pressure signals reflect all phenomena occurring within

the bed and in-bed differential pressure signals registered across two ports within the dense bed are influenced by the phenomena that happen within its ports [99], the planned configuration of pressure transducers made it possible to follow the phenomenon happening inside the well stabilized dense bed with two observers. The pressure probes were mounted flush to the inner wall of the column and the tips of the pressure probes were filled with glass wool to avoid blockage by fine particles.

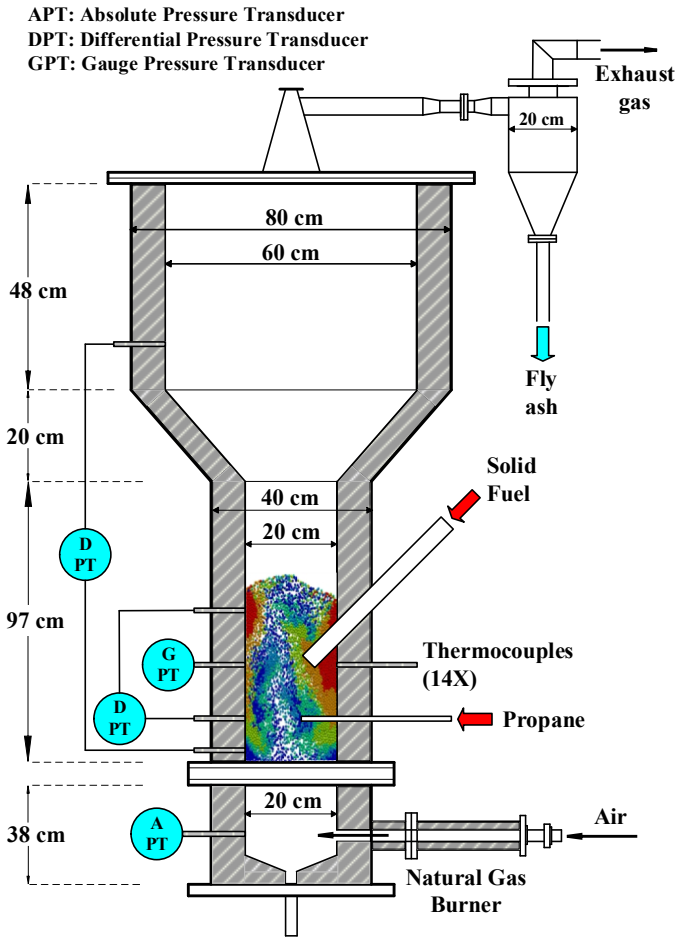

Figure 8.1: Schematic drawing of gas-solid fluidized bed for high temperature experiments.

Coarse silica sand (d_p=820 µm, ρ_p=2650 kg/m^3, ρ_b=1340 kg/m^3; d_p is the mean particle size, ρ_p is the particle density, and ρ_b is the bulk density) and olivine particles (d_p=565 µm, ρ_p=3287 kg/m^3, ρ_b=1615 kg/m^3) were selected as the bed material. They were separately introduced into the fluidized bed for the hydrodynamic study. Values of the minimum fluidization velocity for silica sand and olivine powders at ambient conditions were calculated as 0.54 and 0.39 m/s, respectively, with the help of the Wen and Yu [100] equation and recommended coefficients by

Chitester et al. [101] for coarse particles. Table 8.1 reports the chemical compositions of fresh sand and olivine as provided by the supplier (UNIMIM Corporation). The fresh sand consisted mainly of silica with minor amounts of impurities while magnesium oxide, silica, and iron oxide were the principal components of the fresh olivine. A bed inventory of 26.0 kg of silica sand and 31.2 kg of olivine was fed into the reactor for the corresponding hydrodynamic tests. Considering the amount of solids that were entrapped in the side ports (dead zones) of the reactor, the resulting static bed height for either of these two cases was approximately 55 cm ($h_0/d_c \approx 2.25$; h_0 is the static bed height and d_c is the column diameter).

Table 8.1: Chemical compositions of fresh silica sand and olivine particles (%wt)

Oxides	Fresh silica sand	Fresh olivine
Silicon dioxide (SiO_2)	99.710	41.500
Magnesium oxide (MgO)	0.019	49.700
Iron oxide (Fe_2O_3)	0.040	7.300
Aluminum oxide (Al_2O_3)	0.072	0.490
Calcium oxide (CaO)	0.010	-
Potassium oxide (K_2O)	0.030	-
Sodium oxide (Na_2O)	0.006	-
Chromium oxide (Cr_2O_3)	-	0.300
Nickel oxide (NiO)	-	0.320
Manganese oxide (MnO)	-	0.090
Others	0.107	0.030

Superficial gas velocity U_g was varied in the range of 0.6–1.5 m/s for the purpose of hydrodynamic study at each operating temperature (700, 800, 900, and 1000°C). As will be discussed in section 8.5.1, the bubbling fluidization regime was achieved for both coarse bed materials in the range of gas velocities explored here. The fluidizing gas was measured with a calibrated orifice plate at room temperature and corrected for the temperature.

In order to investigate the influence of temperature on the bed behavior while differentiating the effects of HDFs and IPFs, experiments were divided in two different sets. For the first set of experiments, a bed of either fresh silica sand or olivine was primarily preheated with the natural gas burner to reach a temperature above 630ºC. Upon reaching the condition, the natural gas was stopped and propane was simultaneously fed into the reactor (20 cm above the distributor plate at the bed center) to further increase the bed temperature, up to 1000ºC, while air was continuously going through the distributor to maintain the U_g at 1.0 m/s and supply the required oxygen for the propane combustion. For the second set of experiments, varying degrees of IPFs were initially introduced into a bed of otherwise fresh silica sand or olivine through the combustion of pre-processed solid fuels. The solid fuel was combusted in the fluidized bed at operating temperatures of 800, 900, and 1000ºC for 1 hr each while maintaining the superficial velocity of air entering at 1.0 m/s. A volumetric solid feeder (Schenck AccuRate) with an air assisted assembly was adopted to feed the solid fuel through a tube located 30 cm above the distributor and near the central axis of the bed into the reactor. The bed temperature was increased with the help of the propane combustion between two solid fuel combustion steps. This procedure allowed the bed material to be coated with various degrees of low melting point eutectics, depending on the coating thickness either modifying its surface properties or forming liquid bridges between particles. The solid fuel was a mixture of bituminous coal (1-3 mm) with a pre-processed non-recyclable fraction of municipal solid waste (MSW; ~3mm) in which trace amounts of alkali/alkali earth metal based reagents in the form of fine powders (<35 μm) were embedded. Characteristics of the selected solid fuels are summarized in Table 8.2.

Hydrodynamic tests were commenced upon reaching 1000ºC for the first set of experiments or after the accomplishment of solid fuel combustion for the second set of experiments. Pressure signals were acquired at different superficial gas velocities. For each velocity, signals were logged for 4 min at a frequency of 400 Hz after reaching steady state. The bed temperature was kept constant by the combustion of propane in the bed. Temperature signals were recorded with a sampling frequency of 1 Hz throughout the whole test on a separate computer. The pressure measurements were repeated at 900, 800, and 700ºC. Recorded pressure and temperature signals were subsequently analyzed to highlight the effect of temperature taking into account the variations of both HDFs and IPFs. At the end of each experiment, the bed material was removed and disposed.

Representative samples from the recovered powders were collected for further particle size and density and XPS (X-ray Photoelectron Spectroscopy) measurements.

Table 8.2: Characteristics of selected solid fuels

Solid fuel	Na content	Ca content	Bed material
A (mixture)	low	low	silica sand
B (mixture)	low	medium	silica sand
C (mixture)	medium	Low	silica sand
D (mixture)	medium	medium	silica sand
E (mixture)	low	high	olivine
F (mixture)	high	medium	olivine

8.5 Results and discussion

8.5.1 Effect of temperature on bed hydrodynamics at a minimal level of IPFs

This section of the work aims at investigating the influence of temperature on the bed flow dynamics provided that the magnitudes of IPFs are at minimum. With respect to their physical properties (d_p and ρ_p), the selected coarse particles exhibit identical behavior to powders at the boundary between Geldart groups B and D at ambient conditions. The magnitude of van der Waals IPFs in a dry environment and in the absence of electrostatic forces is negligible in comparison with HDFs for powders with Geldart groups B and/or D behaviors at ambient conditions [102]. As mentioned earlier, increasing the temperature reduces the degree of electrification and, hence, the magnitude of electrostatic forces [18, 38, 39]. Thus, one can anticipate that the bed was minimally affected by the electrostatic forces in the range of operating temperatures explored in this work. Accordingly, in the absence of any liquid phase in the system, if the initial sintering temperatures of the adopted particles take place at thermal levels well above the operating temperature, it can be reliably assumed that the fluidized particles were influenced neither by the plastic deformation, which can enhance the magnitude of the van der Waals forces at elevated temperatures, nor by the sintering phenomenon.

The measurements of the minimum sintering temperatures of fresh silica sand and olivine powders were primarily attempted by dilatometric analysis [103, 104] (DIL402C, Netzsch, Germany). However, owing to the coarse grain sizes of the powder samples, it was difficult to prepare a loosely compacted sample of powders in the sample container of the machine. A traditional approach was subsequently applied through which 5 gr of each powder poured into a crucible and placed in a furnace. The sample was heated, at 5ºC/min, to an elevated temperature, held at the desired temperature for 5 hrs and cooled down by 10ºC/min. The sample was inspected for the presence of an agglomerate at the end of a cycle. The minimum temperature at which particles started to join together was examined by this method. Consistent with the values provided by the supplier, the results showed that the initial sintering of these particles (silica sand≈1400ºC and olivine≈1450ºC) occurred at temperatures well above 1000ºC, the maximum operating temperature of this study.

Due to the spatial position of propane injection within the bed, which was located in the principal passage way of bubbles [105], the propane combustion (required during the heating pass and hydrodynamic tests) would mainly take place in the bubble phase. Therefore, the solid particles could experience a local excess temperature once they were carried up by bubbles between the axial height of the propane injection and the bed surface. Since the mean particle residence time within the bubble phase of a bubbling bed of coarse particles is basically less than a second [106, 107], hot particles experiencing the local excess temperature in the bubble phase could quickly transfer to the emulsion phase, where they spent a considerably longer time at the mean operating temperature. Consequently, the fresh coarse particles were less prone to undergo their initial sintering conditions in the high temperature experiments. This shows that the conjecture above is correct and that fluidized beds of fresh silica sand and olivine particles could be solely influenced by the variations of HDFs when the bed temperature varied in the range of 700–1000ºC.

The standard deviations of in-bed gauge and differential pressure signals for both fresh coarse particles at different operating conditions are illustrated in Figure 8.2. It demonstrates that all systems under investigation were operating in the bubbling regime because there were no conditions for which they exhibited a maximum in the pressure amplitude vs. velocity profile [108]. Figure 8.2 further shows that the standard deviations of in-bed pressure signals decreased with temperature at a given superficial gas velocity for both fresh coarse particles. Consistent observations for the fluidization behavior of coarse particles at high temperature were reported in earlier publications [82, 93-96]. Since the level of IPFs was at minimum for these systems, the

observed modification in the bed behavior can be ascribed to the variation in HDFs. Despite the fact that the fluidizing gas properties change with temperature, i.e., ρ_g decreases and μ_g increases, their influences on the fluidization characteristics must be treated with the particle size information to determine which of these opposing variations is dominant. The particle Reynolds number Re_p for the selected bed materials within the range of tested operating conditions varied between 2.5 and 8.5, which is well beyond the creeping flow condition ($Re_p \ll 1$) for which the viscous effect dominates over inertia [34, 109]. Therefore, a decrease in the gas density principally determined the modification in the fluidization behavior of fresh coarse silica sand and olivine particles at elevated temperatures.

Reducing the gas density decreased the drag force exerted on each single particle by the fluidizing medium. In other words, less energy was transferred to the bed material, which could yield less chaotic particle movements in the bed, i.e., less bed mass oscillation. A decrease in the gas density would also modify the two-phase flow structure of the bed. A higher amount of gas was needed to pass through the bed in the emulsion phase at a higher temperature to compensate for the reduction in the gas density preserving the particles to be well fluidized in this phase. Subsequently, at a given throughput of the fluidizing gas, a lesser amount of gas remained to form bubbles. This portion of the fluidizing gas would appear either in the form of smaller bubbles with a relatively similar passage frequency or identical size/larger bubbles with a lower passage frequency. For a given bubble, a reduced ratio of the drag force to the buoyant weight of particles at a higher temperature could promote the bubble splitting, following Taylor instability [110], and result in the presence of smaller bubbles in the bed. Therefore, the former scenario most likely occurred in the bed; the effect of temperature on the bubble passage frequency will be discussed in Figure 8.3. Since the amplitude of pressure fluctuations is closely related to a characteristic dimension of inhomogenities (bubbles) in the bed [111], the presence of smaller bubbles and less bed mass oscillation led to a decrease in the amplitude of in-bed pressure signals recorded for beds of fresh silica sand and olivine particles.

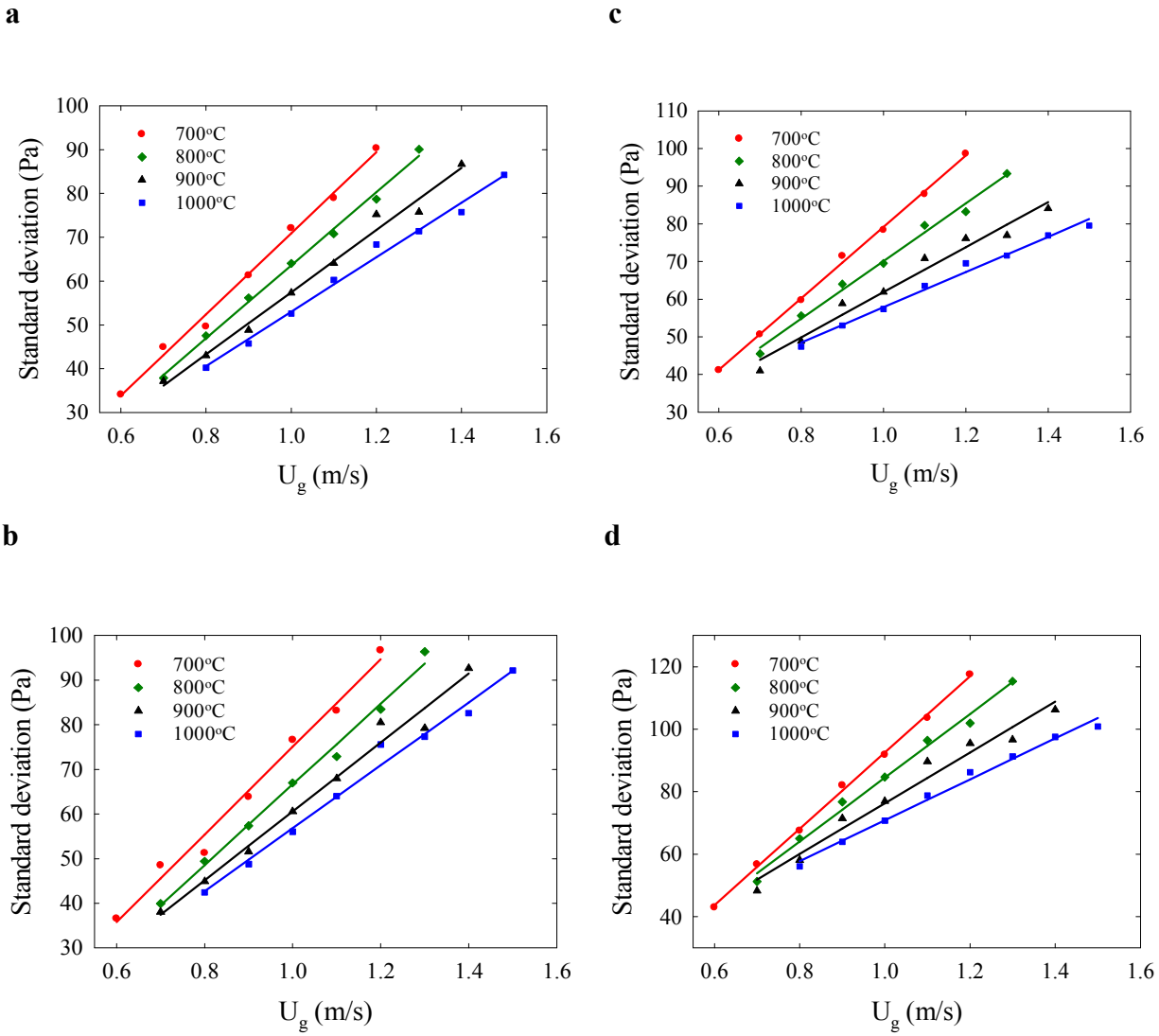

Figure 8.2: Influence of temperature on standard deviations of in-bed pressure signals for fresh silica sand and olivine particles. (a, c) gauge pressure signals, (b, d) differential pressure signals.

To verify this conclusion, the variation in the frequency of bubble passage within the bed should be investigated. An identical approach as presented by Shabanian and Chaouki [112] was adopted in this study to evaluate the frequency of macro-structures, which could be a good representative of the bubble passage frequency in the bed. To this end, the frequency range of three main structures of a bubbling gas-solid fluidized bed, i.e., micro, meso and macro-structures [113], under different operating conditions was initially identified by plotting the power spectral density (PSD) of in-bed gauge pressure signals in a logarithmic scale following Johnsson et al. [114]. Since macro-structures occurred below 1.6 Hz in all conditions, details of D8–D10 from the wavelet

decomposition of treated pressure signals with a 2nd order Daubechies wavelet function (db2), covering the range of frequencies between 0.2 and 1.6, were employed to calculate the frequency of macro-structures; the treated pressure signals were obtained by subtracting a moving average with 0.2 Hz from the original signals to eliminate the effect of gas flow rate fluctuations. Results of this analysis are presented in Figure 8.3. It shows that, in accordance with the above interpretation, the frequency of macro-structures for both systems remained comparatively unaffected in the range of operating temperatures tested. The experimental results presented by Saxena et al. [94] for the variation of the bubble passage frequency in fluidized beds of coarse sand particles (d_p=641 and 1312 μm) in the temperature range of 913–1123 K are in agreement with this observation.

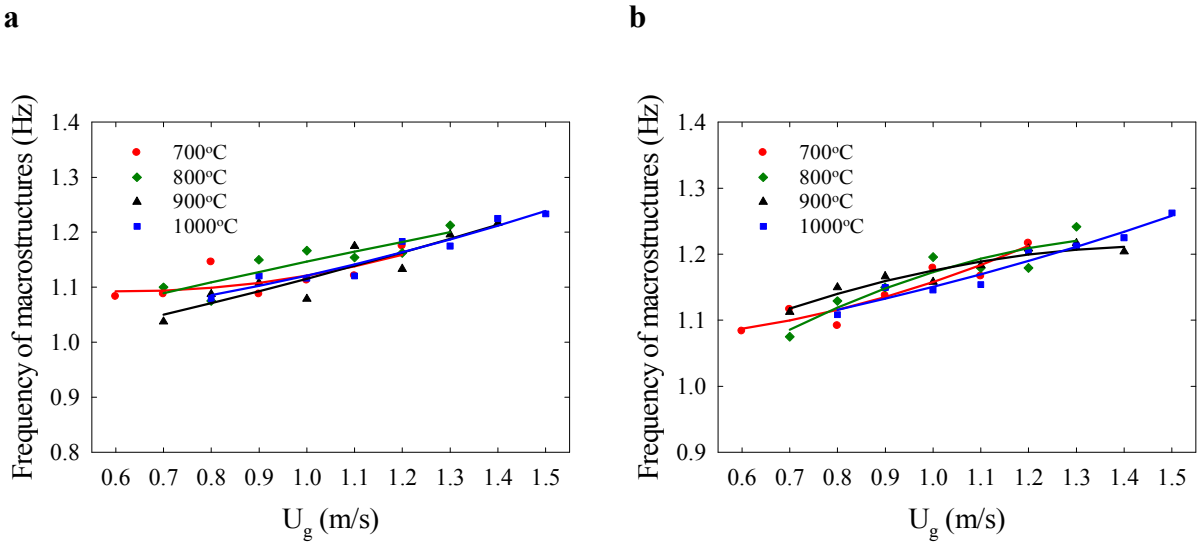

Figure 8.3: Influence of temperature on frequency of macro-structures. (a) fresh silica sand, (b) fresh olivine.

The gas momentum flux $\rho_g U_g{}^2$ is a governing parameter for the hydrodynamic characteristics of a gas-solid fluidized bed when the level of IPFs is at minimum. To further ascertain that the principal reason in the modification of the bed behavior for the fresh coarse particles was a decrease in the gas density, the standard deviations of in-bed gauge pressure signals for fresh silica sand and olivine particles are plotted versus the gas momentum flux in Figure 8.4. Plotting the data versus the gas momentum flux integrates the temperature, or more specifically the gas density, and velocity effects in a single parameter. Figure 8.4 shows that within a certain scatter range all data points are approximated by a straight line. It reveals that the standard deviations of in-bed gauge pressure signals, which is closely dependent on the bubble behavior, were basically a function of

the gas momentum flux. In other words, the bubbling behavior in a bed of coarse particles at operating temperatures well above ambient and in the virtual absence of IPFs followed a unique mechanism being solely influenced by the variation of HDFs resulting either from the variation of the superficial gas velocity or gas density. Therefore, the variation of the gas density at a given volumetric fluidizing gas flowrate governed the modifications in the fluidization behavior for the cases under investigation. Similar trends were recognized for the differential pressure signals recorded from beds of both types of particles.

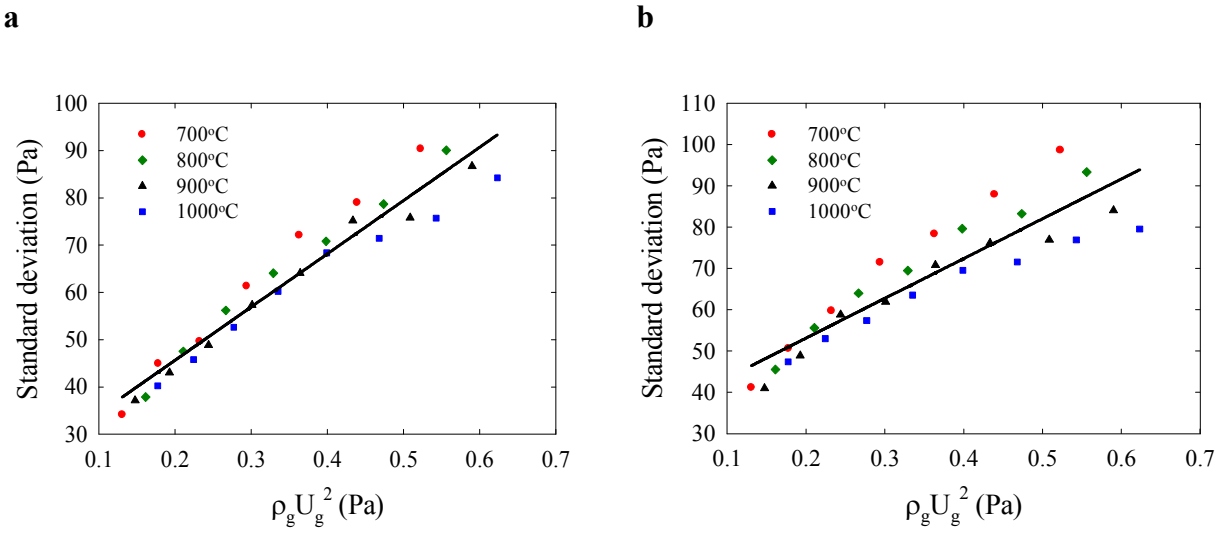

Figure 8.4:Variation of standard deviations of in-bed gauge pressure signals versus the gas momentum flux. (a) fresh silica sand, (b) fresh olivine.

Decreasing the bubble size and a reduced effective drag force on each single particle in a bed of coarse particles at elevated temperatures can yield two subsequent effects. They can primarily decrease the quality of solids mixing in the bed and, in turn, postpone U_c to higher velocities due to the existence of a few strong particle-particle collisions in the bed, which are responsible for vigorous solids mixing and enhanced energy dissipation and, therefore, the formation of aggregate flows as characteristics of the turbulent regime [115]. Cai et al. [82] observed that U_c increased with temperature for coarse particles, which is in broad agreement with the discussion. The second impact concerns the variation of the solids entrainment rate with temperature. The presence of smaller bubbles reduces the bubble rise velocity, resulting in smaller ejection velocities of bubbles erupting at the bed surface. When integrated with a less effective drag force on each single particle, a reduction in the entrainment rate of coarse particles can be anticipated at high temperature.

Experimental results of Choi et al. [88] in a 0.3m × 0.3 m combustor showed that the entrainment rate for coarse sand particles (d_p=560 μm) decreased as temperature increased from 700 to 900ºC. They attributed this observation to a decrease in the gas density.

8.5.2 Effect of IPFs on bed hydrodynamics at high temperature

The second phase of this study was aimed at highlighting the influence IPFs at high temperature on the fluidization characteristics of a bubbling gas-solid fluidized bed. It required the availability of beds at varying degrees of IPFs. Beds of fresh coarse silica sand and olivine particles were subjected to the combustion of different solid fuels containing various amounts of alkali/alkali earth metal based reagents to prepare the desired paradigms. The mechanism through which the level of IPFs increased in the bed could be summarized as the following: upon injection of the solid fuel into the reactor the alkali/alkali earth metal based reagents, which were embedded in the MSW portion of the fuel, could experience a thermal decomposition in favor of producing sodium oxide, sodium carbonate, and calcium oxide. The Na-based compounds could melt or become sticky over the temperature range of solid fuel combustion. Thus, the bed particles would be coated with an adhesive layer, which could also host Ca-based compounds with a considerably higher melting temperature upon collision. In a subsequent step, an interaction would occur between the silica from the sand or olivine particles and impurities in the adhesive layer to form low melting silicates, characterized by a lower melting point than the individual compounds. Since this step is strongly influenced by temperature [6], the local excess temperature around the burning coal particles [116] could promote the formation of eutectics. This could happen since a burning coal particle can stay in the vicinity of the coated particles in the emulsion phase during the idle time of the system, which would be in the order of a few to several seconds depending on the gas velocity, physical properties of particles, and level of IPFs [107]. With this strategy, relying on the amounts of alkali/alkali earth metal based reagents in the solid fuel and the availability of silica on the surface of bed materials, different levels of IPFs could be achieved.

Retrieved particles after each test were subjected to further characterization tests to ascertain that different behaviors observed from beds with varying levels of IPFs (will be discussed later) were principally the result of a surface modification in the bed materials and not other physical properties, i.e., ρ_p and d_p. A MASTERSIZER 3000 (Malvern Instrument Ltd.) and a helium pycnometer (micromeritics AccuPyc II 1340) were employed to measure the particle size and

density of samples, respectively. The variations of ρ_p and d_p of recovered particles after different tests were less than 2% for both parameters (Table 3). The sole exception was associated with the size of recovered olivine after test F for which an increase of about 40% was recognized. It could be due to the strong influence of IPFs, originating from the presence of a high Na content in the combusting solid fuel. The results reveal that particles essentially remained identical from Geldart classification's point of view over the course of solid fuel combustion with different recipes. It confirms that if beds of spent particles behave differently, it is the major consequence of variation in the level of IPFs. Values reported in Table 8.3 are the average of 10 measurements.

Table 8.3: Physical properties of particles before and after different tests

Status	d_p (μm)	ρ_p (kg/m^3)
Fresh coarse sand	820 ± 30	2650 ± 1
Fresh Olivine	565 ± 15	3287 ± 1
Coarse sand after prone alone	811 ± 25	2640 ± 1
Olivine after propane alone	567 ± 10	3286 ± 1
Coarse sand after test A	815 ± 35	2639 ± 1
Coarse sand after test B	838 ± 40	2635 ± 1
Coarse sand after test C	835 ± 50	2636 ± 1
Coarse sand after test D	806 ± 40	2635 ± 1
Olivine after test E	563 ± 15	3298 ± 1
Olivine after test F	806 ± 40	3240 ± 1

The XPS measurements were conducted by VG ESCALAB 3 MKII (Thermo VG Scientific) to show that the surface properties of particles varied following the combustion of different solid fuels in the bed. It was approached through the identification and relative quantification of different elements on the surface of particulate samples since the machine could perform a survey scan with a depth of 5–10 nm on the sample. The presence of different elements on the surface of particles leads to the variation in the level of van der Waals forces, in the absence of capillary force, through the modification of the Liftshits-van der Waals/Hamaker constants. If these elements form eutectics, particles are coated with a liquid phase and, hence, the capillary force can drastically modify the bed hydrodynamics. The reaction between the alkali metals (like Na) with the SiO_2

based bed materials can result in the formation of eutectic compounds, like $Na_2O.2SiO_2$ with T_m=874°C (T_m is the melting temperature) [47, 117]. Since the sample holder was approximately 1 cm across, a large enough number of particles could be placed on the sample holder to provide a reliable Table 4 represents the results of the XPS measurements for fresh and spent particles. They are in good agreement with the characteristic information of the selected solid fuels in this study (refer to Table 8.2) and prove that the surface modification occurred for the spent particles. A few traces of Na and Ca elements on the surface of spent silica sand and olivine after the combustion of propane alone might come from the previous experiments although a cleaning test, i.e., the combustion of coal alone at 900°C and U_g=1.0 m/s for at least 10 hrs, was conducted before these tests.

The values reported in Table 8.4 are the relative atomic percentages $RA\%$ and calculated as follows:

$$RA_i\% = \frac{A_i/SF_i}{\sum_{j=1}^{n} A_j/SF_j} \qquad 8.1$$

where A_i represents the area of the peak for a given element in the resulted XPS measurement and SF_i is the sensitivity factor for the corresponding element. The sensitivity factors were adopted from the Wagner table [118].

Table 8.4: Identification and relative quantification of elements on the surface of different particle samples from survey scans by XPS measurements

Sample/element	Mg	Al	Si	C	Ca	O	Fe	Na
Fresh coarse sand	-	5.3	14.4	17.9	-	61.3	1.1	-
Fresh Olivine	13.7	4.3	10.5	5.4	-	65.1	1.0	-
Coarse sand after propane alone	-	5.8	19.5	8.7	0.3	64.4	1.3	-
Olivine after propane alone	11.8	5.2	9.1	15.2	0.4	56.3	1.7	0.3
Coarse sand after test A	-	4.9	15.0	10.0	5.1	62.3	1.0	1.7

Coarse sand after test B	-	3.3	11.9	16.1	7.7	58.8	0.7	1.5
Coarse sand after test C	-	2.7	15.0	17.9	2.5	56.8	0.6	4.5
Coarse sand after test D	-	3.2	13.9	11.3	5.1	60.7	0.8	5.0
Olivine after test E	6.1	4.6	1.0	17.0	5.3	57.8	1.0	1.2
Olivine after test F	2.6	3.3	12.2	17.8	2.8	53.5	0.5	7.3

Gas-solid fluidized beds are well known for the homogeneous temperature distribution in the bed. This attractive feature results from an intense solids mixing within the bed [106, 119]. In gas-solid fluidized bed technology, temperature measurements contain information on the degree of solids mixing [6] through the evaluation of the uniformity of the temperature profile throughout the bed. The quality of solids mixing decreases in a bubbling bed upon increasing the level of IPFs [107]. Accordingly, an uneven distribution of temperature could be a direct consequence of enhancing IPFs in the bed. This measurement was thus adopted to verify which type of the particles exploited here, i.e., either silica sand or olivine, could demonstrate a greater influence by the presence of IPFs after the combustion of a given solid fuel. The experimental results presented in Figure 8.5 show that a bed of silica sand particles defluidized during the heating pass to 900^{o}C after a 1 hr solid fuel combustion around 800^{o}C whereas a bed of olivine could remain acceptably fluidized after combustion of the same fuel at 800, 900, and 1000^{o}C for 1 hr at each temperature. The solid fuel employed for these runs had the same amount of Ca content as the solid fuel F yet with a slightly lower Na content. This observation indicates that a bed of olivine particles experiences a lower level of IPFs after the combustion of a given solid fuel in comparison with a bed of coarse silica sand particles.

a

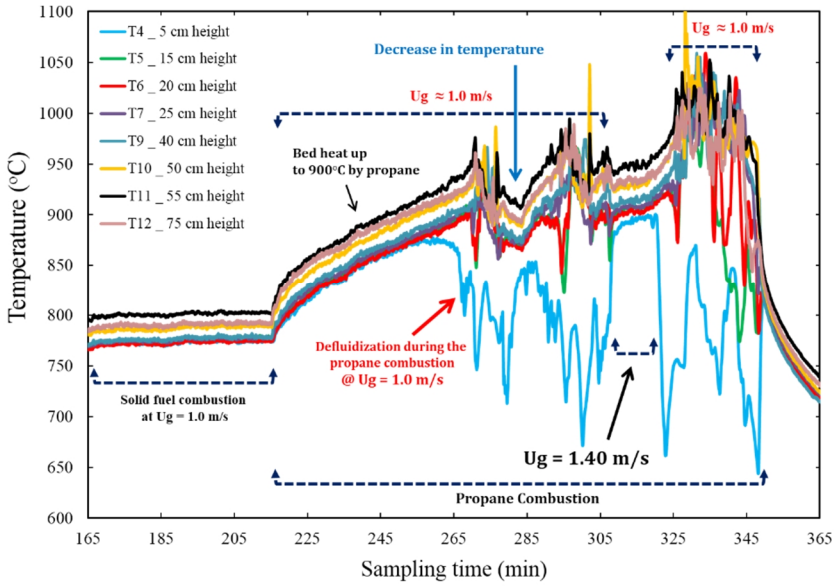

b

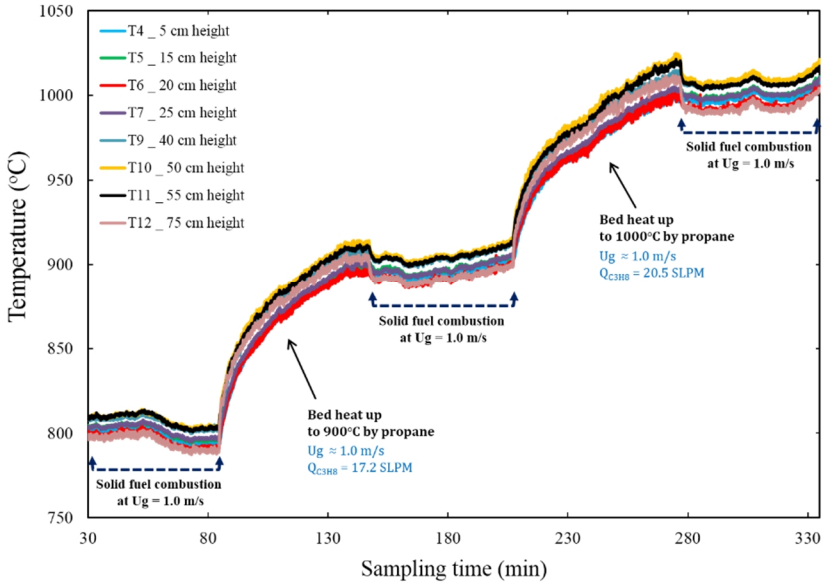

Figure 8.5: Temperature profile during the combustion of a solid fuel with a high Na content at different temperatures. (a) silica sand, (b) olivine particles were employed as the bed material.

It has been reported that Mg and Al can prevent/prolong the agglomeration phenomenon driven by the presence of alkali metals and SiO_2 based bed materials at elevated temperatures [117, 120-123]. The former is beneficial most likely due to the formation of high melting point compounds, such as MgO, $MgSiO_3$, and Mg_2SiO_4 (T_m=2852, 1910, and 1890°C, respectively) in the bed that increases the overall melting temperature of the system and reduces the generation of compounds

with low melting points [121]. Al can react with $Na_2O/Na_2O.Si_2O_3$ and form sodium aluminate ($Al_2O_3.Na_2O$) or sodium aluminosilicate ($Al_2O_3.Na_2O.Si_2O_3$) with high melting points [117, 122, 123] and, hence, decrease the quantity of low-melting eutectics in the bed. These effects are equivalent to a decrease in the level of IPFs. Therefore, by the application of olivine particles in the bed, it could benefit from the presence of both Mg and Al elements and, thus, experience a lower level of IPFs after the combustion of a given solid fuel containing a Na element.

Figure 8.6 exhibits the temperature profiles of some sample beds (silica sand particles as the bed material) under investigation during the hydrodynamic tests. It elucidates that the temperature gradient along the axis, particularly between the bottommost thermocouple and others in the higher levels of the bed, increased for beds with spent particles/IPFs. Fig. 6 also shows that the application of a solid fuel with low Na and medium Ca contents slightly increased the level of IPFs while the fuel with a medium Na content enhanced the level of IPFs more evidently. Since a large temperature gradient was present between the lowermost section and the higher levels of the bed at U_g=1.0 m/s and 1000ºC for test C, the hydrodynamic tests for lower gas velocities had to be skipped to prevent a defluidization condition.

a

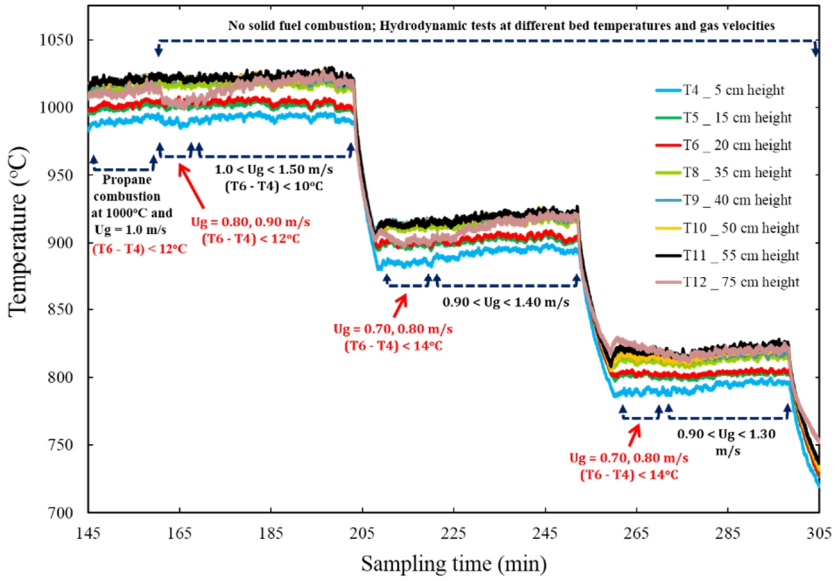

b

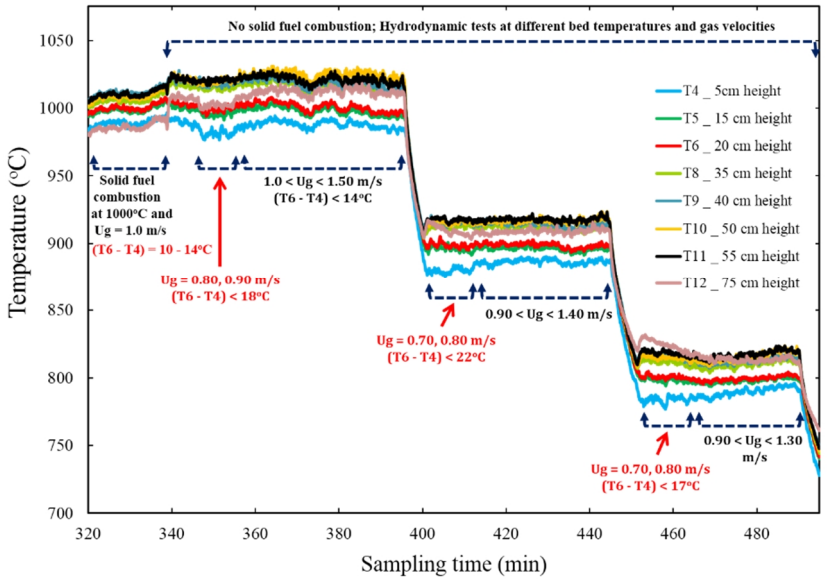

c

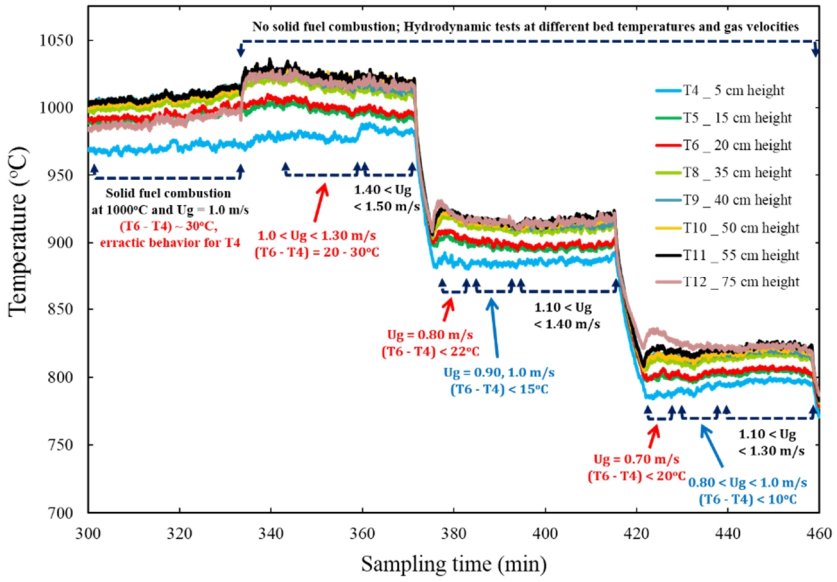

Figure 8.6: Temperature profile during the hydrodynamic tests. (a) fresh silica sand, (b) spent sand after test B, (c) spent sand after test C.

Figure 8.7 illustrates the temperature and total bed pressure drop profiles for a bed of spent silica sand with a high level of IPFs (higher than in test C). The bed was acceptably fluidized during the solid fuel combustion at 900ºC and heat-up pass to 1000ºC, which can be inferred from the uniformity of temperature distribution and the relatively stable oscillations in the total bed pressure

drop. The bed with severe IPFs became defluidized at the beginning of the solid fuel combustion at 1000ºC. This is evident from the discontinuity between the readings of all thermocouples accompanied by a sharp decrease in the bed pressure drop, as suggested by Siegel [44]. Following the defluidization incident, the fluidized bed was recovered by increasing U_g to 1.2 m/s. Although a bed of fresh sand could easily remain fluidized at U_g as low as 0.80 m/s at 1000ºC, the cohesive bed would not remain fluidized at superficial gas velocities lower than 1.1 m/s at 1000ºC. This observation clearly reveals that U_{mf} for a given powder increased with IPFs. This is well in accordance with the results of Shabanian and Chaouki [112], who increased the level of IPFs with the help of a polymer coating approach and temperature adjustment. Also, Gluckman et al. [124] and Compo et al. [104] reported an identical observation when increasing the level of IPFs through sintering of particles at operating temperatures higher than their minimum sintering temperatures. An increase in U_{mf} with IPFs can be interpreted as the need for an additional drag force by the fluidizing gas in excess of the apparent weight of the bed to compensate for the yield stress of the particulate bed resulting from IPFs.

a

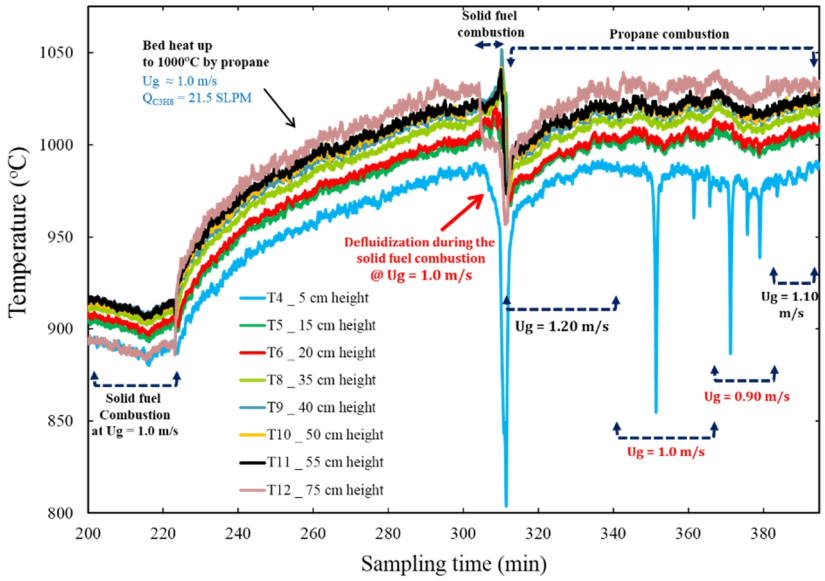

b

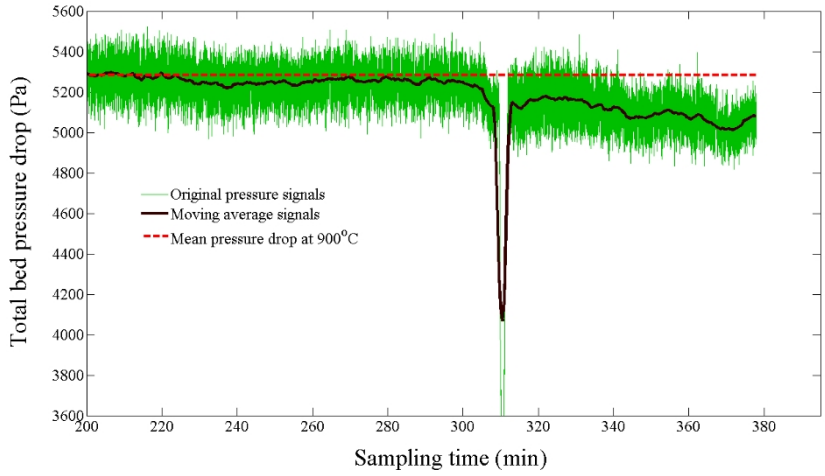

Figure 8.7: (a) Temperature and (b) bed pressure drop profiles for a bed with a high level of IPFS; the bed material was silica sand.

The standard deviations of in-bed gauge pressure signals for beds of fresh and spent silica sand and olivine particles are plotted in Figure 8.8 under different operating conditions. It shows that a bed of spent sand particles after the combustion of solid fuel A with low Na and Ca contents demonstrated very similar behavior to the fresh sand after the combustion of propane alone. The bed of spent sand after test A also showed an identical temperature distribution during the hydrodynamic tests to that of the fresh sand (results not shown here). These observations indicate that the fluidization characteristics were relatively insensitive to the variation of IPFs when HDFs were dominant. Nevertheless, the bed behavior was slightly modified following the combustion of fuel B with a higher Ca content compared to fuel A through a small decrease in the uniformity of temperature distribution (refer to Figure 8.6) and a modest decrease in the amplitude of pressure fluctuations at all superficial gas velocities. Identical to silica sand, a bed of spent olivine after the combustion of a solid fuel with low Na and high Ca contents (mixture E) was slightly influenced by the presence of IPFs.

This modification in the fluidization behavior could be attributed to the formation of some eutectic/peritectic compounds, including Ca, Na, Si, and O elements within the bed, which resulted in a slight increase in the level of IPFs. The role of Ca in enhancing IPFs can be deducted from the ternary Na_2O-SiO_2-CaO phase diagram [125, 126]. Pure CaO melts above 2500^oC and CaO-SiO_2 can form eutectic around 1440^oC [125]. Both temperature ranges are far from those under study. However, when CaO is added to a Na_2O-SiO_2 system, a eutectic of Na_2O-CaO-$5SiO_2$, which has a

melting point as low as 755°C, or a peritectic of Na_2O-3CaO-6SiO_2 at operating temperatures above 827°C would form. It was consistently reported by Olofsson et al. [127] that the addition of CaO into a Na_2O-SiO_2 system can accelerate the agglomeration process.

A bed of spent olivine after test F had the highest level of IPFs among all beds of olivine particles. However, since the bed temperature profile during the hydrodynamic tests after test F was slightly influenced by the presence of IPFs compared to the temperature distribution for a bed of fresh olivine, a moderate level of IPFs could be present in the bed of spent olivine particles after test F. Figure 8.8 elucidates that a bed of spent olivine after test F had a higher growth rate of standard deviation of pressure fluctuations with U_g in comparison with the fresh olivine. A trend inversion occurred under the conditions presented in Figure 8.8c and d, i.e., a smaller and higher amplitude of pressure signals with respect to that of fresh olivine can be recognized for a bed of spent olivine after test F at gas velocities below and above the inversion point, respectively. This behavior is similar to the influence of artificial IPFs, introduced by the polymer coating approach in a bed of coarse sugar beads (d_p=580 µm), on the standard deviations of in-bed pressure signals reported in a separate work by the present authors (Shabanian and Chaouki [112]).

a

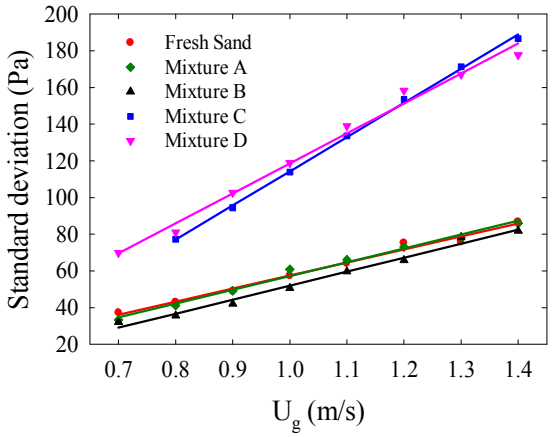

b

c

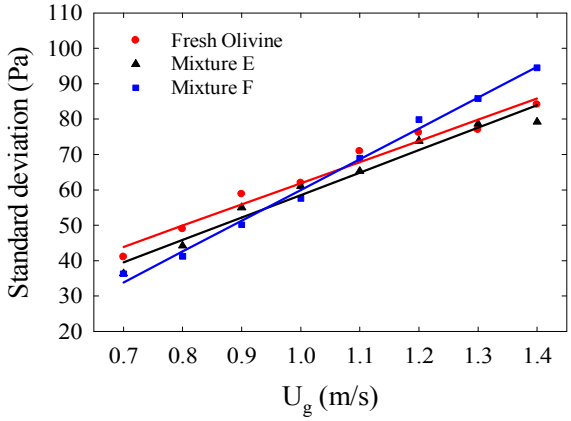

d

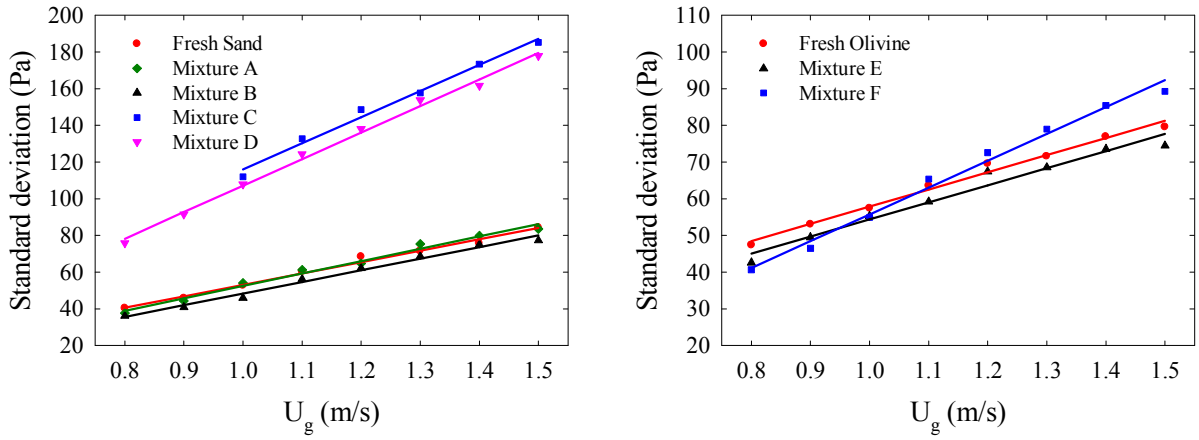

Figure 8.8: Standard deviation of in-bed gauge pressure signals for fresh and spent silica sand and olivine particles at different temperatures. Fresh and spent silica sand particles at (a) 900°C and (b) 1000°C; fresh and spent olivine particles at (c) 900°C and (d) 1000°C.

The fluidization behavior of spent silica sand particles was less affected by the Ca content at moderate levels of Na in the combusting solid fuel. An evident increase at all superficial gas velocities can, however, be realized for the standard deviations of in-bed gauge pressure signals after tests C and D compared to the fresh sand. This could be ascribed to a greater level of increase in cohesive IPFs by introducing more Na elements into the bed of silica sand particles, which increased the chance of low-melting silicate formation.

Since the magnitude of the standard deviation of pressure fluctuations recorded from a gas-solid fluidized bed has an intense relation with the mean bubble size [111], Figure 8.8 indicates that a small increase in the level of IPFs can slightly reduce the size of bubbles moving through the bed. The rate of increase in the mean amplitude of pressure fluctuations, or the bubble size, with the superficial gas velocity can increase when a higher level of IPFs are present in the bed whereas it practically remained unaffected at low levels of IPFs. This can result in the appearance of an inversion trend at moderate levels of IPFs in a bubbling bed while a high level of IPFs can yield the presence of much larger bubbles within the bed at all superficial gas velocities in the bubbling regime.

Increasing the level of IPFs increases the capability of the emulsion phase to hold more gas inside its structure [128] and enhances its resistance to any changes [112, 128]. Since the fluidizing gas is less prone to pass through a bubbling cohesive bed in the bubble phase [128], the bubble size

decreases leading to smaller pressure fluctuations at a given superficial gas velocity in the bubbling fluidization regime. When the level of IPFs is low, this evolution can extend over the whole range of gas velocities in the bubbling regime as the stalactites of particles can be effectively formed on the bubble's roof and contribute to the bubble splitting due to the minimal influence of a low level of IPFs on the quality of solids mixing. Nevertheless, increasing the magnitude of IPFs to a moderate level decreases the quality of solids mixing in the bubbling regime [107] and increases the apparent viscosity of the emulsion phase [129], which can reduce the formation frequency of stalactite of particles from the bubble's roof. It can, subsequently, yield less bubble splitting following Taylor instability [110]. As a consequence, the bubble size and, thus, the amplitude of pressure fluctuations increase at a higher rate with U_g at moderate levels of IPFs compared to a non-cohesive bed resulting in larger pressure fluctuations at a given superficial gas velocity above the inversion point whereas smaller pressure fluctuations can be observed at a given superficial gas velocity below the inversion point. When the level of IPFs is sufficiently high, larger bubbles with higher momentum can form within the bed even at low superficial gas velocities to compensate for the greater resistance of the emulsion phase against the flow. Bubbles under this condition can undergo a considerably faster enlargement with U_g as observed for the spent silica sands after tests C and D.

The variations in the standard deviations of in-bed gauge pressure signals for beds of fresh and spent silica sand and olivine particles versus the gas momentum flux are illustrated in Figure 8.9. It shows that, for each system tested, this parameter practically falls on a single straight line for the entire range of operating conditions investigated here. Nonetheless, different characteristic lines can be realized for different systems. In broad agreement with the results presented in Figure 8.8, it demonstrates that the presence of IPFs could effectively alter the bubble behavior resulting in completely different fluidization characteristics that cannot be predicted solely with the hydrodynamic considerations. Application of the in-bed differential pressure signals led to an identical conclusion.

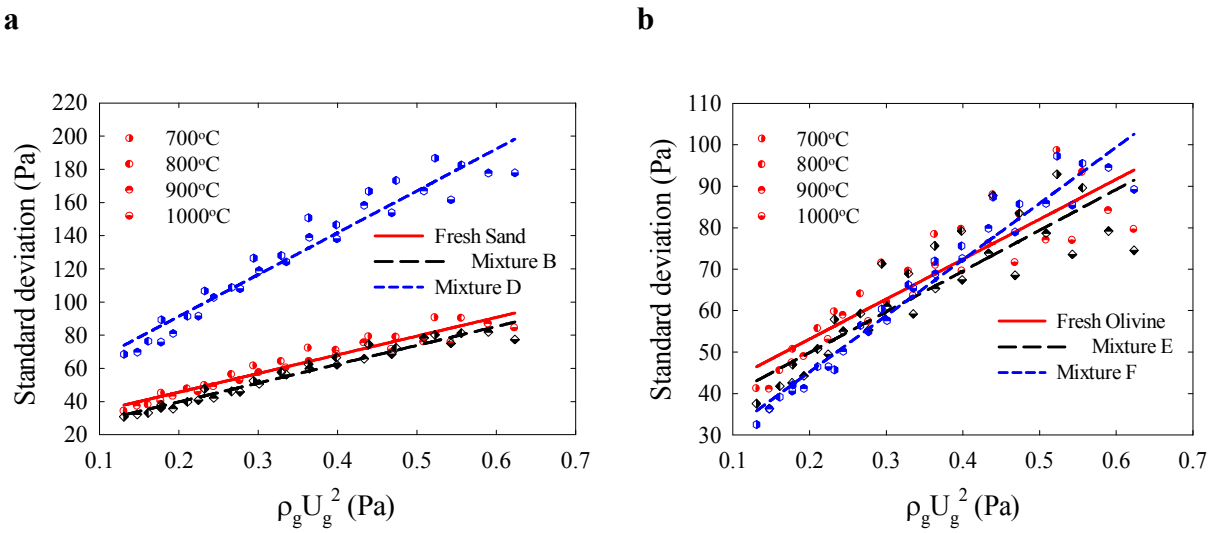

Figure 8.9: Variation of standard deviations of in-bed gauge pressure signals versus the gas momentum flux. (a) fresh and spent silica sand particles, (b) fresh and spent olivine particles.

8.6 Conclusion

1) As the temperature increases in a bed of fresh coarse particles, at temperatures well below the corresponding initial sintering temperature, the bubble size decreases while the bubble passage frequency remains relatively unaffected.

2) Increasing the level of IPFs increases the minimum fluidization velocity for a given powder.

3) The presence of different levels of IPFs in the bed can differently alter the fluidization characteristics in the bubbling regime.

4) A slight decrease in the bubble size is predicable when there is a minor increase in the level of IPFs within the bed.

5) In comparison with a non-cohesive bed, a bed with a moderate level of IPFs can contain smaller bubbles at superficial gas velocities close to U_{mf} and larger bubbles at higher gas velocities of the bubbling regime owing to an increase in the growth rate of bubble size with U_g at higher levels of IPFs. The inversion point shifts toward lower gas velocities upon increasing the level of IPFs.

6) The presence of a high level of IPFs in the bed, however, results in the formation of much larger (oblong) bubbles that pass through the bed less frequently.

8.7 Nomenclature

8.7.1 Acronyms

HDFs	hydrodynamic forces
IPFs	interparticle forces
MSW	municipal solid waste
PSD	power spectral density
XPS	X-ray photoelectron spectroscopy

8.7.2 Symbols

A_i	area of the peak for a given element in the resulted XPS measurement (eV.count/s)
d_c	column diameter (m)
d_p	mean particle size (μm)
h_0	static bed height (m)
n	power of absolute temperature; $\mu_g \propto T^n$, 0.6< n <1.0 (-)
Re_p	particle Reynolds number (-)
$RA\%$	relative atomic percentage (-)
SF_i	sensitivity factor for an element in XPS measurement (-)
T	absolute temperature (K)
T_m	melting temperature (°C)
U_c	transition velocity from bubbling to turbulent fluidization regime (m/s)
U_g	superficial gas velocity (m/s)
U_i	interstitial gas velocity (m/s)
U_{mf}	minimum fluidization velocity (m/s)
U_{mb}	minimum bubbling velocity (m/s)

8.7.3 Greek letters

ε_0	settled bed voidage (-)
ε_{mb}	minimum bubbling voidage (-)
ε_{mf}	minimum fluidization voidage (-)
μ_g	gas viscosity (Pa.s)
ρ_g	gas density (kg/m^3)
$\rho_g {U_g}^2$	gas momentum flux (Pa)
ρ_p	particle density (kg/m^3)

8.8 Acknowledgements

The financial support from the Total American Services, Inc. and the National Sciences and Engineering Research Council of Canada (NSERC) is acknowledged with gratitude. The authors would like to thank Mrs. Seyedeh Laleh Dashtban Kenari, Dr. Pierre Sauriol, Dr. Abdelmajid Rakib, and Mr. Diego Alejandro López Del Ángel for their assistance during the experimental activities. Thanks are also due to Dr. Rafael Salomão for dilatometry measurements at the University of São Paulo.

8.9 References

1) D. Kunii, O. Levenspiel, Fluidization Engineering, Butterworth-Heinemann, Boston, 1991.
2) J.G. Yates, Effects of temperature and pressure on gas-solid fluidization, Chem. Eng. Sci. 51 (1996) 167-205.
3) Jr.A.A. Wiltsee, C.R. McGowin, E.E. Hughes, Biomass combustion technologies for power generation, in: Proceedings of the First Biomass Conference of the Americas, 1993, pp. 347-367.
4) B. Formisani, R. Girimonte, L. Mancuso, Analysis of the fluidization process of particle beds at high temperature, Chem. Eng. Sci. 53 (1998) 951-961.
5) P. McKendry, Energy production from biomass (part 3): gasification technologies, Bioresour. Technol. 83 (2002) 55-63.

6) M. Bartels, W. Lin, J. Nijenhuis, F. Kapteijn, J.R. van Ommen, Agglomeration in fluidized beds at high temperatures: Mechanisms, detection and prevention, Prog. Energy Combust. Sci. 34 (2008) 633-666.

7) T.M. Knowlton, Pressure and temperature effects in fluid-particle systems, in: W.C. Yang (Ed.), Fluidization, Solids Handling and Processing: Industrial Applications, Noyes, New Jersy, 1999, pp. 111-152.

8) P. Lettieri, J.G. Yates, D. Newton, The influence of interparticle forces on the fluidization behaviour of some industrial materials at high temperature, Powder Technol. 110 (2000) 117-127.

9) P. Lettieri, D. Newton, J.G. Yates, High temperature effects on the dense phase properties of gas fluidized beds, Powder Technol. 120 (2001) 34-40.

10) J.S.M. Botterill, Y. Teoman, K.R. Yüregir, The effect of operating temperature on the velocity of minimum fluidization, bed voidage and general behavior, Powder Technol. 31 (1982) 101-110.

11) J.S.M. Botterill, Y. Teoman, K.R. Yüregir, The Effect of temperature on fluidized bed behavior, Chem. Eng. Commun. 15 (1982) 227-238.

12) A. Lucas, J. Arnaldos, J. Casal, L. Puigjaner, High temperature incipient fluidization in mono and polydisperese systems, Chem. Eng. Commun. 41 (1986) 121-132.

13) A. Mathur, S.C. Saxena, Particle classification scheme of saxena and ganzha and high-temperature bed voidage data at minimum fluidization, Powder Technol. 45 (1986) 287-289.

14) A. Mathur, S.C. Saxena, Z.F. Zhang, Hydrodynamic characteristics of gas-fluidized beds over a broad temperature range, Powder Technol. 47 (1986) 247-256.

15) S. Rapagna, P.U. Foscolo, L.G. Gibilaro, The influence of temperature on the quality of gas fluidization, Int. J. Multiphase Flow 20 (1994) 305-313.

16) H. Cui, J. Chaouki, Effects of temperature on local two-phase flow structure in bubbling and turbulent fluidized beds of FCC particles, Chem. Eng. Sci. 59 (2004) 3413-3422.

17) H. Cui, J. Chaouki, Interparticle forces in high temperature fluidization of geldart a particles, China Particuology 2 (2004) 113-118.

18) T.A. Alsmari, J.R. Grace, X.T. Bi, Effects of superficial gas velocity and temperature on entrainment and electrostatics in gas–solid fluidized beds, Chem. Eng. Sci. 123 (2015) 49-56.

19) G. Raso, M. D'Amore, B. Formisani, P.G. Lignola, The influence of temperature on the properties of the particulate phase at incipient fluidization, Powder Technol. 72 (1992) 71-76.

20) P. Lettieri, D. Newton, J.G. Yates, The effect of temperature on the deaeration rate of two silica powders. Comparison with standard correlations for a Group A and a Group C material, in: Proceedings of the 3rd World Congress on Particle Technology, Brighton, UK, 1998, pp. 2239-2250.

21) B. Formisani, R. Girimonte, G. Pataro, The influence of operating temperature on the dense phase properties of bubbling fluidized beds of solids, Powder Technol. 125 (2002) 28-38.

22) C. Xu, J.X. Zhu, Effects of gas type and temperature on fine particle fluidization, China Particuology 4 (2006) 114-121.

23) R. Girimonte, B. Formisani, The minimum bubbling velocity of fluidized beds operating at high temperature, Powder Technol. 189 (2009) 74-81.

24) G.H. Hong, R. Yamazaki, T. Takahashi, G. Jombo, Minimum fluidization velocity in a fluidized bed at high temperatures, Kagaku Kogaku Ronbunshu 6 (1980) 557-562.

25) R. Yamazaki, G.H. Hong, G. Jimbo. The behavior of a gas-solid fluidized bed at elevated temperatures, in: D. Kunii, R. Toei (Eds.), Proceedings of the 4th International Conference on Fluidization, Kashikojima, Japan, 1984, pp. 121-128.

26) R. Yamazaki, N. Ueda, G. Jimbo, Mechanism of incipient fluidization in fluidized bed at elevated temperature, J. Chem. Eng. Jpn. 19 (1986) 251-257.

27) R. Yamazaki, N.-S. Han, Z.-F. Sun, G. Jimbo, Effect of chemisorbed water on bed voidage of high temperature fluidized bed, Powder Technol. 84 (1995) 15-22.

28) D. Geldart, Types of gas fluidization, Powder Technol. 7 (1973) 285-292.

29) C.-L. Lin, M.-Y. Wey, S.-D. You, The effect of particle size distribution on minimum fluidization velocity at high temperature, Powder Technol. 126 (2002) 297-301.

30) Y. Zhong, Z. Wang, Z. Guo, Q. Tang, Defluidization behavior of iron powders at elevated temperature: Influence of fluidizing gas and particle adhesion, Powder Technol. 230 (2012) 225-231.

31) T.M. Knowlton, Pressure and temperature effects in fluid-particle systems, in: O.E. Potter, D.J. Nicklin (Eds.), Proceedings of the 7th International Conference on Fluidization, Engineering Foundation, New York, 1992, pp. 27-46.

32) S.Y. Wu, J. Baeyens, Effect of operating temperature on minimum fluidization velocity, Powder Technol. 67 (1991) 217-220.

33) Visser, J., Van der Waals and other cohesive forces affecting powder fluidization, Powder Technol. 58 (1989) 1-10.

34) J. Shabanian, R. Jafari, J. Chaouki, Fluidization of ultrafine powders-Review, Int. Rev. Chem. Eng. (IRECHE) 4 (2012) 16-50.

35) H. Krupp, Particle adhesion: theory and experiment, Adv. Colloid Interface Sci. 1 (1967) 111-239.

36) H. Rumpf, Particle adhesion, in: Proceedings of the 2nd International Symposium on Agglomeration (Agglomeration 77), AIME, 1977, pp. 97-129.

37) R.A. Bowling, A theoretical review of particle adhesion, in: K. Mittal (Ed.), Particles on Surfaces 1, Plenum Press, New York, 1988, pp. 129-142.

38) T. Kai, S. Furusaki, Behavior of fluidized beds of small particles at elevated temperatures, J. Chem. Eng. Jpn. 18 (1985) 113-118.

39) W.O. Moughrabiah, J.R. Grace, X.T. Bi, Effects of pressure, temperature, and gas velocity on electrostatics in gas−solid fluidized beds, Ind. Eng. Chem. Res. 48 (2009) 320-325.

40) S. Boggs, D.H. Damon, J. Hjerrild, J.T. Holboll, M. Henriksen, Effect of insulation properties on the field grading of solid dielectric DC cable, IEEE Trans. Power Delivery 16 (2001) 456-461.

41) P.K. Jain, N. Saxena, Temperature and composition dependence of electrical conductivity of Se90In10–xSbx (x=0, 2, 4, 6, 8, 10) chalcogenide glasses, J. Non-Oxide Photonic Glasses 1 (2009) 43-52.

42) P. Pagliai, S.J.R. Simons, D. Rhodes, Towards a fundamental understanding of defluidisation at high temperatures: a micro-mechanistic approach, Powder Technol. 148 (2004) 106-112.

43) J.P.K. Seville, C.D. Willett, P.C. Knight, Interparticle forces in fluidisation: a review, Powder Technol. 113 (2000) 261-268.

44) J.H. Siegell, High-temperature de fluidization, Powder Technol. 38 (1984) 13-22.

45) G. Tardos, R. Pfeffer, Chemical reaction induced agglomeration and defluidization of fluidized beds, Powder Technol. 85 (1995) 29-35.

46) A.R. Manzoori, E.R. Lindner, P.K. Agarwal, Inorganic transformation during the circulating fluid bed combustion of low-rank coals with high content of sodium and sulphur, in:

Proceedings of the Engineering Foundation Conference on Inorganic Transformations and Ash Deposition During Combustion, Palm Coast, Florida, USA, 1991, pp. 735-762.

47) J. Werther, M. Saenger, E. U. Hartge, T. Ogada, Z. Siagi, Combustion of agricultural residues, Prog. Energy Combust. Sci. 26 (2000) 1-27.

48) W. Lin, K. Dam-Johansen, F. Frandsen, Agglomeration in bio-fuel fired fluidized bed combustors, Chem. Eng. J. 96 (2003) 171-185.

49) C. Tangsathitkulchai, M. Tangsathitkulchai, Effect of bed materials and additives on the sintering of coal ashes relevant to agglomeration in fluidized bed combustion, Fuel Process. Technol. 72 (2001) 163-183.

50) B.M. Steenari, O. Lindqvist, V. Langer, Ash sintering and deposit formation in PFBC, Fuel 77 (1998) 407-417.

51) M. Öhman, A. Nordin, B.-J. Skrifvars, R. Backman, M. Hupo, Bed agglomeration characteristics during fluidized bed combustion of biomass fuels, Energy Fuels 14 (2000) 169-178.

52) J. van Caneghem, A. Brems, P. Lievens, C. Block, P. Billen, I. Vermeulen, R. Dewil, J. Baeyens, C. Vandecastteele, Fluidized bed waste incinerators: Design, operational and environmental issues, Prog. Energy Combust. Sci. 38 (2012) 551-582.

53) T. Mii, K. Yoshida, D. Kunii, Temperature effects on the characteristics of fluidized beds, J. Chem. Eng. Jpn. 6 (1973) 100-102.

54) T. Otake, S. Tone, M. Kawashima, T. Shibata, Behavior of rising bubbles in gas-fluidized bed at elevated temperature, J. Chem. Eng. Jpn. 8 (1975) 388-392.

55) Geldart, D.S. Kapoor, Bubble sizes in a fluidized bed at elevated temperatures, Chem. Eng. Sci. 31 (1976) 842-843.

56) A. Desai, H. Kikukawa, A.H. Pulsifer, The effect of temperature upon minimum fluidization velocity, Powder Technol. 16 (1977) 143-144.

57) Geldart, A.R. Abrahamsen, Homogeneous fluidization of fine powders using various gases and pressures, Powder Technol. 19 (1978) 133-136.

58) M.A. Doheim, C.N. Collinge, Effect of temperature on incipient fluidization and study of bed expansion, Powder Technol. 21 (1978) 289-293.

59) R.R. Pattipati, C.Y. Wen, Minimum fluidization velocity at high temperatures, Ind. Eng. Chem. Process Des. Dev. 20 (1981) 705-707.

60) K. Svoboda, M. Hartman, Influence of temperature on incipient fluidization of limestone, lime, coal ash, and corundum, Ind. Eng. Chem. Process Des. Dev. 20 (1981) 319-326.

61) K. Svoboda, M. Hartman, Deviations of actual minimum fluidization velocities from theoretical predictions at different temperatures, AIChE J. 27 (1981) 866-869.

62) K. Wittmann, H. Helmrich, K. Schügerl, Measurements of bubble properties in continuously operated fluidized bed reactors at elevated temperatures, Chem. Eng. Sci. 36 (1981) 1673-1677.

63) G. Jimbo, R. Yamazaki, G.H. Hong, Y. Oka, The characteristics of high-temperature fluidized bed, in: M. Kwauk, D. Kunii (Eds.), Proceedings of the Fluidization Science and Technology China-Japan Symposium, 1982, pp. 135-145.

64) J.F. Stubington, D. Barrett, G. Lowry, Bubble size measurements and correlation in a fluidised bed at high temperatures, Chem. Eng. Res. Des. 62 (1984) 173-178.

65) A.W. Weimer, G.J. Quarderer, Effect of temperature on the dense phase in high pressure fluidized beds of fine powders, AIChE Symp. Ser. 80(241) (1984) 79-86.

66) M. Nakamura, Y. Hamada, S. Toyama, A.E. Fouda, C.E. Capes, An experimental investigation of minimum fluidization velocity at elevated temperatures and pressures, Can. J. Chem. Eng. 63 (1985) 8-13.

67) M. Hartman, K. Svoboda, Predicting the effect of operating temperature on the minimum fluidization velocity, Ind. Eng. Chem. Process Des. Dev. 25 (1986) 649-654.

68) C. Sishtla, I. Chan, T.M. Knowlton, The effect of temperature on bubble parameters in gas-fluidized beds, in: K. Ostergaard, A. Sorensen (Eds.), Proceedings of the 5th International Conference on Fluidization, 1986, pp. 127-134.

69) Y. Hatate, K. Ohmagari, A. Ikari, K. Kondo, D.F. King, Behavior of bubbles in a cylindrical fluidized bed at elevated temperature, J. Chem. Eng. Jpn. 21 (1988) 424-425.

70) H.Y. Xie, D. Geldart, Fluidization of FCC powders in the bubble-free regime: effect of types of gases and temperature, Powder Technol. 82 (1995) 269-277.

71) M.F. Llop, J. Casal, J. Arnaldos, Expansion of gas-solid fluidized beds at pressure and high temperature, Powder Technol. 107 (2000) 212-225.

72) Bruni, G., P. Lettieri, D. Newton, J. Yates, The influence of fines size distribution on the behaviour of gas fluidized beds at high temperature, Powder Technol. 163 (2006) 88-97.

73) R. Girimonte, B. Formisani, The effects of thermally induced interparticle forces on the expansion and bubbling behaviour of a fluidized bed, in: F. Berruti, X. Bi, T. Pugsley (Eds.), Proceedings of the 12th International Conference on Fluidization, Engineering Conferences International, Vancouver, Canada, 2007, pp. 177-184.

74) H.J. Subramani, M.B. Mothivel Balaiyya, L.R. Miranda, Minimum fluidization velocity at elevated temperatures for Geldart's group-B powders, Exp. Therm. Fluid Sci. 32 (2007) 166-173.

75) R. Girimonte, B. Formisani, Effects of operating temperature on the bubble phase properties in fluidized beds of FCC particles, Powder Technol. 262 (2014) 14-21.

76) P. Basu, A study of agglomeration of coal-ash in fluidized beds, Can. J. Chem. Eng. 60 (1982) 791-795.

77) P. Basu, A. Sarka, Agglomeration of coal ash in fluidized beds, Fuel 62 (1983) 924-926.

78) B. Liss, T.R. Blake, A.M. Squires, R. Bryson, Incipient defluidization of sinterable solids, in: D. Kunii, R. Toei (Eds.), Proceedings of the 4th International Conference on Fluidization, Kashikojima, Japan, 1984, pp. 249-256.

79) G. Tardos, D. Mazzone, R. Pfeffer, Destabilization of fluidized beds due to agglomeration part I: Theoretical model, Can. J. Chem. Eng. 63 (1985) 377-383.

80) G. Tardos, D. Mazzone, R. Pfeffer, Destabilization of fluidized beds due to agglomeration part II: Experimental verification, Can. J. Chem. Eng. 63 (1985) 384-389.

81) B.J. Ennis, G. Tardos, R. Pfeffer, A microlevel-based characterization of granulation phenomena, Powder Technol. 65 (1991) 257-272.

82) P. Cai, Y. Jin, Z.Q. Yu, Z.W. Wang, Effect of operating temperature and pressure on the transition from bubbling to turbulent fluidization, AIChE Symp. Ser. 85(270) (1989) 37-43.

83) A. Chehbouni, J. Chaouki, C. Guy, D. Klvana, Effect of temperature on the hydrodynamics of turbulent fluidized beds, in: C. Laguerie, J.F. Large (Eds.) Proceedings of the 8th International Conference on Fluidization, Engineering Foundation, New York, 1995, pp. 149-156.

84) H.T. Bi, J.R. Grace, Effects of pressure and temperature on flow regimes in gas-solid fluidization systems, Can. J. Chem. Eng. 74 (1996) 1025-1027.

85) P.K. Peeler, K.S. Lim, R.C. Close, Effect of temperature on the turbulent fluidization regime transition, in: J. Werther (Ed.), Proceedings of the 6th International Conference on Circulating Fluidized Beds, Würzburg, Germany, 1999, pp. 125-130.

86) S.E. George, J.R. Grace, Entrainment of particles from a pilot scale fluidized bed, Can. J. Chem. Eng. 59 (1981) 279-284.

87) J.G. Findlay, T.M. Knowlton, in: Final Report for U. S. Department of Energy, Project DE-AC21-83MC20314, 1985.

88) J.H. Choi, J.E. Son, S.D. Kim, Solid entrainment in fluidized bed combustors, J. Chem. Eng. Jpn. 22 (1989) 597-606.

89) J.-H. Choi, K.-B. Choi, P. Kim, D.-W. Shun, S.-D. Kim, The effect of temperature on particle entrainment rate in a gas fluidized bed, Powder Technol. 92 (1997) 127-133.

90) J.-H. Choi, H.-J. Ryu, D.-W. Shun, J.-E. Son, S.-D. Kim, Temperature effect on the particle entrainment rate in a gas fluidized bed, Ind. Eng. Chem. Res. 37 (1998) 1130-1135.

91) I.M.F. Wouters, D. Geldart, Entrainment at high temperatures, in: L.-S. Fan, T.M. Knowlton (Eds.), Proceedings of the 9th Engineering Foundation Conference on Fluidization, Engineering Foundation, New York, 1998, pp. 341-348.

92) J.-H. Choi, S.D. Kim, J.R. Grace, Entrainment rate of coarse particles at different temperatures in gas fluidized beds, Can. J. Chem. Eng. 85 (2007) 151-157.

93) K. Svoboda, J. Cermak, M. Hartman, J. Drahos, K. Selucky, Pressure fluctuations in gas-fluidized beds at elevated temperatures, Ind. Eng. Chem. Process Des. Dev. 22 (1983) 514-520.

94) S.C. Saxena, N.S. Rao, S.J. Zhou, Fluidization characteristics of gas fluidized beds at elevated temperatures, Energy 15 (1990) 1001-1014.

95) S. Qian, J. Lu, G. Flamant, Fluidization characteristics of gas-solid fluidized bed at elevated temperature, J. Combust. Sci. Technol. 3 (1997) 344-348.

96) Q. Guo, G. Yue, T. Suda, J. Sato, Flow characteristics in a bubbling fluidized bed at elevated temperature, Chem. Eng. Process. Process Intensif. 42 (2003) 439-447.

97) S. Sanaei, N. Mostoufi, R. Radmanesh, R. Sotudeh-Gharebagh, C. Guy, J. Chaouki, Hydrodynamic characteristics of gas-solid fluidization at high temperature, Can. J. Chem. Eng. 88 (2010) 1-11.

98) M.R. Tamadondar, R. Zarghami, H. Azizpour, N. Mostoufi, J. Chaouki, R. Radmanesh, Using S-statistic for investigating the effect of temperature on hydrodynamics of gas–solid fluidization, Particuology 11 (2012) 288-293.

99) J.F. Davidson, The two-phase theory of fluidization: successes and opportunities, AIChE Symp. Ser. 281(87) (1991) 1-12.

100) C.Y. Wen, Y.H. Yu, Mechanics of fluidization, Chem. Eng. Prog. Symp. Ser. 62 (1966) 100-111.

101) D.C. Chitester, R.M. Kornosky, L.-S. Fan, J.P. Danko, Characteristics of fluidization at high pressure, Chem. Eng. Sci. 39 (1984) 253-261.

102) O. Molerus, Interpretation of Geldart's type A, B, C and D powders by taking into account interparticle cohesion forces, Powder Technol. 33 (1982) 81-87.

103) P. Compo, G.I. Tardos, D. Mazzone, R. Pfeffer, Minimum sintering temperatures of fluidizable particles, Part. Part. Syst. Charact. 1 (1984) 171-177.

104) P. Compo, R. Pfeffer, G.I. Tardos, Minimum sintering temperatures and defluidization characteristics of fluidizable particles, Powder Technol. 51 (1987) 85-101.

105) J. Werther, O. Molerus, The local structure of gas fluidized beds-II. The spatial distribution of bubbles, Int. J. Multiphase Flow 1 (1973) 123-138.

106) M. Stein, Y.L. Ding, J.P.K. Seville, D.J. Parker, Solids motion in bubbling gas fluidised beds, Chem. Eng. Sci. 55 (2000) 5291-5300.

107) J. Shabanian, J. Chaouki, Influence of interparticle forces on solids motion in a bubbling gas-solid fluidized bed, Powder Technol. (2015) submitted for publication.

108) J. Yerushalmi, N.T. Cankurt, Further studies of the regimes of fluidization, Powder Technol. 24 (1979) 187-205.

109) R.B. Bird, W.E. Stewart, E.N. Lightfoot, Transport Phenomena, John Wiley & Sons Inc., New York, 2002.

110) R. Clift, J.R. Grace, The mechanism of bubble break-up in fluidised beds, Chem. Eng. Sci. 27 (1972) 2309-2310.

111) N. Sadasivan, D. Barreteau, C. Laguerie, Studies on frequency and magnitude of fluctuations of pressure drop in gas-solid fluidized beds, Powder Technol. 26 (1980) 67-74.

112) J. Shabanian, J. Chaouki, Hydrodynamics of a gas–solid fluidized bed with thermally induced interparticle forces, Chem. Eng. J. 259 (2015) 135-152.

113) G.-B. Zhao, Y.-R. Yang, Multiscale resolution of fluidized-bed pressure fluctuations, AIChE J. 49 (2003) 869-882.

114) F. Johnsson, R.C. Zijerveld, J.C. Schoutten, C.M. van den Bleek, B. Leckner, Characterization of fluidization regimes by time-series analysis of pressure fluctuations, Int. J. Multiphase Flow 26 (2000) 663-715.

115) J. Li, J.A.M. Kuipers, Effect of pressure on gas-solid flow behavior in dense gas-fluidized beds: a discrete particle simulation study, Powder Technol. 127 (2002) 173-184.

116) I. Palchonok, C. Breitholtz, H. Thunman, B. Leckner, Impact of heat and mass transfer on combustion of a fuel particle in CFB boilers, in: F.D.S. Preto (Ed.), Proceedings of the 14th International Conference on Fluidized Bed Combustion, ASME, vol. 2, 1997, pp. 871-878.

117) J.-H. Kuo, C.-L. Lin, M.-Y. Wey, Effect of alkali concentrations and operating conditions on agglomeration/defluidization behavior during fluidized bed air gasification, Powder Technol. 214 (2011) 443-446.

118) C.D. Wagner, L.E. Davis, M.V. Zeller, J.A. Taylor, R.H. Raymond, L.H. Gale, Empirical atomic sensitivity factors for quantitative analysis by electron spectroscopy for chemical analysis, Surf. Interface Anal. 3 (1981) 211-225.

119) X. Fan, D.J. Parker, Z. Yang, J.P.K. Seville, J. Baeyens, The effect of bed materials on the solid/bubble motion in a fluidised bed, Chem. Eng. Sci. 63 (2008) 943-950.

120) C.-L. Lin, M.-Y. Wey, The effect of mineral compositions of waste and operating conditions on particle agglomeration/defluidization during incineration, Fuel 83 (2004) 2335-2343.

121) C.-L. Lin, J.-H. Kuo, M.-Y. Wey, S.-H. Chang, K.-S. Wang, Inhibition and promotion: The effect of earth alkali metals and operating temperature on particle agglomeration/defluidization during incineration in fluidized bed, Powder Technol. 189 (2009) 57-63.

122) J.-H. Kuo, C.-L. Lin, M.-Y. Wey, Effects of agglomeration processes on the emission characteristics of heavy metals under different waste compositions and the addition of Al and Ca inhibitors in fluidized bed incineration, Energy Fuels 23 (2009) 4325-4336.

123) J.-H. Kuo, C.-L. Lin, M.-Y. Wey, Mechanisms of particle agglomeration and inhibition approach in the existence of heavy metals during fluidized bed incineration, Chem. Eng. Sci. 65 (2010) 4955-4966.

124) M.J. Gluckman, J. Yerushalmi, A.M. Squires, Defluidization characteristics of sticky materials on agglomerating bed, in: D.L. Keairns (Ed.), Fluidization Technology, 1976, pp. 395-422.

125) E.M. Levin, H.F. McMurdie, F.P. Hall, Phase Diagrams for Ceramists, The American Ceramic Society, Ohio, 1956.

126) K.A. Shahid, F.P. Glasser, Phase equilibria in the glass forming region of the system Na2O-CaO-SiO2, Phys. Chem. Glasses 12 (1971) 50-57.

127) G. Olofsson, Z. Ye, I. Bjerle, A. Andersson, Bed agglomeration problems in fluidized-bed biomass combustion, Ind. Eng. Chem. Res. 41 (2002) 2888-2894.

128) J. Shabanian, J. Chaouki, Local characterization of a gas-solid fluidized bed in the presence of thermally induced interparticle forces, Chem. Eng. Sci. 119 (2014) 261-273.

129) K. Schügerl, Rheological behaviour of fluidized systems, in: J.F. Davidson, D. Harrison (Eds.) Fluidization, Academic Press, London, 1971, pp. 261-292.

CHAPTER 9 ARTICLE 7: APPLICATION OF TEMPERATURE AND PRESSURE SIGNALS FOR EARLY DETECTION OF DEFLUIDIZATION CONDITIONS

Jaber Shabanian, Pierre Sauriol, Abdelmajid Rakib, Jamal Chaouki*

Department of Chemical Engineering, Ecole Polytechnique de Montreal, Montreal, Quebec, Canada

* Corresponding author: Tel.: +1-514-340-4711 X 4034; fax: +1-514-340-4159.

E-mail address: jamal.chaouki@polymtl.ca

(Published in Procedia Engineering 102 (2015) 1006–1015)

9.1 Abstract

This work shows that simultaneous measurements of temperature and pressure signals for a bubbling gas-solid fluidized bed can be considered as a simple and effective early detection technique of defluidization conditions. The modification of the hydrodynamics of the bed due to the presence of interparticle forces (IPFs) was primarily investigated using different measurement techniques (i.e., pressure transducers, optical fiber probe, and Radioactive Particle Tracking). Different levels of IPFs were attained in the bed with the help of a polymer coating approach at near-ambient temperature (30–40^{o}C) in a 15 cm ID fluidized bed. Experimental results showed that by increasing the degree of IPFs in the bed, larger bubbles were noted at gas velocities well above the minimum fluidization velocity, the emulsion phase voidage increased, and the mean value of the in-bed differential bed pressure drop and the axial solids mixing decreased. The high temperature defluidization tests (800–1000^{o}C) as the second part the experimental campaign were conducted in a 20 cm ID fluidized bed reactor. It was found that the temperature difference between the bottommost thermocouple (located 5 cm above the distributor) and the others located in the dense bed was continuously increasing when the bed was approaching defluidization. Simultaneously, the mean value of the differential pressure signals was successively decreasing from its regular value under normal conditions. A combination of these two conditions was considered as the monitoring method for the early detection of defluidization. It was found that this approach was effectively capable of predicting the onset of defluidization minutes to hours before complete defluidization, allowing time to apply counteracting strategies. Experimental results of the first part of the work clearly demonstrated why the simple integrated approach discovered in

the second part of the study can be efficiently used for timely recognition of defluidization conditions.

Keywords: Defluidization detection; Gas-solid fluidized bed; Temperature measurements; Differential pressure fluctuation measurements

9.2 Introduction

With the rarefaction of conventional energy feedstocks and the efforts to reduce greenhouse gas emissions, it is expected that high temperature fluidized beds are going to be adapted to process new or unconventional energy feedstocks (biomass, various waste materials, low grade coal) or blends (co-firing with conventional fuels). However, these new feedstocks may have high alkali/alkali earth content, which are known to form low melting eutectics at elevated temperatures. The presence of these eutectics inside the bed can induce the formation of agglomerates (bed material and ash), which when accumulating may eventually result in the defluidization of the bed and the unscheduled shut down of the plant. It is thus important to prevent or delay the onset of defluidization incidents. There are a number of counteracting strategies for delaying the onset of defluidization (e.g., lowering the temperature, increasing the superficial gas velocity, high velocity jets, injection of solid additives, semicontinuous replacement of bed material). As these strategies can incur a temporary offset of the fluidized bed performance (e.g., lower efficiency, residue production or added material cost), they should be used sparingly upon opportune detection of the onset of defluidization.

Siegell [1] described the defluidization phenomenon as a direct consequence of the stickiness of bed material. Different methods have been proposed to determine if the bed behavior is moving toward a defluidization state or not. The simplicity, reliability, and robustness of the identification approach as well as its capability for early detection are the most important criteria. Siegell [2] and Tardos et al. [3, 4] were the first to introduce that defluidization is accompanied by a rapid decrease in the total bed pressure drop because most of the fluidizing gas flows through large channels when defluidization occurs. The main drawback with this method is late detection, i.e., when the bed is already partially defluidized. Several other measurement tools, such as capacitance and optical fiber probes, heat transfer probes, and electrodes for measuring triboelectric current [5], which have small measurement volumes, are only useful for determining whether or not small regions are

defluidized [6]. These approaches would require many measurement points for a large-scale fluidized bed. Furthermore, these intricate measurement techniques, which are frequently used in academia, have not seen widespread use in industrial applications. On the other hand, temperature and pressure measurements are the only routine measurements available for industrial fluidized beds [7].

In comparison to the other measurement techniques considered, pressure probes have a much larger detection volume (in the order of some tens of centimeters) [8, 9]. Accordingly, they can provide more practical information with the least number of measurement points about the quality of the fluidization. Moreover, the measurement of pressure signals in a gas-solid fluidized bed is relatively easy to perform, nonintrusive, cost-effective and includes the impact of many phenomena happening in the bed, such as bubble formation, coalescence, eruption, movement and bed mass oscillations [10, 11]. Chirone et al. [12] had applied a relatively simple method, i.e., variance of pressure signals, for the early detection of defluidization. However, since the standard deviation/variance of pressure signals recorded from a gas-solid fluidized bed depends on fluctuations in the gas flow [13], this method is too sensitive to other process changes, leading to false alarms. Hence, this is not considered as a reliable approach for the advanced detection of defluidization in an industrial process [14]. Van Ommen et al. [15] developed an attractor comparison approach that is based on the measurement of pressure signals in the bed for the early warning of defluidization. Although, this technique demonstrated a good performance in the timely recognition of defluidization on both laboratory and pilot scale fluidized beds, it requires many mathematical manipulations and suffers from occasional false alarms, especially when an operational strategy is applied to the system to prevent complete defluidization [14]. This could be principally due to the sole dependence of the detection method on the pressure measurements. The temperature measurements can provide indirect information about the fluidization characteristics, but require considerable insight into the corresponding process to result in a correct interpretation [7].

It can be inferred that the sole application of either temperature or pressure signals alone cannot yield a simple, robust and efficient method for the early detection of defluidization, as the risk of false positives and false negatives has been observed, especially when applying operational changes to a system. The present work will attempt to propose a robust criterion for the early detection of the defluidization phenomenon using temperature and pressure signal data, specifically

targeted at the conditions that may exist in a bubbling fluidized bed combustor using coarse sand particles as bed material.

Before attempting to implement the technique at high temperature conditions, the first part of the work focused on the study of bubbling fluidized beds of model particles with varying degrees of IPFs at near-ambient conditions (e.g., 30–40oC). In particular, the polymer coating approach [16, 17] was used to introduce different levels of IPFs into a gas-solid fluidized bed. Different measurement techniques (i.e., pressure transducers, optical fiber probe, and Radioactive Particle Tracking (RPT)) were applied with this approach to both locally and globally highlight the effect of IPFs on the fluidization behavior of the bed. The findings were then extrapolated to high temperature conditions.

9.3 Experimental

9.3.1 Investigation of the effect of IPFs on the hydrodynamics of the bed

The first experimental step was to study the influence of IPFs on the fluidization behavior of the bed. A polymer coating approach [16, 17] was employed to enhance and adjust the level of cohesive IPFs in a gas-solid fluidized bed. The experimental work initially required the production of base particles uniformly coated with a thin polymer film of PMMA/PEA (Poly Methyl MethAcrylate/Poly Ethyl Acrylate). It was achieved through an atomization process in a spheronizer machine. A 450-700 μm cut of spherical sugar beads (dp=580 μm, ρp=1556 kg/m^3), which belong to Geldart group B particles at ambient conditions, was used as the inert base particles. The thickness of the coating layer was approximately 5.0 μm. Details of the coating procedure and its operating conditions have been previously outlined [16, 18-20].

Following the coating process, the coated particles and the fresh sugar beads were separately used in a cold gas-solid fluidized bed operating under atmospheric pressure with a 15.2 cm internal diameter. Dried and filtered air was used as the fluidizing gas and introduced through a perforated distributor plate (consisting of 157 holes 1 mm in diameter) into the column. In order to investigate the effect of IPFs on the fluidization behavior of the bed, experiments with fresh sugar beads as the base system without IPFs were conducted at 20^{o}C while experiments with the coated sugar beads were carried out at 30^{o}C and 40^{o}C. For the sake of simplicity these systems are referred to by their corresponding operating temperatures, SB20, CSB30, and CSB40, which stand for fresh sugar

beads at 20°C, and coated sugar beads at 30°C and 40°C, respectively. At each temperature tested, different superficial gas velocities were used (up to 1.3 m/s), covering both bubbling and turbulent fluidization regimes.

The fluidization tests were carried out for the purpose of hydrodynamic study employing different measurement techniques, i.e., pressure transducers, optical fiber probe, and RPT. Measurements of the pressure signals were taken by the application of four individual pressure transducers and carried out by measuring the bed pressure drop (0.95–300 cm above the distributor), and registering the gauge and differential pressure signals in the dense bed (17.5 cm and 10–25 cm above the distributor, respectively) and the gauge pressure signals in the windbox. A reflective type solids concentration optical fiber probe, located at the center of the column and 20 cm in height above the distributor, was also used to measure the instantaneous local bed voidage. For the fluidization tests with these two measurement techniques 4.0 kg of material were introduced into the bed, which resulted in a static bed height of approximately 26 cm (h/D≈1.7) at ambient conditions. Measurements of the pressure signals and the instantaneous local bed voidage were simultaneously carried out for a period of four minutes with a sampling frequency of 400 Hz at each superficial gas velocity and temperature tested. The calibration curve developed by Cui et al. [21] was employed to calibrate the optical fiber probe. Hydrodynamic tests with the application of the RPT technique were carried out for SB20 and CSB40 at two different superficial gas velocities (0.30 and 0.50 m/s) in the bubbling regime while 3 kg of material were introduced into the column. A sampling time of 10 ms was used in these tests and each experiment lasted 4 hours. More detail about the RPT experiment can be found elsewhere [20].

9.3.2 High temperature defluidization tests

All experiments related to high temperature defluidization were conducted in an atmospheric pressure pilot scale fluidized bed reactor with a 20 cm internal diameter. Air was used as the fluidizing gas and injected through a bubble cap distributor plate (with 9 caps each having 4 holes on its perimeter) into the column. For this investigation, the bed consisted of about 30 kg of coarse silica sand (dp=830 μm, ρ_p=2650 kg/m^3). Thermocouples were positioned along the length of the fluidized bed with the bottommost one located only 5 cm above the distributor. Using these thermocouples the uniformity of the temperature profile along the bed could be monitored. Also, two differential pressure transducers recorded pressure signals from the bed. One was used to

approximately measure the total pressure drop across the bed (5–130 cm above the distributor). The other one recorded the differential pressure drop from the central part of the dense bed (15–45 cm above the distributor). Throughout the runs, the superficial velocity of the air entering the fluidized bed was kept constant at 1 m/s. The bed defluidization was induced by combusting coal coated with alkali/alkali-earth containing materials. The bed was successively operated for periods of 1 hour at a time at 800, 900 and 1000ºC using the same solid fuel. Propane gas was used between each temperature point to increase the bed temperature. In cases where the alkali content was high enough, the bed became defluidized either in the heat-up pass with propane or during the solid fuel combustion. Pressure and temperature measurements were simultaneously conducted during the test with the sampling frequencies of 400 and 1 Hz, respectively.

9.4 Results and discussion

9.4.1 Effect of IPFs on the hydrodynamics of the bed

Van der Schaaf et al. [10] proposed a frequency-domain-based approach to be applied on the pressure signals recorded in the dense bed to estimate the bubble length scale in the bed. In this method, the registered in-bed gauge/absolute pressure signals are decomposed into their coherent (≈ COP) and incoherent (≈ IOP) power spectral densities by a frequency-domain-based coherence function in relation to identical types of pressure signals recorded in the windbox. The IOP component represents the power spectral density of pressure signals arising from the local bubble passage. Therefore, according to Parseval's theorem, the integral of IOP in the frequency domain yields the variance of the IOP components of pressure signals in the time domain. This is proportional to the characteristic length scale of the bubble, which is an approximation of the exact volume-based average bubble size [22].

Figure 9.1 illustrates the bubble sizes estimated by the IOP method as a function of gas velocity Ug for systems differing in the level of IPFs. An approximately linear increase in the estimated bubble size with the gas velocity can be found in Figure 9.1 for all systems studied. The slope in the bubble size versus gas velocity increased with IPFs while a bed with a higher level of IPFs contained slightly smaller bubbles at low gas velocities. It covered the range of gas velocities approximately below 3Umf, SB20, where Umf, SB20 is the minimum fluidization for SB20 (0.18 m/s). This behavior resulted in a trend inversion at moderate gas velocity. The CSB40, a system with the

highest level of IPFs, contained the largest bubbles at gas velocities above 0.65 m/s. It should be noted that depending on the level of IPFs and physical properties of the fluidizing gas and particles, the inversion trend can happen at different ratios of Ug/Umf, No IPFs. It can be also found that by increasing the level of IPFs, the transition velocity from bubbling to turbulent regime Uc, where large bubbles are replaced by smaller and transient voids [23], increased toward higher gas velocities.

The method of the minimum probability of local bed voidage [24] was employed to distinguish the emulsion phase from the bubble phase from the instantaneous local bed voidage signals measured by the optical fiber probe. Subsequently, the time-averaged voidage of the emulsion phase was calculated at each operating condition and plotted in Figure 9.2. It shows that the emulsion phase voidage εe progressively increased with the level of IPFs for the gas velocities below 0.7 m/s, where all systems were operating in the bubbling regime from the meso-scale point of view [20]. This implies that the capacity of the emulsion phase for holding the fluidizing gas inside its structure increased with the degree of IPFs in the gas-solid fluidized bed. The presence of a plateau-like region for the variation of the emulsion phase voidage with the gas velocity confirms the resistance shown by the emulsion phase against the complete breakdown of its continuous structure. The complete breakdown of the emulsion phase, which can be translated into the disappearance of the stable two-phase flow structure with a clear boundary between the bubble and emulsion phases, is necessary for the local flow regime transition from bubbling to turbulent [20, 25]. It can be observed from Figure 9.2 that this stable level occurred at lower gas velocities and covered a narrower velocity range for systems with a lower amount of IPFs. This indicates that IPFs can stabilize the emulsion phase from any changes that can be imposed on its structure; hence, the formation of the stalactite of particles on the bubble's roof, which is responsible for the bubble splitting [26], decreases with IPFs. Accordingly, the rate of bubble splitting decreases by increasing the level of IPFs in the bed. This results in a slight increase in the growth rate of bubbles with the gas velocity and also an increase in Uc for a system with a higher degree of IPFs (refer to Figure 9.1).

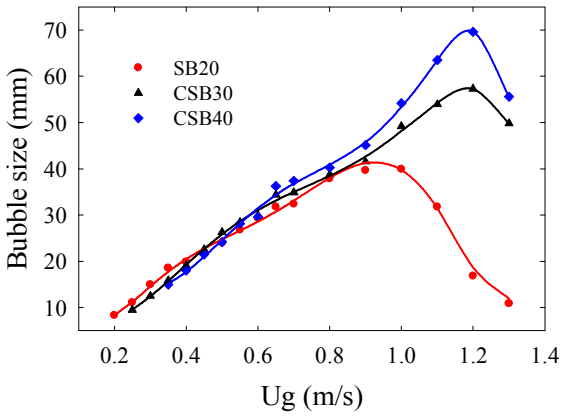

Figure 9.1: Influence of IPFs on the bubble size estimated by IOP method.

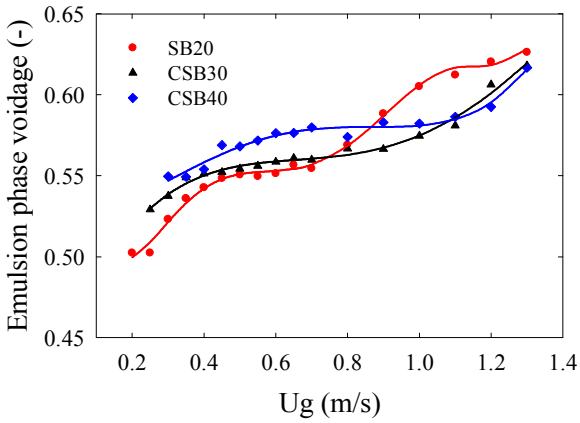

Figure 9.2: Influence of IPFs on the emulsion phase voidage.

By considering Figure 9.1 in conjunction with Figure 9.2, it can be found that εe was perceptibly smaller for SB20 in comparison with CSB30 and CSB40 for gas velocities below 0.5 m/s. In this range of low gas velocities, the emulsion phase was the main constituent of the bed while slightly smaller bubbles were noted for a bed with a higher degree of IPFs. These hydrodynamic modifications suggest that if differential pressure drop signals are measured for the central (well stabilized) part of the dense bed while it is operating at low gas velocities, the average in-bed differential pressure drop decreases with IPFs since the permeability of the emulsion phase can be greatly enhanced by IPFs. At moderate and high gas velocities (0.5-0.9 m/s), where all beds were operating in the bubbling regime (refer to Figure 9.1), the emulsion phase remained more diluted for a bed with a higher level of IPFs while it contained larger bubbles. Thus, an increase in the level of IPFs under such operating conditions offers a higher reduction in the mean value of the in-bed differential pressure drop measurement. In a consistent manner, it can be found in

Figure 9.3 that the average in-bed differential pressure drop measured by a corresponding pressure sensor for the stabilized section of the bubbling dense bed was lower for beds with stronger IPFs, while the total bed pressure drops of systems with different levels of IPFs were closely identical to each other. By a progressive increase in the level of IPFs, it is expected that the mean value of the in-bed differential pressure drop further decreases and even demonstrates a sudden decrease once the bed is at the final defluidization state. This could be accompanied by a rapid decrease in the total pressure drop of the bed. The presence of large channels that form throughout the bed by the

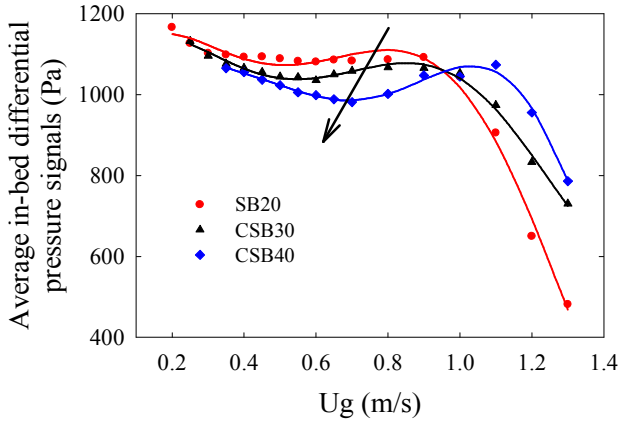

Figure 9.3: Influence of IPFs on the average in-bed differential pressure signals.

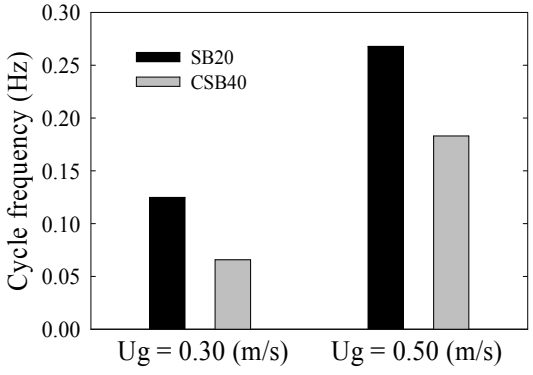

Figure 9.4: Influence of IPFs on the cycle frequency.

fluidizing gas under that operating condition is primarily responsible for this behavior. At gas velocities higher than 0.9 m/s, complex trends for the in-bed differential pressure drops of systems with different levels of IPFs can be noted since SB20 transferred into the turbulent regime first and the amount of bed material decreased due to entrainment. Accordingly, the reduction in the mean value of the in-bed differential pressure drop due to the increase in the level of IPFs is credible for the span of gas velocities below the transition velocity from bubbling to turbulent regime for a bed without IPFs (Uc,No IPFs).

In the bubbling fluidized beds, the passage of bubbles plays the principle role in the formation and evolution of the flow structure of the bed as well as the movements of particles, more generally solids mixing. Also, the heat and mass transfer rates are in close relation with the solids motion in the bed [27]. Particles are carried by the rising bubbles to the splash zone. To compensate this upward movement, a downward flow of particles along the annulus exists in the bed. Stein et al. [28] defined the cycle frequency, as the average frequency of a tracer particle to complete a cycle that starts in the bottom 30% of the dense bed height, takes it to the top 30% and returns it back to the bottom, as a characteristic of the axial solids mixing in the bed.

The time-position trajectory of particles obtained from the RPT experiments was used to calculate the cycle frequency under different operating conditions.

Figure 9.4 illustrates the results of this evaluation. It shows that the cycle frequency increased by the gas velocity for both SB20 and CSB40 in the bubbling regime. This can be attributed to the

increase in the turbulent activity of bubbles in the bed; hence, particles can be more frequently picked up by the rising bubbles, move with them toward the splash zone and return back to the bottom zone of the bed with a higher rate to maintain the continuity. The cycle frequency decreased by increasing the level of IPFs. It reveals that axial movement of particles occurred with a higher degree of difficulty in a bed with stronger IPFs. In general, the high degree of solids mixing is responsible for the uniformity of temperature and composition in the fluidized bed [27]. Therefore, this result suggests that increasing the level of IPFs decreases the axial solids mixing in the bubbling fluidized bed. This can in turn reduce the temperature uniformity (increase the temperature gradient) along the bed height.

The experimental results obtained from the first part of this study provided two promising findings in relation to the early detection of defluidization for a bubbling gas-solid fluidized bed. It can be inferred that by moving toward the defluidization condition the average in-bed differential bed pressure drop decreases whereas the axial temperature gradient increases. The simultaneousness of the two observations as the bubbling fluidized bed approaches defluidization lends credence to the two independent measurement techniques that could be used to yield a robust defluidization early detection criterion. The second part of this study focuses on high temperature defluidization experiments to verify this hypothesis.

9.4.2 Early detection of defluidization conditions

Defluidization occurred in many high temperature experiments either during the solid fuel combustion or the subsequent heating step between the predefined operating temperatures (800, 900, and 1000^{o}C) by the in-bed combustion of propane. All high temperature defluidization experiments exhibited a qualitatively similar behavior. Hence, a typical example is provided here.

Figure 9.5-7 show the temperature, total bed pressure drop, and in-bed differential pressure drop profiles as function of operating time for a fluidized bed that became defluidized during the experimental campaign. The bed was fluidizing well during the solid fuel combustion at 900^{o}C, which can be observed from the bed axial temperature profile. However, upon increasing the bed temperature, starting around the operating time 460 min, the readings of T4 (the bottommost thermocouple located only 5 cm above the distributor) began to deviate from those of other in-bed thermocouples. Simultaneously, a slight decrease in the in-bed differential pressure drop was observed. Nonetheless, no sensible change was noted for the total bed pressure drop. While not

applying counteractive methods, these trends persisted until the complete defluidization of the bed some 40 minutes after the initial observation. Around the operating time 470 min, the difference between the readings of T4 and T6 (20 cm above the distributor) was about 15-20^{o}C while this difference was less than 8oC under normal conditions. Also, a reduction of about 8% in the average in-bed differential pressure drop could be noted at the same time. In addition to the decrease in the quality of axial solids mixing when the bed is affected by the presence of IPFs, there could be also some small agglomerates being present in the lower section of the bed, hence, further deteriorating the solids mixing and resulting in a higher temperature gradient. It is worth mentioning that a variation of less than 3% was measured for the average in-bed differential pressure drop for the span of gas velocities and bed temperatures between 0.8–1.2 m/s and 800–1000^{o}C, respectively, when the bed was operating in the bubbling regime. This shows the relative independence of this parameter from variations in the gas velocity and operating temperature in the ranges tested. The decrease in the average in-bed differential pressure drop and increase in the temperature gradient clearly accelerated as the bed was further approaching the point of defluidization. The bed eventually became partially/completely defluidized around the operating time 500 min, where rapid decreases in the whole bed and in-bed differential pressure drops were noted, most likely due to the passage of fluidizing gas within the bed through channels. They were accompanied by a completely erratic behavior in the temperature profile in the bed, as the loss of fluidization (locally) results in a decrease in the heat transfer rate between the solid-gas and the thermocouple.

This experimental sample confirms that monitoring the whole bed pressure drop results in a very late detection of the defluidization condition. It also demonstrates that the simultaneous monitoring of the temperature profile with a special attention to the temperature difference between the bottommost level and higher levels in the dense bed and the in-bed differential pressure drop for the bed material considered can effectively identify the defluidization phenomenon much earlier than the final state. It also shows that both of these trends can concurrently take place when the level of IPFs is high enough to drive a bubbling bed of coarse silica sand toward the final defluidization point. Although this is a simple approach, its promising performance in the advanced recognition of defluidization allows appropriate measures to be taken to avoid a potential shutdown. According to this method, the operating time at which both of these trends are simultaneously noted for a bubbling gas solid fluidized bed (while the gas velocity remains relatively constant) can be considered as the starting point for applying counteracting measures

against the defluidization phenomenon. Moreover, since the monitoring parameters of the method (temperature profile and the average in-bed differential pressure drop) are relatively insensitive to variations of the gas velocity (in the bubbling regime) and operating temperature (800–1000°C, tested here), it can show a great robustness (in light of avoiding false alarms) in the early detection of defluidization.

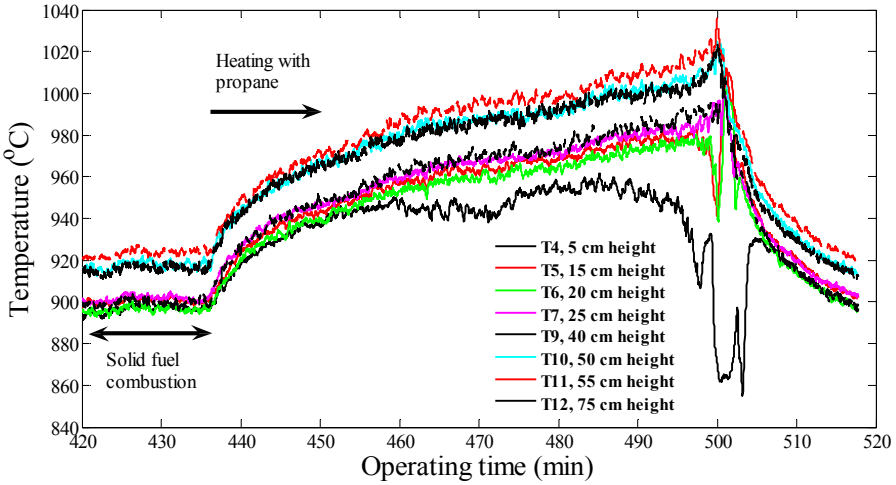

Figure 9.5: Typical temperature profile versus operating time for a fluidized bed approaching the defluidization condition.

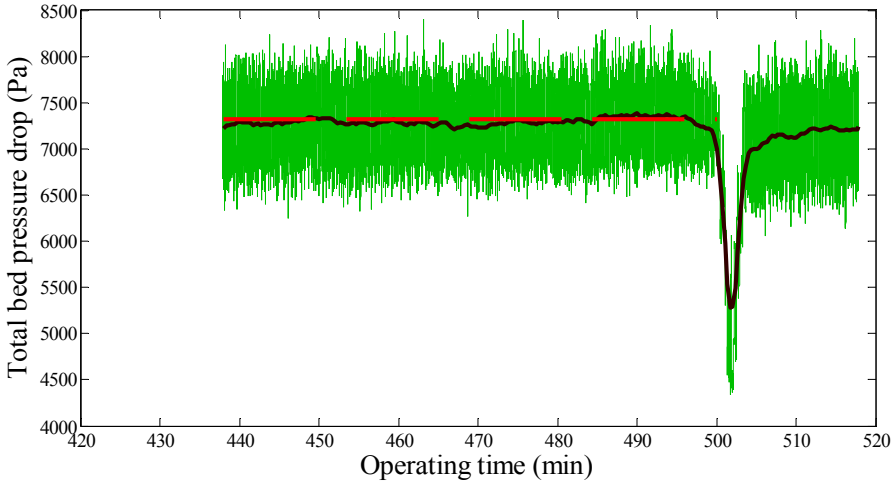

Figure 9.6: Typical bed pressure drop profile versus operating time for a fluidized bed approaching the defluidization condition.

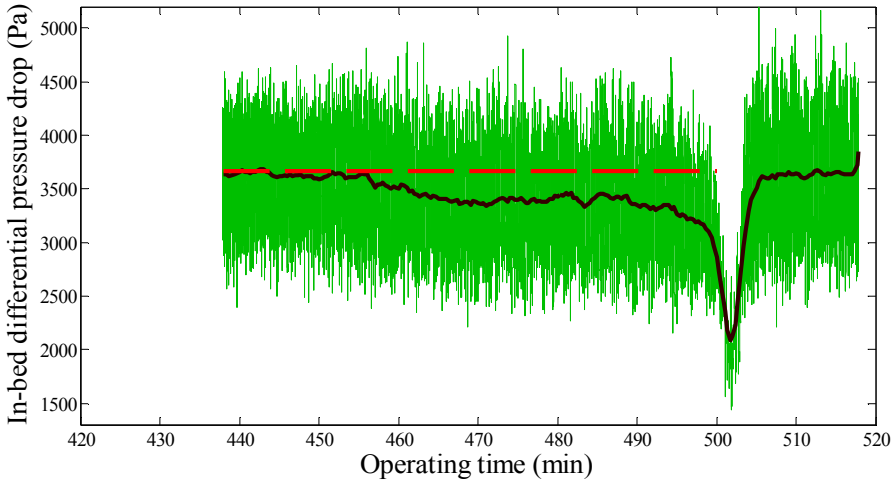

Figure 9.7: Typical in-bed differential pressure drop profile versus operating time for a fluidized bed approaching the defluidization condition.

It is worth mentioning that the defluidization sample provided here occurred during the combustion of propane inside the bed, which was fed through a horizontal tube, located some 20 cm above the distributor plate near the central axis of the bed. This was the case with most observed defluidization incidents and is explained by the fact that the reaction rates of propane and solid fuels differ significantly in the temperature range under investigation (<1 s for propane and ~1 min for coal). As a result, the combustion of propane and the ensuing heat release occurs in the vicinity of the propane injection point resulting in a higher temperature locally, which will have accelerated the formation of eutectics at the surface of bed materials in contact with this hot gas. Accordingly,

the defluidization incident shown took place at an accelerated rate in comparison to that which would take place with solid fuels. In the case of solid fuels having high alkali content, defluidization can take place several hours after the early detection, allowing for a wider range of counteracting methods. As exhibited in Figure 9.5-7, such a counteracting method could include an increase in superficial velocity combined with a reduction of the bed temperature to gain more time in case of rapid defluidization systems, such as a gas combusting system, to pace the implementation of more delicate corrective measures with potential system impacts, such as the replacement of the bed material, the injection of counteracting minerals, or the modification in fuel composition.

9.5 Conclusion

With the help of different experimental techniques, it was found that by increasing the level of IPFs in a bubbling gas-solid fluidized bed the hydrodynamics of the bed alters toward the presence of a more diluted emulsion phase, the formation of slightly smaller bubbles at gas velocities slightly higher than Umf, No IPFs and larger bubbles at high velocities of the bubbling regime as well as a reduction in the quality of axial solids mixing in the bed. These modifications suggest that the temperature gradient along the height of the bed increases and the average in-bed differential pressure drop decreases with IPFs.

With this phenomenological background, a simple and robust method is introduced for the early recognition of the defluidization condition for a bed of coarse particles operated in the bubbling regime. The method is based on simultaneous monitoring of temperature and pressure signals recorded for a bubbling gas-solid fluidized bed. According to this method, when a bubbling bed is approaching defluidization, the temperature gradient between readings of thermocouples located just above the distributor and those at higher levels of the bed increases over the operating time. At the same time, the mean value of an in-bed differential pressure drop demonstrates a continuous decrease over the shift toward defluidization. Although either of these two changes occurs in a bubbling fluidized bed that approaches defluidization, in order to make the detection method efficient and robust, a combination of these conditions should be satisfied simultaneously. Since the identification approach is taking advantage of the application of two measurement techniques that are common in industrial fluidized bed applications, it can be easily used in industrial applications. Moreover, the complete independence between temperature and pressure measurements, which are integrated in this method, reduces the chance of a false detection.

9.6 Nomenclature

9.6.1 Acronyms

CSB30	coated sugar beads at 30ºC
CSB40	coated sugar beads at 40ºC
IPFs	interparticle forces
PEA	poly ethyl acrylate
PMMA	poly methyl methacrylate
RPT	radioactive particle tracking
SB20	fresh sugar beads at 20ºC

9.6.2 Symbols

D	column diameter (m)
d_p	mean particle size (μm)
h	bed height (m)
U_c	transition velocity from bubbling to turbulent regime (m/s)
U_g	superficial gas velocity (m/s)
U_{mf}	minimum fluidization velocity (m/s)
$U_{mf,SB20}$	minimum fluidization velocity for SB20 (m/s)
$U_{mf,No\ IPFs}$	minimum fluidization velocity for a bed without IPFs (m/s)
$U_{c,No\ IPFs}$	transition velocity from bubbling to turbulent regime for a bed without IPFs (m/s)

9.6.3 Greek letters

ε	emulsion phase voidage (-)
ρ_p	particle density (kg/m^3)

9.7 Acknowledgements

The authors would like to thank the Total American Services, Inc. and the National Sciences and Engineering Research Council of Canada (NSERC) for their financial support of the present work.

9.8 References

1) J.H. Siegell, Defluidization phenomena in fluidized bed of sticky particles at high temperature, Ph.D. dissertation, The City University of New York, 1976.
2) J.H. Siegell, High-temperature defluidization, Powder Technol. 38 (1984) 13–22.
3) G. Tardos, D. Mazzone, R. Pfeffer, Destabilization of fluidized beds due to agglomeration part I: Theoretical model, Can. J. Chem. Eng. 63 (1985) 377–383.
4) G. Tardos, D. Mazzone, R. Pfeffer, Destabilization of fluidized beds due to agglomeration part II: Experimental verification, Can. J. Chem. Eng. 63 (1985) 384–389.
5) C.L. Briens, L.A. Briens, E. Barthel, J.M. Le Blevec, A. Tedoldi, A. Margaritis, Detection of local fluidization characteristics using the V statistic, Powder Technol. 102 (1999) 95–103.
6) J.R. van Ommen, R.-J. de Korte, C.M. van den Bleek, Rapid detection of defluidization using the standard deviation of pressure fluctuations, Chem. Eng. Process. 43 (2004) 1329–1335.
7) J. Werther, Measurement techniques in fluidized beds, Powder Technol. 102 (1999) 15–36.
8) J.F. Davidson, The two-phase theory of fluidization: successes and opportunities, AIChE Symp. Ser. 281 (1991) 1–12.
9) J. Ruud van Ommen, J. van der Schaaf, J.C. Schouten, B.G.M. van Wachem, M.-O. Coppens, C.M. van den Bleek, Optimal placement of probes for dynamic pressure measurements in large-scale fluidized beds, Powder Technol. 139 (2004) 264–276.
10) J. van der Schaaf, J.C. Schouten, F. Johnsson, C.M. van den Bleek, Non-intrusive determination of bubble and slug length scales in fluidized beds by decomposition of the power spectral density of pressure time series, Int. J. Multiphase Flow 28 (2002) 865–880.
11) J.R. van Ommen, S. Sasic, J. van der Schaaf, S. Gheorghiu, F. Johnsson, M.-O. Coppens, Time-series analysis of pressure fluctuations in gas–solid fluidized beds – A review, Int. J. Multiphase Flow 37 (2011) 403–428.
12) R. Chirone, F. Miccio, F. Scala, Mechanism and prediction of bed agglomeration during fluidized bed combustion of a biomass fuel: Effect of the reactor scale, Chem. Eng. J. 123 (2006) 71–80.
13) J.R. van Ommen, J.C. Schouten, C.M. van den Bleek, An early-warning-method for detecting bed agglomeration in fluidized bed combustors, in: R.B. Reuther (Ed.), Proceedings of the 15th International Conference on Fluidized Bed Combustion, ASME, New York, 1999, Paper No. FBC99–0150.

14) M. Bartels, J. Nijenhuis, J. Lensselink, M. Siedlecki, W. de Jong, F. Kapteijn, J. R. van Ommen, Detecting and counteracting agglomeration in fluidized bed biomass combustion, Energy Fuels 23 (2009) 157–169.

15) J.R. van Ommen, M.-O. Coppens, C. M. van den Bleek, J.C. Schouten, Early warning of agglomeration in fluidized beds by attractor comparison, AIChE J. 46 (2000) 2183–2197.

16) J. Shabanian, F. Fotovat, J. Bouffard, J. Chaouki, Fluidization behavior in a gas-solid fluidized bed with thermally induced inter-particle forces, in: T.M. Knowlton (Ed.), Proceedings of the 10th International Conference on Circulating Fluidized Beds and Fluidization Technology (CFB-10), Engineering Conferences International, New York, 2011.

17) J. Bouffard, F. Bertrand, J. Chaouki, S. Giasson, Control of particle cohesion with a polymer coating and temperature adjustment, AIChE J. 57 (2012) 3685–3696.

18) J. Shabanian, J. Chaouki, Pressure signals in a gas-solid fluidized bed with thermally induced inter-particle forces, in: J.A.M. Kuipers, R.F. Mudde, J.R. van Ommen, N.G. Deen (Eds.), Proceedings of the 14th International Conference on Fluidization – From Fundamentals to Products, ECI Digital Archives, Noordwijkerhout, The Netherlands, 2013.

19) J. Shabanian, J. Chaouki, Hydrodynamics of a gas-solid fluidized bed with thermally induced interparticle forces, Chem. Eng. J. (2014) submitted for publication.

20) J. Shabanian, J. Chaouki, Local characterization of a gas-solid fluidized bed in the presence of thermally induced interparticle forces, Chem. Eng. Sci. (2014) submitted for publication.

21) H.P. Cui, N. Mostoufi, J. Chaouki, Comparison of measurement technique of local particle concentration for gas–solid fluidization, in: M. Kwauk, J. Li, W.C. Yang (Eds.), Proceedings of Fluidization X, United Engineering Foundation, New York, 2001, pp. 779-786.

22) M. Rüdisüli, T.J. Schildhauer, S.M.A. Biollaz, A. Wokaun, J. R. van Ommen, Comparison of bubble growth obtained from pressure fluctuation measurements to optical probing and literature correlations, Chem. Eng. Sci. 74 (2012) 266–275.

23) H.T. Bi, J.R. Grace, Effect of measurement method on the velocities used to demarcate the onset of turbulent fluidization. Chem. Eng. J. 75 (1995) 261-271.

24) H. Cui, N. Mostoufi, J. Chaouki, Characterization of dynamic gas-solid distribution in fluidized beds, Chem. Eng. J. 79 (2000) 133–143.

25) H. Zhu, J. Zhu, New investigation in regime transition from bubbling to turbulent fluidization, Can. J. Chem. Eng. 86 (2008) 553–562.

26) R. Clift, J.R. Grace, The mechanism of bubble break-up in fluidised beds, Chem. Eng. Sci. 27 (1972) 2309–2310.

27) D. Moslemian, Study of solids motion, mixing, and heat transfer in gas fluidized beds, Illinois University, 1987.

28) M. Stein, T.W. Martin, J.P.K. Seville, P.A. McNeil, D.J. Parker, Positron emission particle tracking: particle velocities in gas fluidized beds, mixers and other applications, in: J. Chaouki, F. Larachi, M.P. Dudukovic (Eds.), Non-invasive monitoring of multiphase flows, Elsevier, Amsterdam, The Netherlands, 1997, pp. 309–333.

CHAPTER 10 ARTICLE 8: A SIMPLE AND ROBUST APPROACH FOR EARLY DETECTION OF DEFLUIDIZATION

Jaber Shabanian, Pierre Sauriol, Jamal Chaouki*

Department of Chemical Engineering, Ecole Polytechnique de Montreal, Montreal, Quebec, Canada

* Corresponding author: Tel.: +1-514-340-4711 X 4034; fax: +1-514-340-4159.

E-mail address: jamal.chaouki@polymtl.ca

(Submitted to Fuel)

10.1 Highlights:

- A simple approach is presented for the early detection of defluidization in a bubbling gas-solid fluidized bed.
- The new approach relies on the simultaneous monitoring of temperature and pressure signals.
- It effectively predicted the onset of agglomeration minutes to hours before complete defluidization.
- It was robust with respect to the changes in gas velocity, operating temperature, and bed inventory.

10.2 Abstract

This study presents a simple approach for the early detection of agglomeration in a bubbling gas-solid fluidized bed. The monitoring approach is based on the simultaneous measurements of local temperatures and the in-bed differential pressure drop from the well-stabilized section of the bed. Defluidization experiments (800–1000ºC) showed that when a bubbling gas-solid fluidized bed approaches complete defluidization the average in-bed differential pressure drop progressively decreases from a reference value obtained under normal conditions while the temperature difference along the axis, particularly between a temperature reading right above the distributor plate and others at higher levels within the dense bed, simultaneously increases. The novel approach was thus proposed on the concurrent occurrence of these drifts to provide an opportune

recognition of the onset of agglomeration in a bubbling gas-solid fluidized bed. The results demonstrated that it could effectively detect the defluidization condition minutes to hours before the complete defluidization state depending on the growth rate of agglomeration within the bed. Two pairs of detection thresholds for the timely recognition of agglomeration in bubbling fluidized beds of coarse silica sand particles were introduced according to the observations made in this study. The approach exhibited a minimal sensitivity to variations in the superficial gas velocity (±10%), operating temperature (±100^{o}C), and bed inventory (±20%) while both legs of the in-bed differential pressure transducer were well below the splash zone and above the jetting zone formed in the vicinity of the distributor plate.

Keywords: Defluidization detection, Gas-solid fluidized bed, Bubbling regime, Temperature measurements, Pressure measurements.

10.3 Introduction

Despite their widespread industrial application at elevated temperatures, gas-solid fluidized beds are prone to agglomeration potentially leading to defluidization problems. Processes in the area of polyolefin production and energy conversion (combustion and gasification of a wide variety of solid fuels, including biomass, waste, and coal or their blends) are relevant processes that regularly experience these problems [1]. An increased level of cohesive interparticle forces (IPFs), which can result from different mechanisms, principally governs these unwanted phenomena. Sintering the bed materials at high temperature is the major reason for agglomeration in the case of the fluidized bed production of polyethylene and polypropylene [2]. Alternatively, capillary IPFs due to the formation of low-melting eutectics is the main cause of agglomeration in fluidized bed energy conversion processes [3-7]. The ongoing agglomeration can ultimately lead to a complete blockage of the distributor plate or defluidized state and, hence, a forced plant shutdown [8, 9]. Therefore, it is of great importance to identify the onset of the agglomeration phenomenon at an early stage leaving enough time to implement counteractive measures.

Various approaches differing either in the type of measurement technique employed or the signal analysis have been proposed for the early detection of defluidization conditions [8, 10-18]. The goal of these approaches is to trigger an alarm to apply an operational/counteractive measure. The effectiveness, simplicity to implement and operate, and robustness are regarded as the most

important features to be readily adopted in industry. Pressure and temperature measurements are the only routine measurements in industry to provide hydrodynamic insight about the fluidized state of the particles [19].

The measurement of pressure signals from a gas-solid fluidized bed offers several advantages over other techniques, such as: i) large measurement volume (in the order of some tens of centimeters [20]), ii) moderate cost, iii) nonintrusiveness, iv) ease of implementation [21, 22]. Furthermore, the signal when sampled at a high enough frequency contains a lot of information about the flow dynamics of the fluidized bed (i.e., bubble formation, coalescence, eruption, and passage) [23, 24]. The variation in the particle size distribution resulting from the agglomeration process can effectively alter these hydrodynamics parameters [8]. Compared to pressure probes, thermocouples provide more localized measurements of the bed hydrodynamics. The temperature measurements attained by these probes contain information on the degree of solids mixing within the bed [6], i.e., the presence of a more uniform temperature profile throughout the bed indicates a better quality of solids mixing. These measurements, however, need considerable insight into the corresponding process to yield a correct interpretation [19]. A review of earlier studies reveals that the sole reliance on either temperature or pressure signals was not sufficient to result in a simple, robust, and reliable approach for detecting bed agglomeration. Nevertheless, preliminary results of the simultaneous applications of temperature and in-bed differential pressure signals, reported by our group [25], showed a promising performance.

Since there was not a thorough understanding about the detailed influence of IPFs on the fluidization characteristics of a bubbling gas-solid fluidized bed, the general impression was that analyzing the pressure fluctuations recorded from a fluidized bed can provide more attractive information for the establishment of a monitoring approach than the averaged pressure values. However, through the application of a polymer coating approach [26, 27] at near-ambient conditions [25] to increase the level of IPFs in the bed, it was observed that the average in-bed differential pressure drop decreased with enhancing the degree of IPFs at identical fluidizing gas throughputs in the bubbling regime. An increased capacity of the emulsion phase to hold the fluidizing gas inside its structure at higher levels of IPFs [25, 28] is principally responsible for this evolution [25]. The presence of considerably large/oblong bubbles at high levels of IPFs can additionally reduce the average in-bed differential pressure drop [25]. Also, a less uniform temperature profile is predicable within the bed when the level of IPFs increases in a bubbling gas-

solid fluidized bed, even in the absence of agglomerates. It is due to a decrease in the quality of solids mixing when cohesive IPFs are present in the bed [29]. Thus, the new detection approach was established by the fact that since the level of IPFs progressively increases in a fluidized bed approaching complete defluidization, both observations should co-exist. The simultaneity of these two evolutions combined with the complete independence of pressure and temperature measurements lends credence to the newly proposed approach to result in a reliable early recognition criterion.

This investigation is a continuation of the previous study of our group [25] proposing a simple, efficient, and robust approach for the opportune detection of defluidization conditions by simultaneous applications of pressure and temperature signals. At first, the most sensitive location for the measurement of temperature within the dense bed, with respect to the variation of IPFs, was identified with the help of the radioactive particle tracking (RPT) technique. The validity of the novel recognition approach for the early warning of defluidization incidents occurring during the propane and solid fuel combustion was subsequently verified through defluidization tests in a bubbling bed of coarse silica sand particles at high temperature (800–1000ºC). Two pairs of detection thresholds, relevant to industrial fluidized bed combustion and gasification of different solid fuels employing coarse silica sand as the bed materials, were introduced according to the experimental results. They are based on the percentage of changes in the evaluation selected temperature difference along the axis $(\Delta T_{sel})_{eval}$ and the evaluation average in-bed differential pressure drop $(\overline{\Delta P}_{in-bed})_{eval}$ relative to their reference values, i.e., $(\Delta T_{sel})_{ref}$ and $(\overline{\Delta P}_{in-bed})_{ref}$, obtained under normal conditions. The sensitivity of the approach to the superficial gas velocity (±10%), operating temperature (±100ºC), and bed inventory (±20%) was also tested. Finally, the applicability of the new recognition approach for the timely detection of defluidization conditions when employing fine silica sand particles as the bed materials was explored.

10.4 Experimental

The first step of this study aimed at determining a region within the dense bed to be exploited for the temperature measurements during defluidization tests, which shows the highest sensitivity to a change in the level of IPFs. The polymer coating approach [26, 27] was employed to introduce and control the level of IPFs in the bed. Sugar beads (d_p=580 µm, ρ_p=1556 kg/m^3, U_{mf}=0.16 m/s at

ambient conditions; d_p is the average particle size, ρ_p is the particle density, and U_{mf} is the minimum fluidization velocity) were selected as the base powders. Coated particles with a 5 μm uniform coating layer of PMMA/PEA (poly methyl methacrylate/poly ethyl acrylate) were produced during an atomization process in a spheronizer machine. More details about the coating procedure and its operating conditions are outlined elsewhere [26, 27, 30].

The coated and fresh sugar beads were separately introduced into a Plexiglas column with a 15.2 cm I.D. and 3.0 m in height. The bed inventory was 3 kg of powders, which resulted in a static bed height of approximately 20.5 cm at ambient conditions. Particles were fluidized with the help of dried and filtered air. The fresh sugar beads at 20ºC (SB20) served as the reference system, being minimally influenced by IPFs, and the coated sugar beads at 40ºC (CSB40) represented a system with a moderate level of IPFs although not leading to defluidization. The activated radioactive tracer was then tracked for 4 hours at a sampling frequency of 100 Hz during the RPT tests for each system. Both systems were run at a superficial gas velocity of 0.30, 0.50, and 0.65 m/s in the bubbling regime. Details of the RPT experiments have been previously reported elsewhere [29].

The same experimental rig as employed by Shabanian and Chaouki [31] was adopted for the defluidization tests at elevated temperatures. Hence, only a brief description of the rig will be given here. An atmospheric pressure pilot scale fluidized bed capable of withstanding operating temperatures up to 1050ºC with a fluidizing section of 20 cm I.D. by 97 cm tall was exploited in this study. Air was introduced into the bed through a bubble cap distributor plate containing 9 caps each having 4 holes 6.35 mm in size on its perimeter. The unit was equipped with 14 OMEGA type K thermocouples along the axis with the bottommost one positioned at the bed center and 5 cm above the distributor plate. These thermocouples monitored the temperature profile within the bed, provided an estimate of the expanded bed height, as well as a local measure of the bed behavior. Pressure measurements were achieved with the help of a differential pressure transducer. The differential pressure transducer (JUMO, 404304/000-414-415-28-298, 0–100 mbar) registered the differential pressure drop from the central part of the dense bed (15–45 cm above the distributor plate).

In this study, for most high temperature runs a bed inventory of 26 kg of coarse silica sand (d_p=820 μm, ρ_p=2650 kg/m^3, U_{mf}=0.54 m/s at ambient conditions) was introduced into the reactor. This led to an effective bed inventory of about 23 kg, equivalent to a static bed height of approximately

55 cm, after accounting for side ports (dead zones) of the reactor. The superficial gas velocity was adjusted to 1.0 m/s throughout the runs. The bed defluidization was induced by combusting solid fuel, i.e., alkali/alkali earth metal laden coal. The defluidization condition was achieved either during an in-bed propane combustion after periods of 1 hour solid fuel combustion at 800 and 900^{o}C when heating the bed toward a higher operating temperature (900 or 1000^{o}C) or during a long solid fuel combustion at 900^{o}C.

Normal operation during the combustion of coal alone was exploited to study the influence of superficial gas velocity (0.9, 1.0, and 1.1 m/s) and operating temperature (800, 900, and 1000^{o}C) on the detection approach. The hydrodynamic study reported in a separate work [31] for a bed of similar coarse silica sand particles ascertained that the bed was operating in the bubbling fluidization regime under all conditions explored here. An experiment with stepwise changes in the bed inventory was attempted when combusting propane to keep the bed temperature at 900^{o}C. To inspect the impact of the bed inventory, an initial effective bed inventory of 27.6 kg was fed into the reactor. The bed was operated for a period of 25 minutes after which 2.3 kg of bed inventory was withdrawn. The operation was repeated 2 other times ending up with an effective bed inventory of 20.7 kg in the last step. In order to verify the applicability of the new monitoring approach for finer bed materials, defluidization conditions were achieved during the propane combustion when heating a bed of fine silica sand particles (d_p=370 μm, ρ_p=2656 kg/m^3, U_{mf}=0.16 m/s at ambient conditions) toward 900^{o}C after 1 hour of solid fuel combustion at 800^{o}C. The mass of the bed inventory for this run was 28.3 kg of fine solids resulting in a static bed height of approximately 55 cm. The analysis of the standard deviation of in-bed gauge pressure signals recorded for a bed of fine silica sand particles at different superficial gas velocities ($0.3<U_g<1.20$ m/s) and 800^{o}C confirmed that the bed was operating in the bubbling fluidization regime throughout the conditions tested with this solid. Temperature and pressure signals were simultaneously registered during the runs with the sampling frequencies of 1 and 400 Hz, respectively.

As a crucial requisite for the new detection approach both legs of the in-bed differential pressure transducer must be positioned within the well-stabilized section of the dense bed. This ascertains that the recorded in-bed differential pressure signals are not perturbed by the bubble eruption and jet turbulence at the splash zone and jetting region close to the distributor, respectively. The bed temperature profile could allow for the verification of the upper leg to be well below the expanded

bed height although positioning it well below a height, where the bubble eruption commences, is the ideal. The calculation of the jet penetration length with the help of available correlations in open literature [32-36] at the distributor level for beds of coarse and fine silica sands at operating conditions explored here reveals that the lower leg of the in-bed differential pressure transducer was well above the jetting zone in all conditions. In addition, the bottom temperature probe(s) should be away from the jetting zone or internals.

10.5 Results and discussion

10.5.1 Time-averaged solids concentration profile

Time-averaged solids concentration (occupancy) profiles obtained from the RPT data are plotted in Figure 10.1. In this figure, the red and blue colors correspond to the higher and lower occurrence of the tracer at a given position. It illustrates that at low gas velocity, the bed of SB20 exhibited a typical gross circulation of solids in the bed (Figure 10.1a). However, since the level of IPFs tends to dominate the hydrodynamic forces (HDFs) for CSB40 at U_g=0.30 m/s, particles were less prone to be involved in the global mixing of the bed (Figure 10.1c). In other words, particles showed a higher tendency to remain fluidized at the bottom of the bed (within 5–10 cm above the distributor referred to Figure 10.1b). This means that particles contribute less in the transfer of heat within the bed when the magnitude of IPFs increases, which can result in a less uniform temperature profile along the bed height in the case of high temperature fluidized beds. In contrast, particles were evidently involved in the gross circulation within the bed at U_g=0.50 m/s (Figure 10.1b and d), where the ratio of the magnitude of IPFs/HDFs decreased. Due to a greater effect of HDFs on the fluidization behavior at higher U_g, particles could be more conveniently caught by the rising bubbles and participate in the global mixing at a higher frequency. Nonetheless, Figure 10.1 also shows that the gross cycle of solids started slightly higher in the beds with IPFs (CSB40), i.e., at bed heights higher than 4 cm above the distributor referred to in Figure 10.1b and d. It indicates that there was less chance for the lowermost section of the bed affected by IPFs to be well fluidized. This observation suggests that the presence of IPFs in a bubbling gas-solid fluidized bed will first impact the bottom of the bed possibly leading to a temperature difference between the bottommost section and higher levels of the bed. Hence, in all high temperature tests, the temperature right above the distributor plate was monitored and

compared with temperatures at other bed heights. It gave rise to the recognition of a fluidization state with an increased level of IPFs when the resulted temperature difference was compared with that obtained under normal conditions.

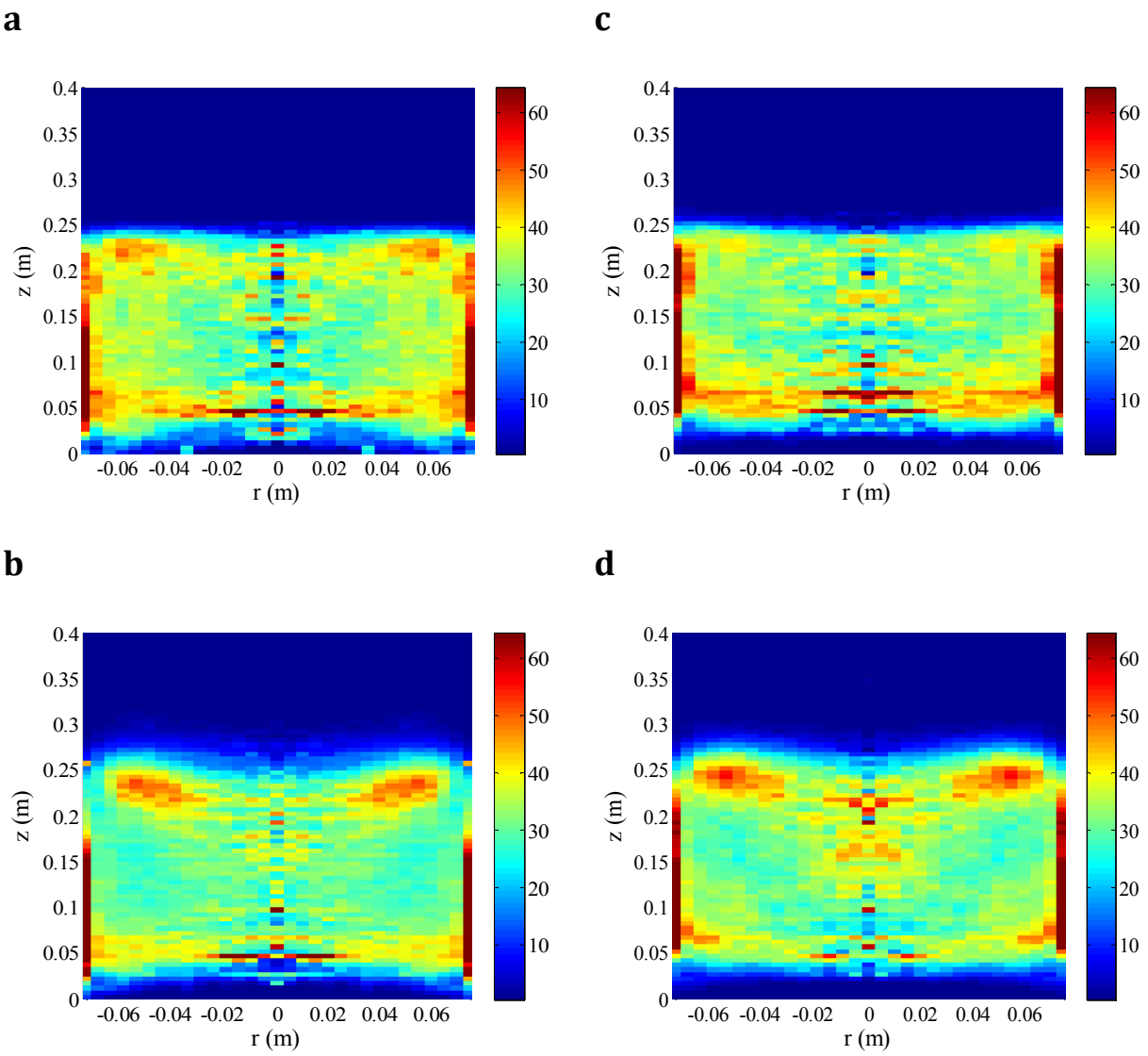

Figure 10.1: Influence of IPFs on the occupancy profile. a) SB20, U_g=0.30; b) SB20, U_g=0.50 m/s; c) CSB40, U_g=0.30 m/s; d) CSB40, U_g=0.50 m/s.

10.5.2 Normal operation during coal and propane combustion

Figure 10.2 demonstrates typical measured and calculated monitoring parameters during a sample normal operation of the bed, which was achieved through the combustion of coal and propane, while keeping U_g at 1.0 m/s throughout the run. Since defluidization tests and those related to the

sensitivity analysis of the new detection approach were carried out at 900°C, the operating data at this temperature was chosen as the reference data. Figure 10.2a exhibits that the temperature profile was more uniform during the coal combustion than propane. This can be explained by the combustion rates per unit of mass, which differ significantly between propane and coal. As a result, coal accumulates in the bed and generates the energy more uniformly over the bed volume. In contrast, propane, which was fed through a horizontal tube near the central axis of the bed and about 20 cm above the distributor plate within the favored passway of bubbles in the bed [37], burnt quickly in the bubble phase above the injector and thus was more dependent upon the solids mixing to achieve bed uniformity even under normal conditions. This observation is also reflected in the calculated temperature difference between the readings of thermocouples $T4$ and $T6$ (Figure 10.2b). We chose this selected temperature difference along the axis, $\Delta T_{sel} = T6 - T4$, as the most relevant one. $T4$ is the bottommost temperature reading, i.e., the first one impacted by the onset of agglomeration. $T6$ was chosen as a the thermocouple representative of the bed because as opposed to the thermocouples located higher in the bed, it was less impacted by the fuel type (coal vs. propane). Despite being at the same axial level as the propane injection point was far enough from it not to be impacted directly by the burning bubbles. When comparing ΔT_{sel} during the coal combustion at 800 (32–95 min) and 1000°C (265–315 min) to that at 900°C (140–200 min), a maximum variation of 25% can be observed. The average increase in ΔT_{sel} during the heating pass from 900 to 1000°C (200–245 min; with propane) with respect to the reference condition was 45%.

Figure 10.2b also illustrates the evolution of the in-bed differential pressure drop during the process. Although this parameter demonstrated a minor decreasing trend for the operating temperature, which could be due to the reduction in the gas density, it showed very stable behavior over the span of temperatures explored here (800–1000°C). A maximum change of 3% for the average in-bed differential pressure drop $\overline{\Delta P}_{in-bed}$ was obtained when compared to the corresponding reference data. Scrutinizing the variations of ΔT_{sel} and $\overline{\Delta P}_{in-bed}$ indicates a simultaneous increase and decrease for the former and latter over the operating time while the bed heated up to 1000°C from the reference condition of 900°C. These changes satisfy the primary condition of the newly proposed defluidization recognition approach. However, through careful selection of agglomeration detection thresholds exceeding the observed variations in these monitoring parameters as a result of a change in operating conditions, such as temperature, U_g, and bed inventory, the approach will not lead to false alarms. This will be discussed later in the text.

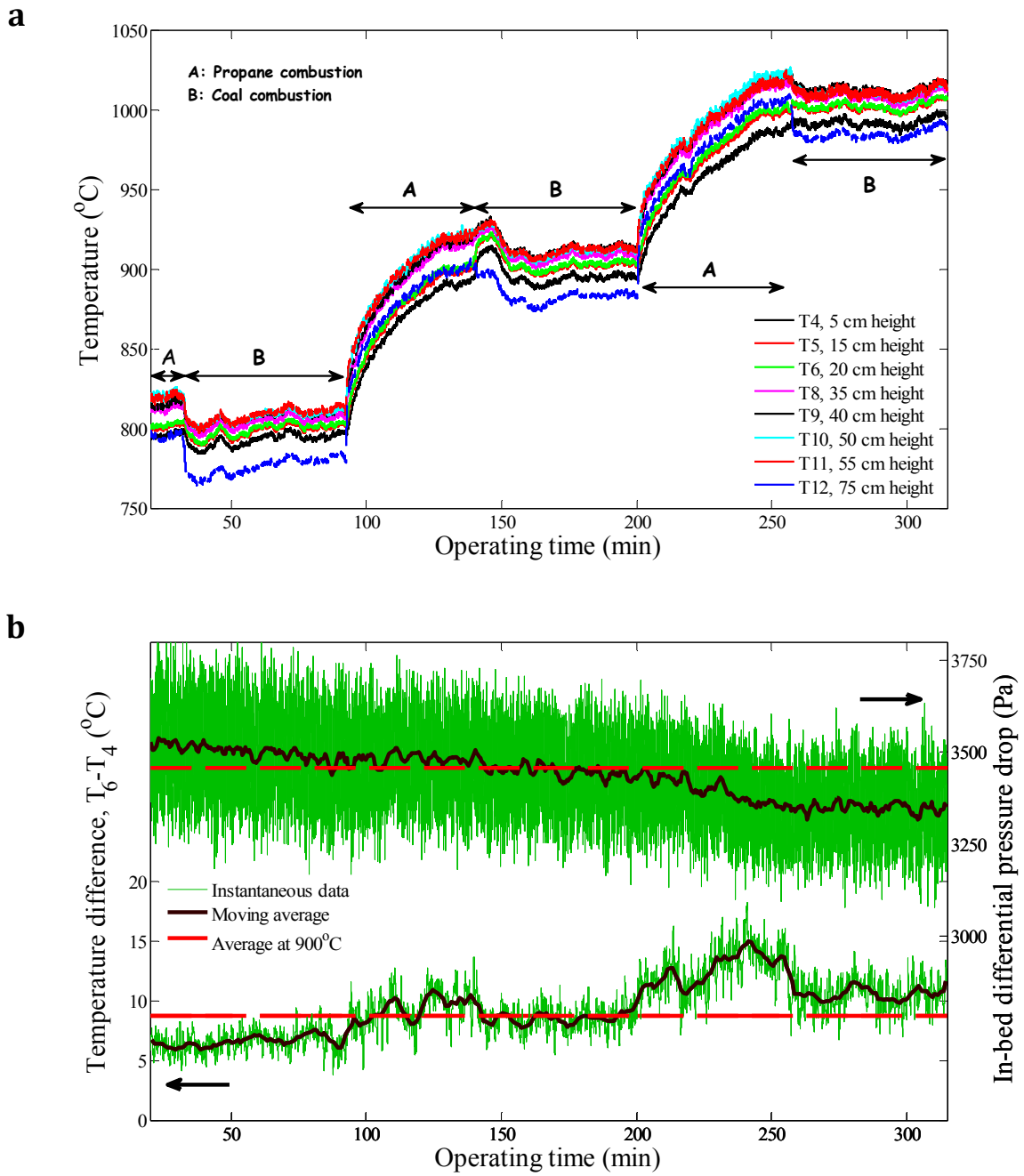

Figure 10.2: a) bed temperature profile, b) a selected in-bed temperature difference and in-bed differential pressure drop during a sample normal operation of the bed when combusting coal and propane.

10.5.3 Defluidization during propane combustion

Figure 10.3 illustrates the monitoring parameters throughout a defluidization test in which a defluidization incident occurred during the in-bed combustion of propane while attempting to

increase the bed temperature from 900 to 1000°C. The level of IPFs within the bed was deliberately increased by previously combusting a solid fluid with a high alkali metal content. The average values of ΔT_{sel} and $\overline{\Delta P}_{in-bed}$ at 900°C from four identical tests during the normal operation of the bed, as presented in Figure 10.2, were employed as the reference values for the corresponding parameters in Figure 10.3b.

The average values of ΔT_{sel} and $\overline{\Delta P}_{in-bed}$ during the solid fuel combustion at 900°C (160–210 min) were higher (about 25%) and lower (around 3.5%) than the reference values. While the major operating parameters remained constant, the simultaneous changes in these monitoring parameters are attributed to the increase in the level IPFs. This can, accordingly, show a decent sensitivity of the new detection approach to the variation in the level of IPFs in the bed.

Upon increasing the bed temperature with the in-bed combustion of propane toward 1000°C (210–240 min) after the last step of the solid fuel combustion, the monitoring parameters had evolved differently until complete defluidization. The $T4$ progressively deviated from $T6$ along the course of the heating step, thus the deviation between ΔT_{sel} and the corresponding reference value could have a considerably larger variation compared to the same deviation during the identical heating step under normal conditions (refer to Figure 10.2b). The ΔT_{sel} increased to about 100% with respect to the reference value at the operating time of 230 min, i.e., 10 min before complete defluidization, and the variation further increased to 260% at the operating time of 235 min, i.e., 5 min prior to complete defluidization. This trend could be primarily owing to the continuous decrease in the quality of solids mixing within the bed when approaching complete defluidization because of the successive increase in the level of IPFs. Also, if the level of IPFs increases to a greater degree at which point dynamic clusters in the bubbling regime [38] could change their entity into permanent agglomerates, they would rest at the bottom of the bed when their minimum fluidization velocity becomes higher than U_g, i.e., a segregation of bed materials appears in the bed [6]. Hence, the increase in the temperature difference along the bed height could be further increased.

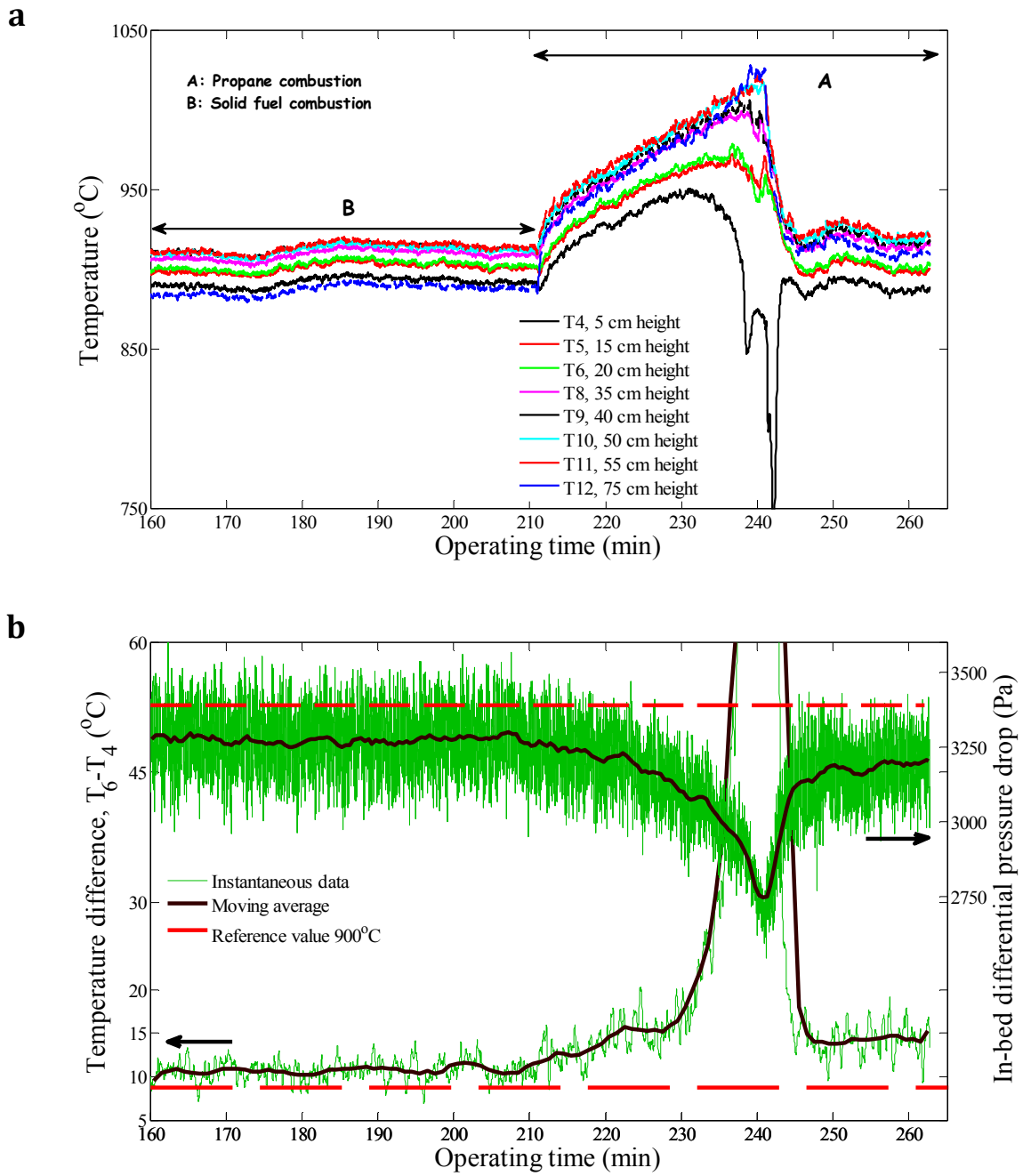

Figure 10.3: a) bed temperature profile, b) a selected in-bed temperature difference and in-bed differential pressure drop during a defluidization test achieved when combusting propane.

The reduction of $\overline{\Delta P}_{in-bed}$ continued throughout the heating pass until the bed reached complete defluidization. This parameter underwent a reduction of around 8.7% at the operating time of 230 min and 11.8% at 235 min. It indicates that when this observation is combined with the growth of ΔT_{sel}, they can adequately identify the defluidization condition much earlier than the eventual state.

The magnitudes of variations in these monitoring parameters for this sample experiment will be integrated with those that will be mentioned in section 10.5.4 to introduce two pairs of detection thresholds for early agglomeration recognition in bubbling fluidized beds of coarse silica sand particles. The defluidization incident can occur at a faster rate when combusting propane in comparison to what could happen during the combustion of solid fuel [25]. Consequently, we anticipate that the new approach will lead to an earlier detection in the case of solid fuel combustion.

The fluidized bed was quickly recovered after the defluidization incident by a 20% increase in the superficial gas velocity (U_g=1.2 m/s) and reducing the propane feed rate. The superficial gas velocity was subsequently adjusted back to 1.0 m/s at the operating time of 250 min with enough propane flow to maintain the operation at 900°C. Figure 10.3b shows that both monitoring parameters after the operating time of 250 min were experiencing values that were markedly different with the corresponding values under normal conditions. It reveals that the retrieved fluidized bed was under the influence of strong IPFs during this span of operating times. Defluidization would quickly occur again when increasing the temperature.

10.5.4 Defluidization during solid fuel combustion

The evolutions of the monitoring parameters during a defluidization test for which the defluidization incident took place during the solid fuel combustion are presented in Figure 10.4. The solid fuel that combusted during the first segment of this experiment (80–160 min) had a low alkali metal content. During the first segment we believe that the fluidized bed operated under normal conditions. Thus, the temperature and pressure signals sampled throughout this segment were exploited to derive the reference values for ΔT_{sel} and $\overline{\Delta P}_{in-bed}$. In the subsequent segments, a solid fuel with a high alkali metal content was employed in order to favor the onset of agglomeration within a few hours of operation. Since a single volumetric solid feeder was adopted in this work, it was necessary to regularly refill it throughout the operation. This was performed manually and took about 5 min during which time the bed temperature was kept constant by burning propane.

Figure 10.4 illustrates that despite ΔT_{sel} exhibiting stable behavior throughout the first segment, it started to deviate from the reference value around the operating time of 200 min, i.e., 35 min into

the second segment. This trend continued at an increasing rate up to the entire defluidization of the bed at the operating time of 440 min. The ΔT_{sel} increased by 120% at the operating time of 330 min, 210% at the operating time of 380 min, and 410% at operating time of 420 min. The average in-bed differential pressure drop simultaneously started to depart from its reference value at the operating time of 200 min. The trend continued at a decreasing rate until complete defluidization, when it experienced a rapid reduction. This monitoring parameter varied by about 6.5%, 10.3%, and 13.2% at the operating times of 330, 380, and 420 min, respectively. The concurrent evolutions of these monitoring parameters confirm the reliability of the new recognition approach for the detection of the onset of agglomeration under different circumstances. Also, providing an initial indication of the agglomeration phenomenon around four hours prior to complete defluidization is very promising.

By increasing the mass flow rate of gas entering the bed (U_g=1.20 m/s at 900ºC) immediately after the defluidization incident, the fluidized bed was retrieved and kept adequately functional approximately 30 min after the event yet at 800ºC (U_g dropped to 1.1 m/s for the same mass flow rate of the fluidizing gas). The superficial gas velocity was set back to 1.0 m/s at the operating time of 480 min. Figure 10.4 demonstrates that the monitoring parameters of the new detection approach were evidently showing that the bed was affected by the presence of a high level of IPFs, as expected.

a

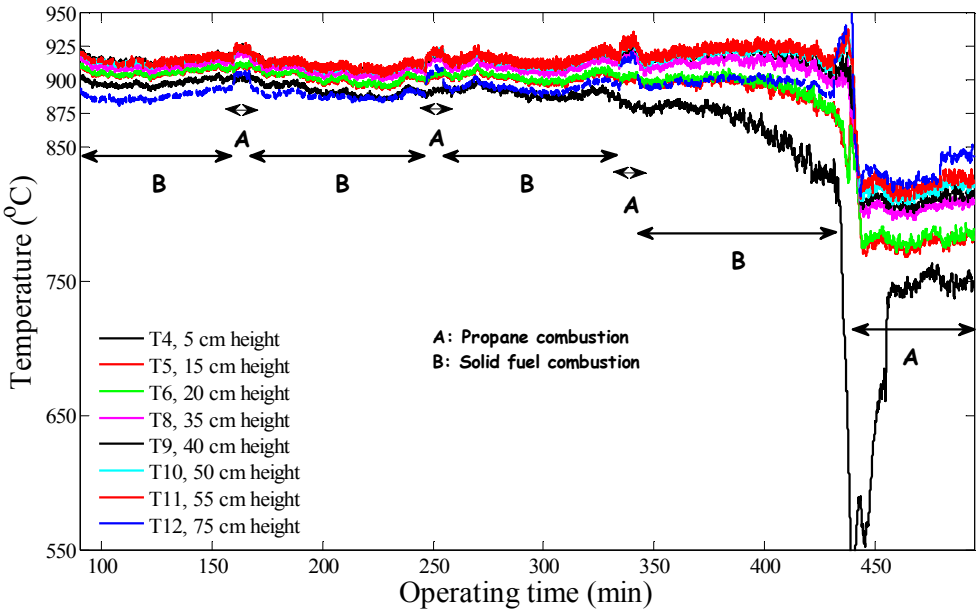

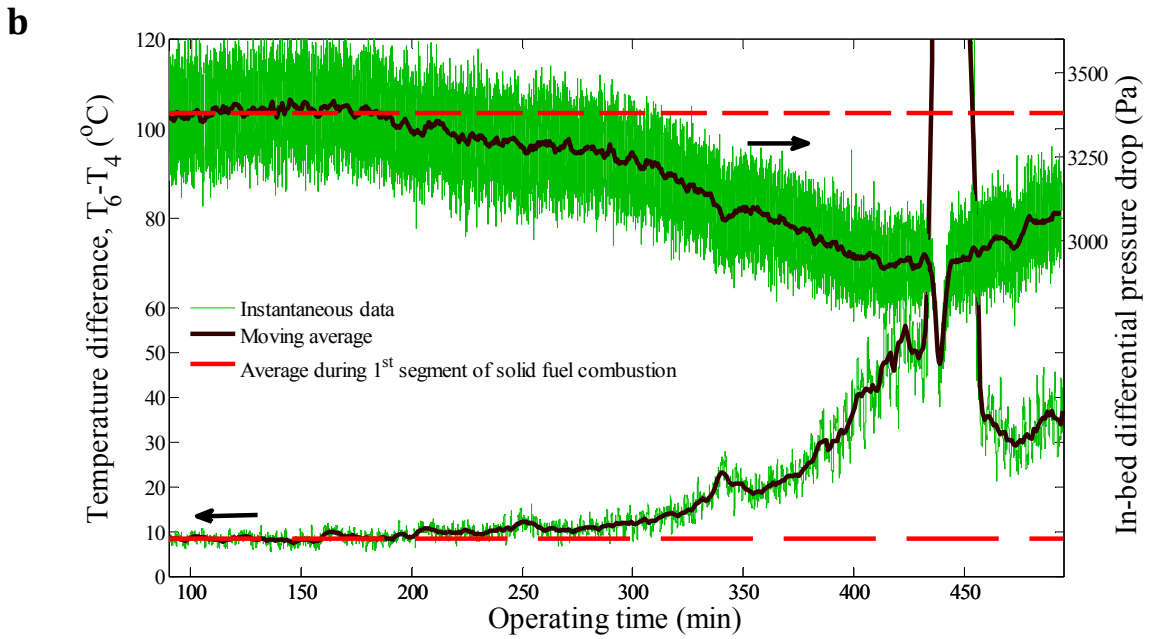

Figure 10.4: a) bed temperature profile, b) a selected in-bed temperature difference and in-bed differential pressure drop during a defluidization test achieved when combusting solid fuel.

On the one hand it is important to identify the defluidization condition at an early stage to prevent an eventual shut down. On the other hand, applying different operational and counteracting strategies [18] to delay the entire defluidization of the bed is often achieved at the cost of a performance reduction, and thus must be utilized sparingly [25]. Therefore, for the new agglomeration recognition approach, two pairs of detection thresholds, resembling the high and high-high alarms in the industry, for the early warning of agglomeration in bubbling fluidized beds of coarse silica sand particles are proposed as follows:

High alarm:

$$\frac{(\Delta T_{sel})_{eval}}{(\Delta T_{sel})_{ref}} \geq 2 \quad \& \quad \frac{(\overline{\Delta P}_{in-bed})_{eval}}{(\overline{\Delta P}_{in-bed})_{ref}} \leq 0.94 \qquad 10.1$$

High-high alarm:

$$\frac{(\Delta T_{sel})_{eval}}{(\Delta T_{sel})_{ref}} \geq 3 \quad \& \quad \frac{(\overline{\Delta P}_{in-bed})_{eval}}{(\overline{\Delta P}_{in-bed})_{ref}} \leq 0.90 \qquad 10.2$$

In order to be on the safe side and prevent any occasional false alarms from the new agglomeration detection approach, a double of the maximum change observed during the sensitivity analysis (sections 10.5.2 and 10.5.5) for $\overline{\Delta P}_{in-bed}$ was chosen for the lower boundary of the variation in this monitoring parameter in the case of the high alarm threshold. Since ΔT_{sel} demonstrated a higher sensitivity to the variation in the level of IPFs in comparison with $\overline{\Delta P}_{in-bed}$, four times the maximum change observed during the sensitivity analysis is selected for the high alarm threshold. With these thresholds, the high alarm affords the operators time to react while a very prompt action will be necessary upon issuing the high-high alarm.

These two pairs of detection thresholds were tested for many defluidization incidents encountered for beds of coarse silica sand particles in this work. They presented promising efficiency in all samples, as shown in Figure 10.3 and Figure 10.4, depending on the rate of agglomeration. The new agglomeration identification approach is based on the information collected from the influence of IPFs on the bed behavior. Also, the degree of modification in the fluidization characteristics due to the presence of IPFs for beds with different properties, varying in particle size and/or chemical composition, could be different. Therefore, the values selected here for the detection thresholds would need to be adapted for other systems.

Scrutinizing the overall bed temperature profile along the course of the experiment (in Figure 10.4a) reveals that similar to ΔT_{sel} the temperature differences between successive thermocouples in the dense bed were progressively increasing up to the point of complete defluidization. Also, since the agglomeration process went on for a longer period of time in comparison with the data in Figure 10.3, an evident increase in the instantaneous fluctuations of each individual temperature reading from the dense bed can be observed after the operating time of ≈380 min. All defluidization incidents during the combustion of different solid fuels showed similar qualitative behavior of temperature fluctuations in the vicinity of the eventual defluidization state. This observation can be added to the newly proposed detection approach in the case of slow defluidization to increase the reliability of the approach.

10.5.5Sensitivity analyses

10.5.5.1 Sensitivity to changes in superficial gas velocity and operating temperature

The sensitivities of the monitoring parameters to changes in U_g (±10%) and a decrease of 100°C in the operating temperature were studied when combusting coal in a bubbling fluidized bed of coarse silica sand particles. Figure 10.5b illustrates the evolutions of both monitoring parameters during this run. The mean values of ΔT_{sel} and $\overline{\Delta P}_{in-bed}$ during the first segment of the combustion of coal alone at 900°C and U_g=1.0 m/s (125–225 min) were selected as the corresponding reference values. The bed temperature was decreased from 900 to 800°C while preserving the mass flow rate of the entering fluidizing gas, which resulted in a U_g of 1.0 m/s at 900°C and 0.9 m/s at 800°C. Finally, the superficial velocity was increased to 1 m/s at 800°C (580–615 min).

Figure 10.5b demonstrates that ΔT_{sel} and $\overline{\Delta P}_{in-bed}$ were stable during all operating changes imposed on the bed. Integrating these observations with those obtained from Figure 10.2b indicates that the new agglomeration detection approach is robust with respect to the changes in the superficial gas velocity (±10%) and operating temperature (±100°C).

a

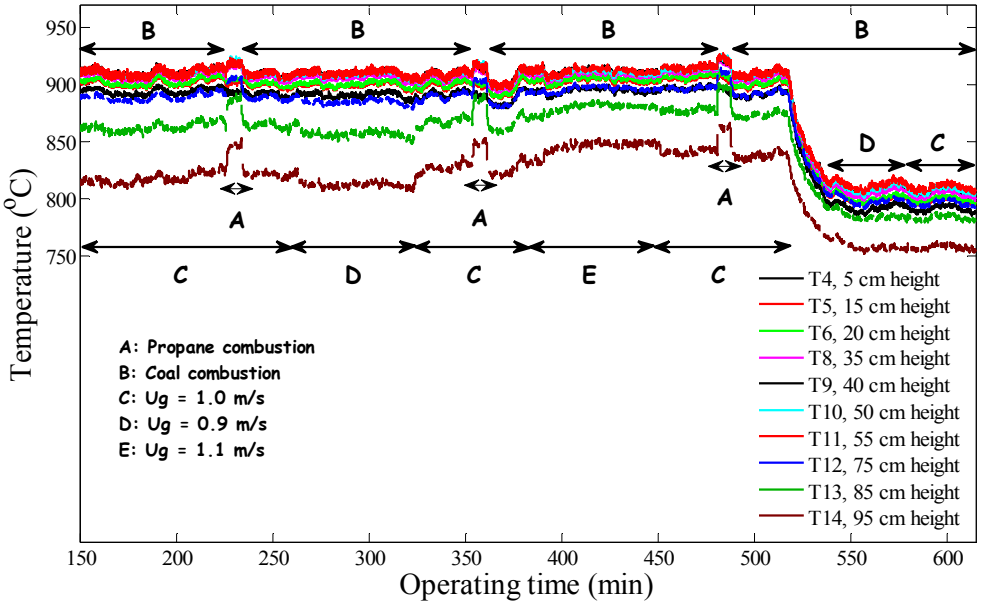

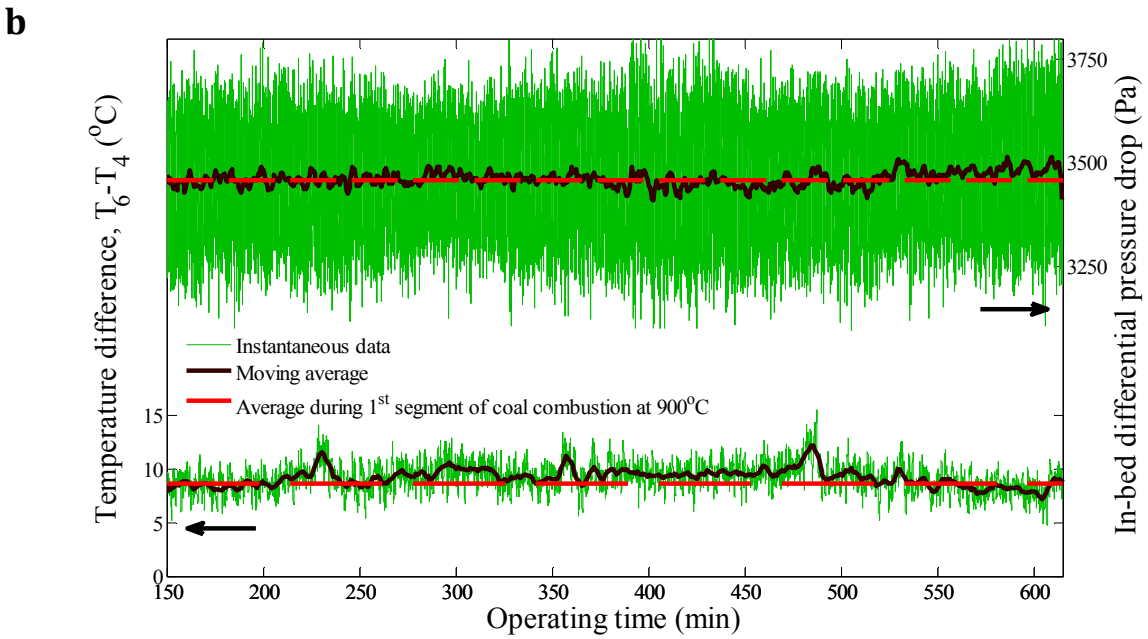

Figure 10.5: a) bed temperature profile, b) a selected in-bed temperature difference and in-bed differential pressure drop during coal alone combustion for sensitivity tests: variations in U_g and operating temperature.

10.5.5.2 Sensitivity to changes in bed inventory

Figure 10.6 demonstrates the variations in the monitoring parameters during a sensitivity test on changes in the bed inventory when combusting propane in a bubbling fluidized bed of coarse silica sand particles (U_g=1.0 m/s at 900°C). In order to ascertain that the upper leg of the in-bed differential pressure transducer was well below the splash zone, the condition during which an effective bed inventory of 25.3 kg was present in the bed (138–158 min) was chosen as the reference condition.

Figure 10.6b illustrates that ΔT_{sel} was very stable with changes in the bed inventory. Scrutinizing the bed temperature profile in the same plot reveals that the expanded bed height was progressively decreasing with the diminishing bed inventory. It shows that the conditions for the new agglomeration detection approach for the upper leg of the in-bed differential pressure transducer were not satisfied when an effective bed inventory of 20.7 kg was present in the bed (190–210 min). Figure 10.6b also exhibits that a change of ±10% in the bed inventory with respect to the reference conditions resulted in a maximum change of 2.7% in $\overline{\Delta P}_{in-bed}$ while change of about 7% was observed with an effective bed inventory of 20.7 kg. Although a source of this variation can

be attributed to the proximity of the upper leg of the in-bed differential pressure transducer to the splash zone, no false alarm would have resulted from the new detection approach since ΔT_{sel} demonstrated stable behavior. On the other hand, if comparing the data from an effective bed inventory of 27.6 kg and that at 23.0 kg (20% change in inventory), the bed inventory difference in $\overline{\Delta P}_{in-bed}$ is around 3.8% while ΔT_{sel} remains relatively unaffected. These observations indicate that when the spatial positions of critical thermocouples for measuring ΔT_{sel} and the legs of the in-bed differential pressure transducer satisfied the requirements of the new agglomeration recognition approach, it showed minimal sensitivity to the 20% variation in the bed inventory.

a

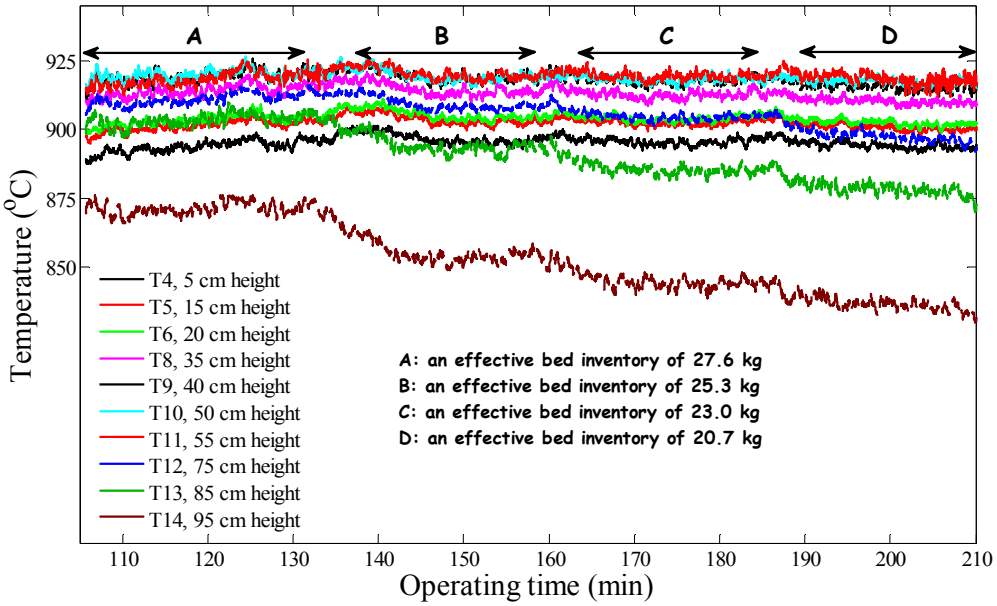

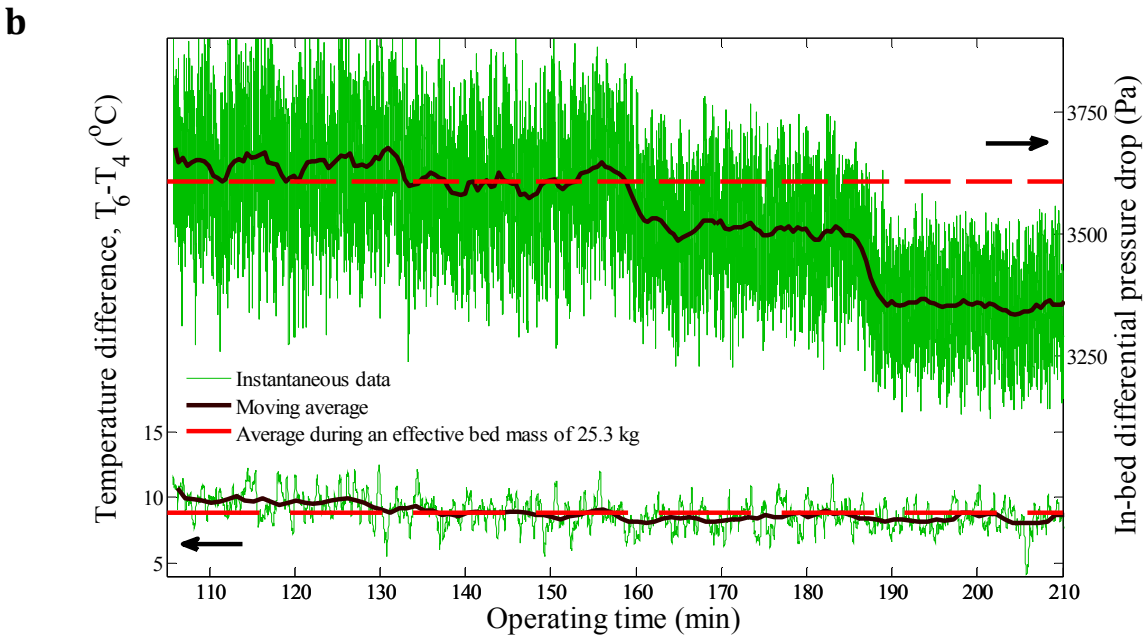

Figure 10.6: a) bed temperature profile, b) a selected in-bed temperature difference and in-bed differential pressure drop during propane combustion for sensitivity tests: variation in bed inventory.

10.5.6 Ability of the new approach for a bed of finer particles

In order to study the ability of the novel agglomeration recognition approach for the advanced detection of agglomeration when fine silica sand particles were employed as the bed materials, defluidization conditions were achieved when heating up the reactor toward 900°C during propane combustion after a 1-hr long combustion of a solid fuel with a high alkali metal content in a bed of otherwise fresh particles at 800°C. Figure 10.7 presents the performance of the new approach throughout this run. An initial 10 min of operation during solid fuel combustion at 800°C (80–90 min) was selected as the reference condition.

The evolutions of the monitoring parameters throughout this sample experiment, presented in Figure 10.7, were similar to those observed in Figure 10.3 for the defluidization in a bed of coarse silica sand particles. The mean values of ΔT_{sel} and $\overline{\Delta P}_{in-bed}$ during the last 50 min of solid fuel combustion at 800°C were higher (around 17%) and lower (about 2.3%) than the reference values. Since other operational parameters were kept constant, these evolutions are consistent with an increase in the level of IPFs in the bed. This indicates that the new recognition approach can show

a good level of sensitivity in the variation of the magnitude of IPFs when particles with varying properties are separately employed as the bed materials.

Upon increasing the operating temperature toward 900ºC (140–163 min), ΔT_{sel} and $\overline{\Delta P}_{in-bed}$ were simultaneously increased and decreased until the point of complete defluidization. The ΔT_{sel} underwent a change of 96% at the operating time of 153 min, i.e., 10 min before complete defluidization, and 128% at the operating time of 158 min, i.e., 5 min before complete defluidization. The variation of $\overline{\Delta P}_{in-bed}$ at the same operating times was 7.8% and 9.3%, respectively. These evolutions satisfy the primary condition of the new agglomeration identification approach. The high alarm threshold introduced in section 10.5.4 for a bed of coarse silica sand particles can identify the defluidization condition in a bed of fine silica sand powders with relatively identical efficiency as observed in Figure 10.3. Nevertheless, the bed of fine silica sand became completely defluidized before the monitoring parameters of the new defluidization detection approach satisfied the conditions of the high-high alarm threshold, proposed in section 10.5.4. It proves the need for a slight modification in the recommended detection thresholds of the new agglomeration recognition approach to achieve its best performance when particles with different properties are separately adopted as the bed materials.

a

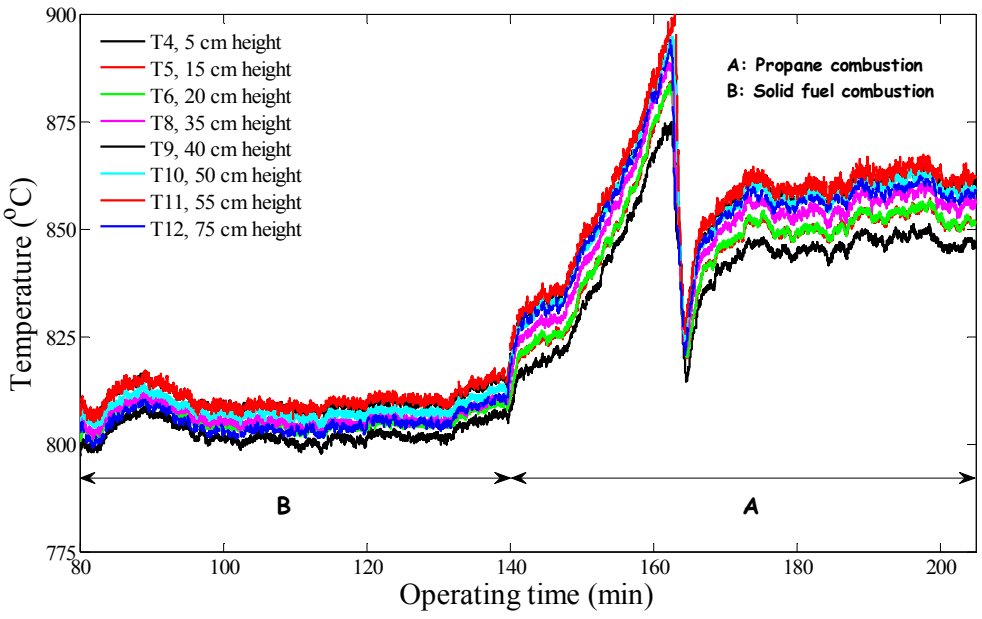

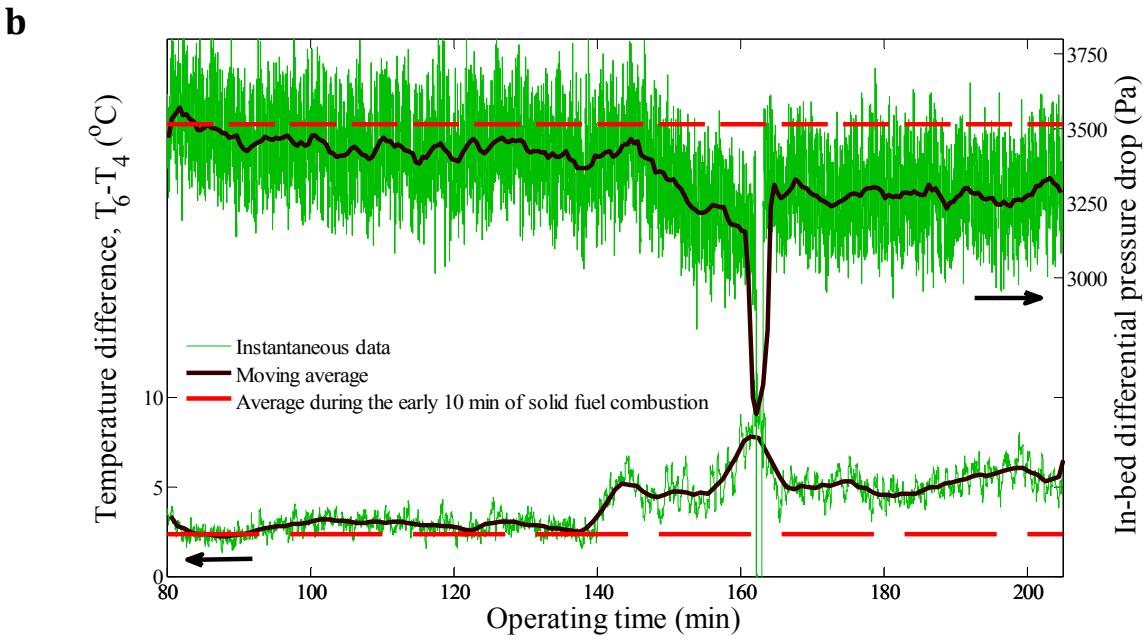

Figure 10.7: a) bed temperature profile, b) a selected in-bed temperature difference and in-bed differential pressure drop during a defluidization test achieved when combusting propane in a bed of fine silica sand particles.

Again after the defluidization incident, the bed was recovered and held at 850°C and U_g=1.0 m/s (172–205 min). The evolutions of ΔT_{sel} and $\overline{\Delta P}_{in-bed}$ after the recovery of the fluidized bed at 850°C and U_g=1.0 m/s indicate that the recovered fluidized bed was under the influence of strong IPFs.

At identical superficial gas velocity in the bubbling regime and in the absence of incremental IPFs, the values of $(\Delta T_{sel})_{ref}$ observed for a bed of fine silica sand particles were smaller than for a bed of coarse ones. This indicates a better quality of solids mixing for the fine particles although the magnitude of HDFs exerted on each single particle is smaller. We believe that the idle time, i.e., the time that particles spend in the emulsion phase [39], mainly explains this difference. The shorter idle time with the finer silica sand reduces the chance of particle agglomeration, thus improving the quality of solids mixing and the temperature uniformity along the axis accordingly. By analogy, this also explains why a cohesive bubbling bed can remain fluidized at a higher U_g whereas it would experience a complete defluidization at a lower U_g.

The average idle times $\bar{t}_{idle}$ for SB20 and CSB40 at different superficial gas velocities were calculated with the help of RPT data and the results are presented in Figure 10.8; the procedure

was explained in detail elsewhere [29]. It shows that $\bar{t}_{idle}$ decreased sharply with U_g near U_{mf} in the bubbling regime to reach a nearly constant value at higher superficial gas velocities in the same regime. This drift is well in accordance with the argument made above. Fig. 8 also illustrates that the rate of increase in $\bar{t}_{idle}$ with IPFs was pronounced at low superficial gas velocities in the bubbling regime, i.e., higher ratios of the magnitude of IPFs/HDFs. This observation suggests that when the level of IPFs progressively increases over the course of the experiment, the agglomeration is an auto-accelerated process, i.e., agglomerates exponentially enlarge from the onset of agglomeration up to the entire defluidization of the bed. We believe that a more general set of thresholds for the early detection of defluidization could be obtained by incorporating idle time observations. Unfortunately, at present, such data is not readily available.

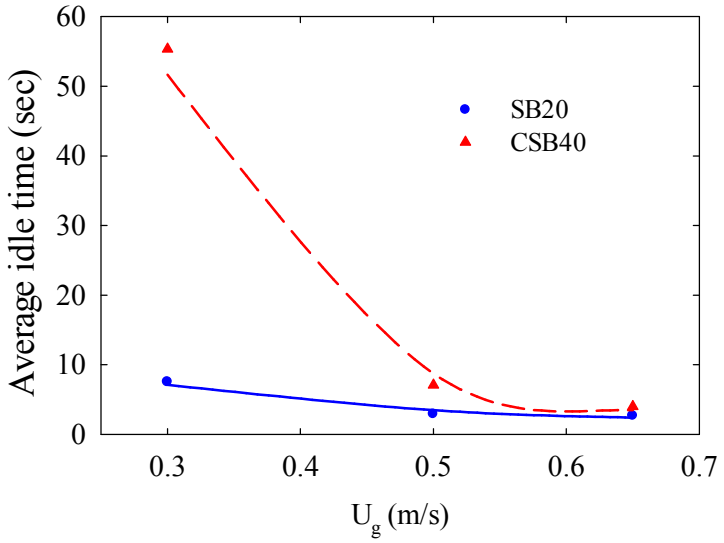

Figure 10.8: Effects of superficial gas velocity and IPFs on the average idle time.

10.6Conclusion

A novel yet simple approach was introduced for the early detection of agglomeration. The new approach was based on the simultaneous applications of temperature and in-bed differential pressure signals. According to this approach, when a cohesive bubbling gas-solid fluidized bed is approaching complete defluidization, the temperature difference between the lowermost section of the bed and the dense bed at higher levels progressively increases over time while the average in-bed differential pressure drop decreases. Based on the experimental observations, two pairs of

detection thresholds for the early warning of agglomeration in bubbling fluidized beds of coarse silica sand particles (d_p=820 μm) were proposed. They function as the high and high-high alarms. The high alarm is issued when the selected temperature difference along the axis increases more than 100% with respect to its reference value while the average in-bed differential pressure drop decreases more than 6% from its reference value. The high-high alarm is issued when the former monitoring parameter increases more than 200% and the latter decreases more than 10% compared to the corresponding reference values. The new approach demonstrated promising performance in the timely recognition of the onset of agglomeration minutes to hours before complete defluidization. The new approach also benefits from its robustness with respect to the variation of influential operating parameters, i.e., bed temperature (±100ºC), U_g (±10%), and bed inventory (±20%). The application of the new approach for the opportune detection of defluidization conditions in a cohesive bubbling bed of fine silica sand particles (d_p=370 μm) would not have triggered the recommended alarms, however the trends for the key measurement parameters were similar to those obtained with the coarse sand but of a lower magnitude. In other words, the approach demonstrated an encouraging performance in this case and pairs of threshold values would need to be adapted to be suitable for changes in particles.

10.7 Nomenclature

10.7.1 Acronyms

CSB40	coated sugar beads at 40ºC
HDFs	hydrodynamic forces
IPFs	interparticle forces
RPT	radioactive particle tracking
SB20	sugar beads at 20ºC

10.7.2 Symbols

d_p	average particle size (μm)
$\bar{t}_{idle}$	average idle time (sec)
$T4$	temperature reading of thermocouples No. 4 (ºC)
$T6$	temperature reading of thermocouples No. 6 (ºC)

U_{mf} minimum fluidization velocity (m/s)

U_g superficial gas velocity (m/s)

10.7.3 Greek letters

$\overline{\Delta P}_{in-bed}$ average in-bed differential pressure drop (Pa)

$(\overline{\Delta P}_{in-bed})_{eval}$ evaluation average in-bed differential pressure drop (Pa)

$(\overline{\Delta P}_{in-bed})_{ref}$ reference average in-bed differential pressure drop (Pa)

ΔT_{sel} selected temperature difference along the axis (°C)

$(\Delta T_{sel})_{eval}$ evaluation selected temperature difference along the axis (°C)

$(\Delta T_{sel})_{ref}$ reference selected temperature difference along the axis (°C)

ρ_p particle density (kg/m^3)

10.8 Acknowledgements

The financial support of this work by the Total American Services, Inc. and the National Sciences and Engineering Research Council of Canada (NSERC) is gratefully acknowledged. The authors would like to thank Mr. Diego Alejandro López Del Ángel for his assistance during the experimental activities. We are also most grateful to Prof. Navid Mostoufi for his constructive comments on this work.

10.9 References

1) Bartels M, Nijenhuis J, Kapteijn F, van Ommen JR. Case studies for selective agglomeration detection in fluidized beds: Application of a new screening methodology. Powder Technol 2010;203:148-166.

2) Mansourpour Z, Mostoufi N, Sotudeh-Gharebagh R. Investigating agglomeration phenomena in an air-polyethylene fluidized bed using DEM–CFD approach. Chem Eng Res Des 2014;92:102-118.

3) Manzoori AR, Lindner ER, Agarwal PK. Inorganic transformation during the circulating fluid bed combustion of low-rank coals with high content of sodium and sulphur. In: Proceedings of the Engineering Foundation Conference on Inorganic Transformations and Ash Deposition During Combustion, Palm Coast, Florida, USA, 1991.

4) Werther J, Saenger M, Hartge EU, Ogada T, Siagi Z. Combustion of agricultural residues. Prog Energy Combust Sci 2000;26:1-27.
5) Lin W, Dam-Johansen K, Frandsen F. Agglomeration in bio-fuel fired fluidized bed combustors. Chem Eng J 2003;96:171-185.
6) Bartels M, Lin W, Nijenhuis J, Kapteijn F, van Ommen JR. Agglomeration in fluidized beds at high temperatures: Mechanisms, detection and prevention. Prog Energy Combust Sci 2008;34:633-666.
7) van Caneghem J, Brems A, Lievens P, Block C, Billen P, Vermeulen I, Dewil R, Vandecasteele C. Fluidized bed waste incinerators: Design, operational and environmental issues. Prog Energy Combust Sci 2012;38:551-582.
8) van Ommen JR, Coppens MO, van den Bleek CM, Schouten JC. Early warning of agglomeration in fluidized beds by attractor comparison. AIChE J 2000;46:2183-2197.
9) Noble LA. Method of preventing or reducing polymer agglomeration on grid in fluidized-bed reactors.2012;US8129482 B2.
10) Siegell JH. High-temperature defluidization. Powder Technol 1984;38:13-22.
11) Tardos G, Mazzone D, Pfeffer R. Destabilization of fluidized beds due to agglomeration part I: Theoretical model. Can J Chem Eng 1985;63:377-383.
12) Tardos G, Mazzone D, Pfeffer R. Destabilization of fluidized beds due to agglomeration part II: Experimental verification. Can J Chem Eng 1985;63:384-389.
13) Schouten JC, van den Bleek CM. Monitoring the quality of fluidization using the short-term predictability of pressure fluctuations. AIChE J 1998;44:48-60.
14) Korbee R, van Ommen JR, Lensselink J, Nijenhuis J, Kiel JHA, van den Bleek CM. Early agglomeration recognition system (EARS). In: 17th International Fluidized Bed Combustion Conference, Jacksonville, Florida USA, 2003.
15) Chirone R, Miccio F, Scala F. Mechanism and prediction of bed agglomeration during fluidized bed combustion of a biomass fuel: Effect of the reactor scale. Chem Eng J 2006;123:71-80.
16) Scala F, Chirone R. Characterization and early detection of bed agglomeration during the fluidized bed combustion of olive husk. Energy Fuels 2006;20:120-132.

17) Nijenhuis J, Korbee R, Lensselink J, Kiel JHA, van Ommen JR. A method for agglomeration detection and control in full-scale biomass fired fluidized beds. Chem Eng Sci 2007;62:644-654.
18) Bartels M, Nijenhuis J, Lensselink J, Siedlecki M, de Jong W, Kapteijn F, van Ommen JR. Detecting and counteracting agglomeration in fluidized bed biomass combustion. Energy Fuels 2009;23:157-169.
19) Werther J. Measurement techniques in fluidized beds. Powder Technol 1999;102:15-36.
20) van Ommen JR, van der Schaaf J, Schouten JC, van Wachem BGM, Coppens MO, van den Bleek CM. Optimal placement of probes for dynamic pressure measurements in large-scale fluidized beds. Powder Technol 2004;139:264-276.
21) de Martín L, van den Dries K, van Ommen JR. Comparison of three different methodologies of pressure signal processing to monitor fluidized-bed dryers/granulators. Chem Eng J 2011;172:487-499.
22) van Ommen JR, Sasic S, van der Schaaf J, Gheorghiu S, Johnsson F, Coppens MO. Time-series analysis of pressure fluctuations in gas–solid fluidized beds – A review. Int J Multiphase Flow 2011;37:403-428.
23) van der Schaaf J, Schouten JC, van den Bleek CM. Origin, propagation and attenuation of pressure waves in gas-solid fluidized beds. Powder Technol 1998;95:220-233.
24) van der Schaaf J, Schouten JC, Johnsson F, van den Bleek CM. Non-intrusive determination of bubble and slug length scales in fluidized beds by decomposition of the power spectral density of pressure time series. Int J Multiphase Flow 2002;28:865-880.
25) Shabanian J, Sauriol P, Rakib A, Chaouki J. Application of temperature and pressure signals for early detection of defluidization conditions. Procedia Eng 2015;102:1006-1015.
26) Shabanian J, Fotovat F, Bouffard J, Chaouki J. Fluidization behavior in a gas-solid fluidized bed with thermally induced inter-particle forces. In: Knowlton TM, Editor. Proceedings of the 10th International Conference on Circulating Fluidized Beds and Fluidization Technology, Engineering Conferences International, New York, USA, 2011.
27) Shabanian J, Chaouki J. Hydrodynamics of a gas–solid fluidized bed with thermally induced interparticle forces. Chem Eng J 2015;259:135-152.
28) Shabanian J, Chaouki J. Local characterization of a gas-solid fluidized bed in the presence of thermally induced interparticle forces. Chem Eng Sci 2014;119:261-273.

29) Shabanian J, Chaouki J. Influence of interparticle forces on solids motion in a bubbling gas-solid fluidized bed. Powder Technol 2015; submitted for publication.
30) Shabanian J, Chaouki J. Pressure signals in a gas-solid fluidized bed with thermally induced inter-particle forces. In: Kuipers JAM, Mudde RF, van Ommen JR, Deen NG, Editors. Proceedings of the 14th International Conference on Fluidization – From Fundamentals to Products, ECI Digital Archives, Noordwijkerhout, The Netherlands, 2013.
31) Shabanian J, Chaouki J. Fluidization characteristics of a bubbling gas-solid fluidized bed at high temperature in the presence of interparticle forces. Chem Eng J 2015; submitted for publication.
32) Zenz FA. Bubble formation and grid design. Inst Chem Eng Symp Ser 1968;30:136-139.
33) Benjelloun F, Liégeois R, Vanderschuren J. Détermination des Longueurs de jets de gazhorizontauxdans les litsfluidisés. In: Laguérie C, Guigon P, Editors. Récentsprogrès en génie des procédés - La fluidisation, Toulouse, 1991.
34) Yates JG, Cobbinah SS, Cheesman DJ, Jordan SP. Particle attrition in fluidized feds containing opposing jets. AIChE Symp Ser 1991;87:13-19.
35) Sauriol P, Cui H, Chaouki J. Gas jet penetration lengths from upward and downward nozzles in dense gas–solid fluidized beds. Powder Technol 2013;235:42-54.
36) Yang X, van Ommen JR, Mudde RF. Gas distribution of a downward micro-nozzle assisted fluidized bed of fine powder. Chem Eng J 2015;264:945-953.
37) Werther J, Molerus O. The local structure of gas fluidized beds —II. The spatial distribution of bubbles. Int J Multiphase Flow 1973;1:123-138.
38) Mostoufi N, Chaouki J. On the axial movement of solids in gas-solid fluidized beds. Chem Eng Res Des 2000;78:911-920.
39) Stein M, Ding YL, Seville JPK, Parker DJ. Solids motion in bubbling gas fluidised beds. Chem Eng Sci 2000;55:5291-5300.

CHAPTER 11 GENERAL DISCUSSION

The main objective of this work was to shed light on the fluidization behavior of a gas-solid fluidized bed at high temperature in the presence of IPFs. To achieve this, the variations in the magnitude of HDFs and IPFs depending on the operating temperature must be simultaneously accounted for. Due to the harsh operating conditions at elevated temperatures, which restrict the application of different types of measurement techniques for hydrodynamic study, this research was divided into two parts. In the first part, studying the influence of IPFs on the global and local hydrodynamic aspects of a gas-solid fluidized bed was targeted with the help a novel approach to introduce different levels of IPFs into the bed at near-ambient conditions. The second part of the work was attempted through an extensive experimental campaign at high temperature with the help of the pressure and temperature measurements when varying levels of IPFs were introduced into the bed. The detailed information collected from these two parts were employed to achieve the main objective of the research program.

A polymer coating approach was adopted in the first part of this study to enhance and control the level of artificial IPFs in a gas-solid fluidized bed. In this technique, spherical inert particles are primarily coated with a polymer material (PMMA/PEA copolymer) having a low glass transition temperature. Since the level of artificial IPFs is dependent on the temperature of the coated particles, they can be easily adjusted by the temperature of the inlet air into the bed when coated particles are employed in the gas-solid fluidized bed for the fluidization study. The operating temperature was thus varied near the glass transition temperature of the polymer, i.e., between 20–40^{o}C, to yield different levels of IPFs in the bed. Operating under mild conditions when applying the polymer coating approach allowed for the application of different reliable and accurate measurement techniques, i.e., pressure transducers, an optical fiber probe, and the radioactive particle tracking (RPT) technique, for the purpose of a comprehensive hydrodynamic study. In addition, by taking advantage of the capability of the polymer coating approach in reproducing and simulating the conditions of a high temperature gas-solid fluidized bed, it was possible to study the same phenomena yet in a much friendlier environment. The study of hydrodynamics was attempted at different superficial gas velocities covering the fixed bed state and bubbling and turbulent fluidization regimes. Sugar beads representing Geldart group B behaviors at ambient conditions for which the level of IPFs was at minimum were adopted as the reference system. The coated

particles with a 5 μm uniform layer of coating were produced through an atomization process in a spheronizer machine.

The measurements of the global hydrodynamic parameters were attempted by the visual observation of the bed height and recording the gauge and differential pressure signals in the dense bed and windbox as well as the total bed pressure drop to investigate the influence of IPFs on the bed behavior. The measurement of the total bed pressure drop showed that the bed behavior shifted from the typical Geldart group B to Geldart group A or even C by increasing the level of IPFs. This observation is in close agreement with those made by Seviller and Clift [1] and McLaughline and Rhodes [2], who increased the level of IPFs in a gas-solid fluidized bed by injection of a liquid. This measurement also demonstrated that the minimum fluidization velocity increased with IPFs. The need for an additional drag force by the fluidizing gas in excess of the apparent weight of the bed to compensate for the yield stress of the particulate bed due to IPFs can explain this modification. An identical trend was also reported in earlier publications [1-3]. The measurement of the bed height in the bubbling regime when combined with a simple two-phase flow assumption and the bubble size data obtained by the pressure measurements showed that the fluidizing gas was more prone to pass through the bed in the emulsion phase in this fluidization regime. This was a promising finding since a better gas-solid contact can be achieved in the emulsion phase. However, further investigation/confirmation by other measurement techniques was required. The measurement of pressure signals was employed to verify this modification and also explore the effect of IPFs on the dilute phase characteristics in the bubbling and turbulent fluidization regimes. The analysis of pressure signals demonstrated that slightly smaller bubbles with a lower passage frequency were present in a bed with a higher level of IPFs in the range of gas velocities similar to the bed height measurements. This showed that the tendency of gas to enter the bubble phase decreased with IPFs in the bubbling regime and, hence, confirmed the finding obtained by the bed height measurements. The calculation of the standard deviation of recorded pressure signals within the dense bed, which is closely related to the characteristic dimension of bubbles in the bed [4], revealed that the growth rate of bubbles with the superficial gas velocity increased with IPFs. This resulted in the presence of larger bubbles in a bed with a moderate level of IPFs at higher gas velocities in the bubbling regime in contrast with the modification observed at lower gas velocities of this regime. The analysis also showed that the presence of IPFs delayed the transition from bubbling to turbulent fluidization regime. The presence of smaller bubbles in a cohesive bed at

superficial gas velocities close to the minimum fluidization velocity in the bubbling regime can be interpreted as the higher capacity of the emulsion phase to hold gas inside its structure, thus decreasing the amount of gas entering to the bubble phase. This modification in the structure of the emulsion phase, which was confirmed by the local measurements, could in turn contribute to the reduction of the bubble size as well as the passage frequency of bubbles in the bed. However, upon increasing the gas velocity, since the emulsion phase could show a greater resistance to any change in its structure at a higher level of IPFs, it could restrict the formation of stalactites of particles on the bubbles' roof [5], leading to the enlargement of bubbles with the superficial gas velocity at a higher rate. The continuous structure of the emulsion phase experiences a complete break-down upon the bubbling to turbulent regime transition giving rise to the presence of clusters of particles in a turbulent bed. The enhanced resistance of the emulsion phase by IPFs can also explain why the bubbling to turbulent regime transition occurred at a higher superficial gas velocity when the level of IPFs was increased in the bed. The visual observations further indicated that the solids entrainment rate decreased with increasing the level of IPFs. This is in line with the observations made by other researchers [6, 7] when measuring the elutriation rate in a bed of fine particles at a constant gas velocity by decreasing the particle size from a typical Geldart group A to group C powders, referred to the fluidization behavior at ambient conditions. An increase in the level of IPFs was argued as the major factor controlling this change.

The local hydrodynamic measurements with the help of an optical fiber probe were subsequently attempted to provide a clear insight into the impact of IPFs on the two-phase flow structure of the bed. The results obtained in this section of the study were also employed to verify the findings achieved through the global hydrodynamic measurements. The analysis of the instantaneous local bed voidage signals demonstrated that the emulsion phase voidage and fraction increased with IPFs. Integrating the data obtained from the optical fiber measurements and the bubble size from the pressure measurements showed that the fluidizing gas tended to interstitially pass through a more cohesive bed in the bubbling regime, i.e., $U_g<U_{c,No\ IPFs}$. This finding confirms the argument made after the global hydrodynamic measurements. It is also in broad accordance with the experimental results of Rowe et al. [8] and Yates and Newton [9]. They observed that increasing the amount of fines (<45 μm), which can be interpreted as an increase in the level of IPFs within the bed, increased the emulsion phase voidage and the amount of gas entering the emulsion phase. A different trend was observed at gas velocities higher than $U_{c,No\ IPFs}$, i.e., a lower amount of gas

was passing through the cohesive bed in the dense phase. This can be ascribed to the bypassing of the fluidizing gas with the larger bubbles in a bed with IPFs at superficial gas velocities higher than $U_{c,No\ IPFs}$. The evaluation of the local bubble passage frequency, the mean contact time of the optical probe with bubbles that indirectly represents the average bubble size, and the meso-scale bubbling to turbulent fluidization regime transition velocities showed that they were in good agreement with similar global hydrodynamic parameters evaluated from the recorded pressure signals. The identical observations made by two different measurement techniques with completely different measurement volumes consolidated the experimental findings achieved in this study.

An increase in the propensity of the fluidizing gas to pass through the bed in the emulsion phase due to the presence of IPFs in the bubbling regime can offer an appreciable advantage for systems requiring good gas-solid contacting, e.g., a catalytic gas-solid fluidized bed reactor, since a better gas-solid contact is achieved in the emulsion phase. In order to verify this hypothesis a simulation study of an industrial-scale fluidized bed reactor was attempted. The catalytic partial oxidation of n-butane into maleic anhydride over the vanadium phosphorus oxide catalyst was chosen as a catalytic example reaction and the corresponding kinetic model was adopted from open literature. To describe the hydrodynamics of the reactor at different levels of IPFs, the simple two-phase model was integrated with the hydrodynamic parameters measured for beds at varying levels of IPFs. As expected, the simulation results demonstrated that enhancing the level of IPFs in a catalytic bubbling fluidized bed reactor, far from defluidization conditions, can improve the overall performance of the reactor. Nevertheless, a higher amount of gas bypassing in a cohesive bed at superficial gas velocities higher than $U_{c,No\ IPFs}$ reduced the performance of the reactor.

Although increasing the level of IPFs in the bubbling regime can favorably divide the fluidizing gas toward the emulsion phase, which is beneficial for a better gas-solid contact, a reduced amount of gas flowing through the bubble phase can have a negative impact on the quality of solids mixing in the bed. The quality of solids mixing governs the uniformity of the temperature profile within the bed and is a critical parameter in the case of gas-solid fluidized bed reactors that host very rapid reactions [10]. Thus, the RPT technique was employed with the polymer coating approach to shed light on the influence of IPFs on the quality of solids mixing in the bubbling regime. The calculation of characteristic parameters of solids mixing for beds with and without IPFs with the help of RPT data revealed that the quality of global and local solids mixing decreased in a bubbling bed with IPFs. The evaluation of the idle and bubble-induced times indicated that this modification in the

bed behavior was principally induced by an increase in the resistance of the emulsion phase resulting from the presence of IPFs. Therefore, the level of IPFs in a catalytic bubbling gas-solid fluidized bed reactor must be increased in a controlled manner to enhance the performance of the reactor. The progressive agglomeration process, which normally occurs for beds approaching complete defluidization at high temperature, is known as a self-promoting phenomenon [11, 12]. By considering the bubble phase as a kinetic energy source and the emulsion phase as a kinetic energy sink [13] an increase in the idle time with IPFs indicates that the cohesive particles spend a longer time in the energy sink portion of the bed. It promotes these particles to adhere to each other and enlarge the new fluidizing entity, i.e., agglomerates. Consequently, the size of agglomerates increases rapidly toward the size of the bed diameter, i.e., the complete defluidization state, when the level of IPFs continuously increases inside the system.

The second part of this study was aimed at understanding the fluidization behavior of a gas-solid fluidized bed in the presence of IPFs under real hot operating conditions. Accordingly, two kinds of coarse particles, i.e., silica sand (d_p=820 μm) and olivine (d_p=565 μm), for which the levels of IPFs were at minimum under the tested span of operating temperatures (700–1000^{o}C), were selected as reference systems. The fresh coarse particles were employed for hydrodynamic study at different operating temperatures at first. The analysis of gauge and differential pressure signals for bubbling beds of these fresh particles indicated that the bubble size decreased with temperature while the bubble passage frequency remained comparatively unchanged. Since the level of IPFs was at minimum for these fresh particles, the observed modification in the bed behavior can be attributed to the variation in HDFs while a decrease in the gas density is dominant for the size of particles adopted here. The level of IPFs was then increased in the bed through the combustion of some solid fuels with varying contents of alkali/alkali earth metals in fluidized beds of otherwise fresh particles. The embedded impurities within the solid fuels formed eutectic compounds with the SiO_2 component from the bed materials and, hence, enhanced the level of IPFs. As the fresh silica sand consisted mainly of SiO_2 while the fresh olivine contained 49.7 wt% MgO, 41.5 wt% SiO_2, and 7.3 % Fe_2O_3 (the rest other components), a lower level of IPFs could be experienced for a bed of olivine particles when combusting a solid fuel with a given Na content in beds of these particles. The experimental results confirmed this expectation. Accordingly, a broad range of conditions with different levels of IPFs was achieved by varying the type of solid fuel and the bed material. The temperature and bed pressure drop measurements showed that the minimum

fluidization velocity increased with IPFs. Also, the analysis of the standard deviation of pressure signals recorded for beds with varying degrees of IPFs demonstrated an identical behavior to what was observed with the help of the polymer coating approach at near-ambient conditions, i.e., an inversion trend was observed at a moderate level of IPFs in the bed. At a high level of IPFs, which was present in a bed of silica sand after combustion of a solid fuel with a moderate Na content, the bed had larger bubbles at all tested superficial gas velocities in comparison with a bed of fresh coarse particles. Increasing the resistance of the emulsion phase of a gas-solid fluidized bed with IPFs at a high/very high level resembles an increase of the liquid phase viscosity in a bubble column. Since larger bubbles with higher momentums are required to pass through the bubble column of a viscous liquid [14], larger bubbles must be present in a gas-solid fluidized bed with a high/very high level of IPFs compared to a non-cohesive bed to be capable of passing through the bed. The appreciable similarity between the results of the first and second parts of the study proved that a suitable strategy was adopted throughout this work to provide a comprehensive understanding on the subject.

The experimental results obtained from this study provided two promising findings in relation to the timely recognition of defluidization conditions for a bubbling gas-solid fluidized bed. The average in-bed differential pressure drop recorded from the well stabilized section of the bed decreased with increasing the level of IPFs at identical fluidizing gas throughput in the bubbling regime. An increased capacity of the emulsion phase to hold gas inside its structure at higher levels of IPFs is mainly responsible for this evolution. The presence of considerably large/oblong bubbles at high levels of IPFs can further decrease the mean in-bed differential pressure drop in the bubbling regime. Also, a decrease in the quality of solids mixing when IPFs are present in the bed reduces the uniformity of the bed temperature profile. Since the level of IPFs progressively increases in a cohesive bed that is approaching complete defluidization conditions, the average in-bed differential pressure drop decreases and the axial temperature gradient simultaneously increases over the processing time. Thus, a new agglomeration detection approach was established on the above developments. The most sensitive position for the measurement of temperature within the dense bed, with respect to the variation of IPFs, was identified with the help of the RPT technique as the lowermost level right above the distributor plate. Accordingly, a temperature measurement at this location was attempted in all high temperature defluidization tests to be compared with other measurements at the higher levels within the dense bed. Although the new technique is simple, it

was very efficient in the timely recognition of the onset of agglomeration minutes to hours before the complete defluidization state. It also showed a low level of sensitivity to the variation of other influential operating parameters, i.e., the bed temperature (±100°C), U_g (±10%), and the bed mass (±20%). Based on the observations made throughout many defluidization incidents, when combusting a solid fuel or propane, two pairs of detection thresholds for the advanced recognition of agglomeration in bubbling fluidized beds of coarse silica sand particles (d_p=820 μm) are introduced. They act as the high and high-high alarms for the purpose mentioned here. The application of the new detection approach for the opportune detection of defluidization conditions in a cohesive bubbling bed of fine silica sand particles (d_p=370 μm) also demonstrated an encouraging performance.

11.1 References

1) J.P.K. Seville, R. Clift, The effect of thin liquid layers on fluidisation characteristics, Powder Technol. 37 (1984) 117-129.
2) L.J. McLaughlin, M.J. Rhodes, Prediction of fluidized bed behaviour in the presence of liquid bridges, Powder Technol. 114 (2001) 213-223.
3) M.J. Espin, J.M. Valverde, M.A.S. Quintanilla, A. Castellanos, Stabilization of gas-fluidized beds of magnetic powders by a cross-flow magnetic field, J. Fluid Mech. 680 (2011) 80-113.
4) N. Sadasivan, D. Barreteau, C. Laguerie, Studies on frequency and magnitude of fluctuations of pressure drop in gas-solid fluidized beds, Powder Technol. 26 (1980) 67-74.
5) R. Clift, J.R. Grace, The mechanism of bubble break-up in fluidised beds, Chem. Eng. Sci. 27 (1972) 2309-2310.
6) K. Smolders, J. Baeyens, Elutriation of fines from gas fluidized beds: mechanisms of elutriation and effect of freeboard geometry, Powder Technol. 92 (1997) 35-46.
7) D. Geldart, A.C.Y. Wong, Entrainment of particles from fluidized beds of fine particles, in AIChE Symp. Ser. (1987) 1-9.
8) P.N. Rowe, L. Santoro, J.G. Yates, The division of gas between bubble and interstitial phases in fluidised beds of fine powders, Chem. Eng. Sci. 33 (1978) 133-140.
9) J.G. Yates, D. Newton, Fine particle effects in a fluidized-bed reactor, Chem. Eng. Sci. 41 (1986) 801-806.

10) N. Mostoufi, J. Chaouki, Local solid mixing in gas-solid fluidized beds, Powder Technol. 114 (2001) 23-31.

11) G. Olofsson, Z. Ye, I. Bjerle, A. Andersson, Bed agglomeration problems in fluidized-bed biomass combustion, Ind. Eng. Chem. Res. 41 (2002) 2888-2894.

12) R. Korbee, J.R. van Ommen, J. Lensselink, J. Nijenhuis, J.H.A. Kiel, C.M. van den Bleek, Early agglomeration recognition system (EARS), in: Proceedings of the 17th International Fluidized Bed Combustion Conference, Jacksonville, Florida USA, 2003.

13) M. Stein, Y.L. Ding, J.P.K. Seville, D.J. Parker, Solids motion in bubbling gas fluidised beds, Chem. Eng. Sci. 55 (2000) 5291-5300.

14) A. Esmaeili, C. Guy, J. Chaouki, The effects of liquid phase rheology on the hydrodynamics of a gas-liquid bubble column reactor, Chem. Eng. Sci. 129 (2015) 193-207.

CHAPTER 12 CONCLUSION AND RECOMMENDATIONS

12.1 Conclusion

The hydrodynamic characterization of a gas-solid fluidized bed at high temperature in the presence of IPFs was regarded as the main target of this work. To approach this study in the most efficient manner, we divided it into two parts. First, a comprehensive investigation was attempted to fundamentally delineate the fluidization characteristics of a gas-solid fluidized bed at varying degrees of IPFs from global and local points of view. Second, the fluidization behavior of a gas-solid fluidized bed at high temperature was subjected to a detailed study while different levels of IPFs were deliberately introduced into a bed of otherwise fresh coarse particles.

The polymer coating approach was adopted for the first part of the study to induce and adjust the level of IPFs in a fluidized bed at near-ambient conditions. This method can simulate the conditions of a gas-solid fluidized bed at high temperature under much milder conditions. Hence, it allows the applicability of nearly all kinds of measurement techniques for the purpose of hydrodynamic study. Fluidization characterization was attempted with the assistance of some gauge and differential pressure transducers, an optical fiber probe, and the RPT technique at different superficial gas velocities covering the fixed bed state, bubbling, and turbulent fluidization regimes. As the most promising findings of this part of the study, the fluidization behavior of powders showing Geldart group B behavior at ambient conditions was altered by enhancing the level of IPFs through an increase in the following: fixed bed voidage/permeability, minimum fluidization velocity (U_{mf}), transition velocity from bubbling to turbulent fluidization regime (U_c), growth rate of bubble size with the superficial gas velocity (U_g) at a moderate/high level of IPFs yielding larger bubbles at gas velocities approaching and above $U_{c,\text{No IPFs}}$, emulsion phase voidage and fraction, idle time, and propensity of gas to pass through the bed in the emulsion phase of a bubbling bed. Bypassing the fluidizing gas at gas velocities above $U_{c,\text{No IPFs}}$ while the bed with IPFs was still operating in the bubbling regime or within the span of bubbling to turbulent regime transition and a decrease in the bubble passage frequency, quality of solids mixing, entrainment rate, and bubble size when the level of IPFs increased by a low level and the bed was operating at low to moderate gas velocities in the bubbling regime were among the promising findings as well. A simulation study of an industrial-scale fluidized bed reactor was then attempted integrating the two-phase flow model and

the hydrodynamic parameters measured for beds with different levels of IPFs while a kinetic model was adopted from open literature. The results showed that increasing the level of IPFs in a bubbling bed, far from defluidization conditions, can enhance the overall performance of a catalytic gas-solid fluidized bed reactor. Increasing the tendency of the gas to interstitially pass through a bubbling bed can explain this behavior. However, it can exhibit a different effect at superficial gas velocities higher than $U_{c,No\ IPFs}$ due to an accelerated gas bypassing that takes place in a bed with IPFs.

In the second part of the study, the influence of temperature on the hydrodynamics of a bubbling gas-solid fluidized bed of fresh coarse particles was primarily investigated. The level of IPFs was at minimum under the operating conditions tested for this case. Upon increasing the operating temperature, the bubble size decreased and the bubble passage frequency remained comparatively unchanged. For the next step, varying degrees of IPFs were induced into a bed of fresh coarse particles through the combustion of different solid fuels with varying contents of alkali/alkali earth metals. Increasing the level of IPFs increased the minimum fluidization velocity and resulted in different fluidization characteristics in the bubbling regime depending on the magnitude of IPFs. The results were in good agreement with those obtained in the first part of this study.

With the help of the detailed information collected in this study about the influence of IPFs on the fluidization behavior of a bubbling fluidized bed of coarse particles, a novel technique was introduced for the early warning of defluidization conditions. The new method benefits from its simplicity, effectiveness, and robustness with respect to the variation of influential operating parameters, i.e., bed temperature (±100^{o}C), U_g (±10%), and bed mass (±20%). It was established on the simultaneous measurements of local temperature and in-bed differential pressure signals. It showed promising performance in the timely detection of the onset of agglomeration minutes to hours before complete defluidization. According to the experimental observations, two pairs of detection thresholds for the advanced recognition of agglomeration in bubbling fluidized beds of coarse silica sand particles were proposed.

12.2 Original contributions

This study provides a large amount of information about the hydrodynamics of gas-solid fluidized beds in the presence of IPFs. By taking advantage of the application of the novel polymer coating

approach and various reliable and accurate measurement techniques, the effect of IPFs on the fluidization behavior at operating conditions that have never been studied before, i.e., well above U_{mf} in the bubbling and turbulent fluidization regimes, were investigated for the first time from both global and local points of view. It was shown for the first time that increasing the level of IPFs in a bubbling bed of a given powder, far from defluidization conditions, enhances the propensity of the fluidizing gas to interstitially pass through the bed. As demonstrated through a simulation study, this modification in the two-phase flow structure of the bed can improve the overall performance of a catalytic bubbling gas-solid fluidized bed reactor. This finding offers a new strategy to favorably enhance the reaction performance of an industrial bubbling gas-solid fluidized bed reactor.

Gas-solid fluidized bed processes operating at high pressure and/or temperature have extensively employed in chemical industries. However, the effects of these operating parameters on changing the bed hydrodynamic aspects have not been well understood. The knowledge acquired in this study can help to interpret these effects on a phenomenological basis when combined with the variations of HDFs. It can also assist, in particular, in improving the performance of industrial processes employing gas-solid fluidized beds at elevated temperatures and establishing a more reliable design criteria and scale-up procedure for these systems. In other words, it can lead to a variety of improvements not only in overall economic efficiency but specifically in the energy- and resource-efficiency of chemical production plants, all of which will make a solid contribution to a sustainable chemistry. Furthermore, with the help of the experimental findings through adopting the novel polymer coating approach, a simple and robust criterion was proposed for the early detection of defluidization conditions. This novel criterion was tested for many defluidization incidents, specifically targeted at the conditions relevant to the high temperature bubbling fluidized bed combustors/gasifiers, and demonstrated very promising performance for the purpose. Since the agglomeration identification method is taking advantage of the application of two measurement techniques that are common in industrial fluidized bed applications, it can be conveniently and securely exploited in industry.

12.3 Recommendations

This research shed light on the influence of IPFs on the hydrodynamic characteristics of gas-solid fluidized beds. In addition to the insight gained here, some avenues for future study are recommended as follows:

- **Investigate the influence of IPFs on the reaction performance of a catalytic bubbling gas solid fluidized bed reactor (under real conditions).** It is recommended to employ a mindful technique to increase the level of IPFs in a gas-solid fluidized bed while the main physical properties of the bed materials (particle size and density) are kept relatively constant. Doping of base catalyst particles by a trace amount of varying species with different sintering temperatures can be considered as the model approach. With this technique it can be attempted to keep the maximum active sites of the catalyst available for the reaction phase while modifying the magnitude of van der Waals forces acting between the particles under the reactive operating conditions.
- **Develop hydrodynamic correlations/models integrating the effects of IPFs and HDFs.** Most of the conventional models/equations describing bed hydrodynamics have been developed based purely on hydrodynamic principals, i.e., included the effects of particle size and density, gas density and viscosity, and superficial gas velocity. It has been proven that these models/equations become increasingly inaccurate when the level of IPFs vary along with HDFs. Since the polymer coating approach can introduce varying degrees of IPFs in the bed at near-ambient conditions, different measurement techniques can be employed to accurately measure the required hydrodynamic parameters for the subsequent model development step. The mild operational conditions of this technique also allows for the measurement of the magnitude of IPFs acting between the particles.
- **Drive correlations predicting the bed hydrodynamic parameters based on the rheological properties of powders.** Results of this study showed that the presence of IPFs changed the interphase interaction between the bubble and emulsion phases, thus led to a modified bed behavior. The structural variation of the emulsion phase resulting from the presence of IPFs principally governed this modification. Rheological properties of sample powders, which are closely linked with the structural properties of the powder emulsion, represent the level of IPFs in a bed of similar powders. With the recent

advancement in the evaluation of the rheological properties of the particulate materials, the measurements of these parameters sound achievable under extreme conditions while the measurement of the magnitude of IPFs is still difficult to obtain. Developing correlations to link the hydrodynamic parameters with the rheological properties, measured at identical conditions of the fluidized bed, offers promising progress in the accurate prediction of the fluidization behavior of a bed operating under extreme conditions. The application of the polymer coating approach could help with the production of powders with different rheological properties, as part of the study at near-ambient conditions.

- **Study the effect of IPFs on the hydrodynamics of spouted beds.** Conical spouted beds are suitable for handling of solids with a wide particle size distribution or cohesive powders that are difficult to handle with other gas-solid contact techniques [1]. Despite their simple construction and easy design, they have been employed in many applications in pharmaceutical and food industries as well as in chemical processes, such as catalytic polymerization and pyrolysis of plastic and sawdust [2], where drying, coating, and granulation as clear process examples with the presence of IPFs are regularly experienced. We believe that the application of the polymer coating approach with particles showing Geldart group D behavior at ambient conditions in a spouted bed can provide valuable insight into the flow dynamics of sticky powders in this gas-solid contacting system.
- **Investigate the influence of IPFs on the fluidization characteristics of Geldart group A powders (referred to the fluidization behavior at ambient conditions).** Fine powders showing typical Geldart group A behavior at ambient conditions are extensively employed in process industries owing to their easily fluidizable property and large specific surface area, which makes them ideal for both catalytic and non-catalytic gas-solids reactions. It has long been known in the industry that adding fines (< 45 μm) to the FCC unit can assist with preventing the blockage of standpipes [3] and enhancing the reaction performance of a catalytic gas-solid fluidized bed reactor [4, 5]. Although increasing the amount of fines in the bed inventory enhanced the degree of IPFs in a gas-solid fluidized bed through an increased available surface for the particle-particle contacts, they can slip in the voids between larger particles, i.e., act as a lubricant and thus reduce the friction forces and decrease the minimum fluidization velocity [6-8]. In

order to determine the relative importance of these two effects, it is recommended to apply the polymer coating approach with some fine particles of Geldart group A powders, referred to the fluidization behavior at ambient conditions, in a gas-solid fluidized bed for the hydrodynamic study. Since physical properties of the base particles, i.e., particle size and density, remain comparatively constant when applying the polymer coating approach, the influence of IPFs on the bed behavior of these fine particles can be exclusively explored.

12.4 References

1) M. Olazar, M. San Jose, R. Llamosas, S. Alvarez, J. Bilbao, Study of local properties in conical spouted beds using an optical fiber probe, Ind. Eng. Chem. Res. 34 (1995) 4033-4039.
2) M.S. Bacelos, J.T. Freire, Flow regimes in wet conical spouted beds using glass bead mixtures, Particuology 6 (2008) 72-80.
3) H.Y. Xie, D. Geldart Fluidization of FCC powders in the bubble-free regime: effect of types of gases and temperature, Powder Technol. 82 (1995) 269-277.
4) M. Pell, S.P. Jordan, Effects of fines and velocity on fluid bed reactor performance, AIChE Symp. Ser. 262 (1988) 68-73.
5) G. Sun, J.R. Grace, The effect of particle size distribution on the performance of a catalytic fluidized bed reactor, Chem. Eng. Sci. 45 (1990) 2187-2194.
6) G.L. Matheson, W.A. Herbst, P.H. Holt, Characteristics of fluid–solid systems, J. Ind. Eng. Chem. 41 (1949) 1098–1104.
7) L. Cheung, A.W. Nienow, P.N. Rowe, Minimum fluidisation velocity of a binary mixture of different sized particles, Chem. Eng. Sci. 29 (1974) 1301-1303.
8) C.-L. Lin, M.-Y. Wey, S.-D. You, The effect of particle size distribution on minimum fluidization velocity at high temperature, Powder Technol. 126 (2002) 297-301.

BIBLIOGRAPHY

A. Ajbar, K. Alhumazi, M. Asif, Improvement of the fluidizability of cohesive powders through mixing with small proportions of group A particles, Can. J. Chem. Eng. 83 (2005) 930-943.

A. Ajbar, Y. Bakhbakhi, S. Ali, M. Asif, Fluidization of nano-powders: effect of sound vibration and pre-mixing with group A particles, Powder Technol. 206 (2011) 327-337.

A. Castellanos, J.M. Valverde, M.A.S. Quintanilla, Aggregation and sedimentation in gas-fluidized beds of cohesive powders, Phys. Rev. E 64 (2001) 041304.

A. Castellanos, , J.M. Valverde, M.A.S. Quintanilla, Physics of Compaction of Fine Cohesive Particles, Phys. Rev. Lett. 94 (2005) 075501.

A. Chehbouni, J. Chaouki, C. Guy, D. Klvana, Characterization of the flow transition between bubbling and turbulent fluidization, Ind. Eng. Chem. Res. 33 (1994) 1889-1896.

A. Chehbouni, J. Chaouki, C. Guy, D. Klvana, Effect of temperature on the hydrodynamics of turbulent fluidized beds, in: C. Laguerie, J.F. Large (Eds.), Proceedings of the 8th International Conference on Fluidization, Engineering Foundation, New York, 1995, pp. 149-156.

A. Desai, H. Kikukawa, A.H. Pulsifer, The effect of temperature upon minimum fluidization velocity, Powder Technol. 16 (1977) 143-144.

A. Dutta, L.V. Dullea, Effects of external vibration and the addition of fibers on the fluidization of a fine powder, AIChE Sym. Ser. 87 (1991) 38–46.

A. Esmaeili, C. Guy, J. Chaouki, The effects of liquid phase rheology on the hydrodynamics of a gas-liquid bubble column reactor, Chem. Eng. Sci. 129 (2015) 193-207.

A. Lucas, J. Arnaldos, J. Casal, L. Puigjaner, High temperature incipient fluidization in mono and polydisperese systems, Chem. Eng. Commun. 41 (1986) 121-132.

A. Mathur, S.C. Saxena, Particle classification scheme of saxena and ganzha and high-temperature bed voidage data at minimum fluidization, Powder Technol. 45 (1986) 287-289.

A. Mathur, S.C. Saxena, Z.F. Zhang, Hydrodynamic characteristics of gas-fluidized beds over a broad temperature range, Powder Technol. 47 (1986) 247-256.

A. Shekari, G.S. Patience, Transient kinetics of n-butane partial oxidation at elevated pressure, Can. J. Chem. Eng. 91 (2013) 291-301.

A.G. Bailey, Electrostatic phenomena during powder handling, Powder Technol. 37 (1984) 71-85.

A.J. Forsyth, S. Hutton, M.J. Rhodes, Effect of cohesive interparticle force on the flow characteristics of granular material, Powder Technol. 126 (2002) 150-154.

A.R. Abrahamsen, D. Geldart, Behavior of gas-fluidized beds of fine powders Part I. Homogeneous expansion, Powder Technol. 26 (1980) 35-46.

A.R. Abrahamsen, D. Geldart, Behavior of gas-fluidized beds of fine powders Part II. Voidage of dense phase in bubbling beds, Powder Technol. 26 (1980) 47-55.

A.R. Manzoori, E.R. Lindner, P.K. Agarwal, Inorganic transformation during the circulating fluid bed combustion of low-rank coals with high content of sodium and sulphur, in: Proceedings of the Engineering Foundation Conference on Inorganic Transformations and Ash Deposition During Combustion, Palm Coast, Florida, USA, 1991, pp. 735-762.

A.S. Monin, A.M. Yaglom, J.L. Lumley, Statistical Fluid Mechanics: Mechanics of Turbulence, Vol. 1., MIT Press, Cambridge, 1971.

A.T. Harris, On the vibration assisted fluidisation of silica nanoparticles, Int. J. Nanotechnol. 5 (2008) 179-194.

A.W. Pacek, A.W. Nienow, Fluidisation of fine and very dense hardmetal powders, Powder Technol. 60 (1990) 145-158.

A.W. Weimer, G.J. Quarderer, Effect of temperature on the dense phase in high pressure fluidized beds of fine powders, AIChE Symp. Ser. 80(241) (1984) 79-86.

B. Esmaeili, J. Chaouki, C. Dubois, An evaluation of the solid hold-up distribution in a fluidized bed of nanoparticles using radioactive densitometry and fiber optics, Can. J. Chem. Eng. 86 (2008) 543-552.

B. Esmaeili, J. Chaouki, C. Dubois, Encapsulation of nanoparticles by polymerization compounding in a gas/solid fluidized bed reactor, AIChE J. 55 (2009) 2271-2278.

B. Formisani, R. Girimonte, G. Pataro, The influence of operating temperature on the dense phase properties of bubbling fluidized beds of solids, Powder Technol. 125 (2002) 28-38.

B. Formisani, R. Girimonte, L. Mancuso, Analysis of the fluidization process of particle beds at high temperature, Chem. Eng. Sci. 53 (1998) 951-961.

B. Liss, T.R. Blake, A.M. Squires, R. Bryson, Incipient defluidization of sinterable solids, in: D. Kunii, R. Toei (Eds.), Proceedings of the 4th International Conference on Fluidization, Kashikojima, Japan, 1984, pp. 249-256.

B.E. Poling, J.M. Prausnitz, J.P. O'Connell, The Properties of Gases and Liquids, McGraw-Hill, New York, 2001.

B.J. Ennis, G. Tardos, R. Pfeffer, A microlevel-based characterization of granulation phenomena, Powder Technol. 65 (1991) 257-272.

B.M. Steenari, O. Lindqvist, V. Langer, Ash sintering and deposit formation in PFBC, Fuel 77 (1998) 407-417.

C. Brereton, J. Chaouki, J. R. Grace, R. Legros, J. Yeung, Hydrodynamic behavior of a silica aerogel powder in a circulating fluidized bed, in: Proceedings of the 37th Canadian Chemical Engineering Conference, Montreal, Canada, 1987.

C. Chavarie, K. Dobson, R. Clift and J.P.K. Seville, Study on the fluidization of group C aerogel powders by spontaneous dynamic agglomeration, in: Proceedings of the 37th Canadian Chemical Engineering Conference, Montreal, Canada, 1987.

C. Lauga, J. Chaouki, D. Klvana, C. Chavarie, Improvement of the fluidisability of Ni/SiO2 aerogels by reducing interparticle forces, Powder Technol. 65 (1991) 461-468.

C. Sishtla, I. Chan, T.M. Knowlton, The effect of temperature on bubble parameters in gas-fluidized beds, in: K. Ostergaard, A. Sorensen (Eds.), Proceedings of the 5th International Conference on Fluidization, 1986, pp. 127-134.

C. Tangsathitkulchai, M. Tangsathitkulchai, Effect of bed materials and additives on the sintering of coal ashes relevant to agglomeration in fluidized bed combustion, Fuel Process. Technol. 72 (2001) 163-183.

C. Vazquez, J.L. Nombela, C. Sobrino, M. de Vega, J. Zubia, D.S. Montero, Plastic fiber-optic probes for characterizing fluidized beds in bubbling regime, in: Proceedings of the 16th International Conference on Plastic Optical Fiber (POF), Turin, Italy, 2007.

C. Xu, J. Zhu, Experimental and theoretical study on the agglomeration arising from fluidization of cohesive particles--effects of mechanical vibration, Chem. Eng. Sci. 60 (2005) 6529-6541.

C. Xu, J.X. Zhu, Effects of gas type and temperature on fine particle fluidization, China Particuology 4 (2006) 114-121.

C. Zhu, G. Liu, Q. Yu, R. Pfeffer, R.N. Dave and C.H. Nam, Sound assisted fluidization of nanoparticle agglomerates, Powder Technol. 141 (2004) 119-123.

C. Zhu, Q. Yu, R.N. Dave, R. Pfeffer, Gas fluidization characteristics of nanoparticle agglomerates, AIChE J. 51 (2005) 426-439.

C. Xu, Y. Cheng, J. Zhu, Fine particle fluidization-effects of mechanical/acoustic vibration, in: Proceedings of Fluidization XI, 2004, pp. 627–634.

C.D. Si, Q.J. Guo, Wavelet analysis of particle concentration signals in an acoustic bubbling fluidized bed, Chem. Eng. Technol. 31 (2008) 1597-1604.

C.D. Wagner, L.E. Davis, M.V. Zeller, J.A. Taylor, R.H. Raymond, L.H. Gale, Empirical atomic sensitivity factors for quantitative analysis by electron spectroscopy for chemical analysis, Surf. Interface Anal. 3 (1981) 211-225.

C.D. Willett, The micromechanics of wet particulate materials, Ph.D. dissertation, University of Birmingham, 1999.

C.H. Nam, R. Pfeffer, R.N. Dave, S. Sundaresan, Aerated vibrofluidization of silica nanoparticles, AIChE J. 50 (2004) 1776-1785.

C.L. Briens, L.A. Briens, E. Barthel, J.M. Le Blevec, A. Tedoldi, A. Margaritis, Detection of local fluidization characteristics using the V statistic, Powder Technol. 102 (1999) 95–103.

C.L. Yaws, Chemical Properties Handbook, McGraw-Hill, New York, 1999.

C.Y. Wen, Y.H. Yu, Mechanics of fluidization, Chem. Eng. Prog. Symp. Ser. 62 (1966) 100-111.

C.-L. Lin, J.-H. Kuo, M.-Y. Wey, S.-H. Chang, K.-S. Wang, Inhibition and promotion: The effect of earth alkali metals and operating temperature on particle agglomeration/defluidization during incineration in fluidized bed, Powder Technol. 189 (2009) 57-63.

C.-L. Lin, M.-Y. Wey, The effect of mineral compositions of waste and operating conditions on particle agglomeration/defluidization during incineration, Fuel 83 (2004) 2335-2343.

C.-L. Lin, M.-Y. Wey, S.-D. You, The effect of particle size distribution on minimum fluidization velocity at high temperature, Powder Technol. 126 (2002) 297-301.

D. Bazic, D. Ahchieva, E. Piskova, S. Heinrich, Z. Grbavcic, Hydrodynamics of shallow fluidized bed of coarse particles, Chem. Eng. J. 114 (2005) 47-54.

D. Geldart, Types of gas fluidization, Powder Technol. 7 (1973) 285-292.

D. Geldart, A.R. Abrahamsen, Homogeneous fluidization of fine powders using various gases and pressures, Powder Technol. 19 (1978) 133-136.

D. Geldart, A.C.Y. Wong, Entrainment of particles from fluidized beds of fine particles, AIChE Symp. Ser. 83 (1987) 1-9.

D. Geldart, A.C.Y. Wong, Fluidization of powders showing degrees of cohesiveness--I. Bed expansion, Chem. Eng. Sci. 39 (1984) 1481-1488.

D. Geldart, D.S. Kapoor, Bubble sizes in a fluidized bed at elevated temperatures, Chem. Eng. Sci. 31 (1976) 842-843.

D. Geldart, N. Harnby, A.C. Wong, Fluidization of cohesive powders, Powder Technol. 37 (1984) 25-37.

D. Klvana, J. Chaouki, C. Lauga, C. Chavarie, D. Kusohorsky, G. Pajonk, Study of the performance of fluidization Ni/SiO2 aerogel for toluene hydrogenation, in: Proceedings of the 6th International Conference on Fluidization, Banff, Canada, 1989.

D. Kunii, O. Levenspiel, Fluidization Engineering, Butterworth-Heinemann, Boston, 1991.

D. Lepek, J.M. Valverde, R. Pfeffer, R.N. Dave, Enhanced nanofluidization by alternating electric fields, AIChE J. 56 (2010) 54-65.

D. Moslemian, Study of solids motion, mixing, and heat transfer in gas fluidized beds, Ph.D. dissertation, Illinois University, 1987.

D. Moslemian, M.M. Chen, B.T. Chao, Experimental and numerical investigation of solids mixing in a gas fluidized bed, Part. Sci. Technol. 7 (1989) 335-355.

D.C. Chitester, R.M. Kornosky, L.-S. Fan, J.P. Danko, Characteristics of fluidization at high pressure, Chem. Eng. Sci. 39 (1984) 253-261.

E. Jaraiz, S. Kimura, O. Levenspiel, Vibrating beds of fine particles: estimation of interparticle forces from expansion and pressure drop experiments, Powder Technol. 72 (1992) 23-30.

E. Marring, A. C. Hoffmann, L.P.B.M. Janssen, The effect of vibration on the fluidization behaviour of some cohesive powders, Powder Technol. 79 (1994) 1-10.

E.C. Eckstein, D.G. Bailey, A.H. Shapiro, Self-diffusion of particles in shear flow of a suspension, J. Fluid Mech. 79 (1977) 191-208.

E.K. Levy, B. Celeste, Combined effects of mechanical and acoustic vibrations on fluidization of cohesive powders, Powder Technol. 163 (2006) 41-50.

E.K. Levy, I. Shnitzer, T. Masaki and J. Salmento, Effect of an acoustic field on bubbling in a gas fluidized bed, Powder Technol. 90 (1997) 53-57.

E.K. Levy, W.J. Shakespears, A.T. Raissi, J.C. Chen, Particle elutriation from centrifugal fluidized beds, AIChE Symp. Ser. 77 (1981) 86-95.

E.M. Levin, H.F. McMurdie, F.P. Hall, Phase Diagrams for Ceramists, The American Ceramic Society, Ohio, 1956.

F. Benjelloun, R. Liégeois, J. Vanderschuren, Détermination des Longueurs de jets de gazhorizontauxdans les litsfluidisés, in: C. Laguérie, P. Guigon (Eds.), Proceedings of the Récentsprogrès en génie des procédés - La fluidisation, Toulouse, 1991.

F. Fotovat, J. Chaouki, J. Bergthorson, The effect of biomass particles on the gas distribution and dilute phase characteristics of sand–biomass mixtures fluidized in the bubbling regime, Chem. Eng. Sci. 102 (2013) 129-138.

F. Ghasemi, J. Rudd van Ommen, M. Sahimi, Analysis of pressure fluctuations in fluidized beds. I. Similarities with turbulent flow, Chem. Eng. Sci. 66 (2011) 2627-2636.

F. Johnsson, R.C. Zijerveld, J.C. Schoutten, C.M. van den Bleek, B. Leckner, Characterization of fluidization regimes by time-series analysis of pressure fluctuations, Int. J. Multiphase Flow 26 (2000) 663-715.

F. Larachi, G. Kennedy, J. Chaouki, A γ-ray detection system for 3-D particle tracking in multiphase reactors, Nucl. Instrum. Methods Phys. Res., Sect. A 338 (1994) 568-576.

F. Larachi, J. Chaouki, G. Kennedy, 3-D mapping of solids flow fields in multiphase reactors with RPT, AIChE J. 41 (1995) 439-443.

F. London, The general theory of molecular forces, Trans. Faraday Soc. 33 (1937) 8-26.

F. Scala, R. Chirone, Characterization and early detection of bed agglomeration during the fluidized bed combustion of olive husk, Energy Fuels 20 (2006) 120-132.

F.A. Zenz, Bubble formation and grid design, Inst. Chem. Eng. Symp. Ser. 30 (1968) 136-139.

G. Bruni, P. Lettieri, D. Newton, J. Yates, The influence of fines size distribution on the behaviour of gas fluidized beds at high temperature, Powder Technol. 163 (2006) 88-97.

G. Centi, G. Fornasari, F. Trifiro, n-Butane oxidation to maleic anhydride on vanadium-phosphorus oxides: kinetic analysis with a tubular flow stacked-pellet reactor, Ind. Eng. Chem. Prod. Res. Dev. 24 (1985) 32-37.

G. Jimbo, R. Yamazaki, G.H. Hong, Y. Oka, The characteristics of high-temperature fluidized bed, in: M. Kwauk, D. Kunii (Eds.), Proceedings of the Fluidization Science and Technology China-Japan Symposium, 1982, pp. 135-145.

G. Lian, C. Thornton, M.J. Adams, A theoretical study of the liquid bridge forces between two rigid spherical bodies, J. Colloid Interface Sci. 161 (1993) 138-147.

G. Lumay, N. Vandewalle, Controlled flow of smart powders, Phys. Rev. E, 78 (2008) 061302.

G. Olofsson, Z. Ye, I. Bjerle, A. Andersson, Bed agglomeration problems in fluidized-bed biomass combustion, Ind. Eng. Chem. Res. 41 (2002) 2888-2894.

G. Raso, M. D'Amore, B. Formisani, P.G. Lignola, The influence of temperature on the properties of the particulate phase at incipient fluidization, Powder Technol. 72 (1992) 71-76.

G. Sun, J.R. Grace, The effect of particle size distribution on the performance of a catalytic fluidized bed reactor, Chem. Eng. Sci. 45 (1990) 2187-2194.

G. Tardos, D. Mazzone, R. Pfeffer, Destabilization of fluidized beds due to agglomeration part I: Theoretical model, Can. J. Chem. Eng. 63 (1985) 377–383.

G. Tardos, D. Mazzone, R. Pfeffer, Destabilization of fluidized beds due to agglomeration part II: Experimental verification, Can. J. Chem. Eng. 63 (1985) 384–389.

G. Tardos, R. Pfeffer, Chemical reaction induced agglomeration and defluidization of fluidized beds, Powder Technol. 85 (1995) 29-35.

G.H. Hong, R. Yamazaki, T. Takahashi, G. Jombo, Minimum fluidization velocity in a fluidized bed at high temperatures, Kagaku Kogaku Ronbunshu 6 (1980) 557-562.

G.H. Qian, I. Bágyi, I.W. Burdick, R. Pfeffer, H. Shaw, J.G. Stevens, Gas–solid fluidization in a centrifugal field, AIChE J. 47 (2001) 1022-1034.

G.H. Qian, R. Pfeffer, H. Shaw, J. Stevens, Fluidization of group C particles using rotating fluidized beds, in: Proceedings of Fluidization X, Engineering Foundation, 2001, pp. 509-516.

G.L. Matheson, W.A. Herbst, P.H. Holt, Characteristics of fluid–solid systems, J. Ind. Eng. Chem. 41 (1949) 1098–1104.

G.R. Duursma, D.H. Glass, S.J.L. Rix, M.I. Yorquez-Ramirez, PIV investigations of flow structures in the fluidised bed freeboard region, Powder Technol. 120 (2001) 2-11.

G.-B. Zhao, Y.-R. Yang, Multiscale resolution of fluidized-bed pressure fluctuations, AIChE J. 49 (2003) 869-882.

H. Cui, J. Chaouki, Effects of temperature on local two-phase flow structure in bubbling and turbulent fluidized beds of FCC particles, Chem. Eng. Sci. 59 (2004) 3413-3422.

H. Cui, J. Chaouki, Interparticle forces in high temperature fluidization of geldart a particles, China Particuology 2 (2004) 113-118.

H. Cui, N. Mostoufi, J. Chaouki, Characterization of dynamic gas-solid distribution in fluidized beds, Chem. Eng. J. 79 (2000) 133–143.

H. Cui, N. Mostoufi, J. Chaouki, Comparison of measurement technique of local particle concentration for gas–solid fluidization, in: M. Kwauk, J. Li, W.C. Yang (Eds.), Proceedings of Fluidization X, Beijing, China, 2001, pp. 779-786.

H. Cui, N. Mostoufi, J. Chaouki, Gas and solids between dynamic bubble and emulsion in gas-fluidized beds, Powder Technol. 120 (2001) 12-20.

H. Cui, P. Sauriol, J. Chaouki, High temperature fluidized bed reactor: measurements, hydrodynamics and simulation. Chem. Eng. Sci. 58 (2003) 1071-1077.

H. Kage, N. Iwasaki, H. Yamaguchi, Y, Matsuno, Frequency analysis of pressure fluctuation in fluidized bed plenum, J. Chem. Eng. Japan, 24 (1991) 76-81.

H. Krupp, Particle adhesion: theory and experiment, Adv. Colloid Interface Sci. 1 (1967) 111-239.

H. Li, R. Hong, Z. Wang, Fluidizing ultrafine powders with circulating fluidized bed, Chem. Eng. Sci. 54 (1999) 5609-5615.

H. Li, R. Legros, C.M.H. Brereton, J.R. Grace, J. Chaouki, Hydrodynamic behaviour of aerogel powders in high-velocity fluidized beds, Powder Technol. 60 (1990) 121-129.

H. Liu, Q. Guo, S. Chen, Sound-assisted fluidization of SiO2 nanoparticles with different surface properties, Ind. Eng. Chem. Res. 46 (2007) 1345-1349.

H. Nakamura, S. Watano, Fundamental particle fluidization behavior and handling of nano-particles in a rotating fluidized bed, Powder Technol. 183 (2008) 324-332.

H. Rumpf, Particle adhesion, in: Proceedings of the 2nd International Symposium on Agglomeration (Agglomeration 77), AIME, 1977, pp. 97-129.

H. Rumpf, Zur theorie der zugfestigkeit vom agglomeraten bei kraftubertragung an kontaktpunkten, Chemie Ingenieur Technik 42 (1970) 538-542.

H. Tong, O. Qiu, H. Li, Fluidization characteristics of ultrafine particles in conical bed, in: Proceedings Fluidization IX, Engineering Foundation, 2004, pp. 715-722.

H. Wang, T. Zhou, J.S. Yang, J.J. Wang, H. Kage, Y. Mawatari, Model for calculation of agglomerate sizes of nanoparticles in a vibro-fluidized bed, Chem. Eng. Technol. 33 (2010) 388-394.

H. Zhu, J. Zhu, New investigation in regime transition from bubbling to turbulent fluidization, Can. J. Chem. Eng. 86 (2008) 553–562.

H. Zhu, J. Zhu, L. Guozheng, L. Fengyun, Detailed measurements of flow structure inside a dense gas-solids fluidized bed, Powder Technol. 180 (2008) 339-349.

H.J. Subramani, M.B. Mothivel Balaiyya, L.R. Miranda, Minimum fluidization velocity at elevated temperatures for Geldart's group-B powders, Exp. Therm. Fluid Sci. 32 (2007) 166-173.

H.P. Cui, N. Mostoufi, J. Chaouki, Comparison of measurement technique of local particle concentration for gas–solid fluidization, in: M. Kwauk, J. Li, W.C. Yang (Eds.), Proceedings of Fluidization X, United Engineering Foundation, New York, 2001, pp. 779-786.

H.R. Norouzi, N. Mostoufi, Z. Mansourpour, R. Sotudeh-Gharebagh, J. Chaouki, Characterization of solids mixing patterns in bubbling fluidized beds, Chem. Eng. Res. Des. 89 (2011) 817-826.

H.S. Fogler, Elements of Chemical Reaction Engineering (4th ed.), Pearson Education Inc., Upper Saddle River, New Jersey, 2006.

H.T. Bi, J.R. Grace, Effects of pressure and temperature on flow regimes in gas-Solid fluidization systems, Can. J. Chem. Eng. 74 (1996) 1025-1027.

H.T. Bi, J.R. Grace, Effect of measurement method on the velocities used to demarcate the onset of turbulent fluidization. Chem. Eng. J. 75 (1995) 261-271.

H.T. Bi, J.R. Grace, J. Zhu, Propagation of pressure waves and forces oscillations in gas-solid fluidized bed and their influences on diagnostics of local hydrodynamics, Powder Technol. 82 (1995) 239-253.

H.T. Bi, N. Ellis, I.A. Abba, J.R. Grace, A state-of-the-art review of gas-solid turbulent fluidization, Chem. Eng. Sci. 55 (2000) 4789-4825.

H.W. Kwon, Y. Kange, S.D. Kim, M. Yashima, L.T. Fam, Bubble-chord length and pressure fluctuations in three-phase fluidized beds, Ind. Eng. Chem. Res. 33 (1994) 1852-1857.

H.Y. Xie, Fluidization of fine particles, Ph.D. Dissertation, University of Bradford, Bradford, UK, 1993.

H.Y. Xie, The role of interparticle forces in the fluidization of fine particles, Powder Technol. 94 (1997) 99-108.

H.Y. Xie, D. Geldart Fluidization of FCC powders in the bubble-free regime: effect of types of gases and temperature, Powder Technol. 82 (1995) 269-277.

I. Palchonok, C. Breitholtz, H. Thunman, B. Leckner, Impact of heat and mass transfer on combustion of a fuel particle in CFB boilers, in: F.D.S. Preto (Ed.), Proceedings of the 14th International Conference on Fluidized Bed Combustion, ASME, vol. 2, 1997, pp. 871-878.

I. Sidorenko, M.J. Rhodes, Pressure effects on gas-solid fluidized bed behavior, Int. J. Chem. Reactor Eng. 1 (2003) Review R5 (1-33).

I. Tomasetta, The effect of temperature on flow properties of powders, Ph.D. Dissertation, Universita Degli Studi Salerno, 2012.

I.M.F. Wouters, D. Geldart, Entrainment at high temperatures, in: L.-S. Fan, T.M. Knowlton (Eds.), Proceedings of the 9th Engineering Foundation Conference on Fluidization, Engineering Foundation, New York, 1998, pp. 341-348.

J. Arnaldos, J. Casal, A. Lucas, L. Puigjaner, Magnetically stabilized fluidization: modelling and application to mixtures, Powder Technol. 44 (1985) 57-62.

J. Baeyens, D. Geldart, Solids Mixing, in: D. Geldart (Ed.), Gas Fluidization Technology, John Wiley & Sons Ltd., New York, 1986, pp. 97-122.

J. Bouffard, F. Bertrand, J. Chaouki, S. Giasson, Control of particle cohesion with a polymer coating and temperature adjustment, AIChE J. 57 (2012) 3685–3696.

J. Chaouki, A. Gonzales, C. Guy, D. Klvana, Two-phase model for a catalytic turbulent fluidized-bed reactor: Application to ethylene synthesis, Chem. Eng. Sci. 54 (1999) 2039-2045.

J. Chaouki, C. Chavarie, D. Klvana, G. Pajonk, Effect of interparticle forces on the hydrodynamic behaviour of fluidized aerogels, Powder Technol. 43 (1985) 117-125.

J. Gascón, R. Valenciano, C. Téllez, J. Herguido, M. Menéndez, A generalized kinetic model for the partial oxidation of n-butane to maleic anhydride under aerobic and anaerobic conditions, Chem. Eng. Sci. 61 (2006) 6385-6394.

J. Li, Compromise and resolution—Exploring the multi-scale nature of gas–solid fluidization, Powder Technol. 111 (2000) 50-59.

J. Li, J.A.M. Kuipers, Effect of pressure on gas-solid flow behavior in dense gas-fluidized beds: a discrete particle simulation study, Powder Technol. 127 (2002) 173-184.

J. Li, L. Wen, G. Qian, H. Cui, M. Kwauk, J.C. Schouten, C.M. van den Bleek, Structure heterogeneity, regime multiplicity and nonlinear behavior in particle-fluid systems, Chem. Eng. Sci. 51 (1996) 2693-2698.

J. Li, L. Wen, G. Wei, H. Cui, R. Jingqiang, Dissipative structure in concurrent-up gas–solid flow, Chem. Eng. Sci. 53 (1998) 3367-3379.

J. Liu, J.R. Grace, X. Bi, Novel multifunctional optical-fiber probe: I. Development and validation. AIChE J. 49 (2003) 1405-1420.

J. Nijenhuis, R. Korbee, J. Lensselink, J.H.A. Kiel, J.R. van Ommen, A method for agglomeration detection and control in full-scale biomass fired fluidized beds, Chem. Eng. Sci. 62 (2007) 644-654.

J. Quevedo, R. Pfeffer, Y. Shen, R. Dave, H. Nakamura, S. Watano, Fluidization of nanoagglomerates in a rotating fluidized bed, AIChE J. 52 (2006) 2401-2412.

J. Shabanian, F. Fotovat, J. Bouffard, J. Chaouki, Fluidization behavior in a gas-solid fluidized bed with thermally induced inter-particle forces, in: T.M. Knowlton (Ed.), Proceedings of the 10th International Conference on Circulating Fluidized Beds and Fluidization Technology (CFB-10), Engineering Conferences International, New York, 2011.

J. Shabanian, J. Chaouki, Hydrodynamics of a gas–solid fluidized bed with thermally induced interparticle forces, Chem. Eng. J. 259 (2015) 135-152.

J. Shabanian, J. Chaouki, Influence of interparticle forces on solids motion in a bubbling gas-solid fluidized bed, Powder Technol. (2015) submitted for publication.

J. Shabanian, J. Chaouki, Local characterization of a gas–solid fluidized bed in the presence of thermally induced interparticle forces, Chem. Eng. Sci. 119 (2014) 261-273.

J. Shabanian, J. Chaouki, Performance of a catalytic gas-solid fluidized bed reactor in the presence of interparticle forces, Int. J. Chem. Reactor Eng. (2015) Published Online: 2015-04-03, DOI: 10.1515/ijcre-2014-0106.

J. Shabanian, J. Chaouki, Pressure signals in a gas-solid fluidized bed with thermally induced inter-particle forces, in: J.A.M. Kuipers, R.F. Mudde, J.R. van Ommen, N.G. Deen (Eds.), Proceedings of the 14th International Conference on Fluidization – From Fundamentals to Products, ECI Digital Archives, Noordwijkerhout, The Netherlands, 2013.

J. Shabanian, P. Sauriol, A. Rakib, J. Chaouki, Application of temperature and pressure signals for early detection of defluidization conditions, Procedia Eng. 102 (2015) 1006-1015.

J. Shabanian, P. Sauriol, A. Rakib, J. Chaouki, Characterization of gas-solid fluidization at high temperature by analysis of pressure signals, in: Proceedings of the 11th International Conference on Fluidized Bed Technology (CFB-11), Beijing, 2014.

J. Shabanian, R. Jafari, J. Chaouki, Fluidization of ultrafine powders-Review, Int. Rev. Chem. Eng. (IRECHE) 4 (2012) 16-50.

J. van Caneghem, A. Brems, P. Lievens, C. Block, P. Billen, I. Vermeulen, R. Dewil, J. Baeyens, C. Vandecastteele, Fluidized bed waste incinerators: Design, operational and environmental issues, Prog. Energy Combust. Sci. 38 (2012) 551-582.

J. van der Schaaf, J.C. Schouten, C.M. van den Bleek, Origin, propagation and attenuation of pressure waves in gas-solid fluidized beds, Powder Technol. 95 (1998) 220-233.

J. van der Schaaf, J.C. Schouten, F. Johnsson, C.M. van den Bleek, Non-intrusive determination of bubble and slug length scales in fluidized beds by decomposition of the power spectral density of pressure time series, Int. J. Multiphase Flow 28 (2002) 865–880.

J. Visser, Van der Waals and other cohesive forces affecting powder fluidization, Powder Technol. 58 (1989) 1-10.

J. Werther, Effect of gas distributor on the hydrodynamics of gas fluidized beds. Ger. Chem. Eng. 1 (1978) 166-174.

J. Werther, Measurement techniques in fluidized beds, Powder Technol. 102 (1999) 15–36.

J. Werther, M. Saenger, E. U. Hartge, T. Ogada, Z. Siagi, Combustion of agricultural residues, Prog. Energy Combust. Sci. 26 (2000) 1-27.

J. Werther, O. Molerus, The local structure of gas fluidized beds —II. The spatial distribution of bubbles, Int. J. Multiphase Flow 1 (1973) 123-138.

J. Yang, , T. Zhou, L. Song, Agglomerating vibro-fluidization behavior of nano-particles, Adv. Powder Technol. 20 (2009) 158-163.

J. Yerushalmi, N.T. Cankurt, Further studies of the regimes of fluidization, Powder Technol. 24 (1979) 187-205.

Jr.A.A. Wiltsee, C.R. McGowin, E.E. Hughes, Biomass combustion technologies for power generation, in: Proceedings of the First Biomass Conference of the Americas, 1993, pp. 347-367.

J.A. Agbim, A.W. Nienow, P.N. Rowe, Inter-particle forces that suppress bubbling in gas fluidized beds, Chem. Eng. Sci. 26 (1971) 1293-1294.

J.A. Quevedo, A. Omosebi, R. Pfeffer, Fluidization enhancement of agglomerates of metal oxide nanopowders by microjets, AIChE J. 56 (2010) 1456-1468.

J.A. Quevedo, J. Flesch, R. Pfeffer, R. Dave, Evaluation of assisting methods on fluidization of hydrophilic nanoagglomerates by monitoring moisture in the gas phase, Chem. Eng. Sci. 62 (2007) 2608-2622.

J.A. Quevedo, R. Pfeffer, In situ measurements of gas fluidized nanoagglomerates, Ind. Eng. Chem. Res. 49 (2010) 5263-5269.

J.B. Romero, L.N. Johanson, Factors affecting fluidized bed quality, Chem. Eng. Prog. Sym. Ser. 58 (1958) 28-37.

J.F. Davidson, Symposium on fluidization discussion, Trans. Inst. Chem. Eng. 39 (1961) 230-232.

J.F. Davidson, The two-phase theory of fluidization: successes and opportunities, AIChE Symp. Ser. 281 (1991) 1–12.

J.F. Davidson, D. Harrison, Fluidised particles, Cambridge University Press, Cambridge, 1963.

J.F. Davidson, R. Clift, D. Harrison, Fluidization (2nd ed.), Academic Press, NewYork, 1985.

J.F. Richardson, W.N. Zaki, Sedimentation and fluidization. Part 1., Trans. Inst. Chem. Eng. 32 (1954) 35-52.

J.F. Stubington, D. Barrett, G. Lowry, Bubble size measurements and correlation in a fluidised bed at high temperatures, Chem. Eng. Res. Des. 62 (1984) 173-178.

J.G. Findlay, T.M. Knowlton, in: Final Report for U. S. Department of Energy, Project DE-AC21-83MC20314, 1985.

J.G. Yates, Effects of temperature and pressure on gas-solid fluidization, Chem. Eng. Sci. 51 (1996) 167-205.

J.G. Yates, D. Newton, Fine particle effects in a fluidized-bed reactor, Chem. Eng. Sci. 41 (1986) 801-806.

J.G. Yates, S.S. Cobbinah, D.J. Cheesman, S.P. Jordan, Particle attrition in fluidized feds containing opposing jets, AIChE Symp. Ser. 87 (1991) 13-19.

J.H. Choi, J.E. Son, S.D. Kim, Solid entrainment in fluidized bed combustors, J. Chem. Eng. Jpn. 22 (1989) 597-606.

J.H. Siegell, Defluidization phenomena in fluidized bed of sticky particles at high temperature, Ph.D. dissertation, The City University of New York, 1976.

J.H. Siegell, High-temperature defluidization, Powder Technol. 38 (1984) 13–22.

J.M. Valverede, Fluidization of fine powders: Cohesive versus dynamical aggregation, Springer, Part. Technol. Ser. 18 (2013).

J.M. Valverde, A. Castellanos, Effect of vibration on agglomerate particulate fluidization, AIChE J. 52 (2006) 1705-1714.

J.M. Valverde, A. Castellanos, Fluidization of nanoparticles: a modified Richardson-Zaki law, AIChE J. 52 (2006) 838-842.

J.M. Valverde, A. Castellanos, Fluidization of nanoparticles: a simple equation for estimating the size of agglomerates, Chem. Eng. J. 140 (2008) 296-304.

J.M. Valverde, A. Ramos, A. Castellanos, P. Keith Watson, The tensile strength of cohesive powders and its relationship to consolidation, free volume and cohesivity, Powder Technol. 97 (1998) 237-245.

J.M. Valverde, M.A.S. Quintanilla, A. Castellanos, D. Lepek, J. Quevedo, R. N. Dave, R. Pfeffer, Fluidization of fine and ultrafine particles using nitrogen and neon as fluidizing gases, AIChE J. 54 (2008) 86-103.

J.M. Valverde, M.A.S. Quintanilla, A. Castellanos, P. Mills, The settling of fine cohesive powders, EPL 54 (2001) 329.

J.M. Valverde, M.A.S. Quintanilla, M.J. Espin, A. Castellanos, Nanofluidization electrostatics, Phys. Rev. E 77 (2008) 031301.

J.M. Valverde, M.J. Espin, M.A.S. Quintanilla, A. Castellanos, Electrofluidized bed of silica nanoparticles, J. Electrostatics 67 (2009) 439-444.

J.R. Grace, Fluidized beds as chemical reactors, in: D. Geldart, (Ed.), Gas Fluidization Technology, John Wiley & Sons, Chichester, 1986.

J.R. van Ommen, J. van der Schaaf, J.C. Schouten, B.G.M. van Wachem, M.-O. Coppens, C.M. van den Bleek, Optimal placement of probes for dynamic pressure measurements in large-scale fluidized beds, Powder Technol. 139 (2004) 264–276.

J.R. van Ommen, J.C. Schouten, C.M. van den Bleek, An early-warning-method for detecting bed agglomeration in fluidized bed combustors, in: R.B. Reuther (Ed.), Proceedings of the 15th International Conference on Fluidized Bed Combustion, ASME, New York, 1999, Paper No. FBC99–0150.

J.R. van Ommen, M.O. Coppens, C.M. van den Bleek, J.C. Schouten, Early warning of agglomeration in fluidized beds by attractor comparison, AIChE J. 46 (2000) 2183-2197.

J.R. van Ommen, R. Pfeffer, Fluidization of nanopowders-experiments, modeling, and applications, in: D. Kim, Y. Kang, J.K. Lee, Y. C. Seo (Eds.), Proceedings of the 13th International Conference on Fluidization, Gyeong-ju, Korea, 2010, Article 8, pp. 1-8.

J.R. van Ommen, R.F. Mudde, Measuring the gas-solids distribution in fluidized beds: a review, Int. J. Chem. Reactor Eng. 6 (2012) 1-29.

J.R. van Ommen, R.-J. de Korte, C.M. van den Bleek, Rapid detection of defluidization using the standard deviation of pressure fluctuations, Chem. Eng. Process. 43 (2004) 1329–1335.

J.R. van Ommen, S. Sasic, J. van der Schaaf, S. Gheorghiu, F. Johnsson, M.-O. Coppens, Time-series analysis of pressure fluctuations in gas–solid fluidized beds – A review, Int. J. Multiphase Flow 37 (2011) 403–428.

J.R. Wank, S.M. George, A.W. Weimer, ALD of aluminum films on nanosized boron nitride particles in a fluidized bed, AIChE annual meeting, San Francisco, CA, USA (2003).

J.R. Wank, S.M. George, A.W. Weimer, Vibro-fluidization of fine boron nitride powder at low pressure, Powder Technol. 121 (2001) 195-204.

J.S. Buchanan, S. Sundaresan, Kinetics and redox properties of vanadium phosphate catalysts for butane oxidation, Appl. Catal. 26 (1986) 211-226.

J.S.M. Botterill, Y. Teoman, K.R. Yüregir, The effect of operating temperature on the velocity of minimum fluidization, bed voidage and general behavior, Powder Technol. 31 (1982) 101-110.

J.S.M. Botterill, Y. Teoman, K.R. Yüregir, The Effect of temperature on fluidized bed behavior, Chem. Eng. Commun. 15 (1982) 227-238.

L.J. McLaughlin, M.J. Rhodes, Prediction of fluidized bed behaviour in the presence of liquid bridges, Powder Technol. 114 (2001) 213-223.

J.P.K. Seville, C.D. Willett, P.C. Knight, Interparticle forces in fluidisation: a review, Powder Technol. 113 (2000) 261-268.

J.P.K. Seville, H. Silomon-Pflug, P.C. Knight, Modelling of sintering in high temperature gas fluidization, Powder Technol. 97 (1998) 160-169.

J.P.K. Seville, R. Clift, The effect of thin liquid layers on fluidisation characteristics, Powder Technol. 37 (1984) 117-129.

J.-H. Choi, H.-J. Ryu, D.-W. Shun, J.-E. Son, S.-D. Kim, Temperature effect on the particle entrainment rate in a gas fluidized bed, Ind. Eng. Chem. Res. 37 (1998) 1130-1135.

J.-H. Choi, S.D. Kim, J.R. Grace, Entrainment rate of coarse particles at different temperatures in gas fluidized beds, Can. J. Chem. Eng. 85 (2007) 151-157.

J.-H. Choi, K.-B. Choi, P. Kim, D.-W. Shun, S.-D. Kim, The effect of temperature on particle entrainment rate in a gas fluidized bed, Powder Technol. 92 (1997) 127-133.

J.-H. Kuo, C.-L. Lin, M.-Y. Wey, Effects of agglomeration processes on the emission characteristics of heavy metals under different waste compositions and the addition of Al and Ca inhibitors in fluidized bed incineration, Energy Fuels 23 (2009) 4325-4336.

J.-H. Kuo, C.-L. Lin, M.-Y. Wey, Effect of alkali concentrations and operating conditions on agglomeration/defluidization behavior during fluidized bed air gasification, Powder Technol. 214 (2011) 443-446.

J.-H. Kuo, C.-L. Lin, M.-Y. Wey, Mechanisms of particle agglomeration and inhibition approach in the existence of heavy metals during fluidized bed incineration, Chem. Eng. Sci. 65 (2010) 4955-4966.

K. Erdész, A. S. Mujumdar, Hydrodynamic aspects of conventional and vibrofluidized beds--a comparative evaluation, Powder Technol. 46 (1986) 167-172.

K. Godard, and J.F. Richardson, The Behaviour of Bubble-Free Fluidized Beds, I. Chem. E. Sym. Ser. 30 (1968) 126-135.

K. Nishii, Y. Itoh, N. Kawakami, M. Horio, A pressure swing granulation, a novel binderless granulation by cyclic fluidization and gas flow compaction, Powder Technol. 74 (1993) 1-6.

K. Noda, , Y. Mawatari, S. Uchida, Flow patterns of fine particles in a vibrated fluidized bed under atmospheric or reduced pressure, Powder Technol. 99 (1998) 11-14.

K. Rietema, The Dynamics of Fine Powders, Elsevier Science Publishers Ltd., New York, 1991.

K. Schügerl, Rheological behaviour of fluidized systems, in: J.F. Davidson, D. Harrison (Eds.), Fluidization, Academic Press, London, 1971, pp. 261-292.

K. Rietema, H.W. Piepers, The effect of interparticle forces on the stability of gas-fluidized beds--I. Experimental evidence, Chem. Eng. Sci. 45 (1990) 1627-1639.

K. Smolders, J. Baeyens, Elutriation of fines from gas fluidized beds: mechanisms of elutriation and effect of freeboard geometry, Powder Technol. 92 (1997) 35-46.

K. Svoboda, J. Cermak, M. Hartman, J. Drahos, K. Selucky, Pressure fluctuations in gas-fluidized beds at elevated temperatures, Ind. Eng. Chem. Process Des. Dev. 22 (1983) 514-520.

K. Svoboda, M. Hartman, Deviations of actual minimum fluidization velocities from theoretical predictions at different temperatures, AIChE J. 27 (1981) 866-869.

K. Svoboda, M. Hartman, Influence of temperature on incipient fluidization of limestone, lime, coal ash, and corundum, Ind. Eng. Chem. Process Des. Dev. 20 (1981) 319-326.

K. Wittmann, H. Helmrich, K. Schügerl, Measurements of bubble properties in continuously operated fluidized bed reactors at elevated temperatures, Chem. Eng. Sci. 36 (1981) 1673-1677.

K.A. Shahid, F.P. Glasser, Phase equilibria in the glass forming region of the system Na2O-CaO-SiO2, Phys. Chem. Glasses 12 (1971) 50-57.

L. Cheung, A.W. Nienow, P.N. Rowe, Minimum fluidisation velocity of a binary mixture of different sized particles, Chem. Eng. Sci. 29 (1974) 1301-1303.

L. de Martín, K. van den Dries, J.R. van Ommen, Comparison of three different methodologies of pressure signal processing to monitor fluidized-bed dryers/granulators, Chem. Eng. J. 172 (2011) 487-499.

L. Massimilla, G. Donsì, Cohesive forces between particles of fluid-bed catalysts, Powder Technol. 15 (1976) 253-260.

L. Massimilla, G. Donsì, C. Zucchini, The structure of bubble-free gas fluidized beds of fine fluid cracking catalyst particles, Chem. Eng. Sci. 27 (1972) 2005-2015.

L. Song, T. Zhou, J. Yang, Fluidization behavior of nano-particles by adding coarse particles, Adv. Powder Technol. 20 (2009) 366-370.

L. Zhou, R. Diao, T. Zhou, H. Wang, H. Kage, Y. Mawatari, Behavior of magnetic Fe3O4 nano-particles in magnetically assisted gas-fluidized beds, Adv. Powder Technol. 22 (2011) 427-432.

L.A. Noble, Method of preventing or reducing polymer agglomeration on grid in fluidized-bed reactors, US Patent (2012) US 8,129,482 B2.

L.D. Enochson, R.K. Otens, Programming and analysis for digital time series data; shock and vibration monograph series, Department of Defense, Shock and Vibration Information Center, Washington, DC, USA, 1968.

L.F. Hakim, J.L. Portman, M.D. Casper, A.W. Weimer, Aggregation behavior of nanoparticles in fluidized beds, Powder Technol. 160 (2005) 149-160.

L.G. Gibilaro, Fluidization Dynamics, Butterworth Heinemann, Oxford, 2001.

L.J. McLaughlin, M.J. Rhodes, Prediction of fluidized bed behavior in the presence of liquid bridge, Powder Technol. 114 (2001) 213-223.

L.R. Glicksman, G. McAndrews, The effect of bed width on the hydrodynamics of large particle fluidized beds, Powder Technol. 42 (1985) 159-167.

L.S. Fan, C. Zhu, Principles of Gas–Solid Flows, Cambridge University Press, New York, 1998.

L.T. Fan, T.C. Ho, S. Hiraoka, W. P. Walawender, Pressure fluctuations in a fluidized bed, AIChE J. 27 (1981) 388-396.

M. Aoyagi, D. Kunii, Importance of dispersed solids in bubbles for exothermic reactions in fluidized beds, Chem. Eng. Commun. 1 (1974) 191-197.

M. Baerns, Effect of interparticle adhesive forces on fluidization of fine particles, Ind. Eng. Chem. Fundam. 5 (1966) 508-516.

M. Bartels, J. Nijenhuis, J. Lensselink, M. Siedlecki, W. de Jong, F. Kapteijn, J. R. van Ommen, Detecting and counteracting agglomeration in fluidized bed biomass combustion, Energy Fuels 23 (2009) 157–169.

M. Bartels, J. Nijenhuis, F. Kapteijn, J.R.van Ommen, Case studies for selective agglomeration detection in fluidized beds: Application of a new screening methodology, Powder Technol. 203 (2010) 148-166.

M. Bartels, J. Nijenhuis, J. Lensselink, M. Siedlecki, W. de Jong, F. Kapteijn, J.R. van Ommen, Detecting and counteracting agglomeration in fluidized bed biomass combustion, Energy Fuels 23 (2009) 157-169.

M. Bartels, W. Lin, J. Nijenhuis, F. Kapteijn, J.R. van Ommen, Agglomeration in fluidized beds at high temperatures: Mechanisms, detection and prevention, Prog. Energy Combust. Sci. 34 (2008) 633-666.

M. Corris, B. Caussat, A. Ayral, J. Durand, Y. Kihn, P. Kalck and P. Serp, Carbon nano-tubes produced by fluidized bed catalytic CVD: first approach of the process, Chem. Eng. Sci. 58 (2003) 4475-4482.

M. Dente, S. Pierucci, E. Tronconi, M. Cecchini, F. Ghelfi, Selective oxidation of n-butane to maleic anhydride in fluid bed reactors: detailed kinetic investigation and reactor modelling, Chem. Eng. Sci. 58 (2003) 643-648.

M. Hartman, K. Svoboda, Predicting the effect of operating temperature on the minimum fluidization velocity, Ind. Eng. Chem. Process Des. Dev. 25 (1986) 649-654.

M. Horio, A. Nonaka, A generalized bubble diameter correlation for gas-solid fluidized beds. AIChE J. 33 (1987) 1865-1872.

M. Kashyap, D. Gidaspow, M. Driscoll, Effect of electric field on the hydrodynamics of fluidized nanoparticles, Powder Technol. 183 (2008) 441-453.

M. Kashyap, D. Gidaspow, T.W. Tsai, Effect of electric field on the hydrodynamics of nanoparticles in a rectangular fluidized bed, AIChE Annual Meeting, San Francisco, CA, US, (2006).

M. Liu, Y. Zhang, H. Bi, J.R. Grace, Y. Zhu, Non-intrusive determination of bubble size in a gas–solid fluidized bed: an evaluation, Chem. Eng. Sci. 65 (2010) 3485-3493.

M. Nakamura, Y. Hamada, S. Toyama, A.E. Fouda, C.E. Capes, An experimental investigation of minimum fluidization velocity at elevated temperatures and pressures, Can. J. Chem. Eng. 63 (1985) 8-13.

M. Öhman, A. Nordin, B.-J. Skrifvars, R. Backman, M. Hupo, Bed agglomeration characteristics during fluidized bed combustion of biomass fuels, Energy Fuels 14 (2000) 169-178.

M. Olazar, M. San Jose, R. Llamosas, S. Alvarez, J. Bilbao, Study of local properties in conical spouted beds using an optical fiber probe, Ind. Eng. Chem. Res. 34 (1995) 4033-4039.

M. Pell, S.P. Jordan, Effects of fines and velocity on fluid bed reactor performance, AIChE Symp. Ser. 262 (1988) 68-73.

M. Poletto, P. Salatino, L. Massimilla, Fluidization of solids with CO_2 at pressures and temperatures ranging from ambient to nearly critical conditions, Chem. Eng. Sci. 48 (1993) 617-621.

M. Punčochář, J. Drahoš, Origin of pressure fluctuations in fluidized beds, Chem. Eng. Sci. 60 (2005) 1193-1197.

M. Rasouli, F. Bertrand, J. Chaouki, A multiple radioactive particle tracking technique to investigate particulate flows, AIChE J. 61 (2015) 384-394.

M. Rüdisüli, T.J. Schildhauer, S.M.A. Biollaz, A. Wokaun, J. R. van Ommen, Comparison of bubble growth obtained from pressure fluctuation measurements to optical probing and literature correlations, Chem. Eng. Sci. 74 (2012) 266–275.

M. Rüdisüli, T.J. Schildhauer, S.M.A. Biollaz, J.R. van Ommen, Scale-up of bubbling fluidized bed reactors - a review, Powder Technol. 217 (2012) 21-38.

M. Stein, T.W. Martin, J.P.K. Seville, P.A. McNeil, D.J. Parker, Positron Emission Particle Tracking: Particle Velocities in Gas Fluidized Beds, Mixers and other Applications, in: J.

Chaouki, F. Larachi, M.P. Dudukovic (Eds.), Non-invasive Monitoring of Multiphase Flows, Elsevier, Amsterdam, 1997, pp. 309-333.

M. Stein, Y.L. Ding, J.P.K. Seville, D.J. Parker, Solids motion in bubbling gas fluidised beds, Chem. Eng. Sci. 55 (2000) 5291-5300.

M.A. Doheim, C.N. Collinge, Effect of temperature on incipient fluidization and study of bed expansion, Powder Technol. 21 (1978) 289-293.

M.A. Howley, R. Pfeffer, The hydrodynamics of a rotating fluidized bed, in: Proceedings of the AIChE Annual Meeting, Cicinati, Ohio, US, October, 2005.

M.F. Llop, J. Casal, J. Arnaldos, Expansion of gas-solid fluidized beds at pressure and high temperature, Powder Technol. 107 (2000) 212-225.

M.J. Espin, J.M. Valverde, M.A.S. Quintanilla, A. Castellanos, Stabilization of gas-fluidized beds of magnetic powders by a cross-flow magnetic field, J. Fluid Mech. 680 (2011) 80-113.

M.J. Gluckman, J. Yerushalmi, A.M. Squires, Defluidization characteristics of sticky materials on agglomerating bed, in: D.L. Keairns (Ed.), Fluidization Technology, 1976, pp. 395-422.

M.J. Lorences, G.S. Patience, F.V. Díez, J. Coca, Butane oxidation to maleic anhydride: kinetic modeling and byproducts, Ind. Eng. Chem. Res. 42 (2003) 6730-6742.

M.J. Lorences, G.S. Patience, F.V. Díez, J. Coca, Transient n-butane partial oxidation kinetics over VPO, App. Catal., A 263 (2004) 193-202.

M.J. Rhodes, X.S. Wang, A.J. Forsyth, K.S. Gan, S. Phadtajaphan, Use of a magnetic fluidized bed in studying Geldart Group B to A transition, Chem. Eng. Sci. 56 (2001) 5429-5436.

M.J. Rhodes, X.S. Wang, M. Nguyen, P. Stewart, K. Liffman, Study of mixing in gas-fluidized beds using a DEM model, Chem. Eng. Sci. 56 (2001) 2859-2866.

M.M. Yazdanpanah, A. Forret, T. Gauthier, A. Delebarre, Modeling of CH4 combustion with NiO/NiAl2O4 in a 10 kW_{th} CLC pilot plant, Appl. Energy 113 (2014) 1933-1944.

M.R. Tamadondar, R. Zarghami, H. Azizpour, N. Mostoufi, J. Chaouki, R. Radmanesh, Using S-statistic for investigating the effect of temperature on hydrodynamics of gas–solid fluidization, Particuology 11 (2012) 288-293.

M.S. Bacelos, J.T. Freire, Flow regimes in wet conical spouted beds using glass bead mixtures, Particuology 6 (2008) 72-80.

M.A.S. Quintanilla, J.M. Valverde, A. Castellanos, D. Lepek, R. Pfeffer, R.N. Dave, Nanofluidization as affected by vibration and electrostatic fields, Chem. Eng. Sci. 63 (2008) 5559-5569.

N. Ellis, Hydrodynamics of gas-solid turbulent fluidized beds, Ph.D. dissertation, Department of Chemical and Bilogical Engineering, The University of British Columbia Vancouver, 2003.

N. Ellis, H.T. Bi, C.J. Lim, J.R. Grace, Hydrodynamics of turbulent fluidized beds of different diameters, Powder Technol. 141 (2004) 124-136.

N. Fraysse, H. Thomé, L. Petit, Humidity effects on the stability of sandpile, Eur. Phys. J. B, 11 (1999) 615-619.

N. Mostoufi, H. Cui, J. Chaouki, A comparison of two- and single-phase models for fluidized-bed reactors, Ind. Eng. Chem. Res. 40 (2001) 5526-5532.

N. Mostoufi, J. Chaouki, Flow structure of the solids in gas-solid fluidized beds, Chem. Eng. Sci. 59 (2004) 4217-4227.

N. Mostoufi, J. Chaouki, Local solid mixing in gas-solid fluidized beds, Powder Technol. 114 (2001) 23-31.

N. Mostoufi, J. Chaouki, On the axial movement of solids in gas-solid fluidized beds, Chem. Eng. Res. Des. 78 (2000) 911-920.

N. Sadasivan, D. Barreteau, C. Laguerie, Studies on frequency and magnitude of fluctuations of pressure drop in gas-solid fluidized beds, Powder Technol. 26 (1980) 67-74.

O. Gundogdu, P. Jenneson, U. Tuzun, Nano particle fluidisation in model 2-D and 3-D beds using high speed X-ray imaging and microtomography, J. Nanopart. Res. 9 (2007) 215-223.

O. Gundogdu, U. Tuzun, Gas fluidisation of nanoparticle assemblies: modified Geldart classification to account for multiplescale fluidisation of agglomerates and clusters, KONA 24 (2006) 3-14.

O. Levenspiel, Chemical Reaction Engineering (3rd ed.), John Wiley & Sons, New York, 1999.

O. Molerus, Interpretation of Geldart's type A, B, C and D powders by taking into account interparticle cohesion forces, Powder Technol. 33 (1982) 81-87.

P. Ammendola, R. Chirone, Aeration and mixing behaviours of nano-sized powders under sound vibration, Powder Technol. 201 (2010) 49-56.

P. Ammendola, R. Chirone, F. Raganati, Fluidization of binary mixtures of nanoparticles under the effect of acoustic fields, Adv. Powder Technol. 22 (2011) 174-183.

P. Ammendola, R. Chirone, F. Raganati, Sound assisted fluidization of Al2O3and Fe2O3 nanoparticles, in: AIChE Annual Meeting, Salt Lake City, US, 2010.

P. Basu, A study of agglomeration of coal-ash in fluidized beds, Can. J. Chem. Eng. 60 (1982) 791-795.

P. Basu, A. Sarka, Agglomeration of coal ash in fluidized beds, Fuel 62 (1983) 924-926.

P. Cai, Y. Jin, Z.Q. Yu, Z.W. Wang, Effect of operating temperature and pressure on the transition from bubbling to turbulent fluidization, AIChE Symp. Ser. 85(270) (1989) 37-43.

P. Cai, Y. Jin, Z.Q. Yu, Z.W. Wang, Mechanism of flow regime transition from bubbling to turbulent fluidization, AIChE J. 36 (1990) 955-956.

P. Cai, Z. Miu, Z.Q. Yu, Y. Jin, Mathematic feature and analyzing methods of pressure fluctuation signal from a gas-solid fluidized bed, Chem. Metall. Eng. 11 (1990) 114-122 (in Chinese).

P. Compo, G.I. Tardos, D. Mazzone, R. Pfeffer, Minimum sintering temperatures of fluidizable particles, Part. Part. Syst. Charact. 1 (1984) 171-177.

P. Compo, R. Pfeffer, G.I. Tardos, Minimum sintering temperatures and defluidization characteristics of fluidizable particles, Powder Technol. 51 (1987) 85-101.

P. Lettieri, J.G. Yates, D. Newton, The influence of interparticle forces on the fluidization behaviour of some industrial materials at high temperature, Powder Technol. 110 (2000) 117-127.

P. Lettieri, D. Newton, J.G. Yates, High temperature effects on the dense phase properties of gas fluidized beds, Powder Technol. 120 (2001) 34-40.

P. Lettieri, D. Newton, J.G. Yates, Homogeneous bed expansion of FCC catalysts, influence of temperature on the parameters of the Richardson-Zaki equation, Powder Technol. 123 (2002) 221-231.

P. Lettieri, D. Newton, J.G. Yates, The effect of temperature on the deaeration rate of two silica powders. Comparison with standard correlations for a Group A and a Group C material, in: Proceedings of the 3rd World Congress on Particle Technology, Brighton, UK, 1998, pp. 2239-2250.

P. Mars, D.W. van Krevelen, Oxidations carried out by means of vanadium oxide catalysts, Chem. Eng. Sci. 3 (1954) 41-59.

P. McKendry, Energy production from biomass (part 3): gasification technologies, Bioresour. Technol. 83 (2002) 55-63.

P. Pagliai, S.J.R. Simons, D. Rhodes, Towards a fundamental understanding of defluidisation at high temperatures: a micro-mechanistic approach, Powder Technol. 148 (2004) 106-112.

P. Russo, R. Chirone, L. Massimilla, S. Russo, The influence of the frequency of acoustic waves on sound-assisted fluidization of beds of fine particles, Powder Technol. 82 (1995) 219-230.

P. Sauriol, H. Cui, J. Chaouki, Gas jet penetration lengths from upward and downward nozzles in dense gas–solid fluidized beds, Powder Technol. 235 (2013) 42-54.

P. Schneider, G. Emig, H. Hofmann, Kinetic investigation and reactor simulation for the catalytic gas-phase oxidation of n-butane to maleic anhydride, Ind. Eng. Chem. Res. 26 (1987) 2236-2241.

P. Zeng, T. Zhou, G. Chen, Q. Zhu, Behavior of mixed ZnO and SiO2 nano-particles in magnetic field assisted fluidization, China Particuology 5 (2007) 169-173.

P. Zeng, T. Zhou, J. Yang, Behavior of mixtures of nano-particles in magnetically assisted fluidized bed, Chem. Eng. Process. 47 (2008) 101-108.

P.C. Carman, Fluid flow through granular beds, Trans. Inst. Chem. Eng. 15 (1937) 150-167.

P.D. Welch, The use of a fast Fourier transform for the estimation of power spectra, IEEE Trans. on Audio and Electroacoustics, AU-15 (1967) 70-73.

P.E. Ege, Investigation of the flow structure of turbulent fluidized beds, Ph.D. dissertation, University of Trondheim, Norway, 1995.

P.L. Mills, H.T. Randall, J.S. McCracken, Redox kinetics of VOPO4 with butane and oxygen using the TAP reactor system, Chem. Eng. Sci. 54 (1999) 3709-3722.

P.K. Jain, N. Saxena, Temperature and composition dependence of electrical conductivity of Se90In10–xSbx (x=0, 2, 4, 6, 8, 10) chalcogenide glasses, J. Non-Oxide Photonic Glasses 1 (2009) 43-52.

P.K. Peeler, K.S. Lim, R.C. Close, Effect of temperature on the turbulent fluidization regime transition, in: J. Werther (Ed.), Proceedings of the 6th International Conference on Circulating Fluidized Beds, Würzburg, Germany, 1999, pp. 125-130.

P.M. Jenneson, O. Gundogdu, In situ x-ray imaging of nanoparticle agglomeration in fluidized beds, Appl. Phys. Lett. 88 (2006) 034103-3.

P.N. Rowe, L. Santoro, J.G. Yates, The division of gas between bubble and interstitial phases in fluidised beds of fine powders, Chem. Eng. Sci. 33 (1978) 133-140.

Q. Guo, H. Liu, W. Shen, X. Yan, R. Jia, Influence of sound wave characteristics on fluidization behaviors of ultrafine particles, Chem. Eng. J. 119 (2006) 1-9.

Q. Guo, G. Yue, T. Suda, J. Sato, Flow characteristics in a bubbling fluidized bed at elevated temperature, Chem. Eng. Process. Process Intensif. 42 (2003) 439-447.

Q. Guo, M. Wang, Y. Lim C. Yang, Fluidization of ultrafine particles in a bubbling fluidized bed with sound assistance, Chem. Eng. Technol. 28 (2005) 1117-1124.

Q. Guo, X. Yang, W. Shen and H. Liu, Agglomerate size in an acoustic fluidized bed with sound assistance, Chem. Eng. Process. 46 (2007) 307-313.

Q. Guo, Y. Li, M. Wang, W. Shen, C. Yang, Fluidization characteristics of SiO2 nanoparticles in an acoustic fluidized bed, Chem. Eng. Technol. 29 (2006) 78-86.

Q. Lin, F. Wei, Y. Jin, Transient density signal analysis and two-phase micro-structure flow in gas–solids fluidization, Chem. Eng. Sci. 56 (2001) 2179-2189.

Q. Yu, R. N. Dave, C. Zhu, J. A. Quevedo, R. Pfeffer, Enhanced fluidization of nanoparticles in an oscillating magnetic field, AIChE J. 51 (2005) 1971-1979.

Q. Zhu, H. Li, Study on magnetic fluidization of group C powders, Powder Technol. 86 (1996) 179-185.

Q.S. Zhu, H.Z. Li, Fluidization of group C powder with external magnetic force, in: Proceedings of the 5th China-Japan Symposium on Fluidization, Nagoya, Japan, 1994.

R. Chirone, F. Miccio, F. Scala, Mechanism and prediction of bed agglomeration during fluidized bed combustion of a biomass fuel: Effect of the reactor scale, Chem. Eng. J. 123 (2006) 71–80.

R. Chirone, L. Massimilla, S. Russo, Bubbling fluidization of a cohesive powder in an acoustic field, in: Proceedings of Fluidization VII, 1992, pp. 545-553.

R. Chirone, L. Massimilla, S. Russo, Bubble-free fluidization of a cohesive powder in an acoustic field, Chem. Eng. Sci. 48 (1993) 41-52.

R. Clift, J.R. Grace, The mechanism of bubble break-up in fluidised beds, Chem. Eng. Sci. 27 (1972) 2309-2310.

R. Girimonte, B. Formisani, Effects of operating temperature on the bubble phase properties in fluidized beds of FCC particles, Powder Technol. 262 (2014) 14-21.

R. Girimonte, B. Formisani, The effects of thermally induced interparticle forces on the expansion and bubbling behaviour of a fluidized bed, in: F. Berruti, X. Bi, T. Pugsley (Eds.),

Proceedings of the 12th International Conference on Fluidization, Engineering Conferences International, Vancouver, Canada, 2007, pp. 177-184.

R. Girimonte, B. Formisani, The minimum bubbling velocity of fluidized beds operating at high temperature, Powder Technol. 189 (2009) 74-81.

R. Jafari, R. Sotudeh-Gharebagh, N. Mostoufi, Performance of the wide-ranging models for fluidized bed reactors, Adv. Powder Technol. 15 (2004) 533-548.

R. Korbee, J.R. van Ommen, J. Lensselink, J. Nijenhuis, J.H.A. Kiel, C.M. van den Bleek, Early agglomeration recognition system (EARS), in: Proceedings of the 17th International Fluidized Bed Combustion Conference, Jacksonville, Florida USA, 2003.

R. Krishna, J.M. van Baten, J. Ellenberger, Scale effects in fluidized multiphase reactors, Powder Technol. 100 (1998) 137-146.

R. Radmanesh, Fluidized bed biomass gasification, Ph.D. dissertation, Ecole Polytechnique de Montreal, 2006.

R. Yamazaki, G.H. Hong, G. Jimbo. The behavior of a gas-solid fluidized bed at elevated temperatures, in: D. Kunii, R. Toei (Eds.), Proceedings of the 4th International Conference on Fluidization, Kashikojima, Japan, 1984, pp. 121-128.

R. Yamazaki, N. Ueda, G. Jimbo, Mechanism of incipient fluidization in fluidized bed at elevated temperature, J. Chem. Eng. Jpn. 19 (1986) 251-257.

R. Yamazaki, N.-S. Han, Z.-F. Sun, G. Jimbo, Effect of chemisorbed water on bed voidage of high temperature fluidized bed, Powder Technol. 84 (1995) 15-22.

R.A. Bowling, A theoretical review of particle adhesion, in: K. Mittal (Ed.), Particles on Surfaces 1, Plenum Press, New York, 1988, pp. 129-142.

R.B. Bird, W.E. Stewart, E.N. Lightfoot, Transport Phenomena, John Wiley & Sons Inc., New York, 2002.

R.D. Morse, Sonic energy in granular solid fluidization, Ind. Eng. Chem. Res. 47 (1955) 1170-1175.

R.D. Toomey, H.F. Johnstone, Gaseous fluidization of solid particles, Chem. Eng. Prog. 48 (1952) 220–225.

R.D. Venkatesh, J. Chaouki, D. Klvana, Fluidization of cryogels in a conical column, Powder Technol. 89 (1996) 179-186.

R.E. Treybal, Mass-Transfer Operations, McGraw-Hill, London, 1981.

R.J. De Vries, W.P.M. van Swaaij, C. Mantovani, A. Heijkoop, Design criteria and performance of the commercial reactor for the Shell Chlorine Process, in: Proceedings of the 2nd International Symposium on Chemicla Reaction Engineering, Amesterdam, 1972, B9 (59 - 69).

R.K. Sharma, D.L. Cresswell, E.J. Newson, Kinetics and fixed-bed reactor modeling of butane oxidation to maleic anhydride, AIChE J. 37 (1991) 39-47.

R.L. Varma, D.N. Saraf, Selective Oxidation of C4 hydrocarbons to maleic anhydride, Ind. Eng. Chem. Prod. Res. Dev. 18 (1979) 7-13.

R.M. Contractor, Dupont's CFB technology for maleic anhydride, Chem. Eng. Sci. 54 (1999) 5627-5632.

R.R. Pattipati, C.Y. Wen, Minimum fluidization velocity at high temperatures, Ind. Eng. Chem. Process Des. Dev. 20 (1981) 705-707.

S. Boggs, D.H. Damon, J. Hjerrild, J.T. Holboll, M. Henriksen, Effect of insulation properties on the field grading of solid dielectric DC cable, IEEE Trans. Power Delivery 16 (2001) 456-461.

S. Kaliyaperumal, S. Barghi, J. Zhu, L. Briens, S. Rohani, Effects of acoustic vibration on nano and sub-micron powders fluidization, Powder Technol. 210 (2011) 143-149.

S. Kaliyaperumal, S. Barghi, L. Briens, S. Rohani, J. Zhu, Fluidization of nano and sub-micron powders using mechanical vibration, Particuology 9 (2011) 279-287.

S. Karimipour, T. Pugsley, A critical evaluation of literature correlations for predicting bubble size and velocity in gas-solid fluidized beds, Powder Technol. 205 (2011) 1-14.

S. Matsuda, H. Hatano, A. Tsutsumi, Ultrafine particle fluidization and its application to photocatalytic NOx treatment, Chem. Eng. J. 82 (2001) 183-188.

S. Matsuda, H. Hatano, K. Tsuchiya, Effects of operating conditions on photocatalytic reduction of NOx in fluidized beds of TiO2, in: Proceedings of Fluidization IX, Engineering Foundation, 1998, pp. 701-708.

S. Matsuda, H. Hatano, T. Muramoto, A. Tsutsumi, Modeling for size reduction of agglomerates in nanoparticle fluidization, AIChE J. 50 (2004) 2763-2771.

S. Matsuda, H. Hatano, T. Nuramoto, A. Tsutsumi, Particle and bubble behavior in ultrafine particle fluidization with high G, in: Proceedings of Fluidization X, Engineering Foundation, 2001, pp. 501–508.

S. Mori, A. Yamamoto, S. Iwata, T. Harahan, I. Yamada, Vibro-fluidization of Group C particles and its industrial applications, AIChE Sym. Ser. 86 (1990) 88–94.

S. Mori, C.Y. Wen, Estimation of bubble diameter in gaseous fluidized beds, AIChE J. 21 (1975) 109-115.

S. Morooka, K. Kusakabe, A. Kobata, Y. Kato, Fluidization state of ultrafine powders, J. Chem. Eng. J. 21 (1988) 41–46.

S. Qian, J. Lu, G. Flamant, Fluidization characteristics of gas-solid fluidized bed at elevated temperature, J. Combust. Sci. Technol. 3 (1997) 344-348.

S. Rapagna, P.U. Foscolo, L.G. Gibilaro, The influence of temperature on the quality of gas fluidization, Int. J. Multiphase Flow 20 (1994) 305-313.

S. Roy, F. Larachi, M.H. Al-Dahhan, M.P. Dudukovic, Optimal design of radioactive particle tracking experiments for flow mapping in opaque multiphase reactors, Appl. Radiat. Isot. 56 (2002) 485-503.

S. Sanaei, N. Mostoufi, R. Radmanesh, R. Sotudeh-Gharebagh, C. Guy, J. Chaouki, Hydrodynamic characteristics of gas-solid fluidization at high temperature, Can. J. Chem. Eng. 88 (2010) 1-11.

S. Sasic, B. Leckner, F. Johnsson, Characterization of fluid dynamics of fluidized beds by analysis of pressure fluctuations, Prog. Energy Combust. Sci. 33 (2007) 453-469.

S. Satij, L.S. Fan, Characterization of slugging regime and transition to turbulent regime for fluidized beds of large coarse particles, AIChE J. 31 (1985) 1554-1562.

S.C. Saxena, N.S. Rao, S.J. Zhou, Fluidization characteristics of gas fluidized beds at elevated temperatures, Energy 15 (1990) 1001-1014.

S.M. Tasirin, N. Anuar, Fluidization behavior of vibrated and aerated beds of starch powders, J. Chem. Eng. J. 34 (2001) 1251-1258.

S.E. George, J.R. Grace, Entrainment of particles from a pilot scale fluidized bed, Can. J. Chem. Eng. 59 (1981) 279-284.

S.K. Bej, M.S. Rao, Selective oxidation of n-butane to maleic anhydride. 1. Optimization studies, Ind. Eng. Chem. Res. 30 (1991) 1819-1824.

S.M. Iveson, J.A. Beathe, N.W. Page, The dynamic strength of partially saturated powder compacts: the effect of liquid properties, Powder Technol. 127 (2002) 149-161.

S.Y. Wu, J. Baeyens, Effect of operating temperature on minimum fluidization velocity, Powder Technol. 67 (1991) 217-220.

T. Kai, S. Furusaki, Behavior of fluidized beds of small particles at elevated temperatures, J. Chem. Eng. Jpn. 18 (1985) 113-118.

T. Li, K. Pougatch, M. Salcudean, D. Grecov , Mixing of secondary gas injection in a bubbling fluidized bed, Chem. Eng. Res. Des. 87 (2009) 1451-1465.

T. Mii, K. Yoshida, D. Kunii, Temperature effects on the characteristics of fluidized beds, J. Chem. Eng. Jpn. 6 (1973) 100-102.

T. Otake, S. Tone, M. Kawashima, T. Shibata, Behavior of rising bubbles in gas-fluidized bed at elevated temperature, J. Chem. Eng. Jpn. 8 (1975) 388-392.

T. Weigert, S. Ripperger, Calculation of the liquid bridge volume and bulk saturation from the half-filling angle, Part. Part. Syst. Charact. 16 (1999) 238-242.

T. Zhou, H. Li, Effects of adding different size particles on fluidization of cohesive particles, Powder Technol. 102 (1999) 215-220.

T. Zhou, H. Li, Estimation of agglomerate size for cohesive particles during fluidization, Powder Technol. 101 (1999) 57-62.

T. Zhou, H. Li, Force balance modelling for agglomerating fluidization of cohesive particles, Powder Technol. 111 (2000) 60-65.

T.A. Alsmari, J.R. Grace, X.T. Bi, Effects of superficial gas velocity and temperature on entrainment and electrostatics in gas–solid fluidized beds, Chem. Eng. Sci. 123 (2015) 49-56.

T.A. Witten, L.M. Sander, Diffusion-limited aggregation, a kinetic critical phenomenon, Phys. Rev. Lett. 47 (1981) 1400.

T.G. Mason, A.J. Levine, D. Ertascedil, T.C. Halsey, Critical angle of wet sandpiles, Phys. Rev. E 60 (1999) R5044.

T.M. Knowlton, Pressure and temperature effects in fluid-particle systems, in: O.E. Potter, D.J. Nicklin (Eds.), Proceedings of the 7th International Conference on Fluidization, Engineering Foundation, New York, 1992, pp. 27-46.

T.M. Knowlton, Pressure and temperature effects in fluid-particle systems, in: W.C. Yang (Ed.), Fluidization, Solids Handling and Processing: Industrial Applications, Noyes, New Jersy, 1999, pp. 111-152.

V.L. Ganzha, S.C. Saxena, Heat-transfer characteristics of magnetofluidized beds of pure and admixtures of magnetic and nonmagnetic particles, IJHMT 41 (1998) 209-218.

W. Lin, K. Dam-Johansen, F. Frandsen, Agglomeration in bio-fuel fired fluidized bed combustors, Chem. Eng. J. 96 (2003) 171-185.

W. Qian , F. Wei, Z. Wang, T. Liu, H. Yu, G. Luo, L. Xiang, X. Deng, Production of carbon nano-tubes in a packed bed and fluidized bed, AIChE J. 49 (2003) 619-625.

W. Yao, G. Guangsheng, W. Fei, W. Jun, Fluidization and agglomerate structure of SiO2 nanoparticles, Powder Technol. 124 (2002) 152-159.

W. Zhang, M. Zhao, Fluidisation behaviour of silica nanoparticles under horizontal vibration, J. Exp. Nanosci. 5 (2010) 69-82.

W.C. Yang, Fluidization of fine cohesive powders and nanoparticles—a review, J. Chin. Inst. Chem. Eng. 36 (2005) 1–15.

W.O. Moughrabiah, J.R. Grace, X.T. Bi, Effects of pressure, temperature, and gas velocity on electrostatics in gas−solid fluidized beds, Ind. Eng. Chem. Res. 48 (2009) 320-325.

W.Y. Wu, A. Navada, S.C. Saxena, Hydrodynamic characterization of a magnetically stabilized air fluidized bed of an admixture of magnetic and non-magnetic particles, Powder Technol. 90 (1997) 39-46.

X. Fan, D.J. Parker, B. Armstrong, Prediction of bubble behaviour in fluidised beds based on solid motion and flow structure, Chem. Eng. J. 140 (2008) 358-369.

X. Fan, D.J. Parker, Z. Yang, J.P.K. Seville, J. Baeyens, The effect of bed materials on the solid/bubble motion in a fluidised bed, Chem. Eng. Sci. 63 (2008) 943-950.

X. Fan, Z. Yang, D.J. Parker, Impact of solid sizes on flow structure and particle motions in bubbling fluidization, Powder Technol. 206 (2011) 132-138.

X. Lu, H. Li, Fluidization of CaCO3 and Fe2O3 particle mixtures in a transverse rotating magnetic field, Powder Technol. 10 (2000) 66-78.

X. Yang, J.R. van Ommen, R.F. Mudde, Gas distribution of a downward micro-nozzle assisted fluidized bed of fine powder, Chem. Eng. J. 264 (2015) 945-953.

X.S. Wang, F. Rahman, M.J. Rhodes, Nanoparticle fluidization and Geldart's classification, Chem. Eng. Sci. 62 (2007) 3455-3461.

X.S. Wang, V. Palero, J. Soria, M.J. Rhodes, Laser-based planar imaging of nano-particle fluidization: Part I--determination of aggregate size and shape, Chem. Eng. Sci. 61 (2006) 5476-5486.

X.S. Wang, V. Palero, J. Soria, M. J. Rhodes, Laser-based planar imaging of nano-particle fluidization: Part II--mechanistic analysis of nanoparticle aggregation, Chem. Eng. Sci. 61 (2006) 8040-8049.

X.-F. Huang, C.-Y. Li, B.-H. Chen, P.L. Silveston, Transient kinetics of n-Butane oxidation to maleic anhydride over a VPO catalyst, AIChE J. 48 (2002) 846-855.

Y. Hatate, K. Ohmagari, A. Ikari, K. Kondo, D.F. King, Behavior of bubbles in a cylindrical fluidized bed at elevated temperature, J. Chem. Eng. Jpn. 21 (1988) 424-425.

Y. Iwadate, M. Horio, Prediction of agglomerate sizes in bubbling fluidized beds of group C powders, Powder Technol. 100 (1998) 223-236.

Y. Mawatari, T. Koide, Y. Tatemoto, S. Uchida, K. Noda, Effect of particle diameter on fluidization under vibration, Powder Technol. 123 (2002) 69-74.

Y. Wang, F. Wei, Y. Jin, T. Luo, Agglomerate particulate fluidization and E-particles, in: Proceedings of the 3rd Joint China/USA Chemical Engineering Conference (CUChE-3), Beijing, China, 2000.

Y. Zhang, H.T. Bi, J.R. Grace, C. Lu, Comparison of decoupling methods for analyzing pressure fluctuations in gas-fluidized beds, AIChE J. 56 (2010) 869-877.

Y. Zhong, Z. Wang, Z. Guo, Q. Tang, Defluidization behavior of iron powders at elevated temperature: Influence of fluidizing gas and particle adhesion, Powder Technol. 230 (2012) 225-231.

Z. Mansourpour, N. Mostoufi, R. Sotudeh-Gharebagh, Investigating agglomeration phenomena in an air-polyethylene fluidized bed using DEM–CFD approach, Chem. Eng. Res. Des. 92 (2014) 102-118.

Z. Wang, M. Kwauk, H. Li, Fluidization of fine particles, Chem. Eng. Sci. 53 (1998) 377-395.

APPENDIX A – EFFECTS OF TEMPERATURE, PRESSURE, AND INTERPARTICLE FORCES ON THE HYDRODYNAMICS OF A GAS-SOLID FLUIDIZED BED - REVIEW

When one contemplates a range of industrial processes including FCC regeneration, coal combustion, iron ore or mineral sand reduction a very broad range of parameters is encountered: gas molecular weight 2–31 kg/kmol, particle size 50–5000 μm, particle density 1400–4800 kg/m^3, temperature to 1000ºC, and pressure to 20 bar [1-3]. Variation in operating conditions (temperature and/or pressure) can change the gas properties and the level of interparticle forces (IPFs) in a gas-solid fluidized bed. Accordingly, in order to provide a comprehensive understanding of the bed hydrodynamics under different operating conditions variations in both hydrodynamic forces (HDFs) and IPFs must be taken into account.

Increasing the bed temperature causes the gas viscosity μ_g to increase (μ_g being proportional to T^n, where n is usually between 0.6 and 1.0) and the gas density ρ_g to decrease (ρ_g being inversely proportional to the absolute temperature T) [4, 5]. These modifications can change the magnitude of fluid forces exerted on the particles. Electrostatic and van der Waals forces mainly determine the magnitude of IPFs in a dry environment [6, 7]. When the system temperature increases, the magnitude of the electrostatic forces decreases [8-10] due to an increase in the electrical conductivity of particles with temperature [11, 12]. Since the molecular dipole pulsation around the contact point between particles in the mutual contacts is enhanced by thermal excitation, the magnitude of the van der Waals forces increases with the bed temperature [13]. The viscous flattening of solid particles occurring before sintering [14] results in a larger interparticle contact area and, hence, increases the magnitude of the van der Waals forces. The formation/addition of a liquid or the structural/chemical changes at the particle surface, e.g., through sintering, crystallization or plastic deformation, can give place to the presence of a material bridge between the particles at elevated temperatures [15]. The electrostatic and van der Waals forces are insignificant compared to the cohesive force resulting from the material bridge, either liquid or solid [7, 15-17]. Materials migrates during sintering due to diffusion, viscous flow or some other mechanism or combination of mechanisms to the contact area [17, 18], thus yielding a solid-solid

bond between the particles in contact at its final stage. The formation of compounds with low melting temperature, i.e., eutectics, principally causes the presence of a trace amount of liquid in high temperature fluidized beds. The presence of impurities with a low sintering temperature within the bed, which sinter/melt under the high temperature operating conditions and further react with each other or other solids, leads to the formation of eutectics [19]. For example, the ash sintering and chemical reaction between the alkali/alkali earth metal elements in the solid fuels/ash and the bed material, usually silica sand, is known as the main cause of the particle stickiness in the bed when combusting and/or gasifying low rank coals, biomass, and wastes [20-27]. The bed hydrodynamics can alter if one of the IPFs is in the same order of magnitude as the weight of the particle [21].

Different from temperature, changing the system pressure has essentially a sole effect on the gas density because the gas viscosity is a very weak function of pressure [28]. Increasing the bed pressure can also enhance the gas adsorption on the surface of particles and, thus, the magnitude of IPFs while they can additionally modify the fluidization behavior of a gas-solid fluidized bed [29-31]. When the magnitude of IPFs is very low and/or does not change with the operating condition, the variation in the gas properties defines the change in the fluidization characteristics for a given powder. The particle size information, in this case, helps to find the modification in the bed hydrodynamics is governed either by the viscous effect or inertia, or even the combination of two. The prediction of bed behavior becomes more complicated when variations in the level of IPFs and the magnitude of HDFs occur simultaneously during the process.

The inertia effect is dominant in the following conditions when the level of IPFs is at minimum: i) fluidization of coarse particles at high temperature (due to a decrease in the gas density) and ii) when increasing the operating pressure (as a result of an increase in the gas density). For larger particles of Geldart group D powders, referred to the fluidization behavior at ambient conditions, the minimum fluidization velocity U_{mf} increases with temperature while the minimum fluidization voidage ε_{mf} remain essentially insensitive to temperature [32-36]. For coarse particles exhibiting typical behavior of powders close to the boundary of Geldart groups B and D at ambient conditions, which undergo a fluidization behavior in the transition region between the viscous and inertia flow regimes, U_{mf} would be independent of temperature [35, 37-39] while ε_{mf} can slightly increase with temperature at atmospheric pressure [35, 37]. Upon raising the operating pressure, since the

counteractive influence of viscous and inertial forces on U_{mf} tends to shift toward the inertia effect, U_{mf} increases with temperature for these powders [35] keeping a similar dependency of ε_{mf} to temperature. For smaller particles of Geldart group B powders, referred to the fluidization behavior at ambient conditions, U_{mf} decreases as temperature increases [32-35, 37, 39-42] while ε_{mf} can lightly increase with temperature [33-35, 37]. The dependence of other fluidization characteristics of these moderate sized powders with the operating temperature would be an intermediate between those of coarser particles and fine powders, as discussed below. Also, no particulate bed expansion was reported for coarse particles at elevated temperatures.

A decrease in the bubble size with relatively no change in the bubble passage frequency are the main hydrodynamic modifications that can take place for coarse particles at high temperature in the bubbling regime [40, 43-47]. Thus, for the same fluidizing gas throughput in the bubbling regime, less gas will flow as bubbles. In other words, an increased amount of gas would be required to keep the particles well fluidized in the emulsion phase at elevated temperatures as a direct consequence of a reduction in the effective drag force acting on each particle by the fluidizing gas. A decrease in the magnitude of the ratio of the drag force to the buoyant weight of the particle at a higher temperature can accelerate the formation of fingers of particles falling in from the bubble's roof [47]. It can, consequently, increase the bubble break up, based on Taylor instability [48], and contribute in formation of smaller bubbles in the bed. The presence of smaller bubbles together with a reduction in the net energy being transferred to the fluidizing particles at a given superficial gas velocity U_g in the bubbling regime can decrease the quality of solids mixing and particle ejection from the bed surface into the freeboard. These modifications in bed behavior can reduce the bed expansion in the bubbling regime, which is in broad agreement with the experimental results of Llop et al. [49]. They can also postpone the transition velocity from bubbling to turbulent fluidization regime U_c [43] and decrease the solids entrainment rate [50].

While ε_{mf} remain unaffected [51-54], an increase in the system pressure for particles larger than about 200 μm, where the inertia effect begins to predominate [55], reduces the minimum fluidization velocity [35, 39, 51-54, 56-69]. This effect becomes more pronounced with increasing the particle size. Although no homogeneous bed expansion was observed for coarse particles when fluidizing them with nitrogen up to 25 bar [51], increasing the operating pressure to nearly critical conditions for particles behaving similar to Geldart group B powders at ambient conditions led to

the appearance of a bubble-free regime when fluidizing with CO_2 [66, 70]. An increase in the level of IPFs due to the gas adsorption at elevated pressures, which is highly dependent on the type of fluidizing gas [29], along with the variation of HDFs can explain this shift in fluidization behavior [70]. The flow dynamics of powders belong to Geldart groups B and D, referred to the fluidization behavior at ambient conditions, can further modify with increasing pressure at identical excess gas velocity, $U_g - U_{mf}$, through a decrease in the bubble stability [55, 71] and bubble size [43, 55, 60, 71-81] when $U_g - U_{mf}$ is not very low [82], and through-flow velocity of gas inside the bubbles [60, 71, 75-77]. An increase in the bed pressure at a given $U_g - U_{mf}$ can otherwise yields an increase in the bed expansion [49, 60, 71, 75-78], bubble splitting and coalescence rates [55, 71], bubble passage frequency [55, 60, 71-77, 80, 83], visible bubble flowrate [60, 71, 74-77] when the pressure is not too high to yield a less distinct bubble-emulsion structure [53, 72, 78, 79], bubble rise velocity U_b [55, 60, 71, 72, 74-77], emulsion phase voidage [71, 79, 80], solids concentration of the bubble phase [79, 80], granular temperature [79], and tendency of bubbles to pass through the bed close to the central axis [55, 60, 71, 74]. All these modifications result in smoother fluidization and excellent solids mixing in high pressure bubbling gas-solid fluidized bed of coarse particles.

Although the variation in the interphase interaction between gas and coarse solids is believed to be the principal reason for the change in the bed behavior at high pressure, three mechanisms have reported to explain the decreased bubble stability under such operating conditions. Rowe et al. [72] observed that bubble splitting, which occurred by stalactites of particles from the bubble's roof at atmospheric pressure, was governed by the wake intrusion into the bubble, breaking the bubble upon reaching the roof, at elevated pressures. Since the bubble rise velocity increased and the terminal velocity U_t of single coarse particle decreased with pressure, experiencing $U_b > U_t$ at higher pressures, an increased instability of bubbles was recognized at pressures well above the ambient following the bubble splitting theory proposed by Harrison et al. [84] from the rear. Yates [85] suggested a different school of thought to explain the growing instability of bubbles at elevated pressures. He attributed this drift to the reduced drag force exerted by the through-flowing gas on particles in bubble's roof since this drag force is responsible for the bubble stability [86] and the through-flow velocity of gas inside the bubbles decreases by pressure [60, 71, 75-77]. Hoffmann and Yates [55], however, reported that bubble splitting occurred both from the roof and rear of bubbles at high pressure. According to Olowson and Almstedt [71] the stability of bubbles is governed by fluctuations in the particle drag force resulted from fluctuations in the gas velocity.

The gas velocity fluctuations in a gas-solid fluidized bed is largely caused by the gas shortening between adjacent bubbles. Albeit fluctuations in the through-flow velocity of gas inside the bubbles remained comparatively identical under different operating pressures, a greater relative fluctuation in the particle drag force can be achieved at higher pressures for a given fluctuation in the gas velocity. An accelerated fluctuations of the drag force increases the tendency for both bubble splitting and coalescence and that when coupled with a decrease in the through-flow velocity of gas inside the bubbles, at higher pressures, leads to the presence of smaller bubbles in the bed.

The redistribution of bubble flow toward the central axis of the bed at a higher pressure can be primarily ascribed to an increased rate of bubble coalescence with the gas pressure [55, 71]. Since coalescence generally causes the bubbles to move laterally toward the vessel center-line [87], increasing the coalescence rate by operating pressure enhances this lateral movement resulting in a parabolic distribution of bubbles over the bed cross-section. A concentrated bubble flow along the axis promotes the gross circulation of solids within the bed [55, 87]. This can in turn direct the rising bubbles to merge together and move toward the bed center and, hence, additionally accelerate the bubble redistribution [71, 74]. The concentrated bubble flow at the center of the bed can also explain the increase in U_b with pressure even when smaller bubbles are present in the bed [71]. An increase in the effective drag force exerted by the fluidizing gas on particles and improved quality of solids mixing due to the increased gross solids circulation and local granular temperature at higher pressures may lead to reach U_c at lower gas velocities. Experimental results reported in the literature [43, 58, 64, 65, 88] are well in accordance with this interpretation showing a clear decrease in U_c for fluidized beds of coarse particles as the bed pressure was increased. The better quality of solids mixing within the bed at elevated pressures can also boost the particle-particle and particle-wall contacts. A higher degree of electrostatic charge generation on the particles and the column wall can accordingly resulted from the increased number of contacts. Experimental findings indicated that the degree of electrification and fouling of particles on the column wall due to the electrostatic effect enhanced with pressure in beds of coarse particles [9, 89, 90]. An increase in the gas density with the operating pressure, which raises the level of HDFs in a bed of coarse particles, can further yield a decrease in U_t and an increase in solids entrainment. Supporting observations were reported for these modifications in the literature [53, 56, 69, 88, 91-93].

Since fine powders, which show typical Geldart group A behavior at ambient conditions, undergo fluidization in the viscous flow regime and the gas viscosity remain essentially unchanged with

pressure [28], increasing the bed pressure has no influence on U_{mf} [29, 51-53, 67, 94]. Also, ε_{mf} is insensitive to pressure for these powders [51-53]. Nonetheless, increasing the system pressure expands the particulate fluidization regime between U_{mf} and the minimum bubbling velocity U_{mb}, i.e., the minimum bubbling voidage ε_{mb} and U_{mb} increase with pressure [29, 51, 52, 65, 66, 73, 95, 96]. At elevated pressures close to the critical conditions, where a fluidizing medium with physical properties intermediate between those of a liquid and a low pressure gas is attained, the fluidization can remain fully particulate at all fluid velocities between U_{mf} and the start of bulk transport for fine powders [95]. As pressure increases, the fluidization behavior of these fine powders in the bubbling regime at constant volumetric gas flowrate alter through an increase in the bed expansion [29, 97-99], emulsion phase voidage [29, 98-101], interstitial gas velocity [29, 100, 101], bubble instability [102], bubble splitting and coalescence rates [99], and bubble passage frequency [1, 29, 73, 99] and a decrease in the bubble size [1, 29, 73, 74, 94, 97-99, 101, 102] and visible bubble hold up [1, 98, 99] and flow rate [1, 29, 73, 98, 99, 101]. In addition, either an increase or no significant change was observed for the mean bubble rise velocity at higher system pressures [1, 73, 74, 102]. Therefore, fluidization of fine powders becomes smoother with increased pressure.

Theories explaining as to what causes stability in fluidized beds have been the source of great controversy and two broad schools of thought have been made [85, 103]. One theory assumes that IPFs dominate the bed stability [29, 104-107] and the other one is established on the assumption that HDFs are purely the controlling factors [108, 109]. Albeit different experimental observations have provided to support one and prove the failure of the other to explain the increased bed stability of fine powders at high pressure, some experimental data obtained by Jacob and Weimer [96], Poletto et al. [70], and Marzocchella and Salatino [65] show that an appropriate theory would be based on combination of both hydrodynamic and IPFs.

Since less gas flows as bubbles and more flows interstitially as the operating pressure increases in a bubbling fluidized bed of fine powders, the simple two-phase flow theory of fluidization [110], which postulates that any gas in excess of the minimum quantity to fluidize particles results in bubble formation, becomes increasingly invalid at higher pressures [1, 73, 101, 102]. The modification in the bubble behavior in a bubbling fluidized bed of these powders could be due either to a reduced portion of gas flowing through the bubble phase or to an instability phenomenon

that restricts the bubble growth [85, 101]. Rowe and MacGilivray [1] showed that the former hypothesis explains the reduced bubble size in a bubbling bed of fine silicon carbides, d_p=58 μm, ρ_p=3186 kg/m^3 (d_p is the mean particle size and ρ_p is the particle density), up to 4 bar. However, clear evidences have provided to emphasize on the latter assumption in conjunction with the former when pressure increases to 83 bar [99, 101]. Bubble splitting both from the roof [98, 101, 102] and the rear [94, 99] have reported in fluidized beds of fine particles at elevated pressures while the dominant mechanism of splitting being disputed. The first group [98, 101] argued that the bubble instability increases with pressure owing to a decrease in the apparent viscosity of the emulsion phase resulting from an increase in the voidage of this phase at higher pressures. Measurements of the apparent kinematic viscosity of dense fluidized bed of fine particles at just below U_{mb} and pressures up to 20 bar showed a substantial decrease with an increase in the operating pressure, which is in accordance with this argument. However, the second group [94] believed that since U_t decreases with pressure, the point where $U_b > U_t$ can be met more conveniently at higher gas pressures, which leads to a more frequent bubble break up. Although their X-ray observations of freely bubbling gas-fluidized bed of fine particles revealed a bubble division from the rear, Barreto et al. [99], however, argued the phenomenon with a slightly different approach. By application of experimental data and postulating a three-phase model for a bubbling fluidized bed (comprised of bubble, emulsion, and wake phases), Barreto et al. showed that either the volume fraction of bed occupied by wake or the difference in voidage between wake and emulsion phases, or even both, increases with pressure. With this modification, more gas will flow in bubbles wakes and less in bubbles as pressure is raised. This conclusion is well in line with others, who stressed on an increase in the interstitial flowrate with pressure while Barreto et al. discriminated between flow in the emulsion phase and the wake.

It was shown by Mostoufi and Chaouki [111] that fine particles move as clusters in dense bubbling and turbulent gas-solid fluidized beds. Thus, if a bubbling bed of fine powders is viewed with this standpoint, since the effective fluidizing entity is far larger than the primary particle, an increase in gas density resulting from the increased operating pressure can have an effective impact on the emulsion phase by the inertia effect. In other words, an increase in the net drag force acting on the fluidizing entities at higher pressures leads the complete breakage of the emulsion phase to occur at a lower gas velocity, i.e., U_c decreases [2, 43, 65, 88]. Consistently, it is expected that the

elutriation rate increases by the operating pressure at a given superficial gas velocity, which is in broad agreement with the experimental findings reported by researchers [88].

An increase in the operating temperature for a fluidized bed of fine powders with typical fluidization behavior of Geldart group A powders at ambient conditions can primarily change the bed behavior as a result of an increase in the gas viscosity if the level of IPFs remains relatively unchanged. Under this circumstance, since U_{mf} for fine particles is inversely proportional to μ_g in the laminar flow regime, it decreases with temperature [37, 112-117]. Experimental observations, however, reveal that high temperature causes an increase in the fixed bed and/or incipient fluidization voidage [37, 112, 117-124] and extension of the homogeneous bed expansion [113, 114, 124-126] for these particles. While the increase in the settled bed voidage ε_0 and/or ε_{mf} with temperature was attributed to the thermal growth of IPFs [37, 112, 117-121, 123, 124], similar to the fluidization of fine powders under pressure, two different approaches were adopted to interpret the extension of the particulate fluidization regime at high temperature; one with purely hydrodynamic considerations [113, 114, 125] and the other one ascribing the modification to the variation in the level of IPFs [124, 126]. The bed behavior in the bubbling regime can be altered through an increase in the bubble size and passage frequency [127] and a decrease in the interstitial gas velocity [115, 116, 122, 123, 126, 128], emulsion phase fraction [127], and solids concentration in this phase [100, 123, 124, 126-128].

An increase in the flowrate of visible bubble in a bed of fine powders at high temperature can be deducted from the increased bubble size and passage frequency. The presence of a viscous gas in the emulsion phase would enhance the viscosity of this phase. This evolution would either decrease the formation of stalactite of particles from the bubble's roof or the intrusion of wake particles into the bubble. This can in turn promote the presence of larger bubbles in the bed. In addition, a larger bubble with a higher momentum is required to pass through a bed of viscous emulsion phase, as the virtual continuous phase in a gas-solid fluidized bed. The effect is in good agreement with increasing the viscosity of the liquid phase in a bubble column reactor [129, 130]. Bubbles in a bed of fine particles experience a maximum stable size due to the appreciable bubble splitting effect [131-133] and elated gas-particle interaction [77]. As a consequence of such special fluidization characteristics, an increased bubble flow does not merely contribute to the formation of larger bubbles. It can, otherwise, increase the bubble frequency as well as the size, which was verified by

Cui and Chaouki [127]. The presence of larger bubbles that more frequently pass through a bed of fine particles at high temperature, where the role of IPFs is not well pronounced, can increase the bed turbulency shifting the fluidization behavior from typical Geldart group A to B behavior. This modification can in turn lead to a decrease in U_c [3, 43, 127, 134] and an increase in the entrainment rate of powders at a given superficial gas velocity.

Findlay and Knowlton [135] studied the effect of temperature on the solids entrainment rate from a fluidized bed of char and limestone while adjusting the system pressure so that the gas viscosity was only altered keeping the gas density constant. Accordingly, a significant increase in the solids entrainment rate was observed most likely due to the increased drag force on the particles by a viscous gas. Ellis et al. [136] investigated the solid circulation rate in a circulating fluidized bed of fine FCC particles by manipulating the fluidizing gas properties. By increasing the helium concentration in the fluidizing air from 0 to 96% vol., the gas density decreased and viscosity increased simultaneously, changes which are identical to when the operating temperature is increased. Consistent to Findlay and Knowlton [135], an increase in solids circulation rate was observed with increasing the helium concentration.

Increasing the level of IPFs below U_{mb} can cause an increase in ε_0 and/or ε_{mf} [30, 137-141], U_{mf} for a given powder [138, 139, 141-145], the span of particulate fluidization regime if exists [125, 144, 146, 147] or yield the appearance of a bubble-free regime in beds of medium sized and coarse particles [137, 148-151]. With these modifications, the fluidization characteristics of the bed can shift from typical Geldart group B behavior toward A and/or even C behavior upon enhancing the magnitude of IPFs [137-139, 141, 148, 149, 151]. A critical review about the fluidization behavior of ultrafine powders, which is known to be greatly influenced by the presence of IPFs, has been given by Shabanian et al. [7].

At a given superficial gas velocity above U_{mb}, if there is a slight increase in the level of IPFs in a bubbling bed of coarse particles, e.g., Geldart group B powders referred to the fluidization behavior at ambient conditions, the bed behavior can change through a modest decrease in the bubble size and passage frequency and an increase in the emulsion phase fraction and voidage [140, 141]. The fluidizing gas, thus, shows a higher tendency to interstitially pass through the bed. This helps keeping the particles to remain well fluidized in the emulsion phase in order to compensate for the increase in U_{mf}. Since the quality of solids mixing can be minimally influenced by the presence of

a low level of IPFs within the bed, the stalactites of particles can be effectively formed on the bubble's roof and contribute to the bubble splitting. Therefore, the bubble size and passage frequency undergo a slight decrease giving rise to a less bubble flow. These changes can subsequently reduce the bubble activity and existence of particle-particle collisions with high intensity in the bed, which are responsible for the bubbling to turbulent fluidization regime transition. Accordingly, U_c and the solids entrainment rate slightly increases [139-141] and decreases [141], respectively, in this case.

A progressive increase in the level of IPFs toward the complete defluidization state can differently modify the bed hydrodynamics. At similar fluidizing gas volumetric flowrate, the presence of a moderate/high level of IPFs in the bed, away from defluidization conditions, results in an increase in the bubble growth rate with U_g [139, 141], emulsion phase fraction and voidage [140, 152] and a discernable decrease in the bubble passage frequency [140, 141]. Depending on the physical properties of the base particles and the ratio of the magnitude of IPFs/HDFs a bed with a moderate level of IPFs can contain smaller bubbles with respect to a system with no IPFs at low and moderate gas velocities in the bubbling regime and larger bubbles at gas velocities approaching U_c; an inversion trend takes place at moderate gas velocities [139, 141]. The trend inversion can take place at a lower superficial gas velocity when the level of IPFs increases. Therefore, a bed with a high level of IPFs can have larger bubbles at all superficial gas velocities above U_{mb} [47].

The minimum fluidization velocity and the capacity of the emulsion phase to hold gas inside its structure steadily increase with a gradual growth of the level of IPFs [140, 141]. Consequently, a higher amount of the fluidizing gas is prone to pass through the bed in the emulsion phase and keep the particles adequately fluidized in this phase. The presence of a moderate/high level of IPFs reduces the quality of solids mixing while an increase in the resistance of the emulsion phase to any changes on the stability of its structure by enhancing the level of IPFs is principally responsible for this drift [153]. It can in turn decrease the formation of the stalactites of particles from the bubble's roof and, hence, promote the bubble growth rate with the superficial gas velocity. Also, reinforcing the emulsion phase of a gas-solid fluidized bed with a moderate/high level of IPFs resembles an increase of the liquid viscosity in a bubble column reactor. This analogy provides an additional justification for the presence of larger bubbles with higher momentum in a bed with a higher apparent viscosity [129, 130] of the emulsion phase, i.e., a cohesive bed, compared to a non-cohesive bed. A progressive increase in the level of IPFs while approaching the complete

defluidization state advances the bubble enlargement, which would result in the presence of oblong bubbles that functions similar to channels in the bed. An exponential increase in idle time that simultaneously occurs with this change speeds up the agglomeration phenomenon [153] and leads to an eventual partial/complete defluidization of the bed. A less bubble activity can take place in a bed with a high level of IPFs since the bubbles pass through the reinforced emulsion phase at a lower frequency even though they are larger in size. This yields less particle-particle collisions with high intensity to occur within the bed, which in turn increases the transition velocity from the bubbling to turbulent fluidization regime [139-141] and decreases the elutriation rate [141].

As mentioned before, an increase in the operating temperature and pressure can change the level of both HDFs and IPFs. Thus, all modifications in both groups of forces must be taken into account to shed light on the bed hydrodynamics under different operating conditions. It is generally expected that the presence of IPFs at high temperature would have a greater impact on the fluidization behavior than those might be present at elevated pressures. This might be due to two accounts: i) an increase in the bed temperature causes the presence and intensification of different types of IPFs that can easily overcome the magnitude of HDFs while it decreases with temperature in the case of coarse particles or moderately increase when fluidizing fine powders at elevated temperatures (for instance, raising the bed temperature from ambient to 1100^{o}C increases the gas viscosity by a factor or 3–4 depending on the type of gas and decreases the gas density by a factor of 4.7 at constant system pressure [28]); ii) despite an increase in the operating pressure can enhance the level of van der Waals forces through the accelerated gas adsorption or increase the degree of electrification within the bed, it significantly increases the level of HDFs (at identical temperature the gas density increases by the same factor as the pressure ratio [28]), which could lead to a less pronounced effect of IPFs on the bed flow dynamics through a reduced magnitude of the ratio of IPFs/HDFs. This can explain the advantage of pressurized gas-solid fluidized beds to treat cohesive particles [2].

The emulsion phase is highly effective in bringing about chemical reaction between gas and particles [154]. In cases, where the bubbles are a serious cause of bypassing, changing the operating condition to increase the interstitial flow improve contacting efficiency and, hence, reactor performance. Nevertheless, since gas mixing is extremely poor in the emulsion phase and bubbles are necessary to provide a good solids mixing within the bed for the purpose of appropriate heat transfer with immersed surfaces [1], the division of gas between the bubble and emulsion phases

should be attempted with a great attention. In other words, depending on the goal and limitations of the process, the operating condition should be modified to direct the gas toward the emulsion or bubble phase or even change the bubble population. Moreover, further hydrodynamic study at simultaneously high pressure and temperature is required to complete the puzzle.

A.1 Nomenclature

A.1.1 Acronyms

HDFs	hydrodynamic forces
IPFs	interparticle forces

A.1.2 Symbols

d_p	mean particle size (μm)
n	power of absolute temperature; $\mu_g \propto T^n$, 0.6< n <1.0 (-)
T	absolute temperature (K)
U_c	transition velocity from bubbling to turbulent fluidization regime (m/s)
U_b	bubble rise velocity (m/s)
U_g	superficial gas velocity (m/s)
U_{mf}	minimum fluidization velocity (m/s)
U_{mb}	minimum bubbling velocity (m/s)
U_t	terminal velocity (m/s)
$U_g - U_{mf}$	excess gas velocity (m/s)

A.1.3 Greek letters

ε_0	settled bed voidage (-)
ε_{mb}	minimum bubbling voidage (-)
ε_{mf}	minimum fluidization voidage (-)
μ_g	gas viscosity (Pa.s)
ρ_g	gas density (kg/m^3)
ρ_p	particle density (kg/m^3)

A.2 References

1) P.N. Rowe, H.J. MacGillivray, A preliminary X-ray study of the effect of pressure on a bubbling gas fluidised bed, in: Proceedings of the Fluidised Combustion: Systems and Applications, Institute of Energy, London, 1980, pp. 1-9.
2) M. Tsukada, D. Nakanishi, M. Horio, The effect of pressure on the phase transition from bubbling to turbulent fluidization, Int. J. Multiphase Flow 19 (1993) 27-34.
3) P.K. Peeler, K.S. Lim, R.C. Close, Effect of temperature on the turbulent fluidization regime transition, in: J. Werther (Ed.) Proceedings of the 6th International Conference on Circulating Fluidized Beds, Würzburg, Germany, 1999, pp. 125-130.
4) T.M. Knowlton, Pressure and temperature effects in fluid-particle systems, in: O.E. Potter, D.J. Nicklin (Eds.) Proceedings of the 7th International Conference on Fluidization, Engineering Foundation, New York, 1992, pp. 27-46.
5) S.Y. Wu, J. Baeyens, Effect of operating temperature on minimum fluidization velocity, Powder Technol. 67 (1991) 217-220.
6) J. Visser, J., Van der Waals and other cohesive forces affecting powder fluidization, Powder Technol. 58 (1989) 1-10.
7) J. Shabanian, R. Jafari, J. Chaouki, Fluidization of ultrafine powders, Int. Rev. Chem. Eng. (IRECHE) 4 (2012) 16-50.
8) T. Kai, S. Furusaki, Behavior of fluidized beds of small particles at elevated temperatures, J. Chem. Eng. Jpn. 18 (1985) 113-118.
9) W.O. Moughrabiah, J.R. Grace, X.T. Bi, Effects of pressure, temperature, and gas velocity on electrostatics in gas−solid fluidized beds, Ind. Eng. Chem. Res. 48 (2009) 320-325.
10) T.A. Alsmari, J.R. Grace, X.T. Bi, Effects of superficial gas velocity and temperature on entrainment and electrostatics in gas–solid fluidized beds, Chem. Eng. Sci. 123 (2015) 49-56.
11) S. Boggs, D.H. Damon, J. Hjerrild, J.T. Holboll, M. Henriksen, Effect of insulation properties on the field grading of solid dielectric DC cable, IEEE Trans. Power Delivery 16 (2001) 456-461.
12) P.K. Jain, N. Saxena, Temperature and composition dependence of electrical conductivity of Se90In10–xSbx (x=0, 2, 4, 6, 8, 10) chalcogenide glasses, J. Non-Oxide Photonic Glasses 1 (2009) 43-52.

13) H. Krupp, Particle adhesion: theory and experiment, Adv. Colloid Interface Sci. 1 (1967) 111-239.

14) H. Rumpf, Particle adhesion, in: Proceedings of the 2nd International Symposium on Agglomeration (Agglomeration 77), AIME, 1977, pp. 97-129.

15) P. Pagliai, S.J.R. Simons, D. Rhodes, Towards a fundamental understanding of defluidisation at high temperatures: a micro-mechanistic approach, Powder Technol. 148 (2004) 106-112.

16) R.A. Bowling, A theoretical review of particle adhesion, in: K. Mittal (Ed.) Particles on Surfaces 1, Plenum Press, New York, 1988, pp. 129-142.

17) J.P.K. Seville, C.D. Willett, P.C. Knight, Interparticle forces in fluidisation: a review, Powder Technol. 113 (2000) 261-268.

18) J.H. Siegell, High-temperature de fluidization, Powder Technol. 38 (1984) 13-22.

19) G. Tardos, R. Pfeffer, Chemical reaction induced agglomeration and defluidization of fluidized beds, Powder Technol. 85 (1995) 29-35.

20) A.R. Manzoori, E.R. Lindner, P.K. Agarwal, Inorganic transformation during the circulating fluid bed combustion of low-rank coals with high content of sodium and sulphur, in: Proceedings of the Engineering Foundation Conference on Inorganic Transformations and Ash Deposition During Combustion, Palm Coast, Florida, USA, 1991, pp. 735-762.

21) M. Bartels, W. Lin, J. Nijenhuis, F. Kapteijn, J.R. van Ommen, Agglomeration in fluidized beds at high temperatures: Mechanisms, detection and prevention, Prog. Energy Combust. Sci. 34 (2008) 633-666.

22) J. Werther, M. Saenger, E. U. Hartge, T. Ogada, Z. Siagi, Combustion of agricultural residues, Prog. Energy Combust. Sci. 26 (2000) 1-27.

23) W. Lin, K. Dam-Johansen, F. Frandsen, Agglomeration in bio-fuel fired fluidized bed combustors, Chem. Eng. J. 96 (2003) 171-185.

24) C. Tangsathitkulchai, M. Tangsathitkulchai, Effect of bed materials and additives on the sintering of coal ashes relevant to agglomeration in fluidized bed combustion, Fuel Process. Technol. 72 (2001) 163-183.

25) B.M. Steenari, O. Lindqvist, V. Langer, Ash sintering and deposit formation in PFBC, Fuel 77 (1998) 407-417.

26) M. Öhman, A. Nordin, B.-J. Skrifvars, R. Backman, M. Hupo, Bed agglomeration characteristics during fluidized bed combustion of biomass fuels, Energy Fuels 14 (2000) 169-178.

27) J. van Caneghem, A. Brems, P. Lievens, C. Block, P. Billen, I. Vermeulen, R. Dewil, J. Baeyens, C. Vandecastteele, Fluidized bed waste incinerators: Design, operational and environmental issues, Prog. Energy Combust. Sci. 38 (2012) 551-582.

28) T.M. Knowlton, Pressure and temperature effects in fluid-particle systems, in: W.C. Yang (Ed.), Fluidization, Solids Handling and Processing: Industrial Applications, Noyes, New Jersy, 1999, pp. 111-152.

29) H.W. Piepers, E.J.E. Cottar, A.H.M. Verkooijen, K. Rietema, Effects of pressure and type of gas on particle-particle interaction and the consequences for gas–solid fluidization behavior, Powder Technol. 37 (1984) 55-70.

30) K. Rietema, The Dynamics of Fine Powders, Elsevier Science Publishers Ltd, New York, 1991.

31) H.Y. Xie, The role of interparticle forces in the fluidization of fine particles, Powder Technol. 94 (1997) 99-108.

32) R.R. Pattipati, C.Y. Wen, Minimum fluidization velocity at high temperatures, Ind. Eng. Chem. Process Des. Dev. 20 (1981) 705-707.

33) J.S.M. Botterill, Y. Teoman, K.R. Yüregir, The effect of operating temperature on the velocity of minimum fluidization, bed voidage and general behavior, Powder Technol. 31 (1982) 101-110.

34) J.S.M. Botterill, Y. Teoman, K.R. Yüregir, The Effect of temperature on fluidized bed behavior, Chem. Eng. Commun. 15 (1982) 227-238.

35) M.F. Llop, J. Casal, J. Arnaldos, Incipient fluidization and expansion in fluidized beds operated at high pressure and temperature, in: J.-F. Large, C. Laguerie (Eds.) Proceedings of the 8th International Conference on Fluidization, Engineering Foundation, New York, 1995, pp. 131-138.

36) N. Sitthiphong, A.H. George, D. Bushnell, Bubble eruption diameter in a fluidized bed of large particles at elevated temperatures, Chem. Eng. Sci. 36 (1981) 1259-1260.

37) B. Formisani, R. Girimonte, L. Mancuso, Analysis of the fluidization process of particle beds at high temperature, Chem. Eng. Sci. 53 (1998) 951-961.

38) D. Geldart, R.R. Cranfield, The gas fluidisation of large particles, Chem. Eng. J. 3 (1972) 211-231.

39) M. Nakamura, Y. Hamada, S. Toyama, A.E. Fouda, C.E. Capes, An experimental investigation of minimum fluidization velocity at elevated temperatures and pressures, Can. J. Chem. Eng. 63 (1985) 8-13.

40) K. Svoboda, J. Cermak, M. Hartman, J. Drahos, K. Selucky, Pressure fluctuations in gas-fluidized beds at elevated temperatures, Ind. Eng. Chem. Process Des. Dev. 22 (1983) 514-520.

41) M. Hartman, K. Svoboda, Predicting the effect of operating temperature on the minimum fluidization velocity, Ind. Eng. Chem. Process Des. Dev. 25 (1986) 649-654.

42) T. Mii, K. Yoshida, D. Kunii, Temperature effects on the characteristics of fluidized beds, J. Chem. Eng. Jpn. 6 (1973) 100-102.

43) P. Cai, Y. Jin, Z.Q. Yu, Z.W. Wang, Effect of operating temperature and pressure on the transition from bubbling to turbulent fluidization, AIChE Symp. Ser. 85(270) (1989) 37-43.

44) S.C. Saxena, N.S. Rao, S.J. Zhou, Fluidization characteristics of gas fluidized beds at elevated temperatures, Energy 15 (1990) 1001-1014.

45) S. Qian, J. Lu, G. Flamant, Fluidization characteristics of gas-solid fluidized bed at elevated temperature, J. Combust. Sci. Technol. 3 (1997) 344-348.

46) Q. Guo, G. Yue, T. Suda, J. Sato, Flow characteristics in a bubbling fluidized bed at elevated temperature, Chem. Eng. Process. Process Intensif. 42 (2003) 439-447.

47) J. Shabanian, J. Chaouki, Fluidization characteristics of a bubbling gas-solid fluidized bed at high temperature in the presence of interparticle forces, Chem. Eng. J. (2015) submitted for publication.

48) R. Clift, J.R. Grace, The mechanism of bubble break-up in fluidised beds, Chem. Eng. Sci. 27 (1972) 2309-2310.

49) M.F. Llop, J. Casal, J. Arnaldos, Expansion of gas-solid fluidized beds at pressure and high temperature, Powder Technol. 107 (2000) 212-225.

50) J.H. Choi, J.E. Son, S.D. Kim, Solid entrainment in fluidized bed combustors, J. Chem. Eng. Jpn. 22 (1989) 597-606.

51) D.F. King, D. Harrison, The dense phase of a fluidized bed at elevated pressures, Trans. Inst. Chem. Eng. 60 (1982) 26-30.

52) L.E.L. Sobreiro, J.L.F. Monteiro, The effect of pressure on fluidized bed behavior, Powder Technol. 33 (1982) 95-100.

53) D.C. Chitester, R.M. Kornosky, L.-S. Fan, J.P. Danko, Characteristics of fluidization at high pressure, Chem. Eng. Sci. 39 (1984) 253-261.

54) B.U. Kozanoglu, J. Welti Chanes, D. García Cuautle, J.P. Santos Jean, Hydrodynamics of large particle fluidization in reduced pressure operations: an experimental study, Powder Technol. 125 (2002) 55-60.

55) A.C. Hoffmann, J.G. Yates, Experimental observations of fluidized beds at elevated pressures, Chem. Eng. Commun. 41 (1986) 133-149.

56) T.M. Knowlton, High-pressure fluidization characteristics of several particulate solids, primarily coal and coal-derived materials. AIChE Symp. Ser. 161(73) (1977) 22-28.

57) S.C. Saxena, G.J. Vogel, The measurement of incipient fluidization velocities in a bed of coarse dolomite at temperature and pressure, Trans. Inst. Chem. Eng. 55 (1977) 184-189.

58) G.S. Canada, M.H. MacLaughlin, Large particle fluidization and heat transfer at high pressure, AIChE Symp. Ser. 74(176) (1978) 27-37.

59) J.-I. Kawabata, M. Yumiyama, Y. Tazaki, S. Honma, T. Chiba, T. Sumiya, K. Endo, Characteristics of gas-fluidised beds under pressure, J. Chem. Eng. Jpn. 14 (1981) 85-89.

60) P.A. Olowson, A.E. Almstedt, Influence of pressure and fluidization velocity on the bubble behaviour and gas flow distribution in a fluidized bed, Chem. Eng. Sci. 45 (1990) 1733-1741.

61) P.A. Olowson, A.E. Almstedt, Influence of pressure on the minimum fluidization velocity, Chem. Eng. Sci. 46 (1991) 637-640.

62) R. Bouratoua, Y. Molodtsof, A. Koniuta, Hydrodynamic characteristics of a pressurized fluidized bed, in: Proceedings of the 12th International Conference on Fluidized Bed Combustion, La Jolla, California, 1993, pp. 63-68.

63) M.F. Llop, F. Madrid, J. Arnaldos, J. Casal, Fluidization at vacuum conditions. A generalized equation for the prediction of minimum fluidization velocity, Chem. Eng. Sci. 51 (1996) 5149-5157.

64) A. Marzocchella, P. Salatino, The dynamics of fluidized beds under pressure, AIChE Symp. Ser. 92(313) (1996) 25-30.

65) A. Marzocchella, P. Salatino, Fluidization of solids with CO_2 at pressures from ambient to supercritical, AIChE J. 46 (2000) 901-910.

66) C. Vogt, R. Schreiber, J. Werther, G. Brunner, Fluidization at supercritical fluid conditions, in: M. Kwauk, J. Li, W.C. Yang (Eds.) Proceedings of the 10th International Conference on Fluidization, Engineering Foundation, New York, 2001, pp. 117-124.

67) I. Sidorenko, M.J. Rhodes, Influence of pressure on fluidization properties, Powder Technol. 141 (2004) 137-154.

68) A. Orta, B. Wu, M. Ghods, A. Guerrero, C. Bellehumeur, A. Kantzas, Pressure effect on hydrodynamics of a high pressure X-ray transparent polyethylene fluidized bed, Int. J. Chem. Reactor Eng. 9 (2011) Article A97.

69) J. Li, Z. Cheng, Y. Fang, H. Wang, W. Nie, J. Huang, Y. Wang, Minimum and terminal velocity in fluidization of coal gasification materials and coal blending of gasification under pressure, Fuel 110 (2013) 153-161.

70) M. Poletto, P. Salatino, L. Massimilla, Fluidization of solids with CO_2 at pressures and temperatures ranging from ambient to nearly critical conditions, Chem. Eng. Sci. 48 (1993) 617-621.

71) P.A. Olowson, A.E. Almstedt, Hydrodynamics of a bubbling fluidized bed: influence of pressure and fluidization velocity in terms of drag force, Chem. Eng. Sci. 47 (1992) 357-366.

72) P.N. Rowe, P.U. Foscolo, A.C. Hoffmann, J.G. Yates, X-ray observation of gas fluidized beds under pressure, in: D. Kunii, R. Toei (Eds.) Proceedings of the 4th International Conference on Fluidization, Kashikojima, Japan, 1984, pp. 53-60.

73) I.H. Chan, C. Sishtla, T.M. Knowlton, The effect of pressure on bubble parameters in gas-fluidized beds, Powder Technol. 53 (1987) 217-235.

74) J. Schweinzer, O. Molerus, Bubble flow in pressurized gas/solid fluidized beds, Chem. Eng. Technol. 10 (1987) 368-375.

75) S.E. Olsson, J. Wiman, A.E. Almstedt, Hydrodynamics of a pressurized fluidized bed with horizontal tubes: Influence of pressure, fluidization velocity and tube-bank geometry, Chem. Eng. Sci. 50 (1995) 581-592.

76) J. Wiman, A.E. Almstedt, Hydrodynamics, erosion and heat transfer in a pressurized fluidized bed: influence of pressure, fluidization velocity, particle size and tube bank geometry, Chem. Eng. Sci. 52 (1997) 2677-2695.

77) J. Wiman, A.E. Almstedt, Influence of pressure, fluidization velocity and particle size on the hydrodynamics of a freely bubbling fluidized bed, Chem. Eng. Sci. 53 (1998) 2167-2176.

78) J. Li, J.A.M. Kuipers, Effect of pressure on gas–solid flow behavior in dense gas-fluidized beds: a discrete particle simulation study, Powder Technol. 127 (2002) 173-184.

79) W. Godlieb, N.G. Deen, J.A.M. Kuipers, On the relationship between operating pressure and granular temperature: A discrete particle simulation study, Powder Technol. 182 (2008) 250-256.

80) Z. Mansourpour, S. Karimi, R. Zarghami, N. Mostoufi, R. Sotudeh-Gharebagh, Insights in hydrodynamics of bubbling fluidized beds at elevated pressure by DEM-CFD approach, Particuol. 8 (2010) 407-414.

81) G.C. Brouwer, E.C. Wagner, J.R. van Ommen, R.F. Mudde, Effects of pressure and fines content on bubble diameter in a fluidized bed studied using fast X-ray tomography, Chem. Eng. J. 207-208 (2012) 711-717.

82) P. Cai, M. Schiavetti, G. De Michele, G.C. Grazzini, M. Miccio, Quantitative estimation of bubble size in PFBC, Powder Technol. 80 (1994) 99-109.

83) M. Cárský, M. Hartman, B.K. Ilyenko, K.E. Makhorin, The bubble frequency in a fluidized bed at elevated pressure, Powder Technol. 61 (1990) 251-254.

84) D. Harrison, J.F. Davidson, J.W. de Kock, On the nature of aggregative and particulate fluidisation, Trans. Inst. Chem. Eng. 39 (1961) 202–211.

85) J.G. Yates, Effects of temperature and pressure on gas-solid fluidization, Chem. Eng. Sci. 51 (1996) 167-205.

86) J.B.L.M. Campos, J.R.F. Guedes de Carvalho, Drag force on the particles at the upstream end of a packed bed and the stability of the roof of bubbles in fluidised beds, Chem. Eng. Sci. 47 (1992) 4057-4062.

87) J.R. Grace, D. Harrison, The distribution of bubbles within a gas fluidized bed, Inst. Chem. Eng. Symp. Ser. 30 (1968) 105–113.

88) W.C. Yang, D.C. Chitester, Transition between bubbling and turbulent fluidization at elevated pressure, AIChE Symp. Ser. 84 (262) (1988) 10-21.

89) F. Salama, D. Song, P. Mehrani, Characterizing electrostatic charges in high-pressure gas-solid fluidized beds: Experimental design and preliminary results, in: J.A.M. Kuipers, R.F. Mudde, J.R. van Ommen, N.G. Deen (Eds.) Proceedings of the 14th International Conference on Fluidization – From Fundamentals to Products, ECI Digital Archives, Noordwijkerhout, The Netherlands, 2013.

90) D. Song, F. Salama, J. Matta, P. Mehrani, Implementation of Faraday cup electrostatic charge measurement technique in high-pressure gas–solid fluidized beds at pilot-scale, Powder Technol. (2015) Published Online: 2015-06-11, DOI: http://dx.doi.org/10.1016/j.powtec.2015.05.049.

91) I.H. Chan, T.M. Knowlton, The effect of pressure on entrainment from bubbling gas-fluidized beds, in: D. Kunii, R. Toei (Eds.) Proceedings of the 4th International Conference on Fluidization, Kashikojima, Japan, 1984, pp. 283-290.

92) I.H. Chan, T.M. Knowlton, The effect of system pressure on the transport disengaging height (TDH) above bubbling gas-fluidized beds, AIChE Symp. Ser. 80(241) 1984 24-33.

93) S.T. Pemberton, J.F. Davidson, Elutriation of fine particles from bubbling fluidized beds, in: D. Kunii, R. Toei (Eds.) Proceedings of the 4th International Conference on Fluidization, Kashikojima, Japan, 1984, pp. 275-282.

94) J.R.F. Guedes de Carvalho, D.F. King, D. Harrison, Fluidization of fine particles under pressure, in: J.F. Davidson, D.L. Keairns (Eds.) Proceedings of the 2nd Engineering Foundation Conference on Fluidization, Cambridge, England, 1978, pp. 59-64.

95) M.E. Crowther, J.C. Whitehead, Fluidization of fine particles at elevated pressure, in: J.F. Davidson, D.L. Keairns (Eds.) Proceedings of the 2nd Engineering Foundation Conference on Fluidization, Cambridge, England, 1978, pp. 65-70.

96) K.V. Jacob, A.W. Weimer, High-pressure particulate expansion and minimum bubbling of fine carbon powders, AIChE J. 33 (1987) 1698-1706.

97) J.R.F. Guedes de Carvalho, D. Harrison, Fluidization under pressure, in: D.L. Keairns (Ed.) Fluidization Technology 1, 1976. pp. 59-61.

98) M.P. Subzwari, R. Clift, D.L. Pyle, Bubbling behavior of fluidized beds at elevated pressures, J.F. Davidson, D.L. Keairns (Eds.) Proceedings of the 2nd Engineering Foundation Conference on Fluidization, Cambridge, England, 1978, pp. 50-54.

99) G.F. Barreto, J.G. Yates, P.N. Rowe, The effect of pressure on the flow of gas in fluidized beds of fine particles, Chem. Eng. Sci. 38 (1983) 1935-1945.

100) A.W. Weimer, G.J. Quarderer, Effect of temperature on the dense phase in high pressure fluidized beds of fine powders, AIChE Symp. Ser. 80(241) (1984) 79-86.

101) A.W. Weimer, G.J. Quarderer, On dense phase voidage and bubble size in high pressure fluidized beds of fine powders, AIChE J., 31 (1985) 1019-1028.

102) D.F. King, D. Harrison, The bubble phase in high pressure fluidized beds, in: J.R. Grace, J.M. Matsen (Eds.) Fluidization, Plenum, New York, 1980, pp. 101-107.

103) Sidorenko, M.J. Rhodes, Pressure effects on gas-solid fluidized bed behavior, Int. J. Chem. Reactor Eng. 1 (2003) Review R5 (1-33).

104) S.M.P. Mutsers, K. Rietema, The effect of interparticle forces on the expansion of a homogeneous gas-fluidized bed, Powder Technol. 18 (1977) 239-248.

105) E.J.E. Cottaar, K. Rietema, A theoretical study on the influence of gas adsorption on interparticle forces in powders, J. Colloid Interface Sci. 109 (1986) 249-260.

106) K. Rietema, H.W. Piepers, The effect of interparticle forces on the stability of gas-fluidized beds-I. Experimental evidence, Chem. Eng. Sci. 45 (1990) 1627-1639.

107) K. Rietema, E.J.E. Cottaar, H.W. Piepers, The effects of interparticle forces on the stability of gas-fluidized beds-II. Theoretical derivation of bed elasticity on the basis of van der Waals forces between powder particles, Chem. Eng. Sci. 48 (1993) 1687-1697.

108) G.B. Wallis, One Dimensional Two-phase Flow, McGraw-Hill, New York, 1969.

109) P.U. Foscolo, L.G. Gibilaro, A fully predictive criterion for the transition between particulate and aggregate fluidization, Chem. Eng. Sci. 39 (1984) 1667-1675.

110) R.D. Toomey, H. Johnstone, Gaseous fluidization of solid particles, Chem. Eng. Prog. 48 (1952) 220-226.

111) N. Mostoufi, J. Chaouki, On the axial movement of solids in gas-solid fluidized beds, Chem. Eng. Res. Des. 78 (2000) 911-920.

112) G. Raso, M. D'Amore, B. Formisani, P.G. Lignola, The influence of temperature on the properties of the particulate phase at incipient fluidization, Powder Technol. 72 (1992) 71-76.

113) S. Rapagna, P.U. Foscolo, L.G. Gibilaro, The influence of temperature on the quality of gas fluidization, Int. J. Multiphase Flow 20 (1994) 305-313.

114) H.Y. Xie, D. Geldart, Fluidization of FCC powders in the bubble-free regime: effect of types of gases and temperature, Powder Technol. 82 (1995) 269-277.

115) P. Lettieri, J.G. Yates, D. Newton, The influence of interparticle forces on the fluidization behaviour of some industrial materials at high temperature, Powder Technol. 110 (2000) 117-127.

116) G. Bruni, P. Lettieri, D. Newton, J. Yates, The influence of fines size distribution on the behaviour of gas fluidized beds at high temperature, Powder Technol. 163 (2006) 88-97.

117) C. Xu, J.X. Zhu, Effects of gas type and temperature on fine particle fluidization, China Particuol. 4 (2006) 114-121.

118) G.H. Hong, R. Yamazaki, T. Takahashi, G. Jombo, Minimum fluidization velocity in a fluidized bed at high temperatures, Kagaku Kogaku Ronbunshu 6 (1980) 557-562.

119) R. Yamazaki, G.H. Hong, G. Jimbo. The behavior of a gas-solid fluidized bed at elevated temperatures, in: D. Kunii, R. Toei (Eds.) Proceedings of the 4th International Conference on Fluidization, Kashikojima, Japan, 1984, pp. 121-128.

120) R. Yamazaki, N. Ueda, G. Jimbo, Mechanism of incipient fluidization in fluidized bed at elevated temperature, J. Chem. Eng. Jpn. 19 (1986) 251-257.

121) R. Yamazaki, N.-S. Han, Z.-F. Sun, G. Jimbo, Effect of chemisorbed water on bed voidage of high temperature fluidized bed, Powder Technol. 84 (1995) 15-22.

122) P. Lettieri, D. Newton, J.G. Yates, The effect of temperature on the deaeration rate of two silica powders. Comparison with standard correlations for a Group A and a Group C material, in: Proceedings of the 3rd World Congress on Particle Technology, Brighton, UK, 1998, pp. 2239-2250.

123) B. Formisani, R. Girimonte, G. Pataro, The influence of operating temperature on the dense phase properties of bubbling fluidized beds of solids, Powder Technol. 125 (2002) 28-38.

124) R. Girimonte, B. Formisani, The minimum bubbling velocity of fluidized beds operating at high temperature, Powder Technol. 189 (2009) 74-81.

125) D. Geldart, A.R. Abrahamsen, Homogeneous fluidization of fine powders using various gases and pressures, Powder Technol. 19 (1978) 133-136.

126) R. Girimonte, B. Formisani, The effects of thermally induced interparticle forces on the expansion and bubbling behaviour of a fluidized bed, in: F. Berruti, X. Bi, T. Pugsley (Eds.) Proceedings of the 12th International Conference on Fluidization, Engineering Conferences International, Vancouver, Canada, 2007, pp. 177-184.

127) H. Cui, J. Chaouki, Effects of temperature on local two-phase flow structure in bubbling and turbulent fluidized beds of FCC particles, Chem. Eng. Sci. 59 (2004) 3413-3422.

128) R. Girimonte, B. Formisani, Effects of operating temperature on the bubble phase properties in fluidized beds of FCC particles, Powder Technol. 262 (2014) 14-21.

129) A. Esmaeili, C. Guy, J. Chaouki, The effects of liquid phase rheology on the hydrodynamics of a gas-liquid bubble column reactor, Chem. Eng. Sci. 129 (2015) 193-207.

130) A. Esmaeili, C. Guy, J. Chaouki, Local hydrodynamic parameters of bubble column reactors operating with non-newtonian liquids: Experiments and models development, AIChE J. (2015) submitted for publication.

131) D. Geldart, Types of gas fluidization, Powder Technol. 7 (1973) 285-292.

132) D. Kunii, O. Levenspiel, Fluidization Engineering, Butterworth-Heinemann, Boston, 1991.

133) K. Hilligardt, J. Werther, Influence of temperature and properties of solids on the size and growth of bubbles in gas fluidized beds, Chem. Eng. Technol. 10 (1987) 272-280.

134) A. Chehbouni, J. Chaouki, C. Guy, D. Klvana, Effect of temperature on the hydrodynamics of turbulent fluidized beds, in: C. Laguerie, J.F. Large (Eds.) Proceedings of the 8th International Conference on Fluidization, Engineering Foundation, New York, 1995, pp. 149-156.

135) J.G. Findlay, T.M. Knowlton, in: Final Report for U. S. Department of Energy, Project DE-AC21-83MC20314, 1985.

136) N. Ellis, M. Xu, C.J. Lim, S. Cloete, S. Amini, Effect of change in fluidizing gas on riser hydrodynamics and evaluation of scaling laws, Ind. Eng. Chem. Res. 50 (2011) 4697-4706.

137) M.J. Rhodes, X.S. Wang, A.J. Forsyth, K.S. Gan, S. Phadtajaphan, Use of a magnetic fluidized bed in studying Geldart Group B to A transition, Chem. Eng. Sci. 56 (2001) 5429-5436.

138) J. Shabanian, F. Fotovat, J. Bouffard, J. Chaouki, Fluidization behavior in a gas-solid fluidized bed with thermally induced inter-particle forces, in: T.M. Knowlton (Ed.) Proceedings of the 10th International Conference on Circulating Fluidized Beds and Fluidization Technology, Engineering Conferences International, New York, 2011.

139) J. Shabanian, J. Chaouki, Pressure signals in a gas-solid fluidized bed with thermally induced inter-particle forces, in: J.A.M. Kuipers, R.F. Mudde, J.R. van Ommen, N.G. Deen (Eds.) Proceedings of the 14th International Conference on Fluidization – From Fundamentals to Products, ECI Digital Archives, Noordwijkerhout, The Netherlands, 2013.

140) J. Shabanian, J. Chaouki, Local characterization of a gas–solid fluidized bed in the presence of thermally induced interparticle forces, Chem. Eng. Sci. 119 (2014) 261-273.

141) J. Shabanian, J. Chaouki, Hydrodynamics of a gas–solid fluidized bed with thermally induced interparticle forces, Chem. Eng. J. 259 (2015) 135-152.

142) M. J. Gluckman, J. Yerushalmi, A.M. Squires, Defluidization characteristics of sticky materials on agglomerating bed, in: D.L. Keairns (Ed.) Fluidization Technology 1, 1976, pp. 395-422.

143) P. Lettieri, D. Newton, J.G. Yates, High temperature effects on the dense phase properties of gas fluidized beds, Powder Technol. 120 (2001) 34-40.

144) M.J. Espin, J.M. Valverde, M.A.S. Quintanilla, A. Castellanos, Stabilization of gas-fluidized beds of magnetic powders by a cross-flow magnetic field, J. Fluid Mech. 680 (2011) 80-113.

145) J. Shabanian, P. Sauriol, A. Rakib, J. Chaouki, Characterization of gas-solid fluidization at high temperature by analysis of pressure signals, in: Proceedings of the 11th International Conference on Fluidized Bed Technology, Beijing, China, 2014.

146) D. Geldart, N. Harnby, A.C. Wong, Fluidization of cohesive powders, Powder Technol. 37 (1984) 25-37.

147) D. Geldart, A.C.Y. Wong, Fluidization of powders showing degrees of cohesiveness-I. Bed expansion, Chem. Eng. Sci. 39 (1984) 1481-1488.

148) J.A. Agbim, A.W. Nienow, P.N. Rowe, Inter-particle forces that suppress bubbling in gas fluidised beds, Chem. Eng. Sci. 26 (1971) 1293-1294.

149) J.P.K. Seville, R. Clift, The effect of thin liquid layers on fluidisation characteristics, Powder Technol. 37 (1984) 117-129.

150) W.Y. Wu, A. Navada, S.C. Saxena, Hydrodynamic characteristics of a magnetically stabilized air fluidized bed of an admixture of magnetic and non-magnetic particles, Powder Technol. 90 (1997) 39-46.

151) L.J. McLaughlin, M.J. Rhodes, Prediction of fluidized bed behaviour in the presence of liquid bridges, Powder Technol. 114 (2001) 213-223.

152) J. Shabanian, J. Chaouki, Performance of a catalytic gas-solid fluidized bed reactor in the presence of interparticle forces, Int. J. Chem. Reactor Eng. (2015) Published Online: 2015-04-03, DOI: 10.1515/ijcre-2014-0106.

153) J. Shabanian, J. Chaouki, Influence of interparticle forces on solids motion in a bubbling gas-solid fluidized bed, Powder Technol. (2015) submitted for publication.

154) P.N. Rowe, L. Santoro, J.G. Yates, The division of gas between bubble and interstitial phases in fluidised beds of fine powders, Chem. Eng. Sci. 33 (1978) 133-140.

APPENDIX B – PERFORMANCE EVALUATION OF DIFFERENT APPROACHES FOR EARLY DETECTION OF DEFLUIDIZATION

This appendix reports the performance comparison of different approaches proposed in the open literature for the advanced detection of defluidization. The evaluations are made at identical high temperature conditions as reported in Chapter 10.

B.1 Introduction:

Different approaches have been proposed in the open literature for the early detection of defluidization conditions. They differ either in the type of measurement technique adopted or in the signal analysis. The ultimate goal of these approaches is to trigger an alarm in an early stage of agglomeration phenomenon to apply an operational/counteractive measure preventing a forced plant shutdown.

Siegell [1] and Tardos et al. [2, 3] were among the first to report that a sudden decrease in the total bed pressure drop takes place upon defluidization as most of the fluidizing gas pass through the bed in large channels. With this approach the recognition is often too late [4, 5] and the situation is irreversible without a shutdown. Application of local measurement techniques with small detection volume such as capacitance, optical fiber, heat transfer, and triboelectric probes do not bear high industrial interest because a recognition approach based on these instruments requires many measurement points for an industrial gas-solid fluidized bed [6]. In addition, pressure and temperature measurements are only common in industrial fluidized bed applications to provide hydrodynamic insight about the fluidized state of the particles [7].

Since pressure signals when sampled at a high enough frequency contains a lot of information about the fluidization behavior of a gas-solid fluidized bed (i.e., bubble formation, coalescence, eruption, and passage) [8, 9] and there was a lack of understanding about the detailed impact of interparticle forces (IPFs) on the flow dynamics of a bubbling gas-solid fluidized bed, different detection approaches have been based on analyzing the pressure fluctuations recorded from a fluidized bed rather than monitoring the averaged pressure values. The simplest property of the pressure fluctuations, i.e., variance of pressure signals, was exploited by Chirone et al. [10] and

Scala and Chirone [11] for the timely recognition of defluidization conditions. Nevertheless, the standard deviation (or variance) of pressure fluctuations is strongly sensitive to the variation of the superficial gas velocity U_g. Moreover, increasing the level of IPFs in a bubbling gas-solid fluidized bed can result in multiplicity of behaviors affecting the magnitude of standard deviation of pressure signals in different ways [12]. Therefore, this approach cannot be qualified as a reliable approach for the early recognition of agglomeration in industrial installations, where significant fluctuations in the gas supply are normally encountered [13, 14]. Furthermore, van Ommen et al. [15] demonstrated that the spectral analysis of pressure signals is relatively insensitive to small changes in the particle size distribution, thus cannot be adopted as a suitable detection approach, either.

Among approaches employing non-linear time series analysis, the S-statistic test has shown the best performance for the early detection of defluidization in both laboratory and pilot scale fluidized beds [14, 16]. With this monitoring approach, consecutive pressure (evaluation) time series, which are recorded at a high frequency during the operation, are compared with a reference time series that reflects the normal operation [17]. The comparison is made with the help of the S-statistical test introduced by Diks et al. [18] on the reconstructed attractors from the reference and evaluation time series. An attractor is a collection of points that results from projection of successive pressure values from the corresponding time series into an n-dimensional state space [14]. It represents the dynamics of the system in the state space [19]. With the attractor reconstruction, all properties of the original signal in the time domain are preserved with the exception of the standard deviation, thus decreasing the sensitivity of the approach to changes in the superficial gas velocity [13, 14, 16, 17]. The S-value indicates the dimensionless distance between the two attractors [13, 14, 16]. When the reference and evaluation pressure signals exhibit an identical dynamics, S-value has an expectation of zero and a standard deviation of unity. If the S-value is greater than 3, the dynamics of two time series significantly differ from each other with more than 95% confidence according to the null hypothesis [17]. Therefore, in the case of early detection of agglomeration, the S-values greater than 3 are sought. More details about this approach can be obtained elsewhere [17].

Despite its success in the timely recognition of defluidization conditions based on the earlier reports, the S-statistics suffers from a number of drawbacks. They can be listed as: i) it necessitates registering the pressure signals at a high frequency (>100 Hz); ii) the performance of the test is

highly sensitive to the careful selection of its critical parameters including the embedding dimension m, time delay τ (normally equal to 1), band width d, and segment length L. An inappropriate selection of these parameters would either yield the reconstructed attractors to become too smooth, i.e., not showing any difference when there is a significant difference in the bed behavior, or make the test very sensitive resulting S-values greater than 3 for cases with the similar dynamics. Accordingly, all these parameters should be optimized for the available signals under different operating conditions while the outcome might not satisfy all conditions; iii) it requires conducting many complex mathematical computations; iv) as the approach solely compares the similarity of the reference and evaluation signals to mark the point, where a significant change is realized, a fundamental understanding about how the bed behavior has evolved over the course of the agglomeration process can hardly be achieved; v) it suffers from occasional false alarms, particularly when a corrective measure, e.g., reduction in the operating temperature, is applied to a cohesive agglomerating fluidized bed [14]. The sole dependence of the recognition approach on the pressure measurement reduces its applicability under different operating conditions as stressed here for the last drawback.

The temperature measurements achieved by thermocouples provide a local measure of the bed behavior. Although these measurements can provide indirect information about the degree of solids mixing within the bed [20], they need deep insight into the corresponding process to yield a correct interpretation [7]. Therefore, the sole application of either pressure or temperature signals cannot lead to an efficient and robust approach for the opportune detection of defluidization.

Shabanian et al. [5] have recently proposed a novel approach for the timely recognition of defluidization based on the simultaneous applications of temperature and in-bed differential pressure signals. The detection approach was established on the observations made on influence of IPFs on the hydrodynamics of a gas-solid fluidized bed. Upon increasing the level of IPFs, the average in-bed differential pressure drop measured from the well-stabilized section of the dense bed and the quality of solids mixing decrease at a given superficial gas velocity in the bubbling fluidization regime [5]. The latter drift results in a less uniform temperature profile along the axis of a high temperature fluidized bed [5, 21]. Therefore, since the level of IPFs progressively increases in a cohesive bubbling bed approaching the complete defluidization state, the new recognition approach was based on the fact that the average in-bed differential pressure drop and the temperature difference along the axis simultaneously decreases and increase, respectively. This

approach demonstrated a great performance in prediction of the onset of agglomeration minutes to hours before complete defluidization. Two sets of detection thresholds were introduced by Shabanian et al. [22] to trigger the high and high-high alarms of the onset of agglomeration in the case of industrial fluidized bed combustors and gasifiers of low grade solid fuels, where coarse silica sand particles are adopted as the bed materials. According to the proposed criteria, the high alarm is issued when the evaluation average in-bed differential pressure drop $(\overline{\Delta P}_{in-bed})_{eval}$ decreases more than 6% with respect to its reference value $(\overline{\Delta P}_{in-bed})_{ref}$ while the evaluation selected temperature difference along the axis $(\Delta T_{sel})_{eval}$ increases more than 100% from the corresponding reference value $(\Delta T_{sel})_{ref}$. The high-high alarm is issued when $(\overline{\Delta P}_{in-bed})_{eval}/(\overline{\Delta P}_{in-bed})_{ref} \leq 0.90$ and $(\Delta T_{sel})_{eval}/(\Delta T_{sel})_{ref} \geq 3$.

In the following sections we compare the performance of these approaches for the early detection of defluidization as well as their robustness with respect to the changes in U_g (±10%), operating temperature (±100°C), and bed inventory (±20%).

B.2 Experimental:

Details of the experiments have been previously outlined in section 10.4.

Pressure measurements were attempted with the help of two differential and a gauge pressure transducers. One differential pressure transducer (JUMO, 404304/000-414-415-28-298, 0–160 mbar) approximately measured the total bed pressure drop (5–130 cm in height). The second differential pressure transducer (JUMO, 404304/000-414-415-28-298, 0–100 mbar) recorded the differential pressure drop from the central part of the dense bed (15–45 cm above the distributor plate). A gauge pressure transducer (OMEGA, PX309-002G5V, 0–2 Psig) was located at an axial position of 30 cm above the distributor plate within the dense bed to provide a global picture from the bed.

B.3 Results and discussions:

B.3.1 Normal operation during coal and propane combustion

A normal operation of the bed was attained by the combustion of coal and propane. Figure 12.1 illustrates typical measured and calculated monitoring parameters during a sample normal

operation while the superficial gas velocity U_g was kept constant at 1.0 m/s throughout the run. The experimental data during the operation at 900ºC was adopted as the reference data because defluidization and sensitivity tests were conducted at this operating temperature. To be less dependent on the type of fuel being combusted within the bed, either coal or propane, the temperature difference between the readings of thermocouples $T4$ and $T6$ was chosen as the selected temperature difference along the axis, $\Delta T_{sel} = T6 - T4$. A maximum change of 25% can be observed for ΔT_{sel} from Figure 12.1a when comparing this monitoring parameter during the coal combustion at 800ºC (32–95 min) and 1000ºC (265–315 min) to that reference condition at 900ºC (140–200 min). Figure 12.1b shows that the average in-bed differential pressure drop $\overline{\Delta P}_{in-bed}$ underwent a maximum change of 3% when compared to its reference value, i.e., average of $\overline{\Delta P}_{in-bed}$ during the coal combustion at 900ºC. The reduction in the gas density with the operating temperature can explain the slightly reducing trend observed for $\overline{\Delta P}_{in-bed}$. Although the variations observed for ΔT_{sel} and $\overline{\Delta P}_{in-bed}$ in Figure 12.1a and b satisfy the primary condition of the defluidization detection approach proposed by Shabanian et al. [5], no false alarm would have resulted when applying the detection thresholds introduced by Shabanian et al. [22].

Figure 12.1b also illustrates the evolution of the average total bed pressure drop $\overline{\Delta P}_{in-bed}$. This parameter demonstrated very stable behavior with a maximum change of 1% over the span of temperatures tested here (800–1000ºC). The minor decreasing trend can be ascribed to the reduction in the gas density. The variation of the standard deviation of in-bed gauge pressure signals σ_{gp} is presented in Figure 12.1c. Similar to the pressure drop parameters, it decreased with temperature at a maximum change of 15% with respect to the reference condition. According to Shabanian and Chaouki [12] this modification for a bed of coarse particles at elevated temperatures could be a direct consequence of reduction in the bubble size at higher temperatures.

In order to assess the evolution of the S-value based on the gauge pressure signals along the course of the experiment, four critical parameters of the S-statistic test needed to be optimized beforehand. Since it was intended in this study to check if the S-statistic test provides an early warning of the defluidization condition or not, the optimization step was attempted to let the test issue S-values less than 3 for signals generated by the same dynamics, i.e., normal operation, and greater than 3 for signals showing significantly different fluidization behavior, i.e., approaching complete defluidization compared to the normal condition. The value of τ was selected as 1 according to van

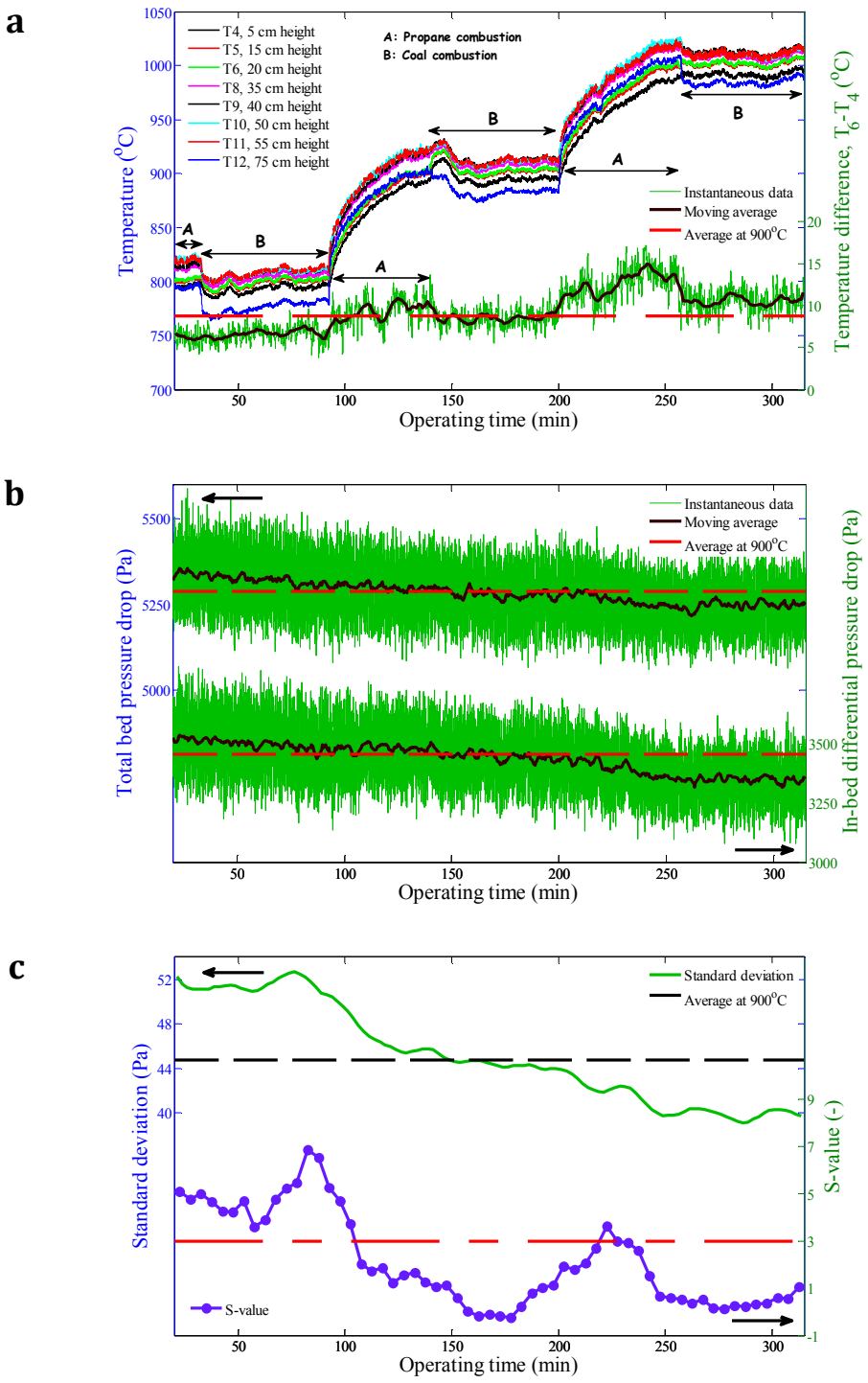

Figure 12.1: a) bed temperature profile and a selected in-bed temperature difference, b) total bed and in-bed differential pressure drops, c) standard deviation of in-bed gauge pressure signals and S-value during a sample normal operation of the bed when combusting coal and propane. Fixed reference data for attractor comparison: 170–175 min.

Ommen et al. [17]. The values of other parameters were varied in the range of 30 to 100 for the embedding dimension, 0.2 to 3 for the band width, and 3 to 6 seconds for the segment length. The best values to relatively satisfy both conditions were achieved as 40, 0.9, and 3 seconds for the embedding dimension, band width, and segment length, respectively. These values were subsequently exploited for calculation of the S-value for different runs in this work. A 5-min long time series of the recorded gauge pressure signals at 900ºC, i.e., between the operating times 170 and 175 min, was selected as the reference set for the assessment of the S-statistic test in this run. A similar 5-min long time window was adopted for the evaluation time series to be successively compared with the reference set during the experiment. Figure 12.1c shows that the S-statistic test had led to values greater than 3 when the bed was adequately fluidized at 800ºC (20–95 min). The test, however, predicted a normal operation after the operating time 105 min, as expected. This observation indicates that the S-statistic test could effectively identify the hydrodynamic changes between the reference (at 900ºC) and evaluation (at 800ºC) sets while they were not originated by agglomeration. This demonstrates a drawback of the test when applied to detect agglomeration in highly dynamic systems. This deficiency could be corrected by modifying the optimized values to have the S-value less than 3 during the normal operation at 800ºC. Nevertheless, the updated set of parameters could yield a reduced performance than those reported in the following sections in the case of timely detection of agglomeration. Therefore, the drawback observed here was tolerated at this step.

B.3.2 Defluidization during propane combustion

The evolutions of the monitoring parameter during a defluidization test for which the defluidization incident took place during the bed heat-up step from 900 to 1000ºC by the in-bed combustion of propane are illustrated in Figure 12.2. The combustion of a solid fuel with a high alkali metal content was previously carried out at 800 and 900ºC for a period of 1-hr at each temperature to increase the level of IPFs within the bed. The reference values for ΔT_{sel}, $\overline{\Delta P}_{tot}$, $\overline{\Delta P}_{in-bed}$, and σ_{gp} were obtained through averaging the corresponding data during the normal operation of the bed in four identical tests, as presented in Figure 12.1, at 900ºC. In order to investigate the effect of dynamic feature of the reference set on the performance of the S-statistic test, the calculations were attempted for two reference sets: i) the same 5-min long time series of gauge pressure signals adopted in Figure 12.1c, which was minimally influenced by the presence of IPFs, and ii) a 5-min

long time series between the operating times 160 and 165 min from the gauge pressure signals recorded in this run being moderately affected by IPFs due to previously combusting the solid fuel at 800°C.

The mean values of ΔT_{sel} and $\overline{\Delta P}_{in-bed}$ during the solid fuel combustion at 900°C (160–210 min) were higher (around 25%) and lower (about 3.5%) than the corresponding reference values. Since other major operational parameters (U_g, operating temperature, and bed inventory) were kept constant, the simultaneous drifts observed for these parameters can be due to the increase in the level of IPFs. This observation indicates that the detection approach proposed by Shabanian et al. [5] can demonstrate a decent sensitivity to the variation in the magnitude of the level of IPFs in the bed. In contrast, $\overline{\Delta P}_{tot}$ during the solid fuel combustion at 900°C remained relatively unchanged (< 0.1% modification) with respect to its reference value. Figure 12.2c exhibits that the values of σ_{gp} were higher than the reference value (25% on average) during the same span of operating times. This variation could be ascribed to the presence of larger bubbles in a bed with a moderate/high degree of IPFs as thoroughly discussed by Shabanian and Chaouki [12]. Figure 12.2c also illustrates that the S-statistic test predicted a normal operation during the solid fuel combustion at 900°C for both reference sets. It reveals that this approach, with the optimized parameters adopted here, was not sensitive enough to detect the hydrodynamic changes resulted from the variation of magnitude of IPFs in the bed achieved in this run.

The monitoring parameters under study had evolved differently during the heating step toward 1000°C (210–240 min) until the complete defluidization state. The ΔT_{sel} and $\overline{\Delta P}_{in-bed}$ increased and decreased progressively during this pass. The variations in these parameters were considerably larger than those observed during the identical heating step under normal conditions (refer to Figure 12.2a and b). These evolutions satisfied the conditions of the high alarm, referred to the defluidization detection thresholds proposed by Shabanian et al. [22], at the operating time of 230 min, i,e., 10 min prior to complete defluidization and those of the high-high alarm [22] at the operating time of 234 min, i.e., 6 min before complete defluidization. These observations show the promising performance of the detection approach introduced by Shabanian et al. [5, 22] even when the defluidization incident took place at an accelerated rate during the combustion of propane.
In Figure 12.2b, $\overline{\Delta P}_{tot}$ demonstrated a minor decreasing trend until complete defluidization at the operating time 240 min, where a sudden decrease was recognized most likely due to the passage

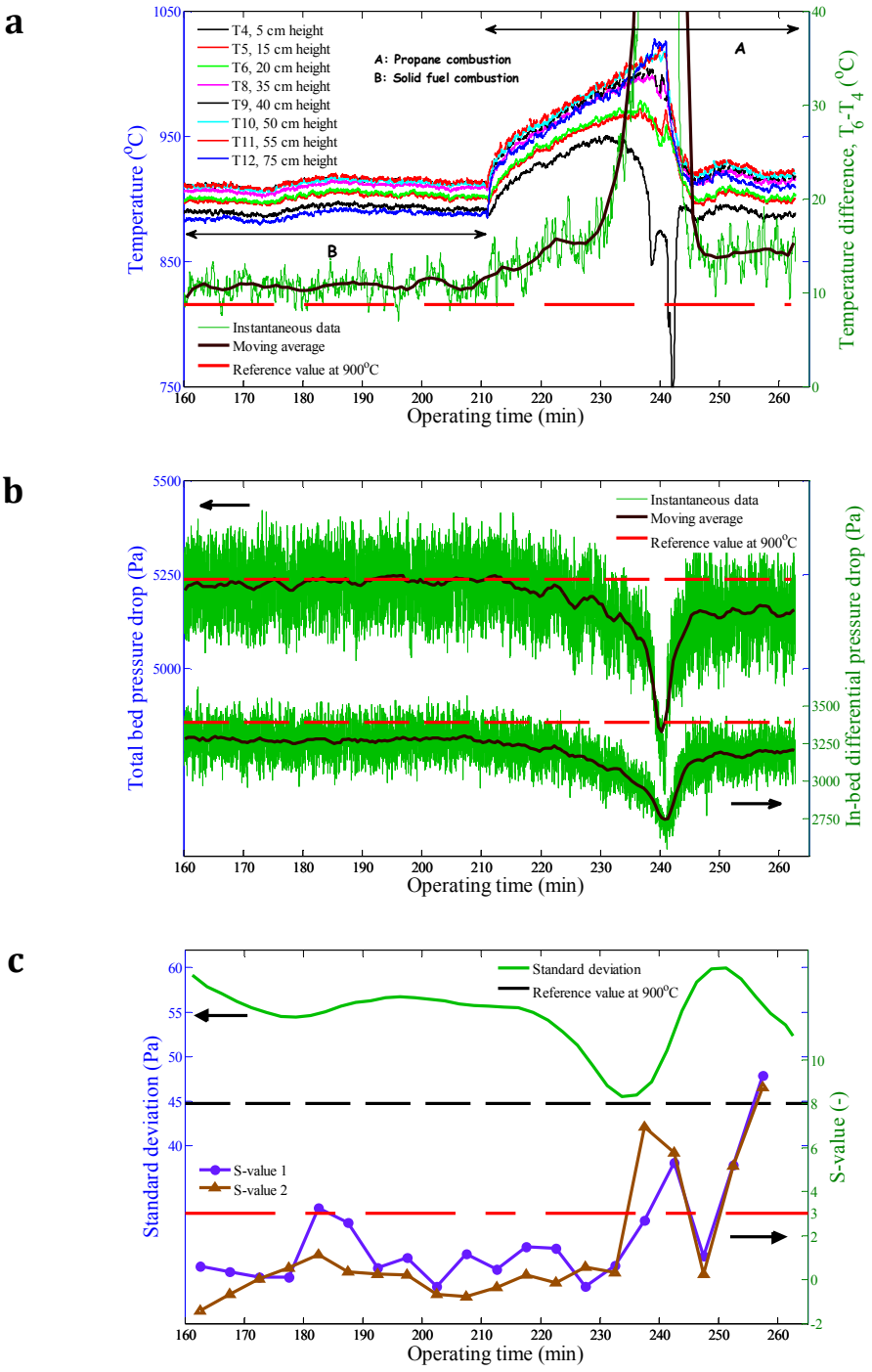

Figure 12.2: a) bed temperature profile and a selected in-bed temperature difference, b) total bed and in-bed differential pressure drops, c) standard deviation of in-bed gauge pressure signals and S-value during a defluidization test achieved when combusting propane. For the *S*-value 1: fixed reference data adopted in Figure 12.1 for attractor comparison. For the *S*-value 2: fixed reference data between 160–165 min of the current test for attractor comparison.

of the fluidizing gas through the bed in channels. The $\overline{\Delta P}_{tot}$ decreased around 1% and less than 3% compared to the reference value at the operating times of 230 and 234 min, respectively. The experimental sample provided here was among those rare samples for which the average total bed pressure drop slowly decreased before the point of complete defluidization. This pressure drop remained comparatively unvaried before the entire defluidization of the bed in most observed defluidization incidents and if altered, as observed here, it tolerated a slight modification. It infers that establishing an early recognition approach on this monitoring parameter will yield a lot of concerns in practice. In other words, it will often lead to a late detection and if otherwise holds true, the magnitude of reduction in this monitoring parameter due to the passage of channel-like oblong bubbles within the bed would be overlapped by the decrease due to the variation of other influential parameters.

The σ_{gp} progressively decreased when approaching the complete defluidization state and returned back to the reference value level at the point of defluidization. Although an increase in the operating temperature could contribute in the reduction of this monitoring parameter, a gradual modification that could occur for the dilute phase behavior of the bed over the course of this evolution looked more influential. It could be presented as a gradual transformation of the dilute phase from a large bubble into a channel-like oblong bubble to reach its final structure in the form of channels. Since σ_{gp} for a bed of coarse particles decreases with temperature, the observation made here suggests that monitoring of this parameter cannot clearly define a time for the onset of agglomeration.

Scanning the variations of S-values during the heating step indicates the S-statistic test was capable of recognizing the occurrence of a significant change in the bed behavior after the operating time 235 min. It is relatively a very late detection. This performance was already anticipated since the attractor comparison approach is not suitable for the detection of a fast agglomeration phenomenon [6]. The nature of this approach, which requires a long pressure time series (in the order of minutes) to be processed [6], explains this feature. Therefore, the application of this approach in similar situations, i.e., rapid defluidization, would let the bed to be completely defluidized without leaving enough time to apply a corrective measure.

Immediately after the defluidization incident, the fluidized bed was retrieved by adjusting the superficial gas velocity at 1.2 m/s and reducing the propane feed rate. The bed temperature was kept constant at 900^{o}C with the help of an enough propane flow after the operating time of 250 min

while U_g was returned back to 1.0 m/s at this operating time. Figure 12.2 illustrates that all monitoring parameters had values considerably different from their corresponding reference values. It shows that the recovered fluidized bed was impacted by the presence of strong IPFs during this span of operating times.

B.3.3 Defluidization during solid fuel combustion

Figure 12.3 exhibits the evolutions of the monitoring parameters during a defluidization test for which the defluidization incident occurred during the solid fuel combustion. A solid fuel with a low alkali metal content was combusted during the first segment of this experiment (90–160 min), which led the fluidized bed to operate under normal conditions. Accordingly, the mean values of ΔT_{sel}, $\overline{\Delta P}_{tot}$, $\overline{\Delta P}_{in-bed}$, and σ_{gp} throughout this step of the experiment were selected as the reference values. A solid fuel with a high alkali metal content was subsequently combusted in the bed to increase the level of IPFs within the bed and in turn result in defluidization conditions within a few hours of operation. The solid fuel combustion had to be stopped intermittently to refill the volumetric solid feeder. The bed temperature was kept constant by burning propane during the refilling. To evaluate the S-statistic test a 5-min long time series of the acquired gauge pressure signals between the operating times 90 and 95 min was selected as the reference set. Similarly, a 5-min long time window was employed for the evaluation sets.

Figure 12.3 shows that although ΔT_{sel} and $\overline{\Delta P}_{in-bed}$ illustrating stable behavior throughout the first segment, they started to depart from the corresponding reference values around the operating time of 200 min, i.e., 35 min into the second segment. The increasing and decreasing trends for ΔT_{sel} and $\overline{\Delta P}_{in-bed}$, respectively, continued up to the entire defluidization of the bed at the operating time of 440 min. The conditions of the high alarm, referred to the defluidization recognition thresholds introduced by Shabanian et al. [22], were satisfied with these evolutions at the operating time of 329 min, i.e., about 2 hrs before complete defluidization. These drifts also fulfilled the conditions of the high-high alarm [22] at the operating time of 380 min, i.e., 1 hr prior to complete defluidization. These observations demonstrate the great efficiency of the detection approach proposed by Shabanian et al. [5], particularly, for the early detection of defluidization during the solid fuel combustion for which the growth rate of agglomeration is generally slow.

The $\overline{\Delta P}_{tot}$ remained nearly constant during the solid fuel combustion before complete defluidization incident. It solely exhibited a minor reduction from its reference value after the

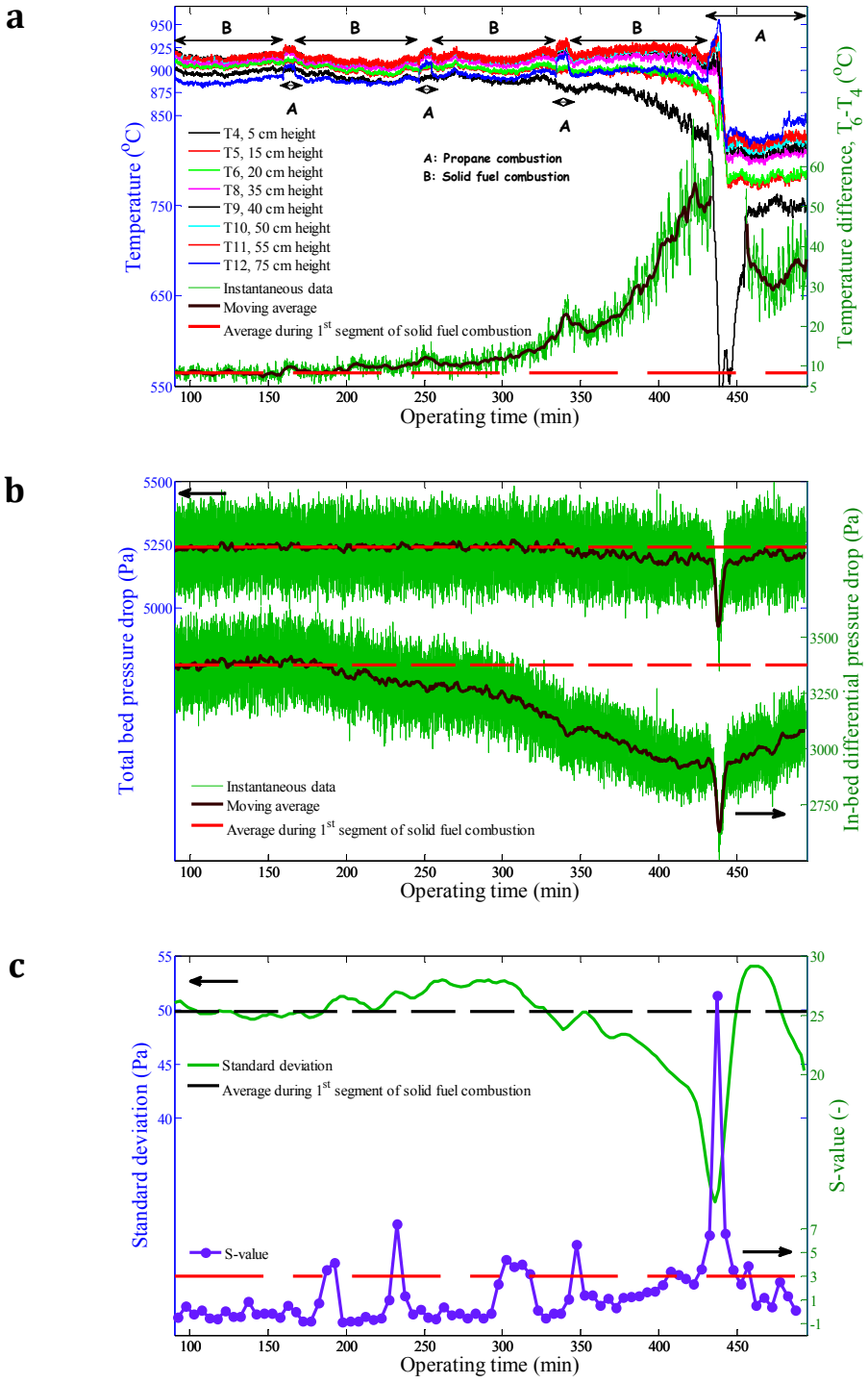

Figure 12.3: a) bed temperature profile and a selected in-bed temperature difference, b) total bed and in-bed differential pressure drops, c) standard deviation of in-bed gauge pressure signals and S-value during a defluidization test achieved when combusting solid fuel. Fixed reference data for attractor comparison: 90–95 min.

operating time of 350 min while the highest change was less than 1.5%. This relatively stable trend persisted until the entire defluidization of the bed, where it underwent a sharp decrease as shown in Figure 12.3b. The late detection drawback of this approach was also valid in this sample experiment confirming its inappropriateness for the timely warning of agglomeration.

The variation of σ_{gp} over the processing time of this experiment is presented in Figure 12.3c. It primarily showed a minute decrease from the reference value (130–185 min), which followed by an inversion trend experiencing higher values than the reference at the operating times between 185 min and 330 min, while ΔT_{sel} and $\overline{\Delta P}_{in-bed}$ showed the accumulating and increasing impact of IPFs. The σ_{gp} subsequently decreased at an accelerating rate until complete defluidization. This eventful evolution is in broad accordance with that observed in Figure 12.2c and the observations made by Shabanian and Chaouki [12]. Upon a slight increase of the level of IPFs in a bed of fresh coarse particles for which the level of IPFs is at minimum, σ_{gp} can slightly decrease at a given U_g in the bubbling fluidization regime [12]. It is due to the presence of slightly smaller bubbles within the bed [12] while the fluidizing gas shows a higher tendency to interstitially pass through the bed as a result of an increase in the emulsion phase voidage and fraction [5, 23]. This modification in the two-phase flow structure of the bed can decrease $\overline{\Delta P}_{in-bed}$. Additional increase in the level of IPFs, reaching to a moderate/high level, increases the resistance of the emulsion phase to any changes on the stability of its structure, thus reduces the rate of bubble splitting since the stalactites of particles can form with a greater difficulty at the bubble's roof [23, 24]. Consequently, larger bubbles with a lower passage frequency can present within the bubbling bed [23, 24]. This can monotonically increase σ_{gp}. However, since the emulsion phase voidage and fraction increase with the magnitude of IPFs [23], $\overline{\Delta P}_{in-bed}$ can show a higher decrease with this evolution. An increase in the bubble size, which occurs along with these modifications in the emulsion phase, can contribute to the further reduction of $\overline{\Delta P}_{in-bed}$.

At a high/very high level of IPFs, approaching complete defluidization, very large/slug-like bubbles would be transferred into channel-like/oblong bubbles since the presence of IPFs at this level between the particles prevents the formation of cake-like structures in the bed to be carried upward with the very large/slug-like bubbles. Particles/agglomerate assembly in the emulsion phase at this state rather tends to undergo a fracture than let the gas to penetrate its structure. The fluidizing gas moving through the bed in the dilute phase under such fluidization state would be

elongated along the fractures leading to the channel-like/oblong bubbles. It is predictable that the dilute phase in this condition has less chance to experience coalescence and breakage. In addition, the resistance of the emulsion phase would be high enough to let it move freely within the bed. Accordingly, the recorded in-bed gauge pressure signals would be minimally influenced by the bubble coalescence and eruption and bed inventory oscillation yielding a reduced magnitude of σ_{gp}. In contrast, the presence of channel-like/oblong bubbles within the bed can speed up the decrease of $\overline{\Delta P}_{in-bed}$ until the complete defluidization point, where all gas would tend to pass through the bed in channels leading to a sharp decrease in the recorded in-bed pressure drop.

A similar eventful evolution of σ_{gp} for a cohesive bed approaching complete defluidization can be recognized by studying the defluidization plots of Chirone et al. [10] and Scala and Chirone [11] for the variance of pressure signals during the progress of agglomeration. An identical qualitative behavior was also obtained for the evolution of σ_{gp} in other defluidization incidents encountered in this work, as observed in Figure 12.3c. Since this monitoring parameter does not vary monotonically with the level of IPFs and is highly influenced by the variation of other operating parameters, it cannot be applied as a reliable approach for the advanced detection of agglomeration.

The performance of the S-statistic test is presented during this sample experiment in Figure 12.3c. Except some occasional alarms, which did not remain persistent, the test was predicting a normal operation throughout the solid fuel combustion until the operating time of 430 min, i.e., 10 min before complete defluidization. It was constantly giving a clear indication of a significant change in the bed behavior after this operating time, which can be considered as a late detection. This approach can potentially provide an earlier detection of agglomeration than the one obtained here if a new set of values for its critical parameters, being particularly optimized for this run, are adopted.

The fluidized bed was recovered after some 30 min from the defluidization incident yet at 800ºC by increasing the mass flow rate of gas entering the bed (U_g=1.20 m/s at 900ºC) immediately after the event. The superficial gas velocity dropped to 1.1 m/s for the same mass flow rate of the fluidizing gas at 800ºC. It was adjusted back to 1.0 m/s at the operating time of 480 min. Figure 12.3 shows that although $\overline{\Delta P_{tot}}$ and S-value were exhibiting relatively normal behavior after the bed recovery, ΔT_{sel} and $\overline{\Delta P}_{in-bed}$ were evidently showing that the bed was influenced by the presence

of strong IPFs, as expected. The σ_{gp} did not illustrate a consistent behavior during and after the recovery trial, which could be mainly attributed to the variations of the superficial gas velocity.

B.3.4 Sensitivity analyses

B.3.4.1 Sensitivity to change in superficial gas velocity and operating temperature

Figure 12.4 illustrates the sensitivities of different defluidization detection approaches to changes in U_g (±10%) and a decrease of 100ºC in the operating temperature. The combustion of coal alone was attempted in a bubbling fluidized bed of coarse silica sand particles to maintain the operating temperature at the desired value. The average values of ΔT_{sel}, $\overline{\Delta P}_{tot}$, $\overline{\Delta P}_{in-bed}$, and σ_{gp} throughout the first step of the coal combustion at 900ºC and U_g=1.0 m/s (125–225 min) were chosen as the reference values. A 5-min long (150–155 min) time series of the in-bed gauge pressure signals registered during the test was chosen as the reference set to evaluate the performance of the S-statistic test. The attractor comparison was attempted for each 5-min long evaluation sets during the run. The coal feed rate was manipulated to decrease the bed temperature from 900 to 800ºC. The mass flow rate of the entering fluidizing air, which resulted in a U_g of 1.0 m/s at 900ºC and 0.9 m/s at 800ºC, was preserved during this step. The superficial velocity was increased to 1 m/s at 800°C (580–615 min) for the last step of this run.

Figure 12.4a and b shows that ΔT_{sel}, $\overline{\Delta P}_{tot}$, and $\overline{\Delta P}_{in-bed}$ were comparatively insensitive to all operating changes imposed on the bed during this test. Integrating the observations made here with those achieved from Figure 12.1a and b indicates that the defluidization detection approach proposed by Shabanian et al. [5, 22] showed a good level of robustness to changes in U_g (±10%) and operating temperature (±100ºC). The total bed pressure drop was also robust to these operational changes.

Figure 12.4c exhibits the evolution of σ_{gp} along the experiment. This monitoring parameter showed a high sensitivity to the variations of U_g and operating temperature, which are undesirable for the advanced detection of agglomeration. The same figure illustrates the sensitivity of the S-statistic test to changes in U_g and the bed temperature. It shows that this monitoring approach with the optimized parameters adopted here was relatively insensitive to the operational changes explored in this run, i.e., the S-values were less than 3 throughout the run.

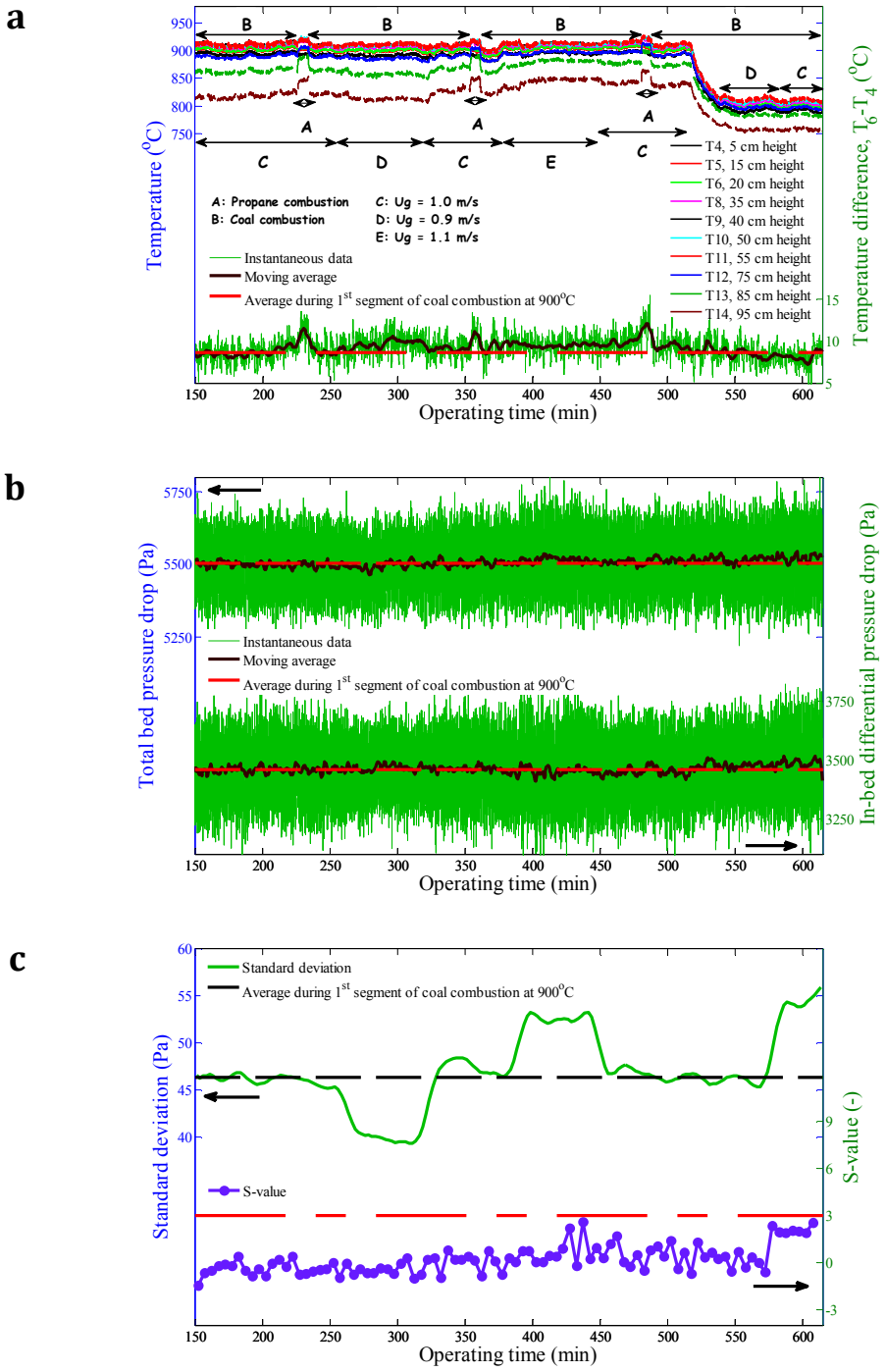

Figure 12.4: a) bed temperature profile and a selected in-bed temperature difference, b) total bed and in-bed differential pressure drops, c) standard deviation of in-bed gauge pressure signals and S-values during coal alone combustion for sensitivity tests: variations in U_g and operating temperature. For the S-value 1: fixed reference data between 125–130 min for attractor comparison. For the S-value 2: fixed reference data between 170–175 min for attractor comparison.

B.3.4.2 Sensitivity to change in bed inventory

The sensitivities of different defluidization detection approaches to changes in the bed inventory was studied when combusting propane in a bubbling fluidized bed of coarse silica sand particles (U_g=1.0 m/s at 900ºC). The reference condition was chosen as the condition during which an effective bed inventory of 25.3 kg was present in the bed (138–158 min). This helped to ascertain that the upper leg of the in-bed differential pressure transducer was well below the splash zone.

The sensitivity of the defluidization detection approach proposed by Shabanian et al. [5] to changes in the bed inventory was thoroughly discussed in section 10.5.5.2. The results presented in Figure 12.5a and b shows that the detection approach based on the simultaneous monitoring of ΔT_{sel} and $\overline{\Delta P}_{in-bed}$ was robust to the variation of 20% in the bed inventory if the conditions of the approach for the spatial positions of critical thermocouples and legs of the in-bed differential pressure transducers are satisfied.

Figure 12.5b and c exhibit that the total bed pressure drop and σ_{gp} were very sensitive to changes in the bed inventory. This is an undesirable feature for these monitoring parameters if adopted for the opportune detection of agglomeration since the bed inventory experiences small variations in industrial fluidized beds that are operated continuously by adding and removing particles [17].

The sensitivity of the S-statistic test applied on the in-bed gauge pressure signals to changes in the bed inventory is presented in Figure 12.5c. It demonstrates that this monitoring approach with the optimized parameters adopted here was relatively insensitive to changes in the bed inventory (up to 30%). It infers that the hydrodynamic features of the bed remained comparatively unchanged when different bed inventories (tested here) presented in the bed. During the three instances when bed inventory was removed, the resulting S-values were greater than 3. This could be due to the gas bypass from the solids removal port of the reactor located at some 30 cm above the distributor plate, resulting in a different dynamic feature in comparison with the reference set. It indicates that the S-statistic test can identify the hydrodynamic changes imposed on the system in addition to the change in particle size distribution resulted from the agglomeration phenomenon.

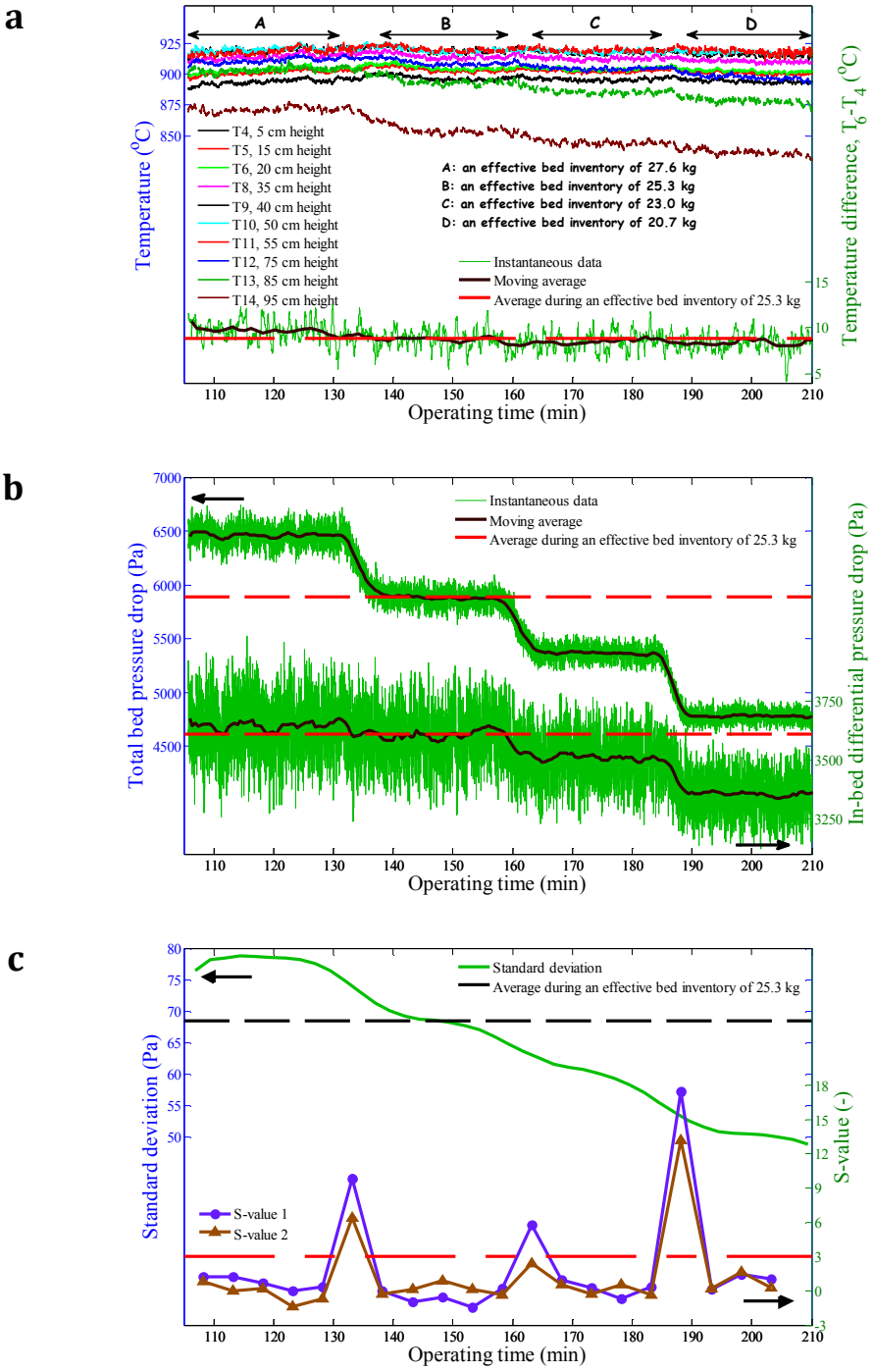

Figure 12.5: a) bed temperature profile and a selected in-bed temperature difference, b) total bed and in-bed differential pressure drops, c) standard deviation of in-bed gauge pressure signals and S-values during propane combustion for sensitivity tests: variation in bed inventory. For the S-value 1: fixed reference data between 150–155 min for attractor comparison. For the S-value 2: fixed reference data between 120–125 min for attractor comparison.

B.4 Conclusion

Comparing the performance of the different defluidization detection approaches reported in the open literature for the advanced recognition of agglomeration indicated that the approach proposed by Shabanian et al. [5], which employs the idea of simultaneous monitoring of temperature and in-bed differential pressured signals, represents an enhanced performance.

B.5 Nomenclature

B.5.1 Acronyms

IPFs	interparticle forces

B.5.2 Symbols

d	band width (-)
L	segment length (sec)
m	embedding dimension (-)
S	dimensionless distance between the two attractors (-)
$T4$	temperature reading of thermocouples No. 4 (°C)
$T6$	temperature reading of thermocouples No. 6 (°C)
U_g	superficial gas velocity (m/s)

B.5.3 Greek letters

$\overline{\Delta P}_{in-bed}$	average in-bed differential pressure drop (Pa)
$(\overline{\Delta P}_{in-bed})_{eval}$	evaluation average in-bed differential pressure drop (Pa)
$(\overline{\Delta P}_{in-bed})_{ref}$	reference average in-bed differential pressure drop (Pa)
$\overline{\Delta P}_{tot}$	average total bed pressure drop (Pa)
ΔT_{sel}	selected temperature difference along the axis (°C)
$(\Delta T_{sel})_{eval}$	evaluation selected temperature difference along the axis (°C)
$(\Delta T_{sel})_{ref}$	reference selected temperature difference along the axis (°C)
σ_{gp}	standard deviation of in-bed gauge pressure signals (Pa)
τ	time delay (-)

B.6 Acknowledgements

The funding of this research by the Total American Services, Inc. and the National Sciences and Engineering Research Council of Canada (NSERC) is gratefully acknowledged. The authors would like to thank Mr. Diego Alejandro López Del Ángel for his contribution to the experimental work. Thanks are also due to Dr. Reza Zarghami, Mr. Mohsen Shiea, and Mr. Hedayat Azizpour for their help with the S-Statistics. The kind hospitality of Prof. Rahmat Sotudeh-Gharebagh to the short stay of Jaber Shabanian at the University of Tehran is acknowledged with gratitude.

B.7 References

1) J.H. Siegell, High-temperature defluidization, Powder Technol. 38 (1984) 13-22.
2) G. Tardos, D. Mazzone, R. Pfeffer, Destabilization of fluidized beds due to agglomeration part I: Theoretical model, Can. J. Chem. Eng. 63 (1985) 377-383.
3) G. Tardos, D. Mazzone, R. Pfeffer, Destabilization of fluidized beds due to agglomeration part II: Experimental verification, Can. J. Chem. Eng. 63 (1985) 384-389.
4) J.C. Schouten, C.M. van den Bleek, Monitoring the quality of fluidization using the short-term predictability of pressure fluctuations, AIChE J. 44 (1998) 48-60.
5) J. Shabanian, P. Sauriol, A. Rakib, J. Chaouki, Application of temperature and pressure signals for early detection of defluidization conditions, Procedia Eng. 102 (2015) 1006-1015.
6) J.R. van Ommen, R.J. de Korte, C.M. van den Bleek, Rapid detection of defluidization using the standard deviation of pressure fluctuations, Chem. Eng. Process. 43 (2004) 1329-1335.
7) J. Werther, Measurement techniques in fluidized beds, Powder Technol. 102 (1999) 15-36.
8) J. van der Schaaf, J.C. Schouten, C.M. van den Bleek, Origin, propagation and attenuation of pressure waves in gas-solid fluidized beds, Powder Technol. 95 (1998) 220-233.
9) J. van der Schaaf, J.C. Schouten, F. Johnsson, C.M. van den Bleek, Non-intrusive determination of bubble and slug length scales in fluidized beds by decomposition of the power spectral density of pressure time series, Int. J. Multiphase Flow 28 (2002) 865-880.
10) R. Chirone, F. Miccio, F. Scala, Mechanism and prediction of bed agglomeration during fluidized bed combustion of a biomass fuel: Effect of the reactor scale, Chem. Eng. J. 123 (2006) 71-80.
11) F. Scala, R. Chirone, Characterization and early detection of bed agglomeration during the fluidized bed combustion of olive husk, Energy Fuels 20 (2006) 120-132.

12) J. Shabanian, J. Chaouki, Fluidization characteristics of a bubbling gas-solid fluidized bed at high temperature in the presence of interparticle forces, Chem. Eng. J. (2015) submitted for publication.

13) R. Korbee, J.R. van Ommen, J. Lensselink, J. Nijenhuis, J.H.A. Kiel, C.M. van den Bleek, Early agglomeration recognition system (EARS), in: Proceedings of the 17th International Fluidized Bed Combustion Conference, Jacksonville, Florida USA, 2003.

14) M. Bartels, J. Nijenhuis, J. Lensselink, M. Siedlecki, W. de Jong, F. Kapteijn, J.R. van Ommen, Detecting and Counteracting Agglomeration in Fluidized Bed Biomass Combustion, Energy Fuels 23 (2009) 157-169.

15) J.R. van Ommen, J.C. Schouten, C.M. van den Bleek, An early-warning method for detecting bed agglomeration in fluidized bed combustors, in: R.B. Reuther (Ed.), Proceedings of the 15thInternational Conference on Fluidized Bed Combustion, ASME: New York, USA, 1999.

16) J. Nijenhuis, R. Korbee, J. Lensselink, J.H.A. Kiel, J.R. van Ommen, A method for agglomeration detection and control in full-scale biomass fired fluidized beds, Chem. Eng. Sci. 62 (2007) 644-654.

17) J.R. van Ommen, M.O. Coppens, C.M. van den Bleek, J.C. Schouten, Early warning of agglomeration in fluidized beds by attractor comparison, AIChE J. 46 (2000) 2183-2197.

18) C. Diks, W.R. van Zwet, F. Takens, J. DeGoede, Detecting differences between delay vector distributions, Phys. Rev. E 53 (1996) 2169-2176.

19) M. Shiea, R. Sotudeh-Gharebagh, H. Azizpour, N. Mostoufi, R. Zarghami, Predicting transition velocities from bubbling to turbulent fluidization by S-statistics on vibration signals, Part. Sci. Technol. 31 (2013) 10-15.

20) M. Bartels, W. Lin, J. Nijenhuis, F. Kapteijn, J.R. van Ommen, Agglomeration in fluidized beds at high temperatures: Mechanisms, detection and prevention, Prog. Energy. Combust. Sci. 34 (2008) 633-666.

21) J. Shabanian, J. Chaouki, Influence of interparticle forces on solids motion in a bubbling gas-solid fluidized bed, Powder Technol. (2015) submitted for publication.

22) J. Shabanian, P. Sauriol, J. Chaouki, A simple and robust approach for early detection of defluidization, Fuel (2015) submitted for publication.

23) J. Shabanian, J. Chaouki, Local characterization of a gas-solid fluidized bed in the presence of thermally induced interparticle forces, Chem. Eng. Sci. 119 (2014) 261-273.

24) J. Shabanian, J. Chaouki, Hydrodynamics of a gas–solid fluidized bed with thermally induced interparticle forces, Chem. Eng. J. 259 (2015) 135-152.